

**A Thesis Submitted for the Degree of PhD at the University of Warwick**

**Permanent WRAP URL:**

<http://wrap.warwick.ac.uk/152561>

**Copyright and reuse:**

This thesis is made available online and is protected by original copyright.

Please scroll down to view the document itself.

Please refer to the repository record for this item for information to help you to cite it.

Our policy information is available from the repository home page.

For more information, please contact the WRAP Team at: [wrap@warwick.ac.uk](mailto:wrap@warwick.ac.uk)

# **In-cell Synchrotron Investigations of Precious-Metal Anticancer Complexes**

A Thesis Submitted for the Degree of Doctor of Philosophy

**Elizabeth May Bolitho BSc (Hons) AMRSC**

Supervisors: Prof. Peter J. Sadler (University of Warwick)

Dr. Paul D. Quinn (Diamond Light Source)



University of Warwick, Department of Chemistry

June 2020

# Table of contents

Acknowledgements	i
Funding	ii
Declaration	ii
Publications	ii
Abstract	iii
Conferences attended	v
Abbreviations	vi
<b>Chapter 1: Introduction</b>	<b>1</b>
<b>1.1 Metal complexes for the treatment of cancer</b>	<b>3</b>
1.1.1 Cancer and the Warburg Effect	3
1.1.2 Metal-based chemotherapy	5
1.1.3 Drug resistance	7
<b>1.2 Development of new metallodrugs</b>	<b>8</b>
1.2.1 Phototherapy: PACT and PDT	8
1.2.2 Half-sandwich anticancer complexes	12
1.2.3 Catalytic metallodrugs	17
<b>1.3 Synchrotron radiation</b>	<b>21</b>
1.3.1 X-Ray Fluorescence (XRF)	22
1.3.2 X-ray Absorption Spectroscopy (XAS)	24
1.3.3 Cryo-X-ray Tomography (cryo-XRT)	26
<b>1.4 Aims of project</b>	<b>28</b>
<b>1.5 References</b>	<b>29</b>
<b>Chapter 2: Materials, methods and instrumentation</b>	<b>39</b>
<b>2.1 Materials</b>	<b>40</b>
2.1.1 Chemical reagents	40
2.1.2 ICP-OES and ICP-MS reagents	41
2.1.3 Synchrotron membranes and grids	41
<b>2.2 Biological materials</b>	<b>42</b>
2.2.1 Human cell lines	42

2.2.2	Biological consumables	42
2.2.3	Biological reagents	43
<b>2.3</b>	<b>Instrumentation at the University of Warwick</b>	<b>44</b>
2.3.1	Mass Spectrometry (MS)	44
2.3.2	Nuclear Magnetic Resonance (NMR)	44
2.3.3	Inductively-Coupled Plasma (ICP) instruments	45
2.3.4	Elemental analysis	46
2.3.5	X-ray crystallography	46
2.3.6	Plunge-freezing and freeze-drying	46
<b>2.4</b>	<b>Biological methods</b>	<b>47</b>
2.4.1	<i>In vitro</i> biological studies	47
2.4.2	ICP-MS acid digestion of cell pellets	49
2.4.3	ICP-MS alkaline digestion of cell pellets	49
<b>2.5</b>	<b>Instrumentation at Diamond Light Source (DLS, Oxford)</b>	<b>50</b>
2.5.1	I14 Beamline	50
2.5.2	B24 Beamline	51
<b>2.6</b>	<b>Synchrotron methods</b>	<b>52</b>
2.6.1	Synchrotron-XRF at the I14 Beamline (DLS, Oxford)	52
2.6.2	Cryo-XRT and cryo-SIM at the B24 Beamline (DLS, Oxford)	56
<b>2.7</b>	<b>Statistical formulae</b>	<b>59</b>
<b>2.8</b>	<b>References</b>	<b>61</b>
 <b>Chapter 3: Catalytic Os<sup>II</sup> arene complexes in cancer cells: ICP-MS and XRF</b>		 <b>63</b>
<b>3.1</b>	<b>Introduction</b>	<b>64</b>
<b>3.2</b>	<b>Experimental</b>	<b>68</b>
3.2.1	Synthesis of BsDPEN ligands	68
3.2.2	Synthesis of Os[( <i>p</i> -cym)BsDPEN] complexes	72
3.2.3	X-ray crystal structures	77
3.2.4	Density functional theory (DFT)	77
3.2.5	Solution stability studies	77
3.2.6	Partition coefficients (Log P)	78
3.2.7	Transfer hydrogenation catalysis	72



3.2.8	Antiproliferative activity (IC <sub>50</sub> )	80
3.2.9	Flow cytometry studies	80
3.2.10	Zebrafish toxicity studies	81
3.2.11	<sup>189</sup> Os ICP-MS cellular accumulation studies	82
3.2.12	<sup>189</sup> Os and <sup>79</sup> Br ICP-MS cellular accumulation studies	83
3.2.13	Synchrotron-XRF	84
3.2.14	Chloroquine inhibition of lysosome activity	84
<b>3.3</b>	<b>Results</b>	<b>86</b>
3.3.1	Synthesis and characterisation	86
3.3.2	Density Functional Theory (DFT)	87
3.3.3	Aqueous stability and solubility	88
3.3.4	Asymmetric Transfer Hydrogenation (ATH) catalysis	90
3.3.5	Antiproliferative activity (IC <sub>50</sub> )	91
3.3.6	In-cell catalysis	92
3.3.7	Flow cytometry studies	94
3.3.8	Zebrafish toxicity studies	96
3.3.9	<sup>189</sup> Os ICP-MS cellular accumulation studies	97
3.3.10	<sup>189</sup> Os and <sup>79</sup> Br ICP-MS cellular accumulation studies	100
3.3.11	<sup>189</sup> Os and <sup>79</sup> Br ICP-MS cellular distribution studies	105
3.3.12	Synchrotron-XRF	106
3.3.13	Chloroquine inhibition of lysosomal activity	116
<b>3.4</b>	<b>Discussion</b>	<b>119</b>
3.4.1	Synthesis of BsDPEN ligands and Os[( <i>p</i> -cym)BsDPEN] complexes	119
3.4.2	X-ray crystal structures and DFT	120
3.4.3	Hydrophobicity studies	121
3.4.4	Asymmetric Transfer Hydrogenation (ATH) catalysis	122
3.4.5	Antiproliferative activity	123
3.4.6	Zebrafish toxicity	131
3.4.7	Combined <sup>189</sup> Os and <sup>79</sup> Br cellular accumulation studies	132
3.4.8	Synchrotron-XRF	141
3.4.9	Chloroquine inhibition of lysosomal activity	150
<b>3.5</b>	<b>Conclusions and future work</b>	<b>151</b>
<b>3.6</b>	<b>References</b>	<b>155</b>

**Chapter 4: Ir<sup>III</sup> photosensitisers in cancer cells: x-ray studies of morphology and elemental mapping** 163

**4.1 Introduction** 164

**4.2 Experimental** 167

4.2.1 Antiproliferative activity (IC<sub>50</sub>) 167

4.2.2 Cryo-XRT at B24 Beamline 168

4.2.3 Synchrotron-XRF at I14 Beamline 170

**4.3 Results** 170

4.3.1 Cryo-XRT of PC3 cells treated with **7** 170

4.3.2 Synchrotron-XRF of A549 cells treated with **8** 177

**4.4 Discussion** 183

4.4.1 Cryo-XRT of PC3 cells treated with **7** 183

4.4.2 Synchrotron-XRF of A549 cells treated with **8** 188

**4.5 Conclusions and future work** 196

**4.6 References** 198

**Chapter 5: X-ray studies of photoactivatable platinum complexes in cancer cells** 205

**5.1 Introduction** 206

**5.2 Experimental** 209

5.2.1 Synthesis of platinum complexes 209

5.2.2 Antiproliferative activity (IC<sub>50</sub>) 209

5.2.3 Cryo-SIM and cryo-XRT 209

5.2.4 Synchrotron-XRF and XANES 212

**5.3 Results** 216

5.3.1 Antiproliferative activity (IC<sub>50</sub>) 216

5.3.2 Cryo-SIM and cryo-XRT 217

5.3.3 Synchrotron-XRF 233

5.3.4 Pt XANES mapping 240

**5.4 Discussion** 243

5.4.1 Cryo-SIM of Pt-treated cancer cells 244

5.4.2 Cryo-XRT of Pt-treated cancer cells 245

5.4.3 Synchrotron-XRF 255

5.4.4 Pt XANES analysis	264
<b>5.5 Conclusions and future work</b>	<b>268</b>
<b>5.6 References</b>	<b>270</b>
<b>Chapter 6: Conclusions and future work</b>	<b>279</b>
<b>6.1 Conclusions</b>	<b>280</b>
<b>6.2 Future work</b>	<b>284</b>
6.2.1 Improving the efficacy of osmium sulfonamide catalysts	284
6.2.2 Targeting of iridium PDT photosensitizers	286
6.2.3 Cellular accumulation, targeting and stability of Ir-Pt	287
6.2.4 Future design of diazido-Pt <sup>IV</sup> complexes	288
6.2.5 Further utilization of synchrotron techniques	291
<b>6.3 References</b>	<b>292</b>
<b>Appendix</b>	<b>296</b>
Tables A1-37	297
Figures A1-23	317
References	329

## Acknowledgements

I would like to thank my supervisors Prof Peter Sadler (University of Warwick) and Dr Paul Quinn (Diamond Light Source) for providing me with this PhD opportunity. I am extremely grateful for the invaluable support and encouragement provided to me, scientifically and otherwise. I have very much enjoyed being part of both the Sadler group and the I14 beamline team.

I would like to thank Dr Carlos Sanchez-Cano for supporting me with synchrotron experiments - from writing proposals, preparing biological samples, running the experiments and analysing the data. I am immensely grateful for all his help throughout my PhD, even if he is grumpy and says I talk too much.

I want to thank Dr James Coverdale for all his help in both chemistry and biology (from synthesis and ICP to *in vitro* assays and endless cell uptake experiments), and for making me work more efficiently. I am extremely grateful for all the help he has offered me. I would also like to thank Dr Hannah Bridgewater for all the help in tissue culture (particularly when I was struggling with the basics), and for attending synchrotron experiments to keep me sane during beamtime.

From the School of Life Sciences I would like to thank Mr Ian Hands-Portman and Dr Saskia Bakker for assistance with plunge-freezing and Mrs Anita Catherwood and Mrs Julie Todd for assistance with freeze-drying. I would also like to thank Mrs Ji Song for training in tissue culture. From the Department of Chemistry I want to thank Dr Lijiang Song for all the help with ICP method optimisation and trusting me not to destroy the instrument. I would also like to acknowledge Dr Huayun Shi for all her hard work involved in the synthesis and *in vitro* analysis of the platinum complexes reported in this thesis.

I would not have been able to achieve as much as I did at both B24 and I14 beamlines without the support of Dr Maria Harkiolaki, Matt Spink, Dr Fernando Cacho-Nerin and Dr Julia Parker from Diamond - for which I am very grateful.

Finally, I would like to thank all of my family and friends for the support over the past few years – particularly to my parents who let me move back in.

## Funding

I would like to thank Diamond Light Source for my PhD studentship, and for funding my attendance to international conferences. I want to acknowledge Warwick Collaborative Postgraduate Research Scholarship (WCPRS), the Engineering and Physical Sciences Research Council (EPSRC) and Cancer Research UK (CRUK) for funding my research. Finally, I would like to thank the Warwick Monash Alliance for funding my research trip to Monash University.

## Declaration

I hereby declare that except where specific reference is made to other sources, the work contained in this thesis is the original work of the author. It has been composed by myself and has not been submitted, in whole or in part, for any other degree, diploma or other qualification

Elizabeth May Bolitho

June 2020

## Publications

1. **E. M. Bolitho**, C. Sanchez-Cano, H. Huang, I. Hands-Portman, P. D. Quinn, M. Harkiolaki, P. J. Sadler, X-ray tomography of cryopreserved human prostate cancer cells: mitochondrial targeting by an organoiridium photosensitiser, *J Biol Inorg Chem*, **2020**, 25(1), 295–303.

## Abstract

Platinum (II) anticancer drugs are used in over 50% of all chemotherapeutic treatments worldwide, however, platinum-resistance is a major clinical concern. Platinum-group complexes are of significant interest in the development of anticancer drugs which overcome such resistance, with improved selectivity for cancer vs. healthy cells, ultimately enhancing the drug efficacy and reducing patient side effects. In this thesis, three families of metal complexes have been investigated: (i) Os<sup>II</sup> half-sandwich complexes for catalytic therapy, (ii) cyclometallated Ir<sup>III</sup> complexes for photodynamic therapy (PDT) and (iii) diazido-Pt<sup>IV</sup> prodrugs for photoactivatable chemotherapy (PACT). Determination of the chemical speciation of such complexes in cancer cells is essential for understanding the antiproliferative mechanisms of action. Herein, the speciation, distribution and stability of such complexes in cancer cells have been probed using Inductively-Coupled Plasma Mass Spectrometry (ICP-MS), synchrotron X-ray Fluorescence (XRF), Differential Phase Contrast (DPC) imaging and synchrotron X-ray Absorption Near Edge Structure (XANES) spectroscopy. Complementary to this, cryogenic fluorescence microscopy, Structured Illumination Microscopy (SIM) and synchrotron soft X-ray Tomography (XRT) have been used to investigate the 3D drug distribution and morphological changes in cancer cells down to a subcellular resolution (40 nm).

Os<sup>II</sup> half-sandwich complexes of the general formula Os<sup>II</sup>[( $\eta^6$ -*p*-cymene)(BsDPEN)] (where BsDPEN=benzylidiphenylethylene diamine) show promise as catalysts for transfer hydrogenation in cancer cells. In this thesis a total of six (1*S*, 2*S*) or (1*R*, 2*R*)-(R)BsDPEN ligands and their corresponding Os<sup>II</sup>[( $\eta^6$ -*p*-cymene)((R)BsDPEN)] complexes have been synthesized and characterized (where R=Br, I, OCH<sub>3</sub>). These complexes exhibited moderate antiproliferative potencies (IC<sub>50</sub>~20-30  $\mu$ M) against four human cancer cell lines. A 16-electron Br-labelled complex (Os<sup>II</sup>[( $\eta^6$ -*p*-cymene)(*p*-Br)BsDPEN]) showed similar chemical properties (x-ray crystal structure, DFT, LogP, solution stability and transfer hydrogenation catalytic activity) to that of parent compound Os<sup>II</sup>[( $\eta^6$ -*p*-cymene)((CH<sub>3</sub>)BsDPEN)]. The Br-probe did not significantly alter the *in vitro* activity, or *in-cell* catalytic activity, thus, was a suitable analogue to probe the intracellular stability and distribution these complexes by ICP-MS (<sup>189</sup>Os; <sup>79</sup>Br) and synchrotron-XRF (Os L<sub>3</sub>M<sub>5</sub>=8.91 keV; Br KL<sub>3</sub>=11.92 keV). The Os and the Br-labelled sulfonamide

ligand strongly co-localised in the cytoplasm. ICP-MS and synchrotron-XRF revealed significantly higher levels of the Br-labelled sulfonamide ligand compared to the Os, implying intracellular degradation. Surprisingly, the Br-labelled sulfonamide ligand was distributed in cell nuclei, whereas Os was not, but it is not yet known whether this contributes to the anticancer activity. Synchrotron-XRF also revealed the co-localisation of Os with the Br-labelled ligand in lysosomes.

Cyclometallated luminescent Ir<sup>III</sup> complexes show promise as photosensitizers for PDT. Potent complex [Ir<sup>III</sup>(C,N)<sub>2</sub>(O,O)] (where C, N=2-phenylpyridine and O,O=diketonate) can generate toxic singlet oxygen (<sup>1</sup>O<sub>2</sub>) and was investigated by cryo-XRT, revealing significant 3D mitochondrial damage in cancer cells treated with this photosensitiser, likely caused by the selective generation of <sup>1</sup>O<sub>2</sub> in close proximity to mitochondria. Additionally, the stability and localisation of a potent photodynamic-photochemotherapeutic Ir<sup>III</sup>-Pt<sup>IV</sup> conjugate under dark conditions was investigated in cancer cells using synchrotron-XRF. This revealed significantly higher levels of Pt vs. Ir, suggestive of in-cell complex cleavage. Pt was distributed homogeneously in cells, whereas Ir localised in organelle-like cytoplasmic regions, providing evidence for a multi-targeting mechanism of action.

The antiproliferative mechanism of action of a potent coumarin-labelled diazido-Pt<sup>IV</sup> prodrug *trans, trans, trans*-[Pt<sup>IV</sup>(OH)(coumarin)(N<sub>2</sub>)<sub>2</sub>(pyridine)<sub>2</sub>] was investigated using cryo-SIM and cryo-XRT. Cryo-XRT revealed the presence of endosomes in treated cells exposed to dark conditions, suggesting that active processes may be involved in the efflux of Pt<sup>IV</sup> prodrugs prior to light activation. Upon irradiation, cells treated with this diazido-Pt<sup>IV</sup> prodrug caused severe cellular damage, including vacuolisation, membrane-blebbing, vesicle-shedding and increased cell granularity. Synchrotron-XRF demonstrated the targeting of cell nuclei by diazido-Pt<sup>IV</sup> prodrugs, in addition to the increased Pt accumulation upon blue light irradiation. XANES studies suggest the presence of predominantly Pt<sup>IV</sup> vs. Pt<sup>II</sup> in treated cancer cells exposed to blue light.

This thesis has utilized a variety of advanced synchrotron imaging techniques to probe the intracellular distribution, speciation and cell damage induced by Os, Ir and Pt complexes in cancer cells in their near-native state, demonstrating how new biological imaging techniques can be exploited in metals in medicine.

## Conferences and courses attended

1. Postgraduate symposium 2020 – University of Warwick (**Oral, May 2020**)
2. Collaborative Computational Project: Electron cryo-Microscopy (CCP-EM) Spring Symposium 2020 - Diamond Light Source (**Oral, April 2020**)
3. Raman and InfraRed spectroscopy of osmium compounds in cancer cells – Research Trip working with Prof Bayden Wood at Monash University, Melbourne -funded by Warwick-Monash Alliance (**March 2020**)
4. Avizo Visualization of X-ray CT Applications – University of Manchester / Thermo Fisher Scientific (**February 2020**)
5. JPAG Pharmaceutical Analysis Research Awards and Careers Symposium 2019 – Royal Society of Chemistry, London (**Oral, poster winner, November 2019**)
6. International Conference on Biological Inorganic Chemistry, ICBIC-19 – Interlaken, Switzerland (**Poster, August 2019**)
7. Postgraduate symposium 2019 – University of Warwick (**Poster, runner-up for best poster, May 2019**)
8. Emerging Analytical Professionals – Analytical Science Network, Leeds (**Poster and flash presentation, May 2019**)
9. ESRF User Meeting 2019 – European Synchrotron Radiation Facility, Grenoble (**Poster and flash presentation, February 2019**)
10. Synchrotron Radiation School – University of Oxford and Diamond Light Source, UK (**September 2018**)
11. European Conference of Biological Inorganic Chemistry, ICBIC – University of Birmingham (**Poster, August 2018**)
12. Biologics Analytical Phenomenex Meeting – London (**July 2018**)
13. Synchrotron Radiation (SR50) Conference – University of Liverpool (**June 2018**)
14. Postgraduate symposium 2018 – University of Warwick (**May 2018**)
15. Dalton Conference 2018 – University of Warwick (**April 2018**)
16. Metals, Peptides and Proteins in Disease and Therapy – Indian Institute of Technology, Kanpur (**Conference organizer/secretary, November 2017**)



## Abbreviations

ATH	Asymmetric Transfer Hydrogenation
ATP	Adenosine triphosphate
ALS	Advanced Light Source
APS	Advanced Photon Source
AuNP	Gold nanoparticles
Azpy	Phenylazopyridine ligand
AXO	Applied X-ray Optics
B24	Soft x-ray tomography beamline
BINAP	(2,2'-bis(diphenylphosphino)-1,1'-binaphthyl)
BsDPEN	Benzylsulfonyldiphenylethylene diamine
CCD	Charge-coupled device
CDDP	Cisplatin
Cryo-XRT	Cryo X-Ray Tomography
Cryo-SIM	Cryo Structured Illumination Microscopy
CTR 1	Copper transporter 1
DCM	Dichloromethane
DFT	Density Functional Theory
DLS	Diamond Light Source
DMEM	Dulbecco's Modified Eagle's Medium
DMSO	Dimethylsulfoxide
DPC	Differential phase contrast
DPEN	Diphenylethylene diamine
ER	Endoplasmic reticulum
ESI-MS	Electrospray ionisation mass spectrometry
ESRF	European Synchrotron Radiation Facility
EXAFS	Extended X-ray Absorption Fine Structure
FCS	Fetal calf serum
FWHM	Full Width at Half Maximum
GC	Gas Chromatography
GC-FID	Gas Chromatography Flame Ionisation Detector
GFP	Green Fluorescent Protein

GSH	Glutathione
HBSS	Hank's Balanced Salt Solution
HR-MS	High Resolution Mass Spectrometry
I14	Hard nano-probe synchrotron beamline
IC <sub>50</sub>	Half maximal inhibitory concentration
ICP-OES	Inductively-Coupled Plasma Optical Emission Spectroscopy
ICP-MS	Inductively-Coupled Plasma Mass Spectrometry
LC <sub>50</sub>	Half maximal lethal concentration
LogP	Octanol-water partition coefficient
MCF-7	Human breast adenocarcinoma
MRC-5	Human lung fibroblasts (primary non-cancerous)
MS	Mass Spectrometry
MTT	3-(4,5-Dimethylthiazol-2-yl)-2,5-diphenyltetrazolium bromide
<i>m/v</i>	Mass / volume (percentage solution)
<i>m/z</i>	Mass-to-charge ratio
NA	Numerical Aperture
NAD <sup>+</sup>	Nicotine adenine dinucleotide (oxidized)
NADH	Nicotine adenine dinucleotide (reduced)
NanoSIMS	Nano-Secondary Ion Mass Spectrometry
NMR	Nuclear Magnetic Eesonance
PACT	Photoactivatable chemotherapy
PBS	Phosphate-Buffered Saline
PC3	Human prostate adenocarcinoma
<i>p</i> -cym	<i>Para</i> -cymene
PDT	Photodynamic therapy
PGP	P-glycoprotein
PI	Propidium iodide
PPB	Parts per billion
PPM	Parts per million
PyMCA	Python Multi-Channel Analyser
ROS	Reactive Oxygen Species
RPMI-1640	Roswell Park Memorial Institute-1640
Si <sub>3</sub> N <sub>4</sub>	Silicon nitride

SIRT	Simultaneous Iterative Reconstructive Technique
SRB	Sulforhodamine B
SuRVoS	Super Resolution Volume Segmentation
TCA	Trichloroacetic acid
TEM	Transmission Electron Microscopy
TFA	Trifluoroacetic acid
TMAH	Tetramethylammonium hydroxide
TMS	Tetramethylsilane
TOF	Turnover frequency
TON	Turnover number
TsDPEN	Tosyldiphenylethylene diamine
UVA	Ultraviolet A
UV-Vis	Ultraviolet-Visible Spectroscopy
$v/v$	Volume / volume (percentage solution)
WBP	Weighted Back Projection
XANES	X-ray absorption spectroscopy
XAS	X-ray absorption near edge structure
XRD	X-ray Diffraction
XRF	X-ray fluorescence
YFP	Yellow fluorescent protein

# **Chapter 1**

## **Introduction**

## Chapter 1: Introduction

The thesis reports the use of cutting-edge synchrotron-based techniques to investigate the speciation, distribution and targeting of three different families of precious metal anticancer complexes: (i)  $[\text{Os}^{\text{II}}(\eta\text{-arene})(\text{diamine})]$  catalysts; (ii) cyclometallated  $\text{Ir}^{\text{III}}$  photosensitisers for photodynamic therapy (PDT); (iii) diazido- $\text{Pt}^{\text{IV}}$  prodrugs for photoactivatable chemotherapy (PACT).

In particular, synchrotron-X-Ray Florescence (XRF), Differential Phase Contrast (DPC) Imaging and X-ray Absorption Near Edge Structure (XANES) spectroscopy techniques are used to probe intracellular drug stability, distribution and speciation by mapping readily detectable exogenous elements (Os, Ir, Pt and Br). Contrastingly, correlative cryo-Structured Illumination Microscopy (cryo-SIM) and cryo-soft-X-Ray Tomography (cryo-XRT) are used to gain both insights into the localisation of fluorescent metallodrugs and drug-induced subcellular morphological changes as close to physiological state as possible.

Platinum-based drugs are the most widely used in cancer treatment, but are limited by poor selectivity and resistance, which ultimately reduces drug efficacy and causes severe patient side effects. There is much potential in the design of metallodrugs which can circumvent platinum-resistance, however, design depends on the understanding of structure-activity relationships: role of the metal, the oxidation state, the coordination geometry, and the number and type of ligands. An understanding of drug speciation in biological media is crucial for elucidating the mechanisms of activation and in-cell antiproliferative activity for clinical translation. Determination of the chemical speciation of metallodrugs is challenging, but can be probed using complementary analytical techniques such as confocal microscopy imaging, mass spectrometry proteomics, Nano-Secondary Ion Mass Spectrometry (Nano-SIMS), Inductively-Coupled Plasma Mass Spectrometry (ICP-MS), Laser-Ablation ICP-MS, synchrotron-XRF and XANES spectroscopy.<sup>1-3</sup>

## **1.1 Metal complexes for the treatment of cancer**

### **1.1.1 Cancer and the Warburg Effect**

Cancer is a major global issue, and statistics from 2018 show that 1 in 2 people in the UK will develop cancer at some point in their lifetime,<sup>4</sup> which puts increasing pressure on the development of new anticancer treatments which combat resistance and reduce off-target effects. Cancer is a generic term which describes the uncontrollable outgrowth or division of a clonal population of cells.<sup>5</sup> In 2001, Weinberg and Hanahan postulated the six main hallmarks of cancer: evasion of apoptosis, sustaining antiproliferative signals, self-sufficient growth, sustained angiogenesis, tissue invasion and metastasis and limitless replication potential which are widely accepted worldwide.<sup>6</sup> Genomic mutations of non-reproductive cells can cause uncontrollable multiplication, eventually producing a malignant cancer. The complication of the design of new treatments to eradicate these malignant tumours stems down to our understanding of the human genome - the sequence of nucleobases encoded into nuclear DNA which encloses our genetic information. If mutations of these nucleobases occur, then they will generate mutated proteins, preventing normal cell function, allowing the cell to become cancerous.<sup>7</sup>

Healthy human cells have a variety of coping mechanisms in response to disruptions or alterations to cell growth through the regulation of growth suppressor factors.<sup>8</sup> Cancer cells inactivate these growth suppressor genes, perturbing the cell homeostasis, ultimately leading to uncontrolled cell growth and division.<sup>9</sup> As a result, premalignant healthy cells try other means of 'cell suicide' to counteract this, for example, the modification of metabolism or programmed-cell death. Cancers evolve and adapt to survive and proliferate under extreme conditions.<sup>10</sup>

Cancer cells have dysfunctional mitochondria compared to healthy cells:<sup>11</sup> one of the hallmarks of cancer. Mitochondria are rod-shaped organelles inside cells where energy (ATP) is generated in the electron-transport chain (ETC), located in the mitochondrial membrane. The ETC is the site of oxidative phosphorylation, a process in which nutrients are oxidised by oxygen to release energy – which plays an essential role in

cellular and tissue metabolism.<sup>12</sup> Non-cancerous cells cannot survive under aerobic conditions, whereas the altered metabolism in cancers permits growth and survival.

Typical features of altered cell metabolism in cancer cells include enhanced glucose uptake and the increased production of lactate *via* glycolysis.<sup>13</sup> Cancer cells increase their availability of energy sources to promote cell growth and survival under hypoxic conditions, primarily utilising aerobic glycolysis to facilitate the uptake and incorporation into biomass (*i.e.* nucleotides, amino acids and lipids) to promote cell growth and survival.<sup>14</sup> They achieve this by increasing the rate at which glucose is taken into the cell – as defined by The Warburg Effect (**Fig. 1.1**). The Warburg Effect describes the phenomenon when cancer cells preferentially rely on aerobic glycolysis to generate energy under hypoxic conditions (as opposed to oxidation to form CO<sub>2</sub>).<sup>14</sup> The distinct differences in redox homeostasis, dysfunctional mitochondrial and cell metabolism between cancer and healthy cells provides the opportunity to develop selective anticancer drugs through the generation of reactive oxygen species (ROS).<sup>15</sup>

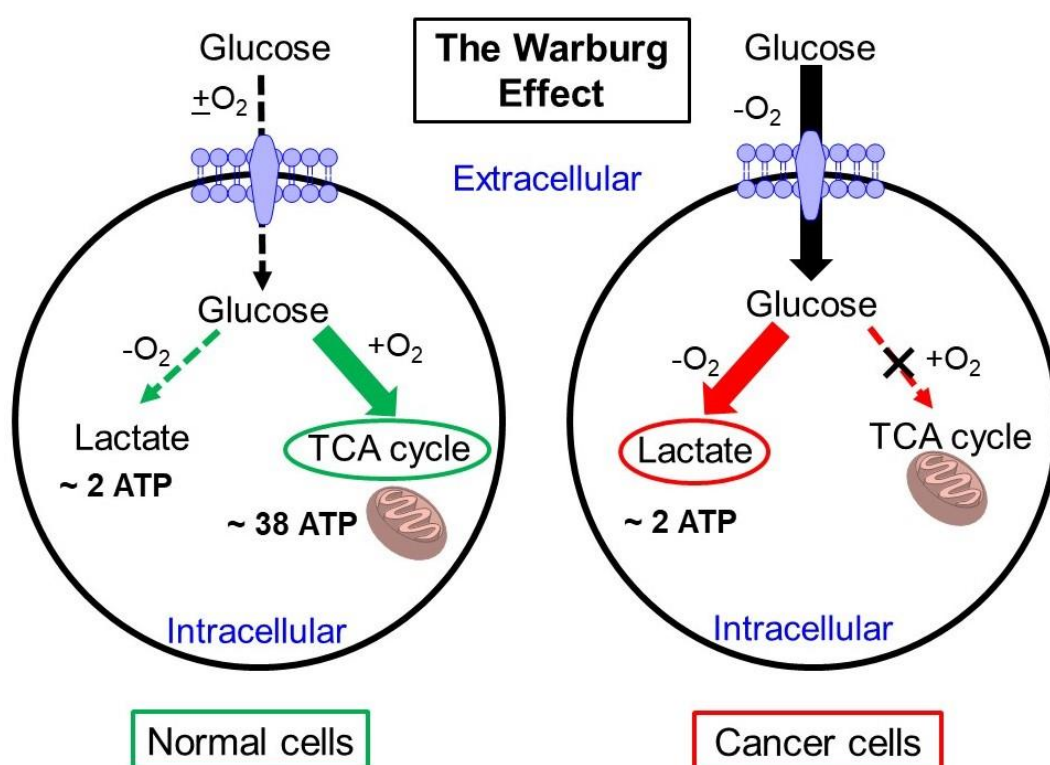


**Figure 1.1.** Schematic depiction of the aerobic glycolysis pathway predominant in cancer cells in the presence or absence of oxygen owing to the Warburg Effect.

### 1.1.2 Metal-based chemotherapy

#### Chemotherapy

Chemotherapy is a treatment in which chemical compounds (drugs) are administered in an attempt to eradicate cancer cells by targeting the proliferation potential and metastasising ability of tumour cells,<sup>16</sup> and has been used to treat cancer for over 70 years. This method has shown to kill cancer cells and is commonly used in combination with other treatments such as surgery or radiotherapy. Interestingly, changes in levels of reactive oxygen species (ROS) and oxidative ‘damage products’ can be accelerated by both chemotherapy and radiotherapy,<sup>17</sup> highlighting the potential advantages of combinational therapies. The overtreatment of cancers by current chemotherapeutics can lead to the development of both intrinsic and acquired multidrug resistance: a major clinical concern.

#### Metal-based chemotherapeutics

Over the years, transition metal complexes have been of increasing interest in medicine, showing promise for the design of viable scaffolds for therapeutic agents in cancer treatment.<sup>18</sup> In particular, platinum-based drugs are used in approximately 50% of chemotherapeutic cancer treatments.<sup>19</sup> However, drug-resistance and poor selectivity of current platinum drugs is becoming increasingly problematic, warranting the development of new anticancer treatments.

In 1978, cisplatin was the first FDA-approved platinum-based anticancer drug for the treatment of testicular and bladder cancers,<sup>20</sup> however (due to poor target selectivity) cisplatin causes severe side effects, including nephrotoxicity - which can lead to long-term kidney problems.<sup>20</sup> This led to the development of other platinum drugs (**Fig. 1.2**), firstly carboplatin (approved in 1989, which reduced nephrotoxicity)<sup>21</sup> and oxaliplatin (approved in 2002, a third-generation platinum drug which showed anticancer activity in cisplatin resistant cells lines).<sup>22</sup>



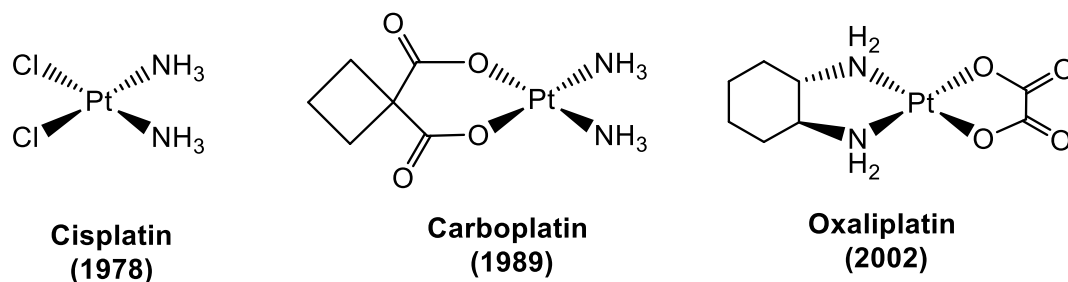


**Figure 1.2.** Structures of clinically-used platinum drugs: cisplatin, carboplatin and oxaliplatin.

The generally accepted mechanism of cisplatin exploits the  $2^+$  oxidation state of platinum.<sup>23</sup> Cisplatin is a square-planar Pt(II) prodrug which is intracellularly hydrolysed to form an activated Pt(II)-aqua species.<sup>24</sup> This species interacts with the N7 nitrogen of guanine (and adenine) of DNA, located in cell nuclei.<sup>24</sup> As a result of two available coordination sites on platinum, both *intra*-strand and *inter*-strand crosslinking occurs,<sup>24</sup> allowing high mobility group (HMG) proteins to insert bulky phenyl groups in the newly-formed gaps. This in turn ‘kinks’ the DNA backbone, preventing the cancer cell from repairing its DNA.<sup>24</sup> Furthermore, these Pt-based drugs induce apoptosis (programmed cell death) through S and G<sub>2</sub>/M phase cell cycle arrest,<sup>25</sup> by preventing DNA replication.

Interestingly, the mechanism of action of oxaliplatin does *not* involve DNA-induced cell damage (despite the structural similarities to cisplatin and carboplatin), but instead induces ribosomal biogenesis stress,<sup>26</sup> highlighting the role of ligand diversity between these mainstay chemotherapeutics. Recent studies have also shown that cisplatin can induce apoptosis by disrupting signalling pathways including calcium signalling, cell death receptor signalling and the activation of mitochondrial pathways.<sup>27</sup> This is somewhat over-looked in platinum-drug research, whereby DNA is considered to be the predominant cellular target of cisplatin, in spite of only 1% of intracellular drug reaching the cell nucleus and interacting with DNA.<sup>28</sup>

### 1.1.3 Drug-resistance

#### Platinum drug resistance

For many cancers, there is growing resistance to chemotherapy – termed multi-drug resistance (MDR). For example, chemotherapy is used to treat early-stage lung cancer, however, as a result of chemotherapeutic resistance, it is ineffective against the treatment of advanced-stage lung cancer.<sup>29</sup> Drug-resistance depends on the type of cancer and the individual patient variability, but mainly on the drug itself, highlighting the need for consideration of patient-specific treatments in the future development of chemotherapeutics. Growing resistance to these administered drugs may reduce patient survival rates, leading to increases in mortality. Additionally, the drugs used in current chemotherapy treatments are not selective for cancer cells, resulting in toxicity (towards non-cancerous cells) making the patient ill with unwanted (and often severe) side effects.<sup>30</sup>

Resistance can be categorized as intrinsic or acquired, both of which have a significant effect on the efficiency of current anticancer treatments, and are considered to be the main reasons for chemotherapy failure. Intrinsic resistance is pre-existent: for example, when cancers do not respond to a drug despite no prior treatment to the drug (*i.e.* as a result of a failing anti-tumour cellular immune response either locally or systematically).<sup>31</sup> In contrast, acquired resistance is drug-induced and can result from specific mutations of cancer cells upon repeated exposure to a drug.<sup>32</sup> For the case of cisplatin, major contributors to resistance are the reduced cellular drug influx and enhanced efflux,<sup>33</sup> DNA repair mechanisms,<sup>34</sup> and over-expressed cellular reducing agents (*i.e.* glutathione and L-ascorbic acid) - which can detoxify drugs in cancer cells.<sup>35</sup> Both intrinsic and acquired platinum resistance are leading causes for the increasing failure of platinum-based cancer chemotherapy, hence, new approaches to drug design are essential to circumvent this. Over the years there has been extensive research into designing new platinum anticancer drugs with alternative cellular targets and mechanisms of action, with the aim of overcoming cisplatin resistance.

## 1.2 Development of new metallodrugs

### 1.2.1 Phototherapy: PDT and PACT

#### Photodynamic therapy (PDT)

Photodynamic therapy (PDT) is a non-invasive, clinically-approved therapeutic technique which exerts cytotoxic activity upon activation of a photosensitiser in the presence of oxygen.<sup>36</sup> Metal based-photosensitizers can display selectivity towards cancer cells over healthy cells through selective tissue irradiation,<sup>37</sup> and are most relevant for the treatment of surface-cancers (*e.g.* skin or prostate cancers) which are accessible to visible light (~mm penetration depth).<sup>38</sup> In general, PDT works by stress response to mitochondrial damage and caspase-dependent apoptosome formation, usually through the generation of toxic singlet oxygen ( $^1\text{O}_2$ )—resulting in cell death.<sup>39</sup>

Metal photosensitisers show advantages over organic photosensitisers as they promote rapid intersystem crossing (due to spin-orbit coupling) and have long excited state lifetimes. Notably, two transition metal photosensitisers are TOOKAD (palladium-based photosensitiser clinically-approved for the treatment of prostate cancer) and TLD-1433 (a cyclometallated Ru(II) photosensitisers in clinical trials for the treatment of bladder cancer).<sup>37</sup>

Cyclometallated luminescent organo-iridium(III) complexes have shown promise as photosensitisers for cancer treatment through the perturbation of intracellular redox balance *via* the generation of toxic singlet oxygen ( $^1\text{O}_2$ ).<sup>40</sup> Mao *et. al.* reported a series of phosphorescent cyclometallated iridium(III) complexes containing 5-membered heterocyclic ligands which can act as both PACT and PDT agents by increasing levels of intracellular ROS and limiting the ATP energy supply.<sup>41</sup> Due to the limited tissue penetration depths of visible light, complexes with extended structures which can be activated with near-IR light are of significant interest. For example, Bryant *et. al.* demonstrated cyclometallated Ir<sup>III</sup> photosensitisers with extended aromatic structures which could be activated with near-IR two-photon light ( $\lambda=760\text{ nm}$ ).<sup>42</sup> However, two-photon photosensitisers reported previously have shown to have low PDT efficiency and usually require large cross sections,<sup>43</sup> which likely hinders their clinical use.

Cyclometallated Ir<sup>III</sup> photosensitisers have been reported to target organelles including mitochondria, lysosomes and endoplasmic reticula,<sup>44</sup> providing an alternative mechanism to that of cisplatin. Although cyclometallated Ir<sup>III</sup> complexes are largely considered to be organelle-targeting, nuclear-specific complexes have also been reported through ROS-mediated DNA damage,<sup>45</sup> highlighting the variety of cellular targets of this family of photosensitisers. In 2017, Sadler *et. al.* reported a series of cyclometallated luminescent Ir<sup>III</sup> complexes which displayed potent antiproliferative activity by inducing specific oxidative attack on proteins upon irradiation with blue light (**Fig. 1.5**).<sup>46</sup> In particular, [Ir(C,N)<sub>2</sub>(S,S)] (where C, N=2-phenylpyridine and S,S=dithione) has a long phosphorescent lifetime, (promoting the generation of highly toxic <sup>1</sup>O<sub>2</sub> in cancer cells), and has shown to disrupt levels of glycolytic enzymes in cancer cells.<sup>46</sup> Interestingly, [Ir(C,N)<sub>2</sub>(S,S)] is less selective for cancer vs. healthy cells compared to [Ir(C,N)<sub>2</sub>(O,O)], highlighting the ligand diversity between metal complexes derivatives.<sup>46</sup>

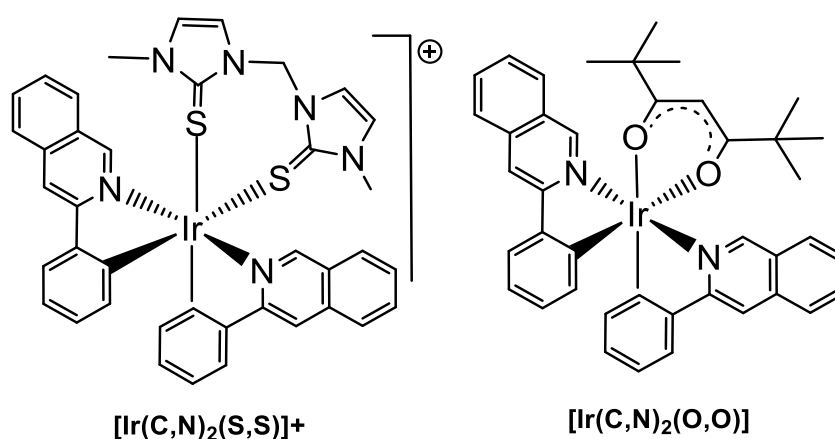


**Figure 1.5.** Structure of cyclometallated iridium(III) octahedral complexes reported by Sadler *et. al.* in 2017: [Ir(C,N)<sub>2</sub>(S,S)]<sup>+</sup> and [Ir(C,N)<sub>2</sub>(O,O)].<sup>46</sup>

Cyclometallated Ir<sup>III</sup> complexes have applications in PDT, photocatalysis and as luminescent imaging probes,<sup>44, 47</sup> however, they are limited by various factors. These complexes are highly lipophilic (poor aqueous solubility),<sup>44</sup> and their mechanisms of action are highly oxygen-dependent (somewhat hindering use in hypoxic tumours). In addition, some photosensitisers exhibit high toxicity under dark conditions. Further approaches such as joining with biocompatible ligands or other metal centres may overcome these concerns by improving selectivity, solubility and cytotoxicity.

### Photoactivatable chemotherapy (PACT)

Photoactivatable chemotherapy (PACT) is an important approach to the treatment of surface tumours which can be accessed by specific wavelengths of light. Photoactivatable platinum prodrugs are of increasing interest in the field of cancer therapeutics, with high photo-toxicity: providing both spatial and temporal selectivity.<sup>48, 49</sup>  $\text{Pt}^{\text{IV}}$  prodrugs can release labile or bioactive ligands upon light irradiation to form reactive  $\text{Pt}^{\text{II}}$  species *in situ* by a dual-action approach.<sup>23, 50-52</sup>

The photo-reductive properties of diazido  $\text{Pt}^{\text{IV}}$  complexes were first reported in 1978 by Vogler *et. al.*,<sup>53</sup> where it was noted that azidyl radicals can be released upon irradiation with UVA light. This has subsequently led to the development of remarkably stable diazido- $\text{Pt}^{\text{IV}}$  prodrugs which exhibit promising cytotoxicity upon *in situ* photoreduction.<sup>51</sup> Photoactivatable diazido- $\text{Pt}^{\text{IV}}$  prodrugs, including ***trans*-[Pt(en)(N<sub>3</sub>)<sub>2</sub>(OH)<sub>2</sub>]** and **FM190 (Fig. 1.3)**,<sup>54, 55</sup> have been reported to have potent anticancer activity against a variety of cancer cell lines.<sup>54-57</sup> These complexes differ from cisplatin by their coordination environment, oxidation state and their ability to release ligands upon irradiation with light. Moreover, these  $\text{Pt}^{\text{IV}}$  prodrugs are remarkable stable under dark conditions (low dark toxicity) and can be activated with blue light (465 nm) to generate  $\text{Pt}^{\text{II}}$  species (which bind to DNA)<sup>58</sup> and toxic radicals (azidyl and hydroxyl),<sup>51, 59</sup> presenting a multi-modal and synergistic mechanism of action.

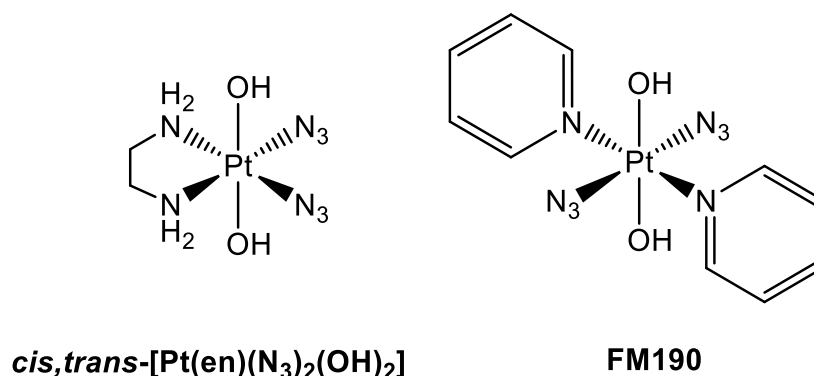


**Figure 1.3.** Structures of photoactivatable diazido- $\text{Pt}^{\text{IV}}$  complexes: ***cis, trans*-[Pt(en)(N<sub>3</sub>)<sub>2</sub>(OH)<sub>2</sub>]** and **FM190**.<sup>54, 55</sup>

The conjugation of biologically active moieties with Pt<sup>IV</sup> prodrugs can improve drug properties such as the pharmacokinetics, cytotoxicity and selectivity through multiple cellular targets and synergistic modes of action. For example, Lippard *et.al* reported Pt<sup>IV</sup> prodrugs conjugated to tumour-specific peptides can selectively target tumour endothelial cells over healthy cells,<sup>60</sup> significantly improving the antiproliferative effect over the non-conjugated analogue. Similarly, Yeow and Xing *et. al.* reported a diazido-Pt<sup>IV</sup> complex conjugated to human serum albumin protein (HSA) which significantly enhanced the cytotoxicity through improved drug delivery and controlled ligand release.<sup>61</sup> This design strategy has also been extended to di- and trinuclear Pt<sup>IV</sup> complexes.<sup>62, 63</sup>

The derivatisation of the axial ligands (OR) of **FM190** (**Fig. 1.3**) can be used to tune the chemical and physical properties of diazido-Pt<sup>IV</sup> PACT complexes, to improve the cytotoxicity, selectivity and targeting in cancer cells.<sup>51</sup> This has been demonstrated by Sadler *et. al.* using TEMPO radicals,<sup>51</sup> and more recently with coumarin (a natural compound which exhibits antitumour properties, **Fig. 1.4**).<sup>64</sup> Dinuclear metal modalities can also be connected at this axial position to improve the potency compared to the mono-metal analogues, as demonstrated with a photodynamic-photoactivatable Ir<sup>III</sup>-Pt<sup>IV</sup> complex recently reported from the Sadler group (**Fig. 1.4**).<sup>65</sup> Diazido Pt<sup>IV</sup> PACT prodrugs can provide a multi-targeting approach to cancer treatment, to overcome resistance to conventional Pt<sup>II</sup> drugs.

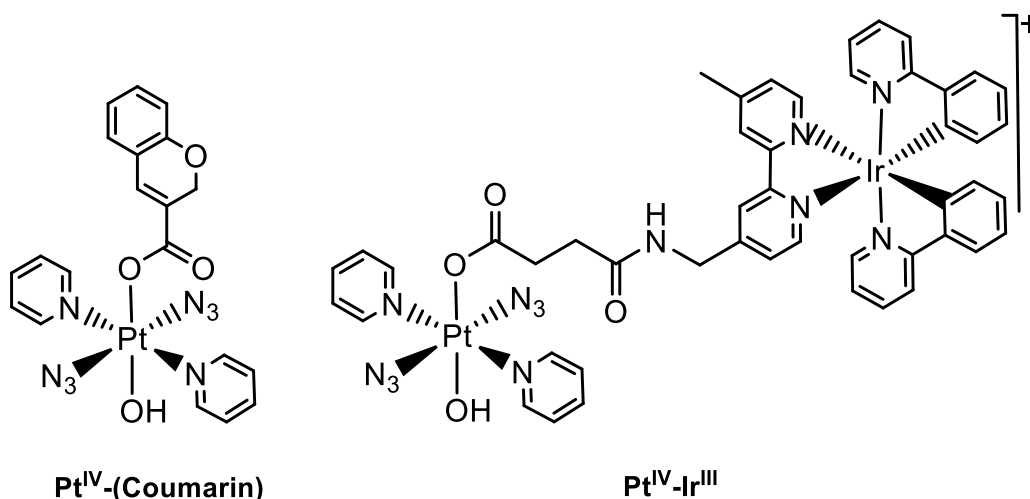


**Figure 1.4.** Photoactivatable diazido-Pt<sup>IV</sup> complexes with varying groups at the axial position reported in the Sadler Group: coumarin and Ir<sup>III</sup>-PDT conjugate.<sup>64, 65</sup>

## PDT vs PACT

PDT and PACT are promising approaches to phototherapy for the treatment of cancer, both of which have potential clinical advantages and disadvantages. PDT is a photocatalytic process: photosensitisers catalytically oxidize biomolecules *via* electron-transfer (Type I) or convert molecular oxygen ( $^3\text{O}_2$ ) to toxic singlet oxygen ( $^1\text{O}_2$ ) *via* energy-transfer (Type II), without being chemically changed themselves. This provides significant advantages over PACT, which typically relies on photodissociation and redox change.<sup>48</sup> However, PDT is more dependent on cellular oxygen levels compared to PACT, somewhat hindering applications in hypoxia.

One of the major limitations of both PDT and PACT agents is that they usually require photo-activation using UV/Vis light (200-700 nm), which has minimal tissue penetration depths (due to the strong absorption by proteins in this region), somewhat limiting the clinical relevance. In addition, they are both confined to localised diseases.

### 1.2.2 Half-sandwich anticancer complexes

#### Half-sandwich “piano-stool” complexes

Half-sandwich metal complexes are of significant interest in the design of new anticancer metallodrugs.<sup>66</sup> In general, half-sandwich complexes are pseudo-octahedral, three-legged “piano stool” complexes containing a cyclic polyhapto ligand. Half-sandwich complexes of platinum-group metals have shown to exhibit antiproliferative activity in human cancer cells. These complexes are composed of four structural components: (i) metal centre; (ii) arene; (iii) bidentate ligand; (iv) leaving group (Fig. 1.6) – all of which contribute to the observed antiproliferative effect.

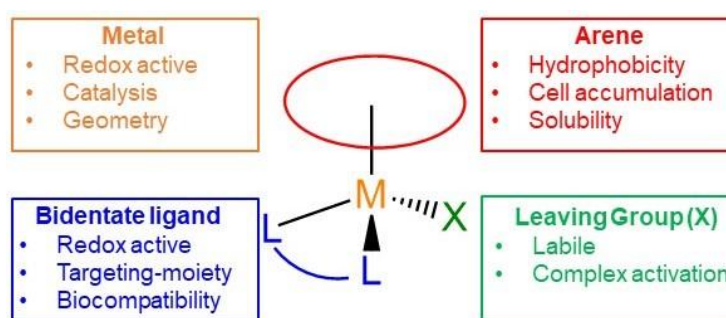


**Figure 1.6.** Structure-activity relationships (SARs) of half-sandwich anticancer complexes.

An understanding of structure-activity relationships (SARs) are crucial for the design of novel therapeutic drugs which circumvent platinum-resistance and reduces toxic side effects. The metal centre plays an essential role in redox activity, catalysis and the coordination geometries. The bidentate ligand contributes to the complex stability (*via*. the chelate effect), redox activity, biocompatibility and targeting of the metal complex. For example, metal complexes bound to natural antitumour organic compounds (such as curcumin) which exhibit pharmacological properties.<sup>67, 68</sup> The arene hapticity controls hydrophobicity - which plays a major role in enhancing cellular accumulation (passage through phospholipid membranes), however, this is a compromise with aqueous solubility - a potential hindrance for clinical translation. Finally, anticancer half-sandwich complexes typically contain a leaving group which is essential for complex activation in a cellular environment (*i.e.* hydrolysis).<sup>69</sup>

### Ruthenium half-sandwich complexes

Ruthenium complexes show desirable properties for use as antitumour drugs.<sup>70-73</sup> A variety of ruthenium candidates have shown high selectivity towards cancer cells with different cellular targets and modes of action to clinical platinum drugs. Ruthenium is in the same group as iron in the periodic table, thus, can mimic Fe-binding to serum transferrin or albumin).<sup>74</sup> Ruthenium-based therapeutics may give rise to novel ligand-dissociation kinetics, cellular transport and activation mechanisms, which may circumvent platinum-resistance and reduce patient side effects.

Two of the most well-known Ru<sup>III</sup> anticancer complexes are octahedral complexes **NAMI-A** and **KP1019/1339** (**Fig. 1.7**), both of which reached clinical trials.<sup>75-78</sup> **NAMI-A** was found to inhibit tumour metastases but lacked cytotoxic properties (limited efficacy), resulting in abandonment at phase II clinical trials.<sup>76</sup> **KP1019** (indazole cation) did not make it past phase I of clinical trials due to low aqueous solubility, and was later replaced with its sodium salt **KP1339**, furthermore emphasizing the importance of the balance between lipophilicity and hydrophilicity for absorption, distribution, metabolism and excretion in a clinical scenario. More recently, an organometallic Ru<sup>II</sup> protein kinase inhibitor (**DW1/2**, **Fig. 1.7**) has shown promise as an anticancer agent, but has not yet made it to clinical trials.<sup>76</sup>



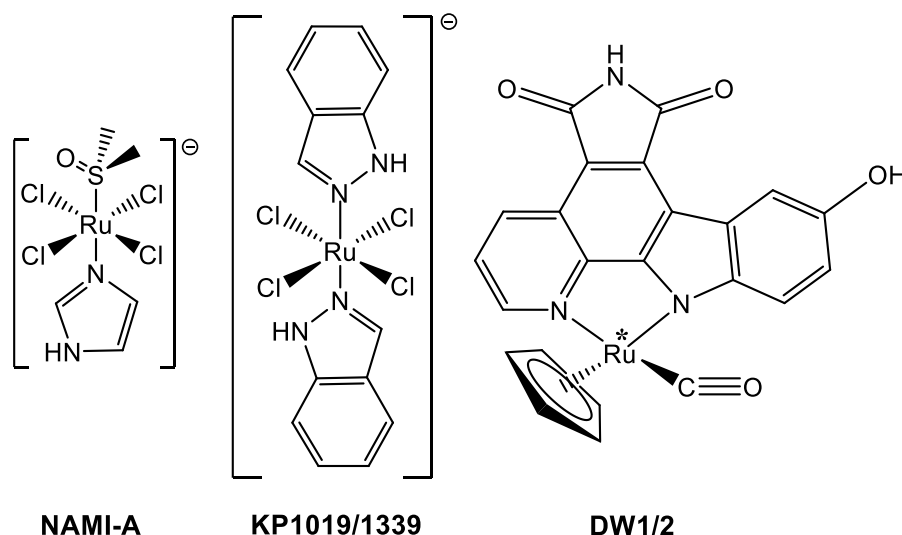


**Figure 1.7.** Structures of ruthenium anticancer lead compounds **NAMI-A**,<sup>76</sup> **KP1019**<sup>75</sup> and **DW1/2** (where \* denotes a chiral centre **DW1**=*R* and **DW2**=*S*).<sup>76</sup>

Half-sandwich ruthenium complexes exhibit remarkable chemical versatility,<sup>79</sup> which makes them attractive pharmacological scaffolds. Ru<sup>II</sup> “half-sandwich” complexes with the general formulae Ru[(arene)(DPEN)X] (where DPEN=diphenylethylenediamine and X=halide) are of great interest in the development of novel anticancer agents. One of the earliest Ru<sup>II</sup> piano-stool complexes which showed promising antitumour activity against carboplatin-resistant cancer cell lines was **RM175** (**Fig. 1.8**), which was discovered in 2001 by Sadler *et al.*<sup>80</sup> **RM175** can induce G<sub>1</sub>/G<sub>2</sub> growth arrest and apoptosis,<sup>81</sup> and can form hydrophobic interactions with nucleobases (DNA adducts).<sup>78</sup> Notably, **RM175** was shown to inhibit matrix metalloproteinase-2 (which contributes to tumour growth and survival),<sup>78,82</sup> providing a novel mechanism of action to that of conventional Pt<sup>II</sup> drugs.

An important biomolecule in cancer cells is glutathione (GSH), which is highly reactive and acts as a natural cellular antioxidant. **RM175** can react with intracellular GSH to form species which may be involved in a postulated redox-mediated pathway towards DNA binding.<sup>83</sup> GSH is over-expressed in many cancer cell lines,<sup>84</sup> hence, novel anticancer agents can exploit these vulnerabilities of cancers. In 2013, organo-ruthenium anticancer agent, **plecstatin-1** (**Fig. 1.7**) demonstrated selectivity for the cytoskeletal linker protein plectin (which is involved in tumour cell migration).<sup>85</sup> However, Ru<sup>II</sup> half-sandwich complexes are susceptible to hydrolysis<sup>86</sup> – which has led to the development of more stable half-sandwich osmium complexes.

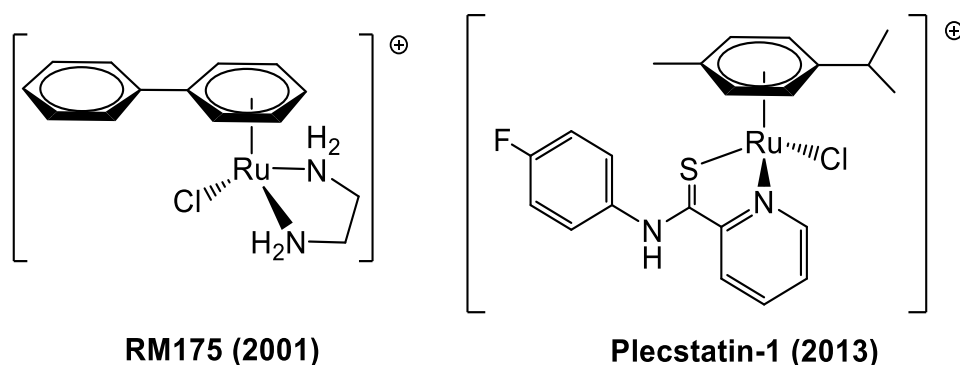


**Figure 1.8.** Structure of **RM175** and **plectstatin-1** lead Ru<sup>II</sup> half-sandwich complexes.<sup>80, 85</sup>

### Osmium half-sandwich complexes

Osmium was discovered before ruthenium,<sup>87</sup> yet its chemical applications are not as well understood (perhaps as a consequence of the known toxicity of osmium tetroxide) - hence, therapeutic applications of osmium are still in their infancy. The use of osmium-based drugs may have significant advantages over ruthenium, including: (i) higher available oxidation states, (ii) strong  $\pi$ -backbonding interactions ( $\pi$ -acceptor ligands, *i.e.* cyclopentadiene), (iii) slower ligand-dissociation kinetics and (iv) stronger spin-orbit coupling, however, this is dependent on the nature of the complex.

Osmium anticancer complexes in a variety of different oxidation states have been reported.<sup>88</sup> High-valent octahedral Os(VI) dinitrido complexes have shown to have potent anticancer activity through highly-controlled intracellular targeting,<sup>89</sup> while octahedral Os(II) complexes can inhibit protein-protein interactions.<sup>90</sup> Os(II), (III) and (IV) analogues of **NAMI-A**, **KP1019** and **RM175** were found to be more inert and stable towards hydrolysis *in vitro*, exhibiting moderate cytotoxicity against a variety of cancers.<sup>82, 88, 91</sup> The osmium analogue of **RM175** (named **AFAP51**, **Fig. 1.9**) was significantly more potent *in vitro*,<sup>82</sup> however, showed limited activity *in vivo* compared to **RM175**,<sup>82</sup> emphasizing the chemical diversity between ruthenium and osmium complexes.

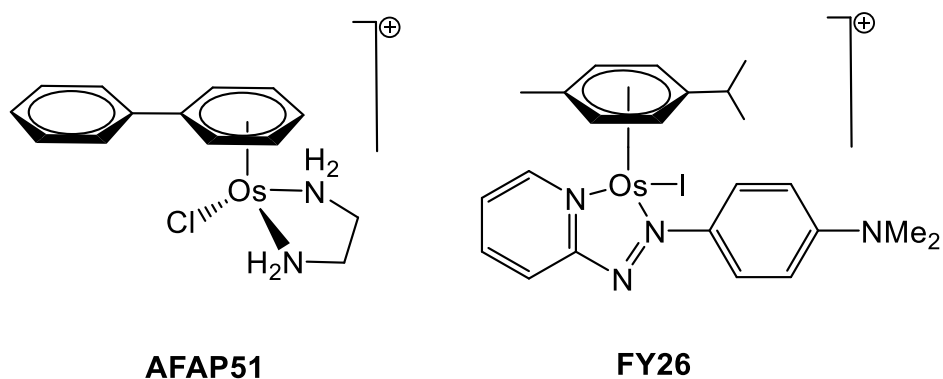


**Figure 1.9.** Structure of half-sandwich Os<sup>II</sup> complexes: **AFAP51**<sup>82</sup> and **FY26**.<sup>92</sup>

In 2010, Sadler *et al.* reported a family of half-sandwich Os<sup>II</sup> complexes containing imino or azo-pyridine bidentate ligands (second-generation analogues of **RM175**) which are remarkably stable and have promising *in vitro* potency against a variety of human cancer cells.<sup>92, 93</sup> These complexes are comprised of (i) arene (*p*-cymene or biphenyl), (ii) imino- or azo-pyridine bidentate ligand and (iii) leaving group (chloride or iodide), all of which play essential roles in structure-activity relationships as described previously (**Fig. 1.6**).<sup>69, 73</sup> In particular, **FY26** with the formula [Os(*p*-cym)(5-Azy-NMe<sub>2</sub>)I]PF<sub>6</sub> (where *p*-cym=*para*-cymene, Azy-NMe<sub>2</sub>=N,N-dimethyl-4-(pyridin-2-yl)diazenyl) (**Fig. 1.9**) is an average of 49× more potent than cisplatin against 809 cancer cell lines.<sup>94</sup> Importantly, these complexes do not predominantly bind to DNA (unlike cisplatin and other platinum drugs) and have promising cytotoxicity in platinum-resistant cancer cells.

Cellular fractionation ICP-MS (<sup>189</sup>Os) studies and synchrotron-XRF (Os L<sub>3</sub>M<sub>5</sub>=8.9 keV) have implicated mitochondria as a cellular target of **FY26**.<sup>95, 96</sup> Potential redox mechanism(s) of action have been investigated, showing that **FY26** can generate ROS both *in vitro* and *in vivo*,<sup>97</sup> and induces S-phase cell cycle arrest.<sup>96</sup> Interestingly, the potency of **FY26** can further be improved upon co-administration with L-buthionine-sulfoximine (which depletes GSH)<sup>98</sup> compromising cellular defence against oxidative stress. Complementary to this, chemical *in situ* reactions (between **FY26** and GSH)<sup>99</sup> and <sup>131</sup>I-labelled **FY26** cellular experiments demonstrated the rapid in-cell hydrolysis of **FY26** and the formation of Os-GSH adducts.<sup>99, 100</sup> Synchrotron-XAS studies have also provided information on the cellular speciation and binding moieties of **FY26** in primary cells and to investigate tumour penetration in cancer spheroid models.<sup>101, 102</sup>

### 1.2.3 Catalytic metallodrugs

The development of catalytic therapies for cancer treatment is emerging in research. Catalytic therapies utilize endogenous biological substrates and an external catalyst to cause oxidative or reductive damage to cancer cells. The first *in vitro* application of catalytic therapy for cancer treatment was reported by Kimoto in 1983,<sup>103</sup> where the antitumour activity of a copper(II) tripeptide complex was significantly enhanced in high concentrations of ascorbate (which is readily oxidised by molecular oxygen) to generate ROS.<sup>103</sup> However, it is only in recent years that promising anticancer catalytic systems have been optimized. Catalytic drugs have additional advantages over non-catalytic drugs: lower dosages (reduces toxicity and side effects)<sup>104, 105</sup> and do not require activation with light or radiation (unlike PACT and radiotherapy).

A catalyst is defined as a species which can promote the progression of a chemical reaction by lowering the activation energy, without being consumed in the reaction itself. In cells, enzymes act as biological catalysts, which can interact with cofactors (*e.g.* NADH and FAD), acting as hydride donors and acceptors to facilitate electron-transfer. In mitochondria there are a variety of enzymes and cofactors which are essential for energy generation under aerobic conditions *via* the ETC. This process is carefully regulated,<sup>106</sup> and disruption to the cellular redox homeostasis (*i.e.* by oxidative stress) can hinder growth, ultimately leading to cell death. The redox vulnerability of cancer cells makes catalytic therapy a promising strategy.

Catalytic therapies can be categorized into oxidative or reductive therapies, depending on the nature of cell death. The generation of ROS, hydrogen peroxide or hydroxyl radicals causes oxidative stress in cancer cells, disrupting the tightly-regulated redox homeostasis. Notably, Sadler *et. al.* reported an Ir<sup>III</sup> photocatalyst which can oxidize NADH to NAD<sup>+</sup> even under hypoxic conditions.<sup>47</sup> In contrast, reductive therapy relies on inducing reductive stress mechanisms of cell death. For example, Ru<sup>II</sup> tethered half-sandwich complexes have shown to catalyse the transfer hydrogenation of NAD<sup>+</sup> to NADH in the presence of formate as a hydride source.<sup>107</sup> This approach can also be extended to external substrates, for example, Meggers *et. al.* demonstrated the biorthogonal catalytic activation of caged anticancer drug doxorubicin by a Ru<sup>II</sup> half-sandwich complex in cancer cells.<sup>108</sup> Other notable contributions to the field of

biorthogonal catalysis includes the work of Salassa *et. al.*, which demonstrated the photocatalytic reduction of  $\text{Pt}^{\text{IV}}$  to  $\text{Pt}^{\text{II}}$  in the presence of flavoproteins<sup>109</sup> – with the metal complex acting as the substrate as opposed to the catalyst.

Catalytic transition-metal complexes have advantages over organic catalysts as they can access a variety of different coordination geometries, oxidation states, and ligand binding modalities, giving rise to different chemical properties. Catalytic metallodrugs can exploit these properties to perturb redox balance and disrupt metabolic processes (*e.g.* oxidative phosphorylation or glycolysis) in cancer cells.<sup>110</sup> One of the major limitations of the development of catalytic metallodrugs is catalyst deactivation due to limited stability in cancer cell environments, which likely hinders their clinical use. Additionally, many transition metal catalysts require activation by ligand dissociation prior to catalysis, with Noyori's ruthenium asymmetric transfer hydrogenation (ATH) catalyst being an well-known example.<sup>111</sup>

Noyori's first generation ruthenium ATH catalysts contained chiral chelating groups; BINAP and diamine ligand (general formula  $\text{Ru}^{\text{II}}(\text{diphosphane})(\text{diamine})\text{Cl}_2$ ),<sup>112, 113</sup> **Fig. 1.10**) which could enantioselectively convert ketones to chiral alcohols with high conversions. Second generation Noyori catalysts with the formula  $[\text{Ru}^{\text{II}}(p\text{-cymene})(\text{TsDPEN})\text{Cl}]$  were developed (**Fig. 1.10**).<sup>111, 114-118</sup> This bifunctional 'piano-stool' complex contains a chiral diamine ligand which directs the enantioselectivity of the reaction to produce high enantiomeric excesses under acidic conditions.<sup>112, 119</sup>

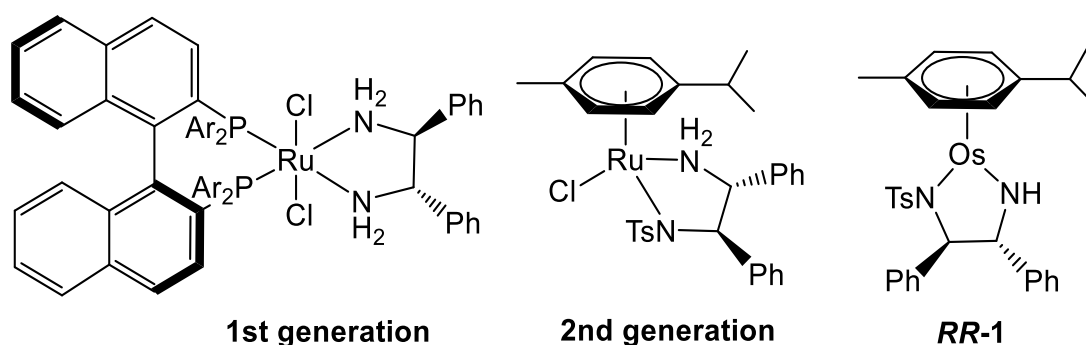


**Figure 1.10.** Structure of Noyori's first and second generation catalysts<sup>111, 113</sup> and  $[\text{Os}^{\text{II}}(p\text{-cym})(\text{TsDPEN})]$  catalyst reported by Sadler *et. al.*<sup>120</sup>

Since the discovery of Noyori's catalyst, there have been significant advances in the design of Ru<sup>II</sup> half-sandwich complexes for the ATH of a diverse range of prochiral substrates under varying experimental conditions. For example, Wills *et. al.* reported a series of tethered [Ru<sup>II</sup>( $\eta^6$ -arene)(TsDPEN)Cl] catalysts which proved effective for the reduction of amino-substituted ketone (which are relatively unreactive) in aqueous solution,<sup>121</sup> achieving high conversions and enantioselectivity.

In 2015, Sadler *et. al.* reported a series of 16-electron, pseudo-octahedral Noyori-type catalysts with the general formulae [Os<sup>II</sup>(*p*-cym)(BsDPEN)] (where *p*-cym=*para*-cymene and BsDPEN=benzylsulfonyldiphenylethylene diamine; **Fig. 1.10**).<sup>120</sup> Correspondingly, these osmium-derivatives can also act as catalysts in the ATH of acetophenone-derived substrates - with high turnover frequencies and enantiomeric excess (>95%) in the presence of formic acid.<sup>120</sup> These osmium complexes are easy to synthesize, remarkably stable and – unlike Noyori's catalysts – do not require activation (*e.g.* ligand dissociation).

This family of Os<sup>II</sup> complexes showed moderate cytotoxicity against a variety of human cancer cell lines.<sup>122</sup> Perhaps more impressively, the antiproliferative activity can be significantly enhanced in the presence of non-toxic concentrations of sodium formate. In particular, parent compound [Os<sup>II</sup>(*p*-cym)(1*R*,2*R*)TsDPEN)] (where TsDPEN=tosyl-(1*R*, 2*R*)-diphenylethylenediamine), was the first reported Os-based ATH catalyst shown to enantioselectively convert pyruvate (an essential metabolic precursor) to unnatural D-lactate in cancer cells in the presence of formate.<sup>122</sup> This process was specific for cancer cells,<sup>122</sup> providing a platform for catalytic selectivity. In nature, cells predominantly produce L-lactate from pyruvate through a carefully NADH-balanced bio-system using lactate dehydrogenase.<sup>123</sup> Upon co-administration of the *RR*-catalyst and formate, levels of intracellular D-lactate were significantly enhanced, implicating in-cell ATH. In comparison, the *SS*-catalyst produced natural L-lactate, suggesting the catalyst chirality is maintained intracellularly.<sup>122</sup>

The catalytic cycle for the enantioselective reduction of pyruvate using [Os(*p*-cym)(TsDPEN)] is thought to be initiated through coordination of formate (*via.* O-atom) at the vacant site, releasing CO<sub>2</sub> to form an active Os-hydride bond (**Fig. 1.11**).<sup>120</sup> The prochiral substrate then forms favourable interactions with the N-H and Os-H in a 6-coordinate transition state,<sup>122</sup> to release the chiral product and regenerate

the catalyst.<sup>120</sup> In 2019, Yang *et. al.* proposed a new catalytic cycle using involving a proton-coupled hydride mechanism for pyruvate reduction.<sup>124</sup> The basis of the stereoselectivity is not fully understood for pyruvate, but it has been proposed that the C-H bond on *p*-cymene is slightly polar, hence, forms electrostatic interactions with the negatively-charged carboxylate of pyruvate in the transition state (**Fig. 1.11**).<sup>122</sup>

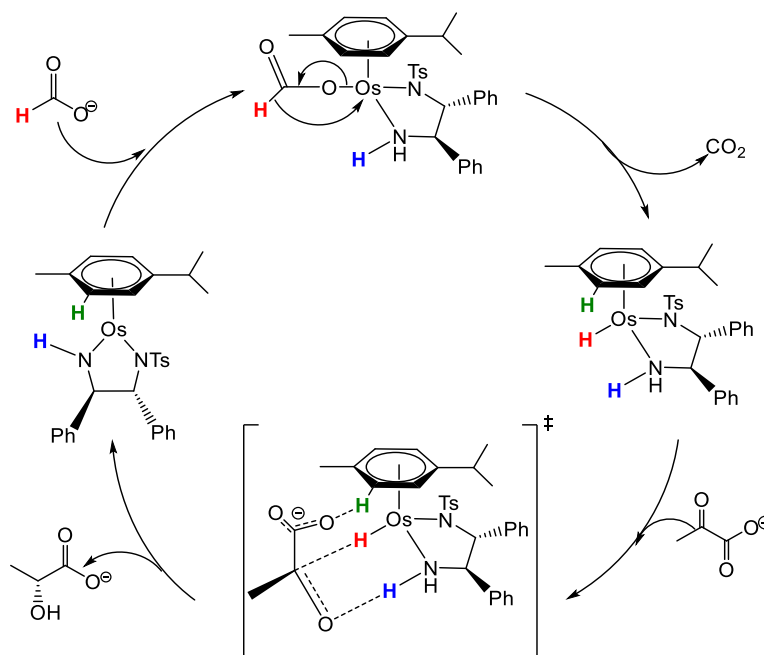


**Figure 1.11.** Proposed catalytic for the enantioselective reduction of pyruvate to D-lactate by  $[\text{Os}(\text{p-cym})(1R,2R)\text{TsDPEN}]$ , adapted from the literature.<sup>122</sup>

One of the major vulnerabilities of cancers is their increased lactate concentrations (*via* the Warburg effect).<sup>14</sup> It was deduced, however, that the increase in lactate concentration by these  $\text{Os}^{\text{II}}$  16-electron catalysts was likely *not* the predominant cause of cell death,<sup>122</sup> but that the contribution of this change likely disrupts important cellular pathways involving lactate. Targeting the vulnerabilities of cancer is one of the most important approaches to cancer therapies. Interestingly, both *in vitro* and *in vivo* confocal microscopy studies of these osmium sulfonamide catalysts have linked the selective generation of ROS with the antiproliferative mechanism of action.<sup>122</sup> Importantly, this moves away from conventional platinum drugs with DNA-targeting mechanisms of action (*i.e.* cisplatin), which may overcome platinum-resistance and minimize off-target toxic effects. These 16-electron osmium catalysts could provide a novel catalytic approach to the treatment of cancer, by exploiting vulnerable redox and metabolic pathways.

### 1.3 Synchrotron Radiation

Synchrotron radiation has shown to be an invaluable tool for investigating *in vitro* and *in vivo* mechanisms of action of metallodrug candidates.<sup>125-127</sup> Typically, hard x-rays can be used to directly monitor the distribution and chemical speciation of exogenous elements in relation to native biological elements. Contrastingly, soft x-rays can be used to gain insights into drug-induced morphological changes in cells or tissues under cryogenic (near-native) conditions. This thesis explores the potential mechanisms of action of metallodrugs using both hard and soft x-rays for XRF, XAS and cryo-XRT studies.

Synchrotron radiation is generated from the acceleration of electrons when they pass through or are re-directed by an undulator, wiggler or bending magnet (dipole). A pulsed beam of electrons is accelerated using a linear accelerator, followed by acceleration with a small booster ring before finally being injected and “stored” in the main ring of the synchrotron. The ring, at Diamond Light Source (DLS, Oxford) is comprised of 24 straight sections and the x-rays generated by oscillating the electrons by the insertion device are directed along the straight section or at a tangent to point of bending into the next straight. Synchrotron radiation can cover a wide range of the electromagnetic spectrum – from ultraviolet and infra-red (<1000 eV) to hard x-rays (>12 keV) - depending on the particle acceleration, which can be exploited for a wide range of scientific applications.

X-rays can generally be categorized as hard (12-120 keV) or soft (0.12-12 keV).<sup>128</sup> Hard x-rays are higher in energy, thus, are less strongly absorbed in materials compared to soft x-rays, but can excite different elements or edges. As a consequence, hard and soft x-rays are utilized in different ways, and can be used to gain diverse, but complementary information on chemical and biological systems. For example, hard x-rays can be used to monitor heavy exogenous metals in biological samples using synchrotron-XRF,<sup>126</sup> whereas, soft-x-rays can be used for contrast of light elements (such as carbon) by exploiting the absorption of soft x-rays by lighter elements.



### 1.3.1 X-ray fluorescence (XRF)

When a sample is bombarded with x-rays with an energy which exceeds the electron-binding energy of an element, a fluorescence phenomenon is observed. This radiation is high enough in energy to eject electrons from lower energy orbitals (*i.e.* K or L-shells), leaving vacant ‘holes’. As a consequence, electrons from higher-energy orbitals fill these holes, resulting in an emission of radiation known as x-ray fluorescence (**Fig. 1.12**). These emissions are elemental-specific and can be simultaneously detected at trace levels (100 ppb) using synchrotron radiation.<sup>129</sup>

Multiple emissions of individual elements can be observed, and are categorized in terms of the final ground state configuration as primary ( $\alpha$ ) or secondary ( $\beta$ ). For example,  $K_\alpha$  emission is observed when an electron is ejected from an inner K-shell forming a vacant hole for which is filled by an electron from the L-shell, whereas,  $K_\beta$  emission is observed when an electron from the M-shell (higher energy) relaxes into the vacated K-shell hole (**Fig. 1.12**). Synchrotron-XRF allows the simultaneous detection of multiple elements, thus, by selecting an incident beam energy greater than that of the element with the highest electron-binding energy, the x-ray emissions of all elements with lower electron-binding energies can be monitored.

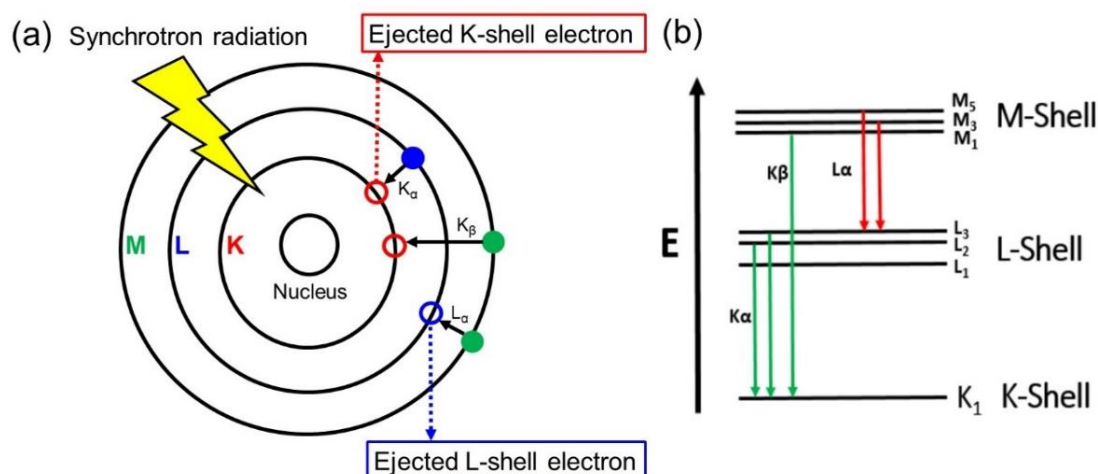


**Figure 1.12.** (a) XRF phenomenon which occurs when an atom is exposed to x-rays (synchrotron radiation), resulting in the ejection of inner-shell electrons and subsequent fluorescence emission by movement of higher-energy electrons into the vacant orbitals. (b)  $K_{\alpha/\beta}$  and  $L_\alpha$  emissions; where alpha ( $\alpha$ ) is the radiation emitted from one orbital above and beta ( $\beta$ ) is the emission from two orbits above the vacated lower-energy shell.

For samples of biological cells, the  $KL_3$ -emissions of native endogenous elements (including Zn, K, S and P) occur within the 2-10 keV range, whereas, that of exogenous heavy elements (Os, Pt, Ir) occur at much higher energies (60-80 keV).<sup>130</sup> Instead, the  $L_3M_5$ -emissions of heavy metals can be monitored using lower energies (9-13 keV). The  $KL_3$ -emissions of relevant endogenous biological elements, and the non-native elements of interest in this thesis (Pt, Ir, Os, Br) are specified in **Table 1.1**.

Synchrotron-XRF can be used to investigate the bio-distribution, stability and localisation of the heavy metal components of metallodrugs in cancer cells (in addition to endogenous biological elements). The use of synchrotron-XRF for the analysis of metal anticancer complexes *in vitro* and *ex vivo* (tumour spheroids or xenograft models) is well-reported for platinum,<sup>131-136</sup> ruthenium,<sup>137, 138</sup> iridium<sup>139</sup> and osmium anticancer agents.<sup>95, 101, 140</sup> XRF can also be used to probe the in-cell stability of metal complexes using exogenous labelling atoms, which has been shown by Hambley *et al.* for Br-labelled Pt complexes,<sup>141</sup> and more recently by Harris *et al.* for an I-labelled rhenium complex in cancer cells.<sup>142</sup> Notably, cryo-XRF is emerging at various beamlines for the analysis of frozen-hydrated cells or tissues as close to their native state as possible including ID16A (ESRF, Grenoble)<sup>139</sup> and 9-ID-B (APS, Illinois).<sup>143</sup>

**Table 1.1.** Summary of the electron-binding energies and XRF emissions of endogenous biological elements and exogenous heavy elements investigated in this thesis.<sup>130</sup>

Element	Electron-binding energy		Relevant XRF emissions	
	Electron	Energy (keV)	XRF emission	Energy (keV)
<b>Ca</b>	$K_{1s}$	4.04	$L_3 (2p_{3/2}^{-1}) \rightarrow K (1s^{-1})$	3.69
<b>Cl</b>	$K_{1s}$	2.82	$L_3 (2p_{3/2}^{-1}) \rightarrow K (1s^{-1})$	2.62
<b>Cu</b>	$K_{1s}$	8.98	$L_3 (2p_{3/2}^{-1}) \rightarrow K (1s^{-1})$	8.05
<b>Fe</b>	$K_{1s}$	7.11	$L_3 (2p_{3/2}^{-1}) \rightarrow K (1s^{-1})$	6.40
<b>K</b>	$K_{1s}$	3.61	$L_3 (2p_{3/2}^{-1}) \rightarrow K (1s^{-1})$	3.31
<b>Mg</b>	$K_{1s}$	1.30	$L_3 (2p_{3/2}^{-1}) \rightarrow K (1s^{-1})$	1.25
<b>Na</b>	$K_{1s}$	1.07	$L_3 (2p_{3/2}^{-1}) \rightarrow K (1s^{-1})$	1.04
<b>P</b>	$K_{1s}$	2.15	$L_3 (2p_{3/2}^{-1}) \rightarrow K (1s^{-1})$	2.01
<b>S</b>	$K_{1s}$	2.47	$L_3 (2p_{3/2}^{-1}) \rightarrow K (1s^{-1})$	2.31
<b>Zn</b>	$K_{1s}$	9.66	$L_3 (2p_{3/2}^{-1}) \rightarrow K (1s^{-1})$	8.64
<b>Os</b>	$L_3 2p_{3/2}$	10.87	$M_5 (3d_{5/2}^{-1}) \rightarrow L_3 (2p_{3/2}^{-1})$	8.91
<b>Br</b>	$K_{1s}$	13.47	$L_3 (2p_{3/2}^{-1}) \rightarrow K (1s^{-1})$	11.92
<b>Ir</b>	$L_3 2p_{3/2}$	11.22	$M_5 (3d_{5/2}^{-1}) \rightarrow L_3 (2p_{3/2}^{-1})$	9.18
<b>Pt</b>	$L_3 2p_{3/2}$	11.56	$M_5 (3d_{5/2}^{-1}) \rightarrow L_3 (2p_{3/2}^{-1})$	9.44

The I14 beamline (DLS, Oxford) is a hard x-ray nanoprobe which operates in the energy range of 5-23 keV, achieving spatial resolution of down to 50 nm. High energy x-rays are generated from an undulator source (forcing electrons into a wave or trajectory) to generate a high energy radiation beam (stabilised with monochromators) which is mirror-directed onto the sample. The sample can be scanned through the beam to obtain chemical and structural information by exploiting XRF. I14 does not yet have the capability for analysis of cryogenic samples (liquid nitrogen conditions), hence, cryo-fixed and freeze-dried cells have been analysed in this thesis.

### 1.3.2 X-ray Absorption Spectroscopy (XAS)

The I14 beamline is also optimized for XAS which uses a scanned energy range as opposed to a fixed energy. XAS can be determined by measuring a transition of an electron from a core energy level to an unoccupied state. When a sample is exposed to synchrotron radiation, a photon interacts with a core electron (typically 1s, 2s or 2p),<sup>126</sup> which causes an electronic transition into a vacant bound or continuum state, resulting in an XAS phenomenon according to Fermi's Golden Rule (**Equation 1.1**). This equation describes the transition probability of a core electron to absorb a photon, which is proportional to the x-ray absorption coefficient and is used to predict XAS.

$$\mu(E) = \sum_{f}^{E_f > E_F} |\langle f | \hat{\epsilon} \cdot \mathbf{r} | i \rangle|^2 \delta(E_f)$$

**Equation 1.1.** XAS equation:  $\mu(E)$ = x-ray absorption coefficient,  $|i\rangle$ = initial state of energy  $E_i$ ,  $\langle f|$  = final (unoccupied) state of energy  $E_f$ ,  $\epsilon$ = photon polarisation,  $r$ = electron position,  $\delta$ = density of states.

XAS can be categorized as two main types, depending on the nature of their absorption regions: (i) X-ray Absorption Near Edge Structure (XANES) and (ii) Extended X-ray Absorption Fine Structure (EXAFS). When an atom absorbs synchrotron radiation, a rapid jump in energy is observed (referred to as an 'edge') followed by a unique and stable fingerprint region (**Fig. 1.13**). The 'edge-jump' corresponds to the XANES region (30 eV before the edge and up to 50 eV after the edge), and the fingerprint region corresponds to the EXAFS region (>50 eV from the edge).<sup>126</sup>

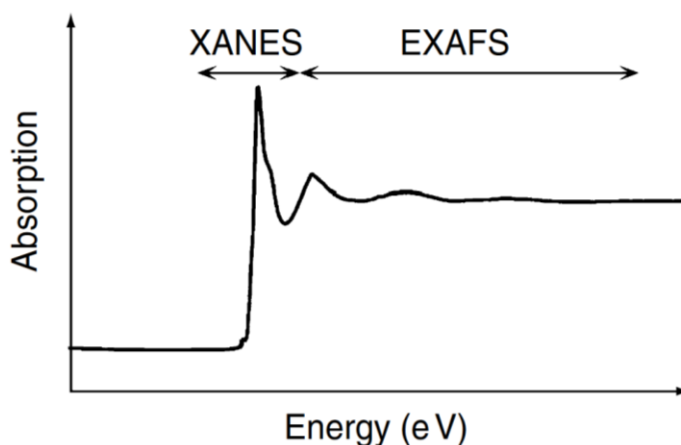


**Figure 1.13.** Characteristic XAS showing the XANES and EXAFS regions.<sup>144</sup>

XANES is observed between 50-100 eV above the ionisation energy of the core level in an atom, and is strongly sensitive to the chemistry of the absorbing atom. XANES spectroscopy can provide information on oxidation state and coordination environment of metal complexes,<sup>145</sup> which may be crucial in understanding the mechanisms of activation of metallodrugs in cancer cells.

In contrast, EXAFS is typically observed at energies greater than 50 eV above the edge of the absorbing atom, and is element-specific. EXAFS occurs as a consequence of the scattering of photo-electrons by neighbouring atoms. In EXAFS, the electrons are promoted from low to high energy states (a continuum), creating a photoelectron which can interact with surrounding atoms, resulting in oscillations in this region. As a result, EXAFS is sensitive to the neighbouring environment around the absorbing atom, providing information on chemical coordination environments (**Equation 1.2**). EXAFS can be used to determine the number and nature of neighbouring atoms up to 4 Å in length.<sup>126</sup>

$$X(k) = \sum_j \frac{N_j f_j(k) \exp(-2k^2 \sigma_j^2) \exp\left(-\frac{2R_j}{\lambda}\right)}{k R_j^2} \sin(2k R_j + \delta_j(k))$$

**Equation 1.2.** EXAFS equation where  $f(k)$ =amplitude,  $\delta(k)$ =phase shift,  $R$ =distance from the wave to the inner shell,  $N$ = coordination number (number of scattering atoms),  $\sigma$ =measure of disorder between neighbouring atoms,  $k$ = photoelectron wave vector.

XAS is a well-established technique for analysing the chemical speciation of metal compounds in biological systems (*in vitro* and *in vivo*). XANES has been used to investigate the *in vitro* and *ex vivo* speciation of platinum,<sup>126</sup> ruthenium<sup>126</sup> and osmium complexes in cancer cells.<sup>99</sup> This includes Pt<sup>IV</sup>-prodrugs of cisplatin (Hambley *et. al.*),<sup>135</sup> ruthenium lead compound **KP1019** (Keppler *et. al.*)<sup>126</sup> and half-sandwich Os<sup>II</sup> azopyridine complex **FY26** (Sadler *et. al.*).<sup>102</sup> In addition, chemical *in situ* experiments between metallodrugs and biomolecules (*e.g.* DNA, GSH, ascorbate and albumin) have been performed on various metallodrugs.<sup>99, 126</sup> More recently, Hambley *et. al.* used XANES spectroscopy to demonstrate the stability of Pt<sup>IV</sup> prodrugs in human blood serum, in addition to the rapid in-cell activation (Pt<sup>IV</sup> → Pt<sup>II</sup>).<sup>146</sup>

### 1.3.3 Cryo X-ray Tomography (cryo-XRT)

The first report of synchrotron radiation microscopy with soft x-rays was that of Horowitz and Howell in 1972.<sup>147</sup> By definition, soft x-rays have lower energies (longer wavelengths) than hard x-rays and an energy range of *ca.* 0.12-2 keV.<sup>128</sup> These x-rays are less penetrating and more strongly absorbed in comparison to hard x-rays. This greater absorption provides stronger contrast for lighter materials which can be exploited for tomographic imaging of biological materials.

Full-field cryo x-ray microscopy can provide 3D images of biological samples under frozen-hydrated conditions, close to their native state. X-ray tomograms (2D images representing slices of a 3D volume) are produced using x-rays (500 eV) close to the K-absorption edges of oxygen and carbon (**Table 1.2**),<sup>148</sup> also referred to as the ‘water-region’ (the region in which water is transparent to incoming soft x-rays). This region is exploited to produce 3D images of biological samples owing to the contrast between carbon-containing cellular components (*i.e.* lipid droplets or mitochondria) with natural ice on the vitrified sample.<sup>149</sup> Cryo-XRT can provide information on subcellular morphology by the identification of carbon-based organelles down to a 25-40 nm spatial resolution,<sup>150, 151</sup> enabling the analysis of intact hydrated cells. This avoids problems induced by chemical fixatives. For example, Moscheni *et. al.* used cryo-XRT to analyse mitochondria in doxorubicin-resistant cancer cells, which may implicate impaired mitochondrial communications in resistant cells.<sup>152</sup>

**Table 1.2.** Electron-binding energies and  $KL_3$  XRF emissions of C, N and O exploited in cryo-XRT.<sup>130</sup>

Element	Electron-binding energy		Relevant XRF emissions	
	Electron	Energy (eV)	XRF emission	Energy (eV)
C	$K_{1s}$	284	$L_3 (2p_{3/2}^{-1}) \rightarrow K (1s^{-1})$	277
N	$K_{1s}$	410	$L_3 (2p_{3/2}^{-1}) \rightarrow K (1s^{-1})$	392
O	$K_{1s}$	543	$L_3 (2p_{3/2}^{-1}) \rightarrow K (1s^{-1})$	525

Cryo-XRT is an up-and-coming technique which can be used to probe drug-induced subcellular damage and cellular events which cannot be achieved using conventional electron or light microscopy.<sup>150</sup> Cryo-XRT is available at various synchrotron beamlines worldwide, including MISTRAL (ALBA, Spain), XM2 (ALS, US), U41-TXM (Bessy II, Germany) and B24 (DLS, UK) beamlines.<sup>153</sup> The use of cryo-XRT in the field of cancer metallodrugs has been demonstrated for iron oxide nanoparticles (Carrascosa *et. al.* 2016)<sup>154</sup> and half-sandwich iridium complexes (Pizarro *et. al.*, 2020) in breast cancer cells,<sup>139</sup> but also recently for cisplatin and gold nanoparticles in skin cancer cells (Gil *et. al.* 2020).<sup>155</sup> In this thesis, cryo-XRT was performed at the B24 beamline (DLS, UK): a transmission microscope operating at 500 eV, achieving a resolution of 30-40 nm.<sup>153</sup> The B24 beamline is capable of analysing cryopreserved biological samples: cancer cells are grown on TEM grids and plunge-frozen in liquid ethane for cryogenic analysis using soft x-rays.

In addition to cryo-XRT, the B24 beamline houses a super-resolution light microscopy facility which allows the analysis of vitrified samples using Structured Illumination Microscopy (SIM) before analysing the same samples by cryo-XRT.<sup>150, 156, 157</sup> Cryo-SIM has advantages over conventional microscopy, including rapid image acquisition (<100 ms), low light doses (minimize sample heating), compatibility with conventional fluorophores and an 8-fold greater volumetric resolution compared to the diffraction limit.<sup>157</sup> Cryo-XRT and cryo-SIM provide cross-correlative analysis which can significantly enhance the understanding of biological systems. This means that biological samples treated with conventional fluorophores or fluorescent drugs can be detected inside cells, and overlaid onto 3D tomograms, providing unambiguous drug localisation in near-native state cells. This cannot be achieved using conventional microscopy as a consequence of the resolution limitations dictated by the Abbe limit.

## 1.4 Aims of project

The aims of this thesis were to elucidate the *in vitro* mechanism(s) of action of osmium, iridium and platinum anticancer metallodrugs in human cancer cells using a variety of synchrotron-based techniques. Specific project aims were as follows:

- **Synthesis, characterisation and screening of Os<sup>II</sup> 16-electron catalysts**

The aim in **Chapter 3** was to synthesize and characterize novel Os<sup>II</sup> arene anticancer complexes containing halide-substituted benzylsulfonyldiamine ligands (**Fig. 1.10**) as potential in-cell transfer hydrogenation catalysts, and screen them for their chemical and biological activity in cancer cells. Further to this, the aim was to synthesise complexes with readily detectable labelling atoms in unreactive positions of the diamine ligand (*e.g.* Br or I) to monitor the in-cell stability, distribution and catalytic efficiency of these complexes by ICP-MS (<sup>189</sup>Os, <sup>79</sup>Br, <sup>127</sup>I) and synchrotron-XRF (Os L<sub>3</sub>M<sub>5</sub>=8.91 keV; Br KL<sub>3</sub>=11.92 keV; I L<sub>3</sub>M<sub>5</sub>=3.94 keV).

- **Distribution and cell damage by cyclometallated Ir<sup>III</sup> photosensitisers**

The aim of **Chapter 4** was to investigate the distribution and cell damage induced by a potent Ir<sup>III</sup> photosensitiser [Ir(C,N)<sub>2</sub>(O,O)] (**Fig. 1.5**) in cryopreserved cancer cells using correlative cryo-SIM and cryo-XRT. Independently of this, the second aim was to probe the cellular distribution, stability and targeting of a potent photodynamic-photochemotherapeutic Ir<sup>III</sup>-Pt<sup>IV</sup> complex (**Fig. 1.4**) by synchrotron-XRF.

- **In-cell x-ray studies of diazido-Pt<sup>IV</sup> photoactivatable prodrugs**

The aim of **Chapter 5** was to investigate the concentration-dependent intracellular distribution and morphological damage induced by a fluorescent coumarin-labelled diazido-Pt<sup>IV</sup> complex (**Fig. 1.4**) in cryopreserved cancer cells using correlative confocal microscopy, cryo-SIM and cryo-XRT. The second aim was to probe the cellular distribution and chemical speciation of diazido-Pt<sup>IV</sup> complexes in cancer cells using synchrotron-XRF (Pt L<sub>3</sub>M<sub>5</sub>=9.44 keV) and XANES (L<sub>3</sub> 2p<sub>3/2</sub>=11.56 keV).

## 1.5 References

1. R. McRae, P. Bagchi, S. Sumalekshmy and C. J. Fahrni, *Chem Rev*, 2009, **109**, 4780-4827.
2. T. J. Stewart, *Metallomics*, 2019, **11**, 29-49.
3. J. F. Collingwood and F. Adams, *Spectrochim Acta B*, 2017, **130**, 101-118.
4. J. L. Oke, J. W. O'Sullivan, R. Perera and B. D. Nicholson, *Sci Rep*, 2018, **8**, 14663-14663.
5. S. Rakoff-Nahoum, *Yale J Biol Med*, 2006, **79**, 123-130.
6. D. Hanahan and R. A. Weinberg, *Cell*, 2000, **100**, 57-70.
7. S. H. Hassanpour and M. Dehghani, *J Cancer Res Prac*, 2017, **4**, 127-129.
8. A. R. M. R. Amin, P. A. Karpowicz, T. E. Carey, J. Arbiser, R. Nahta, Z. G. Chen, J.-T. Dong, O. Kucuk, G. N. Khan, G. S. Huang, S. Mi, E. Niccolai, H. Fujii, K. Aquilano, S. S. Ashraf, S. Nowsheen, X. Yang, A. Bilsland and D. M. Shin, *Semin Cancer Biol*, 2015, **35**, S55-S77.
9. E. Y. H. P. Lee and W. J. Muller, *Cold Spring Harb Perspect Biol*, 2010, **2**, a003236-a003236.
10. K. L. Eales, K. E. R. Hollinshead and D. A. Tennant, *Oncogenesis*, 2016, **5**, e190.
11. M. L. Boland, A. H. Chourasia and K. F. Macleod, *Front Oncol*, 2013, **3**, 292.
12. D. F. Wilson, *J Physiol*, 2017, **595**, 7023-7038.
13. M. V. Liberti and J. W. Locasale, *Trends Biochem Sci*, 2016, **41**, 211-218.
14. M. G. Vander Heiden, L. C. Cantley and C. B. Thompson, *Science*, 2009, **324**, 1029-1033.
15. L. Dong and J. Neuzil, *Cancer Comm*, 2019, **39**, 63.
16. K. Sak, *Chemother Res Pract*, 2012, **2012**, 282570.
17. Y. Zhu, A. E. Dean, N. Horikoshi, C. Heer, D. R. Spitz and D. Gius, *J Clin Invest*, 2018, **128**, 3682-3691.
18. U. Ndagi, N. Mhlongo and M. E. Soliman, *Drug Des Devel Ther*, 2017, **11**, 599-616.
19. T. C. Johnstone, G. Y. Park and S. J. Lippard, *Anticancer Res*, 2014, **34**, 471-476.
20. L. Kelland, *Nat Rev Cancer*, 2007, **7**, 573-584.



21. D. T. Sleijfer, E. F. Smit, S. Meijer, N. H. Mulder and P. E. Postmus, *Br J Cancer*, 1989, **60**, 116-120.
22. A. Ibrahim, S. Hirschfeld, M. H. Cohen, D. J. Griebel, G. A. Williams and R. Pazdur, *Oncologist*, 2004, **9**, 8-12.
23. T. C. Johnstone, K. Suntharalingam and S. J. Lippard, *Chem Rev*, 2016, **116**, 3436-3486.
24. S. Dasari and P. B. Tchounwou, *Eur J Pharmacol*, 2014, **0**, 364-378.
25. G. He, J. Kuang, A. R. Khokhar and Z. H. Siddik, *Gynecol Oncol*, 2011, **122**, 402-409.
26. P. M. Bruno, Y. Liu, G. Y. Park, J. Murai, C. E. Koch, T. J. Eisen, J. R. Pritchard, Y. Pommier, S. J. Lippard and M. T. Hemann, *Nat Med*, 2017, **23**, 461-471.
27. A.-M. Florea and D. Büsselberg, *Cancers*, 2011, **3**, 1351-1371.
28. A. Mandic, J. Hansson, S. Linder and M. C. Shoshan, *J Biol Chem*, 2003, **278**, 9100-9106.
29. E. S. Kim, *Adv Exp Med Biol*, 2016, **893**, 189-209.
30. D. J. Huggins, W. Sherman and B. Tidor, *J Med Chem*, 2012, **55**, 1424-1444.
31. S. Kelderman, T. N. M. Schumacher and J. B. A. G. Haanen, *Mol Oncol*, 2014, **8**, 1132-1139.
32. M. R. Lackner, T. R. Wilson and J. Settleman, *Future Oncol*, 2012, **8**, 999-1014.
33. D.-W. Shen, L. M. Pouliot, M. D. Hall and M. M. Gottesman, *Pharmacol Rev*, 2012, **64**, 706-721.
34. C. R. R. Rocha, M. M. Silva, A. Quinet, J. B. Cabral-Neto and C. F. M. Menck, *Clinics (Sao Paulo)*, 2018, **73**, e478s-e478s.
35. H. H. W. Chen and M. T. Kuo, *Met Based Drugs*, 2010, **2010**, 430939.
36. P. Agostinis, K. Berg, K. A. Cengel, T. H. Foster, A. W. Girotti, S. O. Gollnick, S. M. Hahn, M. R. Hamblin, A. Juzeniene, D. Kessel, M. Korbelik, J. Moan, P. Mroz, D. Nowis, J. Piette, B. C. Wilson and J. Golab, *CA: Cancer J Clin*, 2011, **61**, 250-281.
37. S. A. McFarland, A. Mandel, R. Dumoulin-White and G. Gasser, *Curr Opin Chem Biol*, 2019, **56**, 23-27.
38. S. Mallidi, S. Anbil, A.-L. Bulin, G. Obaid, M. Ichikawa and T. Hasan, *Theranostics*, 2016, **6**, 2458-2487.

39. C. A. Robertson, D. H. Evans and H. Abrahamse, *J Photoch Photobiol B*, 2009, **96**, 1-8.
40. A. Zamora Martínez, G. Viguera Bautista, V. Rodriguez, M. Santana and J. Ruiz, *Coord Chem Rev*, 2018, **360**, 34-76.
41. N. Wu, J.-J. Cao, X.-W. Wu, C.-P. Tan, L.-N. Ji and Z.-W. Mao, *Dalton Trans*, 2017, **46**, 13482-13491.
42. L. K. McKenzie, I. V. Sazanovich, E. Baggaley, M. Bonneau, V. Guerchais, J. A. Williams, J. A. Weinstein and H. E. Bryant, *Chem Eur*, 2017, **23**, 234-238.
43. O. Kazuya and K. Yoshiaki, *Anti-Cancer Agents Med Chem*, 2008, **8**, 269-279.
44. H. Huang, S. Banerjee and P. J. Sadler, *ChemBioChem*, 2018, **19**, 1574-1589.
45. X. Tian, Y. Zhu, M. Zhang, L. Luo, J. Wu, H. Zhou, L. Guan, G. Battaglia and Y. Tian, *Chem Comm*, 2017, **53**, 3303-3306.
46. P. Zhang, C. K. C. Chiu, H. Huang, Y. P. Y. Lam, A. Habtemariam, T. Malcomson, M. J. Paterson, G. J. Clarkson, P. B. O'Connor, H. Chao and P. J. Sadler, *Angew Chem Int Ed*, 2017, **56**, 14898-14902.
47. H. Huang, S. Banerjee, K. Qiu, P. Zhang, O. Blacque, T. Malcomson, M. J. Paterson, G. J. Clarkson, M. Staniforth, V. G. Stavros, G. Gasser, H. Chao and P. J. Sadler, *Nat Chem*, 2019, **11**, 1041-1048.
48. N. J. Farrer, L. Salassa and P. J. Sadler, *Dalton Trans*, 2009, **48**, 10690-10701.
49. C. Imberti, P. Zhang, H. Huang and P. J. Sadler, *Angew Chem Int Ed*, 2020, **59**, 61-73.
50. V. E. Y. Lee, C. F. Chin and W. H. Ang, *Dalton Trans*, 2019, **48**, 7388-7393.
51. H. Shi, C. Imberti and P. J. Sadler, *Inorg Chem Front*, 2019, **6**, 1623-1638.
52. K. Mitra, *Dalton Trans*, 2016, **45**, 19157-19171.
53. A. Vogler, A. Kern and J. Hüttermann, *Angew Chem Int Ed*, 1978, **17**, 524-525.
54. N. J. Farrer, J. A. Woods, L. Salassa, Y. Zhao, K. S. Robinson, G. Clarkson, F. S. Mackay and P. J. Sadler, *Angew Chem Int Ed*, 2010, **49**, 8905-8908.
55. P. Müller, B. Schröder, J. A. Parkinson, N. A. Kratochwil, R. A. Coxall, A. Parkin, S. Parsons and P. J. Sadler, *Angew Chem Int Ed*, 2003, **42**, 335-339.
56. F. S. Mackay, J. A. Woods, H. Moseley, J. Ferguson, A. Dawson, S. Parsons and P. J. Sadler, *Chemistry*, 2006, **12**, 3155-3161.
57. P. J. Bednarski, R. Grunert, M. Zielzki, A. Wellner, F. S. Mackay and P. J. Sadler, *Chem Biol*, 2006, **13**, 61-67.

58. P. J. Bednarski, K. Korpis, A. F. Westendorf, S. Perfahl and R. Grunert, *Philos Trans A Math Phys Eng Sci*, 2013, **371**, 20120118.
59. R. R. Vernooij, T. Joshi, M. D. Horbury, B. Graham, E. I. Izgorodina, V. G. Stavros, P. J. Sadler, L. Spiccia and B. R. Wood, *Chemistry* 2018, **24**, 5790-5803.
60. S. Mukhopadhyay, C. M. Barnés, A. Haskel, S. M. Short, K. R. Barnes and S. J. Lippard, *Bioconjugate Chem* 2008, **19**, 39-49.
61. X. Li, J. Mu, F. Liu, E. W. P. Tan, B. Khezri, R. D. Webster, E. K. L. Yeow and B. Xing, *Bioconjug Chem*, 2015, **26**, 955-961.
62. H. Shi, I. Romero-Canelón, M. Hreusova, O. Novakova, V. Venkatesh, A. Habtemariam, G. J. Clarkson, J.-I. Song, V. Brabec and P. J. Sadler, *Inorg Chem*, 2018, **57**, 14409-14420.
63. X.-D. Yang, H.-J. Xiang, L. An, S.-P. Yang and J.-G. Liu, *New J Chem*, 2015, **39**, 800-804.
64. H. Shi, C. Imberti, G. J. Clarkson and P. J. Sadler, *Inorg Chem Front*, 2020, **7**, 3533-3540.
65. H. Shi, *PhD Thesis (University of Warwick)*, 2019.
66. G. Gasser, I. Ott and N. Metzler-Nolte, *J Med Chem*, 2011, **54**, 3-25.
67. J. P. Mészáros, J. M. Poljarevic, G. T. Gál, N. V. May, G. Spengler and É. A. Enyedy, *J Inorg Biochem*, 2019, **195**, 91-100.
68. A. K. Renfrew, N. S. Bryce and T. Hambley, *Chem Eur J*, 2015, **21**, 15224-15234.
69. Y. Fu, A. Habtemariam, A. M. Basri, D. Braddick, G. J. Clarkson and P. J. Sadler, *Dalton Trans*, 2011, **40**, 10553-10562.
70. L. Zeng, P. Gupta, Y. Chen, E. Wang, L. Ji, H. Chao and Z. S. Chen, *Chem Soc Rev*, 2017, **46**, 5771-5804.
71. A. Levina, A. Mitra and P. A. Lay, *Metallomics*, 2009, **1**, 458-470.
72. U. Ndagi, N. Mhlongo and M. E. Soliman, *Drug Des Devel Ther*, 2017, **11**, 599-616.
73. S. M. Meier-Menches, C. Gerner, W. Berger, C. G. Hartinger and B. K. Keppler, *Chem Soc Rev*, 2018, **47**, 909-928.
74. E. S. Antonarakis and A. Emadi, *Cancer Chemother Pharmacol*, 2010, **66**, 1-9.

75. C. G. Hartinger, S. Zorbas-Seifried, M. A. Jakupec, B. Kynast, H. Zorbas and B. K. Keppler, *J Inorg Biochem*, 2006, **100**, 891-904.
76. S. Thota, D. A. Rodrigues, D. C. Crans and E. J. Barreiro, *J Med Chem*, 2018, **61**, 5805-5821.
77. E. Alessio and L. Messori, *Molecules*, 2019, **24**, 1995.
78. J. Coverdale, T. Laroia-McCarron and I. Romero-Canelón, *Inorganics*, 2019, **7**, 31.
79. P. Kumar, R. K. Gupta and D. S. Pandey, *Chem Soc Rev*, 2014, **43**, 707-733.
80. R. E. Morris, R. E. Aird, P. del Socorro Murdoch, H. Chen, J. Cummings, N. D. Hughes, S. Parsons, A. Parkin, G. Boyd, D. I. Jodrell and P. J. Sadler, *J Med Chem*, 2001, **44**, 3616-3621.
81. R. L. Hayward, Q. C. Schornagel, R. Tente, J. S. Macpherson, R. E. Aird, S. Guichard, A. Habtemariam, P. Sadler and D. I. Jodrell, *Cancer Chemoth Pharm*, 2005, **55**, 577-583.
82. A. Bergamo, A. Masi, A. F. Peacock, A. Habtemariam, P. J. Sadler and G. Sava, *J Inorg Biochem*, 2010, **104**, 79-86.
83. F. Wang, J. Xu, A. Habtemariam, J. Bella and P. J. Sadler, *J Am Chem Soc*, 2005, **127**, 17734-17743.
84. M. P. Gamcsik, M. S. Kasibhatla, S. D. Teeter and O. M. Colvin, *Biomarkers* 2012, **17**, 671-691.
85. S. M. Meier, D. Kreutz, L. Winter, M. H. M. Klose, K. Cseh, T. Weiss, A. Bileck, B. Alte, J. C. Mader, S. Jana, A. Chatterjee, A. Bhattacharyya, M. Hejl, M. A. Jakupec, P. Heffeter, W. Berger, C. G. Hartinger, B. K. Keppler, G. Wiche and C. Gerner, *Angew Chem Int Ed*, 2017, **56**, 8267-8271.
86. P. C. A. Bruijninx and P. J. Sadler, *Adv Inorg Chem*, 2009, **61**, 1-62.
87. P. A. Lay and W. D. Harman, in *Adv Inorg Chem*, ed. A. G. Sykes, Academic Press, 1991, vol. 37, pp. 219-379.
88. M. Hanif, M. V. Babak and C. G. Hartinger, *Drug Discov Today*, 2014, **19**, 1640-1648.
89. K. Suntharalingam, T. C. Johnstone, P. M. Bruno, W. Lin, M. T. Hemann and S. J. Lippard, *J Am Chem Soc*, 2013, **135**, 14060-14063.
90. C. Yang, W. Wang, G.-D. Li, H.-J. Zhong, Z.-Z. Dong, C.-Y. Wong, D. W. J. Kwong, D.-L. Ma and C.-H. Leung, *Sci Rep*, 2017, **7**, 42860.

91. B. Cebrián-Losantos, A. A. Krokhin, I. N. Stepanenko, R. Eichinger, M. A. Jakupec, V. B. Arion and B. K. Keppler, *Inorg Chem* 2007, **46**, 5023-5033.
92. Y. Fu, A. Habtemariam, A. M. Pizarro, S. H. van Rijt, D. J. Healey, P. A. Cooper, S. D. Shnyder, G. J. Clarkson and P. J. Sadler, *J Med Chem*, 2010, **53**, 8192-8196.
93. Y. Fu, M. J. Romero, A. Habtemariam, M. E. Snowden, L. Song, G. J. Clarkson, B. Qamar, A. M. Pizarro, P. R. Unwin and P. J. Sadler, *Chem Sci*, 2012, **3**, 2485-2494.
94. J. M. Hearn, I. Romero-Canelon, A. F. Munro, Y. Fu, A. M. Pizarro, M. J. Garnett, U. McDermott, N. O. Carragher and P. J. Sadler, *PNAS*, 2015, **112**, E3800-3805.
95. C. Sanchez-Cano, I. Romero-Canelón, Y. Yang, I. J. Hands-Portman, S. Bohic, P. Cloetens and P. J. Sadler, *Chem Eur*, 2017, **23**, 2512-2516.
96. S. H. van Rijt, I. Romero-Canelon, Y. Fu, S. D. Shnyder and P. J. Sadler, *Metallomics*, 2014, **6**, 1014-1022.
97. J. P. C. Coverdale, H. E. Bridgewater, J.-I. Song, N. A. Smith, N. P. E. Barry, I. Bagley, P. J. Sadler and I. Romero-Canelón, *J Med Chem*, 2018.
98. I. Romero-Canelón, M. Mos and P. J. Sadler, *J Med Chem*, 2015, **58**, 7874-7880.
99. X. Zhang, F. Ponte, E. Borfecchia, A. Martini, C. Sanchez-Cano, E. Sicilia and P. J. Sadler, *Chem Comm*, 2019, **55**, 14602-14605.
100. R. J. Needham, C. Sanchez-Cano, X. Zhang, I. Romero-Canelón, A. Habtemariam, M. S. Cooper, L. Meszaros, G. J. Clarkson, P. J. Blower and P. J. Sadler, *Angew Chem Int Ed*, 2017, **56**, 1017-1020.
101. C. Sanchez-Cano, I. Romero-Canelón, K. Geraki and P. J. Sadler, *J Inorg Biochem*, 2018, **185**, 26-29.
102. C. Sanchez-Cano, D. Gianolio, I. Romero-Canelón, R. Rucoulou and P. J. Sadler, *Chem Comm*, 2019, **55**, 7065-7068.
103. E. Kimoto, H. Tanaka, J. Gyotoku, F. Morishige and L. Pauling, *Cancer Res*, 1983, **43**, 824-828.
104. J. J. Soldevila-Barreda and P. J. Sadler, *Curr Opin Mol Med*, 2015, **25**, 172-183.
105. J. J. Soldevila-Barreda and N. Metzler-Nolte, *Chem Rev*, 2019, **119**, 829-869.

106. A. P. Trotta, J. D. Gelles, M. N. Serasinghe, P. Loi, J. L. Arbiser and J. E. Chipuk, *J Biol Chem*, 2017, **292**, 11727-11739.
107. F. Chen, I. Romero-Canelón, J. J. Soldevila-Barreda, J.-I. Song, J. P. C. Coverdale, G. J. Clarkson, J. Kasparkova, A. Habtemariam, M. Wills, V. Brabec and P. J. Sadler, *Organometallics*, 2018, **37**, 1555-1566.
108. T. Völker, F. Dempwolff, P. L. Graumann and E. Meggers, *Angew Chem Int Ed*, 2014, **53**, 10536-10540.
109. S. Alonso-de Castro, A. L. Cortajarena, F. López-Gallego and L. Salassa, *Angew Chem Int Ed Engl*, 2018, **57**, 3143-3147.
110. A. L. Noffke, A. Habtemariam, A. M. Pizarro and P. J. Sadler, *Chem Comm*, 2012, **48**, 5219-5246.
111. R. Noyori and S. Hashiguchi, *Acc Chem Res*, 1997, **30**, 97-102.
112. T. Ohkuma, *Proc Jpn Acad Ser B Phys Biol Sci*, 2010, **86**, 202-219.
113. C. A. Sandoval, T. Ohkuma, K. Muñiz and R. Noyori, *J Am Chem Soc*, 2003, **125**, 13490-13503.
114. J. Václavík, P. Sot, B. Vilhanová, J. Pecháček, M. Kuzma and P. Kačer, *Molecules*, 2013, **18**, 6804-6828.
115. T. Ikariya and A. J. Blacker, *Acc Chem Res*, 2007, **40**, 1300-1308.
116. T. Ikariya, K. Murata and R. Noyori, *Org Biomol Chem*, 2006, **4**, 393-406.
117. M. Yamakawa, H. Ito and R. Noyori, *J Am Chem Soc*, 2000, **122**, 1466-1478.
118. M. Yamakawa, I. Yamada and R. Noyori, *Angew Chem Int Ed*, 2001, **40**, 2818-2821.
119. T. Ohkuma, N. Utsumi, K. Tsutsumi, K. Murata, C. Sandoval and R. Noyori, *J Am Chem Soc*, 2006, **128**, 8724-8725.
120. J. P. Coverdale, C. Sanchez-Cano, G. J. Clarkson, R. Soni, M. Wills and P. J. Sadler, *Chem Eur*, 2015, **21**, 8043-8046.
121. R. Soni, T. H. Hall, B. P. Mitchell, M. R. Owen and M. Wills, *J Org Chem*, 2015, **80**, 6784-6793.
122. J. P. C. Coverdale, I. Romero-Canelón, C. Sanchez-Cano, G. J. Clarkson, A. Habtemariam, M. Wills and P. J. Sadler, *Nat Chem*, 2018, **10**, 347.
123. K. G. de la Cruz-López, L. J. Castro-Muñoz, D. O. Reyes-Hernández, A. García-Carrancá and J. Manzo-Merino, *Front Oncol*, 2019, **9**, 1143-1143.
124. W. Wang and X. Yang, *Chem Comm*, 2019, **55**, 9633-9636.

125. R. Zhang, L. Li, Y. Sultanbawa and Z. P. Xu, *Am J Nucl Med Mol Imaging*, 2018, **8**, 169-188.
126. A. A. Hummer and A. Rompel, *Metallomics*, 2013, **5**, 597-614.
127. M. J. Pushie, I. J. Pickering, M. Korbass, M. J. Hackett and G. N. George, *Chem Rev*, 2014, **114**, 8499-8541.
128. X. Ying, N. J. Barlow and M. H. Feuston, in *Reproductive and Developmental Toxicology*, ed. R. C. Gupta, Academic Press, San Diego, 2011, pp. 983-1000.
129. B. De Samber, M. J. Niemiec, B. Laforce, J. Garrevoet, E. Vergucht, R. De Rycke, P. Cloetens, C. F. Urban and L. Vincze, *PLoS One*, 2016, **11**, e0165604.
130. G. P. Williams, W. M. Haynes and D. R. Lide, *Electron binding energies of the elements*, CRC Press, USA, 92 edn., 2011.
131. J. Z. Zhang, N. S. Bryce, A. Lanzirrotti, C. K. J. Chen, D. Paterson, M. D. de Jonge, D. L. Howard and T. W. Hambley, *Metallomics*, 2012, **4**, 1209-1217.
132. B. Laforce, C. Carlier, B. Vekemans, J. Villanova, R. Tucoulou, W. Ceelen and L. Vincze, *Sci Rep*, 2016, **6**, 29999.
133. J. Popović, A. Klajn, T. Paunesku, Q. Ma, S. Chen, B. Lai, M. Stevanović, G. E. J. C. Woloschak and M. Neurobiology, *Cell Mol Neurobiol*, 2019, **39**, 619-636.
134. S. Gil, A. Carmona, G. Martinez-Criado, A. Leon, Y. Prezado and M. Sabes, *Biol Trace Elem Res*, 2015, **163**, 177-183.
135. M. D. Hall, C. T. Dillon, M. Zhang, P. Beale, Z. Cai, B. Lai, A. P. Stampfl and T. W. Hambley, *J Biol Inorg Chem*, 2003, **8**, 726-732.
136. R. Koba, H. Fujita, M. Nishibori, K. Saeki, K. Nagayoshi, Y. Sadakari, S. Nagai, O. Sekizawa, K. Nitta, T. Manabe, T. Ueki, T. Ishida, Y. Oda and M. Nakamura, *Int J Cancer*, 2020, **146**, 2498-2509.
137. J. B. Aitken, S. Antony, C. M. Weekley, B. Lai, L. Spiccia and H. H. Harris, *Metallomics*, 2012, **4**, 1051-1056.
138. S. Antony, J. B. Aitken, S. Vogt, B. Lai, T. Brown, L. Spiccia and H. H. Harris, *J Biol Inorg Chem*, 2013, **18**, 845-853.
139. J. J. Conesa, A. C. Carrasco, V. Rodríguez-Fanjul, Y. Yang, J. L. Carrascosa, P. Cloetens, E. Pereiro and A. M. Pizarro, *Angew Chem Int Ed*, 2020, **59**, 1270-1278.

140. F. Fus, Y. Yang, H. Z. S. Lee, S. Top, M. Carriere, A. Bouron, A. Pacureanu, J. C. da Silva, M. Salmain, A. Vessières, P. Cloetens, G. Jaouen and S. Bohic, *Angew Chem Int Ed*, 2019, **58**, 3461-3465.
141. M. D. Hall, R. A. Alderden, M. Zhang, P. J. Beale, Z. Cai, B. Lai, A. P. Stampfl and T. W. Hambley, *J Struct Biol*, 2006, **155**, 38-44.
142. C. C. Konkankit, J. Lovett, H. H. Harris and J. J. Wilson, *Chem Comm*, 2020, **48**, 6515-6518.
143. S. Chen, T. Paunesku, Y. Yuan, J. Deng, Q. Jin, Y. Hong, D. Vine, B. Lai, C. Flachenecker, B. Hornberger, K. Brister, C. Jacobsen, G. Woloschak and S. Vogt, *AIP Conf Proc*, 2016, **1696**, 020028.
144. J. E. Penner-Hahn, *Physics of X-ray Absorption*, USA, America, 2005.
145. J. Yano and V. K. Yachandra, *Photosynth Res*, 2009, **102**, 241-254.
146. C. K. J. Chen, P. Kappen, D. Gibson and T. W. Hambley, *Dalton Trans*, 2020, **49**, 7722-7736.
147. P. Horowitz and J. A. Howell, *Science*, 1972, **178**, 608-611.
148. J. Groen, J. J. Conesa, R. Valcárcel and E. Pereiro, *Biophys Rev*, 2019, **11**, 611-619.
149. M. Do, S. A. Isaacson, G. McDermott, M. A. Le Gros and C. A. Larabell, *Arch Biochem Biophys*, 2015, **581**, 111-121.
150. R. Carzaniga, M. C. Domart, E. Duke and L. M. Collinson, *Methods Cell Biol*, 2014, **124**, 151-178.
151. E. M. Duke, M. Razi, A. Weston, P. Guttmann, S. Werner, K. Henzler, G. Schneider, S. A. Tooze and L. M. Collinson, *Ultramicroscopy*, 2014, **143**, 77-87.
152. C. Moscheni, E. Malucelli, S. Castiglioni, A. Procopio, C. De Palma, A. Sorrentino, P. Sartori, L. Locatelli, E. Pereiro, J. A. Maier and S. Iotti, *Cancers*, 2019, **11**, 1254.
153. M. Harkiolaki, M. Darrow, M. Spink, E. Kosior, K. Dent and E. Duke, *Emerg Top Life Sci*, 2018, **2**, ETLS20170086.
154. M. Chiappi, J. J. Conesa, E. Pereiro, C. O. S. Sorzano, M. J. Rodríguez, K. Henzler, G. Schneider, F. J. Chichón and J. L. Carrascosa, *J Nanobiotechnology*, 2016, **14**, 15-15.



155. S. Gil, E. Solano, F. Martínez-Trucharte, J. Martínez-Esaín, A. J. Pérez-Berná, J. J. Conesa, C. Kamma-Lorger, M. Alsina and M. Sabés, *PLoS One*, 2020, **15**, e0230022.
156. I. Kounatidis, M. L. Stanifer, M. A. Phillips, P. Paul-Gilloteaux, X. Heiligenstein, H. Wang, C. A. Okolo, T. M. Fish, M. C. Spink, D. I. Stuart, I. Davis, S. Boulant, J. M. Grimes, I. M. Dobbie and M. Harkiolaki, *Cell*, 2020, **182**, 515-530.
157. M. Phillips, M. Harkiolaki, D. Pinto, R. Parton, A. Palanca, M. Garcia-Moreno, I. Kounatidis, J. Sedat, D. Stuart, A. Castello, M. Booth, I. Davis and I. Dobbie, *Optica*, 2020, **2**, 802-812.

# **Chapter 2**

## **Materials, methods and instrumentation**

## 2.1 Materials

### 2.1.1 Chemical reagents

All commercial solvents were purchased from Sigma Aldrich and used as specified by the manufacturer.

**Table 2.1.** List of chemical reagents and suppliers.

Reagent	Supplier
(1 <i>R</i> ,2 <i>R</i> )-(+)-1,2-Diphenylethylenediamine (97%)	Sigma Aldrich
(1 <i>S</i> ,2 <i>S</i> )-(-)-1,2-Diphenylethylenediamine (97%)	Sigma Aldrich
3-bromobenzene sulfonyl chloride (96%)	Sigma Aldrich
4-bromobenzene sulfonyl chloride (98%)	Sigma Aldrich
4-iodobenzenesulfonyl chloride (95%)	Sigma Aldrich
4-methoxybenzenesulfonyl chloride (99%)	Sigma Aldrich
5:2 Formic acid triethylamine azeotrope (>99%)	Sigma Aldrich
Acetophenone (98%)	Sigma Aldrich
d <sub>6</sub> -benzene (99.6%)	Sigma Aldrich
d-chloroform (99.6%)	Sigma Aldrich
d <sub>6</sub> -DMSO (99.7%)	Sigma Aldrich
Magnesium sulfate	Sigma Aldrich
Sodium acetate (>99%)	Sigma Aldrich
Sodium formate (>99%)	Sigma Aldrich
Sodium hydrogen carbonate	Sigma Aldrich
Triethylamine (99.5%)	Sigma Aldrich
Tris-(hydroxymethyl)aminomethane (>99%)	Sigma Aldrich
α-phellandrene (>85%)	Sigma Aldrich
Potassium hydroxide	Fisher Scientific
Sodium acetate anhydrous	Fisher Scientific
Osmium trichloride hydrate (OsCl <sub>3</sub> .xH <sub>2</sub> O)	Heraeus

### **2.1.2 ICP-OES and ICP-MS reagents**

Osmium ( $1000 \pm 10$   $\mu\text{g/mL}$  hexchlorodiammonium osmate in 15% v/v hydrochloric acid, platinum ( $1001 \pm 12$  mg/L TraceCERT® platinum in 5% v/v hydrochloric acid), ruthenium ( $995 \pm 4$   $\mu\text{g/mL}$  ruthenium chloride in 10% v/v hydrochloric acid), iridium ( $995 \pm 3$   $\mu\text{g/mL}$ , iridium chloride in 10% v/v hydrochloric acid) and bromine ( $1000 \pm 5$   $\mu\text{g/mL}$  potassium bromide in water) for ICP trace analysis were purchased from Inorganic Ventures and stored at 276 K. Thiourea (>99%), L-ascorbic acid (>99%) and sodium chloride (99.9999%) were purchased from Sigma Aldrich. 72% v/v nitric acid ( $\text{HNO}_3$ ) was freshly distilled and diluted with milliQ water. 25% m/v tetramethylammonium hydroxide (TMAH) in water was purchased from Fisher Scientific.

### **2.1.3 Synchrotron membranes and grids**

Silicon nitride ( $\text{Si}_3\text{N}_4$ ) membranes were purchased from Silson ltd (5×5 mm frame size, 200  $\mu\text{m}$  frame thickness, 1.5×1.5 mm membrane size, 500 nm membrane thickness, catalogue number SiRN-5.0(0)-200-1.5-500). Quantifoil R2/2 holey carbon films (Au) 200 mesh F1 finder grids were purchased from Quantifoil Micro Tools GmbH (Germany).

## 2.2 Biological Materials

### 2.2.1 Human cell lines

All cell lines were purchased from ECACC (European Collection of Authenticated Cell Cultures). Mycoplasma-free status was confirmed every 6 months.

**Table 2.2.** Summary of human cell lines used in this thesis.

Cell line	Type	Catalogue number
A2780	Human ovarian carcinoma	93112519
A549	Human lung carcinoma	86012804
MCF7	Human breast adenocarcinoma	86012803
PC3	Human prostate adenocarcinoma	90112714
MRC5	Human lung fibroblasts (non-cancerous)	84101801

### 2.2.2 Biological consumables

**Table 2.3.** Summary of biological consumables used in this thesis.

Consumable	Supplier
Filter-capped tissue culture flasks	Greiner Bio-One Ltd
F-bottom tissue culture plates	Greiner Bio-One Ltd
Tissue culture dish (100×20 mm)	Greiner Bio-One Ltd
Tissue culture dish (145×20 mm)	Greiner Bio-One Ltd
C-chip disposable haemocytometers	Labtech International Ltd
15 mL falcon conical centrifuge tube	Scientific Laboratory Supplies
50 mL falcon conical centrifuge tube	Scientific Laboratory Supplies
1.5 mL eppendorf tubes	Scientific Laboratory Supplies

### 2.2.3 Biological reagents

**Table 2.4.** Summary of biological reagents used in this thesis. All reagents used in tissue culture were of biological grade. Further information about trace biological elements and their concentrations present in FCS, DMEM, RPMI-1640, PBS and HBSS are presented in **Appendix (Table A1-5)**. This must be considered for synchrotron-XRF elemental mapping of endogenous elements in cancer cells, particularly for elemental quantification (and less so for elemental distribution).

Reagent	Supplier
Dulbecco's Modified Eagles Medium (DMEM)	Fisher Scientific
LysoTracker Red DND-99 ( $\lambda_{\text{ex/em}}=577/590$ nm)	Fisher Scientific
MitoTracker Deep Red FM ( $\lambda_{\text{ex/em}}=644/665$ nm)	Fisher Scientific
MitoTracker Red FM 580 ( $\lambda_{\text{ex/em}}=581/644$ nm)	Fisher Scientific
Phosphate Buffered Saline (PBS)	Fisher Scientific
Trichloroacetic Acid (TCA)	Fisher Scientific
Methyl- $\beta$ -cyclodextrin	Sigma Aldrich
Chloroquine diphosphate salt	Sigma Aldrich
Ethanol	Sigma Aldrich
Isopropanol	Sigma Aldrich
Poly-L-lysine solution (0.01%)	Sigma Aldrich
Propidium iodide (PI)	Sigma Aldrich
Sulforhodamine B	Sigma Aldrich
Verapamil hydrochloride	Sigma Aldrich
Roswell Park Memorial Institute (RPMI-1640)	Scientific Laboratory
non-phenol red	Supplies
Heat-inactivated fetal calf serum (FCS)	PPA Laboratories
Penicillin streptomycin (penn/strep)	PPA Laboratories
L-glutamine	PPA Laboratories
Trypsin/EDTA	PPA Laboratories
FractionPREP (Biovision) cell fractionation kit	Cambridge Bioscience Ltd
Hank's Balanced Salt Solution (HBSS)	BIOCHROMM (Merck)
Gold nanoparticle fiducials (AuNP, d=250 nm)	BBi Solutions

## 2.3 Instrumentation at the University of Warwick

### 2.3.1 Mass spectrometry (MS)

All low resolution mass spectrometry measurements were performed on an ESI-MS Agilent 6130B, with samples prepared in acetonitrile (unless specified otherwise), using positive ion mode ( $m/z$  range=50-500 and 400-1000). High resolution mass spectrometry measurements were obtained by Dr Lijiang Song (University of Warwick) using a Bruker UHR-Q-TOF MaXis, with a scan range of 50-3000  $m/z$  for positive ions. Samples were prepared in acetonitrile (unless specified otherwise). Analysis was carried out through direct infusion (2  $\mu\text{L}/\text{min}$ ) with a syringe pump. ESI positive ion source conditions were as follows: -500 V end-plate offset, -3000 V capillary, 0.4 bar nebulizer  $\text{N}_2$  gas, dry  $\text{N}_2$  gas flow rate 4 L/min, 453 K dry temperature, RF of funnel 200 Vpp, RF funnel 200 Vpp, 250 Vpp ramping, 121  $\mu\text{sec}$  transfer time, 1  $\mu\text{sec}$  pre-pulse storage time.

### 2.3.2 Nuclear Magnetic Resonance Spectroscopy (NMR)

High resolution  $^1\text{H}$  NMR and  $^{13}\text{C}$  NMR of ligands and complexes (**Chapter 3**) were obtained by Dr. Ivan Prokes on a HD500 Bruker Avance III HD 500 MHz high-field NMR instrument. Samples were prepared in either  $\text{CDCl}_3$  or  $\text{d}_6$ -DMSO in 5 mm NMR tubes at 298 K using standard pulse sequences. The  $^1\text{H}$  NMR kinetic experiments presented in **Chapter 3** were performed on an AV400 Bruker Avance III 400 MHz instrument, using a method published in the literature.<sup>1</sup> Samples were prepared in  $\text{d}_6$ -benzene under an inert  $\text{N}_2$  atmosphere at 310 K in a 5 mm  $\text{N}_2$ -purged NMR tube. All data were processed using TOPSPIN 4.0 NMR software (Bruker).

### 2.3.3 Inductively-coupled plasma (ICP) instruments

Inductively-coupled plasma (ICP) instruments have been used to measure trace amounts of osmium, platinum, iridium and bromine in aqueous cell culture media or in acid or base cell pellet digests. For samples containing osmium, 3.6% v/v stabilized nitric acid was prepared using 10 mM thiourea and 100 mg/L L-ascorbic acid to chelate osmium in solution and prevent the formation of osmium tetroxide ( $\text{OsO}_4$ ).<sup>2, 3</sup> Stabilized solutions were also used for the analysis of platinum and iridium, which were unaffected by the presence of thiourea and L-ascorbic acid.

**ICP-OES.** Solutions of complexes in 5% v/v DMSO and 95% v/v DMEM (or RPMI-1640 as specified) were analysed using PerkinElmer 5300DV ICP-OES. Calibration standards of analytes of interest were prepared in the range 50-700 ppb from a 10'000 ppm certified reference materials (Inorganic Ventures) in 3.6% v/v nitric acid (10 mM thiourea, 100 mg/L L-ascorbic acid). The salinity of the calibration standards were adjusted to the sample matrix of culture media using NaCl. Samples were diluted appropriately to fit the calibration range, so that dissolved solids did not exceed 0.1% w/v. Samples were analysed on a Perkin Elmer Optima 5300 DV Optical Emission Spectrophotometer: Os ( $\lambda=225.585$ ; 228.226 nm), Ir ( $\lambda=237.278$ ; 208.882 nm) and Pt ( $\lambda=204.937$ ; 265.945 nm). Data were processed in WinLab32 Offline 3.4.1 software for Windows.

**ICP-MS.** ICP-MS analysis for cellular accumulation experiments were analysed on an Agilent 7900 series ICP-MS spectrometer in no-gas mode. Calibrations of the elements of interest ( $^{189}\text{Os}$ ,  $^{79}\text{Br}$ ,  $^{195}\text{Pt}$  and  $^{192}\text{Ir}$ ) were prepared in the range 0.1-1000 ppb from 10'000 ppm certified reference materials (Inorganic Ventures) using either 3.6% v/v nitric acid (380.6 mg thiourea, 50 mg L-ascorbic acid in 500 mL) or 1% m/v TMAH, as specified. Dissolved solids did not exceed 0.1% w/v. For TMAH studies of  $^{189}\text{Os}$  and  $^{79}\text{Br}$ ,  $^{101}\text{Ru}$  (50 ppb) was used as an internal standard. For all other ICP-MS experiments,  $^{166}\text{Er}$  (10 ppb) was used.



### 2.3.4 Elemental analysis (CHN)

Elemental analysis of ligands and complexes (**Chapter 3**) were performed by Exeter Analytical (Warwick Analytical Services) using a CE440 Exeter elemental analyser to analyse for carbon (C), hydrogen (H) and nitrogen (N) content.

### 2.3.5 X-ray crystallography

X-ray crystallography data of Os[(*p*-cym)(BsDPEN)] complexes (**Chapter 3**) were obtained by Dr. Guy Clarkson (University of Warwick) from crystals in 1:2 DCM:hexane. A single crystal was mounted onto a glass fibre (using Fromblin oil) and analysed at 150 K on a Oxford Gemini diffractometer (with a ruby CCD). In Olex2,4 and ShelXL5 softwares ('Direct calculation') the chemical structure was determined,<sup>4, 5</sup> and refined using 'Least Square method'.<sup>5</sup> The complexes were enantiospecific (synthesized from chiral reagents) and structure determination was refined using BASF/TWIN in Shelx2014 software to give relatively low Flack parameters. Data were visualised and analysed using Mercury 4.0.<sup>6</sup>

### 2.3.6 Plunge-freezing and freeze-drying

Silicon nitride (Si<sub>3</sub>N<sub>4</sub>) membranes were plunge-frozen using an in-house manufactured manual plunge-freezer with assistance from Dr Saskia Bakker and Mr Ian Hands-Portman (School of Life Sciences, University of Warwick). Freezing was achieved using a 30% propane:ethane mixture liquefied using liquid nitrogen. Si<sub>3</sub>N<sub>4</sub> membranes were freeze-dried using Alpha 2-4 LDplus Christ model, operating at 188 K under vacuum (0.0024 mbar).

## 2.4 Biological methods

### 2.4.1 *In vitro* biological studies

*In vitro* cell culture work was carried out under the guidance of Dr James P. C. Coverdale, Dr Hannah E. Bridgewater and Mrs Ji-Inn Song (School of Life Sciences, University of Warwick). All cell lines used in this thesis were adherent (grown as monolayers on a 2D surface). All cell lines are specified in **Section 2.2.1**.

**Preparation of cell culture media.** DMEM or RPMI-1640 was supplemented with 10% FCS, 1% pen/strep and 1% L-glutamine (2 mM), and incubated at 310 K prior to use.

**Defrosting cells.** A vial of frozen cells (containing *ca.*  $1 \times 10^6$  cells) stored in liquid nitrogen was rapidly defrosted at 310 K. The cell solution was re-suspended in fully prepared DMEM (4 mL) to obtain a single cell suspension. The sample was centrifuged (298 K, 5 min, 1000 rpm), the supernatant removed and the pellet re-suspended in DMEM (3 mL). The solution was transferred to a T25 cell culture flask and incubated (310 K, 5% CO<sub>2</sub>) until a cell confluence of 80-90% was achieved.

**General Cell Maintenance.** Upon 80-90% monolayer cell confluence on the surface of the cell culture flask, the supernatant was removed, cells washed with PBS and 0.25% trypsin/EDTA (1 mL) was added (5 min, 310 K). Once cells were detached and in solution, culture media was added to quench trypsin activity, and the resulting solution pipetted to form a single cell suspension. The cell suspension was transferred to a new culture flask for further incubation (310 K, 5% CO<sub>2</sub>).

**Stock solution preparation.** Stock solutions of test compounds (Os, Ir and Pt) for biological investigations were prepared in 5% v/v DMSO in culture media (95% v/v DMEM or RPMI-1640, as specified) and analysed by ICP-OES to determine the metal concentration prior to use. For photoactivatable experiments (**Chapters 4-5**), RPMI-1640 non phenol red was used to prepare stock solutions, and samples were protected from light. Stocks of test compounds (100  $\mu$ M) were diluted 50-fold in 3.6% v/v stabilised nitric acid (**Section 2.3.3**). Total dissolved solids did not exceed 0.1% w/v. A calibration of elements of interest were prepared in the range 50-700 ppb and the salinity adjusted with NaCl, as described in **Section 2.3.3**.

**Sulforhodamine B (SRB) Assay.** The antiproliferative activities of complexes were determined using the SRB assay.<sup>7</sup> At 80-90% cell confluence, a single cell suspension was obtained as previously described. Cells were counted in duplicate ( $2 \times 10^4$   $\mu$ L) using a haemocytometer and 96-well flat bottom plates were seeded (5000 cells per well in 150  $\mu$ L) and incubated for 48 h (310 K, 5% CO<sub>2</sub>). ICP-OES corrected stock solutions of test compounds (100  $\mu$ M) and CDDP (1000  $\mu$ M) complexes were prepared in 5% v/v DMSO and 95% v/v culture media and diluted to six concentrations in the range 0.01-150  $\mu$ M. The supernatant from each plate was removed and solutions of test compound were added to each well (in duplicate of triplicate), and incubated for a fixed time (24 h, unless specified otherwise). The supernatant was removed, cells were washed with PBS, and complex-free media (200  $\mu$ L) was added (72 h, 310 K, 5% CO<sub>2</sub>). Cells were fixed with 10% TCA (1 h, 277 K). The plates were washed with water (10 $\times$ ) and air-dried. SRB dye (0.4% prepared in 1% acetic acid) was added to each well (50  $\mu$ L) and incubated for 30 min. The plates were washed with 1 % acetic acid (7 $\times$ ) and heat-dried. 10 mM tris base pH 10.5 (150  $\mu$ L) was added to each well and incubated for 1 h. The UV absorbance at 492 nm was measured using SkanIt multiplate analyser (Thermo Scientific). Data were processed in Excel and plotted as a sigmoidal dose-response curve (logarithm of concentration vs. percentage cell survival) in Origin Pro 2016 normalised to the untreated (control) wells.

### 2.4.2 ICP-MS acid digestion of cell pellets

Cell pellets were digested using freshly-distilled 72% *v/v* nitric acid (200  $\mu$ L) at 353 K for 12 h. The samples were then diluted 20-fold using stabilised milliQ water (containing 10 mM thiourea and 100 mg/L L-ascorbic acid) to achieve a final concentration of 3.6% *v/v* nitric acid (total dissolved solids <0.2% *w/v*). Data acquisition was performed using an internal standard of erbium ( $^{166}\text{Er}$ =10 ppb) in no gas mode. Calibration standards of elements of interest were prepared as previously described (Section 2.3.3).

### 2.4.3 ICP-MS alkaline digestion of cell pellets

Cell pellets were digested using an aqueous solution of 25% *m/v* TMAH (500  $\mu$ L) at 353 K overnight, adapted from methods published in the literature.<sup>8, 9</sup> The samples were then diluted 25-fold to achieve 1% *m/v* TMAH (total dissolved solids <0.1% *w/v*) using milliQ water. Data acquisition was performed using an internal standard of ruthenium ( $^{101}\text{Ru}$ =50 ppb). Calibration standards were prepared as previously described (Section 2.3.3).

**Os and Br ICP-MS method validation.** A calibration containing osmium and bromine in 1% *m/v* TMAH was prepared in the range 0.1-1000 ppb. Calibration curves of  $R^2=1.0000$  and  $0.9999$  were obtained for osmium ( $^{189}\text{Os}$ ) and bromine ( $^{79}\text{Br}$ ), using  $^{101}\text{Ru}$  (50 ppb) as an internal standard. Known analyte solutions of osmium and bromine were prepared in 1% *m/v* TMAH in triplicate, in addition to known concentrations of combined osmium-bromine compounds. Spike solutions of potassium bromide (KBr) and osmium trichloride ( $\text{OsCl}_3 \cdot 3\text{H}_2\text{O}$ ) were prepared directly in 1% *m/v* TMAH, achieving >95% recoveries. Additionally, spike solutions of KBr,  $\text{OsCl}_3 \cdot 3\text{H}_2\text{O}$  and osmium and bromine calibration standards were prepared following the alkaline digestion method (*e.g.* digestion in 500  $\mu$ L 25% *m/v* TMAH followed by 25-fold dilution). A known concentration of SS-2 (see Chapter 3) was also prepared following the alkaline digestion protocol to confirm 1:1 ratio of  $^{189}\text{Os}$ : $^{79}\text{Br}$  in aqueous solution prior to commencement of biological studies.

## 2.5 Instrumentation at Diamond Light Source (DLS, Oxford)

### 2.5.1 I14 beamline

All synchrotron X-Ray Fluorescence (XRF) and X-Ray Absorption Near Edge Structure (XANES) experiments were performed at the I14 hard X-ray Nanoprobe beamline. I14 operates in the energy range 5-23 keV and received its first users in March 2017. High energy x-rays are generated by an undulator source, which are directed through an aperture (17 m) to the white beam slits which determine the beam size delivered to the optics. The beam is then directed onto a bent collimating (focussing) mirror, followed by a flat deflecting mirror and then onto the horizontally deflecting double-crystal monochromator (DCM). The beam then passes through a high-precision slit system which acts as a secondary source (50 m) to the focusing optics, a pair of pre-shaped mirrors in Kirkpatrick-Baez (KB) configuration (186m, in the end station), as shown in **Fig. 2.1**.

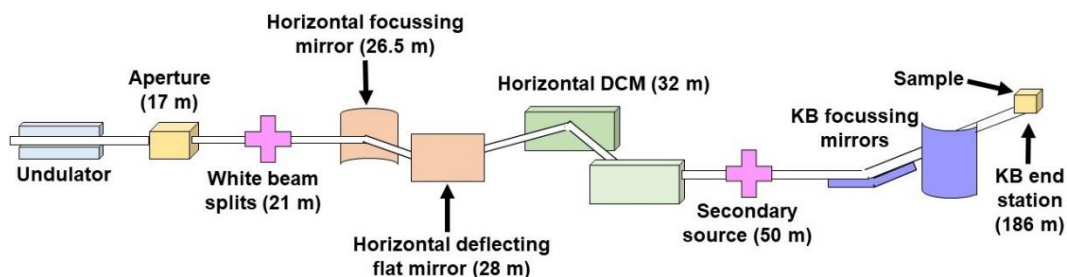


**Figure 2.1.** Schematic for the hard x-ray nanoprobe I14 beamline at DLS (Oxford).

Overall, the beamline is 186 m in length to improve beam demagnification and to provide a coherent beam (**Figure 2.1**).<sup>10</sup> The focused beam can reach spot sizes down to sub-50 nm, with a slight dependence on photon energy (higher energy allows smaller spots). XRF data is collected by a 4-element silicon drift detector (SGX-RaySpec, UK) laid out in backscatter geometry, covering 0.6-0.8 sr solid angle and capable of 1.5 Mcps/channel. Additionally, a Merlin Quad detector (Quantum Detectors, UK) is available for simultaneous imaging techniques using the transmitted beam, such as Differential Phase Contrast (DPC) imaging. Alternative detectors to the Merlin are also available for different techniques such as XRD and near-field ptychography, which goes beyond the scope of this work.

## 2.5.2 B24 beamline

### Cryogenic fluorescence microscopy

Correlative microscopy analysis of plunge-frozen TEM grids was performed on a Zeiss Axioimager M2 (Carl Zeiss X-ray Microscope) coupled to a Linkam cryostage (CMS196M LED) for preliminary grid analysis and mapping (max resolution 50 $\times$ , variable filters) by monitoring the fluorescence of trackers used.

### Cryo-Structured Illumination Microscopy (Cryo-SIM)

Prior to cryo-soft X-ray Tomography (cryo-XRT), super-resolution fluorescence microscopy was performed on plunge-frozen TEM grids using the cryo-SIM facilities (B24 beamline, DLS). The cryo-SIM has 4 excitation lasers (405, 488, 561 and 642nm; 10-100 Wcm<sup>-2</sup> laser power) and a 100X long distance air objective (2 mm, 0.9NA), and can achieve a lateral resolution of 360 nm (when using green light).<sup>11</sup> Cryo-SIM is compatible with conventional fluorophores and can use low light doses, acquiring super-resolution fluorescence information on biological samples 8-fold greater than the diffraction-limit.<sup>11</sup>

### Cryo-XRT

All cryo-XRT and super-resolution cryo-SIM measurements were performed at the full-field transmission microscope at beamline B24 (**Fig. 2.2**), which has a Zeiss UltraXRM-S220C microscope end station.<sup>12</sup> The B24 beamline operates in the soft x-ray region (200-2600 eV), has a beam size of 20  $\mu$ m (allowing a resolution of 40 nm) and delivers a photon flux 10<sup>8</sup> photons/ $\mu$ m<sup>2</sup>.<sup>12</sup> Data were collected by direct detection using a CCD (Pixis, XO 1024B; Princeton Scientific).<sup>12</sup>

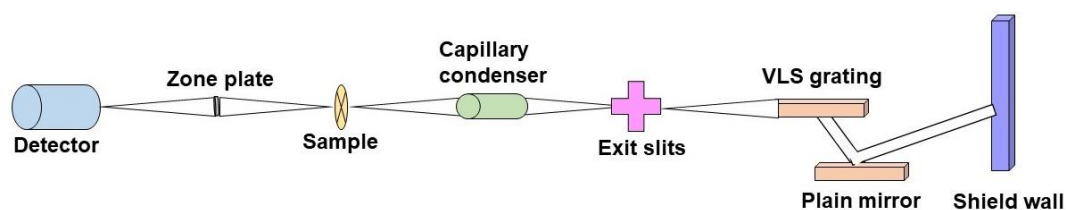


**Figure 2.2.** Schematic layout of the B24 cryo-XRT Beamline (DLS, Oxford).

B24 uses a bending magnet source to generate x-rays, which are directed by a toroidal mirror onto a Variable Line Spacing (VLS) grating monochromator. The mirror focuses the beam onto a focal point downstream of the monochromator, where a slit system removes stray radiation and selects the desired wavelength for the experiment. The beam is then focussed onto the sample using a capillary condenser. Downstream from the sample, a zone plate (40 nm minimum spacing) projects the image onto the Charge Coupled Device (CCD) detector. A schematic diagram of the beamline is depicted in **Figure 2.2**.

## **2.6 Synchrotron methods**

All synchrotron experiments were performed at Diamond Light Source, located in Harwell Campus, South Oxfordshire.

### **2.6.1 Synchrotron-XRF at I14**

In this thesis, cryo-fixed and dehydrated human cancer cells grown on  $\text{Si}_3\text{N}_4$  membranes and treated with Os, Br, Pt or Ir complexes were analysed by synchrotron-XRF at ambient temperature using incident energies of 12-15 keV to monitor the  $\text{L}_3\text{M}_5$  emissions of Os (8.91 keV), Ir (9.18 keV), Pt (9.44 keV), and the  $\text{KL}_3$  emission of Br (11.92 keV).<sup>13</sup> Regions of interest (cancer cells) were identified under the beamline microscope by their endogenous elemental  $\text{KL}_3$  emissions (Zn, K, P and S) using large step sizes (300-500 nm). XRF maps were acquired using 100 nm step size, 50 nm beamsize and 0.1 s exposure. Biological elements present in FCS, RPMI, DMEM, PBS and HBSS are specified (**Appendix, Table A1-5**).

**Sample preparation.**  $\text{Si}_3\text{N}_4$  membranes (suitable growth substrates for cells which are transparent to x-rays)<sup>14</sup> were sterilised with 70% ethanol (5 min) and 100% ethanol (5 min) and air-dried. 0.01% Poly-L-lysine (1-2 drops) was added directly to the membrane and incubated at ambient temperature for 20 min. The poly-L-lysine was removed using PBS (2×3 mL). Cell suspensions of  $8\text{-}10 \times 10^5$  cells/mL

were prepared in culture media, and 50  $\mu\text{L}$  of this suspension was added directly to each membrane. The membranes were incubated for 2 h (310 K, 5%  $\text{CO}_2$ ). After this, 3 mL of the *same* cell suspension was added to each membrane and incubated for a further 24 h (310 K, 5%  $\text{CO}_2$ ). The supernatant was removed, and ICP-OES corrected solutions of Os, Pt or Ir complexes (prepared in 5% v/v DMSO, 95% v/v media) were added to each membrane (3 mL). The supernatant was removed and the membranes were washed with buffer (PBS, tris-glucose, or HBSS as specified). The membranes were dipped in sterile water (3 s), blotted (3 s) and plunge-frozen as previously described (**Section 2.3.6**). The membranes were transferred to cryovials, covered in pierced parafilm, and freeze-dried for 24-48 h.

**Synchrotron-XRF.** Photon energies of greater than the electron-binding energies of Os ( $\text{L}_3$   $2p_{3/2}$ =10.9 keV), Br ( $\text{K}_{1s}$ =13.5 keV), Ir ( $\text{L}_3$   $2p_{3/2}$ =11.2 keV) and Pt ( $\text{L}_3$   $2p_{3/2}$ =11.6 keV) were used in these experiments (12-15 keV).<sup>13</sup> The  $\text{K}_\alpha$ -emissions of native biological elements (P, S, Cl, K, Ca, Zn) can be readily observed at these incident photon energies, and thus cell features such as nuclei or cell membranes can be identified (**Chapter 1, Table 1.1**). Raster scans were performed at the specified step-size (100 nm), using 0.1 s exposure time and a beam size *ca.* 50 $\times$ 70 nm. The fluorescence was detected by Si drift four-element detector.

**Data fitting and analysis.** Data fitting and analysis was performed using PyMCA software (**Fig. 2.3-2.4**).<sup>15</sup> The XRF spectra were fitted to characteristic elemental peaks by specifying the incident energy, exposure time, the matrix composition, geometry and detector characteristics (**Fig. 2.4; Chapter 1, Table 1.1**). The fitted data were analysed in ImageJ software to gain information on cell size, morphology, elemental distribution and co-localisation statistics.<sup>16</sup> A sample with known composition (AXO Dresden GmbH, Germany) was used to calibrate the fitting process and obtain quantitative information (**Equation 2.1**), assuming a density of 0.0012  $\text{g}/\text{cm}^3$  and maximal cell thickness of 6  $\mu\text{m}$ .<sup>17</sup>

$$A = I_0 c \cdot \frac{\Omega}{4\pi} \sum_j R_j^n$$

**Equation 2.1.** Formula for the quantification of elements from XRF spectra, where A=peak area,  $I_0$ = flux, c=mass fraction,  $\Omega/4\pi$ =detector-geometry efficiency,  $R_j$ =relative intensity



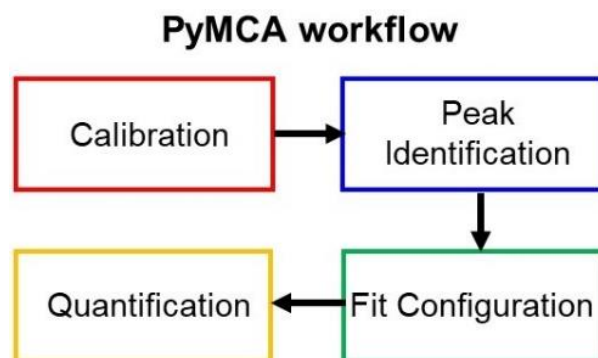


**Figure 2.3.** Summary of the PyMCA workflow for analysing of XRF data. (i) *Calibration*: an internal (1<sup>st</sup> order) calibration is performed on a ROI to calibrate the energy (ii) *Peak Identification*: database proposes theoretical energy emissions, and the user identifies peaks based on knowledge of the sample. (iii) *Fit configuration*: insert instrumental and experimental parameters (detector, distance, matrix, incident beam angle) and user selects elements of interest in sample. The background was removed using strip background model, which applies a baseline to the fit. (iv) *Quantification*: by running an AXO silicon nitride standard contain known concentrations of elements, the photon-flux is back-calculated and used to fit and quantify elements in the sample.

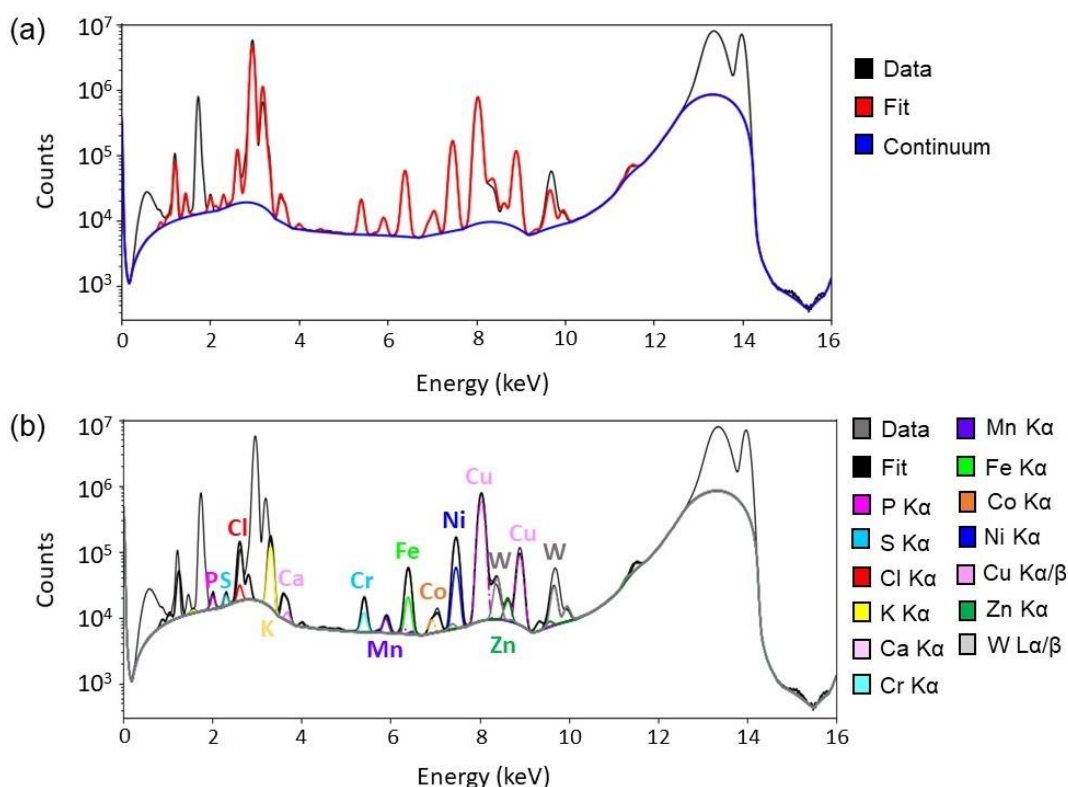


**Figure 2.4.** Typical XRF fit of untreated cancer cells, showing abundant biological elements, in addition to elements prevalent at the synchrotron I14 beamline. (a) Data from a ROI in an untreated cancer cell with the continuum modelled by performing a fit in PyMCA software. (b) Peak identification of elements in the sample or at the beamline including phosphorus, sulfur, chlorine, potassium, calcium, chromium, manganese, iron, cobalt, nickel, copper, zinc and tungsten.

### Limitations of elemental quantification by XRF

In order to quantify elements using synchrotron XRF, one must either have prior knowledge of the system (photon flux, solid angle and acquisition time) *or* use an internal standard (of known chemical composition). As the photon flux at the I14 beamline can vary, an internal standard (AXO Dresden GmbH, Germany) was used for quantification. One of the major problems with quantifying trace biological elements using an internal standard is matrix-matching, in which it is assumed that the matrix in the standard ( $\text{Si}_3\text{N}_4$ ) is an exact representation of the sample matrix (*i.e.* cells grown on  $\text{Si}_3\text{N}_4$ ).<sup>18</sup> As a result of imperfect matrix-matching, XRF is only semi-quantitative.

The quantification will also depend on the sample thickness (assumed to be maximum of 6  $\mu\text{m}$ ).<sup>17</sup> Hard x-rays ( $>10$  keV) can penetrate the full thickness of samples, thus, provides a sum of the XRF emissions from the entire thickness of biological cells. For example, XRF measurements using 100 nm step size achieves 100 nm resolution in the xy-plane, however, the resolution in the z-plane (*i.e.* cell thickness) will be around 6000 nm. This ultimately affects the resulting elemental quantification and resolution in the elemental maps. Moreover, the quantification of biological samples on  $\text{Si}_3\text{N}_4$  membranes is much more reliable with thin samples ( $<1$   $\mu\text{m}$ ), where the sample matrix can be assumed to be the same as the  $\text{Si}_3\text{N}_4$  support (*e.g.* 200 nm thickness). A more reliable way to obtain the ‘real’ cell thickness is to use x-ray tomography, however, this can be time-consuming, expensive and can cause additional damage to samples prior to XRF analysis.

In order to validate the quantification reliability of synchrotron-XRF, LA-ICP-MS (which has similar sensitivity and spatial resolution)<sup>19</sup> can be used on cells prepared and exposed to the same conditions (*e.g.* cryopreserved and freeze-dried). In addition, single-cell ICP-MS could be employed to obtain to quantify elements in individual cells,<sup>20</sup> although these samples will be subject to digestion. Both of these techniques can be used for future quantification validation; however, this goes beyond the scope of the work in this thesis.

### 2.6.2 Cryo-XRT at B24

**Sample preparation.** Quantifoil finder grids (Au-C R2/2 F1 200 mesh, Quantifoil GmbH, Germany) were incubated in FCS (2 mL/well in 6-well plates) for 12 h (310 K, 5% CO<sub>2</sub>). The FCS was removed and 1.5×10<sup>5</sup> cells/ mL of PC3 cell suspension was added to each well (2 mL/well) and incubated for 24 h (310 K, 5% CO<sub>2</sub>). Pt or Ir stock were prepared in non-phenol red RMPI-1640 under dark conditions. The supernatant suspension was removed and Ir or Pt compounds were added and incubated for specified times (310 K, 5% CO<sub>2</sub>). Plates were irradiated with blue light (465 nm, 4.8 mW/cm<sup>2</sup>) for the specified times. The supernatant was removed followed by recovery times in complex-free media. The grids were incubated in conventional fluorescent trackers (100 nM) for 20 min (310 K, 5% CO<sub>2</sub>) before blotting with AuNP fiducials (d=250 nm) and plunge-freezing in liquid ethane.

**Fluorescence Microscopy.** PC3 cells grown as described above and exposed to Ir or Pt complexes were incubated with various trackers: (i) MitoTracker Red ( $\lambda_{\text{ex/em}}$ =581/644 nm); (ii) MitoTracker DeepRed ( $\lambda_{\text{ex/em}}$ =644/665 nm); (iii) LysoTrackerRed ( $\lambda_{\text{ex/em}}$ =577/590 nm). Cells were plunge-frozen in liquid ethane and the fluorophores monitored by fluorescence microscopy on a Zeiss Axioimager M2 microscope coupled to a cryo-stage (model CMS196M, Linkam Scientific, UK) to identify suitable cell candidates for analysis by cryo-XRT.

**Cryo-XRT.** All cryo-XRT experiments were performed at beamline B24 (DLS, Oxford), using a Zeiss UltraXRM-S220C X-ray microscope which uses the synchrotron as the primary source and a direct-detection CCD camera (Pixis XO 1024B, Princeton Scientific). The photon energy was 500 eV for all experiments. Plunge-frozen grids were loaded into the sample chamber of the beamline. X-ray mosaic images were obtained first using short exposures (0.5 s). Regions of interest were brought into focus by mapping the positions of fiducials and dense lipid droplets in the tilt range - 30 and + 30°. The image focus was adjusted by altering the position of the 40 nm zone plate objective. Tomograms were acquired with a tilt range of -65 to +65° using 0.2-0.5° rotations and 1-8 s/frame x-ray exposure.

**Alignment and reconstruction in IMOD.** Tomograms ( $15.8 \times 15.8 \mu\text{m}^2$ ) were aligned and reconstructed using the freely available IMOD software package.<sup>21</sup> The tilt series were aligned to compensate drift and tilt by monitoring the positions of fiducials on the cell surface. Once aligned, tomographic reconstruction follows using standard algorithms (WBP and SIRT). The MRC files produced by the beamline were opened in IMOD using the following settings: single axis; single frame; pixel size=15.8 nm, fiducial diameter=250 nm; image rotation=0°, start angle (-65 to + 65°, unless specified otherwise); increment step=0.2–0.5°. From this, an x-ray model was generated, followed by a fixed stack. Cross-correlation was calculated (high cut-off radius=0.1), and a coarse aligned stack generated. The fiducial model was generated automatically, and corrected manually (by mapping the centre positions of each fiducial throughout the entire tilt series). Tomograms were fine-aligned (relative to neighbouring views; fixed magnification=1; no rotation). The tomogram was positioned (thickness=1000; binning=3) to generate a boundary model (to remove unwanted information). The final aligned stack was generated from the z-shifts and pitch angles (using linear interpolation) to generate tomograms with smooth rotations. The IMOD workflow is summarized in **Fig. 2.5**.

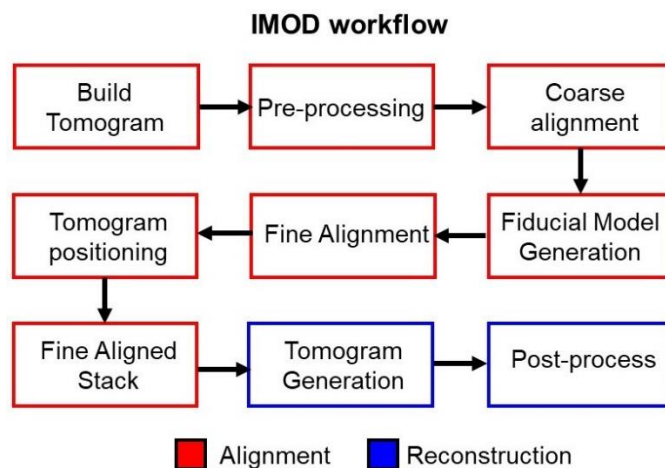


**Figure 2.5.** IMOD workflow for aligning and reconstructing tomograms. (i) *Build tomogram* by inserting experimental parameters (x-ray exposure, tilt range, fiducial size, pixel size), exclude unwanted views (*e.g.* at high tilt angles) and generates an x-ray model. (ii) *Pre-processing* creates a second (fixed) stack with x-rays removed. (iii) *Coarse alignment* corrects for large shifts in xy plane. (iv) *Fiducial model generation* identifies and tracks fiducials through the tilt series. (v) *Fine alignment* solves for displacements, rotation, tilts and magnification and finds the best fit for the data. (vi) *Tomogram positioning* temporarily reduces volume to create a final alignment. (vii) *Fine aligned stack* applies the alignment and creates the final aligned stack of the full volume. (viii) *Tomogram generation* uses WBP or SIRT reconstruction algorithms to computer the tomogram. (IX) *Post-processing* is used to trim the volume and adjust image contrast.

**3D segmentation and visualisation.** The reconstructed tomograms (.rec files) were segmented in SuRVoS software (**Fig. 2.6**),<sup>22</sup> to quantify and image the 3D volumes of organelles of interest. The regions of interest were selected appropriately for each tomogram by deleting specific angle views which were obstructed by thick ice or by gridlines. A Gaussian filter feature channel was used to pre-process the data and supervoxels (hierarchical layers of super-regions, SP= 8×8×8) were generated in Gaussian mode. Organelles of interest were segmented (semi-automatically) using supervoxels for guidance. The exported files (.rec) were visualized in the software package Amira (FEI/Thermo Scientific, The Netherlands, 2016), using the volume-rendering and ortho-slice features to generate 3D images and videos.

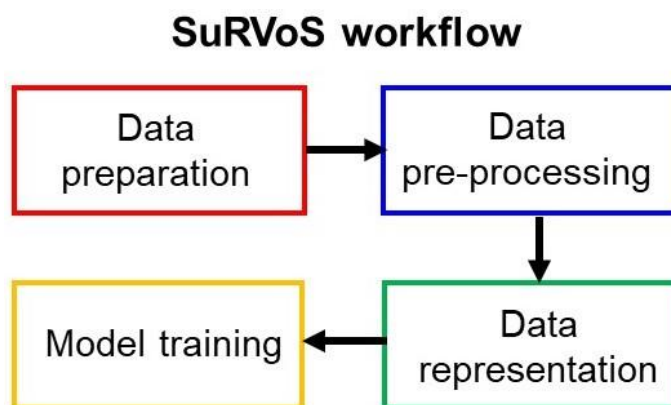


**Figure 2.6.** SuRVoS workflow for volume segmentation analysis. (i) *Data preparation*: reconstructed tomograms (.rec) files are opened and the ROI is selected. (ii) *Data pre-processing*: deionising filters are used to remove noise, adjust contrast and enhance features of interest for discrimination between different cell features. (iii) *Data representation*: voxels, supervoxels or megavoxels are generated to identify specific features (hierachiral layers of super-regions). (iv) *Model training*: user identifies regions of interest and supervoxels colour in these regions (semi-automated volume segmentation), to gain 3D qualitative and quantitative information (*e.g.* organelle volumes). The raw data and annotations can then be exported and visualised in Amira.

## 2.7 Statistical formulae

- **In vitro studies:** All in vitro biological experiments (cell viability assays and ICP-MS cellular uptake) were performed in triplicate to obtain *standard deviations* and the *standard error of the mean*. Statistical significance between different samples was determined using *Welch's unpaired t-test* above the 95% *confidence interval* throughout this thesis.
- **Synchrotron XRF:** The co-localisation between elements in cryo-fixed and freeze-dried samples analysed by XRF were determined using *Pearson's R-value* and *Spearman Rank Correlation*. Statistically significant changes in mass fraction elemental quantities were determined using *Welch's unpaired t-test* above the 95% *confidence interval*.
- **Cryo-XRT:** Statistical differences in volume between segmented organelles in cryopreserved cells analysed by cryo-XRT were determined using *Welch's unpaired t-test* above the 95% *confidence interval*.

### ***Standard deviation***

Measures the variability between the individual data values and the mean value, and is given by the following formula, where  $x_i$ = individual sample value,  $\bar{x}$ =sample mean and  $n$ =sample size.

$$s = \sqrt{\frac{\sum_i^n (x_i - \bar{x})^2}{n - 1}}$$

### ***Standard error of the mean***

A measure of how far the mean is away from the true mean value, and is given by the following formula where  $s$ =standard deviation and  $n$ =sample size.

$$se = \frac{s}{\sqrt{n}}$$

### ***Welch's unpaired t-test***

Assumes that both groups of data have Gaussian distributions, but do not necessarily have the same standard deviation. *Welch's unpaired t-test* (also known as the *two unpaired t-test*) is given by the following formula where  $\bar{x}$ =sample mean,  $S_1$ =sample standard deviation and  $N$ =sample size.

$$t = \frac{\bar{x}_1 - \bar{x}_2}{\sqrt{\frac{S_1^2}{N_1} + \frac{S_2^2}{N_2}}}$$

### ***Confidence intervals***

Describes the range of values for which the true value lies, and is given by the following formula where  $\bar{x}$ =mean,  $se$ =standard error of mean, and  $t$ =critical value.

$$\bar{x} \pm (se \cdot t)$$

### ***Pearson's R-value***

Measures the linearity between two variables, where +1= positive correlation, 0=no correlation and -1= negative correlation. Pearson's R-value is given by the following formulae where  $x_i$  and  $y_i$ = individual sample points,  $n$ =sample size,  $\bar{x}$  and  $\bar{y}$ =sample mean and  $s_x$  and  $s_y$  are the sample standard deviations of  $x$  and  $y$  data sets, respectively.

$$r = \frac{\sum_i^n x_i y_i - n \bar{x} \bar{y}}{(n-1) s_x s_y}$$

### ***Spearman's Rank Correlation***

Measures the monotonic relationships between two variables to obtain a line of best fit. Spearman's Rank Correlation is given by the following formula where  $x_i$  and  $y_i$ = individual sample points,  $n$ =sample size,  $\bar{x}$  and  $\bar{y}$ =sample mean.

$$r = \frac{\sum_i^n x_i y_i - n \bar{x} \bar{y}}{\sqrt{\sum_i^n x_i^2 - n(\bar{x})^2} \sqrt{\sum_i^n y_i^2 - n(\bar{y})^2}}$$

## 2.8 References

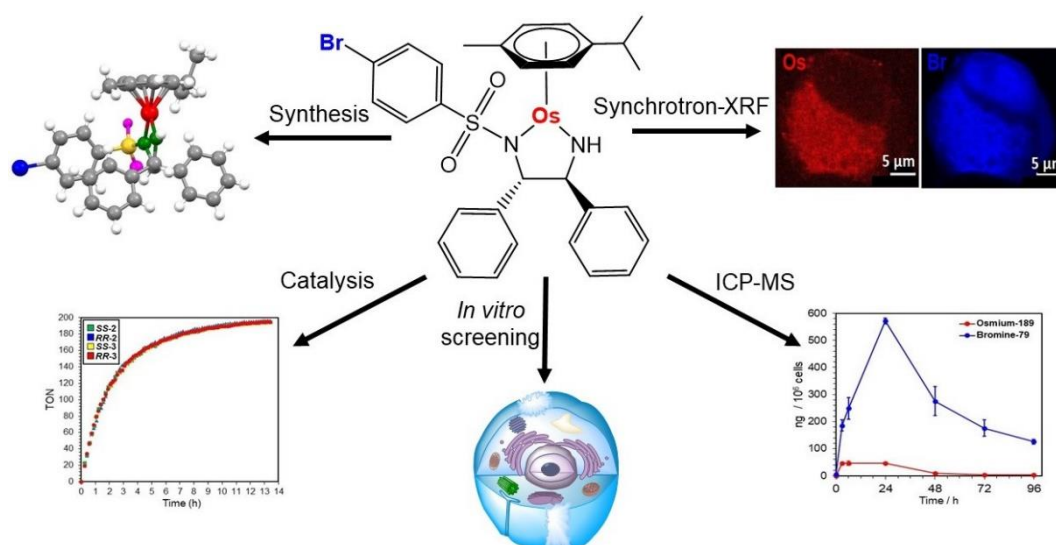
1. J. P. C. Coverdale, C. Sanchez-Cano, G. J. Clarkson, R. Soni, M. Wills and P. J. Sadler, *Chem Eur*, 2015, **21**, 8043-8046.
2. L. Švorc, P. Tomčík, J. Durdiak, M. Rievaj and D. Bustin, *Pol J Environ Stud*, 2012, **21**, 7-13.
3. M. H. M. Klose, M. Hejl, P. Heffeter, M. A. Jakupec, S. M. Meier-Menches, W. Berger and B. K. Keppler, *Analyst*, 2017, **142**, 2327-2332.
4. O. V. Dolomanov, L. J. Bourhis, R. J. Gildea, J. A. K. Howard and H. Puschmann, *J Appl Crystallogr*, 2009, **42**, 339-341.
5. G. Sheldrick, *Acta Crystallogr C*, 2015, **71**, 3-8.
6. C. F. Macrae, I. Sovago, S. J. Cottrell, P. T. A. Galek, P. McCabe, E. Pidcock, M. Platings, G. P. Shields, J. S. Stevens, M. Towler and P. A. Wood, *J Appl Crystallogr*, 2020, **53**, 226-235.
7. I. Romero-Canelón, L. Salassa and P. J. Sadler, *J Med Chem*, 2013, **56**, 1291-1300.
8. D. Pozebon, V. L. Dressler and A. J. Curtius, *Talanta*, 2000, **51**, 903-911.
9. A. E. Egger, C. Rappel, M. A. Jakupec, C. G. Hartinger, P. Heffeter and B. K. Keppler, *J Anal At Spectrom*, 2009, **24**, 51-61.
10. P. Quinn, J. Parker, F. Cacho-Nerin, M. Walker and P. Howes, *Microsc Microanal*, 2018, **24**, 242-243.
11. I. Kounatidis, M. L. Stanifer, M. A. Phillips, P. Paul-Gilloteaux, X. Heiligenstein, H. Wang, C. A. Okolo, T. M. Fish, M. C. Spink, D. I. Stuart, I. Davis, S. Boulant, J. M. Grimes, I. M. Dobbie and M. Harkiolaki, *Cell*, 2020, **182**, 515-530.
12. M. Harkiolaki, M. C. Darrow, M. C. Spink, E. Kosior, K. Dent and E. Duke, *Emerg Top Life Sci*, 2018, **2**, 81-92.
13. G. P. Williams, W. M. Haynes and D. R. Lide, *Electron binding energies of the elements*, CRC Press, USA, 2011.
14. C. Bissardon, S. Reymond, M. Salomé, L. André, S. Bayat, P. Cloetens and S. Bohic, *JoVE*, 2019, e60461.
15. V. A. Solé, E. Papillon, M. Cotte, P. Walter and J. Susini, *Spectchim Acta B*, 2007, **62**, 63-68.



16. C. T. Rueden, J. Schindelin, M. C. Hiner, B. E. DeZonia, A. E. Walter, E. T. Arena and K. W. Eliceiri, *BMC Bioinformatics*, 2017, **18**, 529.
17. J. L. Gregg, K. M. McGuire, D. C. Focht and M. A. Model, *Pflugers Arch*, 2010, **460**, 1097-1104.
18. J. F. Collingwood and M. R. Davidson, *Front Pharmacol*, 2014, **5**, 191.
19. T. J. Stewart, *Metallomics*, 2019, **11**, 29-49.
20. M. Corte Rodríguez, R. Álvarez-Fernández García, E. Blanco, J. Bettmer and M. Montes-Bayón, *Anal Chem*, 2017, **89**, 11491-11497.
21. J. R. Kremer, D. N. Mastronarde and J. R. McIntosh, *J Struct Biol*, 1996, **116**, 71-76.
22. I. Luengo, M. C. Darrow, M. C. Spink, Y. Sun, W. Dai, C. Y. He, W. Chiu, T. Pridmore, A. W. Ashton, E. M. H. Duke, M. Basham and A. P. French, *J Struct Biol*, 2017, **198**, 43-53.

# Chapter 3

## Catalytic Os<sup>II</sup> arene complexes in cancer cells: ICP-MS and XRF



### 3.1 Introduction

In 2015, Coverdale *et al.* reported a series of coordinatively-unsaturated 16-electron pseudo-octahedral osmium(II) complexes with the general formula  $[\text{Os}^{\text{II}}(\eta^6\text{-p-cym})(\text{TsDPEN})]$  (where  $\eta^6\text{-p-cym}$ =*para*-cymene, TsDPEN=tosyldiphenylethylene diamine, **RR-1**, **Fig. 3.1**)<sup>1, 2</sup> as second-generation Noyori ruthenium transfer hydrogenation catalysts. Asymmetric transfer hydrogenation (ATH) is a well-established reaction in which prochiral substrates are enantioselectively converted to chiral products. This is of great industrial interest owing to the importance of optically-active alcohols and amines in both agrochemicals and pharmaceuticals. In the late 20<sup>th</sup> century, Noyori *et al.* reported a series of ruthenium(II) octahedral complexes which can enantioselectively catalyse the reduction of ketones and imines with high enantiomeric excesses, conversions and turnover frequencies.<sup>3</sup> First-generation Noyori catalysts containing asymmetric phosphine (BINAP) and diamine (DPEN) ligands enhanced the catalytic efficiency through steric and electronic effects.<sup>4, 5</sup> Second-generation half-sandwich ruthenium(II) Noyori catalysts were developed, containing: (i) chiral bidentate tosyl-diphenylethylenediamine (TsDPEN(H)) ligand (which directs the enantioselectivity), (ii)  $\eta^6$ -arene and (iii) halide (leaving group) which dissociates to provide an available coordination site for catalysis (**Fig. 3.1**).<sup>5, 6</sup>

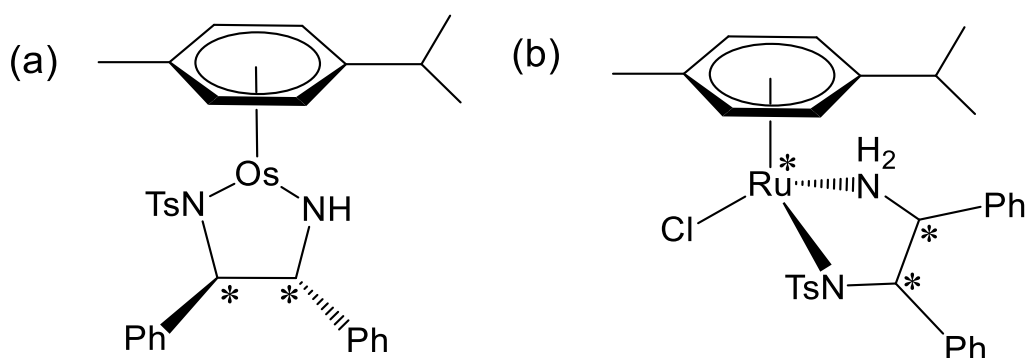


**Figure 3.1.** (a) Coordinatively-unsaturated 16-electron osmium(II) complex  $[\text{Os}^{\text{II}}(\eta^6\text{-p-cym})((1R, 2R)\text{TsDPEN})]$  (**RR-1**).<sup>1</sup> (b) Noyori second-generation half-sandwich ruthenium(II) pre-catalyst  $[\text{Ru}^{\text{II}}(\eta^6\text{-p-cym})((1R, 2R)\text{TsDPEN(H)})\text{Cl}]$ .<sup>5, 6</sup> Where \* denotes chiral centres.

Notably, the amine group of 16-electron [Os<sup>II</sup>( $\eta^6$ -*p*-cym)(TsDPEN)] (**RR-1**) is deprotonated (NH<sup>-</sup>), whereas, the [Ru<sup>II</sup>( $\eta^6$ -arene)(TsDPEN(H)Cl)] pre-catalyst is protonated (NH<sub>2</sub>), leading to initial differences in their catalytic mechanisms. The first stage in the catalytic cycle of Noyori's catalyst requires the base-mediated dissociation of chloride (Cl<sup>-</sup>) to form an active Ru( $\eta^6$ -arene)(TsDPEN(H)) species. Formate (which acts as a hydride source) then directly interacts with both the Ru and the NH<sub>2</sub> group (*via* O-atom), and releases CO<sub>2</sub> to form a highly active Ru-H bond. This mediates the indirect (outer sphere) enantioselective reduction of the prochiral substrate, by forming favourable CH- $\pi$  interactions on the *Re* or *Si* face in the 6-membered coordination state.<sup>7-9</sup>

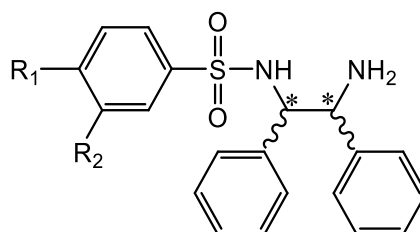
The Os<sup>II</sup> analogues are remarkably stable and can catalytically reduce ketones to optically-pure alcohols with high enantiomeric excesses (>97%) and turnover frequencies in the presence of formic acid.<sup>1</sup> Unlike previous generation Ru<sup>II</sup> catalysts, the Os<sup>II</sup> analogues do not require activation *via* ligand dissociation. It is proposed that formate can bind directly to the vacant coordination site of **RR-1** to form an active Os-H bond (*via* decarboxylation), for which the prochiral ketone (*i.e.* acetophenone) interacts with NH<sub>2</sub> (*via* O-atom) and hydride (H<sup>-</sup>, *via* the carbonyl C-atom). Subsequently, this mediates substrate reduction at the *Si* or *Re*-face (depending on steric interactions between the substrate and the catalyst) – providing an outer sphere catalytic mechanism (**Chapter 1, Fig. 1.11**).<sup>10</sup> Furthermore, the *RR* and *SS* catalysts yield *R* and *S* chiral products, respectively.

These Os<sup>II</sup> complexes have also demonstrated catalysis in a biological context,<sup>10</sup> as an alternative approach to cancer treatment. A hydride source is still required, and the sodium salt of formic acid (an approved food additive) is well-suited for biological use and has been used previously with great success.<sup>11, 12</sup> The potential for half-sandwich Os<sup>II</sup> complexes as anticancer agents with new mechanisms of action(s) has been reported,<sup>13</sup> including this family of “unconventional” 16-electron piano-stool catalysts.<sup>10, 14</sup> Both the *SS/RR* isomers of **1** (**Fig. 3.1**) exhibit moderate antiproliferative activity against a variety of cancer cell lines (*in vitro*).<sup>10</sup> Complex **RR-1** was the first reported osmium-based synthetic catalyst to enantioselectively convert pyruvate (an essential precursor in cell metabolism) to unnatural D-lactate in the presence of non-toxic concentrations of sodium formate in cancer cells,<sup>10</sup> providing a platform for catalytic selectivity. As a consequence of

the Warburg Effect, cancer cells have increased levels of lactate:<sup>15</sup> making metabolism a viable therapeutic target. Interestingly, confocal microscopy studies also revealed that these complexes can selectively generate reactive oxygen species (ROS) both *in vitro* and *in vivo*,<sup>14</sup> providing the opportunity to exploit the redox vulnerability of cancers through catalytic therapy.

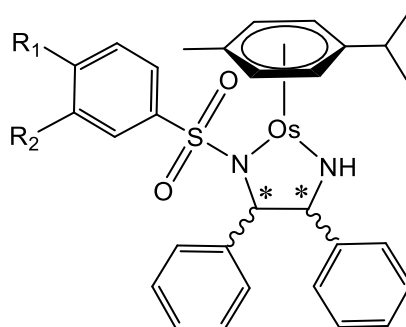
Inductively-Coupled Plasma Mass Spectrometry (ICP-MS) is an analytical technique which can be used to quantify elements down to ppb concentrations and has previously been used to quantify intracellular levels of osmium (<sup>189</sup>Os) in cancer cells treated with **SS/RR-1** under varying conditions (time, temperature, concentration and efflux-inhibition studies),<sup>2</sup> providing insights into the in-cell metal activity. However, this work does not provide information on the stability and speciation of the whole complex – just the osmium centre. Consequently, the fate of the bidentate sulfonamide ligand (which plays a vital role in directing the enantioselectivity of *in-cell* catalysis) has not yet been studied. Labelling this ligand with appropriate exogenous elements which are non-native to cancer cells, are readily detectable by analytical techniques and do not significantly affect the anticancer or catalytic properties, can provide insights into the complex stability, speciation and distribution in cancer cells. This may be crucial in elucidating the mechanism(s) of action for clinical translation.

This Chapter explores the synthesis and characterisation of a series of catalysts derived from parent compound **SS/RR-1** (**Fig. 3.1**), which contain halide substituents on the sulfonamide moiety. Catalytic activities, anticancer potencies and osmium cellular quantities are compared to that of parent compound (**1**). In particular, a Br-labelled complex with the formulae [Os( $\eta^6$ -*p*-cym)((*p*-Br)BsDPEN)] has been used as a molecular probe to investigate the *in-cell* activity of this family of complexes in cancer cells by simultaneously monitoring the osmium centre and the bromine from the bidentate sulfonamide ligand using ICP-MS (<sup>189</sup>Os; <sup>79</sup>Br) and synchrotron-XRF (Os L<sub>3</sub>M<sub>5</sub>=8.9 keV; Br KL<sub>3</sub>=11.9 keV).



Ligand	R <sub>1</sub>	R <sub>2</sub>
<b><i>SS</i>-L1</b>	Br	H
<b><i>RR</i>-L1</b>	Br	H
<b><i>SS</i>-L2</b>	I	H
<b><i>RR</i>-L2</b>	I	H
<b><i>RR</i>-L3</b>	OCH <sub>3</sub>	H
<b><i>SS</i>-L4</b>	H	Br

**Figure 3.2.** Summary of the chiral (*SS* or *RR*) sulfonamide ligands synthesized in this chapter (**L1-L4**), where \* indicates chiral centres *SS* or *RR* as specified.



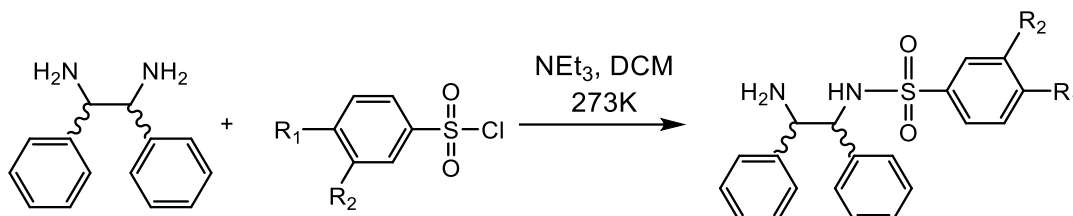
Complex	Ligand	R <sub>1</sub>	R <sub>2</sub>
<b><i>SS</i>-1</b>	N/A	CH <sub>3</sub>	H
<b><i>RR</i>-1</b>	N/A	CH <sub>3</sub>	H
<b><i>SS</i>-2</b>	<b><i>SS</i>-L1</b>	Br	H
<b><i>RR</i>-2</b>	<b><i>RR</i>-L1</b>	Br	H
<b><i>SS</i>-3</b>	<b><i>SS</i>-L2</b>	I	H
<b><i>RR</i>-3</b>	<b><i>RR</i>-L2</b>	I	H
<b><i>RR</i>-4</b>	<b><i>RR</i>-L3</b>	OCH <sub>3</sub>	H
<b><i>SS</i>-5</b>	<b><i>SS</i>-L4</b>	H	Br
<b><i>RR</i>-6</b>	N/A	F	H

**Figure 3.3.** Parent compound ***SS/RR*-1**.<sup>1</sup> Summary of  $Os[(p\text{-cymene})((R)\text{BsDPEN})]$  complexes (**2-5**) synthesized in this chapter, where \* indicates chiral centres *SS* or *RR* as specified. Previously reported complex ***RR*-6** discussed in this Chapter.<sup>2</sup>

## 3.2 Experimental

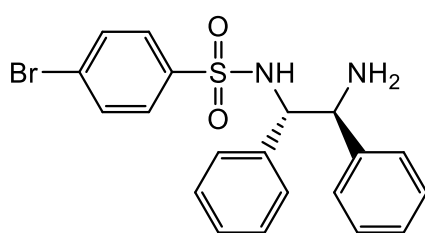
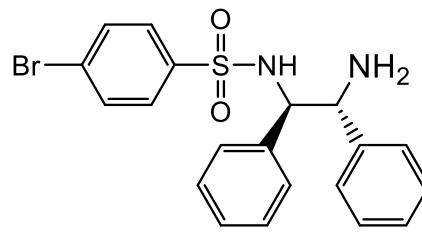
### 3.2.1 Synthesis of BsDPEN ligands

#### General synthesis of BsDPEN ligands



**Scheme 3.1.** General synthetic scheme for the synthesis of BsDPEN (benzenediphenylethylenediamine) ligands using varying benzylsulfonyl chlorides and *SS* or *RR*-DPEN in the presence of base (triethylamine).

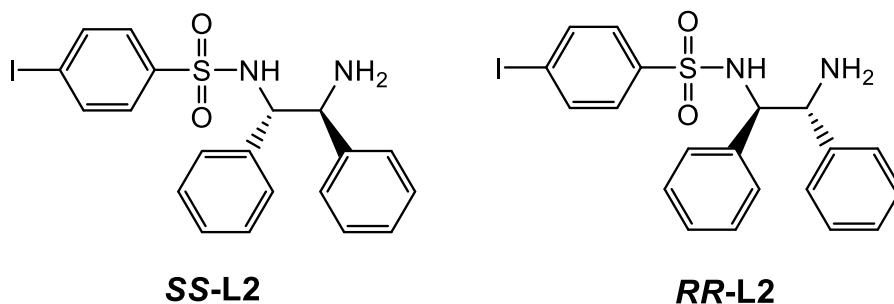
To a solution of (*1S*, *2S*) or (*1R*, *2R*)-diphenylethylenediamine (DPEN, 1.28 g, 6 mmol, 1 mol eq.) and triethylamine (0.83 mL, 6 mmol, 1 mol. eq.) in anhydrous DCM (15 mL) cooled in an ice bath was added dropwise benzenesulfonyl chloride (7.2 mmol, 1.2 mol eq.) in anhydrous DCM (10 mL). The ice bath was removed, the reaction warmed to ambient temperature and stirred for 2 h. Distilled water (30 mL) was added. The organic phase was separated and the aqueous phase extracted with DCM (3×10 mL), combined with the organic phase and dried over magnesium sulphate. The resulting yellow solution was concentrated *in vacuo*, and diethyl ether (10 mL) was added to precipitate a white solid.

**SS-L1****RR-L1**

**(1S, 2S)-BrBsDPEN (SS-L1).** **SS-L1** was synthesized using the general synthesis method using (1*S*, 2*S*)-DPEN (1.28 g, 6.03 mmol), triethylamine (0.8 mL, 5.77 mmol) and 4-bromobenzenesulfonyl chloride (1.84 g, 7.2 mmol) to obtain a white solid (1.12 g, 2.60 mmol, 43%). <sup>1</sup>H NMR (500 MHz, d<sub>6</sub>-DMSO, 298 K, TMS):  $\delta$ =7.43 (d, <sup>3</sup>*J*(H,H)=8.5 Hz, 2H, ArH), 7.31 (d, <sup>3</sup>*J*(H,H)=8.5 Hz, 2H, ArH), 7.12-7.0 (m, 5H, ArH), 7.00 (d, <sup>3</sup>*J*(H,H)=6.6 Hz, 3H, ArH), 6.07-6.92 (m, 2H, ArH), 4.33 (d, <sup>3</sup>*J*(H,H)=7.2 Hz, 1H, CHNHTs), 3.97 (d, <sup>3</sup>*J*(H,H)=7.2 Hz, 1H, CHNH). <sup>13</sup>C NMR (125 MHz, DMSO):  $\delta$ =142.8, 140.9, 140.0, 132.0, 128.6, 128.1, 127.9, 127.8, 127.7, 127.1, 126.9, 125.9, 65.3, 61.0. HRMS (ESI): *m/z* calculated for C<sub>20</sub>H<sub>20</sub>BrN<sub>2</sub>O<sub>2</sub>S [M+H<sup>+</sup>]: 431.0429; found: 431.0427. Elemental analysis: found (calc for C<sub>20</sub>H<sub>19</sub>BrN<sub>2</sub>O<sub>2</sub>S): C 55.05 (55.69), H 4.31 (4.44), N 6.40 (6.49).

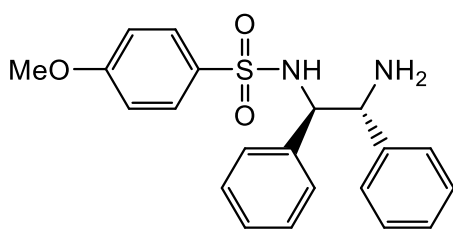
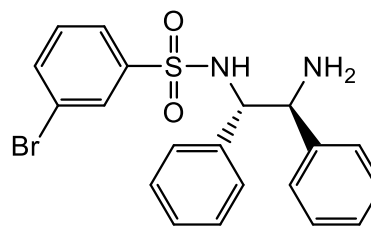
**(1R, 2R)-BrBsDPEN (RR-L1).** **RR-L1** was synthesized using the general synthesis method using (1*R*, 2*R*)-DPEN (1.25 g, 5.9 mmol), triethylamine (0.8 mL, 5.77 mmol) and 4-bromobenzenesulfonyl chloride (1.87 g, 7.32 mmol) to obtain a white solid (1.48 g, 2.91 mmol, 57%). <sup>1</sup>H NMR (500 MHz, d<sub>6</sub>-DMSO, 298 K, TMS):  $\delta$  = 7.43 (d, <sup>3</sup>*J*(H,H)=8.5 Hz, 2H, ArH), 7.31 (d, <sup>3</sup>*J*(H,H)=8.5 Hz, 2H, ArH), 7.14-7.05 (m, 5H, ArH), 7.00 (d, <sup>3</sup>*J*(H,H)=6.7 Hz, 3H, ArH), 6.96-6.92 (m, 2H, ArH), 4.33 (d, <sup>3</sup>*J*(H,H)=7.2 Hz, 1H, CHNHTs), 3.97 (d, <sup>3</sup>*J*(H,H)=7.2 Hz, 1H, CHNH). <sup>13</sup>C NMR (125 MHz, DMSO):  $\delta$ =142.8, 140.9, 140.0, 132.0, 128.6, 128.1, 127.9, 127.8, 127.7, 127.1, 126.9, 125.9, 65.3, 61.0. HRMS (ESI): *m/z* calculated for C<sub>20</sub>H<sub>20</sub>BrN<sub>2</sub>O<sub>2</sub>S [M+H<sup>+</sup>]: 431.0423; found: 431.0429. Elemental analysis: found (C<sub>20</sub>H<sub>19</sub>BrN<sub>2</sub>O<sub>2</sub>S): C 55.02 (55.69), H 4.42 (4.44), N 5.74 (6.49).





**(1S, 2S)-IBsDPEN (SS-L2).** **SS-L2** was synthesized using the general synthesis method using (*1S*, *2S*)-DPEN (1.27 g, 5.98 mmol), triethylamine (0.83 mL, 5.77 mmol) and 4-iodobenzenesulfonyl chloride (2.19 g, 7.20 mmol) to obtain a white solid (0.62 g, 1.30 mmol, 22%). <sup>1</sup>H NMR (500 MHz, d<sub>6</sub>-DMSO, 298 K, TMS): δ=7.60 (d, <sup>3</sup>J(H,H)=8.4 Hz, 2H, ArH), 7.15 (d, <sup>3</sup>J(H,H)=8.4 Hz, 2H, ArH), 7.13-6.78 (m, 10H, ArH), 4.32 (d, <sup>3</sup>J(H,H)=7.3 Hz, 1H, CHNHTs), 3.97 (d, <sup>3</sup>J(H,H)=7.3 Hz, 1H, CHNH). <sup>13</sup>C NMR (125 MHz, DMSO): δ=142.7, 141.2, 140.0, 137.8, 128.3, 128.1, 128.0, 127.8, 127.7, 127.1, 126.9, 100.0, 65.3, 61.0, HRMS (ESI): *m/z* calculated for C<sub>20</sub>H<sub>20</sub>N<sub>2</sub>IO<sub>2</sub>S [M+H<sup>+</sup>]: 479.0290; found: 479.0289. Elemental analysis: found (calculated for C<sub>20</sub>H<sub>19</sub>N<sub>2</sub>IO<sub>2</sub>S): C 49.72 (50.22), H 3.92 (4.00), N 5.73 (5.86).

**(1R, 2R)-IBsDPEN (RR-L2).** **RR-L2** was synthesized using the general synthesis method using (*1R*, *2R*)-DPEN (1.03 g, 4.90 mmol), triethylamine (0.67 mL, 4.83 mmol) and 4-iodobenzenesulfonyl chloride (1.73 g, 5.70 mmol) to obtain a white solid (0.75 g, 1.59 mmol, 27%). <sup>1</sup>H NMR (500 MHz, d<sub>6</sub>-DMSO, 298 K, TMS): δ=7.60 (d, <sup>3</sup>J(H,H)=8.3 Hz, 2H, ArH), 7.15 (d, <sup>3</sup>J(H,H)=8.3 Hz, 2H, ArH), 7.13-6.90 (m, 10H, ArH), 4.38 (d, <sup>3</sup>J(H,H)=7.4 Hz, 1H, CHNHTs), 3.99 (d, <sup>3</sup>J(H,H)=7.4 Hz, 1H, CHNH). <sup>13</sup>C NMR (125 MHz, d<sub>6</sub>-DMSO): δ=141.2, 140.1, 139.8, 137.8, 128.3, 128.1, 128.0, 127.8, 127.7, 127.2, 126.9, 100.1, 65.1, 60.9. HRMS (ESI): *m/z* calculated for C<sub>20</sub>H<sub>20</sub>IN<sub>2</sub>O<sub>2</sub>S [M+H<sup>+</sup>]: 479.0290; found: 479.0288. Elemental analysis: found (calculated for C<sub>20</sub>H<sub>20</sub>N<sub>2</sub>IO<sub>2</sub>S): C 49.70 (50.22), H 3.92 (4.00), N 5.73 (5.86).

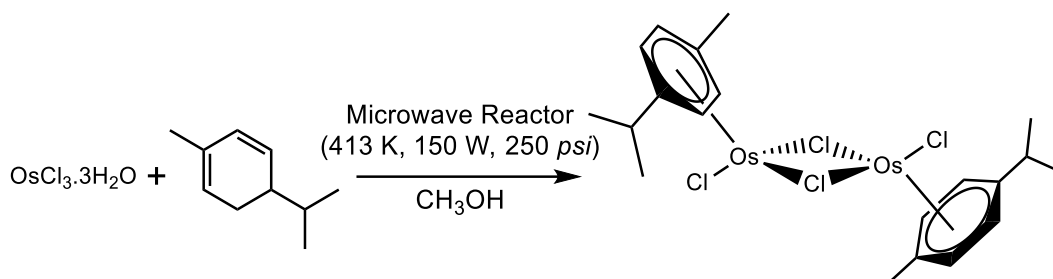
**RR-L3****SS-L4**

**(1R, 2R)-MeOBsDPEN (RR-L3).** **RR-L3** was synthesized using the general synthesis method using (1R, 2R)-DPEN (0.57 g, 2.70 mmol), triethylamine (0.35 mL, 2.5 mmol) and 4-methoxysulfonyl chloride (1.06 g, 5.10 mmol) to obtain a white solid (0.21 g, 0.55 mmol, 22 %). <sup>1</sup>H NMR (500 MHz, d<sub>6</sub>-DMSO, 298 K, TMS): δ=8.76 (s, 1H, NH), 8.66 (d, <sup>3</sup>J(H,H) = 9.6 Hz, 1H, ArH), 8.18 (d, <sup>3</sup>J(H,H)=8.5 Hz, 2H, ArH), 7.56 (d, <sup>3</sup>J(H,H)=8.6 Hz, 2H, ArH), 7.28-7.13 (m, 9H, ArH), 4.50 (d, <sup>3</sup>J(H,H)=8.6 Hz, 1H, TsNCH), 4.02 (d, <sup>3</sup>J(H,H)=8.5 Hz, 1H, CH), 3.70 (s, 3H OCH<sub>3</sub>). <sup>13</sup>C NMR (125 MHz, d<sub>6</sub>-DMSO): δ=161.9, 159.9, 138.5, 133.5, 128.6, 127.9, 127.6, 127.1, 114.0, 113.3, 62.9, 60.3, 55.9, 55.6. HRMS (ESI): *m/z* calculated for C<sub>20</sub>H<sub>23</sub>IN<sub>2</sub>O<sub>2</sub>S [M+H<sup>+</sup>]: 383.1429 found: 383.1423. Elemental analysis: found (calculated for C<sub>21</sub>H<sub>22</sub>N<sub>2</sub>O<sub>3</sub>S): C 67.82 (65.94) H 5.45 (5.80), N 6.12 (6.12).

**(1S, 2S)-*m*-BrBsDPEN (SS-L4).** **SS-L4** was synthesized using the general synthesis method using (1S, 2S)-DPEN (0.36 g, 1.84 mmol), triethylamine (0.25 mL, 1.80 mmol) and 3-bromobenzenesulfonyl chloride (0.32 mL, 2.25 mmol) to obtain a white solid (0.35 g, 0.91 mmol, 50%). <sup>1</sup>H NMR (400 MHz, d<sub>6</sub>-DMSO, 298 K, TMS): δ=8.78 (s, 2H, NH), 7.55 (d, <sup>3</sup>J(H,H)=8.0 Hz, 1H, ArH), 7.50 (d, <sup>3</sup>J(H,H)=7.9 Hz, 2H, ArH), 7.37 (d, <sup>3</sup>J(H,H)=7.8 Hz, 2H, ArH), 7.15 (t, <sup>3</sup>J(H,H)=7.7 Hz, 6H, ArH), 6.83 (m, 3H, ArH), 4.47 (d, <sup>3</sup>J(H,H)=8.2 Hz, 1H, CHNHTs), 4.15 (d, <sup>3</sup>J(H,H)=8.6 Hz, 1H CHNH). <sup>13</sup>C NMR (125 MHz, d<sub>6</sub>-DMSO): δ=142.0, 141.8, 140.0, 139.7, 139.6, 137.8, 128.3, 128.1, 128.0, 127.8, 127.7, 127.1, 126.9, 100.0, 65.3, 61.0. HRMS (ESI): *m/z* calculated for C<sub>20</sub>H<sub>20</sub>BrN<sub>2</sub>O<sub>2</sub>S [M+H<sup>+</sup>]: 431.0429; found: 431.0425. Elemental analysis: found (C<sub>20</sub>H<sub>19</sub>BrN<sub>2</sub>O<sub>2</sub>S): C 55.89 (55.69), H 4.50 (4.44), N 6.38 (6.49).

### 3.2.2 Synthesis of Os[(*p*-cym)BsDPEN] complexes

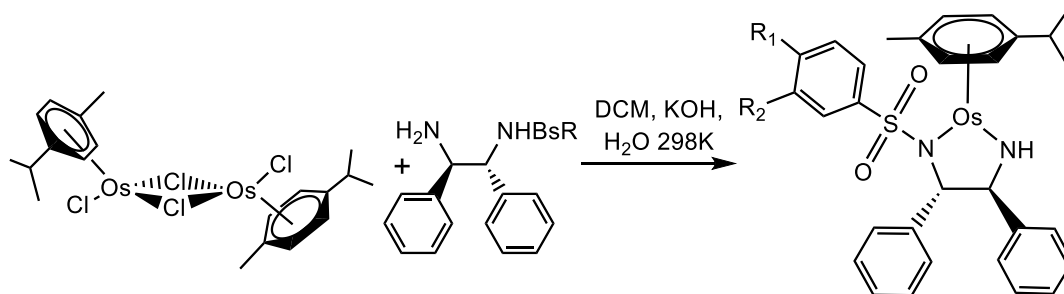
#### Synthesis of [Os(η<sup>6</sup>-*p*-cymene)Cl<sub>2</sub>]<sub>2</sub> dimer



**Scheme 3.2.** Synthetic scheme for [Os(η<sup>6</sup>-*p*-cym)Cl<sub>2</sub>]<sub>2</sub> dimer, used as precursor dimer for the synthesis of [Os(*p*-cym)(BsDPEN)] complexes using an optimized microwave method (413 K, 150 W, 250 *psi*).<sup>16</sup>

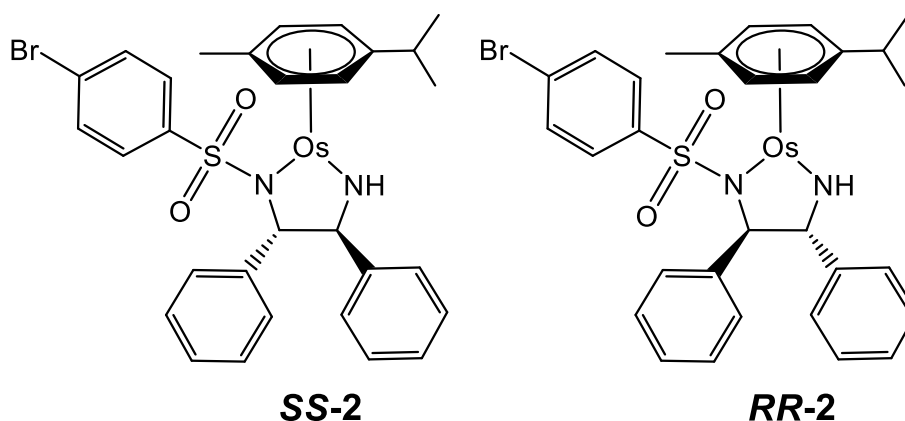
**Synthesis of [Os(η<sup>6</sup>-*p*-cymene)Cl<sub>2</sub>]<sub>2</sub>.** Methanol was sonicated and degassed with nitrogen immediately before use. OsCl<sub>3</sub>·3H<sub>2</sub>O (0.98 g, 2.78 mmol) was dissolved in degassed methanol (10 mL) and α-phellandrene (4.5 mL, 28 mmol) was added while stirring. The reaction vessel was placed in a CEM discovery-SP microwave reactor for 10 min (413 K, 150 W, 250 *psi*). An orange suspension containing crystalline, bright-orange precipitate was observed. The solid was washed with *n*-pentane (3×10 mL) and dried with diethyl ether (10 mL). A pale orange crystalline solid was obtained (0.70 g, 0.88 mmol, 63%). <sup>1</sup>H NMR (500 MHz, d<sub>6</sub>-DMSO, 298 K, TMS): δ=6.09 (d, 4H, <sup>3</sup>J(H,H)=6.1 Hz, Ar-H), 6.04 (d, 4H, <sup>3</sup>J(H,H)=6.1 Hz, Ar-H), 3.00 (sept., 2H, <sup>3</sup>J(H,H)=6.9 Hz, CH(CH<sub>3</sub>)<sub>2</sub>), 2.39 (s, 6H, Ar-CH<sub>3</sub>), 1.21 (d, 12H, <sup>3</sup>J(H,H)=6.9 Hz, CH(CH<sub>3</sub>)<sub>2</sub>).

#### General synthesis of Os[(*p*-cym)BsDPEN] complexes



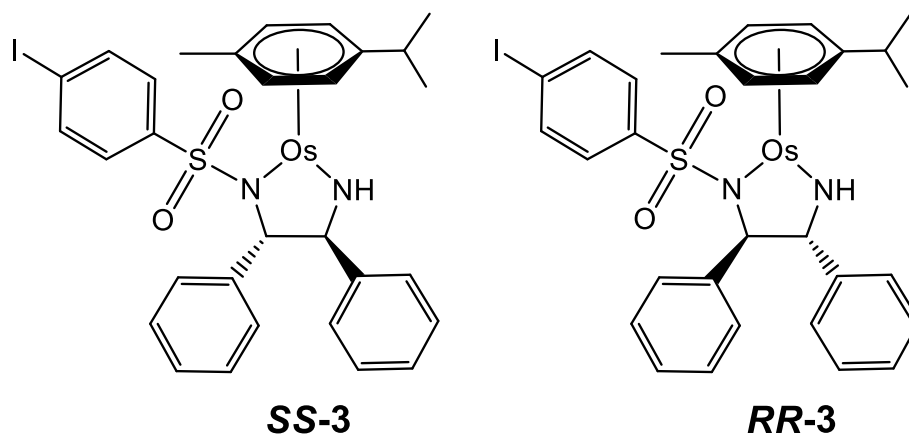
**Scheme 3.3.** General synthetic scheme for [Os<sup>II</sup>(*p*-cym)(R-BsDPEN)] pseudo-octahedral complexes: where *p*-cym=*para*-cymene, RBsDPEN=R-benzylidiphenylethylene diamine with substituent R=Br, I or OMe.

To a stirred solution of [Os( $\eta^6$ -*p*-cymene)Cl<sub>2</sub>]<sub>2</sub> dimer (0.06 mmol, 50 mg, 1 mol eq.) in DCM (10 mL) was added ligand **L1-L4** (0.14 mmol, 2.3 mol eq.) until a yellow solution was formed. Potassium hydroxide (50 mg, 15 mol eq.) was added, followed by distilled water (10 mL) and the solution mixed until a brick-red organic layer was formed. The organic layer was extracted with DCM (3×5 mL) and the resulting solution concentrated *in vacuo*.



**[Os( $\eta^6$ -*p*-cymene)((1*S*, 2*S*)-BrBsDPEN)] (SS-2).** SS-2 was synthesized using the general synthesis method using (1*S*, 2*S*)-BrBsDPEN (**SS-L1**, 60 mg, 0.14 mmol) to obtain a dark orange solid. The product was recrystallized in 1:2 ratio of DCM:hexane (52 mg, 0.07 mmol, 58%). <sup>1</sup>H NMR (500 MHz, d<sub>6</sub>-DMSO, 298 K, TMS):  $\delta$ =8.21 (d, <sup>3</sup>J(H,H)=3.7 Hz, 1H, NH), 7.46 (d, <sup>3</sup>J(H,H)=7.5 Hz, 2H, ArH), 7.31 (d, <sup>3</sup>J(H,H)=8.4 Hz, 2H, ArH), 7.27-7.09 (m, 11H, ArH), 5.95 (d, <sup>3</sup>J(H,H)=5.6 Hz, 1H, Os-ArH), 5.83 (d, <sup>3</sup>J(H,H)=5.5 Hz, 1H, Os-ArH), 5.71 (d, <sup>3</sup>J(H,H)=5.4 Hz, 1H, Os-ArH), 5.64 (d, <sup>3</sup>J(H,H)=5.4 Hz, 1H, Os-ArH), 4.20 (s, 1H, TsNCH), 3.85 (d, <sup>3</sup>J(H,H)=4.3 Hz, 1H, NCH), 2.27 (s, 3H CH<sub>3</sub>), 1.28 (d, <sup>3</sup>J(H,H)=6.8 Hz, 3H, CH(CH<sub>3</sub>)<sub>2</sub>), 1.18 (d, <sup>3</sup>J(H,H)=6.9 Hz, 3H, CH(CH<sub>3</sub>)<sub>2</sub>). <sup>13</sup>C NMR (125 MHz, DMSO):  $\delta$ =146.8, 144.9, 143.9, 131.3, 128.5, 128.2, 127.9, 127.1, 126.7, 126.5, 126.9, 91.1, 82.7, 80.2, 76.8, 73.8, 71.4, 67.9, 40.6, 40.2, 40.1, 32.6, 23.7, 23.5, 20.8. UV/Vis  $\lambda_{\text{max}}$  259, 412, 477 nm; HRMS (ESI): *m/z* calculated for C<sub>30</sub>H<sub>32</sub>BrN<sub>2</sub>O<sub>2</sub>OsS [M+H<sup>+</sup>]: 755.0977; found: 755.0946. Elemental analysis: found (C<sub>30</sub>H<sub>31</sub>BrN<sub>2</sub>O<sub>2</sub>OsS): C 47.17 (47.80), H 4.10 (4.15), N 3.51 (3.72).

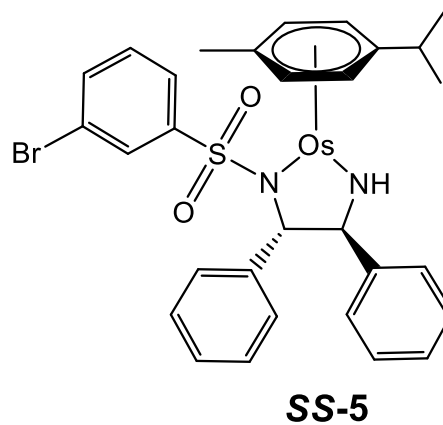
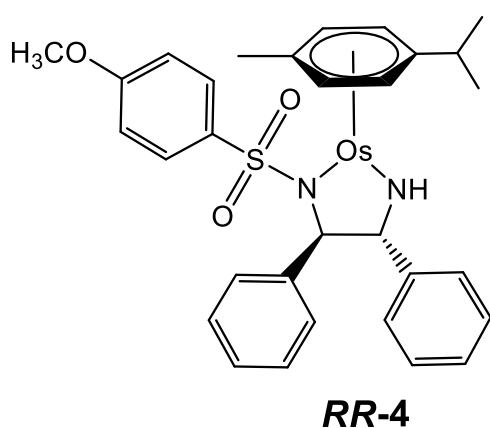
**[Os( $\eta^6$ -*p*-cymene)((1*R*, 2*R*)-BrBsDPEN)] (RR-2).** **RR-2** was synthesized using the general synthesis method using (1*R*, 2*R*)-BrBsDPEN (**RR-L1**, 60 mg, 0.14 mmol) to obtain dark orange solids. The product was recrystallized in 1:2 ratio of DCM:hexane (48 mg, 0.06 mmol, 53%). <sup>1</sup>H NMR (500 MHz, d<sub>6</sub>-DMSO, 298 K, TMS):  $\delta$ =8.21 (d, <sup>3</sup>J(H,H)=4.0 Hz, 1H, NH), 7.46 (d, <sup>3</sup>J(H,H)=7.5 Hz, 2H, ArH), 7.31 (d, <sup>3</sup>J(H,H)=8.5 Hz, 2H, ArH), 7.27-7.11 (m, 11H, ArH), 5.95 (d, <sup>3</sup>J(H,H)=5.7 Hz, 1H, Os-ArH), 5.83 (d, <sup>3</sup>J(H,H)=5.5 Hz, 1H, Os-ArH), 5.71 (d, <sup>3</sup>J(H,H)=5.5 Hz, 1H, Os-ArH), 5.64 (d, <sup>3</sup>J(H,H)=5.6 Hz, 1H, Os-ArH), 4.20 (s, 1H, TsNCH), 3.85 (d, <sup>3</sup>J(H,H)=4.4 Hz, 1H, CH), 2.27 (s, 3H CH<sub>3</sub>), 1.28 (d, <sup>3</sup>J(H,H)=6.9 Hz, 3H, CH(CH<sub>3</sub>)<sub>2</sub>), 1.18 (d, <sup>3</sup>J(H,H)=6.9 Hz, 3H, CH(CH<sub>3</sub>)<sub>2</sub>). <sup>13</sup>C NMR (125 MHz, DMSO):  $\delta$ =146.8, 144.8, 143.8, 131.3, 129.3, 128.5, 128.2, 127.9, 127.4, 127.1, 126.9, 126.6, 91.1, 82.7, 80.2, 76.8, 73.8, 71.4, 40.6, 40.4, 40.3, 32.6, 23.7, 23.5, 20.8. UV/Vis  $\lambda_{\text{max}}$  258, 412, 478 nm HRMS (ESI): *m/z* calculated for C<sub>30</sub>H<sub>32</sub>BrN<sub>2</sub>O<sub>2</sub>OsS [M+H<sup>+</sup>]: 755.0977; found: 755.0969. Elemental analysis: found (calculated for C<sub>30</sub>H<sub>31</sub>BrN<sub>2</sub>O<sub>2</sub>OsS): C 48.48 (47.80), H 4.15 (4.15), N 4.04 (3.72).



**[Os( $\eta^6$ -*p*-cymene)((1*S*, 2*S*)-IBsDPEN)] (SS-3).** **SS-3** was synthesized using the general synthesis method using (1*S*, 2*S*)-IBsDPEN (**SS-L2**, 67 mg, 0.14 mmol) to obtain dark orange solids. The product was recrystallized in 1:2 ratio of DCM:hexane (47 mg, 0.06 mmol, 49%). <sup>1</sup>H NMR (500 MHz, d<sub>6</sub>-DMSO, 298 K, TMS):  $\delta$ =8.19 (d, <sup>3</sup>J(H,H)=4.1 Hz, 1H, NH), 7.49 (d, <sup>3</sup>J(H,H)=8.4 Hz, 2H, ArH), 7.46 (d, <sup>3</sup>J(H,H)=7.7 Hz, 2H, ArH), 7.27-7.11 (m, 9H, ArH), 6.96 (d, <sup>3</sup>J(H,H)=8.3 Hz, 2H, ArH), 5.94 (d, <sup>3</sup>J(H,H)=5.6 Hz, 1H, Os-ArH), 5.82 (d, <sup>3</sup>J(H,H)=5.5 Hz, 1H, Os-ArH), 5.70 (d, <sup>3</sup>J(H,H)=5.5 Hz, 1H, Os-ArH), 5.62 (d, <sup>3</sup>J(H,H)=5.6 Hz, 1H, Os-ArH), 4.19 (s, 1H, TsNCH), 3.84 (d, <sup>3</sup>J(H,H)=4.4 Hz, 1H, CH), 2.27 (s, 3H CH<sub>3</sub>),

1.27 (d,  $^3J(H,H)=6.9$  Hz, 3H,  $CH(CH_3)_2$ ), 1.18 (d,  $^3J(H,H)=6.9$  Hz, 3H,  $CH(CH_3)_2$ ).  $^{13}C$  NMR (125 MHz, DMSO):  $\delta=146.9, 144.9, 144.2, 137.2, 128.3, 128.2, 127.9, 127.4, 127.1, 126.9, 126.6, 98.3, 91.1, 82.7, 80.2, 76.8, 73.8, 71.4, 67.2, 40.6, 40.4, 40.2, 40.1, 32.6, 31.2, 23.7, 23.5, 20.7$ . UV/Vis  $\lambda_{max}$  272, 412, 479 nm; HRMS (ESI):  $m/z$  calculated for  $C_{30}H_{32}IN_2O_2OsS$  [ $M+H^+$ ]: 803.0839; found: 803.0832. Elemental analysis: found (calculated for  $C_{30}H_{31}N_2IO_2OsS$ ): C 45.14 (45.00), H 3.84 (3.90), N 3.60 (3.50).

**[Os( $\eta^6$ -*p*-cymene)((1*R*, 2*R*)-IBsDPEN)] (RR-3).** RR-3 was synthesized using the general synthesis method using (1*R*, 2*R*)-IBsDPEN (RR-L2, 68 mg, 0.14 mmol) to obtain a bright orange solid. The product was recrystallized in 1:2 ratio of DCM:hexane (68 mg, 0.08 mmol, 71%).  $^1H$  NMR (500 MHz,  $d_6$ -DMSO, 298 K, TMS):  $\delta=8.20$  (d,  $^3J(H,H)=4.0$  Hz, 1H, NH), 7.49 (d,  $^3J(H,H)=8.4$  Hz, 2H, ArH), 7.46 (d,  $^3J(H,H)=7.8$  Hz, 2H, ArH), 7.27-7.11 (m, 9H, ArH), 6.96 (d,  $^3J(H,H)=8.3$  Hz, 2H, ArH), 5.94 (d,  $^3J(H,H)=5.6$  Hz, 1H, Os-ArH), 5.82 (d,  $^3J(H,H)=5.5$  Hz, 1H, Os-ArH), 5.70 (d,  $^3J(H,H)=5.5$  Hz, 1H, Os-ArH), 5.62 (d,  $^3J(H,H)=5.6$  Hz, 1H, Os-ArH), 4.19 (s, 1H, TsNCH), 3.84 (d,  $^3J(H,H)=4.4$  Hz, 1H, CH), 2.27 (s, 3H  $CH_3$ ), 1.27 (d,  $^3J(H,H)=6.9$  Hz, 3H,  $CH(CH_3)_2$ ), 1.18 (d,  $^3J(H,H)=6.9$  Hz, 3H,  $CH(CH_3)_2$ ).  $^{13}C$  NMR (125 MHz, DMSO):  $\delta=146.9, 144.9, 144.3, 137.2, 129.3, 128.3, 128.2, 127.9, 127.4, 127.1, 126.9, 126.6, 98.3, 91.1, 82.7, 80.3, 76.8, 73.8, 71.4, 67.2, 40.6, 40.4, 40.2, 40.1, 32.6, 31.2, 23.7, 23.5, 20.8$ . UV/Vis  $\lambda_{max}$  271, 412, 479 nm; HRMS (ESI):  $m/z$  calculated for  $C_{30}H_{32}IN_2O_2OsS$  [ $M+H^+$ ]: 803.0839 ; found: 803.0845. Elemental analysis: found (calculated for  $C_{30}H_{31}N_2IO_2OsS$ ): C 44.71 (45.00), H 3.80 (3.90), N 3.49 (3.50).



**[Os( $\eta^6$ -*p*-cymene)((1*R*, 2*R*)-MeOBsDPEN)] (RR-4).** RR-4 was synthesized using the general synthesis method using (1*R*, 2*R*)-(MeO)BsDPEN (**RR-L3**, 0.054 g, 0.14 mmol) to obtain a bright orange solid (0.043 g, 0.06 mmol, 93%). <sup>1</sup>H NMR (400 MHz, d<sub>6</sub>-DMSO, 298 K, TMS):  $\delta$ =8.10 (s, 1H, NH), 7.47 (d, <sup>3</sup>J(H,H)=7.4 Hz, 2H, ArH), 7.29-7.09 (m, 10H, ArH), 6.68 (d, <sup>3</sup>J(H,H)=7.4 Hz, 2H, ArH), 5.89 (d, <sup>3</sup>J(H,H)=5.6 Hz, 1H, Os-ArH), 5.77 (d, <sup>3</sup>J(H,H)=5.6 Hz, 1H, Os-ArH), 5.58 (d, <sup>3</sup>J(H,H)=5.2 Hz, 1H, Os-ArH), 5.49 (d, <sup>3</sup>J(H,H)=5.2 Hz, 1H, Os-ArH), 4.26 (s, 1H, TsNCH), 3.86 (d, <sup>3</sup>J(H,H)=4.3 Hz, 1H, CH), 3.76 (s, 3H OCH<sub>3</sub>), 2.21 (s, 3H CH<sub>3</sub>), 1.26 (d, <sup>3</sup>J(H,H)=6.7 Hz, 3H, CH(CH<sub>3</sub>)<sub>2</sub>), 1.16 (d, <sup>3</sup>J(H,H)=6.6 Hz, 3H, CH(CH<sub>3</sub>)<sub>2</sub>).  $\delta$ =161.1, 147.3, 145.1, 137.2, 129.3, 128.6, 128.2, 127.8, 127.4, 127.2, 127.0, 126.6, 126.5, 90.8, 82.6, 79.9, 76.7, 74.0, 71.4, 71.3, 67.0, 55.9, 40.6, 40.4, 40.3, 32.6, 24.5, 23.8, 23.4, 20.47. UV/Vis  $\lambda_{\text{max}}$  275, 412, 478 nm; C<sub>31</sub>H<sub>35</sub>N<sub>2</sub>O<sub>3</sub>OsS [M+H<sup>+</sup>]: 707.1978; found: 707.1970. Elemental analysis: found (calculated for C<sub>31</sub>H<sub>34</sub>N<sub>2</sub>O<sub>3</sub>OsS): C 52.32 (52.83), H 4.86 (4.86), N 3.89 (3.97)

**[Os( $\eta^6$ -*p*-cymene)((1*S*, 2*S*)-*m*-BrBsDPEN)] (SS-5).** SS-5 was synthesized using the general synthesis method using (1*S*, 2*S*)-(*m*-Br)BsDPEN (**SS-L4**, 0.019 g, 0.05 mmol) to obtain a bright orange solid (0.043 g, 0.06 mmol, 93%). A bright red oil was formed. The oil was dissolved in a minimum amount of DCM and hexane (10 mL) was added. The resulting cloudy red solution was concentrated *in vacuo* to produce a light orange solid (0.017 g, 23 mg, 45%). <sup>1</sup>H NMR (400 MHz, d<sub>6</sub>-DMSO, 25 °C, TMS):  $\delta$ =8.29 (d, <sup>3</sup>J(H,H)=3.8 Hz, 1H, NH), 7.55 (d, <sup>3</sup>J(H,H)=8.5 Hz, 1H, ArH), 7.46 (d, <sup>3</sup>J(H,H)=7.1 Hz, ArH), 7.40 (s, 1H, ArH), 7.31 (d, <sup>3</sup>J(H,H)=8.0 Hz, 2H, ArH), 7.24 (d, <sup>3</sup>J(H,H)=7.4 Hz, 2H, ArH), 7.22-7.13 (m, 7H, ArH), 5.92 (d, <sup>3</sup>J(H,H)=5.7 Hz, 1H, Os-ArH), 5.80 (d, <sup>3</sup>J(H,H)=5.7 Hz, 1H, Os-ArH), 5.67 (d, <sup>3</sup>J(H,H)=5.2 Hz, 1H, Os-ArH), 5.58 (d, <sup>3</sup>J(H,H)=5.6 Hz, 1H, Os-ArH), 4.23 (s, 1H, TsNCH), 3.85 (d, <sup>3</sup>J(H,H)=4.4 Hz, 1H, CH), 2.29 (s, 3H, CH(CH<sub>3</sub>)<sub>2</sub>), 2.27 (d, <sup>3</sup>J(H,H)=6.8 Hz, 3H, CH(CH<sub>3</sub>)<sub>2</sub>), 1.20 (d, <sup>3</sup>J(H,H)=6.8 Hz, 3H, CH<sub>3</sub>). <sup>13</sup>C NMR (125 MHz, d<sub>6</sub>-DMSO):  $\delta$ =146.8, 146.7, 144.8, 133.8, 130.7, 129.3, 129.1, 128.3, 128.0, 127.3, 126.7, 126.6, 125.6, 121.7, 91.1, 82.8, 80.3, 77.0, 73.6, 71.5, 71.1, 67.6, 40.6, 40.5, 40.4, 33.5, 32.6, 24.5, 23.7, 23.6, 21.0, 20.8. UV/Vis  $\lambda_{\text{max}}$  272, 412, 480 nm; C<sub>30</sub>H<sub>31</sub>BrN<sub>2</sub>O<sub>2</sub>OsS [M+H<sup>+</sup>]: 755.0977; found: 755.0956. C 48.05 (47.80), H 3.56 (4.15), N 3.58 (3.72).

### 3.2.3 X-ray Crystal Structures

Complexes **SS-2** (R=*p*-Br) and **SS-3** (R=*p*-I) were recrystallized in a minimum amount of DCM (4-5 drops) and hexane (9-10 drops) at room temperature over 24 h. X-ray crystal structures were obtained as described in **Chapter 2 (Section 2.3.5)**.

### 3.2.4 Density Functional Theory

Density functional theory (DFT) calculations were carried out by Dr James P. C. Coverdale (University of Warwick) using Gaussian 03W software. Geometry optimization (lowest energy conformation) was calculated in the gas-phase using hybrid PBE0 (Perdew-Burke-Ernzerhof functional) with a combination of 75% DFT (Density functional theory) and 25% (Hartree Fock) computational methods. The Lan12DZ basis set including the effective core potential was used for Os and 6-31+G\*\* basis set for all non-metal elements. Structures were optimized based on the x-ray crystallographic data for **RR-1** (*p*-CH<sub>3</sub>) and were altered appropriately using GaussView 3.0. EPS (electrostatic potential surfaces) were mapped to represent the electron density (isovalue=0.04), ranging from red to blue (-0.025 to +0.250 au).

### 3.2.5 Solution stability studies

Prior to commencement of biological studies (for which osmium complexes are prepared in 5% *v/v* DMSO, 95% *v/v* DMEM), complexes must be stable in DMSO for 24 h. The stabilities of complexes **2-5** in d<sub>6</sub>-DMSO were monitored over 24 h using <sup>1</sup>H NMR (400 MHz, d<sub>6</sub>-DMSO) and UV-Vis spectroscopy (λ=200-800 nm) over 24 h. The 24 h solubility and stability of **2-5** in 5% *v/v* DMSO: 95% *v/v* PBS (physiological conditions) were also determined by UV-Vis spectroscopy (λ=200-800 nm).



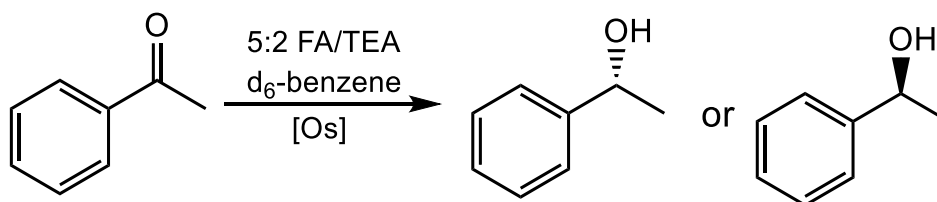
### 3.2.6 Partition Coefficient (LogP)

$$\text{LogP} = \frac{[\text{Os in octanol}]}{[\text{Os in water}]} = \frac{[\text{Os in water before}] - [\text{Os in water after}]}{[\text{Os in water after}]}$$

**Equation 3.1.** Determination of the partition coefficient (LogP) as the ratio of concentrations of osmium complexes in octanol and water using ICP-MS under nitric acid conditions

Octanol-saturated water (OSW) and water-saturated octanol (WSO) solutions were prepared by mixing equivalent volumes of octanol and milliQ water for 24 h. The aqueous and organic phases were extracted. Osmium complex (~3-4 mg) was dissolved in OSW (10 mL) in duplicate, shaken and sonicated (until the solution was fully saturated) and syringe-filtered (0.2 µm) to remove excess solid. From the filtered solution, 2 mL was mixed in triplicate with WSO (2 mL) and shaken (24 h). The remaining filtered solution was analysed by ICP-MS (1:10 dilution) in 3.6% v/v stabilised nitric acid (**Chapter 2, Section 2.3.3**) to calculate the ‘before’ concentration. After 24 h, the OSW bottom (water) layer was extracted using a 2 mL syringe. The resulting samples were diluted in 3.6% v/v stabilized nitric acid and analysed by ICP-MS. From ICP-MS, the quantity of osmium in the OSW layer was obtained, which was used to back-calculate the concentration of osmium in the octanol (WSO) layer, and thus, the LogP (according to **Equation 3.1**).

### 3.2.7 Transfer hydrogenation catalysis



**Scheme 3.4.** Enantioselective reduction of acetophenone to (*S*) or (*R*)-1-phenylethanol in the presence of osmium catalyst ([Os]=**2-5**), 5:2 formic acid/trimethylamine azeotrope (TEA/FA) and d<sub>6</sub>-benzene monitored at 310 K by <sup>1</sup>H NMR and chiral GC-FID.

### Catalytic reduction of acetophenone by <sup>1</sup>H NMR

Osmium catalyst (5 µmol, 0.5% mol eq.) was weighed into a small glass vial and dissolved in d<sub>6</sub>-benzene (100 µL) and 5:2 formic acid/triethylamine azeotrope (500 µL) under nitrogen at 310 K. The mixture was stirred for 30 min. Acetophenone (1 mmol, 200 mol eq.) was added and the mixture transferred to a nitrogen-purged 5 mm NMR tube. <sup>1</sup>H NMR spectra were collected every 2 min over 1 h at 310 K and the experiment was performed in triplicate. <sup>1</sup>H NMR spectra were also acquired every 10 min over a 15 h period. The catalytic conversion of acetophenone to 1-phenylethanol was determined by monitoring the decrease in the integral for the acetophenone singlet (3H, 2.10 ppm) and the increase in the 1-phenylethanol quartet (4.75 ppm, 1H).

### Catalytic reduction of acetophenone by GC

Formic acid: triethylamine 5:2 azeotrope (500 µL) was added to a round-bottom flask containing osmium catalyst (5 µmol, 1 eq.) under nitrogen and acetophenone (1 mmol, 0.17 mL, 200 eq.) was added and stirred at 310 K for 24 h. From the resulting solution, 2-3 drops were placed in 1:1 ethyl acetate/sodium bicarbonate (2 mL). The organic ethyl acetate layer was extracted and filtered through a silica micro-pipette column. The samples were then analysed by chiral GC-FID to determine enantiomeric excesses and conversions. Chiral GC measurements were carried out by Jonathan Barrios-Rivera and Sam Forshaw (University of Warwick) on a Hewlett-Packard 5890 instrument linked to PC running DataApex Clarity software. Measurements were obtained using a CROMPAC CYCLODEXTRIN-β-236M-19, 50 m×0.25 mm×0.25 µm, carrier gas=H<sub>2</sub>, T=383 K, pressure=15 psi, FID temperature=523 K, injection temperature=493 K. Data were analysed on Windows Clarity Chromatography Suite.

### 3.2.8 Antiproliferative activity (IC<sub>50</sub>)

#### IC<sub>50</sub> determination

Half-maximal inhibitory concentrations (IC<sub>50</sub> /  $\mu$ M) of **2-5** were determined using the protocol described in **Chapter 2 (Section 2.5.1)** against A2780 (ovarian carcinoma), A549 (lung adenocarcinoma), PC3 (prostate adenocarcinoma) and MCF7 (breast adenocarcinoma) cancer cells and MRC5 healthy lung fibroblasts.

#### Formate and acetate-dependent inhibition of cell proliferation

The affect of formate and acetate on the cell viability upon co-administration with **SS-2** and **RR-2** was determined in A549 (lung) cancer cells using the general SRB protocol but co-administering a fixed concentration of osmium complex (0.5 or 1.0 $\times$ IC<sub>50</sub>) alongside variable concentrations of sodium formate or acetate (0-2 mM).

### 3.2.9 Flow cytometry studies

#### Membrane integrity

Flow cytometry measurments were conducted by Dr Hannah Bridgewater from the School of Life Sciences (University of Warwick). A suspension of  $1\times 10^6$  A549 cells were seeded in a 6-well plate (2 mL/well) for 24 h (310 K, 5% CO<sub>2</sub>). The supernatant medium was removed and cells were treated with 1 $\times$ IC<sub>50</sub> (30  $\mu$ M) of **SS-2** and sodium formate (0-2 mM) for 24 h (310 K, 5% CO<sub>2</sub>). The supernatant was removed, cells washed with PBS and 0.25% trypsin/EDTA (1 mL) was added to detach cells from the surface. The cell suspensions were centrifuged (1500 rpm, 5 min, 298 K), the pellets collected, washed with PBS and re-suspended in a staining buffer containing 80  $\mu$ g/mL RNase and 50  $\mu$ g/mL propidium iodide (500  $\mu$ L) for 30 min, under dark conditions. The cells were centrifuged (1500 rpm, 5 min, 298 K) and the supernatant removed, before being re-suspended in PBS for analysis by flow cytometry on the BD LSRII flow cytometer with BD FACSDIVA V8.01 for Windows and processed using FlowJo V10.

### Cell cycle analysis

Cell pellets treated with 1×IC<sub>50</sub> (30 μM) of **SS-2** were obtained as described in the membrane integrity section. The pellets were washed in PBS before re-suspending in ice-cold ethanol (fixation) for 30 min. The supernatant ethanol was removed and cells washed with PBS. The cells were then treated with 500 μL of staining buffer (as described for membrane integrity analysis) for 30 min. Cells were pelleted by centrifugation (1500 rpm, 5 min, 298 K), the supernatant removed, before being re-suspended in PBS for analysis by flow cytometry.

### 3.2.10 Zebrafish toxicity studies

The University of Warwick is a member of the Laboratory Animal Science Association and the Institute of Animal Technology.<sup>14</sup> All *in vivo* animal work was approved by the University Ethical Review Committee.<sup>14</sup> Zebrafish experiments were carried out at the School of Life Sciences (University of Warwick) under project AWERB.10/16-17, in collaboration with Dr. Karuna Sampath (Warwick Medical School).<sup>14</sup>

Experiments were carried out by Dr James P. C. Coverdale (University of Warwick). 12-well plates were seeded with a minimum of one Singapore wild-type (SG-WT) zebrafish embryo per well. Embryos were treated with different concentrations of **SS-2** or **RR-2** (0.01, 0.1, 1, 10 and 50 μM) and incubated at 301.5 K for 96 h. The mortality of the embryos was categorized as non-viable upon fulfilment of any of the following: (a) tail detachment from body, (b) somite formation, (c) coagulation of embryo and (d) heartbeat.<sup>14</sup> Sigmoidal dose-response curves were plotted by taking the logarithm of osmium complex concentration against percentage survival to determine half-lethal inhibitory concentrations (LC<sub>50</sub> / μM).

### 3.2.11 <sup>189</sup>Os ICP-MS cellular accumulation studies

Osmium (<sup>189</sup>Os) ICP-MS cellular accumulation studies of **SS-2** and **RR-2** were conducted in A2780 (ovarian) and A549 (lung) cancer cells by varying conditions using the general cellular ICP-MS accumulation method.

#### General ICP-MS cellular accumulation method

Cellular accumulation studies were performed based on a previously reported method.<sup>17</sup> A single cell suspension was obtained as previously described (**Section 2.5.1**). Briefly, 4×10<sup>6</sup> cells were seeded into a 100 cm<sup>2</sup> cell culture petri dish in 10 mL of media for 24 h (310 K, 5% CO<sub>2</sub>). Cells were treated with specific concentrations of ICP-OES corrected test compounds under various conditions. The cells were then washed with PBS, detached with 0.25% trypsin/EDTA and quenched with a known volume of DMEM. Cells were counted in duplicate (using a haemocytometer) before centrifugation (5 min, 1000 rpm, 298 K) to obtain cell pellets. The supernatant was removed, and the cell pellets re-suspended in PBS (1 mL) before further centrifugation (5 min, 1200 rpm). The supernatant was removed and the pellets and stored at 253 K before ICP-MS analysis. Cell pellets were digested using the ICP-MS acid digestion method (**Chapter 2, Section 2.5.2**). Variations in cellular accumulation have been specified:

- (i) **Concentration:** Treated with 0.25, 0.5, 1, 1.5×IC<sub>50</sub> (μM) for 24 h, (no recovery period; 310 K, 5% CO<sub>2</sub>)
- (ii) **Time:** Treated with 1×IC<sub>50</sub> (μM) for 3, 6, 18 h, 24 h (no recovery in complex-free media) and 24 h exposure with 24, 48 and 72 h recovery in complex-free media (310 K, 5% CO<sub>2</sub>).
- (iii) **Temperature:** Treated with 1×IC<sub>50</sub> (μM) for 3 or 6 h at 310 or 277 K (no recovery in complex-free media).
- (iv) **Formate:** Treated with 1×IC<sub>50</sub> and co-administered with 0-2 mM sodium formate for 24 h (310 K, 5% CO<sub>2</sub>), with no recovery in complex-free media.

### 3.2.12 <sup>189</sup>Os and <sup>79</sup>Br ICP-MS cellular accumulation studies

Cell accumulation studies of **SS-2** (R=*p*-Br) were conducted in A549 cells under varying conditions using the general ICP-MS cellular accumulation method. In these experiments, 4×10<sup>6</sup> cells per 20 mL were seeded in 145 mm cell culture petri dishes for 24 h (310 K, 5% CO<sub>2</sub>). Prior to centrifugation, the cell suspensions from two petri dishes were combined to form larger pellets, so as to ensure reliable detection of bromine (<sup>79</sup>Br) by ICP-MS. All cell pellets were analysed by ICP-MS using the alkaline digestion method (**Chapter 2, Section 2.5.3**). Variations in cellular accumulation have been specified:

- (i) **Time:** Treated with 1×IC<sub>50</sub> of **SS-2** (30 μM) for 3, 6, 18 h, 24 h (no recovery in complex-free media) and 24 h exposure with 24, 48 and 72 h recovery in complex-free media (310 K, 5% CO<sub>2</sub>).
- (ii) **Temperature:** Treated with 1×IC<sub>50</sub> **SS-2** (30 μM) for 3 or 6 h at 310 or 277 K (no recovery in complex-free media).
- (iii) **Inhibition of caveolae endocytosis:** The inhibition of caveolae endocytosis was investigated using methyl-β-cyclodextrin, a known endocytotic inhibitor.<sup>17</sup> Cells were treated with 1×IC<sub>50</sub> **SS-2** (30 μM) and co-administered with 0.1-1 mM methyl-β-cyclodextrin (DMEM).
- (iv) **Inhibition of efflux:** The inhibition of efflux was investigated by recovering treated cells in verapamil – a known P-glycoprotein (PGP) inhibitor.<sup>17</sup> Cells were treated with 1×IC<sub>50</sub> **SS-2** (30 μM) for 24 h, washed with PBS and allowed to recover in 20 μM of verapamil hydrochloride (5% v/v DMSO, 95% v/v DMEM) for 24, 48 and 72 h.
- (v) **Cell fractionation:** The cellular distribution of <sup>189</sup>Os and <sup>79</sup>Br was investigated using a FractionPREP BioVision Cell Fractionation Kit using 2× the volumes specified by the manufacturers (to account for larger cell pellet size). Cells were treated with 1×IC<sub>50</sub> of **SS-2** (30 μM) for 3, 6 and 24 h (no recovery) and 24 h exposure with 24, 48 and 72 h recovery in complex-free media.

### 3.2.13 Synchrotron-XRF

**Preparation of Tris-glucose buffer.** Tris-glucose buffer was prepared by mixing D-glucose (11.756 g, 0.065 mol), tris(hydroxymethyl)aminomethane (0.307 g, 2.53 mmol), 9 mM acetic acid (12.9 mL) and made up to 250 mL in milliQ water (pH=7.42). The buffer was sterile-filtered using a 500 mL Millipore Stericup filter unit (Durapore PVDF membrane, low protein-binding, pore size 0.22 µm).

**Preparation of A549 cells on Si<sub>3</sub>N<sub>4</sub> membranes.** Si<sub>3</sub>N<sub>4</sub> membranes were prepared using the general protocol described in **Chapter 2 (Section 2.6.1)**, using a seeding density of 6×10<sup>4</sup> cells/mL of A549 cells. Cells were treated with 1, 3 and 5×IC<sub>50</sub> of **SS-2** (30, 90 or 150 µM, respectively) for 24 h (no recovery). Prior to blotting and plunge-freezing, cells were washed with tris-glucose buffer (2×3 mL).

**Beamline settings and data analysis.** XRF maps were acquired using an incident energy of 15 keV, step size=100 nm, 0.1 s exposure and a beam size of 50×70 nm<sup>2</sup> (**Chapter 2, Section 2.4.1**). Data were fitted in PyMCA and analysed in ImageJ (**Chapter 2, Section 2.6.1**).<sup>18, 19</sup>

### 3.2.14 Chloroquine inhibition of lysosomal activity

**Chloroquine-dependent IC<sub>50</sub>.** Chloroquine toxicity was determined in A549 cells using the general SRB protocol (**Chapter 2, Section 2.5.1**). Cells were treated with chloroquine diphosphate (0-150 µM in DMEM) for variable exposure times, followed by fixing with TCA and continuation of the SRB assay (**Chapter 2, Section 2.5.1**). The chloroquine-dependent IC<sub>50</sub> concentrations of **RR-1** (R=*p*-CH<sub>3</sub>) and **SS-2** (R=*p*-Br) were determined in A549 cancer cells using the general SRB protocol (**Chapter 2, Section 2.5.1**). Prior to treatment with **RR-1** or **SS-2**, cells were pre-incubated chloroquine diphosphate (150 µM in DMEM) for 2 h. The chloroquine supernatant was removed, cells washed with PBS, and then treated with **RR-1** or **SS-2** (0.1-150 µM).

**Chloroquine-dependent <sup>189</sup>Os cellular accumulation.** The chloroquine-dependent cellular accumulation of osmium was determined for A549 cells following the general accumulation protocol (**Chapter 2, Section 2.5.2**). Cells were pre-incubated with 150  $\mu$ M chloroquine disphosphate (DMEM) for 2 h, washed with PBS and treated with 1 $\times$ IC<sub>50</sub> of **RR-1** (21  $\mu$ M) or **SS-2** (30  $\mu$ M) for 24 h (no recovery). This experiment was performed in duplicate for **SS-2** to allow analysis by both the acid and alkaline digestion methods specified in **Chapter 2 (Section 2.5.3)**.

**Chloroquine-dependent membrane integrity.** The chloroquine-dependent effect on membrane integrity was investigated using the same membrane integrity protocol described in this chapter (**Section 3.2.9**). Cells were pre-incubated with 150  $\mu$ M chloroquine disphosphate (DMEM) for 2 h, washed with PBS and treated with 1 $\times$ IC<sub>50</sub> of **RR-1** (21  $\mu$ M) or **SS-2** (30  $\mu$ M) for 24 h (no recovery).



### 3.3 Results

#### 3.3.1 Synthesis and characterisation

All ligands and complexes were characterised by <sup>1</sup>H NMR, <sup>13</sup>C NMR, HR-MS and elemental (CHN) analysis. A total of six BsDPEN ligands (**L1-L4**, including enantiomers) were synthesized from the reaction between (1*R*, 2*R*) or (1*S*, 2*S*)-diphenylethylene diamine (DPEN) with different benzene sulfonyl chlorides from a method reported in the literature.<sup>20</sup> Ligands **L1-L4** were recrystallized from hot ethyl acetate, and cooled to 253 K to produce white solids. From these ligands, six Os<sup>II</sup>[(*p*-cym)BsDPEN] complexes (**2-5**, including enantiomers) were synthesized by reacting [Os(*p*-cym)Cl<sub>2</sub>]<sub>2</sub> dimer with **L1-L4** (BsDPEN ligands) in the presence of a base (potassium hydroxide) following a method reported in the literature.<sup>1</sup>

Single crystals for **SS-2** (R=*p*-Br) and **SS-3** (R=*p*-I) were obtained by dissolving *ca.* 5 mg in a minimum amount of DCM (4-5 drops) and hexane (7-10 drops). Crystallographic data were obtained by Dr. Guy Clarkson (University of Warwick) using the methods and instrumentation described in **Chapter 2 (Section 2.3.5)**. The crystal structures of **SS-2** and **SS-3** were closely comparable to that of parent compound **SS-1** (R=*p*-CH<sub>3</sub>) – all with (1*S*, 2*S*) chiral centres, with orthorhombic space groups P2<sub>1</sub>2<sub>1</sub>2<sub>1</sub> (**Fig. 3.4; Appendix, Table A6**).

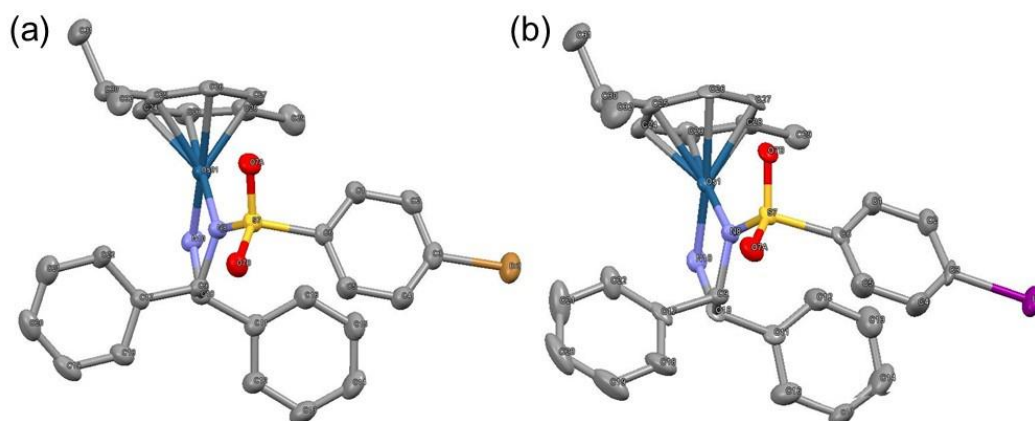


**Figure 3.4.** ORTEP x-ray crystal structures of osmium sulfonamide complexes showing carbon (■), nitrogen (■), oxygen (■), sulfur (■), osmium (■), bromine (■) and iodine (■) for (a) **SS-2** (*p*-Br); (b) **SS-3** (*p*-I), as viewed in Mercury 3.3 software. Thermal ellipsoids (atomic displacement parameters) are presented at 50% probability level.

### 3.3.2 Density Functional Theory (DFT)

Density Functional Theory (DFT) is a valuable tool in bioinorganic chemistry which can be used to model the structure and properties of complexes by providing a solution approximation obtained from the electron-density.<sup>21</sup> Calculated Cartesian coordinates and electrostatic potential surfaces (EPS) for **RR-2** (*p*-Br), **RR-3** (*p*-I) and previously reported complex **RR-6** (*p*-F) were calculated at the PBE0/Lanl2DZ/6-31+G\*\* level (which is commonly used for organometallic compounds) with the EPS shown mapped onto total electron density (**Appendix, Tables A7-10**). The Mulliken partial charges calculated for complexes **RR-6** (*p*-F), **theoretical compound** (*p*-Cl), **RR-2** (*p*-Br) and **RR-3** (*p*-I), at the PBE0/Lanl2DZ/6-31+G\*\* level of theory were determined (**Appendix, Fig. A1, Table A7**). The electrostatic potential correlated with the electronegativity of the halide series: F>Cl>Br>I (**Fig. 3.5**).

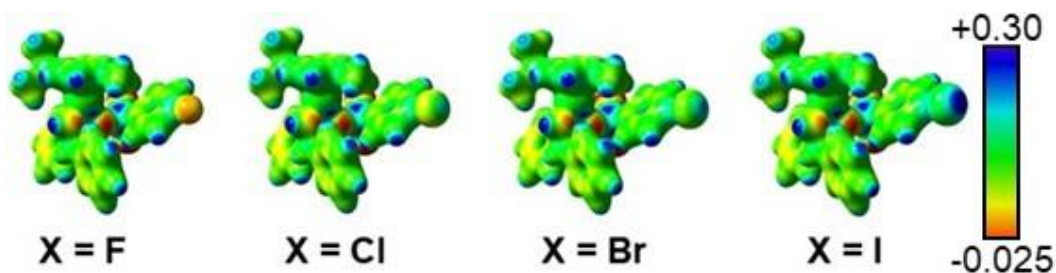


**Figure 3.5.** Calculated electrostatic potential energy surfaces for complexes **RR-6** (X=F), **theoretical compound** (X=Cl), **RR-2** (X=Br) and **RR-3** (X=I), at the PBE0/Lanl2DZ/6-31+G\*\* level of theory. EPS shown mapped onto total electron density. Isovalue = 0.04. (*R,R*)-catalyst only. Surface mapping colours range from red (-0.025 au) to blue (+0.30 au).

The x-ray crystal structures of **SS-2** (R=*p*-Br) and **SS-3** (R=*p*-I; **Appendix, Table A6**) were closely comparable to the ground state structures calculated by DFT (**Appendix, Table A9-10**). Halide-substitution (X=Cl, Br, I) at the *para*-position of the sulfonamide group resulted in localized charge effects, as previously reported for **RR-6** (X=*p*-F).<sup>2</sup> The charge at the osmium centre, the aromatic *p*-cymene ring and the nitrogen atoms of the sulfonamide ligand closely resembled that of parent compound **RR-1** (R=*p*-CH<sub>3</sub>).<sup>2</sup>

### 3.3.3 Aqueous stability and solubility

In order to probe the aqueous stability of complexes **2-5**, solutions in PBS were monitored using UV-Vis spectroscopy over a 24 h period (310 K). The hydrophobic nature of **2-5** limits their solubility in aqueous media, thus a more hydrophobic solubilizing agent is required. Conventionally, aqueous solution stability by UV/Vis for organometallic half-sandwich complexes utilizes a mixture of methanol and water, however, the methanol poses two major issues. Firstly, methanol can act as a hydride source<sup>22</sup> – affecting the catalytic nature of these complexes, and secondly, methanol is toxic to biological cells, so cannot be used as a solubilising agent for *in vitro* antiproliferative assays. As an alternative, complexes **2-5** were tested for their solubility and stability in DMSO over 24 h using <sup>1</sup>H NMR revealing no spectral changes, indicative of high stability in all cases. This also suggests that DMSO is likely not coordinating to the vacant site on the osmium complex (*i.e.* forming a DMSO-complex adduct), or that adduct formation is immediate, hence, is represented in the initial <sup>1</sup>H NMR spectra (t=0 h).

The aqueous stability was investigated in 5% v/v DMSO and 95% PBS by UV-Vis spectroscopy over 24 h – revealing no changes in the absorption spectrum. Importantly, both the <sup>1</sup>H NMR and the UV-Vis spectra show that **2-5** were soluble and stable enough in aqueous media, hence suitable for *in vitro* biological studies.

A balance between lipophilicity and hydrophilicity is essential for the bioavailability and targeting of drugs. Drugs have to be stable enough to pass through a variety of biological barriers (*i.e.* phospholipid membrane bilayers) or enter the cells using pathways such as passive diffusion.<sup>23</sup> The hydrophobic nature of a test compound can influence the cellular influx and efflux pathways, *i.e.* whether the compound enters the cell *via* active transport (*e.g.* endocytosis) or passive diffusion (*e.g.* ion channels). For example, cisplatin enters cancer cells through CTR1 copper transporters, in addition to passive diffusion through cell membranes.<sup>24</sup> Importantly, one major factor enhancing platinum-resistance is reduced drug uptake,<sup>25</sup> thus, novel drugs with alternative uptake mechanisms may be essential to overcome this resistance.

The partition coefficient (LogP) is a measure of the hydrophobic nature of a compound and is determined by its preferential solubility in octanol or water, as defined by **Equation 3.1 (Section 3.2.6)**. The larger the LogP value, the more hydrophobic the complex. In the 1990s, Lipinski and co-workers postulated a set of five rules for which suitable drug candidates should adhere,<sup>26</sup> one in particular states that the partition coefficient (LogP) must not exceed the value 5. The higher the LogP value (LogP>0) the more hydrophobic the compound; the lower the value (LogP<0) the more hydrophilic. The LogP values were determined for complexes **2-5** and compared to that of **RR-1** (*p*-CH<sub>3</sub>), **RR-6** (*p*-F) and cisplatin (**Table 3.1**).

**Table 3.1.** Octanol-water partition coefficients (LogP) for complexes **1-6**, and **cisplatin**.

Complex	Metal	X	LogP
<b>RR-1</b>	Os	<i>p</i> -Me	1.45±0.02 <sup>[a]</sup>
<b>SS-2</b>	Os	<i>p</i> -Br	1.01±0.01
<b>RR-2</b>	Os	<i>p</i> -Br	1.02±0.02
<b>SS-3</b>	Os	<i>p</i> -I	1.02±0.03
<b>RR-3</b>	Os	<i>p</i> -I	1.01±0.01
<b>RR-4</b>	Os	<i>p</i> -OMe	1.11±0.01
<b>SS-5</b>	Os	<i>m</i> -Br	1.04±0.02
<b>RR-6</b>	Os	<i>p</i> -F	0.30±0.03 <sup>[a]</sup>
<b>Cisplatin</b>	Pt	-	-2.21±0.06 <sup>[b]</sup>

<sup>[a]</sup>Literature Log P value of **RR-1** and **RR-6**.<sup>10</sup> <sup>[b]</sup>Literature Log P value of **cisplatin**.<sup>27</sup>

The LogP values of **2-5** were found to range between 1.01-1.11 implying moderate hydrophobicity. Substitution of larger, electron-withdrawing groups (R=*p*-Br or *p*-I; **2** or **3**) decreased the hydrophobicity compared to parent compound **RR-1** (R=*p*-CH<sub>3</sub>). Interestingly, **RR-6** (R=*p*-F) was significantly less hydrophobic (LogP=0.30±0.03) compared to the latter halide-substituents. Substitution of the *para*-methyl group with a methoxy group (**RR-1** vs. **RR-4**) also decreased the hydrophobicity, but to a lesser extent. A comparison of complexes **2** (R=*p*-Br) and **5** (R=*m*-Br) revealed no differences in LogP. Likewise, the LogP values for enantiomers (**SS/RR-2**; **SS/RR-3**) were the same. Complexes **1-6** were all significantly more hydrophobic (higher LogP) compared to cisplatin (-2.21±0.06).<sup>27</sup>

### 3.3.4 Asymmetric Transfer Hydrogenation (ATH) Catalysis

The ability of complexes **2-5** to catalyse the conversion of acetophenone – an important industrial substrate – to (*S*) or (*R*)-1-phenylethanol enantioselectively in the presence of formic acid (which acts as a hydride source for catalysis) was determined by both <sup>1</sup>H NMR and GC-FID. The catalytic reaction was monitored kinetically by <sup>1</sup>H NMR using d<sub>6</sub>-benzene as the NMR lock solvent. The catalytic turnover (h<sup>-1</sup>) was determined from <sup>1</sup>H NMR spectra by monitoring the decrease of the singlet of acetophenone (2.10 ppm) and the formation of the quartet of 1-phenylethanol (4.75 ppm). As acetophenone is prochiral, the chirality of 1-phenylethanol was determined by gas chromatography (GC) against known retention times of the (*S*) or (*R*) alcohol products. Complexes **2-5** all achieved high catalytic conversions (>95%) and enantiomeric excesses (>93%) and exhibited maximal turnover frequencies of greater than 76 h<sup>-1</sup> (**Appendix, Fig. A2**) – significantly higher than that of parent compound **RR-1** (**Table 3.2**).<sup>1</sup> No statistical differences in turnover frequency of enantiomers **SS/RR-2** (*p*-Br) or **SS/RR-3** (*p*-I) were observed (**Table 3.2**). Bromine-substitution at the *meta*-position (**SS-5**) did not significantly alter the observed catalytic activity (compared to **SS-2**; *para*-Br).

**Table 3.2.** Catalytic conversion (%), enantiomeric excesses (%) and turnover frequencies (h<sup>-1</sup>) for the reduction of acetophenone to form (*S*) or (*R*)-1-phenylethanol for complexes **2-5** in the presence of 5:2 formic acid/TEA azeotrope for 24 h at 310 K as determined by <sup>1</sup>H NMR and chiral GC.

Complex	R	Conversion (%) <sup>[a]</sup>	Enantiomeric Excess (%) <sup>[a]</sup>	Enantiomer <sup>[a]</sup>	TOF (h <sup>-1</sup> ) <sup>[b]</sup>
<b>RR-1</b> <sup>[c]</sup>	<i>p</i> -CH <sub>3</sub>	99	99	<i>R</i>	63.6±0.6
<b>SS-2</b>	<i>p</i> -Br	98	98	<i>S</i>	81±5
<b>RR-2</b>	<i>p</i> -Br	99	97	<i>R</i>	81±2
<b>SS-3</b>	<i>p</i> -I	96	94	<i>S</i>	88±5
<b>RR-3</b>	<i>p</i> -I	97	95	<i>R</i>	85±5
<b>RR-4</b>	<i>p</i> -O CH <sub>3</sub>	97	94	<i>R</i>	76±4
<b>SS-5</b>	<i>m</i> -Br	98	98	<i>S</i>	79±4

<sup>[a]</sup> Determined by chiral GC (24 h, 310 K). <sup>[b]</sup> Determined by <sup>1</sup>H NMR spectra (1 h, 310 K). <sup>[c]</sup> Literature value.

### 3.3.5 Antiproliferative activity (IC<sub>50</sub>)

The antiproliferative activities (IC<sub>50</sub> /  $\mu$ M) of **2-5** were determined in A2780 (ovarian), A549 (lung), PC3 (prostate) and MCF7 (breast) cancer cells, and MRC5 healthy (lung) fibroblasts upon 24 h exposure and 72 h recovery in complex-free media (**Table 3.3**). Biological studies were initially carried out in A2780 cells so as to compare directly to the parent compound **RR-1** (*p*-CH<sub>3</sub>),<sup>10</sup> and then in A549 cells due to their large cell surface area,<sup>28, 29</sup> making them an attractive cell line for 2D synchrotron-XRF imaging.<sup>30-32</sup>

Complexes with *para* halido substituents (**2/3**; where R=*p*-Br /I) were consistently less potent than parent compound **RR-1** (*ca.* 2-fold), but, nonetheless, of the same order of magnitude. No statistically significant differences were observed between the antiproliferative activities of complexes **2/3**. Interestingly, methoxy-substitution at the *para*-position (**4**) significantly enhanced the anticancer potency in A2780 cells, compared to **RR-1**, but was less potent in A549 lung cancer cells (**Table 3.3**).

Bromine-substitution at the *meta*-position (**5**) did not significantly alter the antiproliferative activity when compared to substitution at the *para*-position (**SS/RR-2**). Overall, the IC<sub>50</sub> of halide-substituted complexes (**2**, **3** and **5**) were not statistically different when comparing to the same cell line. Complexes **SS/RR-2** exhibited poor selectivity for A549 (lung cancer) cells over MRC5 (healthy lung) fibroblasts (**Table 3.3**) – with comparable antiproliferative activities in both cell lines – closely resembling that reported for **RR-1**.<sup>10</sup>

**Table 3.3.** Half-maximal inhibitory concentrations (IC<sub>50</sub> /  $\mu$ M) of **1-5** and cisplatin against A2780 (ovarian), A549 (lung), PC3 (prostate) and MCF7 (breast) cancer cells and MRC5 healthy lung fibroblasts upon 24 h exposure, 72 h recovery (complex-free media).

Complex	R	A2780	A549	PC3	MCF7	MRC5
<b>RR-1</b> <sup>[a]</sup>	<i>p</i> -CH <sub>3</sub>	15.5±0.5	21.1±0.3	12±0.3	10.9±0.7	21.4±0.7
<b>SS-2</b>	<i>p</i> -Br	31±2	31±1	41±2	32±1	37.8±0.7
<b>RR-2</b>	<i>p</i> -Br	27.4±0.6	29.5±0.5	38.9±4.3	26.3±4.6	37±1
<b>SS-3</b>	<i>p</i> -I	27.5±0.8	33±0.4	37±2	28±3	-
<b>RR-3</b>	<i>p</i> -I	29±3	32±0.4	39.5±0.6	22.7±5.6	-
<b>RR-4</b>	<i>p</i> -OCH <sub>3</sub>	7.3±0.3	33±3	-	-	-
<b>SS-5</b>	<i>m</i> -Br	27±2	32±2	-	-	-
<b>Cisplatin</b>	-	1.2±0.3	3.2±0.1	4.1 ± 0.5	6.6 ± 0.4	12.8 ± 0.5

<sup>[a]</sup> Literature IC<sub>50</sub> values of **RR-1** and **cisplatin** using the specified conditions.<sup>2</sup> Note that all precursor BsDPEN ligands were determined to be non-toxic (IC<sub>50</sub>> 100  $\mu$ M), thus, are not displayed.

### 3.3.6 In-cell catalysis

It has previously been reported that the antiproliferative activity of parent compound **RR-1** ( $R=p\text{-CH}_3$ ) in A2780 and PC3 cancer cells can be enhanced upon co-administration with non-toxic concentrations of sodium formate – which acts as a hydride source.<sup>10</sup> Sodium formate has been reported to be non-toxic to cells up to 2 mM,<sup>10, 11</sup> thus can be utilized as a biologically-compatible hydride source. Herein, the formate-dependent antiproliferative activities have been determined for A549 cells. Cells were treated with 0.5-1.0 $\times$ IC<sub>50</sub> concentrations of **SS-2** ( $29.5\pm 0.5$   $\mu$ M) or **RR-2** ( $31\pm 1$   $\mu$ M) with varying concentrations of sodium formate or acetate (0-2 mM) for 24 h. The normalized cell proliferation of cells treated with **SS-2** or **RR-2** reduced with formate concentration, achieving a maximal decrease of 67-77% (**SS-2**,  $p<0.001$ ) and 71-72% (**RR-2**,  $p<0.001$ ), for cells treated with 0.5 or 1.0 $\times$ IC<sub>50</sub> upon co-administration with 2 mM formate (**Fig. 3.6**). This closely correlates with the 80-83% decrease in cell viability for **RR-1** ( $p\text{-CH}_3$ ) under the same conditions,<sup>10</sup> suggesting a similar formate-dependent mechanism of action for **SS-2** or **RR-2** inside cancer cells. No changes in cell viability were observed in the presence acetate (**Fig. 3.7**).

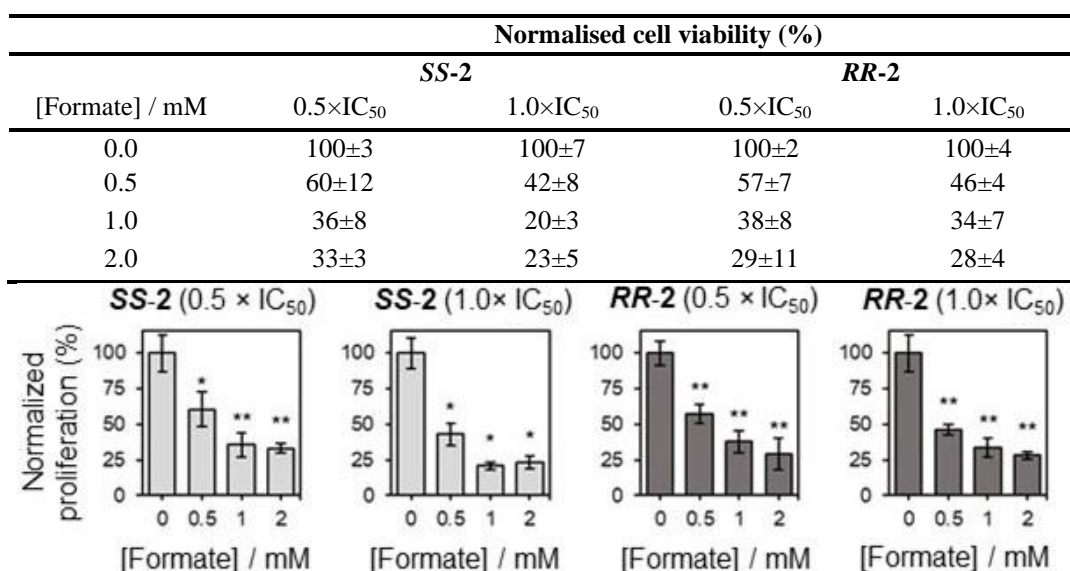


**Figure 3.6.** Normalized cell proliferation (%) of A549 (lung) cancer cells treated with 0.5-1.0 $\times$ IC<sub>50</sub> of **SS-2** and **RR-2** in A549 cancer cells upon co-administration with sodium formate (0-2 mM) for 24 h, followed by 72 h recovery in complex-free media.

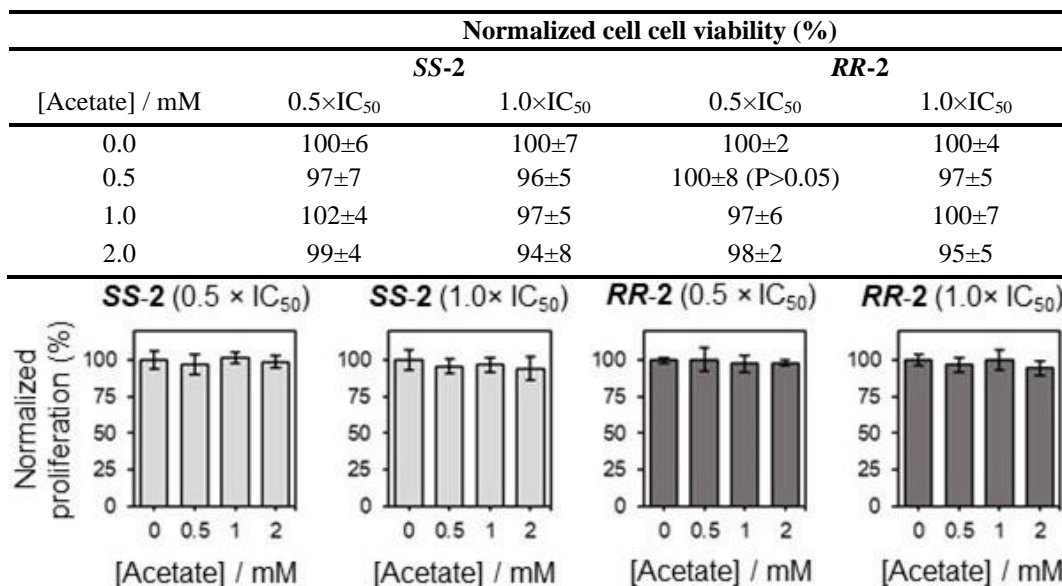


**Figure 3.7.** Normalized cell proliferation (%) of A549 cancer cells treated with 0.5-1.0×IC<sub>50</sub> of **SS/RR-2** upon co-administration with acetate (0-2 mM) for 24 h, followed by 72 h recovery in complex-free media.

The formate and acetate-dependent antiproliferative activity in MRC5 fibroblasts was assessed upon treatment with 0.5×IC<sub>50</sub> of **SS/RR-2** with sodium formate and acetate (0-2 mM) for 24 h (**Fig. 3.8**). No statistical differences in cell proliferation were observed upon co-administration with sodium formate or acetate.

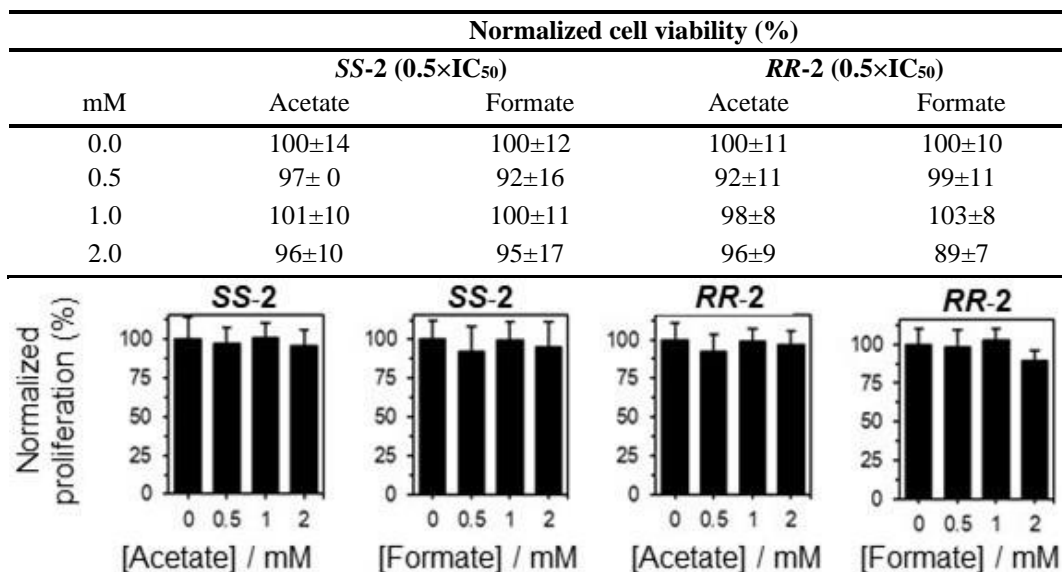


**Figure 3.8.** Normalized cell proliferation (%) MRC5 healthy lung fibroblasts treated with 0.5×IC<sub>50</sub> of **SS-2** or **RR-2** upon co-administration with sodium acetate or formate (0-2 mM) for 24 h, followed by 72 h recovery in drug-free media.



### 3.3.7 Flow cytometry studies

Flow cytometry is a cell analysis technique which can be used to rapidly analyse morphological properties of a population of cells (*i.e.* cell size, DNA content and granularity). Flow cytometry focusses a laser onto biological samples, resulting in characteristic light scattering, allowing the high-throughput processing of a large number of cells. In particular, fluorescent-labelling of cells is commonly used to monitor fluorescence emission by flow cytometry – *i.e.* DNA intercalators such as propidium iodide (PI). In this Chapter, flow cytometry has been used to investigate membrane or cell cycle damage induced by **SS/RR-2** in the presence of non-toxic concentrations of sodium formate (0–2 mM).

#### Membrane integrity

The membrane integrity of A549 cells treated with 1×IC<sub>50</sub> of **SS/RR-2** for 24 h upon co-administration of non-toxic concentrations of sodium formate (0–2 mM) was investigated (**Fig. 3.9**; **Appendix, Table A11**). Cells were stained with PI without fixation and analysed using flow cytometry. PI is non-permeable to cell membranes, hence, damaged membranes would enhance the fluorescence of PI by *ca.* 20 to 30-fold upon intercalation with DNA.<sup>33</sup> The resulting cells were categorized into viable (FL2-) and non-viable (FL2+) membrane populations using FlowJo V10 software. No significant differences in PI fluorescence of cells treated with **SS/RR-2** were observed when compared to that of the untreated controls ( $p > 0.05$ , **Fig. 3.9**), with normalized viable (non-compromised) cell membrane populations of 99.9±0.1 and 99.5±0.1% for **SS-2** and **RR-2**, respectively. Similarly, no differences in PI fluorescence was observed for cells treated with **SS/RR-2** and co-administered with formate (99.8±0.2 and 99.4±0.03%, respectively). This data suggests the membranes of A549 cells are not compromised by **SS-2** or **RR-2** in the presence or absence of sodium formate, correlating with the lack of membrane damage observed for parent compound **RR-1** (R=*p*-CH<sub>3</sub>) under the same conditions.<sup>10</sup>

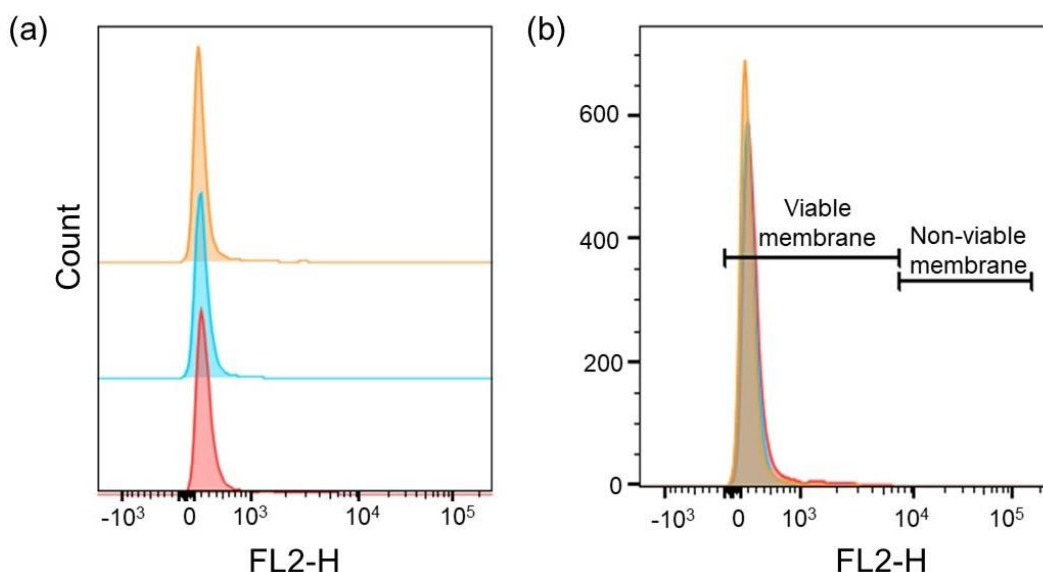


**Figure 3.9.** Membrane integrity assessed by PI (FL2) staining of A549 cancer cells treated with **SS-2** ( $1 \times \text{IC}_{50}$ ) for 24 h (310 K, 5%  $\text{CO}_2$ ) upon co-administration with sodium formate (0-2 mM). (a) untreated control (■), **SS-2** (■) and **SS-2** + 2 mM sodium formate (■); (b) Overlay of propidium iodide fluorescence with gated bars indicating viable (FL2-) and non-viable membranes (FL2+).

### Cell cycle analysis

Cell cycle analysis of A549 cells treated with  $1 \times \text{IC}_{50}$  **SS-2** or **RR-2** for 24 h upon co-administration of non-toxic concentrations of sodium formate (2 mM) was investigated (**Table 3.4**). In contrast to membrane integrity analysis, cells were chemically-fixed with ice-cold ethanol to allow cellular influx of non-permeable PI.<sup>33</sup> Cells were analysed by flow cytometry and the sub- $G_1$ ,  $G_1$ , S and  $G_2$ /M-phase cell cycle populations were fitted using FlowJo V10 software.

Cells treated with **SS-2** or **RR-2** for 24 h showed slight  $G_1$  cell cycle arrest with normalised  $G_1$  populations of  $75.8 \pm 0.4$  and  $78.4 \pm 0.44\%$ , respectively, compared to  $70.4 \pm 0.97\%$  in the untreated control population ( $p=0.012$  and  $p=0.0059$ ). Similarly, cells treated with **SS-2** or **RR-2** and co-administered with formate (2 mM) showed a similar increase in  $G_1$ -phase population compared to the untreated controls (**Fig. 3.10**,  $p=0.031$  and  $p=0.0069$ , respectively) – suggesting formate does not alter the mechanism of action, but merely enhances the observed effect. This is in strong agreement with  $G_1$ -arrest observed for cells treated with parent compound **RR-1** ( $R=p\text{-CH}_3$ ) over 24 h in the presence of sodium formate (0-2 mM).<sup>10</sup>

**Table 3.4.** Cell cycle analysis of a normalized population of A549 (human lung) cancer cells treated with  $1 \times \text{IC}_{50}$  of **SS-2** ( $30.8 \pm 1.6 \mu\text{M}$ ) for 24 h (310 K, 5%  $\text{CO}_2$ ) upon co-administration with sodium formate (0-2 mM), showing the percentage of cells in sub-G<sub>1</sub>, G<sub>1</sub>, S and G<sub>2</sub>/M phases of the cell cycle. P-values were calculated using a two-tailed t-test assuming unequal sample variance (Welch's unpaired t-test). All t-tests were compared to the untreated controls.

Complex	Sub G <sub>1</sub> -phase	G <sub>1</sub> phase	S Phase	G <sub>2</sub> /M Phase
Untreated control	$1.28 \pm 0.23$ ( $p=1.0000$ )	$70.40 \pm 0.97$ ( $p=1.0000$ )	$20.70 \pm 0.67$ ( $p=1.0000$ )	$7.99 \pm 0.51$ ( $p=1.0000$ )
Untreated + formate	$0.00 \pm 0.00$ ( $p=0.0103$ )	$74.13 \pm 1.21$ ( $p=0.0153$ )	$18.82 \pm 0.70$ ( $p=0.0289$ )	$7.05 \pm 0.57$ ( $p=0.0987$ )
<b>SS-2</b>	$2.47 \pm 0.49$ ( $p=0.0353$ )	$75.84 \pm 0.42$ ( $p=0.0044$ )	$17.40 \pm 0.58$ ( $p=0.0032$ )	$4.29 \pm 0.48$ ( $p=0.0008$ )
<b>SS-2 + formate</b>	$2.04 \pm 0.61$ ( $p=0.1524$ )	$77.87 \pm 2.12$ ( $p=0.0137$ )	$16.51 \pm 1.12$ ( $p=0.0090$ )	$3.58 \pm 0.62$ ( $p=0.0008$ )

### 3.3.8 Zebrafish toxicity studies

Zebrafish embryos are becoming of increasing interest in the translation of compounds from *in vitro* to *in vivo* models. Although zebrafish display obvious differences to humans, they possess high genetic homology to mammals,<sup>14, 34-36</sup> thus, can be utilized to as suitable vertebrates to model drug toxicity and efficacy for translation into humans.<sup>14, 37</sup> Zebrafish are transparent (useful for fluorescence microscopy), cheap (unlike rodent models), rapidly reproduce and allow high-throughput genetic and chemical screening of drug candidates.<sup>34-39</sup> The half-lethal concentrations ( $\text{LC}_{50}$  /  $\mu\text{M}$ ) have been determined in SG-WT zebrafish embryos upon treatment with **SS/RR-2** (0.01-50  $\mu\text{M}$ , 301.5 K, 96 h, **Table 3.5**).

**Table 3.5.** Half-maximal lethal concentrations ( $\text{LC}_{50}$  /  $\mu\text{M}$ ) for parent compound **RR-1**, **SS-2**, **RR-2**, **RR-6** and cisplatin in SG-WT zebrafish embryos (96 h drug exposure, no recovery).

Complex	R	$\text{LC}_{50}$ ( $\mu\text{M}$ )
<b>RR-1</b> <sup>[a]</sup>	<i>p</i> -Me	$2.4 \pm 0.4$
<b>SS-2</b>	<i>p</i> -Br	$3.7 \pm 0.3$
<b>RR-2</b>	<i>p</i> -Br	$4.1 \pm 0.1$
<b>RR-6</b> <sup>[a]</sup>	<i>p</i> -F	$0.7 \pm 0.2$
<b>Cisplatin</b> <sup>[a]</sup>	-	$0.6 \pm 0.2$

<sup>[a]</sup>Literature  $\text{LC}_{50}$  values of **RR-1** (R=*p*-CH<sub>3</sub>), **RR-6** (R=*p*-F) and **cisplatin**.<sup>14</sup>

The LC<sub>50</sub> concentrations for **SS-2** and **RR-2** were determined to be 3.7±0.3 and 4.1±0.1 µM, respectively – implying that the complex chirality does not alter the observed toxicity ( $p>0.05$ ). A comparison of **SS-2** or **RR-2** with parent compound **RR-1** (R=*p*-CH<sub>3</sub>) revealed a significantly lower LC<sub>50</sub> (2.4±0.4 µM;  $p=0.0204$  and  $p=0.019$ , for **SS-2** and **RR-2**, respectively).<sup>14</sup> **RR-6** (R=*p*-F) was found to be significantly more toxic than **SS-2** and **RR-2** (LC<sub>50</sub>=0.7±0.2 µM;  $p=0.0007$  and  $p=0.0014$ , respectively).<sup>14</sup> Importantly, cisplatin was significantly more toxic than **SS-2** and **RR-2** (LC<sub>50</sub>=0.6±0.2 µM;  $p=0.0007$  and  $p=0.0014$ , respectively).

### 3.3.9 <sup>189</sup>Os ICP-MS cellular accumulation studies

The cellular accumulation of Os of **SS-2** and **RR-2** was initially determined in A2780 ovarian cancer cells to enable a direct comparison with that reported for **RR-1** (R=*p*-CH<sub>3</sub>),<sup>10</sup> but later determined only for **SS-2** in A549 cells for comparative studies by synchrotron-XRF.

#### Equipotent 24 h accumulation

A2780 cells were treated with equipotent (1×IC<sub>50</sub>) of **SS/RR-2** or **SS/RR-3** for 24 h (Table 3.6). No statistically significant differences in intracellular Os (ng/10<sup>6</sup> cells) were observed between enantiomers ( $p>0.05$ ). The Os accumulation of **SS/RR-2** was the same as that of **SS/RR-1**. Statistically more Os was observed in cells treated with **SS/RR-3** (*p*-I) compared to that of **SS/RR-2** (*p*-Br;  $p=0.0172$  and  $p=0.0436$ ).

**Table 3.6.** Osmium (<sup>189</sup>Os) ICP-MS cellular accumulation (ng Os/10<sup>6</sup> cells) of **1-3** and **RR-6, 7** and **8** in A2780 cells when treated with equipotent 1×IC<sub>50</sub> for 24 h (no recovery).

Complex	R-group	ng Os / 10 <sup>6</sup> cells
<b>SS-1</b> <sup>[a]</sup>	CH <sub>3</sub>	32±3
<b>RR-1</b> <sup>[a]</sup>	CH <sub>3</sub>	30±2
<b>SS-2</b>	Br	29±3
<b>RR-2</b>	Br	30±2
<b>SS-3</b>	I	39±2
<b>RR-3</b>	I	37±3
<b>RR-6</b> <sup>[a]</sup>	F	10±2
<b>RR-7</b> <sup>[a]</sup>	NO <sub>2</sub>	8.1±0.3
<b>RR-8</b> <sup>[a]</sup>	H	5.8±0.7

[a] Literature values for the osmium cellular accumulation of **SS/RR-1**, **RR-6**, **RR-7** and **RR-8**.

### Varying concentration

The dependence of complex concentration on the drug influx or efflux was investigated by treating A2780 cells with 0.25–1.5×IC<sub>50</sub> of **SS-2** or **RR-2** (IC<sub>50</sub>=30.8±1.6 and 27.4±0.6 µM, respectively) for 24 h. Interestingly, the 24 h Os accumulation of **SS-2** (29±3 ng Os/10<sup>6</sup> cells) and **RR-2** (30±2 ng Os/10<sup>6</sup> cells) were identical to that of parent compound **RR-1** (30±2 ng Os/10<sup>6</sup> cells) when treated at equipotent concentrations (**Table 3.7**). This suggests that the Br-substituent of **SS/RR-2** somewhat hinders the cellular accumulation of osmium with respect to **RR-1**, in agreement with the reduced potency (higher IC<sub>50</sub>) exhibited by **SS-2** and **RR-2**. Similarly, A549 cells treated with 1×IC<sub>50</sub> **SS-2** or **RR-2** for 24 h showed no statistical differences in Os accumulation compared to **RR-1** (16±5, 14±3 and 18±2 ng Os/10<sup>6</sup> cells, for **SS-2**, **RR-2** and **RR-1**, respectively).

**Table 3.7.** Concentration-dependent osmium (<sup>189</sup>Os) ICP-MS cellular accumulation (ng Os /10<sup>6</sup> cells) of **RR-1**, **SS-2** and **RR-2** in A2780 (ovarian) cells when treated with 0.25-1.5×IC<sub>50</sub> concentrations for 24 h (no recovery).

Complex	R-group	0.25×IC <sub>50</sub>	0.5×IC <sub>50</sub>	1×IC <sub>50</sub>	1.5×IC <sub>50</sub>
<b>RR-1</b> <sup>[a]</sup>	<i>p</i> -CH <sub>3</sub>	7±1	16±1	30±2	53±7
<b>SS-2</b>	<i>p</i> -Br	7±1	15±1	29±3	48±6
<b>RR-2</b>	<i>p</i> -Br	7±1	16±1	30±2	52±7

<sup>[a]</sup> Literature values for the concentration-dependent Os cellular accumulation of **RR-1** in A2780 cells.<sup>2, 10</sup>

### Varying temperature

Varying the drug incubation temperatures can provide insights into the dependence on active influx or efflux cellular pathways of drugs.<sup>17</sup> A2780 cells treated with 1×IC<sub>50</sub> **SS-2** or **RR-2** for 3 or 6 h at lower incubation temperatures (277 K) revealed a significant decrease in intracellular Os (**Table 3.8**). After 3 h at 277 K, a decrease in intracellular Os (by *ca.* 77% and 75% for **SS-2** and **RR-2**, respectively) was observed. Similarly, further decreases of 43% and 44% were observed upon incubation at 277 K for 6 h, respectively. Overall this suggests that the intracellular Os accumulation may involve active, energy-dependent transport, which was previously hypothesised for parent compound **RR-1** (*p*-CH<sub>3</sub>).<sup>2</sup>

**Table 3.8.** Temperature-dependent osmium (<sup>189</sup>Os) cellular accumulation (ng Os/10<sup>6</sup> cells) of **RR-1** (R=*p*-CH<sub>3</sub>), **SS-2** (R=*p*-Br) and **RR-2** (R=*p*-Br) in A2780 (ovarian) cancer cells when treated with 1×IC<sub>50</sub> concentrations for 3-6 h (no recovery) at 310 K or 277 K.

Compound	3 h		6 h	
	T=277 K	T=310 K	T=277 K	T=310 K
<b>RR-1</b> <sup>[a]</sup>	3±2	32±4	10.2±0.1	42±1
<b>SS-1</b>	9±1	37±2	20±2	35±3
<b>RR-2</b>	8.9±0.9	35±3	20±3	36±3

<sup>[a]</sup> Literature values for the temperature-dependent cellular accumulation of **RR-1** (R=*p*-CH<sub>3</sub>) after 24 h exposure (no recovery in complex-free medium) in A2780 cells.<sup>2</sup>

### Extent of efflux

The time-dependent cellular accumulation of Os was investigated in A2780 cells treated with 1×IC<sub>50</sub> of Br-labelled **SS-2** by varying the exposure times (3, 6, 18 and 24 h). Additionally, the extent of efflux was monitored by treating cells with 1×IC<sub>50</sub> **SS-2** for 24 h, followed by 24, 48 and 72 h recovery periods in complex-free media. The maximal Os accumulation of **SS-2** was observed at *ca.* 6 h exposure (35±3 ng Os/10<sup>6</sup> cells), which closely correlates with that of **RR-1** (Fig. 3.10).<sup>10</sup> Upon recovery in complex-free media, the osmium in cells treated with **SS-2** was removed from cells in the same manner as **RR-1** (Fig. 3.10; Appendix, Table A12)<sup>10</sup> – suggesting Br-labelling has not changed the mechanism of uptake.

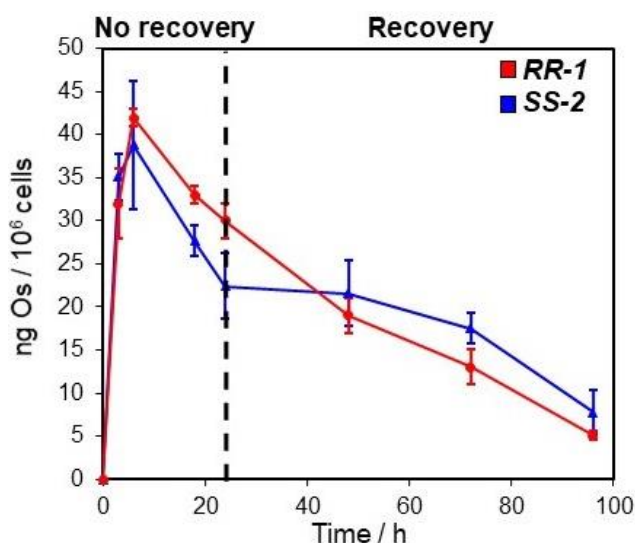


**Figure 3.10.** Time-dependent cellular accumulation of <sup>189</sup>Os in A2780 cells treated with 1×IC<sub>50</sub> concentration of **RR-1** (■) or **SS-2** (■) for 3-24 h, followed by 24-72 h recovery in complex-free media.

### Varying formate

The osmium cellular accumulation in A2780 cells treated with  $1 \times \text{IC}_{50}$  of **SS-2** in the presence of formate (2 mM) was determined upon 24 h exposure (no recovery). No statistically significant differences in Os accumulation were observed between A2780 cells treated with **SS-2** in the presence or absence of sodium formate ( $p > 0.05$ ), nor with that of **RR-1** (Fig. 3.11; Appendix, Table A13).

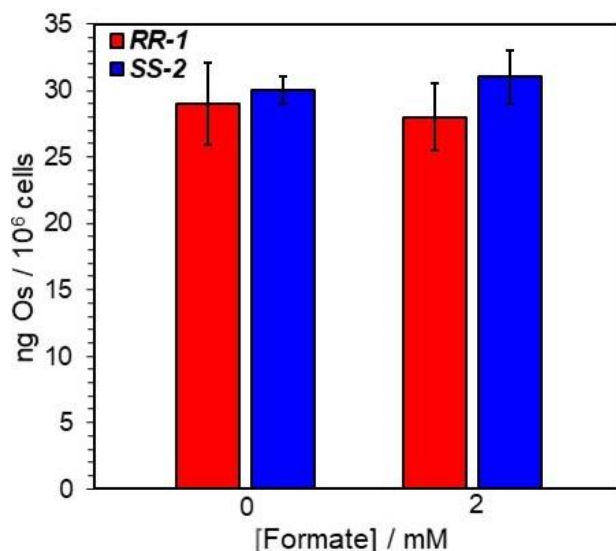


**Figure 3.11.** Cellular accumulation of osmium in A2780 cells treated with  $1 \times \text{IC}_{50}$  of **RR-1** (*p*-CH<sub>3</sub>, ■) and **SS-2** (*p*-Br, ■) for 24 h upon co-administration with sodium formate (0 or 2 mM).

### 3.3.10 <sup>189</sup>Os and <sup>79</sup>Br ICP-MS cellular accumulation studies

Up until now, ICP-MS cellular accumulation studies of half-sandwich organometallic osmium complexes has involved the quantification of osmium (<sup>189</sup>Os) in stabilised 3.6% v/v nitric acid by ICP-MS. However, this only provides information on the Os metal centre, and not the overall metal complex – thus, cannot provide information on the intracellular stability of complexes in cancer cells. In this Chapter, Br (at an apparent inert site of parent compound **RR-1**) has been used as a molecular probe to monitor the *in-cell* stability and catalytic efficiency of this family of complexes in A549 cells. Herein, a method for the simultaneously quantification of osmium (<sup>189</sup>Os) and bromine (<sup>79</sup>Br) in strongly alkaline conditions (1% m/v TMAH) by ICP-MS without the need for chemical stabilisers was used.

### Varying temperature

It has previously been shown that incubating A2780 cells with **RR-1** (R=*p*-CH<sub>3</sub>) or **SS/RR-2** (R=*p*-Br) at lower temperatures (277 K) significantly reduces the cellular accumulation of Os after 3-6 h exposure (Section 3.3.9). Similarly, the Os accumulation in A549 cells treated with 1×IC<sub>50</sub> of **SS-2** for 6 h was reduced by *ca.* 48% when incubated at 277 K (Fig. 3.12, *p*=0.0043). The same trend was observed for Br, but with a more pronounced effect, revealing a *ca.* 75% decrease in intracellular Br (Fig. 3.12, *p*=0.0052).

A comparison of the intracellular molar quantities of Os and Br in cells treated with **SS-2** for 6 h at 310 K revealed *ca.* 12× more intracellular Br (Fig. 3.12, *p*=0.0039). Similarly, *ca.* 5× more Br than Os was present in cells treated with **SS-2** for 6 h at 277 K. Overall these results may suggest: (i) the cellular accumulation of both Os and Br is affected by lower temperatures, implying active, energy-dependent influx or efflux mechanisms; (ii) the Br-labelled sulfonamide ligand is dissociating from the Os centre – indicative of complex degradation; (iii) the Br-labelled ligand remains in cells for longer (significantly higher levels of intracellular Br).

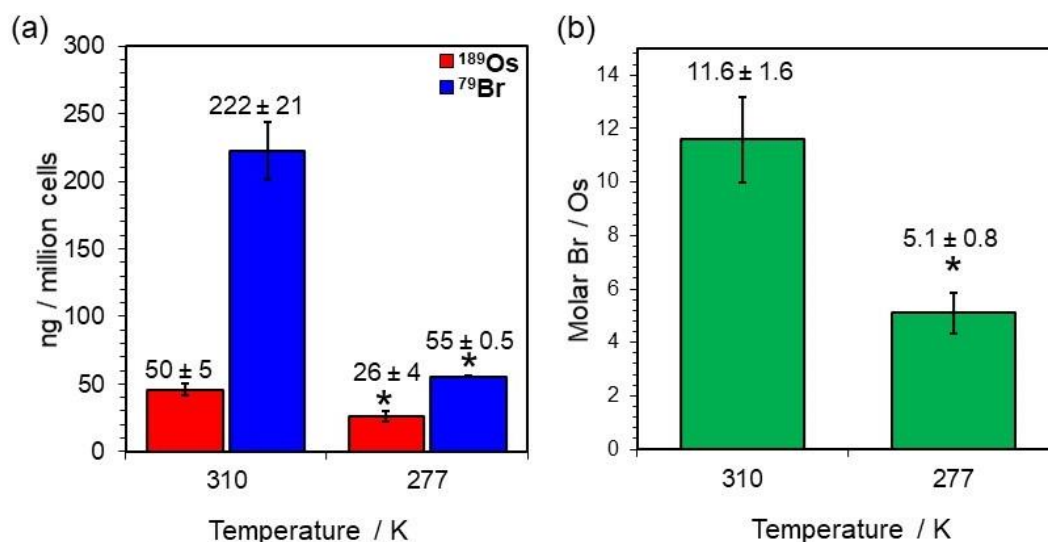


**Figure 3.12.** Temperature-dependent efflux of osmium and bromine in A549 cells treated with 1×IC<sub>50</sub> (30 μM) of **SS-2** at 310 and 277 K for 6 h, respectively: (a) <sup>189</sup>Os (■) and <sup>79</sup>Br (■) cellular accumulation; (b) Intracellular molar bromine-to-osmium (Br/Os) ratios at 310 K and 277 K. Statistical analysis was performed using the Welch's unpaired t-test, assuming unequal variables.



### Inhibition of endocytosis

The potential involvement of active accumulation pathways of **RR-1** (*p*-CH<sub>3</sub>) and **SS-2** (*p*-Br) has already been probed by varying the drug incubation temperatures. Subsequently, the contribution of caveolae endocytosis in the cell uptake of **SS-2** has been probed using methyl- $\beta$ -cyclodextrin - a known endocytotic inhibitor.<sup>17</sup> A549 cells were treated with 1 $\times$ IC<sub>50</sub> (30  $\mu$ M) of **SS-2** and co-administered with methyl- $\beta$ -cyclodextrin (0-1 mM) for 24 h (**Fig. 3.13**).

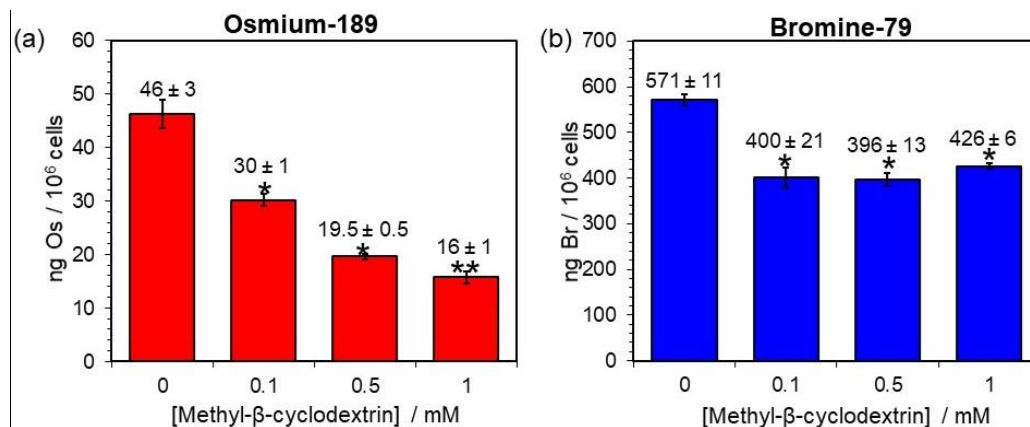


**Figure 3.13.** The effect of methyl- $\beta$ -cyclodextrin co-administration (0-1 mM) on the osmium and bromine accumulation in A549 cells treated with 1 $\times$ IC<sub>50</sub> of **SS-2** for 24 h: (a) <sup>189</sup>Os (■); (b) <sup>79</sup>Br (■). Statistical analysis was performed using Welch's unpaired t-test, assuming unequal variances, and compared to the positive controls (0 mM methyl-  $\beta$ -cyclodextrin)

The amount of intracellular Os (ng/10<sup>6</sup> cells) decreased with increasing methyl- $\beta$ -cyclodextrin concentration ( $p=0.0128$ ,  $p=0.0044$ ,  $p=0.0037$  for 0.1, 0.5 and 1 mM methyl- $\beta$ -cyclodextrin). In contrast, the intracellular quantity of Br decreased by *ca.* 30% in the presence of 0.1 mM methyl- $\beta$ -cyclodextrin ( $p=0.0011$ ). However, the Br accumulation did not continue to decrease upon increasing methyl- $\beta$ -cyclodextrin concentration, but stabilized at *ca.* 400 ng/10<sup>6</sup> cells. The quantity of intracellular Br was found to be significantly higher than Os for all concentrations of methyl- $\beta$ -cyclodextrin ( $p>0.05$ ), with molar bromine-to-osmium ratios (Br/Os) ranging between 30-65 (**Appendix, Fig. A3**) – suggestive of complex degradation. Co-administration of **SS-2** with methyl- $\beta$ -cyclodextrin 0.5-1 mM revealed a larger Br/Os ratio compared to that of lower concentrations, suggestive of increasing complex degradation (Br-sulfonamide ligand dissociating from the Os centre) or decreased ligand efflux, with more of the ligand remaining in the cancer cells.

### Inhibition of efflux

P-glycoprotein (PGP) is a down-regulated efflux membrane protein responsible for actively transporting drugs in cancer cells (particularly lipophilic and positively-charged molecules),<sup>40, 41</sup> and has shown to play a role in the development of platinum-resistance.<sup>42</sup> Herein, verapamil – a known PGP inhibitor<sup>17</sup> – was used to investigate the effect of efflux inhibition. A549 cells were treated with  $1 \times \text{IC}_{50}$  of **SS-2** ( $R=p\text{-Br}$ ) for 24 h, followed by recovery in 20  $\mu\text{M}$  verapamil hydrochloride (5% DMSO; 95% DMEM) for 24–72 h (**Fig. 3.14**). Statistically significant differences in Os accumulation in cells treated with **SS-2** were observed after 48 h recovery in verapamil ( $p=0.0371$ ) – suggesting the PGP-pump is involved in efflux of **SS-2**. This is in agreement with that reported for **RR-1** ( $R=p\text{-CH}_3$ ).<sup>10</sup> In contrast, the intracellular Br was unaffected by recovery with verapamil when compared to that of recovery in medium alone (**Fig. 3.14**,  $p>0.05$ ) – suggesting different efflux pathways of the free sulfonamide ligand and the osmium complex. For treated cells recovered in complex-free media the molar Br/Os ratio increased with recovery time (**Appendix, Table A14-15**), suggesting that the longer the recovery time the more the complex is degraded (*ca.* 60% increase in Br/Os ratio from 24 h to 72 h recovery). Similarly, the Br/Os ratios in treated cells recovered in verapamil increased, but overall maintained lower Br/Os ratios compared to recovery in complex-free media – suggesting **SS-2** is more stable upon PGP-inhibition.

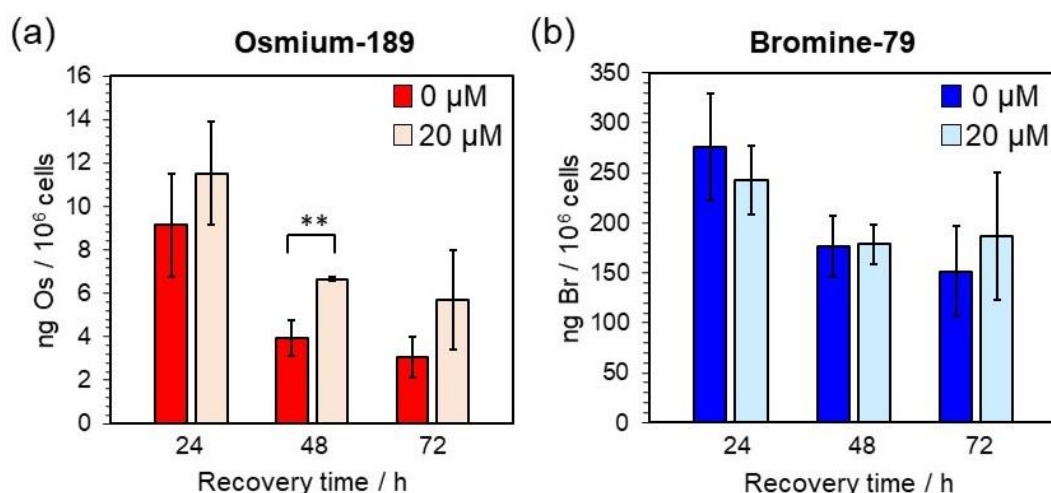


**Figure 3.14.** Verapamil-dependent efflux of osmium and bromine in A549 cells treated with  $1 \times \text{IC}_{50}$  (30  $\mu\text{M}$ ) of **SS-2** for 24 h, and recovery in 0–20  $\mu\text{M}$  of verapamil for 24–72 h: (a) <sup>189</sup>Os (■); (b) <sup>79</sup>Br (■). Statistical analysis was performed using Welch’s unpaired t-test, assuming unequal variances.

**Extent of efflux**

The extent of complex efflux of **SS-2** from A549 cells was investigated by varying the exposure time. Cells were treated with  $1 \times \text{IC}_{50}$  of **SS-2** for 3, 6 and 24 h (no recovery) or 24 h with 24, 48 and 72 h recovery (**Fig. 3.15**; **Appendix, Table A16**). Significantly more intracellular Br vs. Os was observed for all exposure times, suggesting complex degradation and the preferential efflux of the Os modality over the Br-labelled sulfonamide ligand.

The general trend of Os accumulation showed a maximum between 8-24 h, and upon recovery (complex-free media) Os was effluxed from the cells over 72 h, which correlates closely with that observed for parent compound **RR-1** (*p*-CH<sub>3</sub>),<sup>10</sup> and **SS-2** in A2780 cells (**Section 3.3.9**). Maximal levels of intracellular Br were reached after 24 h exposure (no recovery) revealing a remarkable  $571 \pm 11$  ng Br/ $10^6$  cells. Upon recovery (complex-free media) Br is effluxed from the cells, however, even after 72 h recovery period,  $151 \pm 45$  ng Br/ $10^6$  cells still remained intracellularly (**Fig. 3.15**).

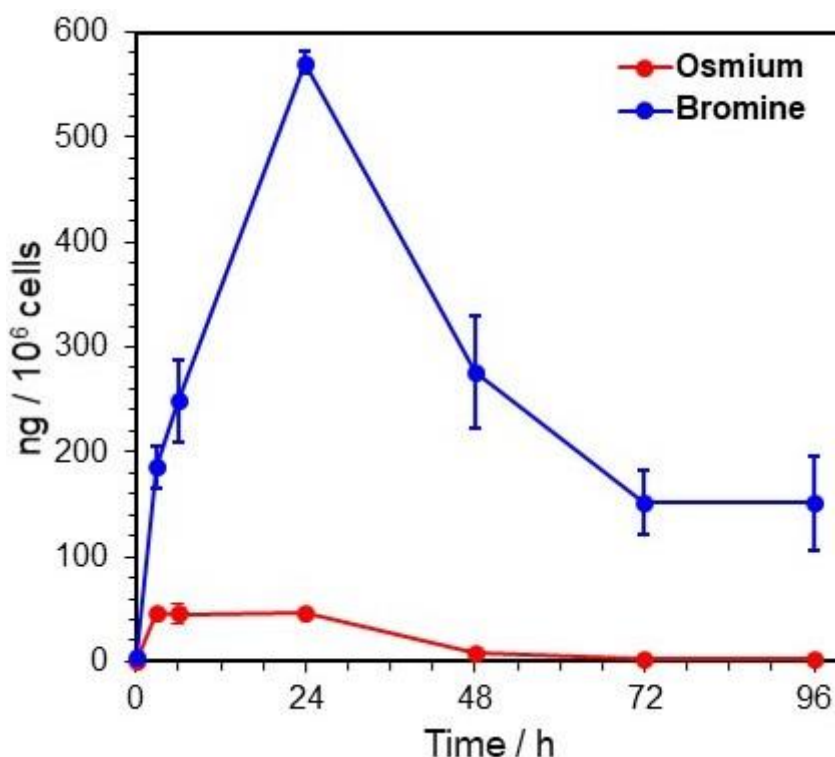


**Figure 3.15.** Time-dependent <sup>189</sup>Os (■) and <sup>79</sup>Br (■) intracellular accumulation in A549 cells treated with  $1 \times \text{IC}_{50}$  (30  $\mu\text{M}$ ) of **SS-2** for different exposure times (3, 6, 18, 24 h) and 24 h with different recovery times (24, 48 and 72 h) as analysed by ICP-MS.

### 3.3.11 <sup>189</sup>Os and <sup>79</sup>Br cellular distribution

The cellular distribution of metals in cancer cells can be probed using cell fractionation kits (FractionPREP kit) which separates cells into four fractions: (i) cytoskeletal (containing insoluble proteins); (ii) nuclear (nuclear proteins and membranes); (iii) membranes (organelles and membrane proteins) and (iv) cytosolic (cytoplasmic proteins). From this, separate cell fractions can be digested and analysed for their Os content, as previously reported for **RR-1** (*p*-CH<sub>3</sub>).<sup>10</sup> Herein, A549 cancer cells treated with 1×IC<sub>50</sub> of **SS-2** for varying exposure times (3, 6 and 24 h) and 24 h exposure with 24–72 h recovery (complex-free media) were fractionated and analysed by ICP-MS for their Os and Br content (**Fig. 3.16**).

Significantly more intracellular Br vs. Os was observed in cells treated with **SS-2** for all measured time points – implying dissociation of the Br-labelled chelated ligand. The majority of intracellular Os was present in the membrane fraction (>65%), but also in the cytoskeletal fraction (**Appendix, Table A17**). Similarly, the majority of intracellular Br was present in the membrane fraction (>58%). However, interestingly 10–20% of Br was distributed in the nuclear fraction (**Fig. 3.16, Appendix, Table A18**), with negligible quantities of nuclear Os (<6%) – suggestive of a different cellular target for the “free” Br-sulfonamide ligand.

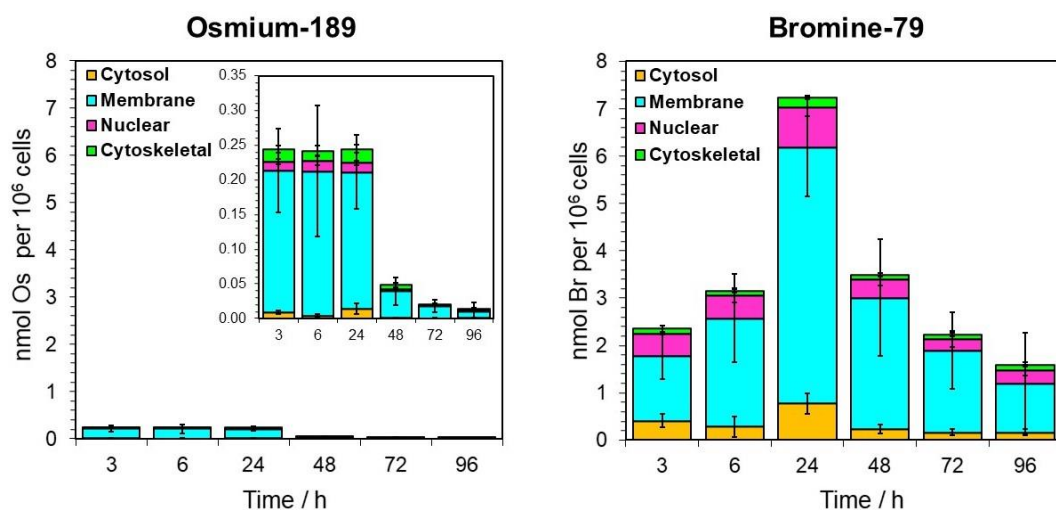


**Figure 3.16.** Time-dependent cellular distribution of (a) <sup>189</sup>Os and (b) <sup>79</sup>Br in A549 cells treated with 1×IC<sub>50</sub> (30 μM) of **SS-2** for different exposure times (3, 6, 24 h and 24 h exposure with 24, 48 and 72 h recovery) showing the cytosolic (■), nuclear (■), membrane (■) and cytoskeletal (■) fractions, as reported in nmol per million cells.

The moles of Os and Br per cell in the nuclear fraction were calculated by normalizing the ratios to the *total* cellular quantities (**Fig. 3.17**; **Appendix, Table A19**). Negligible quantities of Os were observed in the cell nucleus ( $<1.5 \times 10^{-8}$  nmol per cell), whereas, significantly more Br was present ( $>25 \times 10^{-8}$  nmol per cell) – achieving maximal nuclear quantities of *ca*  $85 \times 10^{-8}$  nmol per cell after 24 h (no recovery), as shown in **Fig. 3.17**. Overall, this suggests the nuclear localization of the Br-labelled sulfonamide ligand, but not the Os.

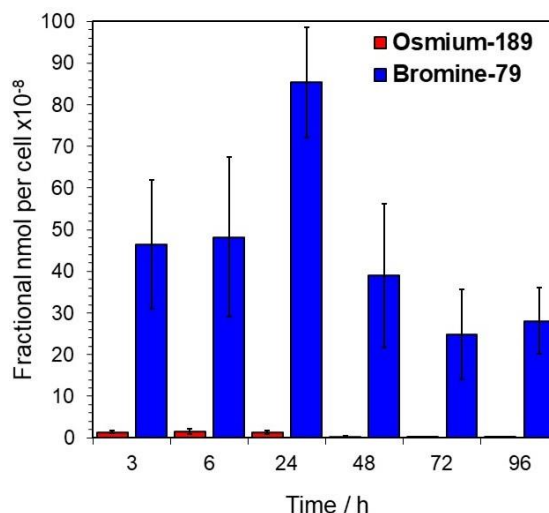


**Figure 3.17.** Normalized fractional moles of osmium and bromine in the nuclear fraction in A549 cells treated with  $1 \times \text{IC}_{50}$  of **SS-2** ( $30 \mu\text{M}$ ) for different exposure times:  $^{189}\text{Os}$  (■) and  $^{79}\text{Br}$  (■), as reported in fractional nmol  $\times 10^{-8}$  per cell.

### 3.3.12 Synchrotron-XRF

Synchrotron-XRF is a well-established technique for probing the *in-cell* localization and distribution of metal complexes in cancer, including platinum,<sup>43-45</sup> ruthenium,<sup>43, 46, 47</sup> iridium<sup>48</sup> and osmium.<sup>49-51</sup> Synchrotron-XRF is not limited to metals and can be used to monitor the emissions of other non-metals which are non-native to cells – including bromine, for which the  $\text{KL}_3$ -emission (11.92 keV) does not overlay with that of endogenous elements.<sup>52</sup> Bromine is non-native to cells and has previously been used to monitor Br-labelled cyclic peptides and platinum complexes in tumour cells using synchrotron-XRF.<sup>31, 53</sup> Complementary to ICP-MS studies, Os and Br in A549 cells treated with  $1-5 \times \text{IC}_{50}$  of **SS-2** for 24 h (no recovery) have been monitored in this work by synchrotron-XRF in a dual-mapping approach.

A population of A549 cells grown on Si<sub>3</sub>N<sub>4</sub> membranes was treated with different concentrations of **SS-2**, before cryo-fixation and dehydration. Individual cells were selected on the membranes based on their distributions of endogenous elements (Zn, S, P, K). An incident energy of 15 keV (which exceeds the electron-binding energy of the elements of interest) was used to monitor the XRF emissions of Os (L<sub>3</sub>M<sub>5</sub>=8.9 keV) and Br (KL<sub>3</sub>=11.9 keV).<sup>52</sup> In cells, the K-emission of endogenous Zn is close to that of the Os L<sub>3</sub>-emission, hence, Zn K-lines were de-convolved from the Os L-lines using the PyMCA fitting toolkit to distinguish between endogenous Zn and exogenous Os (**Fig. 3.18**).<sup>18</sup>

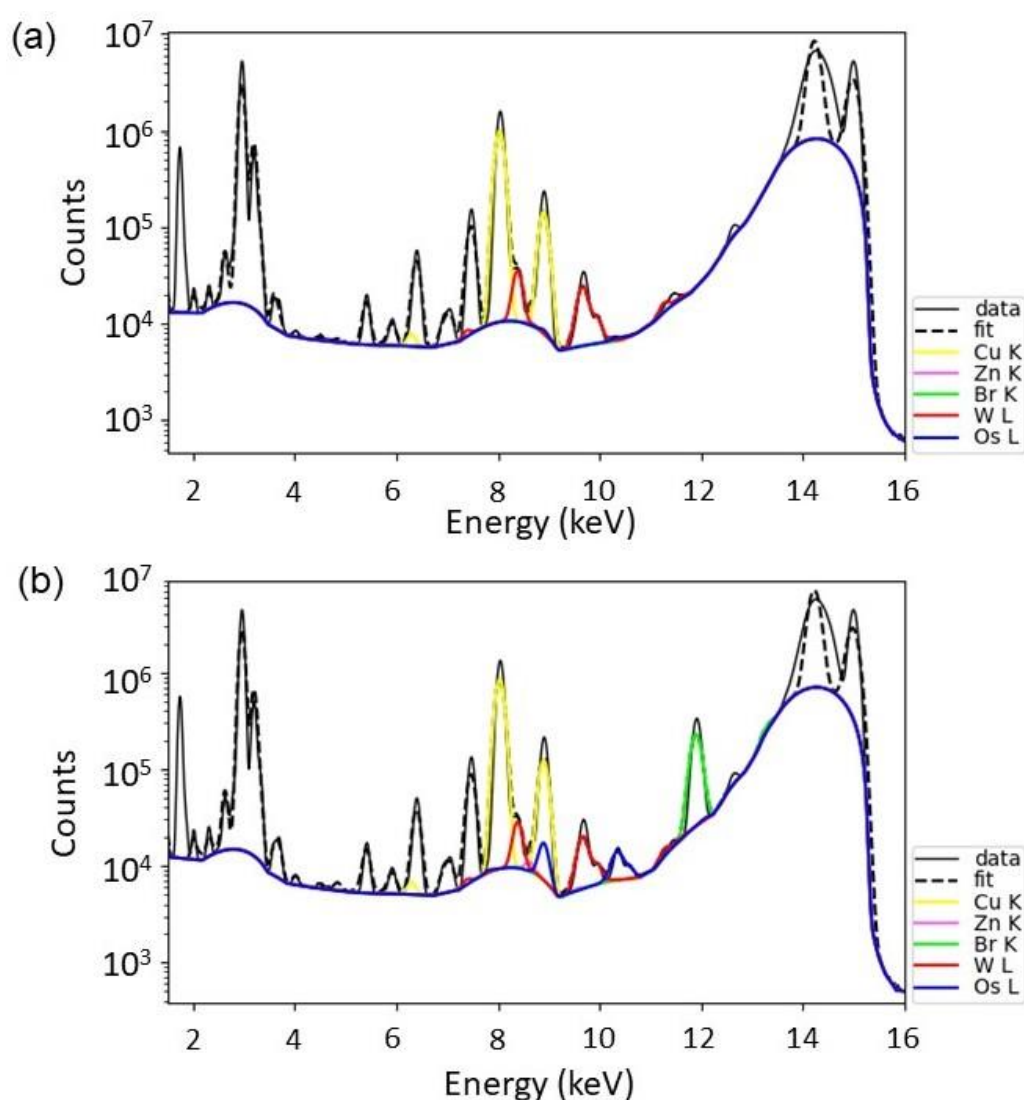


**Figure 3.18.** XRF spectrum and the corresponding fit configuration, showing copper, zinc, bromine, tungsten and osmium: (a) Untreated A549 cell; (b) Treated with 1×IC<sub>50</sub> of **SS-2** for 24 h. Note that the Os K $\beta$  emission has also been fitted as the K $\alpha$  emission overlaps with Cu K $\beta$ . XRF emissions from osmium and bromine were not evident in the untreated control, but were present in cells treated with **SS-2**. Graphs were fitted in PyMCA.<sup>18</sup>



**Elemental XRF maps of A549 cells**

Elements in four untreated (control) cells were mapped (C1-4, Fig. 3.19), showing typical elongated A549 morphologies,<sup>28, 29</sup> with clear elemental distributions allowing the identification of cell nuclei from the highly-localized Zn (containing *ca.* 30-40% of total intracellular Zn).<sup>54</sup> Importantly, Os and Br were not observed in these untreated cells (Fig. 3.18-19), thus, validating the experiment.

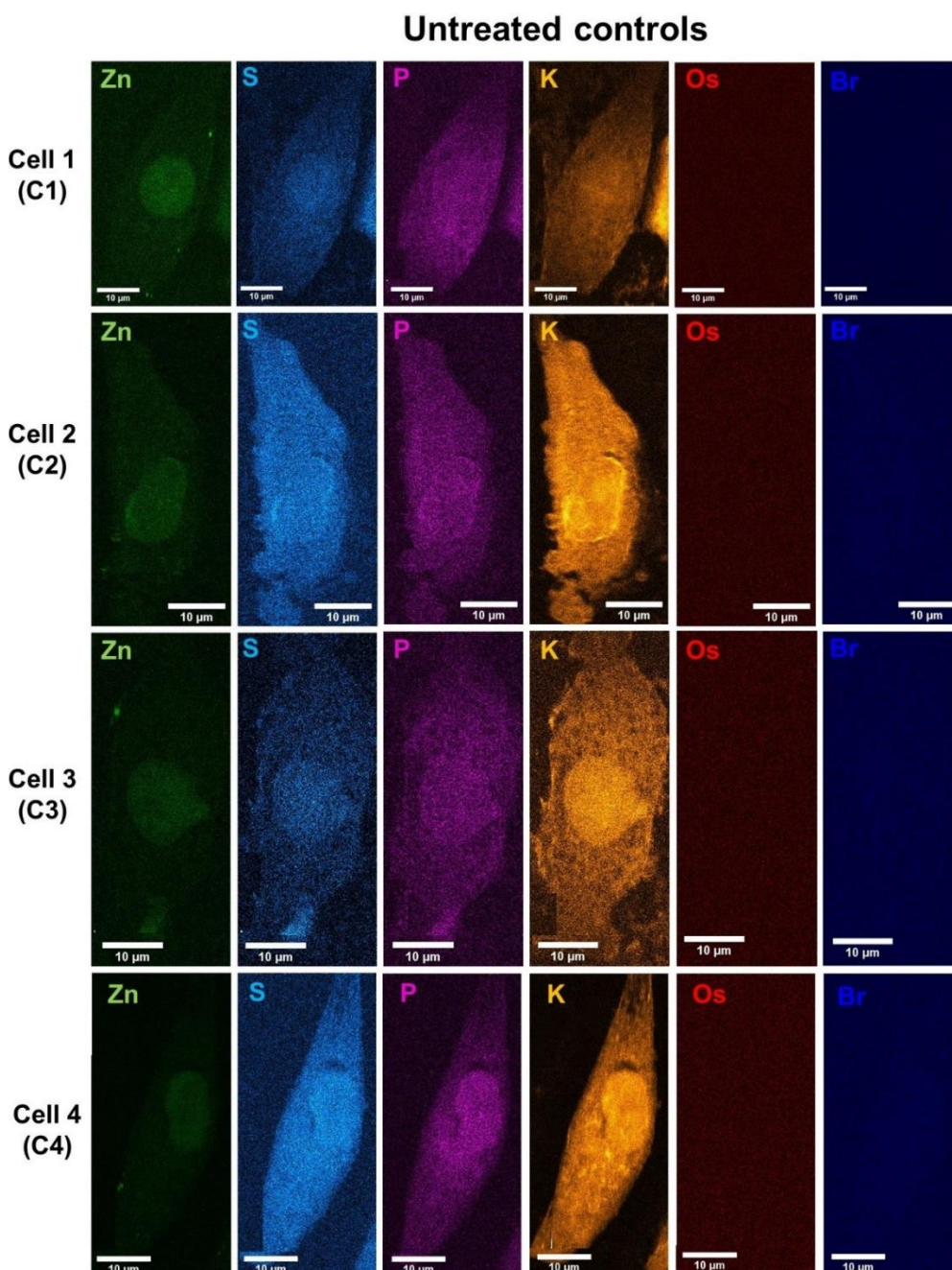


**Figure 3.19.** Synchrotron-XRF elemental maps of untreated cryo-fixed and freeze-dried A549 cells grown on  $Si_3N_4$  membranes (Cells 1-4, C1-4) showing: Zn (■); S (■); P (■); K (■); Os (■) and Br (■). Note that cells have been labelled C1-4 for convenience. Data were acquired using 15 keV energy, 0.1 s exposure, 100 nm step size with *ca.* 50×70 nm<sup>2</sup> beam size. Data were analysed in PyMCA software,<sup>18</sup> and images generated in ImageJ.<sup>19</sup>

A549 cells were treated with  $1\times IC_{50}$  (**C5-8**, **Fig. 3.20**),  $3\times IC_{50}$  (**C9-15**, **Fig. 3.21**) or  $5\times IC_{50}$  (**C16-18**, **Fig. 3.22**) of **SS-2** for 24 h (no recovery), revealing strong cytoplasmic (non-nuclear) localization of both Os and Br in all cases. Interestingly, Br was also observed in the cell nucleus, but Os was not – suggesting *in-cell* complex degradation. Overall, the cells appear less elongated and cobble-stoned shaped compared to the untreated controls (**C1-4**, **Fig. 3.19**). Note that cells analysed by synchrotron-XRF have been numbered **C1-18** for simplicity.

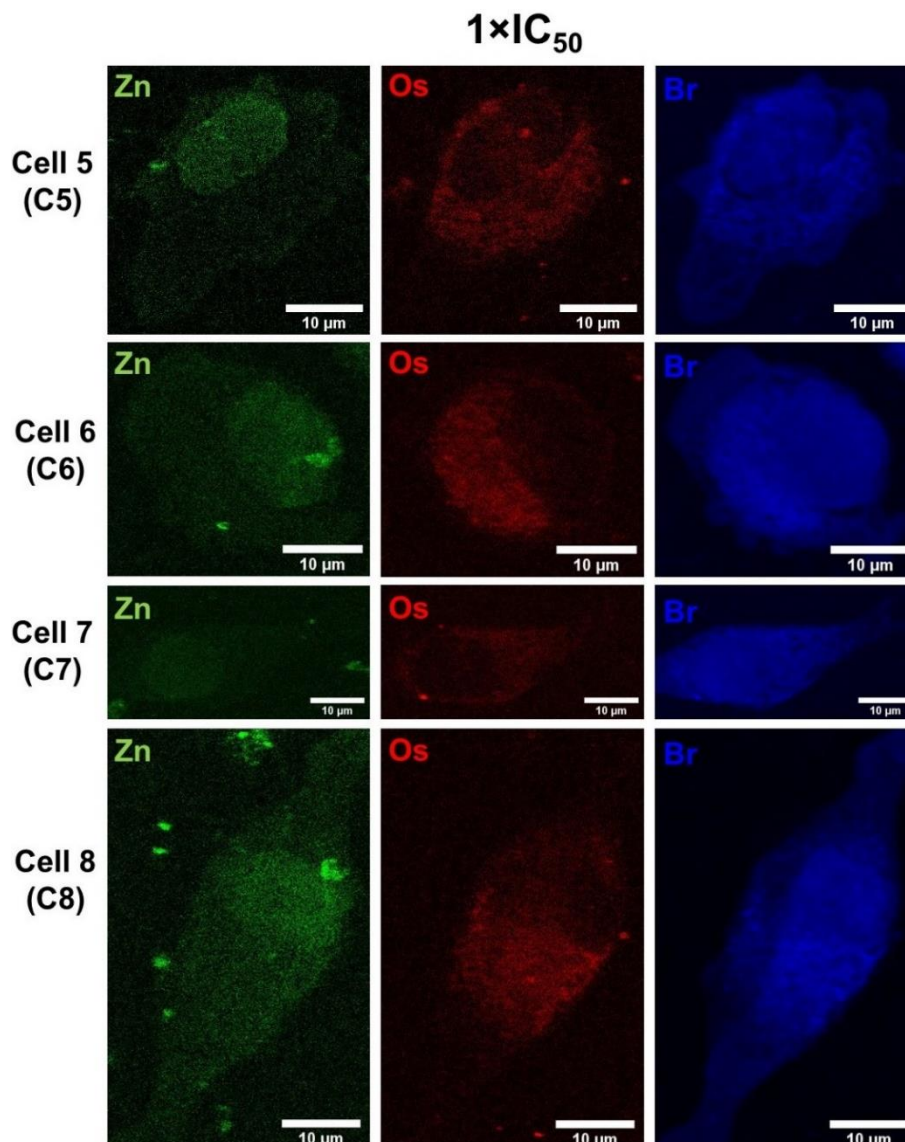


**Figure 3.20.** Synchrotron-XRF elemental maps of cryo-fixed and freeze-dried A549 cells grown on  $Si_3N_4$  membranes and treated with  $1\times IC_{50}$  (30  $\mu M$ ) of **SS-2** for 24 h (**Cells 5-8**, **C5-8**), showing: Zn (■); Os (■) and Br (■). Note that cells have been labelled **C5-8** for convenience. Data were acquired using 15 keV energy, 0.1 s exposure, 100 nm step size with *ca.* 50 $\times$ 70 nm<sup>2</sup> beam size. Data were analysed in PyMCA software,<sup>18</sup> and images generated in ImageJ.<sup>19</sup>



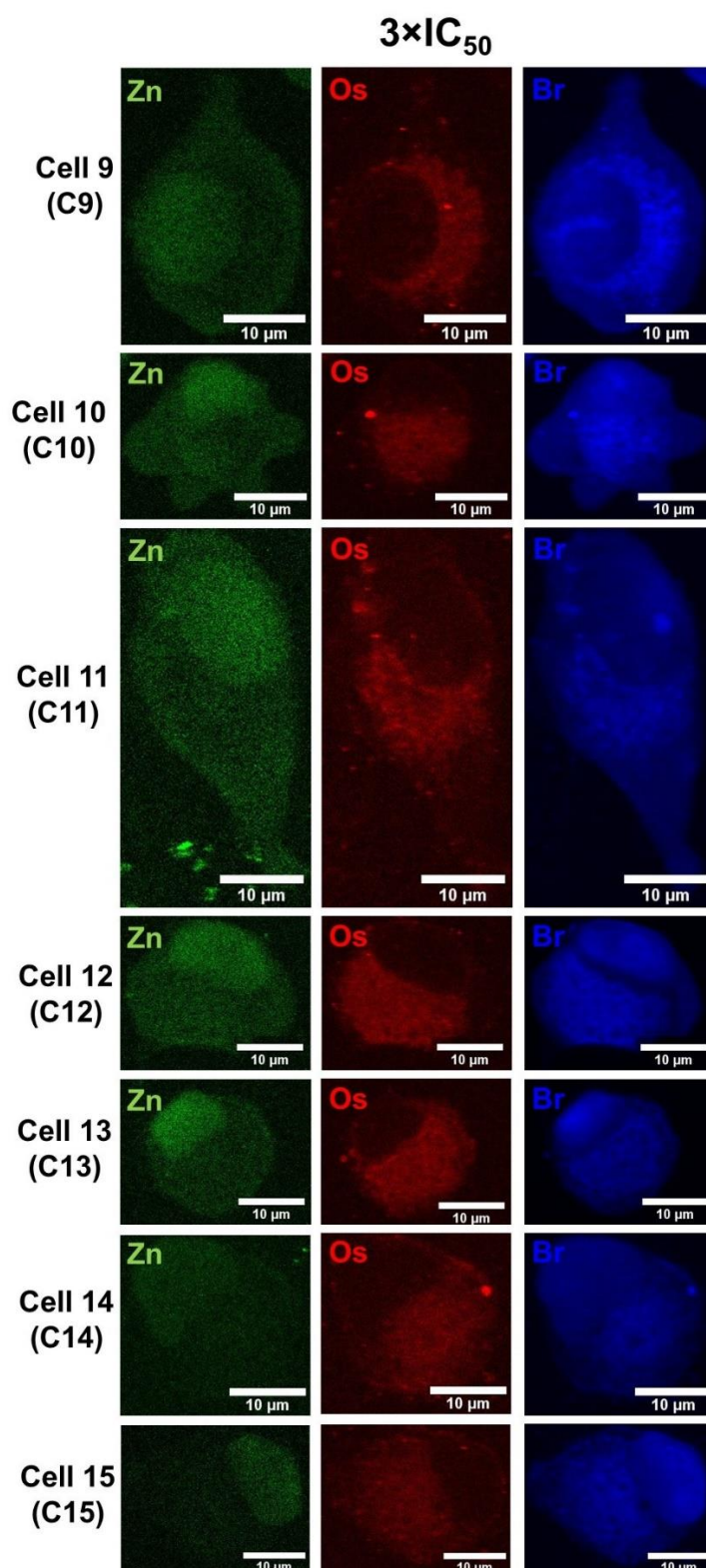


**Figure 3.21.** Synchrotron-XRF elemental maps of cryo-fixed and freeze-dried A549 cells grown on  $Si_3N_4$  membranes and treated with 3×IC<sub>50</sub> (90 μM) of **SS-2** for 24 h (**Cells 9-15, C9-15**), showing: Zn (■); Os (■) and Br (■). Note that cells have been labelled **C9-15** for convenience. Data were acquired using 15 keV energy, 0.1 s exposure, 100 nm step size with *ca.* 50×70 nm<sup>2</sup> beam size. Data were analysed in PyMCA software,<sup>18</sup> and images generated in ImageJ.<sup>19</sup>

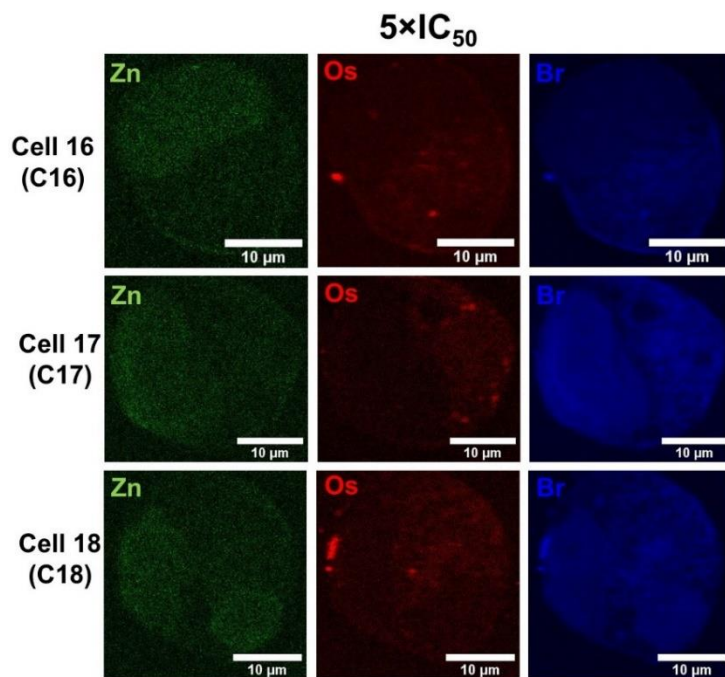


**Figure 3.22.** Synchrotron-XRF elemental maps of cryo-fixed and freeze-dried A549 cells grown on  $Si_3N_4$  membranes and treated with  $5\times IC_{50}$  ( $150\ \mu M$ ) of **SS-2** for 24 h (**cells 16-18, C16-18**), showing: Zn (■); Os (■) and Br (■). Note that cells have been labelled **C16-18** for convenience. Data were acquired using 15 keV energy, 0.1 s exposure, 100 nm step size with *ca.*  $50\times 70\ nm^2$  beam size. Data were analysed in PyMCA software,<sup>18</sup> and images generated in ImageJ.<sup>19</sup>

### Cellular morphology of A549 cells

Changes in cell morphology were quantified by calculating the 2D areas ( $\mu m^2$ ) and roundness factors (a measure of the circularity of an object) of individual cells in triplicate using ImageJ analysis software (**Appendix, Table A20**).<sup>19</sup> A statistically significant decrease in cell area ( $\mu m^2$ ) was observed between cells treated with  $3\times IC_{50}$  of **SS-2** compared to the untreated controls ( $p=0.0074$ , **Fig. 3.22**). However, at the highest concentration ( $5\times IC_{50}$ ) an increase in 2D cell area was observed with respect to  $3\times IC_{50}$  ( $p=0.0236$ ). No statistically significant differences in roundness were observed between cells treated with  $1\times IC_{50}$  of **SS-2** when compared to the untreated controls (**Fig. 3.23**). However, cells treated with 3 and  $5\times IC_{50}$  were significantly more rounded compared to the untreated controls ( $p=0.0002$  and  $p=0.0001$ , respectively). The area of cell nuclei were determined from the Zn XRF maps (**Appendix, Table A21**), revealing no statistically significant differences between nuclei in cells treated with 0- $3\times IC_{50}$  of **SS-2** ( $p>0.05$ ), however, upon exposure to  $5\times IC_{50}$  an increase in nuclei size was observed ( $p=0.0233$ ,  $p=0.013$ ,  $p=0.0234$ , respectively).

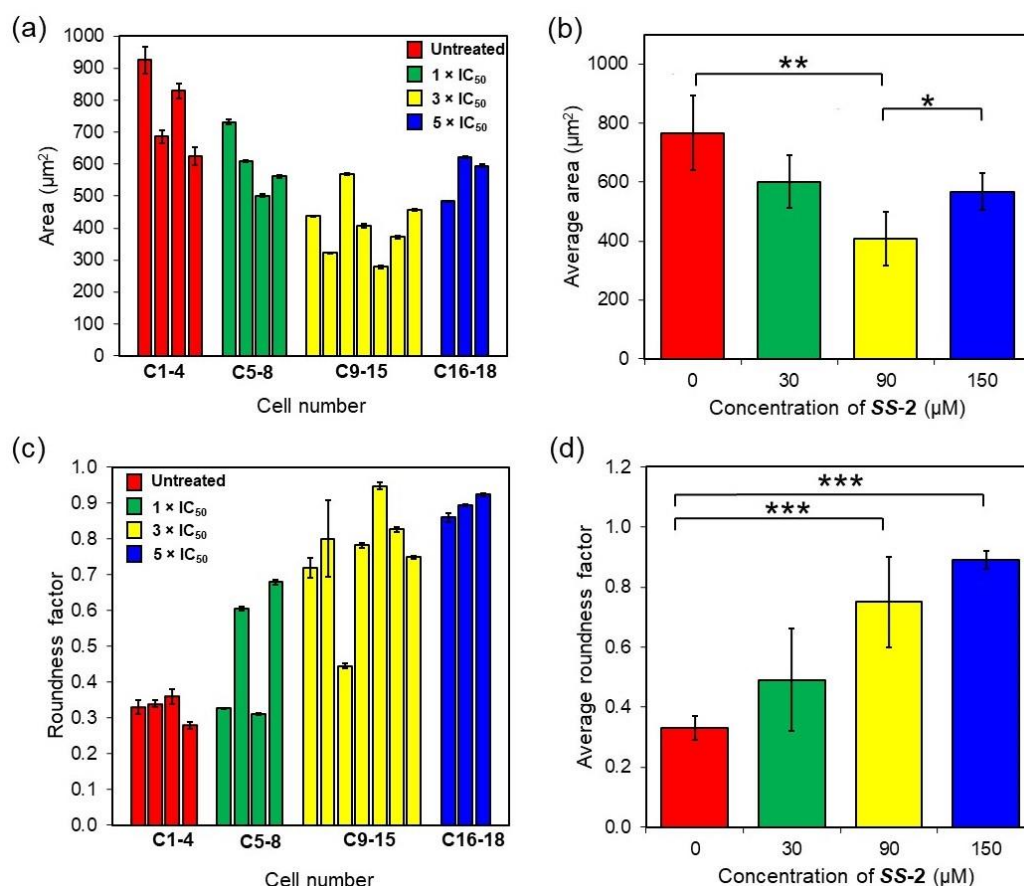


**Figure 3.23.** Cell area (μm<sup>2</sup>) and roundness factor analysis of cryo-fixed and freeze-dried A549 cells grown on Si<sub>3</sub>N<sub>4</sub> membranes and treated with 1-5×IC<sub>50</sub> of **SS-2** (0–150 μM) for 24 h (no recovery), as identified from the S, K, P and Zn XRF elemental maps using ImageJ software:<sup>19</sup> Controls (**C1-4**), 30 μM (**C5-8**), 90 μM (**C9-15**) or 150 μM (**C16-18**) of **SS-2** for 24 h with no recovery, as identified by S, K, P and Zn distributions in the obtained XRF elemental maps. (a) Individual cell areas (μm<sup>2</sup>). (b) Mean cell areas (μm<sup>2</sup>). (c) Individual roundness factors. (d) Mean roundness factors. Statistical analysis was performed using Welch's unpaired t-test, assuming unequal variables.

### Co-localization of Os, Br and Zn

The co-localization statistics (Pearson's R-value and Spearman Rank correlation) between Os, Br and Zn in cells **C4-18** were calculated using ImageJ (**Appendix, Tables A22-24**). Overall, the co-localization between Os and Zn in cells treated with 1-5×IC<sub>50</sub> of **SS-2** revealed *r* and *r<sub>s</sub>* values close to zero, implying little or no correlation (**Appendix, Table A23**). In contrast, the co-localization between intracellular Br and Zn ranged between *r*=0.09-0.36 (**Appendix, Table A24**), implying some correlation between them. There was moderate co-localization between Os and Br: 1×IC<sub>50</sub> (*r*=0.15-0.45); 3×IC<sub>50</sub> (*r*=0.07-0.56); 5×IC<sub>50</sub> (*r*=0.10-0.29) as shown in **Appendix (Table A22)**.

As the nuclei in cells treated with 1-3×IC<sub>50</sub> of **SS-2** were clearly identifiable by the high localization of Zn,<sup>54</sup> the co-localization between Os, Br and Zn in the cell nucleus and the cytoplasm was estimated for each cell (**Appendix, Tables A22-24**). Os did not strongly co-localise with Zn in the cell nucleus ( $r=-0.09$  to  $0.00$ ) or the cytoplasm ( $r=-0.03$  to  $+0.05$ ), whereas, Br co-localized moderately with Zn in the nucleus ( $r=0.06-0.22$ ) and in the cytoplasm ( $r=0.03-0.12$ ), which varied between individual cells. Co-localization between Os and Br was prominent in the cytoplasm ( $r=0.13-0.48$ ), but negligible in the nucleus ( $r=-0.11$  to  $+0.10$ ).

The co-localization statistics between Os, Br and Zn were also determined for cells treated with 5×IC<sub>50</sub> of **SS-2**, however, as the nucleus could not be confidently identified (**C16-18, Section 3.3.12, Fig. 3.22**), the interpretation of the data was more difficult. Nonetheless, Os and Zn did not strongly co-localise in the nucleus nor the cytoplasm ( $r=0.00-0.02$  and  $0.00-0.03$ , respectively); similarly, Br did not strongly co-localise with Zn in the nucleus ( $r=0.02-0.05$ ), but co-localized strongly in the cytoplasmic region of the cell ( $r=0.16-0.21$ ). Finally, Os and Br moderately co-localised in the cytoplasm of cells treated with 5×IC<sub>50</sub> of **SS-2** ( $r=0.16-0.18$ ), but not in the cell nucleus ( $r=0.02-0.08$ ).

### Quantification of Os and Br

The mass fractions of elements can be determined from synchrotron-XRF by calibrating the data to an AXO standard of known elemental concentrations, assuming a maximal cell thickness of 6 μm.<sup>55</sup> Mole fraction quantities of both Os and Br were determined for cells **C5-18** to gain an insight into the concentration-dependent intracellular stability of **SS-2** in A549 cancer cells (**Table 3.9**), revealing significantly higher levels of intracellular Br vs. Os ( $>3\times$ ) for all concentrations, as represented by the molar bromine-to-osmium ratios (Br/Os). Large variations in the mole fraction quantities of both elements were observed for cells treated under the same conditions, with Br/Os ranging from: (i) 4.2–8.6 (1×IC<sub>50</sub>); (ii) 3.8–11.3 (3×IC<sub>50</sub>); (iii) 2.2–2.4 (5×IC<sub>50</sub>), emphasizing the variability in drug uptake in a population of unsynchronized cells. A comparison of the mean Br/Os ratios revealed a statistically significant decrease (by *ca.* 57%) between cells treated with 3×IC<sub>50</sub> (**C9-15**) and 5×IC<sub>50</sub> (**C16-18**,  $p=0.0019$ ) of **SS-2**.

**Table 3.9.** Mole fraction quantities and molar bromine-to-osmium (Br/Os) ratios of Os and Br in cryo-fixed and freeze-dried A549 cells grown on Si<sub>3</sub>N<sub>4</sub> membranes and treated with 1-5×IC<sub>50</sub> of *SS-2* (30-150 μM) for 24 h (no recovery), as determined from synchrotron-XRF in triplicate using ImageJ software.<sup>19</sup>

Cell	Mole Fraction of [Os] × 10 <sup>-8</sup>	Mole Fraction of [Br] × 10 <sup>-8</sup>	[Br]/[Os]	Mean [Br] / [Os]
5	5.41±0.02	46.5±0.3	8.6	5±2.5
6	5.22±0.01	14.86±0.04	2.9	
7	4.70±0.01	19.6±0.1	4.2	
8	5.54±0.02	23.48±0.15	4.2	
9	4.390±0.004	34.1±0.2	7.8	7.1±2.4
10	5.50±0.01	37.0±0.9	6.7	
11	6.82±0.01	25.9±0.1	3.8	
12	8.72±0.05	98.4±0.8	11.3	
13	9.91±0.07	86.4±0.9	8.7	
14	4.20±0.01	26.0±0.2	6.4	
15	6.53±0.01	33.7±0.1	5.2	
16	5.60±0.02	12.55±0.03	2.2	2.3±0.1
17	5.29±0.01	12.89±0.02	2.4	
18	5.47±0.02	12.49±0.04	2.3	

#### Analysis of Os and Br in lysosomes of A549 cells

For cells treated with 3×IC<sub>50</sub> (90 μM) and 5×IC<sub>50</sub> (150 μM) of *SS-2* for 24 h (**C9-15**), small localized regions of Os were observed in the cytoplasm – perhaps indicative of Os accumulation in organelles such as lysosomes, endosomes or mitochondria (**Fig. 3.24**; **Appendix, Fig. A4-12**). The areas of these compartments were initially determined in triplicate from the Os XRF maps, using the and multipoint selection tools in ImageJ software (and reaffirmed using the smoothing tools – see **Appendix, Figure A4**).<sup>19</sup> Further to this, mole fraction quantities of both Os and Br in these compartments were determined. The total number of these cytoplasmic organelles per cell ranged between 16-25 (for 3×IC<sub>50</sub>) and 4-11 (for 5×IC<sub>50</sub>), with average areas of 0.6±0.1 μm<sup>2</sup> and 0.78±0.25 μm<sup>2</sup>. More Br was present in these compartments than Os, with mean molar bromine-to-osmium ratios (Br/Os) of 4±1 and 1.48±0.17 (**Table 3.10**). No correlation was observed between the lysosomal area and the average Br/Os ratio.

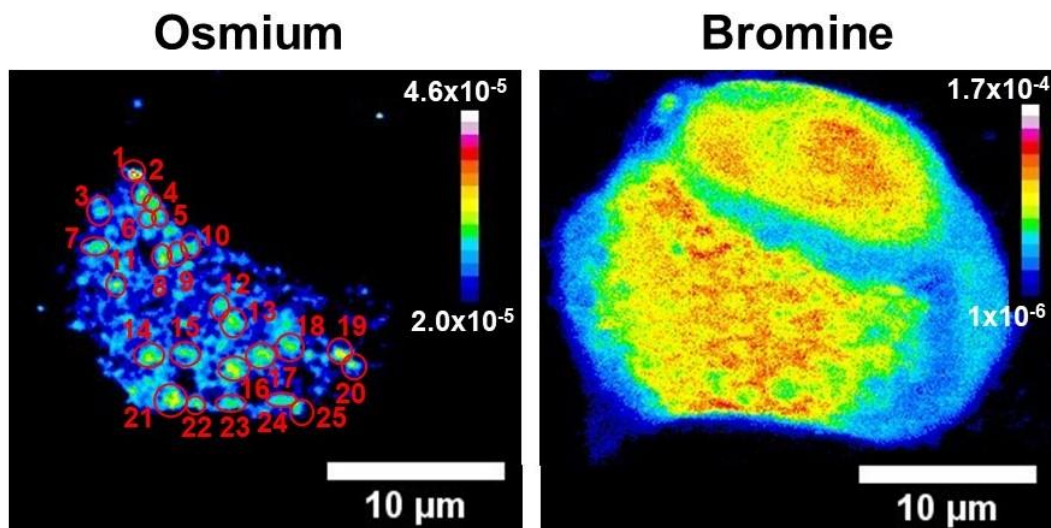


**Figure 3.24.** Representative example of synchrotron XRF elemental maps of a cryopreserved and freeze-dried A549 cell treated with  $3 \times IC_{50}$  ( $90 \mu M$ ) of **SS-2** for 24 h (no recovery) showing the co-localization of Os and Br in small, vesicle-sized compartments as represented identified with red circles (**C13**). Images were prepared in ImageJ using the 16-colour settings, using the multipoint selections tools to identify small compartments. Data were acquired using 15 keV energy, 0.1 s exposure, 100 nm stepsize with *ca.*  $50 \times 70 \text{ nm}^2$  beam size. Data were analysed in PyMCA software,<sup>18</sup> and images generated in ImageJ.<sup>19</sup> Note that, the presented images are shown as using the smoothing tool for clarity and presentation purposes, but all analysis was performed on the original pixelated mass fraction image. See Appendix **Fig. A4** for more information.

**Table 3.10.** A comparison of the average lysosomal area ( $\mu m^2$ ) and the average lysosomal bromine-to-osmium (Br/Os) ratio of A549 cells treated with 3 and  $5 \times IC_{50}$  ( $90 \mu M$ ) of **SS-2** for 24 h, no recovery time, as analysed in triplicate using ImageJ software.<sup>19</sup>

Cell number	No. of lysosomes	Average lysosomal area ( $\mu m^2$ )	Average [Br]/[Os]
9	17	$0.63 \pm 0.29$	$3.4 \pm 0.4$
10	12	$0.57 \pm 0.23$	$3.1 \pm 0.6$
11	12	$0.70 \pm 0.17$	$2.6 \pm 0.3$
12	19	$0.67 \pm 0.19$	$5.7 \pm 0.8$
13	25	$0.45 \pm 0.15$	$8.5 \pm 0.8$
14	n.d	n.d	n.d
15	12	$0.58 \pm 0.18$	$3.6 \pm 0.4$
16	5	$0.84 \pm 0.42$	$1.57 \pm 0.14$
17	11	$0.80 \pm 0.18$	$1.53 \pm 0.12$
18	4	$0.63 \pm 0.05$	$1.24 \pm 0.13$



### 3.3.13 Chloroquine inhibition of lysosomal activity

Chloroquine is the main clinically-approved drug for the treatment of malaria, and has been reported to be relatively non-toxic towards cancer cells at low micromolar concentrations.<sup>56</sup> Importantly, chloroquine can deactivate lysosomes by increasing the pH (decreasing the acidity),<sup>56-59</sup> preventing them from working as efficiently – hence, is suitable for probing the role of lysosomes in A549 cells treated with **RR-1** or Br-labelled **SS-2**. Herein, A549 cells were pre-incubated in chloroquine diphosphate (0 or 150  $\mu\text{M}$ ) for 2 h, washed with PBS and then treated with  $1 \times \text{IC}_{50}$  of **RR-1** ( $21.1 \pm 0.3$   $\mu\text{M}$ ) or **SS-2** ( $29.5 \pm 0.5$   $\mu\text{M}$ ) for 24 h and 72 h complex-free media (**Fig. 3.25**). A statistically significant increase in potency (decrease in  $\text{IC}_{50}$ ) was observed for cells pre-incubated in 150  $\mu\text{M}$  chloroquine and treated with **RR-1** (ca. 50% increase) or **SS-2** (ca 25% increase) when compared to their normal  $\text{IC}_{50}$  concentrations ( $p=0.0001$  and  $p=0.0003$ , respectively). Subsequently, the cellular accumulation of Os (ng/ $10^6$  cells) was determined in A549 cells pre-incubated in chloroquine (0-150  $\mu\text{M}$ , 2 h), washed with PBS, and treated with **RR-1** or **SS-2** for 24 h (no recovery), as shown in **Fig. 3.24**. A statistically significant increase in Os accumulation was observed for cells pre-incubated in chloroquine (0 or 150  $\mu\text{M}$ ) and treated with **RR-1** (ca. 69% increase) or **SS-2** (ca. 35% increase) for 24 h (no recovery), when compared to the latter ( $p=0.0015$  and  $p=0.0251$ , respectively).

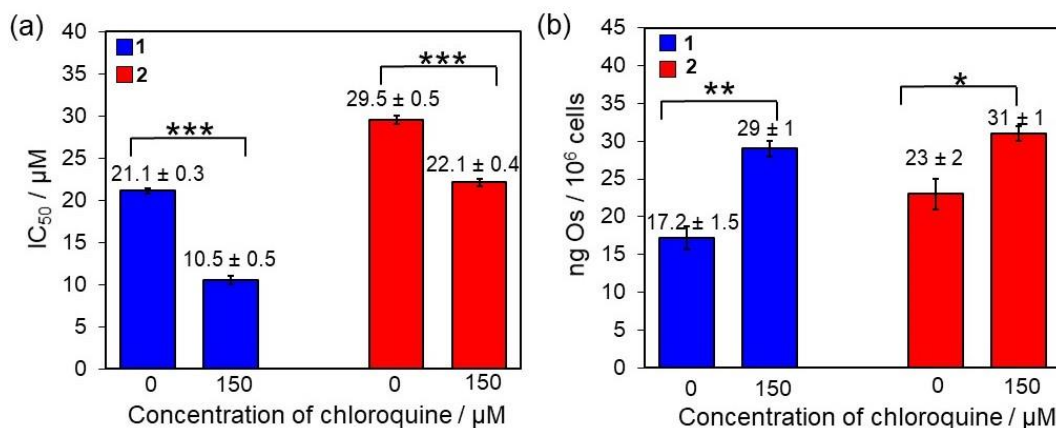


**Figure 3.25.** (a) Antiproliferative ( $\text{IC}_{50}$  /  $\mu\text{M}$ ) of **RR-1** and **SS-2** in A549 (human lung) cancer cells pre-incubated in 0 or 150  $\mu\text{M}$  of chloroquine diphosphate for 2 h, followed by 24 h drug and 72 h recovery time in drug-free media. (b) Osmium cellular accumulation of A549 cells pre-incubated with 0 or 150  $\mu\text{M}$  chloroquine diphosphate for 2 h and treated with  $1 \times \text{IC}_{50}$  **RR-1** (21  $\mu\text{M}$ ) and **SS-2** (30  $\mu\text{M}$ ) for 24 h, no recovery time as analysed using the acid digestion method. Statistical analysis was performed using the Welch's unpaired t-test, assuming unequal variances.

The Os and Br cellular accumulation of **SS-2** was also determined using the alkaline digestion method. The Os accumulation increased by *ca.* 33% from  $42.5 \pm 1.4$  to  $57 \pm 5$  ng Os/ $10^6$  cells ( $p=0.0327$ ) upon pre-incubation with chloroquine (**Fig. 3.26**). The Br accumulation was found to be statistically the same ( $p>0.05$ ). Interestingly, the molar Br/Os ratio decreased by *ca.* 29% upon preincubation with chloroquine (from  $33.7 \pm 0.1$  to  $23.2 \pm 0.2$ ;  $p=0.0001$ ), which implies that more of the complex may be intact upon deactivation of lysosomes.

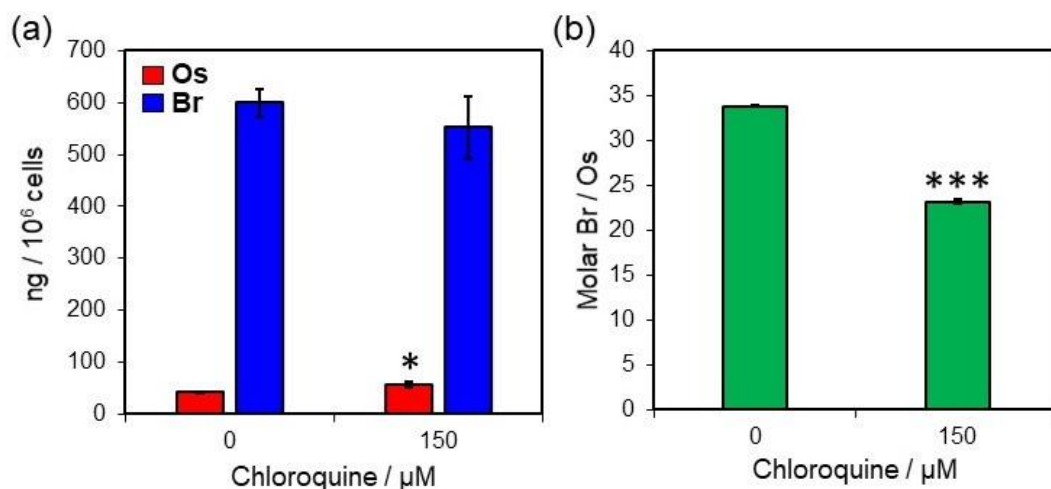


**Figure 3.26.** (a) Osmium and bromine cellular accumulation of A549 cells pre-incubated with 0 or 150  $\mu\text{M}$  chloroquine diphosphate for 2 h and treated with  $1 \times \text{IC}_{50}$  **SS-2** (30  $\mu\text{M}$ ) for 24 h, no recovery time as analysed using the alkaline digestion method. (b) Molar bromine-to-osmium ratio (Br / Os). Statistical analysis was performed using the Welch's unpaired t-test, assuming unequal variances.

Although chloroquine can deactivate lysosomes in cancer cells, it may not just be affecting these vesicles (for example, chloroquine can also affect endosomes),<sup>60</sup> hence, the observed differences in antiproliferative activity ( $\text{IC}_{50}$ ) and Os accumulation (ng/ $10^6$  cells) may not *just* be a result of lysosomal damage. In order to confirm that the increase in potency is a direct consequence of lysosomal deactivation and *not* membrane damage, chloroquine-dependent membrane integrity studies were performed. A549 cells were pre-incubated in chloroquine (0 or 150  $\mu\text{M}$ , 2 h), washed with PBS and then treated with  $1 \times \text{IC}_{50}$  of **RR-1** (*p*-CH<sub>3</sub>) or **SS-2** (*p*-Br) for 24 h (no recovery), followed by staining with PI and analysis by flow cytometry as described in **Section 3.2.9**.



The membrane viability of cells treated with **RR-1** or **SS-2** (negative controls) were comparable to that previously reported (Section 3.3.7), revealing negligible membrane damage (Fig. 3.27, Appendix, Table A25). No statistically significant differences in cell viability in cells pre-incubated in chloroquine or complex-free media were observed (Fig. 3.27). Similarly, no differences in the membrane viability was observed for cells pre-incubated in chloroquine and treated with **RR-1** or **SS-2** suggesting chloroquine does not damage cellular membranes.

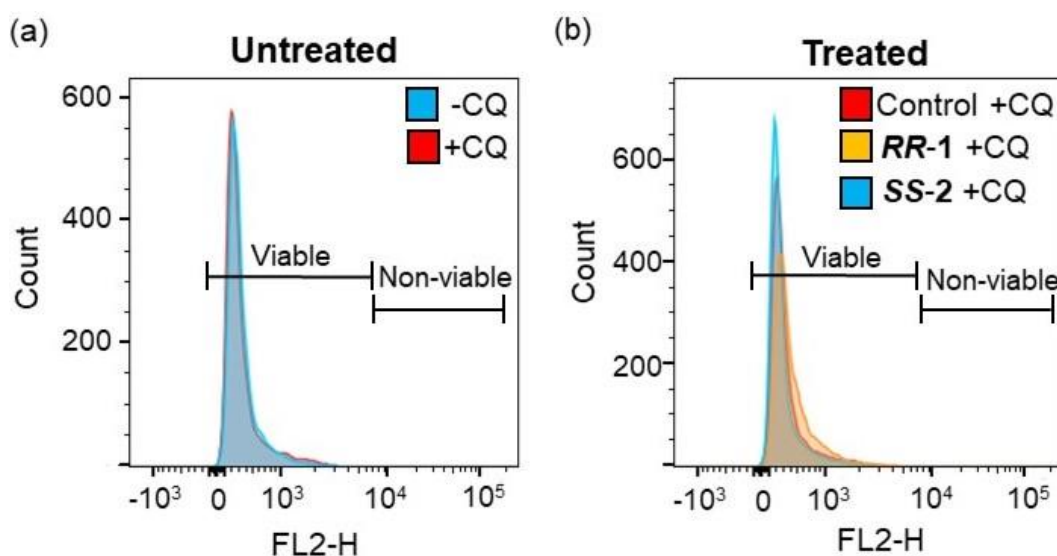


**Figure 3.27.** Membrane integrity analysis determined by flow cytometry for a normalized population of A549 cells. (a) Cells were pre-incubated with either medium alone or with chloroquine diphosphate (**CQ**, 150  $\mu$ M) for 2 h (b) Cells were pre-incubated with chloroquine diphosphate (**CQ**, 150  $\mu$ M) for 2 h followed by treatment with  $1 \times IC_{50}$  **RR-1** or **SS-2** for 24 h, with no recovery.

### 3.4 Discussion

#### 3.4.1 Synthesis of ligands and complexes

A total of six BsDPEN ligands (**SS/RR-L1**, **SS/RR-L2**, **RR-L3** and **SS-L4**) were synthesized through a S<sub>N</sub>2 nucleophilic substitution reaction between a sulfonyl chloride group and a primary amine group in the presence of a base (triethylamine, TEA). The addition of TEA was performed dropwise and at a low temperature to prevent deprotonation of both NH protons; additionally, the respective sulfonyl chlorides were added dropwise to prevent the formation of the disubstituted product. An excess of sulfonyl chloride was used to ensure that all of DPEN reacted (which would have consequences in further reaction with [Os(*p*-cym)Cl<sub>2</sub>]<sub>2</sub>). Any excess sulfonyl chloride was easily removed from the product by chromatography due to differences in polarity compared to the diamines (DPEN or BsDPEN). All ligands were recrystallized in hot ethyl acetate and estimated to be >95% pure (<sup>1</sup>H NMR, <sup>13</sup>C NMR, CHN analysis), suitable for further reaction with [Os(*p*-cym)Cl<sub>2</sub>]<sub>2</sub>.

The precursor dimer [Os(*p*-cym)Cl<sub>2</sub>]<sub>2</sub> for the synthesis of Os[(*p*-cym)BsDPEN] complexes was synthesised using the microwave-assisted synthesis previously reported.<sup>1</sup> Microwave synthesis has advantages over reflux methods, including shorter reaction times (kinetic enhancement), higher yields and simplicity. A solution of [Os(*p*-cym)Cl<sub>2</sub>]<sub>2</sub> and BsDPEN ligand (**L1-4**) in DCM were reacted together to form a yellow solution. This can be attributed to an 18-electron Os<sup>II</sup> species (previously isolated for **RR-1**),<sup>1</sup> in which the BsDPEN ligand is bound *via* one nitrogen atom, with two chlorides (Cl<sup>-</sup>) coordinated to the metal centre. Upon addition of an excess of potassium hydroxide (KOH) and water (to dissolve the base), a red organic layer formed, proceeding through a biphasic (DCM:water) reaction.<sup>1</sup> KOH acts as a base to deprotonate the already-coordinated N-atom, which subsequently eliminates Cl, forming highly stable 16-electron [Os<sup>II</sup>(*p*-cym)(BsDPEN)] complexes (**2-5**).

### 3.4.2 X-ray crystal structures and DFT

Complexes **SS-2** (*p*-Br) and **SS-3** (*p*-I) were isolated as single crystals in DCM:hexane. The crystal structures of **SS-2** and **SS-3** (Section 3.3.1, Fig. 3.4) were closely comparable to that of the parent compound **SS-1** (*p*-CH<sub>3</sub>) with (*1S*, *2S*) chirality. The osmium is  $\eta^6$ -coordinated to *p*-cymene, as reported for a variety of osmium and ruthenium half-sandwich pseudo-octahedral complexes.<sup>1, 61-63</sup> Complexes **SS-2** and **SS-3** both crystallise in the orthorhombic space group P2<sub>1</sub>2<sub>1</sub>2<sub>1</sub>, complementary to that of **SS-1** (*p*-CH<sub>3</sub>).<sup>1</sup> Unlike **SS-1**, H-bonds between the N-H and an O-atom of the sulfonyl group was not observed for **SS-2** and **SS-3** (3.09 Å and 2.97 Å, respectively – which are too long to be H-bonds). Stacking ( $\pi$ - $\pi$ ) interactions of aromatic groups (*p*-cymene and phenyl) were not observed for either **SS-2** or **SS-3**. Overall, the crystal structures of **SS-2** and **SS-3** were found to be remarkably similar to that of **SS-1** and the analogous Ru<sup>II</sup> 16-electron catalysts.<sup>1, 62</sup>

DFT was used to provide insights into the effect of halide substitution on the chemical structure of this family of 16-electron Os<sup>II</sup> complexes, based on the electron density distribution. DFT calculations on organometallic complexes commonly use mixed basis sets (a set of functions which represents the electron wave-function) to provide approximations to Schrödinger's equation.<sup>64</sup> Herein, the DFT calculations revealed close similarities between **RR-2** and **RR-3** (Section 3.3.2, Fig. 3.5), hence, suggesting the transition states in the ATH of acteophenone would be similar. The charge at the Os, arene or the BsDPEN (which are crucial for ATH catalysis)<sup>65</sup> did not change with halide-substitution, reaffirming that only localised charge effects were observed. Comparison of **RR-2** (*p*-Br) and **RR-3** (*p*-I) with **RR-6** (*p*-F) showed no significant changes in the Mulliken partial charges on non-carbon atoms (Appendix, Table A7, Fig. A1), except for the halide atom (X) for which the charge correlated with the electronegativity of the halide series (F>Cl>Br>I).

The crystal structures of the **RR** enantiomers of **2** and **3** (not obtained) were assumed to closely resemble those of the **SS** crystal structures, thus, it can be deduced that their ground state geometries (DFT) closely resembled the crystal structures (mirror images have the same energy). Overall, both the x-ray crystal structures and DFT results of **SS-2** and **SS-3** are closely comparable to that of parent compound **SS-1**.<sup>2</sup>

### 3.4.3 Hydrophobicity studies

Strong similarities in LogP values were observed between enantiomeric pairs **SS/RR-2** (*p*-Br) and **SS/RR-3** (*p*-I), all with LogP values around 1.0 (Section 3.3.3, Table 3.1), implying they have similar lipophilic properties. This was not surprising considering their chemical compositions are identical. Similarly, variation of substituent position did not affect the LogP: **SS-5** (*m*-Br) and **SS/RR-2** (*p*-Br). The LogP of **SS/RR-3** (*p*-I) were closely comparable to that of **SS/RR-2** (*p*-Br) which was expected as bromide and iodide have similar electronegativities, despite the larger size of iodide. This correlates with the electrostatic potentials of *p*-halide substituted Os<sup>II</sup> sulfonamide complexes determined by DFT (Section 3.3.2).

The lipophilicity of **RR-4** (*p*-OMe) was determined to be greater than that of the **SS/RR-2** and **SS/RR-3** (*p*-Br and I), implying increased hydrophobicity. Methoxy groups (OMe) are electron-donating by resonance, so can push electrons into the delocalized benzene ring and towards the SO<sub>2</sub> group, further, strengthening the N-Os bond. In contrast, halides (Br, I) are weakly electron-withdrawing from the aromatic ring, thus, somewhat weaken the N-Os bond. It was expected that the presence of non-polar methoxy group in **RR-4** (*p*-OCH<sub>3</sub>) would increase the hydrophobicity, despite the addition of an O atom (which can H-bond with water), through hydrophobic interactions with octanol. Moreover, the LogP of **RR-4** (*p*-OCH<sub>3</sub>) was intermediate between that of **SS/RR-2** or **SS/RR-3** (R=*p*-Br, I) and parent compound **RR-1** (R=*p*-CH<sub>3</sub>).<sup>10</sup>

Parent compound **RR-1** (*p*-CH<sub>3</sub>) has an even larger partition coefficient of 1.45±0.02 (increased hydrophobicity)<sup>2</sup> than **2-5** as the methyl group in the *para* position is strongly electron-donating by the induction effect and can form favourable hydrophobic interactions with octanol. **RR-6** (*p*-F) was significantly less hydrophobic than **1-5**, which can be attributed to the strong electronegativity of fluoride and the ability to form additional H-bonds with water.

One of the major aims with the development of organometallic complexes as anticancer agents is to optimise their solubility in physiological conditions and improve their accumulation in cancer cells – both of which are largely influenced by LogP. Cisplatin (a clinically-approved metal anticancer agent), is highly

hydrophilic with a negative partition coefficient of  $-2.21 \pm 0.06$ ,<sup>27</sup> making it compatible for formulation in aqueous media. In comparison, many Os<sup>II</sup> and Ru<sup>II</sup> complexes have significantly enhanced lipophilic properties,<sup>66, 67</sup> thus, rely on other means to improve aqueous solubility: for example, changing the nature of counter-anions of half-sandwich complexes.<sup>67</sup> Consequently, lipophilic compounds are somewhat more-dependent on passive diffusion through hydrophobic bilayers of cell membranes. In contrast, cisplatin relies on both passive diffusion and active/facilitated transport.<sup>24</sup> This family of Os<sup>II</sup> sulfonamide complexes have low water solubility ( $\text{LogP} > 1$  for **1-5**, compared to  $-2.21$  of cisplatin), thus, require initial solubilisation in DMSO (5% v/v) - a common solubilising agent for screening of many therapeutic and toxic agents.<sup>68</sup> DMSO is amphiphilic in nature and non-toxic at diluted concentrations, thus, proves suitable for *in vitro* screening.<sup>68</sup>

#### 3.4.4 Asymmetric Transfer Hydrogenation (ATH) catalysis

Acetophenone is a simple prochiral ketone which is a commonly used substrate in ATH.<sup>1</sup> Parent compound **RR-1** ( $R = p\text{-CH}_3$ ) can enantioselectively convert acetophenone to (*R*)-1-phenylethanol with *ca.* 10-fold higher turnover frequency (TOF) compared to Noyori's Ru<sup>II</sup> catalyst, while maintaining high enantioselectivity and conversions.<sup>1, 2</sup> Similarly, **2-5** all displayed high conversions (96-99%) and high enantiomeric excesses (94-98%) for the reduction of acetophenone in the presence of 5:2 formic acid/triethylamine azeotrope at 310 K over 24 h (Section 3.3.4, Table 3.2). The TOF ( $\text{h}^{-1}$ ) were calculated from the initial (linear) rate of reaction over a 3 h period using <sup>1</sup>H NMR by exploiting the differences in hydrogen-environments between the ketone substrate and the alcohol product (Fig. 3.27). Interestingly, the TOF of **SS/RR-2** and **SS/RR-3** (*ca.* 80  $\text{h}^{-1}$ ) were higher than that of **RR-1** (63.6  $\text{h}^{-1}$ ),<sup>1</sup> suggesting that the size or electronic properties of Br or I somewhat enhance the rate of reaction. Nonetheless, the ATH catalytic activity of **2-5** were of the same order of magnitude to parent compound **RR-1** ( $p\text{-CH}_3$ ) – suggesting that the *para*-position is an inert site which does not alter the catalytic ability of these osmium complexes.

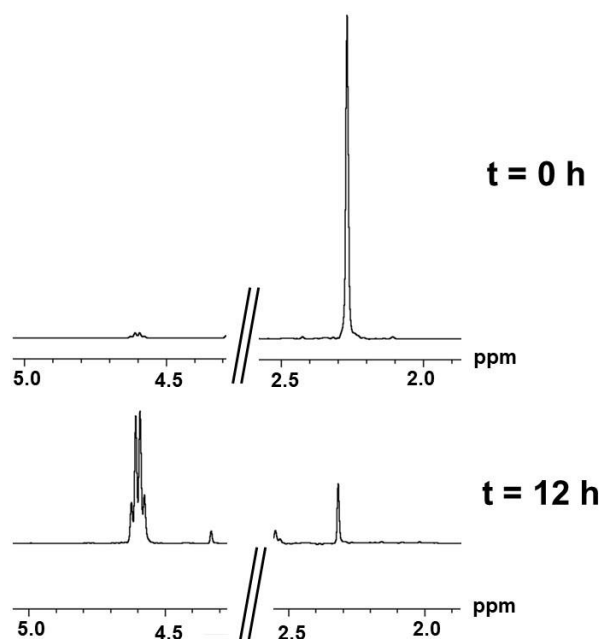


**Figure 3.28.** <sup>1</sup>H NMR spectra for the reduction of acetophenone using *SS-2* in the presence of 5:2 formic acid: TEA azeotrope over time at 310 K (400 MHz, d<sub>6</sub>-benzene): a reduction in singlet of acetophenone (3*H*, 2.3 ppm) and a formation of quartet (1*H*, 4.60 ppm) upon conversion to 1-phenylethanol.

### 3.4.5 Antiproliferative activity

#### Anticancer potency and accumulation

In order to prove that changing the substituent at the *para*-position of the sulfonamide ligand does not drastically change the *in-cell* activity, the antiproliferative activities of **2-5** were determined in four human cancer cell lines (A2780, A549, PC3 and MCF7) and in non-cancerous lung fibroblasts (MRC5). The half-maximal inhibitory concentrations (IC<sub>50</sub>/ μM) were determined using the well-established SRB colorimetric assay, which stains cells based on their protein content. Herein, cells were treated with **2-5** for 24 h, followed by 72 h recovery in complex-free media for pharmacological relevance.

The IC<sub>50</sub> concentrations of enantiomeric pairs were found to be identical across all the cell lines (*SS/RR-2*; *SS/RR-3*), suggesting that the sulfonamide chirality does not change the overall antiproliferative activity. In addition, changing the position of the Br-substituent (**2**=*para*; **5**=*meta*) did not alter the anticancer potency. Overall, **4** (R=*p*-OMe) was the most potent in A2780 cells, implying that increased electron-

donation into the benzene ring might increase the anticancer activity. The methoxy group of **4** is strongly electron-donating by resonance and increases the activity in A2780 cells. Furthermore, it was hypothesized that the ether group pushes electrons through the delocalized ring system towards the N-atom, increasing the electron density on the nitrogen, thus strengthening the Os-N bond. This may improve the complex stability in a cancer cell environment, which may contribute to the improved anticancer activity. The resonance and induction effects of donating or withdrawing substituents on organometallic complexes may significantly influence the *in vitro* activity, which may prove necessary in future drug design.

Complexes **2** (*p*-Br), **3** (*p*-I) and **5** (*m*-Br) were less potent than **1** (*p*-CH<sub>3</sub>) and **RR-6** (*p*-F) – which may be a consequence of reduced cellular accumulation. The improved antiproliferative potency of **RR-6** (*p*-F) compared to **2** (*p*-Br) and **3** (*p*-I) may also be attributed to increased electronegativity and polarisation of fluorine and its ability to form additional H-bonds with water, ultimately lowering the LogP of the complex. The F-atom of **RR-6** may also increase the complex stability in biological media by forming favourable H-bonds with molecules of itself, as previously hypothesised by Coverdale.<sup>2</sup> Complexes **2-5** were not as potent as cisplatin against the analysed cell lines, however, current data implicates an ROS-mediated mechanism of action which has the potential to circumvent Pt-resistance and reduce off-target effects.<sup>14</sup>

The toxicities of **SS/RR-2** in MRC5 (healthy lung) cells demonstrated similar activities in cancer vs. healthy cells (A549 vs. MRC5), which is a major clinical drawback and would likely cause side effects. This was also observed for **RR-1** (*p*-CH<sub>3</sub>).<sup>2, 10</sup> However, this family of osmium complexes have previously been shown to perform intracellular catalysis (when co-administered with sodium formate), which is selective for cancer cells,<sup>10</sup> providing a platform for catalytic therapy.

In order to validate Br-labelled **2** as a molecular probe for elucidating the *in vitro* mechanism(s) of action of parent compound **RR-1** (*p*-CH<sub>3</sub>), <sup>189</sup>Os ICP-MS cellular accumulation studies were performed. A2780 cells treated with equipotent concentrations (1×IC<sub>50</sub>) of **SS/RR-2** for 24 h (no recovery) revealed identical intracellular levels of Os to that found in cells treated with **SS/RR-1**.<sup>2, 10</sup> This suggests that the Br substituent is somewhat hindering the cellular uptake,

correlating with the reduced potency of **2** compared to **1** (2× less potent). The Br-substituent likely does not alter the mechanism of Os accumulation, but merely reduces the amount of intracellular complex available for antiproliferative activity.

Interestingly, the osmium cellular accumulation of **SS/RR-3** (*p*-I) were significantly higher than **SS/RR-2** (*p*-Br) despite their similar potencies (IC<sub>50</sub>~30 μM). This implies that more of the iodide-substituted complex (**3**) has to enter cancer cells to have the same antiproliferative effect. This may prove somewhat more desirable for catalytic therapy (with administered formate) as more of **SS/RR-3** (*p*-I) may be available for in-cell ATH catalysis at lower drug doses.

The cellular accumulation of drugs depend on a variety of factors, including lipophilicity, the type of substituent and the molecular size. A comparison of LogP and the Os cellular accumulation may suggest that the enhanced hydrophobicity of **RR-1** (1.45±0.02) may promote passage through phospholipid membrane bilayers more readily than **SS/RR-2** (1.01±0.01), hence, more accumulates intracellularly. A comparison of LogP and Os cellular accumulation in A2780 cells treated with equipotent (1×IC<sub>50</sub>) for 24 h for **2** (*p*-Br) and **3** (*p*-I) after 24 h drug revealed that a higher LogP is reflected in a greater Os accumulation in cancer cells (**Fig. 3.27**). These are compared to that of **RR-6** (*p*-F), **RR-7** (*p*-NO<sub>2</sub>), and **RR-8** (*p*-H), all of which are less hydrophobic and exhibit lower intracellular quantities of osmium.<sup>2</sup>

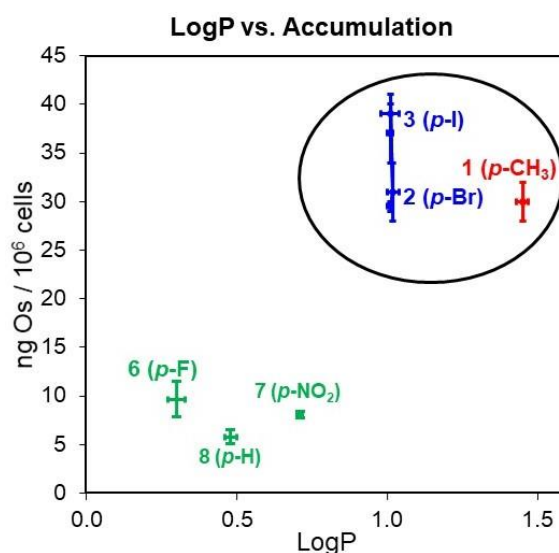


**Figure 3.29.** Comparison between the the partition coefficient (LogP) and the osmium cellular accumulation (ng Os/10<sup>6</sup> cells) in A2780 (ovarian) cancer cells. (i) Parent compound **RR-1** (■).<sup>2</sup> (ii) Complexes **SS/RR-2** and **SS/RR-3** synthesised in this Chapter (■). (iii) Complexes **RR-6**, **7** and **8** previously reported (■).<sup>2</sup>



The concentration-dependence on the Os cellular accumulation was investigated for A2780 cells treated with 0.25-1.50×IC<sub>50</sub> **SS/RR-2** for 24 h (no recovery) to determine whether the system reaches saturation. The intracellular quantities of Os increased linearly with concentration (**Section 3.3.9, Table 3.7**), in agreement with that previously reported for **RR-1**.<sup>2</sup> Concentration-dependent uptake has been reported for various other metallodrugs including Ru<sup>II</sup>-half-sandwich complexes,<sup>17</sup> Ru<sup>III</sup> octahedral complexes,<sup>69</sup> Os<sup>II</sup> octahedral complexes<sup>70</sup> and clinical drug cisplatin,<sup>71</sup> highlighting the importance of dose-dependent uptake in mediating drug efficacy. Upon treatment with 1×IC<sub>50</sub> of **1** (*p*-CH<sub>3</sub>) or **2** (*p*-Br) the same amount of intracellular Os was observed. This means that upon equimolar treatment (equal concentrations) with **1** or **2**, more of **1** will accumulate intracellularly: Br is somewhat hindering the cellular accumulation.

Varying the incubation temperatures can provide information on the dependence of active cellular influx/efflux pathways of drugs. Active mechanisms are energy-dependent and rely on electrochemical gradients to cross cell membranes and enter cells. The temperature-dependent Os accumulation in A2780 cells showed a significant decrease after both 3 and 6 h when treated with **SS/RR-2** at 277 K compared to 310 K (**Section 3.3.9, Table 3.8**), suggesting energy-dependent processes (*e.g.* endocytosis or membrane pumps) are involved in the cell uptake of these complexes. The same trend was reported for parent compound **RR-1** (*p*-CH<sub>3</sub>), but with a more drastic reduction in Os accumulation after 6 h (*ca.* 90% for **RR-1**,<sup>2,10</sup> compared to *ca.* 45% of **SS/RR-2**). Nonetheless, **SS/RR-2** and **RR-1** displayed the same temperature-dependent trend, hence, the Br substituent has likely not altered the mechanism of uptake of **RR-1**.

The extent of efflux was investigated by monitoring the Os accumulation from **SS-2** (*p*-Br) over time, and after cells had recovered in complex-free media (**Section 3.3.9, Fig. 3.11**). The time-dependent accumulation of Os in A2780 cells treated with **SS-2** and **RR-2** indicated very similar efflux to **RR-1** (*p*-CH<sub>3</sub>).<sup>2</sup> The maximum amount of intracellular Os was observed after *ca.* 6 h of drug exposure, after which the Os was gradually removed from the cells (**Section 3.3.9, Fig. 3.10; Appendix, Table A12**). The amount of Os inside the cancer cells decreased by *ca.* 25% of its maximum (6 h) after 24 h. After recovery in complex-free media, the Os was removed from the cells at a rate of *ca.* 0.3 ng/10<sup>6</sup> cells.h<sup>-1</sup> in a linear fashion,

correlating closely with the efflux of **RR-1** (*ca.* 0.34 ng/10<sup>6</sup> cells.h<sup>-1</sup>).<sup>2, 10</sup> One of the major contributors to multidrug resistance is enhanced drug efflux,<sup>25</sup> which reduces drug efficacy and thus, the anticancer effect. This has been reported for clinical anticancer drugs including cisplatin and oxaliplatin.<sup>72</sup> Novel anticancer complexes with different influx and efflux pathways may be able to circumvent multidrug resistance. The Os of **RR-1** and **SS/RR-2** was slowly removed from cells over a 72 h recovery period at the same rate when treated with equipotent concentrations,<sup>2, 10</sup> suggesting the Br substituent does not alter the cellular efflux kinetics. The slow rate of cellular efflux of these complexes may prove appropriate for catalytic therapy, extending the intracellular catalysts lifetime which may enhance catalytic turnover to contribute towards cell death.

### In-cell catalytic activity

It has previously been demonstrated that **RR-1** (R=*p*-CH<sub>3</sub>) can act catalytically inside cancer cells, converting pyruvate to unnatural D-lactate in the presence of non-toxic doses of formate (hydride donor).<sup>10</sup> This work provided an opportunity to increase selectivity for cancer over healthy cells through a catalytic mode of action,<sup>10</sup> by exploiting the redox vulnerability of cancer cells. Formate is a well-established hydride source compatible with cells, and has been used to probe the *in-cell* catalytic properties of hald-sandwich metal complexes, including ruthenium.<sup>11</sup>

In 2018, Coverdale *et al.* proposed a catalytic cycle in which the pyruvate itself can directly interact with the *p*-cymene arene group of **RR-1** *via* a transition state (**Chapter 1, Section 1.2.3, Fig. 1.11**).<sup>10</sup> In this mechanism, formate binds directly to Os and releases CO<sub>2</sub> to form an active Os-H bond, which then facilitates the preferential binding of pyruvate at the Re-face, subsequently releasing D-lactate.<sup>10</sup> The electrostatic interaction between pyruvate and *p*-cymene is thought to be essential for mediating the enantioselectivity of the reaction, however, no evidence has been provided for this proposed transition state.<sup>2</sup> In 2019, Yang *et al.* proposed a proton-coupled hydride transfer catalytic mechanism for the ATH conversion of pyruvate to lactate in the presence of formic acid, using DFT.<sup>73</sup> In this scenario, formate binds directly to pyruvate on the *Re*-face *via* a cationic Os species which facilitates the release of D-lactic acid.<sup>73</sup> The exact nature of the transition states (and

the catalytic cycle) is unknown, however, both proposed mechanisms are in agreement that the electrostatic interaction between *p*-cymene and pyruvate has a crucial influence on the enantioselectivity of the catalytic reaction.<sup>10, 73</sup>

In order to validate Br-labelled **SS-2** or **RR-2** as suitable probes for investigating the in-cell stability of parent compound **RR-1** (*p*-CH<sub>3</sub>) by ICP-MS and XRF, the possible in-cell catalytic anticancer activity was investigated in A549 cells upon treatment with 0.5–1.0×IC<sub>50</sub> of **SS-2** or **RR-2** and sodium formate (0–2 mM) for 24 h, with a 72 h recovery period. Sodium formate was found to be non-toxic towards cancer cells (*p*>0.05). A significant decrease in the normalized cell proliferation (from 100% to 25%) was observed upon co-administration with increasing concentrations of formate (**Section 3.3.6, Fig. 3.6**), suggesting a catalytic contribution to the antiproliferative activity, similar to that reported for **RR-1**.<sup>2, 10</sup> Further affirmation of the role of a hydride source in promoting an increase in potency of **2** (*p*-Br) was obtained using sodium acetate which (unlike formate) cannot act as a hydride source for ATH.<sup>10</sup> As such, no decrease in cell viability was observed upon acetate co-administration (**Section 3.3.6, Fig. 3.7**). In order to confirm that the observed decrease in activity with formate was a consequence of in-cell catalysis and *not* due to increased Os accumulation, cancer cells were treated with 1×IC<sub>50</sub> of Br-labelled **SS-2** and co-administered with sodium formate (0–2 mM) for 24 h. No change in Os accumulation was observed (**Section 3.3.9, Fig. 3.11**), in strong agreement with that reported for **RR-1**.<sup>2, 10</sup>

The catalytic selectivity for cancer vs. healthy cells was investigated using MRC5 cells treated with 0.5–1×IC<sub>50</sub> of **SS** or **RR-2** in the presence of sodium formate or acetate (0–2 mM), revealing no significant differences in cell viability (*p*>0.05; **Section 3.3.6; Fig. 3.8**), as reported for **RR-1**.<sup>2, 10</sup> This suggests that intracellular catalysis is selective for cancer cells and that the biological properties of **2** (*p*-Br) are complementary to that of **1** (*p*-CH<sub>3</sub>). This is likely attributed to higher levels of intracellular pyruvate (Warburg Effect),<sup>74</sup> where cancer cells preferentially rely on aerobic glycolysis to survive under extreme metabolic conditions. Complementary to this, formate-producing enzymes (*e.g.* peptide deformylase) are over-expressed in A549 cancer cells<sup>75</sup> – which may further promote the catalytic activity in cancer cells vs. healthy cells. This has previously been probed for **RR-1** by the inhibition of peptide deformylase with N-formylmethionine in PC3 prostate cancer cells.<sup>2</sup>

### Membrane integrity and cell cycle analysis

Flow cytometry can be used to monitor drug-induced changes in a treated population of cells. The membrane integrity of A549 cells treated with **SS-2** or **RR-2** (*p*-Br) in the presence of sodium formate (0-2 mM) was analysed by flow cytometry, to probe whether the cell membrane is compromised upon treatment. In this assay, a staining solution of red-fluorescent PI (a DNA intercalater with  $\lambda_{\text{ex/em}}$  of 493/636 nm) was used on non-chemically fixed cells.<sup>76</sup> PI is not permeable to cell membranes, thus, only damaged or compromised cell membranes will allow PI to enter the cell and intercalate with DNA, with an approximate 20-fold increase in fluorescence compared to unbound PI.<sup>33</sup> This change in fluorescence can be monitored using flow cytometry (FL2 channel,  $\lambda=488$  nm laser), a laser-based technique which can assess different biological parameters (*i.e.* cell viability) of a population of cells on the basis of the excitation of fluorochromes.<sup>77</sup> The data was 'gated' into two population categories (viable and non-viable membranes), using FlowJo V10 software.

It has been previously reported that A2780 cells treated with parent compound **RR-1** ( $1 \times \text{IC}_{50}$ ) in the presence of sodium formate (0-2 mM) showed no significant variation or disruption of membrane integrity after 24 h exposure when compared with the untreated controls.<sup>2, 10</sup> The same was observed for cells treated with Br-labelled **SS/RR-2** ( $p > 0.05$ , **Section 3.3.7, Fig. 3.9; Appendix, Table A11**), suggesting that the antiproliferative mechanism of action is not a result of membrane damage. No differences in the membrane integrity were observed between cells treated with **SS/RR-2** in the presence or absence of formate, implying that the increased antiproliferative activity is not due to formate-induced membrane damage. This correlates with the formate-dependent osmium accumulation which revealed that co-administration with sodium formate (2 mM) did not enhance intracellular levels of osmium (**Section 3.3.9, Fig. 3.11**).

Cell cycle analysis was performed on A549 cells treated with **SS-2** (*p*-Br), again in the presence of sodium formate (0-2 mM). In this case, cells were fixed with ice-cold ethanol to permit membrane-permeation of PI. The PI fluorescence was monitored using the FL2 channel (red-fluorescence) by flow cytometry and the cell cycle populations (sub-G<sub>1</sub>, G<sub>1</sub>, G<sub>2</sub>/M and S-phases) were fitted to experimental data using FlowJo V10 software.

Cells treated with **SS-2** in the absence of formate revealed slight G<sub>1</sub>-arrest compared to the untreated control cells (*ca.* 7% increase in the G<sub>1</sub> population, **Section 3.3.7, Table 3.4**). Importantly, co-administration of **SS-2** (*p*-Br) with formate revealed a similar extent of G<sub>1</sub>-arrest (*ca.* 11% increase in the G<sub>1</sub> population) which suggests the formate does not alter the mechanism of action, but merely enhances the observed antiproliferative effect. The same trend was observed for **RR-1** under the same conditions (0-2 mM sodium formate) but in A2780 cells.<sup>2, 10</sup> Furthermore, it was deduced that the antiproliferative mechanism of action in A549 cells is likely enhanced by formate co-administration, but not altered – correlating with the observed increase in antiproliferative activity in the presence of formate (**Section 3.3.6, Fig. 3.6**).

Interestingly, this differs from the clinically-approved anticancer drugs cisplatin, which causes G<sub>2</sub>/M phase cell cycle arrest,<sup>78</sup> disrupting the growth and mitotic (cell division) stage through the formation of DNA crosslinking in the cell nucleus. When DNA is damaged, the G<sub>2</sub>-phase checkpoint prevents cells from entering mitosis (M-phase), further preventing the proliferation of cells. In contrast, the G<sub>1</sub>-phase promotes cell growth in preparation for DNA synthesis (S-phase), thus, drug-induced G<sub>1</sub>-arrest implies that DNA is likely not the primary target. Both parent compound **RR-1** and Br-labelled **SS-2** did not demonstrate G<sub>2</sub>/M arrest, which is suggestive of a non-DNA targeting anticancer mechanism of action. This is in strong agreement with reported work demonstrating that **RR-1** is non-apoptotic in nature,<sup>2, 10</sup> and exhibits an antiproliferative effect through the intracellular targeting of pyruvate in response to metabolic stress.

### 3.4.6 Zebrafish toxicity

Zebrafish have been used as well-established models to predict drug toxicity in humans;<sup>79</sup> 75% of the human genes have at least one zebrafish orthologue and share a variety of phenotypes with humans.<sup>80</sup> Zebrafish embryos can be used as high-throughput vertebrate models: they are cheap, easy to handle and can readily be used to investigate solubilized compounds.<sup>14</sup> It has recently been reported that a fluorescently-labelled Os<sup>II</sup> arene sulfonamide complex can selectively generate ROS in zebrafish.<sup>2, 14</sup> Herein, the half-maximal lethal concentrations (LC<sub>50</sub>) of complexes **SS/RR-2** (*p*-Br) in SG-WT zebrafish embryos were determined in order to gain an insight into the *in vivo* biocompatibility and selectivity of this family of osmium complexes (Section 3.3.8, Table 3.5). The LC<sub>50</sub> concentrations (μM) of Br-labelled enantiomers **SS/RR-2** were determined to be the same (3.7±0.3 and 4.1±0.1 μM, respectively), suggesting that the chirality does not alter the *in vivo* toxicity. Interestingly, comparison with parent compound **RR-1** (LC<sub>50</sub>=2.4±0.4 μM) revealed that **SS/RR-2** were 1.5× less toxic towards zebrafish.<sup>14</sup> Nonetheless, the LC<sub>50</sub> concentrations of **RR-1** (*p*-CH<sub>3</sub>) and **SS/RR-2** (*p*-Br) were of the same order of magnitude (*ca.* 3 μM), suggesting that substitution on the sulfonamide moiety does not drastically alter the *in vivo* toxicity.

Drug toxicity is a major concern for clinical platinum drugs - a consequence of limited selectivity (for cancer *vs.* healthy cells), resulting in unwanted patient side effects. The undesired targeting of healthy tissue ultimately reduces drug efficacy, limiting the effectiveness of the treatment. Importantly, the toxicity exhibited by **SS/RR-2** (*p*-Br) was less pronounced in zebrafish embryos compared to cisplatin (LC<sub>50</sub>=0.6±0.2 μM),<sup>14</sup> which is likely associated with the localised generation of ROS by these osmium complexes.<sup>14</sup> Redox-mediated mechanisms of action have been implicated for various half-sandwich Os<sup>II</sup> and Ru<sup>II</sup> complexes,<sup>61, 81, 82</sup> providing novel antiproliferative mechanisms of action compared to conventional Pt<sup>II</sup> drugs. Importantly, due to the extreme redox stress exhibited by cancer cells, this may provide the opportunity to increase drug selectivity to enhance efficacy and lessen toxic side effects. Overall, the toxicities of **2** (*p*-Br) in zebrafish embryos closely resembled that of parent compound **1** (*p*-CH<sub>3</sub>) - both of which were significantly less toxic compared to cisplatin.<sup>2, 14</sup>

### 3.4.7 Combined <sup>189</sup>Os and <sup>79</sup>Br cellular accumulation

#### <sup>189</sup>Os and <sup>79</sup>Br ICP-MS methods optimisation

All of the Os cellular accumulation data discussed thus far in this Chapter have been analysed in stabilised 3.6% v/v stabilised nitric acid (supplemented with 100 mg/L L-ascorbic acid and 10 mM thiourea), to prevent the formation of volatile OsO<sub>4</sub> and stabilize Os in acidic conditions.<sup>83</sup> The objective for synthesizing a Br-labelled catalyst was to quantify both Os and Br concentrations inside cancer cells, to gain information on the localization, speciation and stability of this family of complexes. ICP-MS quantification of Br is even more difficult than Os. Bromine exists as two stable isotopes: <sup>79</sup>Br and <sup>81</sup>Br with natural abundances of 50.54% and 49.46%, respectively.<sup>84</sup> Quantification of Br by ICP-MS is challenging as a consequence of the high first ionisation potential (11.8 eV),<sup>85</sup> and common polyatomic interferences with  $m/z=79$  or  $81$ , including <sup>40</sup>Ar<sup>39</sup>K<sup>+</sup> or <sup>31</sup>P<sup>16</sup>O<sub>3</sub><sup>+</sup> ( $m/z=79$ ) and <sup>32</sup>S<sup>16</sup>O<sub>3</sub><sup>1</sup>H<sup>+</sup> or <sup>40</sup>Ar<sup>40</sup>Ar<sup>1</sup>H<sup>+</sup> ( $m/z=81$ ).<sup>86</sup>

Initially, a calibration of Os and Br in stabilized nitric acid was analysed, which proved unsuccessful for Br detection. This was not surprising as nitric acid is a strong oxidizing agent, which can oxidize bromide to form molecular bromine (Br<sub>2</sub>),<sup>87</sup> which is readily volatile and is released as a gas. To overcome this, tetramethylammonium hydroxide (TMAH) – a strong base - was used as a chemical modifier to form thermally-stable tetramethylammonium (TMA) bromide salt,<sup>88</sup> which is retained until vaporization. A calibration of Os and Br in 1% m/v TMAH formed a linear calibration in the range 0.1-1000 ppb ( $R^2=0.9999$ ), and standard recovery experiments of known analyte concentration (complexes **1** and **2**) were performed, achieving percentage recoveries of >95% for both <sup>189</sup>Os and <sup>79</sup>Br. Subsequently, a cell pellet digestion method in TMAH was optimized based on methods reported in the literature.<sup>89, 90</sup>

Prior to commencement of cellular accumulation studies, triplicate solutions of Br-labelled **SS-2** (of known concentrations) were prepared in 1% m/v TMAH and analysed by ICP-MS. Percentage recoveries >95% were achieved for <sup>189</sup>Os and <sup>79</sup>Br, and an osmium-to-bromine ratio (<sup>189</sup>Os:<sup>79</sup>Br) of 1:1 for **SS-2** was confirmed. The amount of intracellular Os determined in A549 cells treated with **1** (*p*-Br) for 24 h and analysed in nitric acid (16±5 ng Os/10<sup>6</sup> cells, respectively) was

significantly lower than that in TMAH ( $46 \pm 3$  ng Os/ $10^6$  cells;  $p=0.0030$ ). This may imply strongly alkaline conditions may be more efficient at stabilising Os than nitric acid supplemented with thiourea and ascorbic acid – potentially due to a reduction of memory effects. It must also be noted that the protocol for acid digestion involves non-stabilised 72% HNO<sub>3</sub> for at least 12 h (prior to thiourea and ascorbic acid addition), which likely contributes to the lower levels of Os observed.

The use of alkaline solutions (as opposed to strong acid oxidizers) for the analysis of Os by ICP-MS has previously been proposed for the determination of osmium in natural waters.<sup>91</sup> In addition, TMAH digestion of biological samples can promote complete solubilisation (protein and lipid matrices) which remain stable at room temperature (days to months), subsequently, reducing loss of volatile analytes.<sup>92</sup> Furthermore, this data warrants whether ICP-MS cell digest quantification of Os should alternatively be analysed for samples in TMAH. The use of TMAH to detect <sup>79</sup>Br by ICP-MS is well-established in the food industry,<sup>93, 94</sup> with emerging applications in pharmaceutical research.<sup>95</sup> Herein, the simultaneously quantification of <sup>189</sup>Os and <sup>79</sup>Br in TMAH has been optimized to probe the *in-cell* stability and distribution of Br-labelled **SS-2** inside A549 lung cancer cells.

#### <sup>189</sup>Os-<sup>79</sup>Br cellular accumulation

The temperature-dependence on the cellular accumulation of Os in cells treated with **SS-2** (*p*-Br) has previously been demonstrated in this Chapter (**Section 3.3.9**) and in the literature for **RR-1** (*p*-CH<sub>3</sub>).<sup>2</sup> Lower temperatures were shown to significantly reduce the Os accumulation in A2780 ovarian cancers treated with **RR-1** (*p*-CH<sub>3</sub>) or **SS-2** (*p*-Br) – indicating an active contribution to the uptake of these complexes. The same experiment was conducted in A549 cells treated with **SS-2** for 3-6 h, at 310 and 277 K, but analysed in TMAH (to simultaneously quantify Os and Br), revealing a *ca.* 48% reduction in intracellular Os at 277 K compared to 310 K (**Section 3.3.10, Fig. 3.12**). Again, this suggests a dependence on cellular energy (electrochemical gradients) in the cell uptake of **SS-2**. Similarly, a more pronounced reduction in intracellular Br was observed (*ca.* 75% decrease), which may suggest temperature-dependent changes in the rate of efflux of the Br and Os modalities.



Interestingly, a comparison of the intracellular Br/Os ratio revealed *ca.* 12× more Br under physiological conditions (310 K), suggesting that after just 6 h exposure, the chelated Br-ligand dissociates from **SS-2** inside cells. Of course, the potential cleavage of the C-Br aromatic bond must be considered, however, in general aryl halides are highly stable and unreactive towards nucleophilic substitution (S<sub>N</sub>1 or S<sub>N</sub>2) owing to steric hinderance, short C-X bonds (sp<sup>2</sup> hybridization) and resonance delocalisation (partial double bond nature),<sup>96</sup> thus, C-Br bond cleavage likely does not occur in a biological environment. This concept has previously been demonstrated with Ar-Br and Ar-I bonds in rhenium,<sup>97</sup> platinum<sup>53</sup> and ruthenium<sup>32</sup> complexes in cancer cells using XRF. As the Br-substituent is in an apparent inert (unreactive) site of the benzene ring,<sup>14</sup> it was deduced that the <sup>79</sup>Br detected corresponds to either “free” BsDPEN ligand or intact **SS-2**, and not bromide (Br<sup>-</sup>). Furthermore, significantly higher levels of Br inside the cells may suggest the free BsDPEN ligand has dissociated from the Os centre and remains intracellularly for a longer time period.

Cells treated with **SS-2** at lower temperatures (277 K) showed *ca.* 5× more Br vs. Os, implying that at lower temperatures more of the complex may be intact, but at much lower overall quantities. This implies that the uptake of intact **SS-2** is likely dependent on active uptake pathways. Cellular accumulation studies do not give a direct indication of cellular uptake, but instead a combination of both influx *and* efflux, thus, active efflux mechanisms may also be involved. Incubating cells at lower temperatures reduces the rate of cell growth, and may also affect the optimal activity of organelles or biomolecules responsible for the detoxification and excretion of drugs. For example, temperature changes can alter features including membrane nuclei acid topology and protein function.<sup>98</sup> This may explain the increased intracellular stability of **SS-2** (smaller Br/Os ratio) at 277 K compared to 310 K. Overall, this data reaffirms that the cellular accumulation of Br-labelled **SS-2** and parent compound **RR-1** (*p*-CH<sub>3</sub>) are somewhat reliant on active cellular accumulation mechanisms.<sup>2, 10</sup>

The dependence on active cellular uptake pathways has been reported for a variety of organometallic complexes including half-sandwich Os<sup>II</sup>,<sup>99</sup> Ru<sup>II</sup> and Ir<sup>III</sup> complexes,<sup>17, 100</sup> which may be essential in overcoming the reduced cellular uptake of Pt<sup>II</sup> chemotherapeutics. This data also provides evidence into the poor

intracellular stability of this family of Os<sup>II</sup> sulfonamide complexes, which may explain the low catalytic turnover of pyruvate to lactate of **RR-1** (*p*-CH<sub>3</sub>) in cancer cells co-administered with sodium formate over 24 h.<sup>2</sup>

To further explore the dependence of active mechanisms of uptake of **SS-2** (*p*-Br) in cancer cells, accumulation studies were conducted using a known endocytotic inhibitor: methyl- $\beta$ -cyclodextrin.<sup>101</sup> Endocytosis is a process for which molecules are taken into cells *via*. membrane invaginations, which then bud off into vesicles inside cells. Endocytotic pathways are modified in cancer cells,<sup>102</sup> which play crucial roles in the development of multi-drug resistance, thus, are of much interest in the development of chemotherapeutics. In particular, caveolae (lipid raft membrane invaginations) have an important role in endocytosis and is a highly-regulated mechanism of uptake.<sup>101</sup> Methyl- $\beta$ -cyclodextrin is a known caveolae endocytotic inhibitor which prevents the uptake of small molecules *via* fusion with vesicles.<sup>101</sup> Herein, A549 cells were treated with **SS-2** for 24 h and co-administered with non-toxic concentrations of methyl- $\beta$ -cyclodextrin (0-1 mM).

The Os accumulation decreased by around 60% with increasing inhibitor concentration (**Section 3.3.10, Fig. 3.13**), suggesting that the uptake of **SS-2** (*p*-Br) is caveolae-dependent. As **RR-1** (*p*-CH<sub>3</sub>) and **SS-2** (*p*-Br) are mildly hydrophobic (LogP=1.01 and 1.45, respectively), the dependence of these complexes on caveolae for cellular uptake is not surprising. In contrast however, the intracellular Br initially decreased by *ca.* 30% upon co-administration with the lowest concentration of inhibitor (0.1 mM), before plateauing at *ca.* 400 ng Br/10<sup>6</sup> cells (**Section 3.3.10, Fig. 3.13**). This may suggest that caveolae endocytosis mediates the uptake of the intact 16-electron complex **SS-2**, but upon entering the cell, the complex is degraded thus, demonstrating higher levels of Br-labelled BsDPEN (*ca.* 30 $\times$  more Br *vs.* Os) which are retained intracellularly. It can be hypothesized that Br-labelled **SS-2** enters cells intact (where it can perform enantioselective *in-cell* catalysis), but is degraded intracellularly over time. Moreover, the free Br-labelled BsDPEN ligand may be less susceptible to efflux from the cell compared to the remaining Os fragment, thus, is retained intracellularly for longer.

In cancer cells there are various reducing agents including GSH, L-ascorbic acid, and low molecular weight antioxidants (*e.g.* metalloproteins) which have been associated with drug detoxification.<sup>103</sup> In particular, GSH has been implicated in the detoxification of **RR-1** in cancer cells (shown using L-BSO assays),<sup>2</sup> hence, the intracellular breakdown of **SS-2** is not surprising. In addition, the dependence on active “energy-dependent” cell accumulation pathways may implicate active breakdown mechanisms, for example by lysosomes/endosomes or efflux pumps (including PGP) which are modified in cancers and are implicated in resistance.<sup>40</sup>

The speciation of the dissociated sulfonamide ligand is not known, and requires further investigation using advanced techniques (*e.g.* XANES or EXAFS analysis). Overall, the hydrophobicity of **RR-1** (*p*-CH<sub>3</sub>) and **SS-2** (*p*-Br) likely facilitates cellular uptake *via* caveolae endocytosis (active transport). Caveolae-specific drug uptake can have benefits in the development of targeted drug delivery (*e.g.* through specific interactions with membrane receptors),<sup>104</sup> however, caveolin-1 has also shown to promote chemotherapeutic resistance.<sup>105</sup> This may have detrimental consequences in the future development of these Os<sup>II</sup> catalysts for sustainable use.

Alternatively – although the BsDPEN ligand itself does not exhibit antiproliferative activity against cancer cells (IC<sub>50</sub>>100 μM) – this cannot rule out extracellular complex degradation and internalisation of the “free” ligand. Complex **SS-2** exhibits sufficient stability in DMSO and PBS (shown by NMR and UV-Vis), and exhibits a 1:1 ratio of Os:Br (ICP-MS) in aqueous solution, however, cell culture medium is highly supplemented with components including inorganic salts, amino acids and vitamins. This may alter the chemical speciation or stability of metallodrugs, which ultimately dictates the *in vitro* activity.<sup>106</sup> For example, cisplatin can bind to serum proteins transferrin and albumin which can influence the Pt accumulation in cancer cells.<sup>107</sup> Moreover, <sup>79</sup>Br cellular accumulation studies of the Br-labelled BsDPEN ligand are required to confirm extracellular complex degradation (in culture medium), which may prove necessary for *in vivo* translation.

Cellular influx and efflux mechanisms play a major role in multidrug resistance.<sup>25</sup> In order to investigate the potential active efflux of **SS-2** from cancer cells, cellular accumulation studies in the presence of a known inhibitor of PGP were performed. Cells were treated with 1×IC<sub>50</sub> of **SS-2** for 24 h, washed with PBS and recovered in

20  $\mu$ M verapamil hydrochloride for 24, 48 and 72 h recovery. PGP is an efflux membrane transporter which is over-expressed in cancer cells,<sup>40</sup> and is responsible for the enhanced efflux of chemotherapeutics leading to multidrug resistance.<sup>40</sup> Verapamil is an inhibitor of PGP which blocks “active” efflux *via* competitive inhibition,<sup>17</sup> thus, can be used to gain an understanding on drug efflux.

It has previously been shown for **RR-1** (*p*-CH<sub>3</sub>) that verapamil significantly reduced Os efflux after 24 or 48 h recovery, however no significant change in intracellular Os was observed after 72 h.<sup>2, 14</sup> Verapamil had the same effect on Br-labelled **SS-2** but only after 48 h (**Section 3.3.10, Fig. 3.14**) suggesting that Br-substitution does not change the PGP-dependent efflux compared to **RR-1**.<sup>2</sup> Multidrug efflux pumps - like PGP - can recognize and excrete a wide variety of structurally diverse substrates,<sup>108</sup> presenting a major challenge in the development of cancer chemotherapeutics. Interestingly, cisplatin is not a substrate for PGP, but over-treatment with cisplatin can lead to MDR (*e.g.* it may cause PGP expression).<sup>109</sup> PGP-dependent efflux plays a considerable role in enhancing the efflux of clinical anticancer drugs,<sup>110</sup> and for organometallic ruthenium,<sup>17, 111</sup> osmium<sup>14</sup> and iridium complexes.<sup>112, 113</sup> Furthermore, the need for new anticancer drugs which can circumvent PGP-dependent efflux and other such efflux pathways may be crucial for overcoming resistance in cancer cells. For example, Dyson *et. al.* synthesised a half-sandwich Ru<sup>II</sup> complex tethered to a PGP-inhibitor (phenoxazine) which improved drug cytotoxicity and reduced PGP-dependent efflux.<sup>114</sup> This work would further benefit from investigating other means of cellular efflux, for example the inhibition of expression of epidermal growth factor receptor (EGFR) expression which reduced the efflux of Os and Ru complexes.<sup>115</sup>

Interestingly, intracellular quantities of Br were unaffected by verapamil – revealing no changes in Br accumulation compared to recovery in complex-free media (**Section 3.3.10, Fig. 3.14**). This observation (in addition to significantly higher quantities of Br *vs.* Os) provides evidence for complex degradation *via* BsDPEN ligand dissociation. Importantly, the differences observed between Os and Br upon verapamil recovery suggest that the excretion of the Os moiety (assumed to be the intact complex) is PGP-dependent, but the ‘free’ Br-BsDPEN ligand is not. Moreover, it may be possible that the BsDPEN sulfonamide ligand is less susceptible to cellular excretion compared to the Os metal modality.

Alternatively, the ligand may not be a compatible PGP substrate (which can further be predicted through molecular docking studies),<sup>116</sup> or may be strongly bonded to other cellular modalities (*i.e.* by metal chelation). Sulfonamides themselves constitute an important class of drugs,<sup>117</sup> many of which have shown to exhibit antitumour activity both *in vitro* and *in vivo*. As Br-labelled BsDPEN *alone* is non-toxic towards cancer cells (**Section 3.3.5, Table 3.3**), complexation with Os may facilitate passage into cells, where it can be released intracellularly. The delivery of bioactive ligands *via* transition metal complexes is emerging as a feasible approach in the design of chemotherapeutics. Notably, Hambley *et al.* used fluorescence lifetime imaging and XAS to demonstrate the release of bioactive curcumin into cancer cells *via* a cobalt chaperone, which significantly enhanced drug stability and efficacy compared to the free drug.<sup>118</sup> The formate-dependent antiproliferative activity of **RR-1** (*p*-CH<sub>3</sub>) and **SS-2** (*p*-Br) depend on the BsDPEN ligand remaining coordinated to Os, however, catalysis is likely not the only mechanism of action. It is not yet known whether the “free” organic sulfonamide moiety is contributing to the antiproliferative effect.

The time-dependent intracellular stability of complex **SS-2** (*p*-Br) was investigated in A549 cells treated with 1×IC<sub>50</sub> for 3, 6 and 24 h (no recovery) and 24 h with 24, 48 and 72 h recovery, respectively (**Section 3.3.10, Fig. 3.15; Appendix, Table A12**). The time-dependent influx/efflux of Os of **SS-2** closely correlates with that of parent compound **RR-1** (reaching a maximum at *ca.* 6-8 h),<sup>2, 10</sup> reaffirming that Br-labelling of the sulfonamide ligand does not dramatically alter the Os efflux (**Section 3.3.9, Fig. 3.10**). Importantly, upon removal of the extracellular drug solution, the Os was slowly removed from the cell over 72 h – presenting a longer *in-cell* lifetime of **SS-2** suitable for catalytic therapy (maximizing the catalytic efficiency). Similar accumulation properties of conventional half-sandwich Os<sup>II</sup>-azopyridine complexes have also been reported,<sup>23, 119</sup> suggesting that slow detoxification is non-specific for these 16-electron Os<sup>II</sup> complexes. Similarly, even slower influx/efflux profiles were observed for structurally-similar Ru<sup>II</sup> half-sandwich complexes – reaching maximal intracellular Ru quantities between 24-48 h exposure, before gradual detoxification and excretion.<sup>17</sup> Moreover, despite the poor antiproliferative potency of **RR-1** (IC<sub>50</sub>=21.1 μM),<sup>2, 10</sup> slow complex influx/efflux proves more appropriate for intracellular catalytic activation.<sup>2, 10</sup>

Significantly higher levels of intracellular Br were observed for all the time points monitored (**Section 3.3.10, Fig. 3.15**), reaffirming complex degradation and dissociation of the Br-labelled BsDPEN ligand. After just 3 h exposure to **SS-2**, *ca.* 11×more Br *vs.* Os was present intracellularly, suggesting rapid complex degradation in a cellular environment. Again, this provides an explanation to the low 24 h catalytic turnover of pyruvate to lactate by **RR-1** (*p*-CH<sub>3</sub>) in cancer cells.<sup>10</sup>

#### <sup>189</sup>Os-<sup>79</sup>Br cellular distribution studies

In order to probe the potential intracellular targets of **SS-2** (*p*-Br) in A549 cells, the subcellular distributions of both <sup>189</sup>Os and <sup>79</sup>Br were determined using a cell fractionation kit and ICP-MS (**Section 3.3.11, Fig. 3.16; Appendix, Table A17-18**). Os was predominantly in the membrane fraction (>65%) – which contains particulates (*e.g.* mitochondrial and lysosomal organelles), in strong agreement with that reported for **RR-1** (*p*-CH<sub>3</sub>).<sup>2</sup> The development of mitochondrial-targeting organometallic complexes is of significant interest as an alternative approach to DNA-targeting cisplatin, through redox mechanisms of action. In particular, Os<sup>II</sup> azopyridine half-sandwich complexes have been reported to localize in small elliptical compartments and induce mitochondrial-mediated apoptosis<sup>23, 50</sup> – implicating mitochondria as a major therapeutic target. However, as the membrane fraction also contains other cytoplasmic organelles, the observed Os accumulation may be suggestive of other targeting moieties, such as lysosomes – which play a role in the excretion and degradation of unwanted cellular materials by exocytosis. Importantly, negligible amounts of Os (<6% of total cellular Os) were present in the nuclear fraction over the analysed period, which suggests the nucleus is *not* the primary therapeutic target – ruling out a DNA-binding mechanism of action. This is in strong agreement with the low nuclear quantities (<2%) of parent compound **RR-1** (*p*-CH<sub>3</sub>) observed in A2780 cancer cells and quantified by ICP-MS.<sup>2, 10</sup>

Significantly higher quantities of intracellular Br *vs.* Os were observed in A549 cells treated with **SS-2** over the analysed period (**Section 3.3.11, Fig. 3.16**), in agreement with the cellular accumulation studies described in this Chapter. This supports the hypothesis of intracellular complex degradation *via* BsDPEN ligand dissociation, resulting in different quantities of intact Os complex and free

sulfonamide ligand. This could mean that Os complexation acts as a chaperone for delivering sulfonamide ligands into cancer cells, where the (potentially) toxic ligand is released. However, further work is required to corroborate this: <sup>79</sup>Br ICP-MS uptake studies of the Br-BsDPEN ligand to see whether osmium complexation is crucial for cell permeation.

The majority of intracellular Br was distributed in the membrane fraction (>58%), correlating with that of Os (**Section 3.3.11, Fig. 3.16**), suggesting there might be some intact complex present in cytoplasmic organelles (*e.g.* mitochondria or lysosomes). Significantly more intracellular Br was observed in the cytosolic fraction (6-12%), compared to Os (<3%), which may imply potential interactions of the BsDPEN ligand with cytoplasmic proteins. This may suggest different cellular targets of the intact Os complex (for *in-cell* catalysis) and the dissociated BsDPEN ligand – for which any possible binding moieties are unknown. Moreover, this may suggest a multi-targeting mechanism of action of this family of complexes.

Remarkably, 10-20% of the intracellular Br was present in the nuclear fraction, which may implicate a potential DNA-binding antiproliferative mechanism mediated by the dissociated BsDPEN ligand. However, this contradicts cell cycle flow cytometry studies in cells treated with **SS-2 (Section 3.3.7)**, which revealed slight G<sub>1</sub>-arrest (growth stage) and *not* S (DNA-synthesis) or G<sub>2</sub>/M-arrest (growth and mitosis), implying minimal DNA-damage. The nature of the interactions between BsDPEN ligand and DNA (if any) is unknown, and could involve binding to metals involved in the stabilisation of DNA (*e.g.* Zn<sup>2+</sup> or Mg<sup>2+</sup>), interacting with nucleobases, intercalating DNA or high mobility group proteins (positively-charged). This is difficult to probe without further knowledge of the ligand speciation in the nuclear environment.

The overall intracellular micromolar quantities of Os and Br per cell were estimated from the cell fractionation data by normalizing total cellular quantities to the average volume of an A549 cell (1.67 pL).<sup>29</sup> This revealed *total* cellular Os and Br concentrations of 0.14 and 4.3 mM, respectively, after 24 h exposure (no recovery). Although the *overall* intracellular Os quantity can be normalized to the average cell volume, the volume of individual fractions cannot be determined, thus, fractional nanomoles of Os and Br per fraction have been reported. Negligible nuclear

quantities of Os ( $<1.5 \times 10^{-8}$  nmol per cell) were observed, compared with that of Br ( $>25 \times 10^{-8}$  nmol per cell), reaffirming that **SS-2** is primarily non-DNA targeting – as reported for **RR-1** (*p*-CH<sub>3</sub>).<sup>2, 10</sup> This also supports the hypothesis of multiple mechanisms of action: in-cell catalysis, ROS generation and intracellular targeting of the sulfonamide ligand.

### 3.4.8 Synchrotron-XRF

The elemental preservation of biological elements in frozen-dehydrated cells on Si<sub>3</sub>N<sub>4</sub> membranes has been reported in the literature.<sup>120</sup> Ideal analysis would be performed on frozen-hydrated samples (cryogenic temperatures) as demonstrated at beamlines ID16A (ESRF, Grenoble)<sup>48</sup> and 9-ID-B (APS, Chicago),<sup>121</sup> however, these facilities are not yet available at DLS (Oxford). Nonetheless, room temperature analysis of frozen-dried cells reported in this thesis have avoided the use of chemical fixatives (which can distort morphology chemical integrity).

#### Elemental preservation and cellular morphology

A population of A549 lung cancer cells was grown on Si<sub>3</sub>N<sub>4</sub> membranes and treated with **SS-2** ( $1-5 \times \text{IC}_{50}$ , 24 h), cryo-fixed and dried were analysed by synchrotron-XRF. An incident x-ray energy of 15 keV – exceeding the electron-binding energies of Os (L<sub>3</sub> 2p<sub>3/2</sub>=10.9 keV) and Br (K 1s=13.5 keV) was used - resulting in element-specific XRF. Individual cells in the population were selected for high-resolution XRF analysis (100 nm resolution), with at least 3 cells mapped per condition. In turn, the XRF of native biological elements (Zn, S, P and K) were monitored allowing cells to be identified and imaged. It must also be noted that cellular elements are also present in biological media (FCS and DMEM) used in this experiment (**Appendix, Table A1-2**), which may affect the elemental quantities but likely does not affect the distribution.



Zn, S, P and K are highly abundant elements, distributed within the cell in different regions and concentrations. Sulfur has roles in energy-generation (*i.e.* ferredoxins in the mitochondrial electron-transport chain), and is a major component of proteins (*e.g.* cysteine and methionine), which are essential for enzymatic catalysis in metabolic processes. Phosphorus is present in the cell in a variety of different forms, from phospholipid bilayers in membranes to the phosphodiester backbone of DNA, in addition to ATP (energy molecule) and RNA. Potassium is the primary cation found intracellularly (*ca.* 140 mM)<sup>122</sup> and is necessary for the regulation of metabolism and intercellular communication. Finally, intracellular zinc (0.2-0.3 mM)<sup>123</sup> plays essential roles in enzyme catalysis, protein regulation and DNA synthesis, allowing cell nuclei to be identified through highly localized zinc.<sup>54</sup> The high biological abundance of these elements has been exploited to locate cells on the supporting membrane, but also to identify the overall shape of the cell nucleus.

In general, the untreated cells (**C1-4**, **Section 3.3.12**, **Fig. 3.19**) were largely stretched out (cobblestone-shaped) on the membrane, with a clear distribution of P, S and K showing the overall cell outline, with nuclei visible from the strongly localized intracellular Zn. Importantly, the endogenous distributions of Zn, S and K observed correlate with the XRF maps of A549 cells previously reported.<sup>31, 32</sup> Cells **C1-4** ranged in size from 624–925  $\mu\text{m}^2$  ( $766 \pm 126 \mu\text{m}^2$ ) and an average roundness factor of  $0.33 \pm 0.04$  (where perfect circularity=1; **Appendix, Table A20**) supporting the elongated nature typical of that of A549 cells.<sup>28, 29</sup> As expected, these untreated A549 cells did not contain detectable Os or Br, thus, validating the experiment. It must be noted that differences in transparency of this population of A549 cells were observed (**Fig. 3.30**), most likely as a result of damage during cryo-fixation or freeze-drying. To address this, cells exposed to the same conditions but on independent Si<sub>3</sub>N<sub>4</sub> membranes were selected to ensure a reliable representation of the population of cells. In general, A549 cells have elongated 2D morphologies with large cytoplasmic-to-nuclear volume ratios.<sup>28, 29</sup> The mapped cells showed consistent morphologies and elemental distributions typical of native A549 cells.

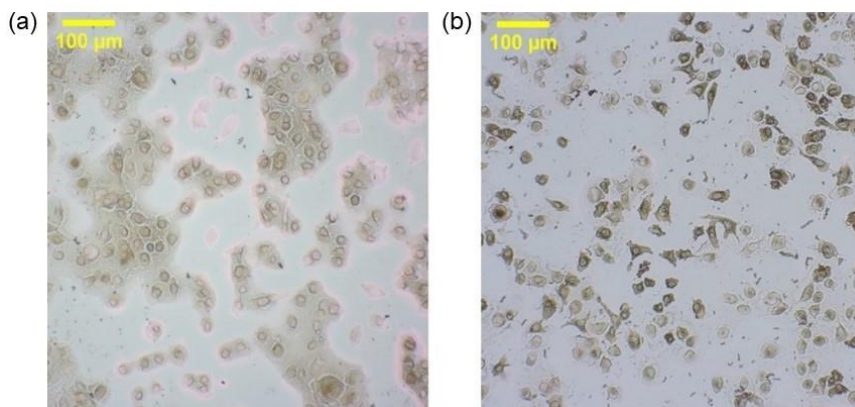


**Figure 3.30.** Light microscopy images of cryo-fixed and dried A549 cells grown on  $Si_3N_4$  membranes and exposed to the same conditions (24 h complex-free media), showing the differences in cell transparency. Differences are likely attributed to blotting and washing.

Cells were treated with 1, 3 and  $5 \times IC_{50}$  of *SS-2* (*p*-Br) for 24 h, and a total of 14 cells were mapped by XRF (**Section 3.3.12**, **C5-18**, **Fig. 3.20-22**): (i)  $1 \times IC_{50}$  (**C5-8**); (ii)  $3 \times IC_{50}$  (**C9-15**); (iii)  $5 \times IC_{50}$  (**C16-18**). Cells treated with  $1 \times IC_{50}$  of *SS-2* (**C5-8**) showed variance in cell morphologies, with respect to their 2D shape (circular, rounded or elongated), size (area, length and width) and their nuclear-to-cytoplasm ratios (**Section 3.3.12**, **Fig. 3.20**). The ‘rounding-up’ of a cell can be indicative of significant cell damage, and commonly accompanies cell death pathways.<sup>124</sup> The efficiency of surface adhesion of cells also decreases upon increasing damage, resulting in less stretched-out cells (**C5-8**, **Section 3.3.12**, **Fig. 3.20**). Cell nuclei in these treated cells (**C5-8**) were clearly distinguishable from the rounded and highly-localized Zn distributions, indicative of an intact and non-compromised cell nucleus.

Correspondingly, cells treated with a higher concentration ( $3 \times IC_{50}$ ) of Br-labelled *SS-2* (**C9-15**, **Section 3.3.12**, **Fig. 3.21**) were significantly smaller in size compared to those treated with  $1 \times IC_{50}$  (**C5-8**, **Fig. 3.20**) and the untreated controls ( $p=0.0074$ ; **C1-4**, **Fig. 3.19**), with significantly more rounded features (*ca.*  $2 \times$  more rounded, mean RF= $0.33 \pm 0.04$  and  $0.75 \pm 0.16$ , respectively). This observation may be suggestive of dose-dependent cell death, complementing the linear concentration-dependent Os accumulation studies reported in this Chapter (**Section 3.3.9**).

Cells treated with the highest concentration of **SS-2** ( $5\times\text{IC}_{50}$ ) exhibited similar roundness properties compared to  $3\times\text{IC}_{50}$  (**C16-18**, **Section 3.3.12**, **Fig. 3.22**), however, showed an increase in cell area compared to  $3\times\text{IC}_{50}$  ( $p=0.0288$ ) subsequently deviating from the observed trend in cell ‘shrinkage’. In these cells (treated with  $5\times\text{IC}_{50}$ ), the nuclei appear elongated, and take up a large proportion of the now-rounded cells (mean RF= $0.88\pm0.04$ ). Identification of the nucleus in **C18** is ambiguous due to the sparse intracellular distribution of Zn owing to cell damage. No trends in the size of individual cell nuclei of cells treated with  $0-3\times\text{IC}_{50}$  of **SS-2** were observed (**Appendix, Table A21**), with mean areas of  $130\pm21\ \mu\text{m}^2$ , however, nuclei in cells treated with  $5\times\text{IC}_{50}$  were significantly larger ( $266\pm34\ \mu\text{m}^2$ ) suggesting that high concentrations of **SS-2** inflict increased intracellular damage. It is hypothesised that at high doses of **SS-2**, nuclear membranes are damaged allowing Zn to leak freely into the cytoplasm. Cell shrinkage, membrane-blebbing and nuclear fragmentation are typical morphological changes which are indicative programmed-cell death.<sup>124</sup> Nuclear membrane blebbing and fragmentation can also be associated with mitochondrial damage, through the generation of ROS<sup>49</sup> – a mechanism which has been implicated for these complexes.<sup>14</sup>

It is known that this family of Os<sup>II</sup> complexes do not induce apoptosis,<sup>10</sup> thus, the observed swelling and membrane damage may be suggestive of a potential necrotic cell death pathway.<sup>124</sup> Necrosis is defined as a type of cell death which lacks the features of apoptosis or autophagy and is somewhat uncontrollable.<sup>124</sup> Necrotic cell death can be either unregulated (chaotic breakdown under intolerable conditions) or programmed (*i.e.* specific signalling pathways or regulation by genetic/epigenetic factors). Typical features of necrosis includes swelling of cells and organelles, rupturing of the plasma membrane and leaking of cellular contents,<sup>124</sup> and been reported for a variety of organometallic complexes including rhenium,<sup>125</sup> rhodium,<sup>126</sup> gold,<sup>127</sup> ruthenium and osmium.<sup>128</sup> Importantly, necrosis is more efficient in reducing cell survival compared to autophagic and apoptotic cell death<sup>124</sup> – which may be crucial in circumventing cisplatin resistance (which predominantly causes apoptosis).<sup>126</sup> Although a necrotic (non-apoptotic) cell death pathway induced by **SS-2** can be proposed, further experimental evidence is needed to substantiate this.

### Elemental co-localization

As predicted, Os and Br co-localised moderately in the cytoplasm of cells treated with 1-5×IC<sub>50</sub> of **SS-2** (**Appendix, Table A22**) which has been represented by Pearson's R-value (r), suggesting that some of the BsDPEN ligand remains coordinated to the metal centre: a necessity for the enantioselective catalytic conversion of pyruvate to lactate.<sup>10</sup> Moreover, the co-localization of Os with Br in non-nuclear regions of cancer cell supports the hypothesis that ATH catalysis occurs in the cytoplasm.<sup>10</sup> Os and Zn showed very little correlation (mean r=-0.03, **Appendix, Tables A23**), implying the Os likely does not localize in the nucleus, complementing cell fractionation data reported in this Chapter (**Section 3.3.11**). Interestingly, Br moderately co-localized with Zn in the cell nucleus (mean r=0.21; **Appendix; Table A24**), confirming dissociation of the BsDPEN ligand from the Os centre after 24 h.

The coordination of this BsDPEN ligand to the Os centre is essential for catalysis as it provides a chiral platform for the reaction to proceed. The observation of Br in the cell nucleus may therefore provide an explanation for the previously reported low catalytic conversion of pyruvate to lactate after 24 h exposure to **RR-1** (*p*-CH<sub>3</sub>), in the presence of formate.<sup>10</sup> Although **SS-2** is stable in aqueous conditions (water, PBS), the coordinatively-unsaturated nature of these 16-electron complexes makes them vulnerable in the highly reducing environment of cancer cells. For example, GSH has shown to alter the potency of **RR-1** (L-BSO assays),<sup>2</sup> implicating GSH as a cellular defence mechanism. The limited stability of Br-labelled **SS-2** in the intracellular environment of A549 cells is therefore not surprising. However, it can be hypothesized that *some* complex must remain intact after 24 h in order to perform *in-cell* catalysis, in agreement with formate-enhanced potency (**Section 3.3.6**).

The co-localization statistics seem to support that **SS-2** (*p*-Br) remains intact in cytoplasmic regions of cells, however, is not fully stable due to the distribution of the Br-labelled ligand within the cell nucleus, indicative of complex degradation and instability after 24 h. Nonetheless, these statistics support the hypothesis that intact **SS-2** is not primarily DNA-targeting (due to the lack of nuclear Os), and may act as a chaperone to deliver the BsDPEN ligand into the nucleus.

### Quantification of Os and Br

In order to calculate mole fraction quantities of elements in individual cancer cells, a reference AXO Si<sub>3</sub>N<sub>4</sub> membrane (of known elemental concentrations) was analysed by XRF and used to estimate the photon flux (photons/second), assuming a maximal cell thickness of 6  $\mu$ m.<sup>55</sup> When quantifying element by XRF, two factors must be considered: (i) matrix-matching between the sample and the internal standard is difficult and imperfect<sup>129</sup>; (ii) an assumption about sample thickness and homogeneity is assumed. As a consequence, XRF quantification is only semi-quantitative, and requires cross-correlation with techniques such as LA-ICP-MS.<sup>130</sup>

The Os in cells treated with 1 or 3 $\times$ IC<sub>50</sub> **SS-2** revealed predominant cytoplasmic (non-nuclear) localization (*ca.* 80%), implying that the cell nucleus is not the major *in-cell* target. This is in agreement with <sup>189</sup>Os-<sup>79</sup>Br ICP-MS cellular fractionation studies of **SS-2**, which revealed <6% of Os in the cell nucleus (**Section 3.3.11**). Additionally, flow cytometry analysis of parent compound **RR-1** (*p*-CH<sub>3</sub>) demonstrated non-apoptotic cell death,<sup>2</sup> supporting the hypothesis of a non DNA-mediated mechanism of action. However, the lack of Os in the cell nucleus cannot *completely* eliminate the prospect of DNA-targeting: DNA is a major target of cisplatin, despite only 1% reaching the cell nucleus.<sup>131</sup>

Correspondingly, cells treated with 5 $\times$ IC<sub>50</sub> of **SS-2** revealed *ca.* 60% of Os in the cytoplasm. A reduction in cytoplasmic Os was observed in cells treated with 5 $\times$ IC<sub>50</sub> of **SS-2** compared to those treated with lower concentrations. This is likely attributable to concentration-dependent cell damage (membrane damage, elemental leaching and cell swelling – typical features of necrosis)<sup>124</sup> which made distinguishing between the cell nucleus and cytoplasm ambiguous. In comparison, the localization of Br in the cytoplasm decreased from *ca.* 70% to 50% with concentration (1-5 $\times$ IC<sub>50</sub>) of **SS-2**, whilst the nuclear Br increased from *ca.* 30% to 50%. An increase in intranuclear Br with concentration may be a consequence of cell damage: for example, ruptured nuclear membrane or nuclear fragmentation.<sup>49</sup>

Significantly higher intracellular levels of Br *vs.* Os were observed in cells treated with **SS-2**, with at least 3 $\times$  more Br in all of the individually analysed cells (**Section 3.3.12, Table 3.8**), which is indicative of complex degradation (as previously discussed). The reduced intracellular levels of Os may also suggest that the Os

moiety is more susceptible to rapid excretion from the cell, with more Br-labelled BsDPEN remaining intracellularly. Herein, ICP-MS cellular accumulation studies revealed the potential PGP-dependent efflux of the Os component of **SS-2**, but *not* the Br component (**Section 3.3.10, Fig. 3.14**) - implicating different excretion pathways of intact complex and the unbound sulfonamide ligand. The excretion of Os is likely facilitated through binding to efflux proteins, whereas the chelating sulfonamide may favour binding to alternative cellular modalities, for example, chelating endogenous metal ions (*e.g.* Zn, Cu, Fe – although the concentration of “free” unbound ions is low) or forming interactions with biomolecules (proteins, lipids, DNA) – which may enhance the intracellular lifetime compared to Os.

The mean bromine-to-osmium (Br/Os) molar ratio in cells treated with  $1.5 \times \text{IC}_{50}$  of **SS-2** revealed a significant decrease between 3 and  $5 \times \text{IC}_{50}$  ( $p=0.0019$ ), implying more of the complex is intact at higher concentrations of **SS-2**. Furthermore, it may be possible that either detoxification is less pronounced (due to increased cell damage) at higher drug concentrations, or that the uptake of **SS-2** is faster.

It has already been shown by <sup>189</sup>Os ICP-MS that the accumulation of osmium is linearly dependent on the concentration of **SS-2** (**Section 3.3.9, Table 3.7**), in addition to sigmoidal dose-response in cell viability assays, thus, it is likely that the antiproliferative activity is enhanced with concentration. Moreover, treatment with higher drug concentrations likely causes increased cell damage – potentially a consequence of reduced cellular defence mechanisms. Drug-induced changes in cell homeostasis renders cells more vulnerable, preventing the efficient excretion of drugs, which usually leads cell death. Furthermore, this may explain why cells treated with  $5 \times \text{IC}_{50}$  showed a higher percentage of intracellular intact complex (mean Br/Os= $2.3 \pm 0.1$ ; **Section 3.3.12, Table 3.8**). As the linear dependence on concentration of Os accumulation in cells treated with **SS-2** was only demonstrated up to  $1.5 \times \text{IC}_{50}$ , this hypothesis can be further probed by performing <sup>189</sup>Os-<sup>79</sup>Br uptake studies at  $5 \times \text{IC}_{50}$  concentration (however, this will require a larger cell seeding population to account for expected increases in cell death). Likewise, time-dependent <sup>189</sup>Os-<sup>79</sup>Br accumulation at higher doses of **SS-2** can be performed to probe whether the rate of uptake / efflux changes with drug concentration.

Drug-induced damage to the plasma membrane of cells treated with 5×IC<sub>50</sub> of **SS-2** may also cause elemental-leeching of Os, Br and Zn making the discrimination between intracellular and extracellular elements challenging. High concentrations of **SS-2** may cause the cancer cells to swell or burst, supporting the hypothesis of necrotic-mediated cell death.<sup>124</sup> This can be probed using membrane integrity flow cytometry at higher concentrations of **SS-2** to determine whether very high concentrations of these osmium catalysts compromise cell membranes.

### Lysosomal sequestration

The most intriguing discovery from synchrotron-XRF was the co-localization of Os and Br in small, vesicle-sized compartments in the cell cytoplasm, which were identified only in cells treated with 3-5×IC<sub>50</sub> of **SS-2** (*p*-Br). The area of each compartment was calculated in triplicate using the multipoint selection tools in ImageJ,<sup>19</sup> which also enabled the quantification of both Os and Br in each ‘vesicle’. These compartments revealed mean areas of 0.59±0.22 and 0.78±0.25 μm<sup>2</sup> for 3 and 5×IC<sub>50</sub>, respectively. The mean bromine-to-osmium ratio (Br/Os) in the vesicle-sized compartments in 6 different cells (treated with 3×IC<sub>50</sub> of **SS-2**) was calculated to be 4.5±2 (**Section 3.3.12, Table 3.10**) again implying *ca.* 4× more intracellular Br *vs.* Os. Interestingly, the vesicle-like structures observed in cells treated with 5×IC<sub>50</sub> of **SS-2** revealed mean Br/Os ratios of 1.48±0.18. This may suggest some co-localisation between Os and the Br-labelled BsDPEN ligand (intact complex) in these vesicle-like structures, which may be attributed to cytoplasmic organelles. As there are significantly higher levels of Br *vs.* Os for all cases, this may implicate degradative organelles (*e.g.* lysosomes or endosomes) in the breakdown of these complexes.

Lysosomes are acidic intracellular organelles in eukaryotic cells (0.1-1.2 μm in diameter)<sup>132</sup> which have important roles in the excretion and degradation of unwanted cellular components, and also partake in cellular processes including repairing membrane damage and apoptosis. Lysosome-targeted anticancer therapy is becoming of increasing interest to mediate multidrug resistance, providing new modes of action through sub-organelle localization. The sequestration of hydrophobic anticancer agents (*e.g.* doxorubicin) in lysosomes has been reported in

the literature,<sup>133</sup> which impacts lysosomal biogenesis and exocytosis. This may provide the opportunity to overcome resistance, and prevent procurement of aggressive tumour phenotypes.

The acidic nature of lysosomes (pH 4.5–5) may promote the protonation of complex **SS-2** – most likely at the basic NH<sup>+</sup> of the coordinated BsDPEN ligand – facilitating ligand dissociation and complex degradation. Upon protonation, the altered structure of the complex may prevent passage through the lysosomal membrane, subsequently becoming entrapped in the lysosome.<sup>133</sup> Furthermore, the potential lysosomal sequestration of **SS-2** (*p*-Br) likely reduces the drug efficacy by preventing it reaching its chemotherapeutic *in-cell* target. This is well-documented for platinum in tumour cells,<sup>59</sup> and is a major concern in drug resistance. The quantity of Br in these compartments was significantly higher than Os which suggests that lysosomes may detoxify both the intact complex and the excess dissociated Br-labelled BsDPEN ligand. The lysosomal accumulation of weak bases is well-reported in the literature, and is predominantly attributed to pH-partitioning,<sup>134</sup> preventing membrane permeation out of the lysosomes. Both the intact osmium complex and the unbound sulfonamide ligand can be considered as weak bases, hence, it may be conceivable that both the intact complex and the BsDPEN ligand may be encapsulated within lysosomes. Moreover, as there is significantly more Br vs. Os in the cell cytoplasm, it may be hypothesised that complex breakdown occurs in both the cytoplasm and in endosomes/lysosomes. As synchrotron-XRF alone cannot identify different cellular organelles, further lysosomal-based *in vitro* assays were performed.



### 3.4.9 Chloroquine inhibition of lysosomal activity

Chloroquine is the mainstay clinically-approved drug for the treatment of malaria, and has been reported to be relatively non-toxic towards cancer cells at low micromolar concentrations, thus can be utilized as a lysosomotropic agent.<sup>56-59</sup> Incubation of cells with chloroquine causes de-acidification of lysosomes by preventing autophagy,<sup>57, 58</sup> hence, can be used to investigate the potential for lysosome-targeting chemotherapeutics. Cells pre-incubated with non-toxic concentrations of chloroquine diphosphate (150  $\mu$ M, 2 h), followed by 24 h exposure to **RR-1** (*p*-CH<sub>3</sub>) or **SS-2** (*p*-Br) revealed a significant increase in potency (by 50% and 25%, respectively), implying that lysosomes may be contributing to the detoxification and reduced efficacy of these complexes (**Section 3.3.13, Fig. 3.25**). Chloroquine has been reported to improve the cytotoxicity of multiple anticancer drugs, including doxorubicin and cisplatin,<sup>135, 136</sup> with considerable implications on reversing multi-drug resistance in cancer cells.

It must be considered that chloroquine itself may not *just* affect the lysosomes,<sup>60</sup> hence, to demonstrate that the enhanced potency of **RR-1** and **SS-2** is a consequence of lysosomal activity and *not* due to membrane damage, chloroquine-dependent membrane integrity analysis was performed by flow cytometry upon treatment with **RR-1** and **SS-2** (**Section 3.3.13, Figure 3.27**). Treatment of cells with chloroquine prior to exposure to **RR-1** or **SS-2** did not reveal cause membrane damage, thus, the increased potency was not due to a compromised membrane.

Further to this, the Os cellular accumulation in A549 cells pre-incubated with chloroquine (150  $\mu$ M, 2 h) with 24 h exposure to **RR-1** or Br-labelled **SS-2** (1 $\times$ IC<sub>50</sub>) showed a significant increase in intracellular Os ( $p=0.0015$  and  $p=0.0251$ , respectively). This implies that the deactivation of lysosomes results in higher intracellular levels of Os (ng/10<sup>6</sup> cells, which is accompanied by increased antiproliferative potency (**Section 3.3.13, Fig. 3.25**). In addition, the molar Br/Os ratio decreased in cells preincubated with chloroquine and exposed to **SS-2**, implying that more of **SS-2** remains intact intracellularly upon deactivation of lysosomes (**Section 3.3.13, Fig. 3.26**). Overall, this implicates lysosomes in the detoxification of this family of osmium catalysts.

### 3.5 Conclusions and future work

A series of Os<sup>II</sup> 16-electron sulfonamide catalysts with the formula [Os<sup>II</sup>(*p*-cym)(R-BsDPEN)] (**2-5**, where R=*p*-Br, I, OMe and *m*-Br, respectively) have been synthesized and characterised. Their properties were closely comparable to parent compound **RR-1** (R=*p*-CH<sub>3</sub>) with respect to structure (x-ray crystallography; DFT), hydrophobicity (Log P), solvent stability (DMSO; PBS) and catalytic activity (ATH reduction of acetophenone). Complexes **2-5** exhibited high enantiomeric excesses (>95%) and turnover frequencies (*ca.* 80 h<sup>-1</sup>) in the presence of formic acid (hydride source), for the catalytic conversion of acetophenone to (*S/R*)-1-phenylethanol. Substituents which were large, and electron-withdrawing (**2** and **3**, R=*p*-Br, I, respectively) moderately improved the turnover frequency reported for **1** (*p*-CH<sub>3</sub>) by approximately 27%.<sup>1,2</sup> Overall, it was deduced that substitution of Br at the *para* site of **1** (R=*p*-CH<sub>3</sub>) did not significantly alter the chemical activity of the catalyst.

Remarkably, the Br-probe did not significantly alter the *in vitro* biological activity, demonstrating similarities in antiproliferative potency (IC<sub>50</sub>), selectivity factors (A549 *vs.* MRC5), *in-cell* catalytic activity, alterations in membrane integrity and cell cycle and osmium cellular accumulation (concentration; time; temperature; extent of efflux; formate-dependent) to that of **RR-1** (*p*-CH<sub>3</sub>). Notably, the cellular accumulation of Os in cells treated with **SS/RR-2** (*p*-Br) was found to be identical to that of **RR-1** (*p*-CH<sub>3</sub>) when using equipotent concentrations (1×IC<sub>50</sub>), despite the difference in potency between **RR-1** (IC<sub>50</sub>=21.1±0.3 μM) and **SS-2** (IC<sub>50</sub>=29.5±0.5 μM), which implies Br is somewhat hindering the cellular accumulation. This correlated with the increased hydrophobicity of **RR-1** *vs.* **SS-2** (LogP=1.45 and 1.01, respectively), which may promote cellular accumulation of **RR-1** through the highly lipophilic cell membrane. Overall, it was deduced that the antiproliferative mechanism of action of **RR-1** was unchanged upon Br-substitution, hence, Br-labelled **SS-2** can be utilized as a suitable analogue to elucidate the *in-cell* activity of this family of Os<sup>II</sup> complexes by correlative ICP-MS and synchrotron-XRF.

A method for the simultaneous quantification of both Os and Br by ICP-MS was optimised using alkaline digestion in TMAH, allowing analysis of readily-oxidised analytes (<sup>189</sup>Os and <sup>79</sup>Br) in a matrix with sufficient reactivity to achieve complete digestion of cell pellets. Cellular accumulation of Os and Br in A549 lung cancer

cells treated with **SS-2** (*p*-Br) was determined under varying conditions (temperature, methyl- $\beta$ -cyclodextrin, verapamil, time and cell fractionation). In all cases, significantly higher concentrations of Br compared to Os were found (>10-fold) suggesting that these complexes may have limited stability in a cellular environment. This begins to provide an explanation as to why the intracellular catalytic turnover of parent compound **RR-1** (*p*-CH<sub>3</sub>) was so low.<sup>2, 10</sup>

The endocytic contribution to the accumulation of **SS-2** (*p*-Br) was investigated using a known endocytotic inhibitor (methyl- $\beta$ -cyclodextrin), which was shown to reduce the quantity of intracellular Os with increasing concentration of inhibitor (by *ca.* 65%). Interestingly, intracellular levels of Br were initially reduced at the lowest inhibitor concentration (0.1 mM), but plateaued with increasing concentration, thus it may be hypothesized that caveolae endocytosis mediates the uptake of the intact complex, but once inside the cell the complex is degraded to release the Br-labelled ligand, which is retained intracellularly for longer.

Similarly to **SS-2**, the dependence on drug efflux *via.* pathways associated with PGP (determined by incubating cells in verapamil - a known PGP-inhibitor – after Os treatment) revealed that the efflux of the Os moiety (assumed to be intact complex) is dependent on PGP.<sup>2</sup> As verapamil is not entirely specific for PGP-inhibition, it was deduced that efflux of these complexes is reliant on pathways associated with verapamil-inhibition. However, Br accumulation was unaffected by verapamil treatment, suggesting that the Br-labelled BsDPEN ligand is not removed from cells by PGP. The *extent* of cellular efflux of **SS-2** was monitored using varying exposure times and recovery in complex-free media, revealing maximum intracellular levels of Os after *ca.* 3-6 h, as reported for parent compound **RR-1**.<sup>2</sup> Contrastingly, the intracellular Br reached a maximum after 24 h exposure with around 30× more Br *vs.* Os, indicative of severe complex instability.

Cellular fractionation studies of A549 cells treated with **SS-2** revealed significantly more Br *vs.* Os (>10-fold), with the majority of Os and Br observed in the membrane and cytoskeletal fractions. This suggests that some of complex **SS-2** is intact in the cell cytoplasm, where *in-cell* catalysis likely occurs, as previously hypothesized for **RR-1**.<sup>2, 10</sup> Negligible quantities of Os were present in the nuclear fraction (<6%) – which may rule out a DNA-binding mechanism of action.

Interestingly, 10-20% Br was present in the nuclear fraction, perhaps as unbound Br-labelled BsDPEN. Approximately 32× more Br vs. Os was present in the nuclear fraction after 24 h exposure to **SS-2**. It may be hypothesized that the Os complex may facilitate the delivery of the BsDPEN into the cell (verified by the lack of toxicity of BsDPEN, IC<sub>50</sub>>100 μM), where it can then be released and enter the nucleus. Whether the presence of BsDPEN is contributing to the anticancer activity is unknown, and requires further investigation.

Synchrotron-XRF confirmed that some of **SS-2** is likely to remain intact as judged by the co-localization of Os and Br in the cytoplasm of A549 cells, but again with significantly higher levels of Br vs. Os – in agreement with ICP-MS accumulation studies. Interestingly, XRF revealed the co-localization of Os and Br in small, spherical compartments (*ca.* 0.6 μm<sup>2</sup>) in A549 cells treated with 3-5×IC<sub>50</sub> of **SS-2**, which may imply lysosomal breakdown and complex efflux. This was probed using chloroquine (which de-acidifies lysosomes), revealing a significant increase (*ca.* 25-50%) in potency, accompanied by an increase in Os accumulation (ng/10<sup>6</sup> cells).

Future work confirming the lysosomal-mediated detoxification of this family of osmium catalysts may involve utilizing complementary lysosomotropic bioassays, including Neutral Red (rhodamine dye that stains lysosomes of viable cells) or LysoTracker staining assays (fluorescence microscopy). Furthermore, correlative cryo-SIM (Structured Illumination Microscopy) and cryo-XRT (X-Ray Tomography)<sup>137</sup> can be used on cryopreserved cancer cells treated with the fluorescent sulforhodamine complex (used in zebrafish toxicity studies)<sup>14</sup> will provide complementary information into the in-cell localisation, distribution and detoxification of this family of Os complexes in cryopreserved cells (as close to their native state as possible). Correlative cryo-XRT and cryo-XRF can also provide unambiguous information on the subcellular distribution metallodrugs.<sup>48</sup>

The potential necrotic (non-apoptotic and non-autophagic) mechanism of cell death induced by **RR-1** (*p*-CH<sub>3</sub>) or **SS-2** (*p*-Br) can be further probed using flow cytometry using immunofluorescent staining with 7-aminoactinomycin D or annexin V.<sup>125, 138</sup> Consideration of the formate-dependent distribution of **SS-2** requires investigations either using cellular fractionation (ICP-MS) or synchrotron-XRF studies. In addition, as **SS-2** is only *ca.* 2-fold selective for cancer vs. healthy

cells (without formate), the *in-cell* distribution and localisation in MRC5 fibroblasts can be investigated by ICP-MS and synchrotron-XRF, to gain an insights into the *in vitro* toxicity.

The Br molecular probe of complex **SS-2** can further be utilized to perform both Os and Br XANES analysis of treated cancer cells,<sup>139-141</sup> to gain essential insights into the potential *in-cell* binding moieties of the ‘intact’ complex and the unbound sulfonamide ligand. Complementary to this, mass spectrometry proteomics of osmium and bromine (<sup>79</sup>Br; <sup>81</sup>Br) can be performed.<sup>142</sup> Finally, the concept of triple-mapping *via* molecular labelling may be possible, to elucidate the overall complex stability: labelling the *para*-cymene arene group with a molecular probe (*i.e.* iodine) and monitor this by ICP-MS (<sup>189</sup>Os, <sup>79</sup>Br and <sup>127</sup>I), or by synchrotron-XRF (Os L<sub>3</sub>M<sub>5</sub>=8.9, Br K<sub>L3</sub>=11.9 and I L<sub>3</sub>M<sub>5</sub>=3.9 keV).

### 3.6 References

1. J. P. C. Coverdale, C. Sanchez-Cano, G. J. Clarkson, R. Soni, M. Wills and P. J. Sadler, *Chem Eur*, 2015, **21**, 8043-8046.
2. J. P. C. Coverdale, *PhD Thesis (University of Warwick)*, 2017.
3. R. Noyori and S. Hashiguchi, *Acc Chem Res*, 1997, **30**, 97-102.
4. R. Noyori, M. Kitamura and T. Ohkuma, *PNAS*, 2004, **101**, 5356-5362.
5. T. Ohkuma, *Proc Jpn Acad Ser B Phys Biol Sci*, 2010, **86**, 202-219.
6. T. Ohkuma, N. Utsumi, K. Tsutsumi, K. Murata, C. Sandoval and R. Noyori, *J Am Chem Soc*, 2006, **128**, 8724-8725.
7. P. A. Dub and J. C. Gordon, *Dalton Trans*, 2016, **45**, 6756-6781.
8. M. Yamakawa, I. Yamada and R. Noyori, *Angew Chem Int Ed*, 2001, **40**, 2818-2821.
9. P. Kačer, J. Václavík, J. Přech and M. Kuzma, *J Cheminform*, 2012, **4**, 16.
10. J. P. C. Coverdale, I. Romero-Canelón, C. Sanchez-Cano, G. J. Clarkson, A. Habtemariam, M. Wills and P. J. Sadler, *Nat Chem*, 2018, **10**, 347.
11. J. J. Soldevila-Barreda, I. Romero-Canelón, A. Habtemariam and P. J. Sadler, *Nat Comm*, 2015, **6**, 6582.
12. J. J. Soldevila-Barreda and N. Metzler-Nolte, *Chem Rev*, 2019, **119**, 829-869.
13. P. Zhang and H. Huang, *Dalton Trans*, 2018, **47**, 14841-14854.
14. J. P. C. Coverdale, H. E. Bridgewater, J.-I. Song, N. A. Smith, N. P. E. Barry, I. Bagley, P. J. Sadler and I. Romero-Canelón, *J Med Chem*, 2018.
15. I. San-Millan and G. A. Brooks, *Carcinogenesis*, 2017, **38**, 119-133.
16. J. Tönnemann, J. Risse, Z. Grote, R. Scopelliti and K. Severin, *Eur J Inorg Chem*, 2013, **1**, 4558-4562.
17. I. Romero-Canelon, A. M. Pizarro, A. Habtemariam and P. J. Sadler, *Metallomics*, 2012, **4**, 1271-1279.
18. V. A. Solé, E. Papillon, M. Cotte, P. Walter and J. Susini, *Spectrochim Acta B*, 2007, **62**, 63-68.
19. C. T. Rueden, J. Schindelin, M. C. Hiner, B. E. DeZonia, A. E. Walter, E. T. Arena and K. W. Eliceiri, *BMC Bioinform*, 2017, **18**, 529-529.
20. G. Kang, S. Lin, A. Shiwakoti and B. Ni, *Catal Commun*, 2014, **57**, 111-114.

21. M. Orio, D. A. Pantazis and F. Neese, *Photosynth Res*, 2009, **102**, 443-453.
22. A. H. Aboo, E. L. Bennett, M. Deeprose, C. M. Robertson, J. A. Iggo and J. Xiao, *Chem Comm*, 2018, **54**, 11805-11808.
23. S. H. van Rijt, I. Romero-Canelon, Y. Fu, S. D. Shnyder and P. J. Sadler, *Metallomics*, 2014, **6**, 1014-1022.
24. N. D. Eljack, H.-Y. M. Ma, J. Drucker, C. Shen, T. W. Hambley, E. J. New, T. Friedrich and R. J. Clarke, *Metallomics*, 2014, **6**, 2126-2133.
25. D.-W. Shen, L. M. Pouliot, M. D. Hall and M. M. Gottesman, *Pharmacol Rev*, 2012, **64**, 706-721.
26. M. P. Pollastri, *Curr Protoc Pharmacol*, 2010.
27. J. J. Wilson and S. J. Lippard, *J Med Chem*, 2012, **55**, 5326-5336.
28. R. Camerlingo, R. Miceli, L. Marra, G. Rea, I. D'Agnano, M. Nardella, R. Montella, A. Morabito, N. Normanno, V. Tirino and G. Rocco, *PLoS One*, 2019, **14**, e0219597.
29. R. D. Jiang, H. Shen and Y. J. Piao, *Rom J Morphol Embryol*, 2010, **51**, 663-667.
30. I. M. Rio-Echevarria, J. Ponti, A. Bogni, D. Gilliland, M. Altissimo, L. Pascolo, G. Ceccone and A. Gianoncelli, *X-Ray Spectrometry*, 2019, **48**, 94-101.
31. E. J. Sheridan, C. J. D. Austin, J. B. Aitken, S. Vogt, K. A. Jolliffe, H. H. Harris and L. M. Rendina, *J Synchrotron Radiat*, 2013, **20**, 226-233.
32. S. Antony, J. B. Aitken, S. Vogt, B. Lai, T. Brown, L. Spiccia and H. H. Harris, *J Biol Inorg Chem*, 2013, **18**, 845-853.
33. P. Stiefel, S. Schmidt-Emrich, K. Maniura-Weber and Q. Ren, *BMC Microbiol* 2015, **15**, 36-36.
34. J. Gehrig, G. Pandey and J. H. Westhoff, *Front Pediatr*, 2018, **6**, 183.
35. K. Howe and e. al, *Nature*, 2013, **496**, 498-503.
36. C. Santoriello and L. I. Zon, *J Clin Invest*, 2012, **122**, 2337-2343.
37. D. Raldúa and B. Piña, *Expert Opin Drug Metab Toxicol* 2014, **10**.
38. T. Wang, C. Wang, Q. Wu, K. Zheng, J. Chen, Y. Lan, Y. Qin, W. Mei and B. Wang, *Molecules*, 2017, **22**.
39. J. Schur, A. Lüning, A. Klein, R. W. Köster and I. Ott, *Inorg Chim Acta*, 2019, **495**, 118982.
40. M. L. Amin, *Drug Target Insights*, 2013, **7**, 27-34.

41. A. K. Nanayakkara, C. A. Follit, G. Chen, N. S. Williams, P. D. Vogel and J. G. Wise, *Sci Rep*, 2018, **8**, 967.
42. J. Wang, H. Wang, L. Zhao, S. Fan, Z. Yang, F. Gao, L. Chen, G. G. Xiao, J. Molnar and Q. Wang, *Anticancer Res*, 2010, **30**, 3593-3598.
43. A. A. Hummer and A. Rompel, *Metallomics*, 2013, **5**, 597-614.
44. R. Koba, H. Fujita, M. Nishibori, K. Saeki, K. Nagayoshi, Y. Sadakari, S. Nagai, O. Sekizawa, K. Nitta, T. Manabe, T. Ueki, T. Ishida, Y. Oda and M. Nakamura, *Int J Cancer*, 2019, **146**, 2498-2509.
45. J. Z. Zhang, N. S. Bryce, A. Lanzirotti, C. K. J. Chen, D. Paterson, M. D. de Jonge, D. L. Howard and T. W. Hambley, *Metallomics*, 2012, **4**, 1209-1217.
46. L. Wielopolski, R. Zhang, M. J. Clarke and S. H. Cohn, *Biol Trace Elem Res*, 1987, **13**, 283-290.
47. J. B. Aitken, S. Antony, C. M. Weekley, B. Lai, L. Spiccia and H. H. Harris, *Metallomics*, 2012, **4**, 1051-1056.
48. J. J. Conesa, A. C. Carrasco, V. Rodríguez-Fanjul, Y. Yang, J. L. Carrascosa, P. Cloetens, E. Pereiro and A. M. Pizarro, *Angew Chem Int Ed*, 2020, **59**.
49. C. Sanchez-Cano, D. Gianolio, I. Romero-Canelon, R. Tucoulou and P. J. Sadler, *Chem Comm*, 2019, **55**, 7065-7068.
50. C. Sanchez-Cano, I. Romero-Canelón, Y. Yang, I. J. Hands-Portman, S. Bohic, P. Cloetens and P. J. Sadler, *Chem Eur*, 2017, **23**, 2512-2516.
51. F. Fus, Y. Yang, H. Z. S. Lee, S. Top, M. Carriere, A. Bouron, A. Pacureanu, J. C. da Silva, M. Salmain, A. Vessieres, P. Cloetens, G. Jaouen and S. Bohic, *Angew Chem Int Ed*, 2019, **58**, 3461-3465.
52. C. A. Lawrence Berkeley Lab, *X-ray data booklet Revision*, 1986.
53. M. D. Hall, R. A. Alderden, M. Zhang, P. J. Beale, Z. Cai, B. Lai, A. P. Stampfl and T. W. Hambley, *J Struct Biol*, 2006, **155**, 38-44.
54. E. Bafaro, Y. Liu, Y. Xu and R. E. Dempski, *Signal Transduct Target Ther*, 2017, **2**, 17029.
55. J. L. Gregg, K. M. McGuire, D. C. Focht and M. A. Model, *Pflugers Arch*, 2010, **460**, 1097-1104.
56. C. Fan, W. Wang, B. Zhao, S. Zhang and J. Miao, *Biorg Med Chem*, 2006, **14**, 3218-3222.



57. A. Kondratskyi, K. Kondratska, F. Vanden Abeele, D. Gordienko, C. Dubois, R.-A. Toillon, C. Slomianny, S. Lemi re, P. Delcourt, E. Dewailly, R. Skryma, C. Biot and N. Prevarskaya, *Sci Rep*, 2017, **7**, 15896-15896.
58. M. Mauthe, I. Orhon, C. Rocchi, X. Zhou, M. Luhr, K.-J. Hijlkema, R. P. Coppes, N. Engedal, M. Mari and F. Reggiori, *Autophagy*, 2018, **14**, 1435-1455.
59. B. Zhitomirsky and Y. G. Assaraf, *Drug Resist Update*, 2016, **24**, 23-33.
60. M. A. A. Al-Bari, *Pharmacol Res Perspect*, 2017, **5**, e00293-e00293.
61. Y. Fu, A. Habtemariam, A. M. Pizarro, S. H. van Rijt, D. J. Healey, P. A. Cooper, S. D. Shnyder, G. J. Clarkson and P. J. Sadler, *J Med Chem*, 2010, **53**, 8192-8196.
62. J. M. Zimbron, M. Dauphinais and A. B. Charette, *Green Chem*, 2015, **17**, 3255-3259.
63. L. Biancalana, S. Fulignati, C. Antonetti, S. Zacchini, G. Provinciali, G. Pampaloni, A. M. Raspolli Galletti and F. Marchetti, *New J Chem*, 2018, **42**, 17574-17586.
64. Y. Yang, M. N. Weaver and K. M. Merz, *J Phys Chem A*, 2009, **113**, 9843-9851.
65. R. Soni, F. K. Cheung, G. C. Clarkson, J. E. D. Martins, M. A. Graham and M. Wills, *Org Biomol Chem*, 2011, **9**, 3290-3294.
66. S. M. Meier-Menches, C. Gerner, W. Berger, C. G. Hartinger and B. K. Keppler, *Chem Soc Rev*, 2018, **47**, 909-928.
67. P. C. A. Bruijninx and P. J. Sadler, *Adv Inorg Chem*, 2009, **61**, 1-62.
68. J. E. Camp, S. B. Nyamini and F. J. Scott, *RSC Med Chem*, 2020, **11**, 111-117.
69. A. E. Egger, C. Rappel, M. A. Jakupiec, C. G. Hartinger, P. Heffeter and B. K. Keppler, *J Anal At Spectrom*, 2009, **24**, 51-61.
70. K. S. Gkika, A. Byrne and T. E. Keyes, *Dalton Trans*, 2019, **48**, 17461-17471.
71. P. Mistry, L. R. Kelland, S. Y. Loh, G.  bel, B. A. Murrer and K. R. Harrap, *Cancer Res*, 1992, **52** **22**, 6188-6193.
72. J. Zhou, Y. Kang, L. Chen, H. Wang, J. Liu, S. Zeng and L. Yu, *Front Pharmacol*, 2020, **11**.
73. W. Wang and X. Yang, *Chem Comm*, 2019, **55**, 9633-9636.

74. M. G. Vander Heiden, L. C. Cantley and C. B. Thompson, *Science*, 2009, **324**, 1029-1033.
75. H. Randhawa, S. Chikara, D. Gehring, T. Yildirim, J. Menon and K. M. Reindl, *BMC Cancer*, 2013, **13**, 321.
76. A. Banerjee, P. Majumder, S. Sanyal, J. Singh, K. Jana, C. Das and D. Dasgupta, *FEBS Open Bio*, 2014, **4**, 251-259.
77. M. Veldhoen, *Immun Inflamm Dis*, 2017, **5**, 384-385.
78. S. Mueller, M. Schittenhelm, F. Honecker, E. Malenke, K. Lauber, S. Wesselborg, J. T. Hartmann, C. Bokemeyer and F. Mayer, *Int J Oncol*, 2006, **29**, 471-479.
79. A. J. Hill, H. Teraoka, W. Heideman and R. E. Peterson, *Toxicol Sci*, 2005, **86**, 6-19.
80. W. B. Barbazuk, I. Korf, C. Kadavi, J. Heyen, S. Tate, E. Wun, J. A. Bedell, J. D. McPherson and S. L. Johnson, *Genome Res*, 2000, **10**, 1351-1358.
81. J. M. Hearn, I. Romero-Canelón, A. F. Munro, Y. Fu, A. M. Pizarro, M. J. Garnett, U. McDermott, N. O. Carragher and P. J. Sadler, *Proc Natl Acad Sci USA*, 2015, **112**, E3800-E3805.
82. Z. Xu, D. Kong, X. He, L. Guo, X. Ge, X. Liu, H. Zhang, J. Li, Y. Yang and Z. Liu, *Inorg Chem Front*, 2018, **5**, 2100-2105.
83. M. H. M. Klose, M. Hejl, P. Heffeter, M. A. Jakupiec, S. M. Meier-Menches, W. Berger and B. K. Keppler, *Analyst*, 2017, **142**, 2327-2332.
84. L. Bluck and D. A. Volmer, *Spectroscopy (Springf)* 2009, **23**, 36-36.
85. X. Bu, T. Wang and G. Hall, *J Anal At Spectrom*, 2003, **18**, 1443-1451.
86. T. W. May and R. H. Wiedmeyer, *At Spectrosc*, 1998, **19**, 150-155.
87. Z. Marczenko and M. Balcerzak, in *Analytical Spectroscopy Library*, Elsevier, 2000, vol. 10, ch. 12, pp. 129-132.
88. H. Kataoka, S. Tanaka, C. Konishi, Y. Okamoto, T. Fujiwara and K. Ito, *Rapid Commun Mass Spectrom*, 2008, **22**, 1792-1798.
89. D. Pozebon, V. L. Dressler and A. J. Curtius, *Talanta*, 2000, **51**, 903-911.
90. A. E. Egger, C. Rappel, M. A. Jakupiec, C. G. Hartinger, P. Heffeter and B. K. Keppler, *J Anal*, 2009, **24**, 51-61.
91. Y. Gao, S. Li, H. He, T. Li, T. Yu, R. Liu, S. Ni and Z. Shi, *Microchem J*, 2017, **130**, 281-286.

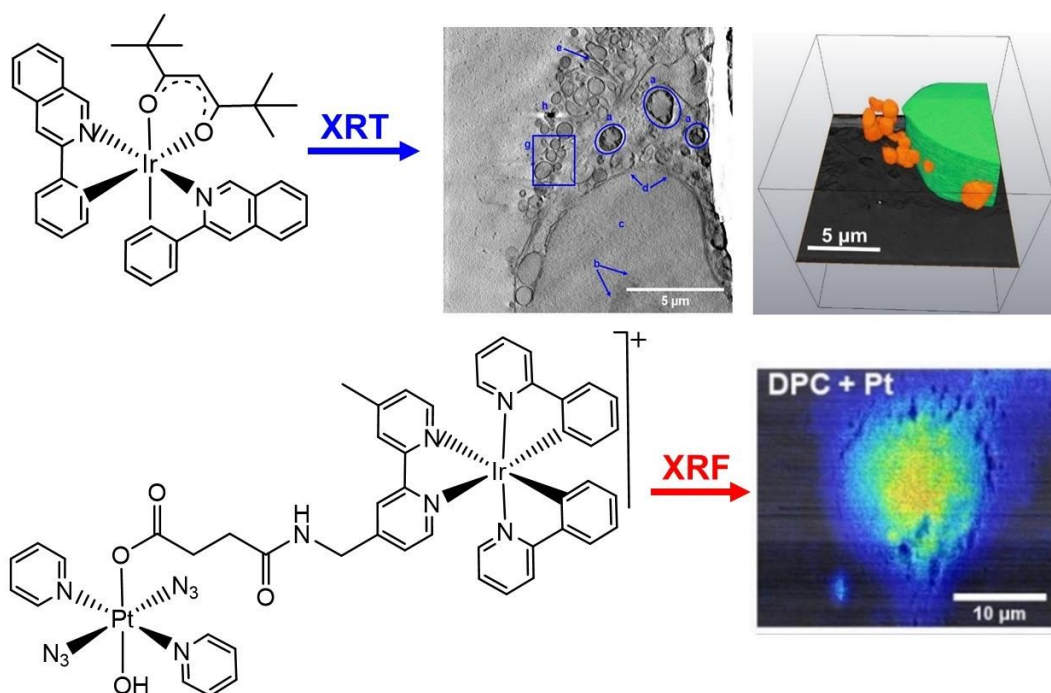
92. C. Silva, A. Nunes, E. Oreste, T. Acunha, M. Vieira and A. Ribeiro, *J Braz Chem Soc*, 2012, **23**, 1623-1629.
93. J. H. Chen, K. E. Wang and S. J. Jiang, *Electrophoresis*, 2007, **28**, 4227-4232.
94. M. F. Mesko, V. C. Costa, R. S. Picoloto, C. A. Bizzi and P. A. Mello, *J Anal At Spectrom*, 2016, **31**, 1243-1261.
95. A. L. H. Muller, P. A. Mello, M. F. Mesko, F. A. Duarte, V. L. Dressler, E. I. Muller and E. M. M. Flores, *J Anal At Spectrom*, 2012, **27**, 1889-1894.
96. F. Pellegrini, *Cliffs Quick Review: Organic Chemistry II*, Cliffs Notes, USA, 1 edn., 2011.
97. C. C. Konkankit, J. Lovett, H. H. Harris and J. J. Wilson, *Chem Comm*, 2020.
98. I. Digel, P. Kayser and G. M. Artmann, *J Biophys*, 2008, **2008**, 602870.
99. A. Ballesta, F. Billy, J. Coverdale, J.-I. Song, C. Sanchez-Cano, I. Romero-Canelón and P. Sadler, *Metallomics*, 2019, **11**, 1648-1656.
100. J. Li, L. Guo, Z. Tian, S. Zhang, Z. Xu, Y. Han, R. Li, Y. Li and Z. Liu, *Inorg Chem* 2018, **57**, 13552-13563.
101. A. L. Kiss and E. Botos, *J Cell Mol Med*, 2009, **13**, 1228-1237.
102. Y. Mosesson, G. B. Mills and Y. Yarden, *Nat Rev Cancer*, 2008, **8**, 835-850.
103. D. Gibson, *Dalton Trans*, 2016, **45**, 12983-12991.
104. L. M. Bareford and P. W. Swaan, *Adv Durg Deliv Rev*, 2007, **59**, 748-758.
105. W. Zou, X. Ma, W. Hua, B. Chen and G. Cai, *Oncol Rep*, 2015, **34**, 3256-3263.
106. A. Levina, D. C. Crans and P. A. Lay, *Coord Chem Rev*, 2017, **352**, 473-498.
107. H. U. Holtkamp, S. Movassaghi, S. J. Morrow, M. Kubanik and C. G. Hartinger, *Metallomics*, 2018, **10**, 455-462.
108. C. A. Puckett, R. J. Ernst and J. K. Barton, *Dalton Trans*, 2010, **39**, 1159-1170.
109. X. Yang and M. Page, *Oncol Res*, 1995, **7**, 619-624.
110. T. Yamagishi, S. Sahni, D. M. Sharp, A. Arvind, P. J. Jansson and D. R. Richardson, *J Biol Chem*, 2013, **288**, 31761-31771.

111. R. E. Aird, J. Cummings, A. A. Ritchie, M. Muir, R. E. Morris, H. Chen, P. J. Sadler and D. I. Jodrell, *Br J Cancer*, 2002, **86**, 1652-1657.
112. V. Novohradsky, Z. Liu, M. Vojtiskova, P. J. Sadler, V. Brabec and J. Kasparkova, *Metallomics*, 2014, **6**, 682-690.
113. J.-S. Choi, A. Maity, T. Gray and A. J. Berdis, *J Biol Chem*, 2015, **290**, 9714-9726.
114. C. A. Vock, W. H. Ang, C. Scolaro, A. D. Phillips, L. Lagopoulos, L. Juillerat-Jeanneret, G. Sava, R. Scopelliti and P. J. Dyson, *J Med Chem*, 2007, **50**, 2166-2175.
115. C. Licona, J.-B. Delhorme, G. Riegel, V. Vidimar, R. Cerón-Camacho, B. Boff, A. Venkatasamy, C. Tomasetto, P. da Silva Figueiredo Celestino Gomes, D. Rognan, J.-N. Freund, R. Le Lagadec, M. Pfeffer, I. Gross, G. Mellitzer and C. Gaiddon, *Inorg Chem Front*, 2020, **7**, 678-688.
116. E. Dolgih, C. Bryant, A. R. Renslo and M. P. Jacobson, *PLoS Comput Biol*, 2011, **7**, e1002083-e1002083.
117. A. Casini, A. Scozzafava, A. Mastrolorenzo and C. Supuran, *Curr Cancer Drug Targets*, 2002, **2**, 55-75.
118. A. K. Renfrew, N. S. Bryce and T. W. Hambley, *Chem Sci*, 2013, **4**, 3731-3739.
119. A. Ballesta, F. Billy, J. P. C. Coverdale, J.-I. Song, C. Sanchez-Cano, I. Romero-Canelón and P. J. Sadler, *Metallomics*, 2019, **11**, 1648-1656.
120. C. Bissardon, S. Reymond, M. Salome, L. Andre, S. Bayat, P. Cloetens and S. Bohic, *J Vis Exp*, 2019, **154**, e60461.
121. S. Chen, T. Paunesku, Y. Yuan, J. Deng, Q. Jin, Y. P. Hong, D. J. Vine, B. Lai, C. Flachenecker, B. Hornberger, K. Brister, C. Jacobsen, G. E. Woloschak and S. Vogt, *AIP Conf Proc*, 2016, **1696**, 20028.
122. V. Langlois, in *Comprehensive Pediatric Nephrology*, eds. D. F. Geary and F. Schaefer, Mosby, Philadelphia, 2008, pp. 39-54.
123. W. Maret, *Metallomics*, 2015, **7**, 202-211.
124. Q. Chen, J. Kang and C. Fu, *Signal Transduct Tar Ther*, 2018, **3**, 18.
125. C. C. Konkankit, B. A. Vaughn, S. N. MacMillan, E. Boros and J. J. Wilson, *Inorg Chem*, 2019, **58**, 3895-3909.
126. G. Gasser, I. Ott and N. Metzler-Nolte, *J Med Chem*, 2011, **54**, 3-25.
127. M. Zaki, S. Hairat and E. S. Aazam, *RSC Adv*, 2019, **9**, 3239-3278.

128. G. Mühlgassner, C. Bartel, W. F. Schmid, M. A. Jakupec, V. B. Arion and B. K. Keppler, *J Inorg Biochem*, 2012, **116**, 180-187.
129. J. F. Collingwood and M. R. Davidson, *Front Pharmacol*, 2014, **5**, 191.
130. T. J. Stewart, *Metallomics*, 2019, **11**, 29-49.
131. A. Mandic, J. Hansson, S. Linder and M. C. Shoshan, *J Biol Chem*, 2003, **278**, 9100-9106.
132. R. Young and S. Francis, in *Pharmacognosy*, eds. S. Badal and R. Delgoda, Academic Press, Boston, 2017, pp. 459-475.
133. B. Zhitomirsky and Y. G. Assaraf, *Oncotarget*, 2017, **8**, 45117-45132.
134. A. M. Kaufmann and J. P. Krise, *J Pharm Sci*, 2007, **96**, 729-746.
135. Y. Li, Y. Sun, L. Jing, J. Wang, Y. Yan, Y. Feng, Y. Zhang, Z. Liu, L. Ma and A. Diao, *Chemother*, 2017, **62**, 85-93.
136. L. Qin, T. Xu, L. Xia, X. Wang, X. Zhang, X. Zhang, Z. Zhu, S. Zhong, C. Wang and Z. Shen, *Drug Des Devel Ther*, 2016, **10**, 1035-1045.
137. R. Carzaniga, M. C. Domart, E. Duke and L. M. Collinson, *Methods Cell Biol*, 2014, **124**, 151-178.
138. N. Zembruksi, V. Stache, W. Haefeli and J. Weiss, *Anal Biochem*, 2012, **429**, 79-81.
139. K. Lomachenko, C. Garino, E. Gallo, D. Gianolio, R. Gobetto, P. Glatzel, N. Smolentsev, G. Smolentsev, A. Soldatov, C. Lamberti and L. Salassa, *Phys Chem Chem Phys*, 2013, **15**, 16152-16159.
140. K. Uno, Y. Notoya, T. Fujikawa, H. Yoshikawa and K. Nishikawa, *Jpn J Appl Phys*, 2005, **44**, 4073-4079.
141. A. C. Leri and B. Ravel, *J Synchrotron Radiat*, 2014, **21**, 623-626.
142. C. A. Wootton, C. Sanchez-Cano, H.-K. Liu, M. P. Barrow, P. J. Sadler and P. B. O'Connor, *Dalton Trans*, 2015, **44**, 3624-3632.

# Chapter 4

## Ir<sup>III</sup> photosensitisers in cancer cells: x-ray studies of morphology and elemental mapping



## 4.1 Introduction

In this Chapter, synchrotron cryo-X-Ray Tomography (XRT) has been used to probe the effect of a potent cyclometallated Ir<sup>III</sup> photodynamic therapy (PDT) photosensitiser (**7**, **Fig. 4.1**) on cancer cell organelles. Such studies can provide new information on cellular damage and mechanisms of cell death down to a remarkable 30-40 nm resolution. Additionally, synchrotron-XRF and differential phase contrast (DPC) imaging have been used to gain insights into the distribution, targeting and intracellular stability of a photodynamic-photochemotherapeutic Ir<sup>III</sup>-Pt<sup>IV</sup> conjugate (**8**, **Fig. 4.1**) by monitoring the L<sub>3</sub>M<sub>5</sub> XRF emissions of Ir and Pt (9.18 and 9.44 keV, respectively).

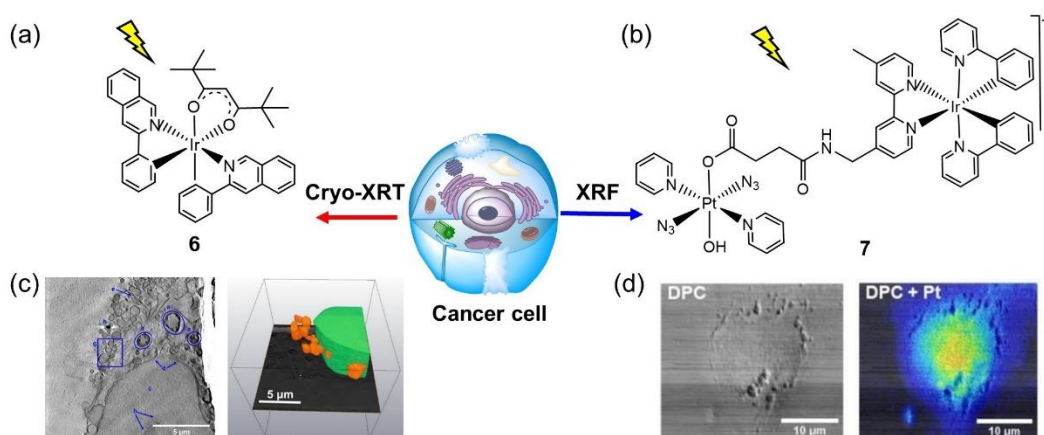


**Figure 4.1.** Graphical representation of the techniques used to investigate the intracellular mechanisms of action and cellular targets of iridium photosensitisers (**7**; **8**). (a) Structure of **7**. (b) Structure of **8** (c) Cryo-XRT of PC3 cancer cells treated with **7**. (d) XRF and DPC imaging of frozen-dehydrated A549 cancer cells treated with **8**.

PDT is a non-invasive therapeutic approach in which a non-toxic photosensitiser is irradiated locally in tumours by spatially-directed light,<sup>1</sup> often generating reactive oxygen species (ROS) and inducing cellular apoptosis.<sup>2, 3</sup> PDT photosensitisers are usually activated by longer wavelength visible light ( $\lambda=500-800$  nm).<sup>4</sup> The limited penetration depths means that use in cancer treatment is somewhat confined to light-accessible cancers such as prostate or lung cancers.<sup>5, 6</sup> The lack of photosensitiser toxicity under dark conditions, combined with the controlled activation with light may reduce unwanted patient side effects compared to conventional chemotherapeutics.<sup>7</sup>

Cyclometalated luminescent organo-iridium(III) octahedral complexes have been reported as promising photosensitisers for PDT,<sup>8-10</sup> and have been shown to induce oxidative attack on proteins in cancer cells upon irradiation with light.<sup>11</sup> The photophysical properties of such complexes mediates their PDT efficiency: fast singlet to triplet intersystem crossing (ISC) allows longer excited state lifetimes, leading to high yields of toxic ROS and singlet oxygen (<sup>1</sup>O<sub>2</sub>).<sup>12</sup> In particular, [Ir(C,N)<sub>2</sub>(O,O)] (**7**, where C,N=2-phenylpyridine and O,O=diketone; **Fig. 4.2**) has a moderate phosphorescent lifetime ( $\tau_p=59$  ns,  $\lambda_{ex}=458$  nm;  $\lambda_p=620$  nm) which promotes the generation of toxic <sup>1</sup>O<sub>2</sub> in carcinoma cells through energy transfer.<sup>11</sup> In addition, oxidative stress induced by **7** in cancer cells was shown to increase the expression of glycolytic enzymes (including aldehyde dehydrogenase),<sup>11</sup> suggesting a cellular dependency on glucose metabolism.

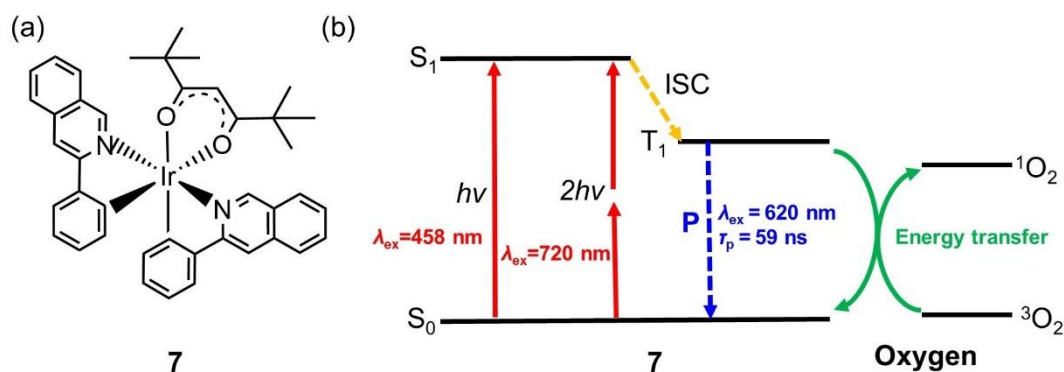


**Figure 4.2.** (a) Structure of **7**. (b) Jablonski diagram showing the one- and two-photon excitation of **7** in the presence of oxygen: (i)  $h\nu$ =photon energy required for irradiation, (ii)  $S_0$ =singlet ground state; (iii)  $S_1$ =singlet excited state; (iv)  $T_1$ =triplet excited state; (v) ISC=intersystem crossing; (vi) P=phosphorescence.

The conjugation of cyclometalated Ir<sup>III</sup> complexes with additional metal modalities may significantly improve the antiproliferative activity and other pharmacokinetic factors, which has been shown for various photoactivatable di-iridium and di-platinum complexes.<sup>13-15</sup> The combination of a photosensitiser (PDT) with a photoactivatable drug (PACT) in the same compound may improve the antiproliferative activity by providing a dual mechanism of action, and improving factors such as solubility, pharmacokinetics and cell uptake. In 2020, the Sadler group reported the synthesis of a Ir<sup>III</sup>-Pt<sup>IV</sup> conjugate with the formula *trans, trans*,



*trans*-[Pt<sup>IV</sup>(py)<sub>2</sub>(N<sub>3</sub>)<sub>2</sub>(OH)(OOCCH<sub>2</sub>CH<sub>2</sub>CONHCH<sub>2</sub>)-Ir<sup>III</sup>(bpy)<sub>2</sub>]Cl (**8**, where py=pyridine, N<sub>3</sub>=azide, OH=hydroxyl, bpy=bipyridine), which is comprised of a cyclometalated Ir<sup>III</sup> photosensitizer conjugated to a diazido-Pt<sup>IV</sup> complex (**Fig. 4.2**).<sup>16</sup> Diazido-Pt<sup>IV</sup> PACT complexes show promising antiproliferative activity towards a variety of cancer cells upon irradiation with blue light (465 nm).<sup>17-21</sup> Some cyclometallated iridium complexes have limited aqueous solubility and dark cytotoxicity (owing to their increased lipophilicity) and are highly oxygen-dependent. In contrast, diazido-Pt<sup>IV</sup> compounds exhibit high dark stability and can release toxic radicals and O<sub>2</sub> upon photoactivation.<sup>18</sup> Combining these modalities may improve the solubility, lower the dark cytotoxicity and overcome the hypoxic-limitations of Ir<sup>III</sup> photosensitisers (by utilising O<sub>2</sub> release from diazido-Pt<sup>IV</sup> complexes for PDT),<sup>22</sup> providing a synergistic mechanism of action.

Interestingly, combining these Ir<sup>III</sup>-PDT and Pt<sup>IV</sup>-PACT agents together significantly enhanced the photocytotoxicity compared to their mono-metal analogues. Photoactivated complex **8** can oxidize NADH to NAD<sup>+</sup> *via* radical formation (•NAD) and can generate ROS inside cancer cells, causing severe damage to cell nuclei.<sup>21</sup> The mechanism of action of **8** has previously been probed using LC-MS through reactions with 5'-guanine monophosphate (GMP, a model DNA base) upon irradiation with indigo light.<sup>21</sup> This revealed the formation of platinum - but not iridium-GMP adducts – implying the cell nucleus may not be a predominant target for the iridium moiety. Since **8** is luminescent ( $\lambda_{\text{ex/em}}$ =405/460-560 nm), the cellular accumulation in A549 cells was monitored by confocal microscopy (using conventional fluorophores), revealing the predominant localisation in the cytoplasm.<sup>21</sup>

This Chapter utilises cryo-XRT to probe the effects of a cyclometallated Ir<sup>III</sup> photosensitiser (**7**) on cellular organelles in cryopreserved PC3 prostate cancer cells – as close to their native state as possible. Separately, the intracellular stability, distribution and localisation of the potent Ir<sup>III</sup>-Pt<sup>IV</sup> conjugate (**8**) in frozen-dried A549 lung cancer cells was probed using nano-focussed synchrotron-XRF and DPC imaging, to gain insights into the intracellular stability and localisation of both the Ir and Pt metal centres.

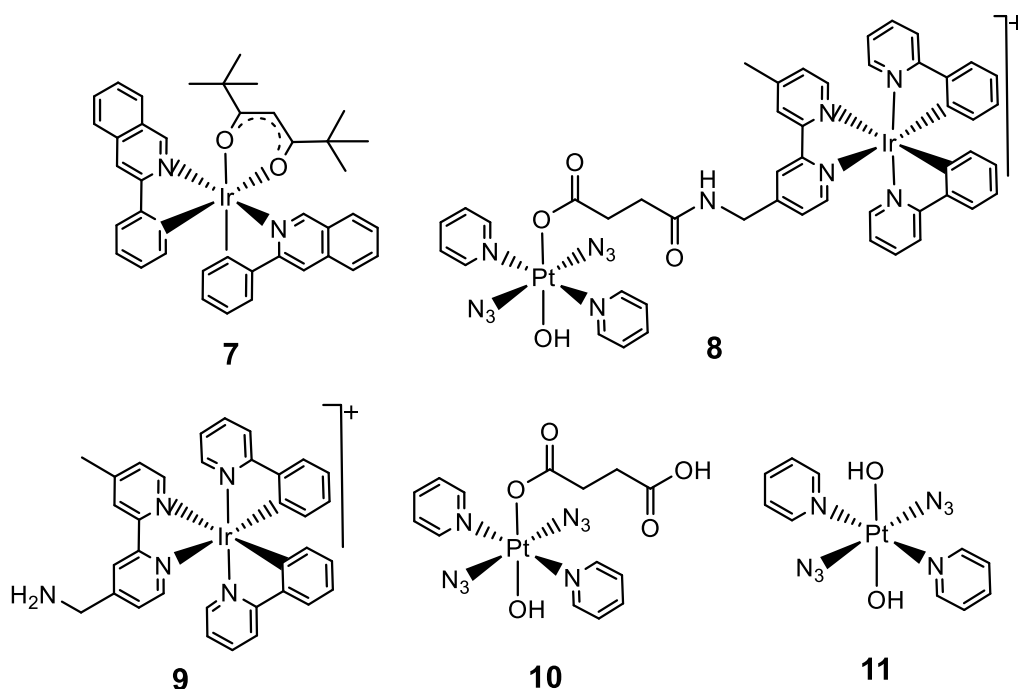


**Figure 4.3.** Chemical structures of complexes **7-11** investigated in this Chapter. The complexes investigated by synchrotron techniques are **7** (Cryo-XRT) and **8** (synchrotron-XRF and DPC imaging).

## 4.2 Experimental

### 4.2.1 Antiproliferative activity (IC<sub>50</sub>)

The half-maximal inhibitory concentration (IC<sub>50</sub>/ μM) of **7** was determined in PC3 (prostate) cancer cells. Cells were treated with **7** for 2 h (protected from the light), washed with PBS and complex-free medium was added. Plates were then irradiated (λ=465 nm, 4.8 mW/cm<sup>2</sup>) or kept in the dark for 10 min, before incubation for 24 h protected from light (310 K, 5% CO<sub>2</sub>). Cell viability was determined using the SRB protocol (**Chapter 2, Section 2.5.1**).

IC<sub>50</sub> concentrations of **8-11** were determined by Dr. Huayun Shi and Dr. Huaiyi Huang (University of Warwick).<sup>21</sup> A549 (lung) cancer cells were treated with **8-11** for 1 h followed by 1 h exposure to blue light (λ=465 nm, 4.8 mW/cm<sup>2</sup>) or kept in the dark, before 24 h recovery in complex-free medium (310 K, 5% CO<sub>2</sub>). Cell viability was determined using the SRB protocol (**Chapter 2, Section 2.5.1**).

#### 4.2.2 Cryo-XRT at B24 Beamline (DLS, Oxford)

##### Preparation of TEM grids for cryo-XRT

Quantifoil Au-C R2/2 F1 200 mesh finder grids were irradiated with UV light for 20 min (**Chapter 2, Section 2.6.2**) and  $1 \times 10^5$  PC3 cells/well were seeded, and incubated for 24 h (310 K, 5% CO<sub>2</sub>). Cells were treated with 0 or 1  $\mu$ M of **7** for 2 h, then washed with PBS followed by either (i) irradiation (10 min, 465 nm, 4.8 mW/cm<sup>2</sup>), or (ii) kept in the dark (10 min), before a 24 h recovery period in complex-free media (protected from light). The medium was removed, and cells washed with PBS ( $\times 2$ ) followed by sterile water ( $\times 1$ ). Fiducials (AuNP, d=250 nm, *ca.*  $3.5 \times 10^7$  particles in 10  $\mu$ L) were added to each grid, before blotting with pin filter paper and plunge-freezing in 30% liquid propane:ethane mixture using an in-house manufactured plunge-freezer (**Chapter 2, Section 2.3.6**). Samples were stored in liquid nitrogen (110 K) until cryo-XRT analysis at the B24 beamline.

##### Fluorescence mapping of TEM grids

Preliminary correlative microscopy analysis of cryopreserved grids was performed on a Zeiss Axioimager M2 fitted with a Linkam Scientific cryostage by monitoring the fluorescence of MitoTracker Red ( $\lambda_{\text{ex/em}}$ =647/665 nm) and the phosphorescence of **7** ( $\lambda_{\text{ex/em}}$ =458/620 nm) using the YFP and GFP filters, respectively.

##### Sample loading onto the beamline

Up to four pre-mapped quantifoil grids were loaded into the sample holder at B24 beamline under cryogenic conditions (110 K). Initial 2D inspection was performed by generating a mosaic (consecutive images stitched together) of a  $100 \times 100 \mu\text{m}^2$  regions using short x-ray exposure (0.5 s, 500 eV) in continuous acquisition mode (Pixis, XO 1024B; Princeton Scientific; **Chapter 2, Section 2.4.2**). The view was brought into focus by monitoring the positions of lipid droplets or fiducials at  $-30^\circ$  and  $+30^\circ$  sample tilt angles and the depth altered by moving the zone plate objective. Once focussed, the tilt limit was identified by rotating the sample to no more than  $-70^\circ$  and  $+70^\circ$ , respectively. Depending on sample thickness, varying x-ray exposure times were required to collect tomograms (**Table 4.1**).

**Table 4.1.** Summary of the x-ray exposure times used for different samples at high ( $< -30^\circ$ ,  $> +30^\circ$ ) and low tilt angles ( $0^\circ$ ).

Conditions	High tilt exposure (s)	Low tilt exposure (s)
Untreated (Dark) control	6	3
Untreated (465 nm) control	2	1
<b>7 (Dark)</b>	4	2
<b>7 (465 nm)</b>	8	4

### Tomogram reconstruction in IMOD

Tomograms were aligned and reconstructed manually by registering the positions of AuNP fiducials ( $d=250$  nm) using IMOD imaging software,<sup>23</sup> as described in **Chapter 2 (Section 2.6.2)**. Representative tomograms for each condition were selected for further 3D analysis: (i) **T1** (untreated, dark); (ii) **T2** (untreated, 465 nm); (iii) **T3** (**7**, dark); (iv) **T4** (**7**, 465 nm).

### 3D segmentation and visualization

The mitochondria and nuclei in each representative (reconstructed) tomograms (**T1-4**) were volume segmented using SuRVoS imaging software to determine average mitochondrial volumes ( $\mu\text{m}^3$ ) per tomogram (**Chapter 2, Section 2.6.2**).<sup>24</sup> The segmented tomograms were visualised in Amira (FEI/Thermo Scientific, The Netherlands, 2016), and 3D videos were generated (**Chapter 2, Section 2.6.2**).

### 4.2.3 Synchrotron-XRF at I14 Beamline (DLS, Oxford)

#### Preparation of Si<sub>3</sub>N<sub>4</sub> membranes for XRF

Silicon nitride (Si<sub>3</sub>N<sub>4</sub>) membranes were prepared as described in **Chapter 2** (**Section 2.6.1**) using a seeding density of *ca.* 7×10<sup>4</sup> cells/mL of A549 cells. Following an incubation period, A549 cells were treated with 500 µM of **8** (dark IC<sub>50</sub>>100 µM) for 2 h under dark conditions. The supernatant medium was removed and cells washed with HBSS (2 mL/well).

#### Beamline settings

XRF data were acquired at I14 beamline (DLS, Oxford) using a beam size=75×47 nm<sup>2</sup>; incident energy=12.5 keV and step size=100 nm. Differential phase contrast (DPC) imaging was simultaneously performed using a Merlin Quad detector (Quantum Detectors, UK). Data were fitted using the PyMCA software developed by the ESRF,<sup>25</sup> assuming a cell thickness of 6 µm.<sup>26</sup> Fitted data were analysed in ImageJ software.<sup>27</sup> All other information is specified in **Chapter 2** (**Section 2.4.1** and **Section 2.6.2**).

## 4.3 Results

### 4.3.1 Cryo-XRT of PC3 cells treated with **7**

#### Fluorescence microscopy

The antiproliferative activity (IC<sub>50</sub> / µM) of **7** was determined in PC3 prostate cancer cells under dark (protected from light) and blue light (direct irradiation, λ=465 nm) conditions using the SRB assay. Under dark conditions (2 h), **7** was inactive (IC<sub>50</sub>>100 µM), however, upon irradiation with blue light (10 min, 465 nm) the IC<sub>50</sub> was determined to be 6±1 µM. Fluorescence microscopy imaging was used to locate cryopreserved cells on the TEM grids by monitoring the red fluorescence of MitoTracker Red (λ<sub>ex/em</sub>=581/644 nm) using the YFP filter (**Fig. 4.4**). Subsequently, suitable cell candidates for cryo-XRT were identified.

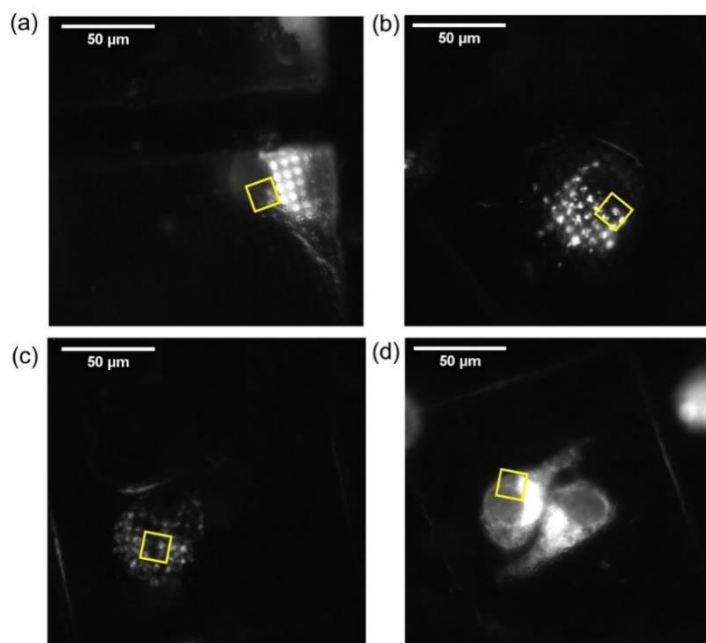


**Figure 4.4.** Microscopy images of cryopreserved PC3 cells grown on carbon-gold TEM grids treated with **7** (0 or 1  $\mu\text{M}$ ) for 2 h (protected from light), followed by 10 min exposure to (i) dark conditions or (ii) blue light conditions (465 nm, 4.8  $\text{mW}/\text{cm}^2$ ), before 24 h recovery (complex-free media). Images were recorded on a Zeiss Axioimager M2 coupled to a Linkam cryostage, monitoring the fluorescence of MitoTracker Red ( $\lambda_{\text{ex/em}}=581/644$  nm): (a) Untreated control (10 min, dark); (b) Untreated control (10 min, 465 nm); (c) Treated with **7** (1  $\mu\text{M}$ , dark); (d) Treated with **7** (1  $\mu\text{M}$ , 10 min, 465 nm). Images were generated in ImageJ software.<sup>27</sup> The yellow box indicates the  $15.8 \times 15.8 \mu\text{m}^2$  region of interest mapped by cryo-XRT.

Faint green fluorescence was observed in cells treated with **7** upon blue light exposure ( $\lambda_{\text{ex}}=465$  nm, **Fig. 4.5**) when using the GFP microscopy filter ( $\lambda_{\text{ex/em}}=488/510$  nm). This was attributed to the tail of the phosphorescence emission band of **7** (deep-red emission,  $\lambda_{\text{p}}=620$  nm).<sup>11</sup> Green fluorescence was not observed for the untreated PC3 cells. An overlay of brightfield, red-fluorescent microscopy images allowed the determination of suitable PC3 cancer cell candidates for cryo-XRT. Grid samples were cryogenically loaded into the autosampler chamber at the B24 beamline (DLS, Oxford) and transferred to the x-ray microscope, where they were maintained under cryogenic conditions (liquid nitrogen, 110 K) throughout cryo-XRT data acquisition.

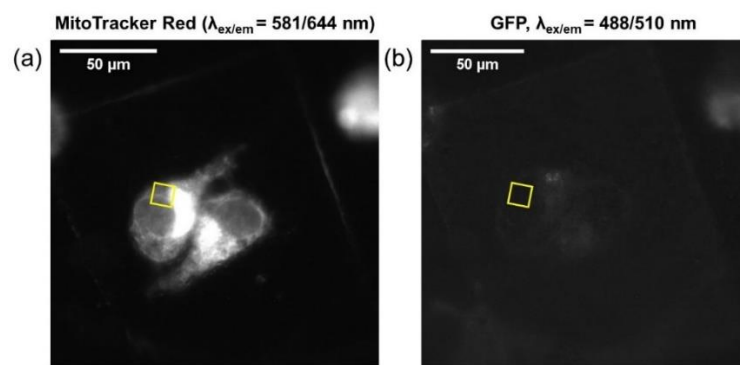


**Figure 4.5.** Microscopy images of two cryopreserved PC3 cells (**Figure 4.3, d**) treated with **7** (1  $\mu\text{M}$ ) for 2 h (protected from light), followed by exposure to blue light (465 nm, 10 min, 4.8  $\text{mW}/\text{cm}^2$ ) and 24 h recovery (complex-free media, protected from light). Images were recorded on a Zeiss Axioimager coupled to a Linkam cryostage, monitoring the phosphorescence of **7** ( $\lambda_{\text{p}}=620$  nm) using the GFP filter ( $\lambda_{\text{ex/em}}=488/510$  nm). The yellow box indicates the  $15.8 \times 15.8 \mu\text{m}^2$  region of interested mapped by cryo-XRT.

### X-ray tomography

Cryo-XRT can be used to gain ultrastructural information on cancer cells in 3D as close to their native physiological state, avoiding the use of chemical fixatives.<sup>28, 29</sup> X-ray tomograms were obtained using soft x-rays (500 eV), producing contrast between carbon-containing structures and natural ice on the sample. Cryopreserved PC3 cells treated with  $1/6^{\text{th}} \times$  irradiated  $\text{IC}_{50}$  of **7** were analysed under both dark and irradiated ( $\lambda=465$  nm) conditions by cryo-XRT at B24 (**Table 4.2**).

**Table 4.2.** Summary of the tomograms of cryopreserved PC3 cells treated with 0 or 1  $\mu\text{M}$  of **7** for 2 h, followed by 10 min in the dark or irradiated with blue light (465 nm, 4.8  $\text{mW}/\text{cm}^2$ ) and 24 h recovery in complex-free media (protected from light).

Tomogram number	Conditions	Figure	Video
<b>T1</b>	Untreated (Dark)	<b>4.6</b>	C4_Video_T1
<b>T2</b>	Untreated (465 nm)	<b>4.7</b>	C4_Video_T2
<b>T3</b>	<b>7</b> (Dark)	<b>4.8</b>	C4_Video_T3
<b>T4</b>	<b>7</b> (465 nm)	<b>4.9</b>	C4_Video_T4
<b>T5</b>	Untreated (Dark)	<b>Appendix A13</b>	C4_Video_T5
<b>T6</b>	<b>7</b> (Dark)	<b>Appendix A14</b>	C4_Video_T6
<b>T7</b>	<b>7</b> (Dark)	<b>Appendix A15</b>	C4_Video_T7
<b>T8</b>	<b>7</b> (Dark)	<b>Appendix A16</b>	C4_Video_T8
<b>T9</b>	<b>7</b> (465 nm)	<b>Appendix A17</b>	C4_Video_T9
<b>T10</b>	<b>7</b> (465 nm)	<b>Appendix A18</b>	C4_Video_T10

### Untreated control (dark)

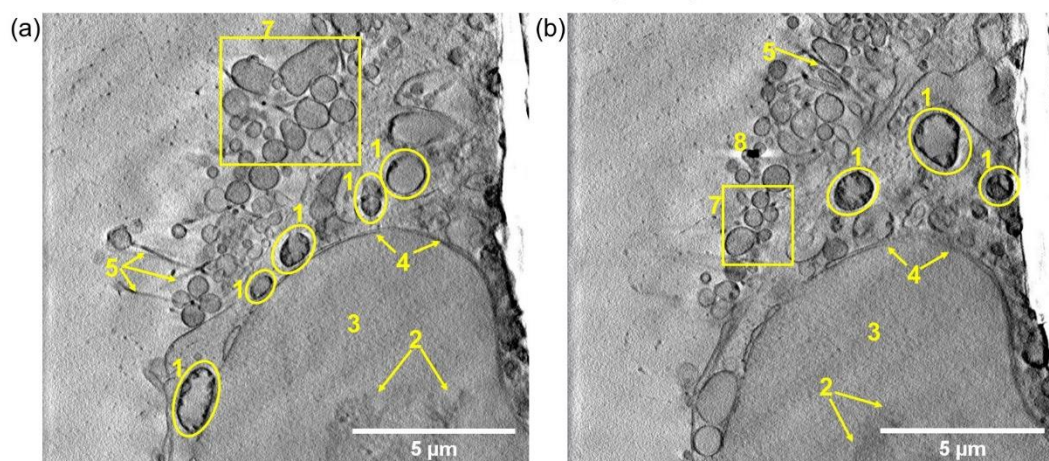


**Figure 4.6.** 2D projections of a reconstructed x-ray tomogram ( $15.8 \times 15.8 \mu\text{m}^2$ ) showing cellular and organelle morphology of a cryopreserved PC3 cell grown on carbon-gold TEM grid under dark conditions (protected from light) followed by 24 h recovery in complex-free medium (310 K, 5%  $\text{CO}_2$ ; **T1**, **C4\_Video\_T1**). Images were generated in IMOD software.<sup>23</sup> Two different sample views (tilt angles): (a)  $0^\circ$ ; (b)  $+28^\circ$ , showing 1. mitochondria, 2. nucleolus, 3. nucleus, 4. nuclear membrane, 5. features of lamellipodium, 6. plasma membrane, 7. spherical vesicles, 8. AuNP fiducials ( $d=250 \text{ nm}$ ).

### Untreated control (465 nm)

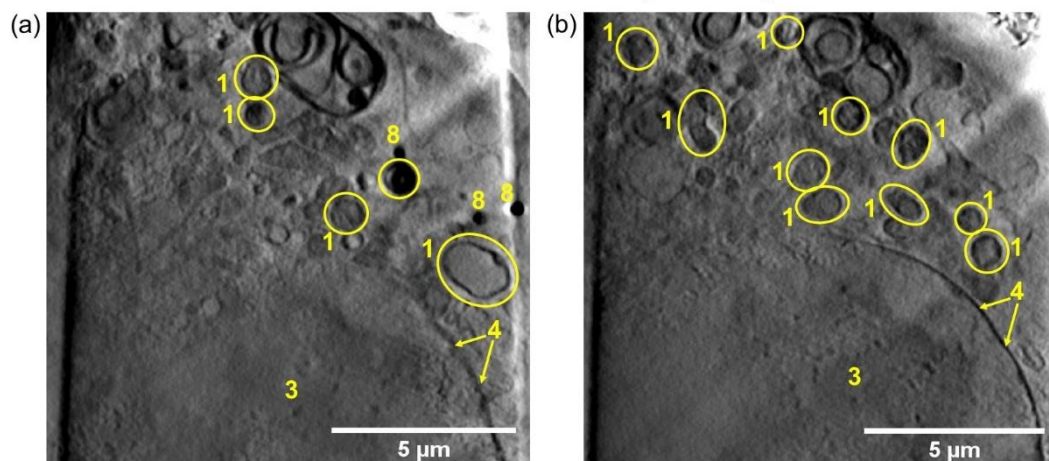


**Figure 4.7.** 2D projections of a reconstructed x-ray tomogram ( $15.8 \times 15.8 \mu\text{m}^2$ ) showing cellular and organelle morphology of a cryopreserved PC3 cell grown on carbon-gold TEM grid under dark conditions and irradiated for 10 min followed by 24 h recovery in complex-free medium (310 K, 5%  $\text{CO}_2$ ; **T2**, **C4\_Video\_T2**). Images were generated in IMOD software,<sup>23</sup> showing two different sample views (tilt angles): (a)  $0^\circ$ ; (b)  $+8^\circ$ , showing 1. mitochondria, 2. nucleolus, 3. nucleus, 4. nuclear membrane, 5. features of lamellipodium, 6. plasma membrane, 7. spherical vesicles, 8. AuNP fiducials ( $d=250 \text{ nm}$ ).



**1  $\mu\text{M}$  of 6 (dark)**

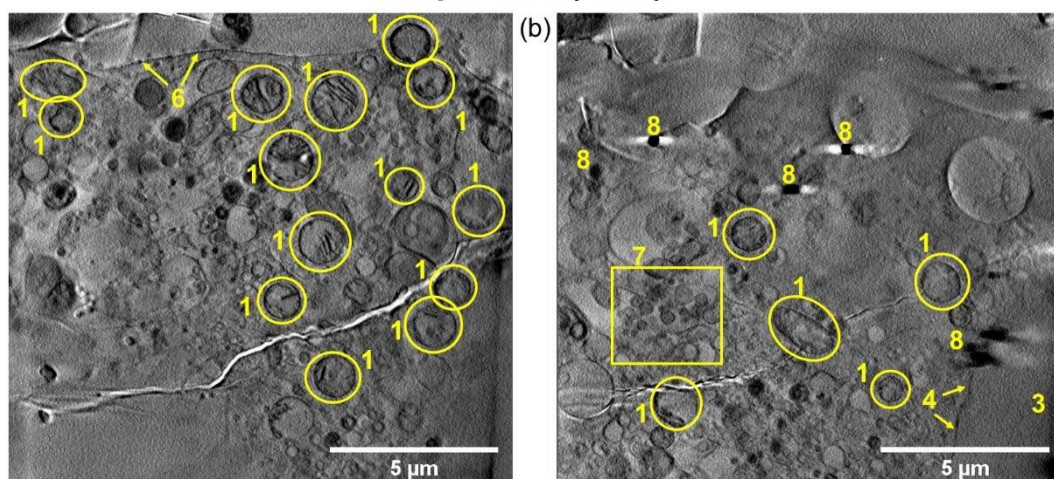


**Figure 4.8.** 2D projections of a reconstructed x-ray tomogram ( $15.8 \times 15.8 \mu\text{m}^2$ ) showing cellular and organelle morphology of a cryopreserved PC3 cell grown on carbon-gold TEM grid and treated with **7** ( $1 \mu\text{M}$ ) for 2 h (protected from the light), followed by 24 h recovery in complex-free medium (310 K, 5%  $\text{CO}_2$ ; **T3**, **C4\_Video\_T3**). Images were generated in IMOD software,<sup>23</sup> showing two different sample views (tilt angles): (a)  $0^\circ$ ; (b)  $+54^\circ$ , showing 1. mitochondria, 2. nucleolus, 3. nucleus, 4. nuclear membrane, 5. features of lamellipodium, 6. plasma membrane, 7. spherical vesicles, 8. AuNP fiducials ( $d=250 \text{ nm}$ ).

**1  $\mu\text{M}$  of 6 (465 nm)**

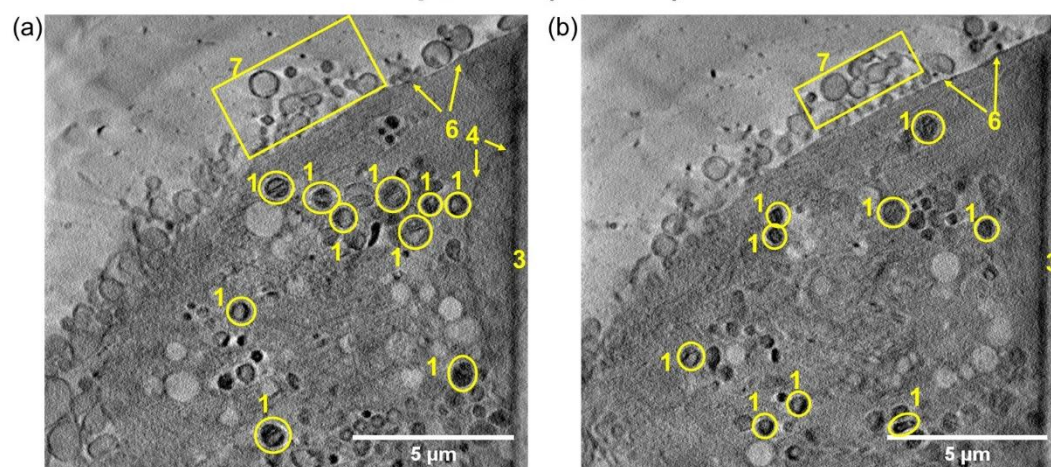


**Figure 4.9.** 2D projections of a reconstructed X-ray tomogram ( $15.8 \times 15.8 \mu\text{m}^2$ ) showing cellular and organelle morphology of a cryopreserved PC3 cell grown on carbon-gold TEM grid and treated with **7** ( $1 \mu\text{M}$ ) for 2 h (protected from the light), 10 min irradiation (465 nm) followed by 24 h recovery in complex-free medium (310 K, 5%  $\text{CO}_2$ ; **T4**, **C4\_Video\_T4**). Images were generated in IMOD software,<sup>23</sup> showing two different sample views (tilt angles):  $0^\circ$ ; (b)  $+10^\circ$ , showing 1. mitochondria, 2. nucleolus, 3. nucleus, 4. nuclear membrane, 5. features of lamellipodium, 6. plasma membrane, 7. spherical vesicles, 8. AuNP fiducials ( $d=250 \text{ nm}$ ).

Prior to cryo-XRT analysis, short bursts of x-rays (0.5 s; 500 eV; 40×40 nm<sup>2</sup> spot size) were used to identify regions of interest (15.8×15.8 μm<sup>2</sup>) within individual PC3 cells (2D projections). For the four conditions analysed, a total of 10 tomograms were obtained and manually reconstructed in IMOD imaging software.<sup>23</sup> One tomogram for each condition is presented in this Chapter (**T1-4**, **Fig. 4.6-9**), with the additional tomograms presented in **Appendix (Fig. A13-18)**. Mitochondria can be identified by their ellipsoidal shape and the presence of cristae (**T1**, **Fig. 4.6**), and features of *lamelipodia* (flat cellular protrusions) affiliated with vesicle-shedding at the plasma membrane are visible in the tomograms (**T1**, **Fig. 4.6**; **Appendix, Fig. A13**). Analysis of the tomograms demonstrated that irradiation with blue light (465 nm, 10 min) in the absence of complex **7** did not significantly alter the morphology of native PC3 cells when compared to cells exposed to dark conditions: revealing defined cell nuclei, and similarities in cytoplasmic organelles (**T2**, **Fig. 4.7**).

PC3 cells treated with 1 μM of **7** (**T3**, **Fig. 4.8**; **Appendix, Fig. A14-16**) and under dark conditions (non-irradiated and protected from light) revealed organelle morphologies comparable to those of the untreated cells in the dark (**T1**, **Fig. 4.6**; **Appendix, Fig. A13**) or blue light (**T2**, **Fig. 4.7**) conditions. Tomograms in the latter showed uncompromised plasma membranes, vesicle-shedding, *lamellopodia*, well-defined nuclei and unambiguous mitochondria. In contrast, cells treated with 1 μM of **7** and exposed to blue light (**T4**, **Fig. 4.9**; **Appendix, Fig. A17-18**) revealed significant morphological differences in organelles compared to the treated cells under dark conditions. The size of mitochondria in cells treated with **7** under photo-conditions appeared significantly smaller, and severe membrane-blebbing was observed. To further probe the mitochondrial damage induced by **7** (upon blue light exposure), 3D volume segmentation of individual mitochondria in **T1-4** was performed using SuRVoS imaging software.<sup>24</sup> It must also be noted that samples treated with **7** (regardless of the photo-conditions) were significantly darker in appearance, likely due to increased x-ray absorption caused by the presence of Ir in the samples. Consequently, longer x-ray exposure times at high tilt angles were required to obtain tomographic information (6-8 s, for **T3-4**).

### 3D segmentation and visualisation

The 3D volumes of mitochondria and cell nuclei were segmented from tomograms **T1-4** using SuRVoS imaging software (**Fig. 4.6-9**),<sup>24</sup> and visualized using Amira (**Fig. 4.10**). Total numbers of mitochondria per tomogram ( $15.8 \times 15.8 \mu\text{m}^2$ ) were determined: (i) **T1**=14; (ii) **T2**=20; (iii) **T3**=26; (iv) **T4**=19), and individual mitochondrial volumes ( $\mu\text{m}^3$ ) in each tomogram were calculated (**Fig. 4.11**; **Appendix, Table A26**). Statistical analysis was performed using Welch's unpaired t-test (assuming unequal sample variance) which revealed significant reductions in mitochondrial size in the cell treated with **7** under photo-irradiation conditions (**T4**), compared to both untreated controls (**T1-2**;  $p < 0.05$  and  $p < 0.01$ , respectively) and cells treated with **7** under dark conditions (**T3**;  $p < 0.001$ ), as shown in **Fig. 4.11**.

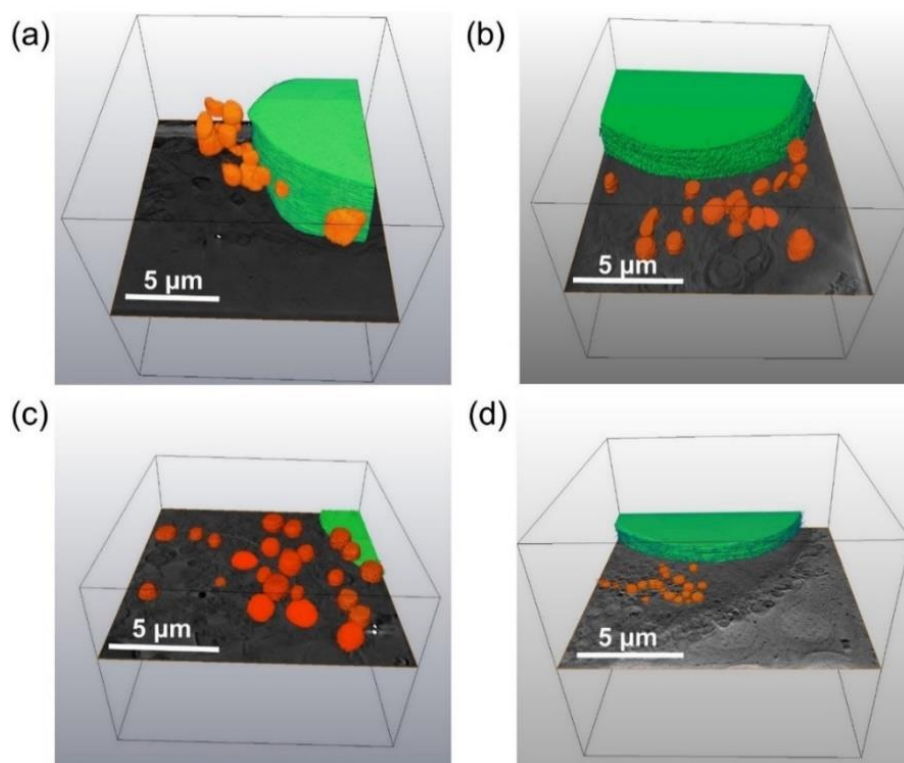


**Figure 4.10.** 3D projections of segmented tomograms (**T1-4**) showing the mitochondria (■) and nuclei (■) of cryopreserved PC3 cells grown on carbon-gold TEM grids. (a) Untreated controls under dark conditions (**T1**, **C4\_Video\_T1\_Seg**). (b) Untreated controls exposed 10 min blue light irradiation (465 nm; **T2**, **C4\_Video\_T2\_Seg**). (c) Treated with 1  $\mu\text{M}$  of **7** under dark conditions (2 h, followed by 24 h recovery period; **T3**, **C4\_Video\_T3\_Seg**). (d) Treated with 1  $\mu\text{M}$  of **7** under irradiated conditions (2 h + 10 min 465 nm, 24 h recovery period; **T4**, **C4\_Video\_T4\_Seg**).

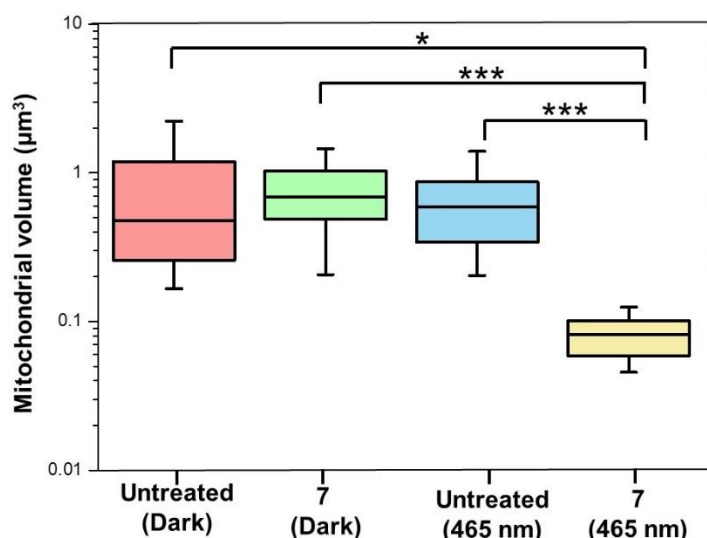


**Figure 4.11.** Comparison of the calculated mitochondrial size ( $\mu\text{m}^3$ ) in cryopreserved PC3 cells treated with 0 or 1  $\mu\text{M}$  (**T1-4**) of **7** for 2 h, and exposed to 10 min in the dark (protected from light) or irradiation (blue light, 465 nm), followed by 24 h recovery in complex-free media (310 K, 5%  $\text{CO}_2$ ). Statistical analysis was performed using Welch's unpaired t-test, revealing statistically smaller mitochondrial volumes in **T4**, compared to the untreated controls (**T1-2**, \*  $p < 0.05$  and \*\*  $p < 0.01$ ) and **7** under dark conditions (**T3**, \*\*\*  $p < 0.001$ ).

### 4.3.2 Synchrotron-XRF of A549 cells treated with **8**

The antiproliferative activities ( $\text{IC}_{50}$  /  $\mu\text{M}$ ) of complexes **8-11** (Table 4.3) were determined by Dr. Huayun Shi and Dr. Huaiyi Huang (University of Warwick).<sup>21</sup>

**Table 4.3.** Antiproliferative activities ( $\text{IC}_{50}$  /  $\mu\text{M}$ ) in A549 (lung) cancer cells treated with **8-11** and **cisplatin** as determined using the SRB assay.

Complex	$\text{IC}_{50}/\mu\text{M}$ (dark) <sup>[a]</sup>	$\text{IC}_{50}/\mu\text{M}$ (irradiated) <sup>[b]</sup>	Photocytotoxicity index (PI) <sup>[c]</sup>
<b>8</b>	>100	3.5±0.1	>28.5
<b>9</b>	>100	20.2±2.3	>4.9
<b>10</b>	>100	n.d.	n.d.
<b>11</b> <sup>[d]</sup>	>100	51.9±2.5	>1.9
<b>Cisplatin</b>	>100	>100	n.d.

<sup>[a]</sup> 2 h drug exposure followed by 24 h recovery in drug-free medium. <sup>[b]</sup> 1 h drug exposure, 1 h irradiation (465 nm, 4.8  $\text{mW}/\text{cm}^2$ ) and 24 h recovery in drug-free medium. <sup>[c]</sup> Photocytotoxicity indexes (PI) as determined by comparing the antiproliferative activities under dark and irradiated (465 nm) conditions. <sup>[d]</sup> Literature  $\text{IC}_{50}$  values.<sup>21</sup>



### Cell morphology, co-localization and quantification

Synchrotron-XRF was used to probe the intracellular localisation, distribution and stability of **8** in A549 lung cancer cells. A population of A549 cells were grown on Si<sub>3</sub>N<sub>4</sub> membranes and treated with **8** (500  $\mu$ M, IC<sub>50</sub>>100  $\mu$ M) for 2 h under dark conditions (protected from light), before cryo-fixation (liquid ethane) and freeze-drying. Unfortunately, cells treated with **8** under blue light conditions could not be mapped by synchrotron-XRF due to poor sample quality (poorly preserved and damaged cells), but nonetheless, information on the dark stability and distribution of **8** was obtained. The Ir (L<sub>3</sub>M<sub>5</sub>=9.18 keV) and Pt (L<sub>3</sub>M<sub>5</sub>=9.44 keV) emissions were monitored by synchrotron-XRF using an incident energy of 12.5 keV.<sup>30</sup> A total of 6 elemental maps of cells were obtained: (i) Untreated A549 cells (**C1-3**, **Fig. 4.12**); (ii) treated with **8** (**C4-6**, **Fig. 4.13**). The XRF maps of K, P, S and Zn were used to locate cells on the membrane using XRF, as previously described (**Chapter 3**).

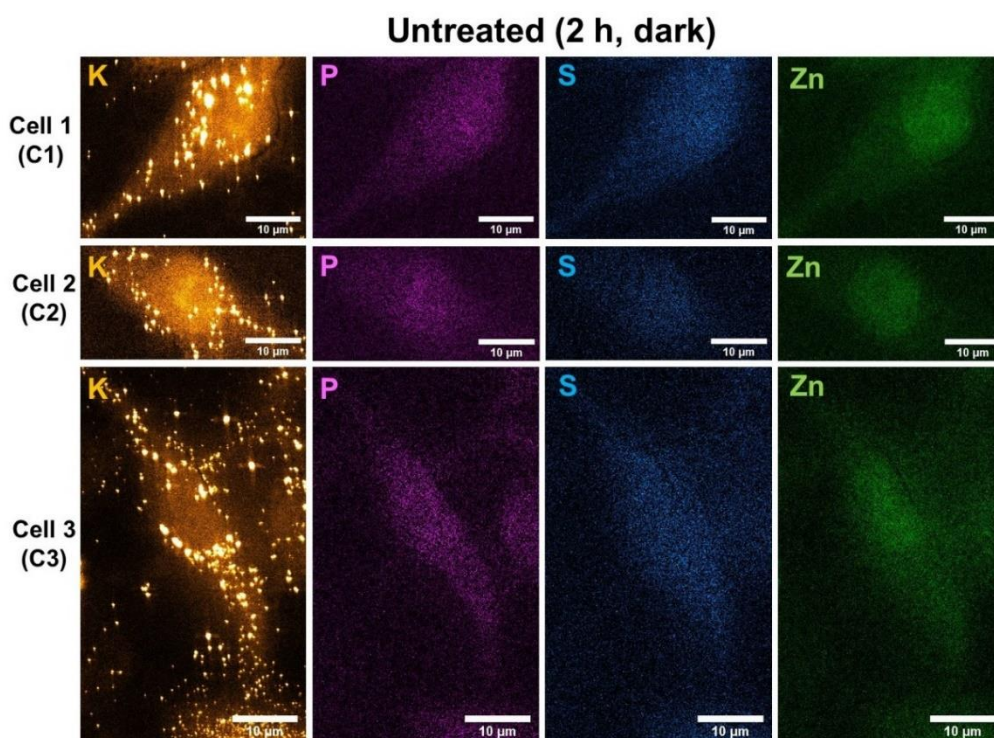


**Figure 4.12.** Synchrotron-XRF elemental maps of cryo-fixed and freeze-dried A549 cells grown on a Si<sub>3</sub>N<sub>4</sub> membrane (**C1-3**) exposed to 1 h irradiation (465 nm) as obtained using an incident energy of 12.5 keV: K (■), P (■), S (■) and Zn (■).<sup>30</sup> Note that the observed spots in the K maps are likely due to K from residual HBSS (contains KCl) prior to plunge-freezing. Data were acquired using 15 keV energy, 0.1 s exposure, 100 nm step size with *ca.* 50×70 nm<sup>2</sup> beam size. Data were analysed in PyMCA software,<sup>25</sup> and images generated in ImageJ.<sup>27</sup>

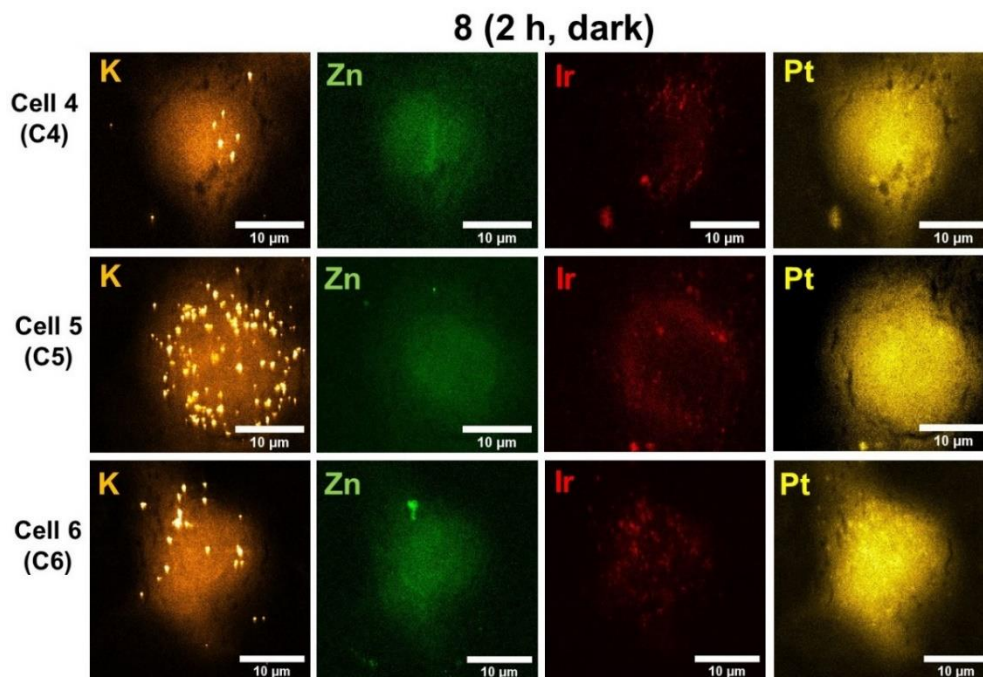


**Figure 4.13.** Synchrotron-XRF elemental maps of cryo-fixed and freeze-dried A549 cells (C4-6) grown on a Si<sub>3</sub>N<sub>4</sub> membrane and treated with 5×IC<sub>50</sub> (500 µM) **8** for 2 h under dark conditions as obtained using incident energy 12.5 keV: K (■), Zn (■), Ir (■) and Pt (■).<sup>30</sup> Note that the observed spots in the K maps are likely due to K from residual HBSS (contains KCl) prior to plunge-freezing. Data were acquired using 15 keV energy, 0.1 s exposure, 100 nm step size with *ca.* 50×70 nm<sup>2</sup> beam size. Data were analysed in PyMCA software,<sup>25</sup> and images generated in ImageJ.<sup>27</sup>

The untreated cells (C1-3, Fig. 4.12) showed elongated morphologies typical of healthy A549 cells,<sup>31-33</sup> with cell nuclei identified by the highly-concentrated intracellular Zn. The mean cell area (µm<sup>2</sup>) of the untreated cells was determined to be 438±82 µm<sup>2</sup> (Appendix, Table A27), which was statistically different from A549 cells reported in Chapter 3 (766±126 µm<sup>2</sup>; *p*=0.0143). However, the mean roundness factor (where perfect circularity=1) of the untreated cells in this Chapter strongly correlated with that of the cryo-fixed and dehydrated A549 untreated cells in Chapter 3 (0.37±0.07 and 0.33±0.01, respectively), reaffirming the elongated nature of this cell line.<sup>31, 33</sup> Importantly, XRF from Ir or Pt was not observed for the untreated cells. Furthermore, no statistically significant differences in cell area (µm<sup>2</sup>) were observed for cells treated with **8** (C4-6, Appendix, Table A27) compared to the untreated controls (438±82 and 407±31 µm<sup>2</sup>, *p*=0.7185, respectively). However, upon treatment with **8** (C4-6), cells were significantly more rounded compared to the untreated controls (*p*=0.0056; Appendix, Table A27).

In cells treated with **8** (**C4-6**), Pt was well-distributed, localizing in nucleus and the cytoplasm, closely resembling the elemental map of K. In contrast, Ir seemed to be distributed in the cytoplasm and somewhat concentrate in small, intracellular compartments (**Fig. 4.13**). The region of interest was selected from the K map, and used to determine the co-localisation between elements in the cells: Pearson's R-value ( $r$ ) and Spearman Rank Coefficient ( $r_s$ ) in ImageJ software (**Appendix, Table A28-29**).<sup>27</sup> Pt co-localized strongly with Zn (mean  $r=0.65\pm0.05$ ; mean  $r_s=0.55\pm0.08$ ), which may implicate nuclear localization. In contrast, Ir only moderately co-localized with Zn (mean  $r=0.33\pm0.12$ ; mean  $r_s=0.26\pm0.08$ ). Intracellular Ir and Pt were found to co-localize partially in cells treated with **8** (mean  $r=0.51\pm0.10$ ; mean  $r_s=0.44\pm0.07$ ).

Mole fraction quantities of Ir and Pt were determined for each cell by calibrating the data to an AXO thin-film standard (**Chapter 2, Section 2.6.1**), assuming uniform cell thickness. XRF images revealed that cells treated with **8** (**C4-6**, **Fig. 4.13**) contained significantly more intracellular Pt than Ir (**Fig. 4.14; Appendix, Table A30**). The molar ratios of platinum-to-iridium (Pt/Ir) for **C4-6** were determined to be 4.13, 4.63 and 4.15, respectively.

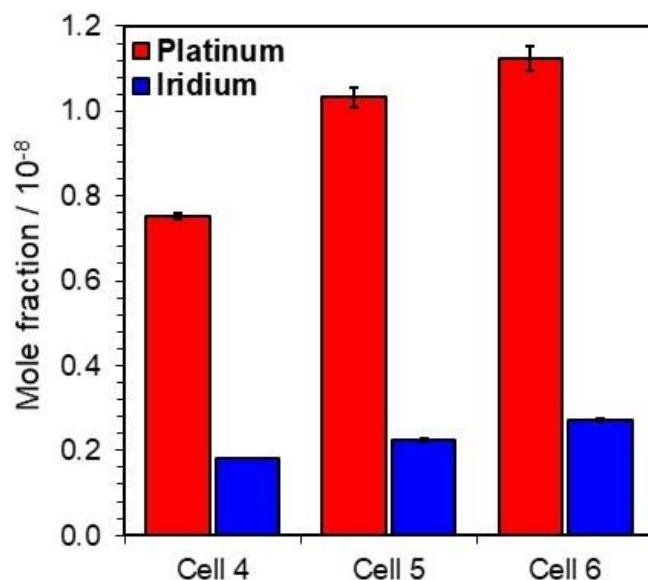


**Figure 4.14.** Normalized mole fraction quantities of Pt (■) and Ir (■) in cryo-fixed and freeze-dried A549 cells grown on Si<sub>3</sub>N<sub>4</sub> membranes and treated with **8** (500 μM) for 2 h under dark conditions, as determined from synchrotron-XRF (**C4-6**, **Fig. 4.13**). Data were acquired using 15 keV energy, 0.1 s exposure, 100 nm step size with *ca.* 50×70 nm<sup>2</sup> beam size. Data were analysed in PyMCA software,<sup>25</sup> and images generated in ImageJ.<sup>27</sup>

### Differential Phase Contrast (DPC) Imaging

Differential phase contrast (DPC) imaging is a well-established technique used in microscopy, which provides structural information by measuring the deflection of x-rays as they pass through an object. DPC imaging differs from XRT in that it provides phase-contrast (phase-sensitive), whereas, XRT provides full-field absorption-contrast.<sup>34</sup> Phase contrast is a consequence of the imaginary character of the refractive index (**Equation 4.1**),<sup>35</sup> which is enhanced with hard x-rays (stronger coherence). The real part of the refractive index describes the phase delays as light pass through a sample, whereas the imaginary part describes the absorption.<sup>35</sup> Phase contrast provides the opportunity to quantify values for both the real and imaginary parts of refractive indices, whereas, absorption contrast is only concerned with the imaginary part.<sup>34</sup>

$$m(\lambda) = m_r(\lambda) + im_i(\lambda)$$

**Equation 4.1.** Equation for complex refractive index,  $m(\lambda)$ , where  $\lambda$ =free-space wavelength,  $m_r$  is the real part of the refractive index and  $m_i$  is the imaginary part.

DPC imaging relies on a change in refractive index when passing through a sample and the resulting deflections which are more easily observed compared to absorption changes. More specifically, DPC imaging exploits differences in electron density when x-rays pass through a sample (monitors changes in phase). Synchrotron DPC imaging has recently been implemented at the I14 beamline (coherent hard x-rays), enabling the simultaneous acquisition of XRF and phase-contrast images to monitor **8** in A549 cancer cells.

The DPC images of **C4-6** show dark indentations surrounding nuclei (**Fig. 4.15**) which may be attributed to cytoplasmic organelles (*e.g.* mitochondria, endoplasmic reticula, lysosomes or lipid droplets). As DPC imaging monitors the *changes* in phase when x-rays pass through a sample (rather than *phase-retrieval*), the observed indentations may also be attributed to holes in the cell (*e.g.* vacuoles).

These dense bodies were perinuclear as identified by overlaying the DPC images with the Zn XRF maps (**Fig. 4.15**). Pt strongly correlates with Zn, but did not closely correlate with the dense structures. In contrast, Ir was localized in small compartments, most likely in the cytoplasm, but did not closely correlate with the



dense bodies (**Fig. 4.15**). Overall, the nature of these structures cannot be identified using just DPC imaging, but nonetheless highlights the capabilities of hard x-ray nanoprobe beamlines for biological applications.

The lengths and areas of the darker and more elongated dense structures (represented in red, **Fig. 4.16**) were determined for **C4-6** using ImageJ (**Appendix, Table A31-32**).<sup>27</sup> The mean organelle lengths in **C4-6** were  $1.2 \pm 0.4$ ,  $2.5 \pm 1.1$  and  $2.6 \pm 0.6$   $\mu\text{m}$ , respectively (**Appendix, Table A31**). The elongated nature of these organelles may correspond to mitochondria (*e.g.* fused interconnecting networks), or even the perinuclear endoplasmic reticula. The individual 2D areas ( $\mu\text{m}^2$ ) of these structures were also determined (**Appendix, Table A32**), revealing mean areas of  $1.5 \pm 0.6$ ,  $1.6 \pm 0.8$  and  $1.9 \pm 1.0$   $\mu\text{m}^2$ , for **C4-6**, respectively.

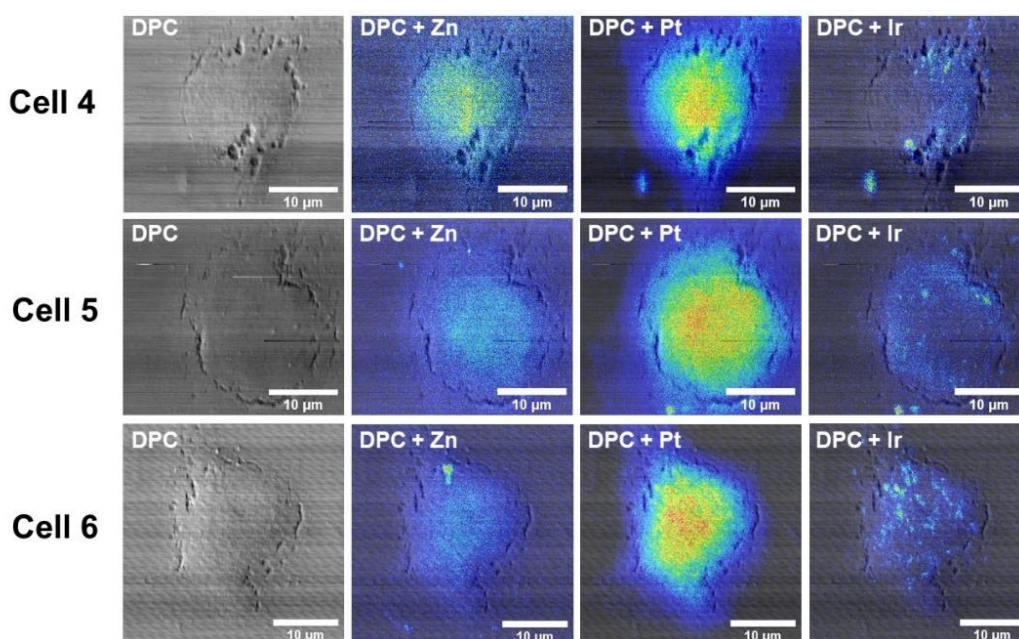


**Figure 4.15.** Overlay of DPC images with Zn, Pt and Ir synchrotron-XRF elemental maps of cryo-fixed and dehydrated A549 lung cancer cells grown on a  $\text{Si}_3\text{N}_4$  membrane and treated with **8** (500  $\mu\text{M}$ ) under dark conditions (2 h), as analysed using synchrotron-XRF (12.5 keV, 100 nm step, 0.1 s).

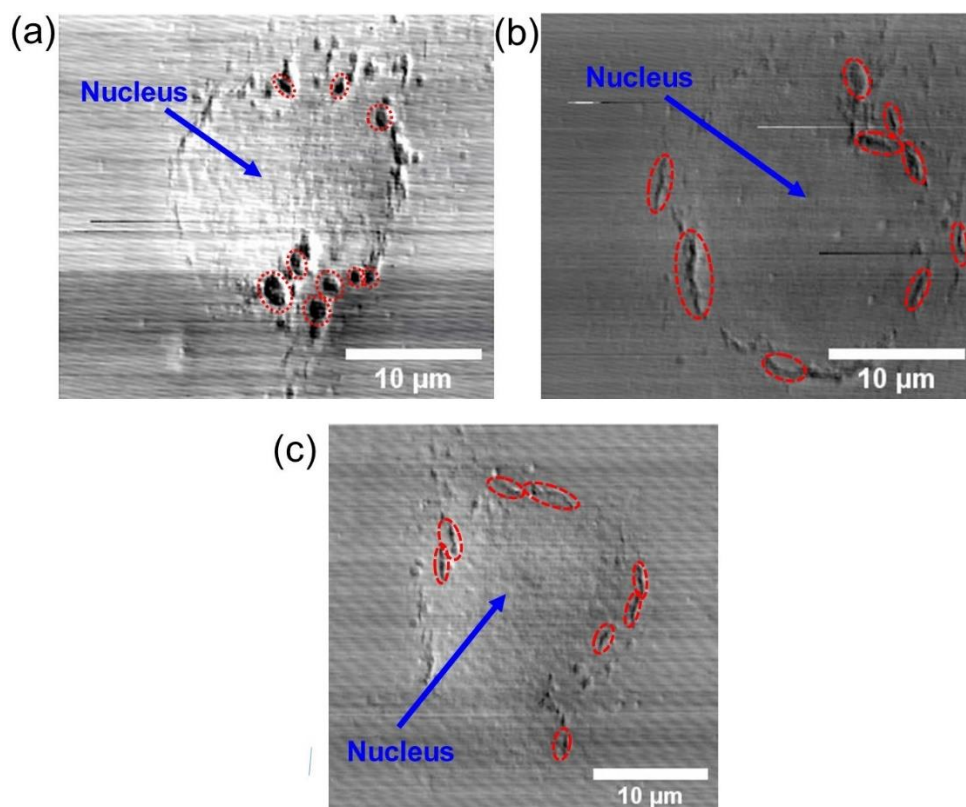


**Figure 4.16.** DPC images of cryo-fixed and dehydrated A549 cells grown on a  $\text{Si}_3\text{N}_4$  membrane and treated with **8** (500  $\mu\text{M}$ , 2 h) under dark conditions, as analysed using synchrotron-XRF and DPC imaging at I14 (12.5 keV, 100 nm step, 0.1 s), Showing the cell nucleus in blue and dark, elongated structures in red: (a) **C4**; (b) **C5**; (c) **C6**.

## 4.4 Discussion

### 4.4.1 Cryo-XRT of PC3 cells treated with **7**

Cryo-XRT can provide near-native state information down to subcellular 25-40 nm resolution, and can be combined with other techniques (*e.g.* super-resolution fluorescence or cryo-XRF) to gain essential insights into drug-targeting, cell death mechanisms and drug-induced physiological damage.<sup>28, 29, 36</sup> Cryo-XRT imaging of intact cells has been performed at various synchrotron beamlines worldwide, including XM-2 (ALS, US), MISTRAL (ALBA, Spain), U41-TXM (Bessy II, Germany) and B24 (DLS, UK).<sup>28</sup> Of interest in this research, cryo-XRT has previously been used for imaging *in vitro* cancer cells,<sup>36, 37</sup> including probing the cellular effects of a half-sandwich iridium complex and iron oxide nanoparticles in

breast cancer cells.<sup>38, 39</sup> Recently, cryo-XRT has been used to probe the effect of cisplatin and gold nanoparticles in skin cancer cells.<sup>40</sup> A similar approach has been adopted here to gain insights into the ultrastructural and morphological changes to cellular organelles induced by a potent organometallic Ir<sup>III</sup> photosensitizer (**7**) under dark (non-toxic) and irradiated (blue light) conditions.

Complex **7** ([Ir(C,N)<sub>2</sub>(O,O)] (where (C,N)=2-phenylpyridine and O,O=diketone) exhibits good antiproliferative activity (IC<sub>50</sub>=6±1 µM) in PC3 cells upon irradiation with blue light (λ=465 nm), and is non-toxic to the same cells under dark conditions. Its high photo-stability, long luminescence lifetime and ability to form toxic <sup>1</sup>O<sub>2</sub> makes **7** of significant interest as a PDT photosensitizer.<sup>11</sup> The generation of <sup>1</sup>O<sub>2</sub> by **7** is highly-confined through spatially-directed light,<sup>11</sup> with the hope of reducing patient side effects experienced by current chemotherapeutics.<sup>7</sup> Generation of ROS by **7** is known to cause oxidative damage to proteins (*e.g.* HSP-70 – a heat shock protein that is expressed in response to stress), and can disrupt glycolysis by increasing enzyme expression.<sup>11</sup> The dependence of glucose metabolism in cancer cells can be described by the Warburg Effect,<sup>41</sup> allowing them to survive under extreme conditions. This makes the glycolytic pathway a viable therapeutic target. Since glycolysis is indirectly associated with mitochondrial organelles,<sup>42</sup> the observed photocytotoxicity may implicate mitochondrial damage in the mechanism of action of **7**. This hypothesis was probed using cryo-XRT to investigate the effect of **7** on cancer cell organelles under both dark and irradiated conditions.

The preparation of cryopreserved samples for soft x-ray analysis is challenging for various reasons: (i) delicacy of quantifoil grids; (ii) rapid accumulation of ice on grid surface (which prevents soft x-ray penetration); (iii) multi-step process (increased risk of sample damage). A general problem with the majority of grids imaged was the accumulation of thick ice on the surface, likely caused during plunge-freezing. Tweezer-damage (from the handling of grids in tissue culture, plunge-freezing and sample loading) were also evident, which led to tears and perforation of grids. Furthermore, cells preferentially adhere to the mesh grid – a more supportive environment for cell growth - compared to the thin carbon material. Thick ice layers present challenges for cryo-XRT as low energy x-rays can only penetrate *ca.* 10 µm of ice.<sup>43</sup> Thick ice and mesh grid lines will produce darkened tomograms (higher x-ray absorbance) with limited tomographic

information (*e.g.* restricted views at high tilt angles). Nonetheless, suitable cell candidates from each population of PC3 cancer cells were identified on the grids, and analysed by cryo-XRT.

Cryo-XRT is a soft x-ray synchrotron technique that can probe the 3D structures of biological samples without the need for chemical staining.<sup>28</sup> Chemical fixation can alter biomolecules including proteins and nucleic acids, which can indirectly affect morphological features such as cell volume and ATP content.<sup>44</sup> If these fixatives interact with the same cellular targets as the therapeutic agents, then they may disrupt the observed drug distribution. To overcome this, cryogenic analysis of samples can be used to monitor cellular response to drugs close to their native state. Cryo-XRT operates in the “water-window” (the energy of x-rays at which the absorbance of O is significantly lower than that of C and N, 280-530 eV).<sup>45</sup> This not only provides natural contrast, but also permits the analysis of vitrified samples down to 25-40 nm resolution.<sup>43</sup> Herein, cryo-XRT has been utilized to monitor morphological changes of PC3 cells treated with **7**.

A comparison of the untreated dark controls (**Section 4.3.1, Fig. 4.6; Appendix, Fig. A13**) and the irradiated controls (**Section 4.3.1, Fig. 4.7**) reaffirmed that 10 min irradiation with blue light (of this intensity) did not alter the ultrastructure of the cell – with uncompromised nuclear membranes, features of *lamellopodia* and vesicle-shedding, correlating with that reported for prostate cancer cells (including this cell line).<sup>46-48</sup>

In order to probe mitochondrial damage induced by **7**, volume segmentation was performed, which has previously been demonstrated by cryo-XRT for doxorubicin sensitive and resistant colon cancer cells.<sup>37</sup> In x-ray tomography, the entirety of biological samples (tilt range  $\pm 180^\circ$ ) cannot be analysed due to the ‘missing-wedge’ problem, which results in loss of 3D information at high tilt angles.<sup>49</sup> Consequently, 3D structures are distorted or elongated along the z-axis.<sup>50</sup> In order to reduce artefacts and limit the amount of missing 3D information, tomographic data can be acquired from multiple tilt axes (*i.e.* conical tilt or double tilt axes).<sup>49</sup> The mitochondrial volumes reported in this Chapter were obtained under the same experimental parameters, hence, mitochondrial volumes between different samples are directly comparable.

Volume segmentation revealed wide variations in mitochondrial size ( $0.98 \pm 1.20$  and  $0.65 \pm 0.35 \mu\text{m}^3$ , for **T1-2**, respectively), but no statistically significant differences ( $p=0.335$ ; **Appendix, Table A26**). This correlates with the area of mitochondrial organelles in healthy cells, typically ranging from  $0.75\text{--}3 \mu\text{m}^2$  in size.<sup>51</sup> Furthermore, this confirms that blue light (of this intensity and dosage) does not significantly damage or alter mitochondrial physiology. Representative mitochondria in the untreated control tomograms (**T1-2**) are shown in **Fig. 4.17**.

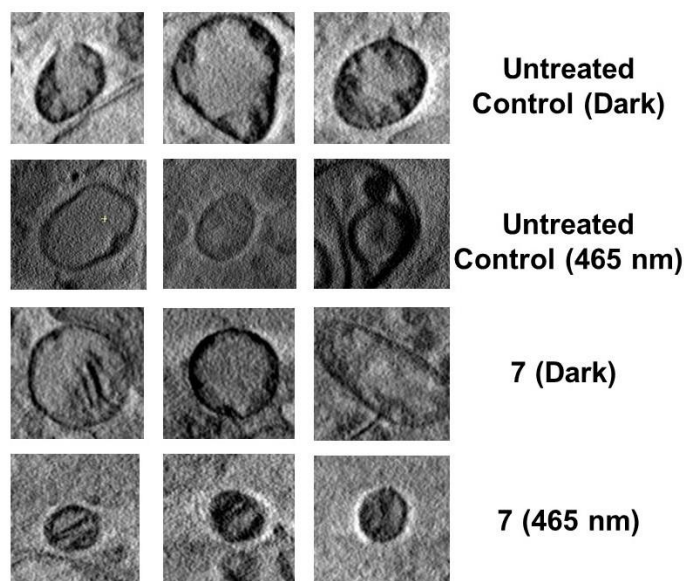


**Figure 4.17.** Representative 2D regions ( $1 \times 1 \mu\text{m}^2$ ) of mitochondrial organelles in cryopreserved PC3 cells treated with **7** (0 or  $1 \mu\text{M}$ ) for 2 h followed by 10 min of dark or blue light (465 nm), followed by 24 h recovery in complex-free media (**T1-4**, 310 K, 5%  $\text{CO}_2$ ). Images were generated in IMOD imaging software.<sup>23</sup>

Cryo-XRT analysis of cells treated with **7** under dark conditions did not reveal any obvious damage to PC3 cells, which showed typical vesicle-shedding, *lamellopodia* and unambiguous mitochondria (identified by cristae in the mitochondrial matrix; **T3**, **Fig. 4.8**; **Appendix, Fig. A14-16**). Moreover, the mean mitochondrial volume in **T3** was determined to be  $0.77 \pm 0.38 \mu\text{m}^3$ , which was statistically the same as the mitochondria found in untreated controls ( $p=0.534$  and  $p=0.273$ , respectively, **Fig. 4.17**). As the sizes of mitochondria in cells treated with **7** under dark conditions (**T3**) were not statistically different from the controls (**T1-2**), this reaffirms that **7** in dark conditions did not result in morphological changes to mitochondria (**Section 4.3.1, Fig. 4.8**). This also correlates with the low dark cytotoxicity of **7** determined by cell viability assays ( $\text{IC}_{50} > 100 \mu\text{M}$ ).

In contrast, the mitochondria in cells treated with **7** followed by direct irradiation with blue light (465 nm) were significantly smaller than the ones in untreated cells or cells exposed to the drug under dark conditions (**Section 4.3.1**, **Fig. 4.9**; **Fig. 4.17**). Severe plasma membrane-blebbing on drugged and irradiated cells also suggested the initiation of cell death pathways, and can be commonly associated with apoptosis and necrosis.<sup>52</sup> As  $^1\text{O}_2$  is short-lived (<200 ns),<sup>53, 54</sup> and possesses inadequate diffusion capacity (<1  $\mu\text{m}$ )<sup>55</sup> the mitochondrial damage observed upon photo-activation of **7** may be attributed to the generation of  $^1\text{O}_2$  in close proximity to mitochondria. This is in strong agreement with the cytosolic distribution of **7** in cancer cells, as probed using optical microscopy.<sup>11</sup>

Complementary to this, cells treated with **7** under dark conditions revealed dark mitochondrial membranes and cristae compared to the untreated controls, with light (low-density) interiors (**Section 4.3.1**, **Fig. 4.8**; **Appendix**, **Fig. A14-16**). Heavy metals have high x-ray absorption properties in comparison to cellular material (due to increased electron scattering), hence, iridium localised in the mitochondria would impede x-ray penetration. This coincides with the increased x-ray exposure (6-8 s) required to obtain tomographic information at high tilt angles ( $x < -30^\circ$ ,  $x > +30^\circ$ ) from cryopreserved PC3 cells treated with **7**, regardless of the photo-conditions. The mitochondria in cells exposed to **7** and irradiated with blue light appear overall darker in contrast (**Section 4.3.1**, **Fig. 4.9**, **Appendix**, **Fig. A17-18**) - which was not observed for cells treated with **7** and protected from light. This is likely a result of a reduced volume (*e.g.* condensation of cristae or volume reduction of the mitochondrial outer membrane). Overall, this provides complementary evidence that the increase in levels of glycolytic enzymes in cells treated with **7** upon exposure to blue light is associated with changes in mitochondria physiology.<sup>11</sup>

Glycolysis is controlled by various metabolic enzymes (*i.e.* hexokinase and pyruvate kinase) which are up-regulated in various cancers.<sup>56</sup> The inherent differences in metabolism between healthy tissues and tumours can be exploited to selectively target cancer. Interestingly, the enhanced glycolysis phenotype in cancer cells has been implicated in chemotherapeutic resistance (including cisplatin),<sup>57</sup> which has major consequences on drug efficacy. Various inhibitors of glycolysis have been shown to reverse platinum resistance in cancer cells,<sup>58</sup> rendering it a viable approach to improving cytotoxicity and selectivity.

Unlike the majority of cancers which utilize aerobic glycolysis, prostate cancer cells exhibit higher levels of activity involving the Krebs cycle.<sup>59</sup> The Krebs cycle differs from glycolysis in that it occurs within the mitochondria and pyruvate is oxidised to carbon dioxide, whereas glycolysis occurs in the cytoplasm and involves the metabolism of glucose in 10 enzyme-catalysed steps to form pyruvate. The mitochondrial damage observed in PC3 cells treated with **7** under photo-conditions (465 nm) may therefore *also* be associated with disruption to the Krebs cycle. The nature of mitochondrial damage caused by **7** may also be a consequence of direct disruption of the Krebs cycle or indirectly perturbation of glycolysis *via* the generation <sup>1</sup>O<sub>2</sub> in the vicinity of mitochondria. Evidence directly linking **7** to the Krebs cycle might be achieved by use of fluorometric or colorimetric assays specific to the Krebs cycle (citrate synthase) or by mass spectrometry metabolomic studies. Overall, cryo-XRT has provided direct insights into the morphological and structural damage induced by a cyclometallated Ir<sup>III</sup> photosensitiser, which may accelerate their progression towards *in vivo* studies.

#### 4.4.2 Synchrotron-XRF of A549 cells treated with **8**

The concept of dual-mapping of anticancer complexes by synchrotron-XRF was demonstrated with Br-labelled Os<sup>II</sup> catalysts in **Chapters 3**. In this Chapter, correlative mapping of the two metal centres (Ir and Pt) of a photodynamic-photochemotherapeutic complex (**8**) in cancer cells was monitored by synchrotron-XRF. The intracellular distribution and stability of **8** in cryo-fixed and freeze-dried A549 (lung) cancer cells was probed using synchrotron-XRF, by directly monitoring the XRF emissions of Ir (L<sub>3</sub>M<sub>5</sub>=9.18 keV) and Pt (L<sub>3</sub>M<sub>5</sub>=9.44 keV).<sup>30</sup>

#### Elemental preservation and cellular morphology

The sufficient preservation of endogenous cellular elements in cryo-fixed and dehydrated cells grown on Si<sub>3</sub>N<sub>4</sub> membranes has been reported with great success in the literature,<sup>60</sup> and in **Chapter 3**. The Zn, S and K XRF distributions allowed the identification of the cell nuclei and the cell outline, comparable to that of A549 cells in the literature – with elongated morphologies, and rounded cell nuclei



(identified by localised Zn).<sup>61-63</sup> Ideally, frozen-hydrated samples (*e.g.* cryo-XRF) would provide information closer to the native state of the cells so as to avoid alterations to subcellular structures, membranes and cell morphology upon drying. Cryo-XRF enables the 2D of biological elements with their close-to-native state cells, in addition to mapping exogenous metallodrugs, and is emerging at various synchrotron beamlines worldwide including ID16A (ESRF, Grenoble)<sup>40</sup> and 9-ID-B (APS, Illinois).<sup>64</sup> Cryo-XRF facilities are not yet available at the I14 beamline, thus, cells were cryo-fixed and dried for analysis at room temperature. Importantly, chemical fixatives were avoided by cryo-fixation and drying of samples, providing much more reliable elemental distributions.

Synchrotron-XRF maps of three untreated (control) A549 cells grown on  $\text{Si}_3\text{N}_4$  membranes were obtained (**C1-3**, **Section 4.3.2**, **Fig. 4.12**), revealing elongated morphologies, correlating closely with the typical morphology of A549 cells,<sup>31, 33</sup> and those reported in **Chapter 3**. The elongated nature of these untreated cells was reflected in the mean roundness factor ( $0.37 \pm 0.07$ ), in strong agreement with that of A549 cells prepared under the same conditions in **Chapter 3** ( $0.33 \pm 0.01$ ). Interestingly, the A549 cells reported in this Chapter were smaller than others imaged (**Chapter 3**;  $p=0.0143$ ). This may be attributable to factors including the differences in the stage of cell growth of individual cells in a population, the cell seeding density ( $6-7 \times 10^4$  cells/mL), the buffer system used to wash cells before cryogenic fixation (tris-glucose or HBSS), or the efficiency of cryo-fixation/dehydration. In contrast, cells treated with **8** (500  $\mu\text{M}$ , 2 h protected from light) demonstrated more rounded morphologies compared to the untreated controls (**C4-6**, **Section 4.3.2**, **Fig. 4.13**). Rounding of a cell can be associated with cell damage and commonly accompanies cell death pathways.<sup>65</sup> This may imply that high concentrations of **8** (500  $\mu\text{M}$ ) causes morphological damage to cells under dark conditions. Furthermore, analysis of cells treated with *lower* concentrations of **8** in the dark, and upon irradiation are required to provide further insights into the antiproliferative mechanism of action.



### Distribution of Ir and Pt

Iridium in cells treated with **8** somewhat localising in small compartments which may be indicative of organelle-targeting (**C4-6**, **Section 4.3.2**, **Fig. 4.13**). This correlates with the predominant cytoplasmic localization of **8** observed in A549 cells using fluorescence microscopy with conventional trackers (LysoTracker Deep Red and MitoTracker Red) upon irradiation.<sup>21</sup> For the case of **C6**, Ir appears localised within the nuclear region (with concentrated Zn), however, it cannot be determined whether this is *within* the nucleus or not. Synchrotron-XRF provides information in 2D, however cells grown on a monolayer surface are not entirely flat (as shown from XRT), hence, the distribution of elements is a 2D projection of an inherently 3D object. For example, the ‘bulky’ cell nucleus has been reported to take up *ca.* 28% of the volume of A549 cells.<sup>66</sup> Subsequently, this may mean that observed Ir may reside *above* the cell nucleus (in the cytoplasmic space), and not *in* the cell nucleus. This correlates with the lack of adducts formed between the Ir-PDT counterpart of **8** or the analogous Ir complex (**9**) with model DNA nucleobases.<sup>21</sup> Complementary to this, only moderate co-localisation between Ir and Zn was observed ( $r=0.20-0.42$ ; **Appendix, Table A28**). Methods involving cellular fractionation <sup>192</sup>Ir ICP-MS studies (which separates cells into nuclear, cytosolic, membrane and cytoskeletal fractions) or correlative cryo-SIM and XRT could be used in future studies to probe the organelle-localisation of intact and cleaved **8**.

Multi-targeting drugs with synergistic mechanisms of action might improve drug efficacy and circumvent multidrug resistance. In particular, it is hypothesized that diazido-Pt<sup>IV</sup> PACT complexes can be photo-reduced *in situ* (Pt<sup>IV</sup> → Pt<sup>II</sup>) to form square planar Pt<sup>II</sup> species (which can bind to nuclear DNA), whilst releasing toxic azidyl radicals intracellularly – presenting a synergistic mode of action.<sup>18</sup> In contrast, Ir<sup>III</sup> photosensitisers have been reported to target a variety of cytoplasmic organelles. In general, Ir<sup>III</sup> PDT agents are highly lipophilic and cationic,<sup>8</sup> promoting localization in negatively-charged mitochondria or lysosomes. The mitochondrial-targeting of Ir<sup>III</sup> photosensitizers is well-reported,<sup>67, 68</sup> where they can generate highly reactive and toxic singlet oxygen (<sup>1</sup>O<sub>2</sub>) (with high quantum yields,  $\Phi\Delta$  0.5-0.9)<sup>69</sup> to disrupt cancer redox homeostasis. In this Chapter, mitochondrial damage by photosensitiser **7** was also demonstrated by cryo-XRT

(Section 4.4.1). Lysosomal targeting has also been reported for various cyclometallated Ir<sup>III</sup> complexes.<sup>70-72</sup> Lipophilic compounds can pass freely through lysosomal membranes and can become protonated in the acidic lysosomal environment (pH 4-5),<sup>73</sup> ultimately becoming entrapped. This has led to the development of pH-activated Ir<sup>III</sup> photosensitisers,<sup>72</sup> to control the selective production of <sup>1</sup>O<sub>2</sub> inside lysosomes. The ER has also been explored as a target for cyclometalated Ir<sup>III</sup> photosensitisers.<sup>74</sup> Combining diazido-Pt<sup>IV</sup> PACT modalities with cyclometalated Ir<sup>III</sup> PDT complexes provides a novel multi-modal approach to treating cancer.

The XRF of Pt revealed 2D distributions in the nucleus and cytoplasm, with significantly higher levels of Pt vs. Ir (4× more; Section 4.3.2, Fig. 4.14). The sparse intracellular distribution of Pt has been reported for a variety of platinum compounds (including cisplatin),<sup>75-77</sup> hence, the observed Pt distribution in cells treated with **8** is perhaps not surprising. Further to this, Pt strongly co-localised with Zn in cells treated with **8** (r=0.59-0.69, Appendix, Table A28-29) - supporting the hypothesis of nuclear-targeting of the Pt component. Diazido-Pt<sup>IV</sup> prodrugs can be photo-reduced *in situ* to form square planar Pt<sup>II</sup> species (*via*. the loss of azidyl radicals), which can bind to nuclear DNA in a different manner to that of cisplatin.<sup>78</sup> In the absence of light, it is conceivable that the reductive cancer cell environment can cause the chemical reduction of Pt<sup>IV</sup>→Pt<sup>II</sup>, though this conflicts with the apparent lack of antiproliferative activity in dark conditions and the ‘inertness’ of the Pt<sup>IV</sup> prodrug.

Confocal microscopy of A549 cells treated with **8** under dark conditions revealed the predominant cytoplasmic localization of **8** ( $\lambda_{\text{ex/em}}$ =405/460-560 nm),<sup>21</sup> however, the cleaved Ir-PDT fragment of **8** likely exhibits luminescence itself, hence, the observed fluorescence may not be directly mapping intact complex **8**, but cleaved **9** instead (providing no information on the cleaved Pt PACT component). The cleavage of the Ir part may explain the lack of the fluorescence of **8** observed in the nucleus by confocal microscopy,<sup>21</sup> compared to the nuclear-localised Pt observed by XRF (C4-6, Section 4.3.2, Fig. 4.13). This highlights the advantages of XRF mapping combined with conventional fluorescence microscopy techniques.

The higher levels of Pt vs. Ir are strongly indicative of intracellular cleavage of **8**. When quantifying elements by XRF, assumptions are made about cell thickness and density,<sup>26</sup> whereas, biological cells are inhomogenous (non-uniform). Subsequently, these assumptions are likely only valid for very thin samples,<sup>79</sup> thus, the quantification of Ir and Pt *in* or *above* the thick cell nucleus may not be entirely reliable. Moreover, ICP-MS cellular fractionation studies of **8** prove necessary for reaffirming the Pt/Ir ratio. Alternatively, techniques such as hard x-ray ptychography or nanotomography can be used to gain insights into 3D cellular features for more reliable elemental quantification.<sup>80, 81</sup> Nonetheless, it is evident that there is more intracellular Pt vs. Ir, which is suggestive of two things: (i) the Ir fragment may be more susceptible to efflux compared to Pt; (ii) less Ir is entering the cells (influx).

It is hypothesized that the antiproliferative mechanism of action of **8** involves photodecomposition upon irradiation with blue light (465 nm),<sup>21</sup> through a combined PDT-PACT effect. In chemical HPLC/LC-MS experiments, **8** has shown to release the axial carboxylato ligand upon irradiation with light.<sup>21</sup> The amide bond of **8** may also be susceptible to cleavage by proteolytic enzymes, for example by cathepsins (an over-expressed group of lysosomal cysteine proteases) which play a role in drug resistance.<sup>82</sup> The higher levels of Pt vs. Ir is suggestive of intracellular cleavage, with the cleaved Ir-PDT moiety being more susceptible to cellular efflux. Cancer cells have various reducing agents (*i.e.* metalloproteins and low molecular weight antioxidants) which can reduce Pt<sup>IV</sup> → Pt<sup>II</sup>,<sup>83</sup> which likely contribute to the breakdown of **8**. The intracellular reduction of the Pt centre of **8** may explain the nuclear localisation of Pt observed by XRF – which is a well-known target for Pt<sup>II</sup> drugs (including cisplatin).<sup>18</sup>

The co-localisation statistics between Ir and Pt for A549 cells treated with **8** under dark conditions, revealed moderate co-localization (0.44-0.63; **Appendix, Table A28**), suggesting that some of **8** is likely intact intracellularly– which may prove essential for enhancing the antiproliferative activity compared to the mono-metal complexes (upon photo-activation). The protocol for screening the antiproliferative activity of **8** under dark conditions involves 2 h (dark) drug exposure, followed by 24 h recovery. In contrast, the antiproliferative activity upon photoactivation involves 1 h drug exposure followed by 1 h irradiation with blue light. With this in

mind, the low dark toxicity of **8** in cancer cells may also be a consequence of intracellular complex cleavage after 2 h (longer) exposure. The extent of complex cleavage of **8** after 1 h drug exposure (irradiated protocol) is likely less pronounced compared to 2 h (dark protocol), which may be why photoactivation after 1 h leads to photocytotoxicity. Herein, the lack of toxicity of **8** under dark conditions ( $IC_{50} > 100 \mu M$ ) was assumed to be due to absence of  $^1O_2$ , azidyl radicals and Pt<sup>II</sup> square-planar species (all formed upon blue light exposure),<sup>21</sup> however, this may *also* be ascribed to enhanced drug efflux prior to photoactivation. This may reduce quantities of complex available for photo-activation, limiting the photodynamic-photochemotherapeutic effect. However, XRF quantification of cells treated with **8** under photo-conditions is required to confirm this.

In aqueous cell culture media, **8** exists in a 1:1 ratio (as confirmed by ICP-OES),<sup>21</sup> however, this does not necessarily verify whether the Ir and Pt moieties are intact or not. The differences between intracellular levels of Ir and Pt may be a consequence of different influx mechanisms. For example, Pt complexes typically rely on copper transporters and organic cation transporters to enter cells,<sup>84</sup> whereas, lipophilic Ir<sup>III</sup> photosensitisers may rely more heavily on passive transport.<sup>85</sup> Moreover, an alternative hypothesis may be that the cellular *influx* mechanism of intact **8** may vary from that of the cleaved Ir and Pt modalities, hence, complex dissociation prior to uptake may be preferential for cell permeation. The chemical speciation of metallodrugs in biological media is of great importance in understanding drug activation mechanisms, and usually requires techniques such as ICP-MS, XANES, EXAFS, NMR or MS-proteomics.<sup>86</sup> For example, Hartinger *et al.* used capillary electrophoresis ICP-MS to demonstrate the vulnerability of cisplatin in extracellular culture media.<sup>87</sup> This research would benefit from further studies into the biological speciation of **8**, which may prove necessary for elucidating mechanisms of drug activation and cell death.

Synchrotron-XRF can be used to gain insights into the distribution of metallodrugs and endogenous biological elements both *in vitro* and *in vivo* down to a high spatial resolution (typically *ca.* 50-100 nm),<sup>88</sup> however, cannot distinguish organelles or subcellular features without using complementary techniques. Additionally, beam damage upon repeated exposure to hard x-rays can damage biological samples, and disrupt metal distribution and speciation (particularly for nanofocussed XANES).

Other analytical techniques can provide complementary information. For example, Laser Ablation ICP-MS (LA-ICP-MS) and NanoSIMS have been used to investigate metallodrug distributions in both cells and tissues down to a subcellular level.<sup>89-92</sup> Single-cell ICP-MS is emerging as a high-throughput method for investigating metal quantities in individual cells,<sup>93</sup> overcoming concerns of unsynchronized cells. Top-down FT-ICR-MS proteomics can be utilized to investigate potential biomolecule targeting of metallodrugs as demonstrated by O'Connor *et. al.* with platinum anticancer drugs.<sup>94</sup> This work may also benefit from fluorescence sensor techniques (*e.g.* FRET ratiometric sensors), which can be used to quantify metal concentrations in biological systems.<sup>95, 96</sup>

### Differential Phase Contrast (DPC) Imaging

Correlative DPC imaging has provided insights into 3D structures in A549 cells treated with **8** by exploiting the varying refractive properties of different objects. At I14, the XRF detector is located *before* the sample (to collect back-scattering), whereas, the DPC detector is *after* the sample (to collect transmitted beam). Objects refract light in different ways to produce phase-contrast images. Thus, objects appearing darker in DPC images implicate a stronger *change* in electron density.

The nuclei in each of the DPC images were clearly identifiable from the lighter phase-contrast regions (overlayed with Zn XRF), as nuclei have lower mass densities and refractive indices than the cytoplasm (**Section 4.3.2, Fig. 4.15**).<sup>97</sup> DPC imaging is sensitive to changes in density, which means that the contents of highly dense cell nuclei are difficult to identify (non-uniform electron density). Dark phase-contrast regions in the image appear to somewhat surround the central nucleus, implying they may be cytoplasmic organelles. When light passes through thicker regions of the sample (nucleus), there is a phase shift relative to the light passing through thinner regions of the sample (cytoplasm) which causes interference.<sup>98</sup> This is exploited in DPC imaging to visualize cells. As a result, the thick cell nucleus appears lighter in the image, whereas, cytoplasmic organelles appear much darker. Alternatively – as DPC imaging relies on phase gradients- the observed dark contrast regions may be attributed to holes in the cell (*e.g.* vacuoles – which can be associated with cell damage and programmed cell death).<sup>99</sup>

The dense cytoplasmic organelles ranged between 0.76-4.14  $\mu\text{m}$  in length (mean=2.1 $\pm$ 0.9  $\mu\text{m}$ ) and areas between 0.81-3.98  $\mu\text{m}^2$  (**Appendix, Table A31-32**). These lengths were statistically smaller than the reported mean mitochondrial length in A549 cells determined independently using immunofluorescence assays - which reported mitochondrial lengths of between 7-8  $\mu\text{m}$  length.<sup>100</sup> The wide variability in 3D mitochondrial size has already been demonstrated in this Chapter by cryo-XRT, which will also depend on the analysis conditions (*i.e.* fixed or live cells *etc.*). The elongated nature of these dense organelles somewhat resembled that of fused mitochondrial networks, which are atypical of other dense structures – including lipids droplets (dark and rounded, typically ranging between 0.1–5  $\mu\text{m}$ )<sup>101</sup> and lysosomes (ranging between 50-500 nm).<sup>102</sup> Alternatively, these organelles could also comprise the endoplasmic reticulum.

The Ir and Pt XRF maps of A549 cells treated with **8** were overlaid with the DPC images (**Section 4.3.2, Fig. 4.15**). Pt nor Ir did not strongly correlate or overlay with the resolved organelles/vacuoles from the DPC image. DPC imaging is limited in that it only provides a preliminary indication of potential 3D structures in a 2D sample, and cannot identify the nature of these organelles. DPC imaging can be used in combination with soft cryo-XRT to identify organelles/vacuoles once cryo-XRF is implicated at the I14 beamline.<sup>43</sup> Alternatively, hard x-ray ptychography can be used to monitor endogenous and exogenous cellular elements in addition to 3D features, as demonstrated by Jacobsen *et. al* on frozen-hydrated cells at the 21-ID-D beamline, APS (Chicago).<sup>80</sup>

Overall, it can be postulated that some of intact **8** may concentrate in cytoplasmic organelles, with excess cleaved Pt species predominantly targeting the cell nucleus, providing a multi-targeted mechanism of action, however, more evidence is required to support this hypothesis.

## 4.5 Conclusions and future work

Soft cryo-XRT of cryopreserved PC3 prostate cancer cells treated with a neutral diketone Ir<sup>III</sup> photosensitiser (**7**) upon blue light exposure revealed extensive and significant alterations to mitochondria physiology (reduction in volume), most likely caused by the selective generation of singlet oxygen species (<sup>1</sup>O<sub>2</sub>) in close proximity to these organelles. The observed changes in mitochondrial morphology upon photo-treatment with **7** may be associated with the previously reported increase in the expression of glycolytic enzymes in cancer cells.<sup>11</sup>

The mitochondrial-targeting of **7** can be probed further using correlative cryo-XRT and cryo-XRF to confirm the localisation of Ir using hard x-rays.<sup>40</sup> XAS on localised regions of intracellular Ir may provide information on the oxidation state, coordination environment and binding modalities of **7** in cancer cells – although this is dependent on the in-cell metal concentration. Alternatively, mitochondrial-dependent cell viability assays (*e.g.* inhibition of peptide formylase), can be performed to gain information on the mitochondria damage induced by **7**. Information on the mechanisms of cell death induced by **7** can be further investigated using flow cytometry (*e.g.* using Annexin V/ PI assay).

Synchrotron-XRF has been used to probe the intracellular distribution and stability of a potent photodynamic-photochemotherapeutic Ir-Pt complex (**8**) in A549 cancer cells under dark conditions. Interestingly, Pt was distributed in both the cell nucleus and cytoplasm, but Ir seemed to localise in non-nuclear regions (most likely in cytoplasmic organelles) – however, ICP-MS cellular fractionation studies are required to confirm this. Complementary to this, significantly higher intracellular levels of Pt *vs.* Ir were observed (*ca.* 4×), suggestive of the intracellular cleavage of **8**. The Ir and Pt of **8** co-localized in small cytoplasmic regions, most likely organelles - in agreement with similar Ir<sup>III</sup> photosensitizers reported in the literature.<sup>8</sup> This correlates with confocal microscopy studies in which **8** (under dark conditions) predominantly localised in the cytoplasm (particularly with mitochondria).<sup>21</sup> Cells treated with **8** were more rounded compared to the elongated untreated controls, suggesting some cellular damage upon drug exposure under dark conditions (likely owing to the high photosensitiser concentration).

Differential phase contrast (DPC) imaging provided preliminary insights into dense elongated organelles located around the cell nucleus (perinuclear). The intracellular Pt or Ir did not correlate with that of the observed dense organelles from the DPC images. Since DPC only gives an indication of 3D features of a cell, the nature of these organelles cannot be identified using this technique alone.

The conjugation of metal moieties with different mechanisms of action to form binuclear complexes may significantly improve the cytotoxicity, aqueous solubility and pharmacokinetics of organometallic anticancer complexes. Conjugation of potent Ir-PDT and Pt-PACT modalities may provide a combined PDT-PACT targeting mechanism of antiproliferative activity through the generation of singlet oxygen, toxic radicals and Pt<sup>II</sup>-species. Additionally, **8** can readily be monitored by fluorescence microscopy ( $\lambda_{\text{ex/em}}$ =405/460-560 nm) and synchrotron-XRF (Ir L<sub>3</sub>M<sub>5</sub>:9.18 keV; Pt L<sub>3</sub>M<sub>5</sub>:9.44 keV).

ICP-MS studies (<sup>192</sup>Ir and <sup>195</sup>Pt), may be employed to gain further insights into the cellular uptake mechanism(s) of intact or cleaved **8** under both dark and blue light (irradiated) conditions, and compared to that of the mono-metal complexes (**9**; **11**). Antiproliferative screening and cellular accumulation ICP-MS studies of co-administered Ir-PDT (**9**) and Pt-PACT (**11**) compared to intact Ir-Pt (**8**) will provide insights into the necessity of conjugation. The intracellular detoxification of **8** in cancer cells can further be explored using cellular antioxidants such as GSH, either chemically (by monitoring the formation of metal-GSH adducts by HPLC/LC-MS),<sup>103</sup> or biologically (using L-buthionine sulfoximine – which depletes cellular levels of GSH).<sup>104</sup>

The multi-targeting of **8** can be investigated using mitochondrial/lysosomal bioassays (peptide deformylase, NeutralRed) or more advanced biological techniques including PCR amplification of isolated mitochondrial DNA or cytochrome c release assays.<sup>105, 106</sup> Correlative cryo-SIM, XRT and XRF would provide unambiguous information on the organelle-targeting of **8**, as close to physiological state as possible.<sup>40</sup> Moreover, advanced techniques such as LA-ICP-MS and NanoSIMS can be used to gain information into the quantification and distribution of metals in cells.<sup>89-92</sup>



## 4.6 References

1. M. Stapleton and L. E. Rhodes, *J Dermatolog Treat*, 2003, **14**, 107-112.
2. L. V. Chekulayeva, I. N. Shevchuk, V. A. Chekulayev and K. Ilmarinen, *J Environ Pathol Tox*, 2006, **25**, 51-77.
3. H. Guo, H. Qian, N. M. Idris and Y. Zhang, *Nanomedicine*, 2010, **6**, 486-495.
4. Z. Huang, H. Xu, A. D. Meyers, A. I. Musani, L. Wang, R. Tagg, A. B. Barqawi and Y. K. Chen, *Technol Cancer Res T*, 2008, **7**, 309-320.
5. T. Gheewala, T. Skwor and G. Munirathinam, *Oncotarget*, 2017, **8**, 30524-30538.
6. C. B. Simone, 2nd and K. A. Cengel, *Semin Oncol*, 2014, **41**, 820-830.
7. T. C. Johnstone, G. Y. Park and S. J. Lippard, *Anticancer Res* 2014, **34**, 471-476.
8. H. Huang, S. Banerjee and P. J. Sadler, *ChemBioChem*, 2018, **19**, 1574-1589.
9. C. Imberti, P. Zhang, H. Huang and P. J. Sadler, *Angew Chem Int Ed*, 2020, **59**, 61-73.
10. H. Huang, S. Banerjee, K. Qiu, P. Zhang, O. Blacque, T. Malcomson, M. J. Paterson, G. J. Clarkson, M. Staniforth, V. G. Stavros, G. Gasser, H. Chao and P. J. Sadler, *Nat Chem*, 2019, **11**, 1041-1048.
11. P. Zhang, C. K. C. Chiu, H. Huang, Y. P. Y. Lam, A. Habtemariam, T. Malcomson, M. J. Paterson, G. J. Clarkson, P. B. O'Connor, H. Chao and P. J. Sadler, *Angew Chem Int Ed*, 2017, **56**, 14898-14902.
12. L. K. McKenzie, I. V. Sazanovich, E. Baggaley, M. Bonneau, V. Guerchais, J. A. G. Williams, J. A. Weinstein and H. E. Bryant, *Chem Eur J*, 2017, **23**, 234-238.
13. V. Ramu, S. Gautam, P. Kondaiah and A. R. Chakravarty, *Inorg Chem*, 2019, **58**, 9067-9075.
14. M. A. Nazif, R. Rubbiani, H. Alborzinia, I. Kitanovic, S. Wölfl, I. Ott and W. S. Sheldrick, *Dalton Trans*, 2012, **41**, 5587-5598.
15. H. Shi, I. Romero-Canelón, M. Hreusova, O. Novakova, V. Venkatesh, A. Habtemariam, G. J. Clarkson, J.-i. Song, V. Brabec and P. J. Sadler, *Inorg Chem*, 2018, **57**, 14409-14420.

16. H. Shi, *PhD Thesis (Univerisity of Warwick)*, 2019.
17. P. J. Bednarski, F. S. Mackay and P. J. Sadler, *Anticancer Agents Med Chem*, 2007, **7**, 75-93.
18. H. Shi, C. Imberti and P. J. Sadler, *Inorg Chem Front*, 2019, **6**, 1623-1638.
19. C. Vallotto, E. Shaili, H. Shi, J. S. Butler, C. J. Wedge, M. E. Newton and P. J. Sadler, *Chem Comm*, 2018, **54**, 13845-13848.
20. P. J. Bednarski, R. Grunert, M. Zielzki, A. Wellner, F. S. Mackay and P. J. Sadler, *Chem Biol*, 2006, **13**, 61-67.
21. H. Shi, Q. Wang, V. Venkatesh, G. Feng, L. S. Young, I. Romero-Canelón, M. Zeng and P. J. Sadler, *Dalton Trans*, 2019, **48**, 8560-8564.
22. S. Xu, X. Zhu, C. Zhang, W. Huang, Y. Zhou and D. Yan, *Nat Comm*, 2018, **9**, 2053.
23. J. R. Kremer, D. N. Mastronarde and J. R. McIntosh, *J Struct Biol*, 1996, **116**, 71-76.
24. M. C. Darrow, I. Luengo, M. Basham, M. C. Spink, S. Irvine, A. P. French, A. W. Ashton and E. M. H. Duke, *J Vis Exp*, 2017, **126**, 56162.
25. V. Solé, E. Papillon, M. Cotte, P. Walter and J. Susini, *Spectrochim Acta B*, 2007, **62**, 63-68.
26. J. L. Gregg, K. M. McGuire, D. C. Focht and M. A. Model, *Pflugers Arch*, 2010, **460**, 1097-1104.
27. C. T. Rueden, J. Schindelin, M. C. Hiner, B. E. DeZonia, A. E. Walter, E. T. Arena and K. W. Eliceiri, *BMC Bioinformatics*, 2017, **18**, 529-529.
28. M. Harkiolaki, M. C. Darrow, M. C. Spink, E. Kosior, K. Dent and E. Duke, *Emerging Topics in Life Sciences*, 2018, **2**, 81-92.
29. J. Groen, J. J. Conesa, R. Valcárcel and E. Pereiro, *Biophys Rev*, 2019, **11**, 611-619.
30. A. Thompson, A. D., E. Gullikson, H. M., K.-J. Kim, J. Kirtz, J. Kortright, I. Lindau, Y. Liu, P. Pianetta, A. Robinson, J. Scofield, J. Underwood, G. Williams and H. Winick, *X-ray Data Booklet*, Lawrence Berkeley National Laboratory, Berkeley, 2 edn., 2009.
31. P. Stiefel, S. Schmidt-Emrich, K. Maniura-Weber and Q. Ren, *BMC Microbiol* 2015, **15**, 36-36.

32. Z.-X. Ren, H.-B. Yu, J.-S. Li, J.-L. Shen and W.-S. Du, *Biosci Rep*, 2015, **35**, e00202.
33. R. Camerlingo, R. Miceli, L. Marra, G. Rea, I. D'Agnano, M. Nardella, R. Montella, A. Morabito, N. Normanno, V. Tirino and G. Rocco, *PloS One*, 2019, **14**, e0219597-e0219597.
34. C. Nave, *J Synchrotron Radiat*, 2018, **25**, 1490-1504.
35. M. Chen, L. Tian and L. Waller, *Biomed Opt Express*, 2016, **7**, 3940-3950.
36. J.-H. Chen, A. Ekman, V. Weinhardt, G. McDermott, M. Gros and C. Larabell, *Biophys J*, 2019, **116**, 439a.
37. C. Moscheni, E. Malucelli, S. Castiglioni, A. Procopio, C. De Palma, A. Sorrentino, P. Sartori, L. Locatelli, E. Pereiro, J. A. Maier and S. Iotti, *Cancers (Basel)*, 2019, **11**, 1254.
38. J. J. Conesa, A. C. Carrasco, V. Rodriguez-Fanjul, Y. Yang, J. L. Carrascosa, P. Cloetens, E. Pereiro and A. M. Pizarro, *Angew Chem Int Ed*, 2020, **59**, 1270-1278.
39. M. Chiappi, J. J. Conesa, E. Pereiro, C. O. S. Sorzano, M. J. Rodríguez, K. Henzler, G. Schneider, F. J. Chichón and J. L. Carrascosa, *J Nanobiotechnology*, 2016, **14**, 15-15.
40. S. Gil, E. Solano, F. Martínez-Trucharte, J. Martínez-Esaín, A. Pérez-Berná, J. J. Conesa, C. Kamma-Lorger, M. Alsina and M. Sabés, *PloS One*, 2020, **15**, e0230022.
41. M. G. Vander Heiden, L. C. Cantley and C. B. Thompson, *Science*, 2009, **324**, 1029-1033.
42. R. Shiratori, K. Furuichi, M. Yamaguchi, N. Miyazaki, H. Aoki, H. Chibana, K. Ito and S. Aoki, *Sci Rep*, 2019, **9**, 18699.
43. E. M. H. Duke, M. Razi, A. Weston, P. Guttman, S. Werner, K. Henzler, G. Schneider, S. A. Tooze and L. M. Collinson, *Ultramicroscopy*, 2014, **143**, 77-87.
44. A. Penttilä, H. Kalimo and B. F. Trump, *J Cell Biol*, 1974, **63**, 197-214.
45. M. Berglund, L. Rymell, M. Peuker, T. Wilhein and H. M. Hertz, *J Microsc*, 2000, **197**, 268-273.
46. D. Millimaggi, C. Festuccia, A. Angelucci, S. D'Ascenzo, N. Rucci, S. Flati, M. Bologna, A. Teti, A. Pavan and V. Dolo, *Int J Oncol*, 2006, **28**, 909-914.

47. V. Vlaeminck-Guillem, *Front Oncol*, 2018, **8**, 222-222.
48. T. Lorenc, K. Klimczyk, I. Michalczywska, M. Słomka, G. Kubiak-Tomaszewska and W. Olejarz, *Int J Mol Sci*, 2020, **21**, 2118.
49. L. Paavolainen, E. Acar, U. Tuna, S. Peltonen, T. Moriya, P. Soonsawad, V. Marjomäki, R. H. Cheng and U. Ruotsalainen, *PloS One*, 2014, **9**, e108978-e108978.
50. A. Bartesaghi, P. Sprechmann, J. Liu, G. Randall, G. Sapiro and S. Subramaniam, *J Struct Biol*, 2008, **162**, 436-450.
51. L. Wiemerslage and D. Lee, *J Neurosci Methods*, 2016, **262**, 56-65.
52. Y. Zhang, X. Chen, C. Gueydan and J. Han, *Cell Res* 2018, **28**, 9-21.
53. G. G. Kramarenko, S. G. Hummel, S. M. Martin and G. R. Buettner, *J Photochem Photobiol*, 2006, **82**, 1634-1637.
54. V. Dogra and C. Kim, *Front Plant Sci*, 2020, **10**, 1640-1640.
55. E. Skovsen, J. W. Snyder, J. D. Lambert and P. R. Ogilby, *J Phys Chem B*, 2005, **109**, 8570-8573.
56. X.-B. Li, J.-D. Gu and Q.-H. Zhou, *Thorac Cancer*, 2015, **6**, 17-24.
57. B. Bhattacharya, S. H. H. Low, C. Soh, N. Kamal Mustapa, M. Belouèche-Babari, K. X. Koh, J. Loh and R. Soong, *Br J Pharmacol*, 2014, **171**, 3255-3267.
58. Y. Xu, W. Gao, Y. Zhang, S. Wu, Y. Liu, X. Deng, L. Xie, J. Yang, H. Yu, J. Su and L. Sun, *Int J Oncol*, 2018, **53**, 1055-1068.
59. E. Eidelman, J. Twum-Ampofo, J. Ansari and M. M. Siddiqui, *Front Oncol*, 2017, **7**, 131.
60. C. Bissardon, S. Reymond, M. Salome, L. Andre, S. Bayat, P. Cloetens and S. Bohic, *J Vis Exp*, 2019.
61. S. Antony, J. Aitken, S. Vogt, B. Lai, T. Brown, L. Spiccia and H. Harris, *J Biol Inorg Chem*, 2013, **18**, 845-353.
62. E. J. Sheridan, C. J. D. Austin, J. B. Aitken, S. Vogt, K. A. Jolliffe, H. H. Harris and L. M. Rendina, *J Synchrotron Radiat*, 2013, **20**, 226-233.
63. I. M. Rio-Echevarria, J. Ponti, A. Bogni, D. Gilliland, M. Altissimo, L. Pascolo, G. Ceccone and A. Gianoncelli, *X-Ray Spectrometry*, 2019, **48**, 94-101.

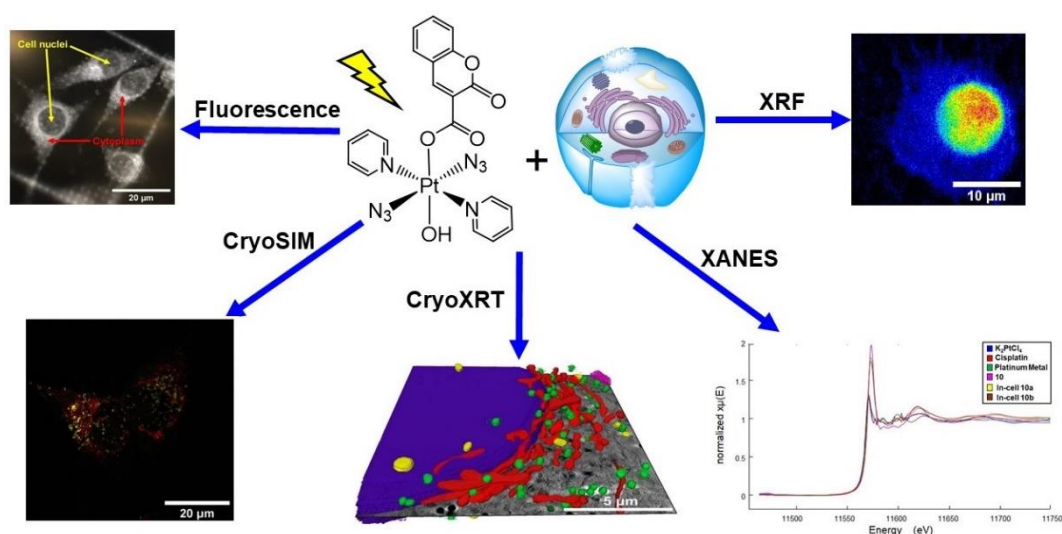
64. S. Chen, T. Paunesku, Y. Yuan, J. Deng, Q. Jin, Y. Hong, D. Vine, B. Lai, C. Flachenecker, B. Hornberger, K. Brister, C. Jacobsen, G. Woloschak and S. Vogt, *AIP Conf Proc*, 2016, **1696**, 020028.
65. Q. Chen, J. Kang and C. Fu, *Signal Transduct Tar Ther*, 2018, **3**, 18.
66. R. D. Jiang, H. Shen and Y. J. Piao, *Rom J Morphol Embryol*, 2010, **51**, 663-667.
67. W. Y. Zhang, Q. Y. Yi, Y. J. Wang, F. Du, M. He, B. Tang, D. Wan, Y. J. Liu and H. L. Huang, *Eur J Med Chem*, 2018, **151**, 568-584.
68. W.-W. Qin, Z.-Y. Pan, D.-H. Cai, Y. Li and L. He, *Dalton Trans*, 2020, **49**, 3562-3569.
69. P. I. Djurovich, D. Murphy, M. E. Thompson, B. Hernandez, R. Gao, P. L. Hunt and M. Selke, *Dalton Trans*, 2007, DOI: 10.1039/B704595F, 3763-3770.
70. Q. Du, L. Zhao, L. Guo, X. Ge, S. Zhang, Z. Xu and Z. Liu, *App Organomet Chem*, 2019, **33**, e4746.
71. F.-X. Wang, M.-H. Chen, Y.-N. Lin, H. Zhang, C.-P. Tan, L.-N. Ji and Z.-W. Mao, *ACS Appl Mater Interfaces*, 2017, **9**, 42471-42481.
72. L. He, Y. Li, C. P. Tan, R. R. Ye, M. H. Chen, J. J. Cao, L. N. Ji and Z. W. Mao, *Chem Sci*, 2015, **6**, 5409-5418.
73. F. Kazmi, T. Hensley, C. Pope, R. S. Funk, G. J. Loewen, D. B. Buckley and A. Parkinson, *Drug Metab Dispos*, 2013, **41**, 897-905.
74. J. S. Nam, M.-G. Kang, J. Kang, S.-Y. Park, S. J. C. Lee, H.-T. Kim, J. K. Seo, O.-H. Kwon, M. H. Lim, H.-W. Rhee and T.-H. Kwon, *J Am Chem Soc*, 2016, **138**, 10968-10977.
75. A. V. Klein and T. W. Hambley, *Chem Rev*, 2009, **109**, 4911-4920.
76. R. Ortega, P. Moretto, A. Fajac, J. Benard, Y. Llabador and M. Simonoff, *Cell Mol Biol* 1996, **42**, 77-88.
77. R. F. S. Lee, T. Riedel, S. Escrig, C. Maclachlan, G. W. Knott, C. A. Davey, K. Johnsson, A. Meibom and P. J. Dyson, *Metallomics*, 2017, **9**, 1413-1420.
78. N. J. Farrer, J. A. Woods, L. Salassa, Y. Zhao, K. S. Robinson, G. Clarkson, F. S. Mackay and P. J. Sadler, *Angew Chem Int Ed*, 2010, **49**, 8905-8908.
79. K. Vogel-Mikus and P. Kump, *J Instrum*, 2018, **13**.

80. J. Deng, D. J. Vine, S. Chen, Q. Jin, Y. S. G. Nashed, T. Peterka, S. Vogt and C. Jacobsen, *Sci Rep*, 2017, **7**, 445.
81. T. W. Victor, L. M. Easthon, M. Ge, K. H. O'Toole, R. J. Smith, X. Huang, H. Yan, K. N. Allen, Y. S. Chu and L. M. Miller, *Sci Rep*, 2018, **8**, 13415.
82. Y. Yang, H. Hong, Y. Zhang and W. Cai, *Cancer Growth Metastasis*, 2009, **2**, 13-27.
83. D. Gibson, *Dalton Trans*, 2016, **45**, 12983-12991.
84. S. Harrach and G. Ciarimboli, *Front Pharmacol*, 2015, **6**, 85-85.
85. X. Liu, B. Testa and A. Fahr, *Pharm Res*, 2011, **28**, 962-977.
86. R. McRae, P. Bagchi, S. Sumalekshmy and C. J. Fahrni, *Chem Rev*, 2009, **109**, 4780-4827.
87. H. U. Holtkamp, S. Movassaghi, S. J. Morrow, M. Kubanik and C. G. Hartinger, *Metallomics*, 2018, **10**, 455-462.
88. A. A. Hummer and A. Rompel, *Metallomics*, 2013, **5**, 597-614.
89. A. A. Legin, S. Theiner, A. Schintlmeister, S. Reipert, P. Heffeter, M. A. Jakupiec, J. Mayr, H. P. Varbanov, C. R. Kowol, M. Galanski, W. Berger, M. Wagner and B. K. Keppler, *Chem Sci*, 2016, **7**, 3052-3061.
90. K. Wu, F. Jia, W. Zheng, Q. Luo, Y. Zhao and F. Wang, *J Biol Inorg Chem*, 2017, **22**, 653-661.
91. R. Lee, S. Escrig, M. Croisier, S. Clerc-Rosset, G. Knott, A. Meibom, C. Davey, K. Johnsson and P. Dyson, *Chem Comm*, 2015, **51**, 16486-16489.
92. K. Löhr, H. Traub, A. J. Wanka, U. Panne and N. Jakubowski, *J Anal At Spectrom* 2018, **33**, 1579-1587.
93. M. Corte Rodríguez, R. Álvarez-Fernández García, E. Blanco, J. Bettmer and M. Montes-Bayón, *Anal Chem*, 2017, **89**, 11491-11497.
94. H. Li, T.-Y. Lin, S. L. Van Orden, Y. Zhao, M. P. Barrow, A. M. Pizarro, Y. Qi, P. J. Sadler and P. B. O'Connor, *Anal Chem*, 2011, **83**, 9507-9515.
95. K. Hwang, Q. Mou, R. J. Lake, M. Xiong, B. Holland and Y. Lu, *Inorg Chem* 2019, **58**, 13696-13708.
96. R. Berrocal-Martin, C. Sanchez-Cano, C. K. C. Chiu, R. J. Needham, P. J. Sadler and S. W. Magennis, *Chem Eur J*, 2020, **26**, 4980-4987.
97. M. Schürmann, J. Scholze, P. Müller, J. Guck and C. J. Chan, *J Biophotonics*, 2016, **9**, 1068-1076.

98. B. Alberts, A. Johnson, J. Lewis and e. al., in *Molecular Biology of the Cell. 4th edition.*, Garland Science, New York, 2002.
99. A. V. Shubin, I. V. Demidyuk, A. A. Komissarov, L. M. Rafieva and S. V. Kostrov, *Oncotarget*, 2016, **7**, 55863-55889.
100. K. J. Thomas and M. R. Jacobson, *PloS One*, 2012, **7**, e45319-e45319.
101. T. Fujimoto and R. G. Parton, *Cold Spring Harb Perspect Biol*, 2011, **3**, a004838.
102. D. Bandyopadhyay, A. Cyphersmith, J. A. Zapata, Y. J. Kim and C. K. Payne, *PloS One*, 2014, **9**, e86847-e86847.
103. R. J. Needham, C. Sanchez-Cano, X. Zhang, I. Romero-Canelón, A. Habtemariam, M. S. Cooper, L. Meszaros, G. J. Clarkson, P. J. Blower and P. J. Sadler, *Angew Chem Int*, 2017, **56**, 1017-1020.
104. I. Romero-Canelón, M. Mos and P. J. Sadler, *J Med Chem*, 2015, **58**, 7874-7880.
105. N. J. Waterhouse and J. A. Trapani, *Cell Death & Differ*, 2003, **10**, 853-855.
106. S. P. Wisnovsky, J. J. Wilson, R. J. Radford, M. P. Pereira, M. R. Chan, R. R. Laposa, S. J. Lippard and S. O. Kelley, *Chem Biol*, 2013, **20**, 1323-1328.

# Chapter 5

## X-ray studies of photoactivatable platinum complexes in cancer cells





## 5.1 Introduction

In this Chapter, the intracellular mechanisms of action of diazido-Pt<sup>IV</sup> PACT prodrugs have been investigated using complementary synchrotron techniques. Firstly, the localisation of a coumarin-labelled diazido-Pt<sup>IV</sup> complex which exhibits fluorescence upon photoactivation with light (**12**, **Fig. 5.1**,  $\lambda_{\text{ex/em}}=405/450 \text{ nm}$ )<sup>1</sup> in PC3 prostate cancer cells was investigated using cryogenic fluorescence microscopy and cryo-Structured Illumination Microscopy (cryo-SIM). Correlative cryo-X-ray Tomography (Cryo-XRT) was used to gain insight into the morphological and ultrastructural changes induced by **12** in PC3 cells down to a remarkable subcellular 40 nm resolution. These studies provide a crucial understanding of cellular targets, mechanisms of cell death and drug efficacy. Importantly, cells were analysed cryogenically (without the use of chemical stains or labels), allowing investigations of treated cancer cells close to their native states. Complementary to this, nanofocused synchrotron-XRF and XANES were used to probe the intracellular distribution of Pt ( $L_3M_5=9.44 \text{ keV}$ ) and its oxidation state in cryo-fixed and freeze-dried PC3 cancer cells to provide a further understanding into the cellular targets, drug activation and the mechanism of action.

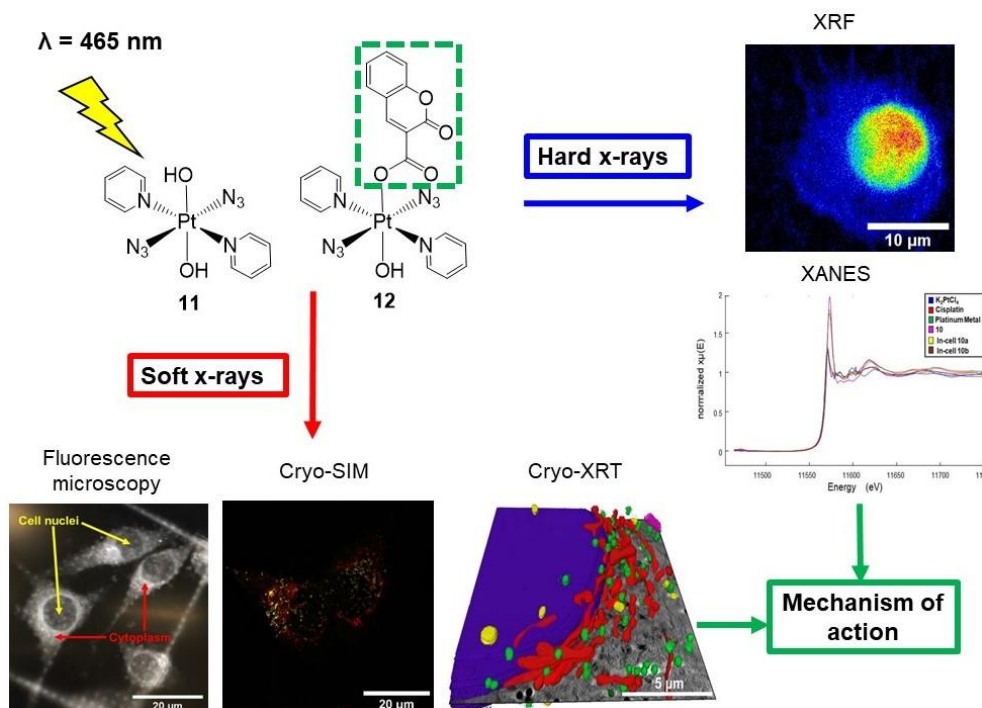


**Figure 5.1.** Graphical representation of the techniques used in this Chapter to investigate the intracellular mechanisms of action and cellular targets of complexes **11** and **12**.

In contrast to PDT (discussed in **Chapter 4**), PACT involves the chemical activation of a prodrug upon irradiation with a specific wavelengths of light (*e.g.* ligand loss) and is much less-dependent on oxygen levels.<sup>2</sup> In particular, Pt<sup>IV</sup> photoactivatable prodrugs are of significant interest in the development of chemotherapeutics which can circumvent cisplatin-resistance by utilizing *in situ* photodecomposition, allowing both temporal and spatial control over metal complex activation.<sup>3,4</sup>

In 1978, the photo-reductive properties of a series of Pt<sup>IV</sup> diazidyl complexes were first reported.<sup>5</sup> This has since led to the development of remarkably stable photoactivatable diazido-Pt<sup>IV</sup> complexes with promising anticancer activity.<sup>6-14</sup> The development of photoactivatable Pt<sup>IV</sup> prodrugs has the potential to overcome intrinsic and acquired resistance of cancer cells towards Pt<sup>II</sup> clinical drugs through a multi-targeting approach, while reducing off-target toxic effects using spatially-directed light.<sup>15</sup> In particular, *trans, trans, trans*-[Pt(N<sub>3</sub>)<sub>2</sub>(OH)<sub>2</sub>(py)<sub>2</sub>] (**11**, where py=pyridine, **Figure 5.1**) has shown promise as a PACT anticancer agent against a variety of human cancer cells,<sup>11</sup> and is significantly more potent than cisplatin with lower dosages and shorter drug exposure times.<sup>11</sup> It is hypothesised that **11** can be photo-reduced intracellularly to form an active Pt<sup>II</sup> species *in situ*.<sup>16</sup> As such, **11** is a prodrug which can be used to improve factors such as pharmacokinetics, targeting and toxicity.<sup>17,18</sup> The remarkable stability and slow ligand-exchange kinetics of Pt<sup>IV</sup> compounds can be advantageous over Pt<sup>II</sup> clinical drugs as they can resist premature aquation and the unwanted binding to plasma proteins, which ultimately reduces Pt<sup>II</sup> drug efficacy.<sup>19</sup>

The family of diazido-Pt<sup>IV</sup> prodrugs from which **11** is derived achieve high photocytotoxicity through blue light activation ( $\lambda=465$  nm), while retaining high chemical stability under dark conditions.<sup>4</sup> These complexes can be photo-reduced to form both toxic Pt<sup>II</sup> species and release cytotoxic ligands (*e.g.* azidyl or hydroxyl radicals, **Fig. 5.2**), as shown by UV-visible spectroscopy,<sup>13, 20</sup> ESI-MS,<sup>11</sup> IR spectroscopy<sup>21</sup> and NMR (<sup>1</sup>H, <sup>195</sup>Pt, <sup>13</sup>C and <sup>15</sup>N).<sup>11</sup> The potential interactions of **11** with nuclear DNA have also been investigated using electrophoresis, which revealed that the cellular response and the nature of DNA lesions were distinct to that of clinical drug cisplatin.<sup>11</sup> This may provide an alternative mechanism of action to conventional Pt<sup>II</sup> chemotherapeutics.

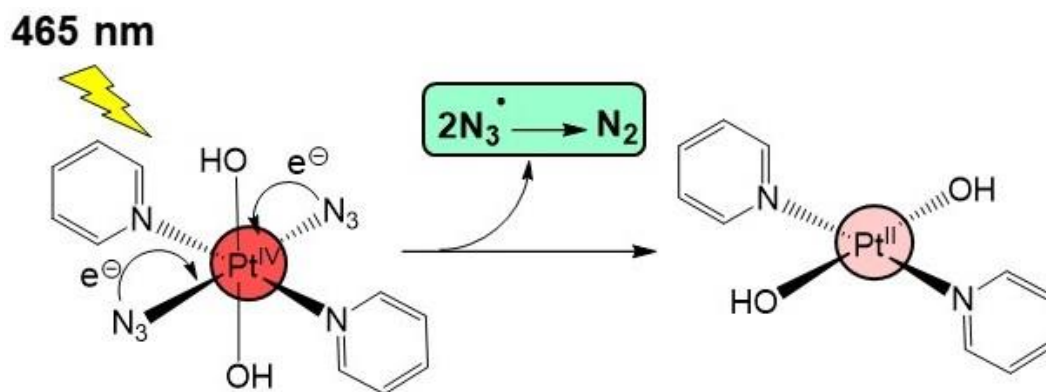


**Figure 5.2.** The main proposed mechanism for the photo-reduction of **11** using blue light ( $\lambda=465$  nm) via the release of azidyl radicals, to form a Pt<sup>II</sup> species.<sup>4</sup>

Interestingly, the antiproliferative activity of **11** can be significantly enhanced by coordinating detachable ligands in the axial position. For example, using the axial OR position to join different dinuclear Pt modalities using bisamide dicarboxylato linkers,<sup>22</sup> bioactive ligands (*i.e.* biotin)<sup>23</sup> or radical markers (*e.g.* TEMPO=2,2,6,6-tetramethylpiperidine-1-oxyl).<sup>24</sup> This labelling strategy provides an opportunity for multi-targeting by releasing pharmacologically-active ligands upon irradiation, whilst maintaining the “inactive” form in the dark. This has been previously been probed using FTIR which revealed that reduction of Pt<sup>IV</sup> to Pt<sup>II</sup> (in **11**) proceeds *via* the release of at least one hydroxyl and one azidyl radical, or by two hydroxyl radicals upon irradiation.<sup>21</sup>

Conjugation of coumarin (a biologically active fluorophore with antitumour properties)<sup>25</sup> to the axial position of diazido-Pt<sup>IV</sup> prodrugs (**12**, **Fig. 5.1**) significantly increased the potency in PC3 prostate cancer cells compared to parent compound **11** (by *ca.* 8×) upon blue light irradiation.<sup>26</sup> Interestingly, photo-activated **12** can exhibit blue fluorescence (attributed to 7-hydroxycoumarin-3 carboxylate and radical photo-products containing hydroxido and coumarin-3 carboxylato ligands),<sup>26</sup> thus, can be used as a fluorescent probe to elucidate potential cellular targets using correlative cryo-SIM and cryo-XRT. As coumarin itself displays antitumour properties, it cannot be assumed that **12** has the same mechanism of action as **11**. Nonetheless, it can still be used to gain essential insights into the potential in-cell activities of **12** and other such diazido-Pt<sup>IV</sup> prodrugs.

## 5.2 Experimental

### 5.2.1 Synthesis of platinum complexes

Complex **11** used in these experiments was synthesized by Dr Cinzia Imberti (University of Warwick) using a published literature method.<sup>11</sup> Complex **12** was synthesized by Dr Huayun Shi (University of Warwick) as previously reported.<sup>26</sup> Both complexes were >95% pure and were stored under dark conditions prior to commencement of biological *in vitro* studies.

### 5.2.2 Antiproliferative activity (IC<sub>50</sub>)

The half-maximal inhibitory concentration (IC<sub>50</sub> /  $\mu\text{M}$ ) of **11** in PC3 cells was previously reported in the literature using an optimized protocol: 1 h incubation in the dark, followed by 1 h blue light irradiation ( $\lambda=465\text{ nm}$ ,  $4.8\text{ mW/cm}^2$ ), and 24 h recovery in the dark and complex-free media.<sup>11</sup> The IC<sub>50</sub> of **12** in PC3 cells was determined by Dr. Huayun Shi (University of Warwick) under the same conditions, using the SRB assay protocol (**Chapter 2, Section 2.5.1**).

### 5.2.3 Cryo-XRT sample preparation

#### Preparation of TEM grids

Quantifoil Au-C R2/2 F1 200 mesh finder grids were prepared using the general method described in **Chapter 2 (Section 2.6.2)**. Cells were treated with 0.25–1 $\times$  irradiated IC<sub>50</sub> (IC<sub>50</sub>=6.5  $\mu\text{M}$ ) of **12** (prepared in non-phenol red RPMI-1640, protected from light) for 1 h, followed by irradiation with blue light (465 nm, 1 h,  $4.8\text{ mW J/cm}^2$ ) or dark conditions (2 h, protected from light). The supernatant was removed and cells recovered in complex-free RMPI-1640 for 0 or 2 h (protected from light). Grids were then incubated in MitoTracker FarRed (100 nM) and LysoTracker Red (100 nM) for 20 min (310 K, 5% CO<sub>2</sub>) before blotting with AuNP fiducials (d=250 nm) and plunge-freezing in liquid ethane.

### Fluorescence mapping of TEM grids

Preliminary correlative microscopy analysis on plunge-frozen grids was performed on a Zeiss Axioimager M2 optical microscopy (50×) coupled to a Linkam Scientific cryostage (CMS196M LED) to monitor: (i) MitoTracker DeepRed, (ii) LysoTracker Red, and (iii) blue fluorescent photo-products of **12** (Table 5.1). Suitable cell candidates were selected for cryo-XRT analysis.

**Table 5.1.** Excitation and emission wavelengths of MitoTracker DeepRed, LysoTracker Red and **12**, and the fluorescence filters used to map them.

Fluorophore	Fluorophore $\lambda_{\text{ex/em}}$ (nm)	Filter	Filter $\lambda_{\text{ex/em}}$ (nm)
<b>MitoTracker DeepRed</b>	644/665	<b>mPlum</b>	585/645
<b>LysoTracker Red</b>	577/590	<b>YFP</b>	514/527
<b>12</b>	405/450	<b>DAPI</b>	358/461

### Cryo-SIM

Prior to cryo-XRT measurements, cryo-SIM was performed (B24 beamline, DLS). The cryo-SIM has a long distance air objective (100X, 2 mm, 0.9NA) with 4 available excitation lasers: 405, 488, 561 and 642nm (10-100 Wcm<sup>-2</sup> laser power).<sup>27</sup> A maximal lateral resolution of 360 nm (with green light) can be achieved at this facility, allowing the imaging of conventional fluorophores with low doses and rapid image acquisition (<100 ms).<sup>27, 28</sup> Cryo-SIM was used to generate super-resolution fluorescence information on cryopreserved PC3 cells treated with (i) MitoTracker Deep Red ( $\lambda_{\text{ex/em}}$ =644/665 nm); (ii) LysoTracker Red ( $\lambda_{\text{ex/em}}$ =577/590 nm); (i) blue fluorescent complex **12** ( $\lambda_{\text{ex/em}}$ =405/450 nm) on quantifoil grids (Table 5.2). Three maps per grid were obtained: (i) z-stack brightfield mosaic; (ii) Red ( $\lambda_{\text{em}}$ =605 nm) + Blue (DAPI,  $\lambda_{\text{em}}$ =452 nm) and (iii) FarRed ( $\lambda_{\text{em}}$ =655 nm) + Blue (DAPI,  $\lambda_{\text{em}}$ =452 nm). A total of 15 images per z-plane were collected (3× angles at 60° apart, 5× phases) at 125 nm increments.<sup>27, 28</sup> The blue laser parameters were kept consistent throughout all sample measurements ( $\lambda$ =405 nm, 100 ms, 149.963 mW). Images of 512×512 pixel were obtained and reconstructed for form stacks of images (voxel size=0.0625×0.0625×0.0125  $\mu\text{m}^3$ ).

**Table 5.2.** Excitation and emission wavelengths of MitroTracker DeepRed, LysoTracker Red and **11** with the excitation laser wavelengths and emission filters available at the B24 beamline cryo-SIM facility.

Fluorophore	Fluorophore $\lambda_{\text{ex/em}}$ (nm)	Excitation wavelength (nm)	Emission filter (nm)
MitoTracker DeepRed	644/665	642	655
LysoTracker Red	577/590	561	605
<b>12</b>	405/450	405	452

### Cryo-SIM data analysis

Data were processed in SoftWoRX 6.5.2 (GE Healthcare) using real optical transfer functions (generated from 3D-SIM images of fluorescent beads of 175  $\mu\text{m}$ ) to produce image stacks. Processed data were then analysed in Fiji imaging software to separate the fluorescence channels.<sup>29</sup> The brightness of the blue channel was adjusted to eliminate blue fluorescence in the untreated control cells. The same parameters were then used to separate the channels in cells treated with  $1 \times \text{IC}_{50}$  of **12** under dark and irradiated (465 nm) conditions. For all samples, the blue laser conditions were kept the same ( $\lambda=405$  nm, 100 ms, 149.963 mW).

### Cryo-XRT Sample loading onto the beamline

Pre-mapped quantifoil grids were cryogenically loaded into 4 sample holders at the B24 beamline (**Chapter 2, Section 2.6.2**). Cells of interest were analysed by cryo-XRT in the tilt range  $-65$  to  $+65^\circ$  using an energy of 500 eV, 0.1 s exposure, 0.2-0.5° sample rotation steps, as specified.

### Tomogram reconstruction in IMOD

Tomograms were aligned and reconstructed automatically (unless specified otherwise). Tomograms which did not reconstruct sufficiently were manually modified in IMOD (**Chapter 2, Section 2.6.2**).<sup>30</sup>

### **Volume segmentation and visualization**

Volume segmentation was performed in SuRVoS imaging software,<sup>31</sup> as described in **Chapter 2 (Section 2.6.2)**. Segmentation of mitochondria and lipid droplets in each tomogram was performed to determine 3D volumes ( $\mu\text{m}^3$ ). Full segmentation of two representative tomograms was performed (**T3**=dark, untreated control; **T17**= $1 \times \text{IC}_{50}$  of **12**; 1 h incubation followed by 1 h irradiation with 465 nm), which included: mitochondria, lipid droplets, nucleus, dense organelles/vesicles, the plasma membrane and cytoplasmic vacuoles.

## **5.2.4 Synchrotron-XRF and XANES**

### **Preparation of $\text{Si}_3\text{N}_4$ membranes**

Silicon nitride ( $\text{Si}_3\text{N}_4$ ) membranes were prepared as described in **Chapter 2 (Section 2.6.1)** using a seeding density of  $8 \times 10^4$  cells / mL of PC3 cells. Cells were treated with  $5 \times \text{IC}_{50}$  of **11** ( $\text{IC}_{50}=55 \mu\text{M}$ ), **12** ( $\text{IC}_{50}=6.5 \mu\text{M}$ ) or **cisplatin** ( $\text{IC}_{50}>100 \mu\text{M}$ ) for (i) 2 h in the dark or (ii) 1 h incubation (protected from light) followed by 1 h irradiation (in drug) with blue light ( $\lambda=465 \text{ nm}$ ,  $4.8 \text{ mW/cm}^2$ ). The supernatant drug was removed and cells washed with HBSS (2 mL per well).

### **Synchrotron-XRF beamline settings**

$\text{Si}_3\text{N}_4$  membranes were loaded into the sample holders provided at the I14 beamline (DLS, Oxford) and analysed at room temperature (298 K), as described in **Chapter 2 (Section 2.6.1)**. All synchrotron-XRF maps were obtained by raster scanning using an incident energy of 14 keV, 100 nm step size and 0.1 s exposure.

### **Data analysis**

All elemental maps were fitted using PyMCA toolkit software developed by the ESRF.<sup>32</sup> The photon flux (photons per second) was estimated by running an AXO standard  $\text{Si}_3\text{N}_4$  membrane containing known elemental concentrations to further enable quantification of platinum. Data were analysed in Image J software.<sup>33</sup> All other information is specified in **Chapter 2 (Section 2.6.1)**.

### XANES pellets

Reference samples were prepared for XANES analysis. In addition to a metallic Pt foil, solid pellet samples of **cisplatin**, potassium tetrachloroplatinate ( $\text{K}_2\text{PtCl}_4$ ) and **11** were prepared by grinding 3–4 mg with 25–30 mg of dried cellulose using a pestle and mortar and formed in a 10 mm die by applying a 1.5 T force with a pellet press (Specac, UK). The resulting pellets were sealed in Kapton tape to protect them from the environment and to allow labelling. Because of the light sensitivity of  $\text{Pt}^{\text{IV}}$  photoactivatable complex **11**, the pellet was formed under dark conditions and taped in aluminized mylar to protect it from light.

### Experimental setup for XANES

**Solid pellets & metal sheet:** In order to improve signal quality and offer a user-friendly experience when dealing with pellets and foils, reference samples are measured upstream from the focusing optics by placing them between two ion chambers which monitor the position of the full beam (**Fig. 5.3**). XANES spectra were acquired in the energy range 11.46–11.73 keV, across the Pt  $L_3$ -edge (11.57 keV).<sup>34</sup> The energy step was variable, with step sizes ranging from 8 eV away from the edge to 0.5 eV across the edge. Typical analysis of solid pellets and the metal sheet took no longer than 30 min each, as spatial resolution was not required.

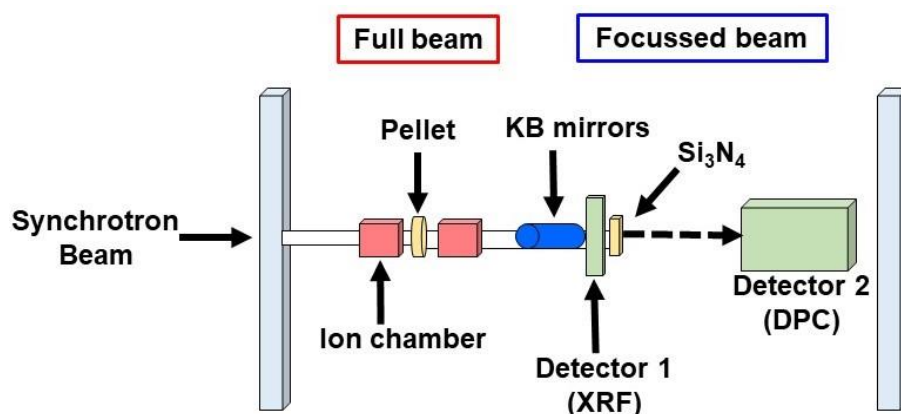


**Figure 5.3.** Schematic of the experimental hutch. Solid pellets and foils were analysed upstream with the full beam (left), whereas,  $\text{Si}_3\text{N}_4$  cell samples were analysed further downstream with the focussed beam. There are two detectors used: Detector 1 (back-scattered XRF detector) and Detector 2 (DPC detector used in **Chapter 4**).



**Si<sub>3</sub>N<sub>4</sub> cell samples:** In this case the beam was focussed to a 50 nm spot, and the sample is raster-scanned across the region of interest (ROI). At each point of the ROI a full XRF spectrum is acquired, and element-specific images are derived by extracting the corresponding signal from the spectrum. Two different 5×5 μm<sup>2</sup> Pt-containing regions (in cryo-fixed and freeze-dried PC3 cells treated with 5×IC<sub>50</sub> of **11** under blue light conditions) were analysed. XANES mapping of the Si<sub>3</sub>N<sub>4</sub> cell samples were acquired in the energy range 11.46–11.73 keV, across the Pt L<sub>3</sub>-edge (11.57 keV).<sup>34</sup> The energy step was variable, with step sizes ranging from 8 eV away from the edge to 0.5 eV across the edge (dwell time=0.2 s, 200 nm steps, 50×70 nm<sup>2</sup>). Spatially-resolved XANES spectra were constructed from XRF scans at the specified energies, generating a full spatially-resolved XRF map at each energy over the Pt-edge. In addition to the traditional data acquisition method of scanning the energy with the monochromator, a compressed sensing approach currently in development at I14 was applied to some samples as a method test. This involved acquiring data at only 7 selected energy points in the energy range, rather than the 150 of the default method. The analysis of 5×5 μm<sup>2</sup> region using conventional “Energy-scanning” method took *ca.* 10-12 h, whereas to analyse a 5×5 μm<sup>2</sup> region using the “Compressed-Sensing” method took *ca.* 1-1.5 h.

### Obtaining XANES spectra

For in-cell Pt XANES measurements (for which we require spatial resolution using a focussed beam), multiple XRF spectra of the 5×5 μm<sup>2</sup> ROI were acquired. The XRF peaks of alignment elements (known elements in the sample) were integrated to produce 1 value per pixel using Python software. The images were then stacked and unwanted information removed. From this, the same alignment parameters were applied to the Pt XRF peak (L<sub>3</sub>M<sub>5</sub>=9.44 keV).<sup>34</sup> Principle Component Analysis (mathematical decomposition) was performed on the XRF spectra, followed by cluster analysis (both in Python) to obtain XANES spectra.

### Normalisation of XANES spectra

XANES spectra were analysed in Athena XAS Data Analysis Software.<sup>35</sup> Data were normalised using edge-step normalisation formulae (**Equation 5.1**). Edge-step normalisation extrapolates the difference between pre-edge subtraction and post-edge regression to the edge itself. In this case, pre-edge normalisation was performed in the energy range 11.47-11.54 keV and the post-edge normalisation was performed in the range 11.59-11.75 keV, and a normalisation order=2.

$$X(E) = \frac{\mu(E) - \mu_0(E)}{\mu_0(E_0)}$$

**Equation 5.1.** Equation for edge-step normalisation of XANES spectra, where  $X(E)$  is the theoretical absorption coefficient,  $\mu(E)$  is the experimental absorption coefficient and  $\mu_0(E_0)$  is the energy-independent edge jump.

### XANES data analysis

A linear combination fit (LCF) was performed on both sets of cellular Pt regions (obtained by the “Compressed sensing” and “Energy-scanning” methods, respectively) with respect to the solid pellets (**cisplatin**, **K<sub>2</sub>Cl<sub>4</sub>Pt** and **11**) and platinum foil. Conventional curve-fitting techniques cannot be used to reliably determine the relative proportions of Pt<sup>II</sup>:Pt<sup>IV</sup> species in a mixture (due to similarities in peak energy and shape), hence, a method developed by Hambley *et al* specifically for Pt<sup>IV</sup>/Pt<sup>II</sup> systems was also used to analyse the data. This method normalises the maximal edge-absorption (height of peak) with the post-edge minima after the white line (**Fig. 5.4**).<sup>36, 37</sup>

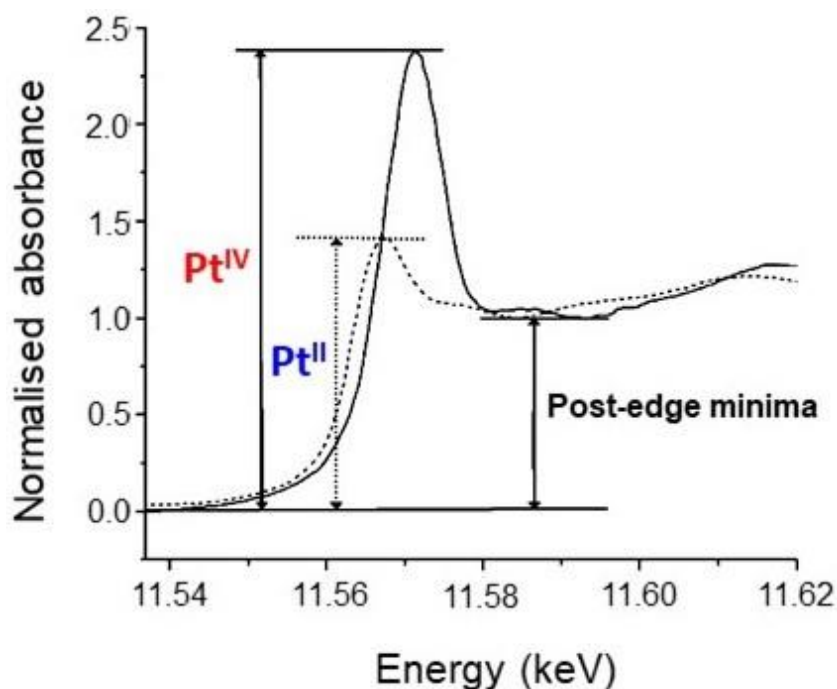


**Figure 5.4.** XANES spectra of Pt<sup>IV</sup> and Pt<sup>II</sup> compounds, showing the maximum peak absorptions for each oxidation state (a) and the post-edge minima. Reprinted (adapted) with permission from (M. D. Hall, G. J. Foran, M. Zhang, P. J. Beale and T. W. Hambley, *J Am Chem Soc*, 2003, 125, 7524-7525.). Copyright (2003) American Chemical Society as modified from a literature figure.<sup>37</sup>

## 5.3 Results

### 5.3.1 Antiproliferative activity (IC<sub>50</sub>)

The antiproliferative activities of **11** and **12** were determined in PC3 prostate cancer cells upon 1 h drug exposure (protected from light), 1 h light irradiation (465 nm, 4.8 mW J/cm<sup>2</sup>) and 24 h recovery in complex-free media, protected from the light. Coumarin-labelled **12** was 8× more potent than that of parent compound **11** in PC3 cells upon exposure to blue light of the same intensity and dosage (**Table 5.3**,  $p=0.0001$ ). Additionally, antiproliferative activities of **11** and **12** were determined under dark conditions (2 h exposure under dark conditions, 24 h recovery in complex-free medium). Both complexes exhibited low dark antiproliferative activity (IC<sub>50</sub>>100 μM). For comparison, the antiproliferative activity of **cisplatin** was determined under the same conditions, revealing inactivity (IC<sub>50</sub>>100 μM) under both dark and irradiated conditions (**Table 5.3**).

**Table 5.3.** Half-maximal inhibitory concentration ( $IC_{50}$  /  $\mu M$ ) and cellular accumulation of platinum in PC3 cancer cells treated with **11**, **12** and **cisplatin**.<sup>26</sup>

Complex	$IC_{50}$ / $\mu M$ (dark) <sup>[a]</sup>	$IC_{50}$ / $\mu M$ (465 nm) <sup>[b]</sup>
<b>11</b>	>100**	55.6 $\pm$ 0.9
<b>12</b>	>100**	6.48 $\pm$ 0.84
<b>Cisplatin</b>	>100**	>100**

<sup>[a]</sup> 1 h drug exposure + 1 h in dark conditions, then 24 h in drug-free media; <sup>[b]</sup> 1 h drug exposure + 1 h blue light irradiation (465 nm), then 24 h in drug-free media. <sup>[c]</sup> Literature  $IC_{50}$  value for **11**.<sup>11</sup>  
 \*\*100  $\mu M$  concentration is higher than the test range, thus, are deemed inactive.

### 5.3.2 Synchrotron cryo-XRT

#### Cryogenic light microscopy

TEM grids were analysed under cryogenic conditions using correlative light microscopy. Bright-field mosaics of full grids were acquired to identify suitable cell candidates. YFP ( $\lambda_{ex/em}$ =514/527 nm), mPlum ( $\lambda_{ex/em}$ =585/645 nm) and DAPI ( $\lambda_{ex/em}$ =358/461 nm) filters were used to map the LysoTracker Red ( $\lambda_{ex/em}$ =577/590 nm), MitoTracker FarRed ( $\lambda_{ex/em}$ =644/665 nm and **12** ( $\lambda_{ex/em}$ =405/450 nm).

PC3 cells were located within the finder grid, looking for individual cells positioned in the centre of the different quadrants (not located on or near the mesh grid lines; to ensure they allow penetration of soft x-ray and can be accessed by cryo-XRT) and in areas showing a reduced ice layers and no tweezer damage. Unfortunately, the blue fluorescence ( $\lambda_{em}$ =450 nm) of the photoproducts of **12** was not observed on the Zeiss Axioimager microscope under the concentration used to treat cells for the experiment (0.25–1.0 $\times IC_{50}$ ; 1.5–6.5  $\mu M$ ). Nonetheless, suitable cells were selected and analysed by cryo-SIM prior to cryo-XRT. A representative example of suitable cryopreserved PC3 cells grown on TEM grids is shown in **Fig. 5.5**.

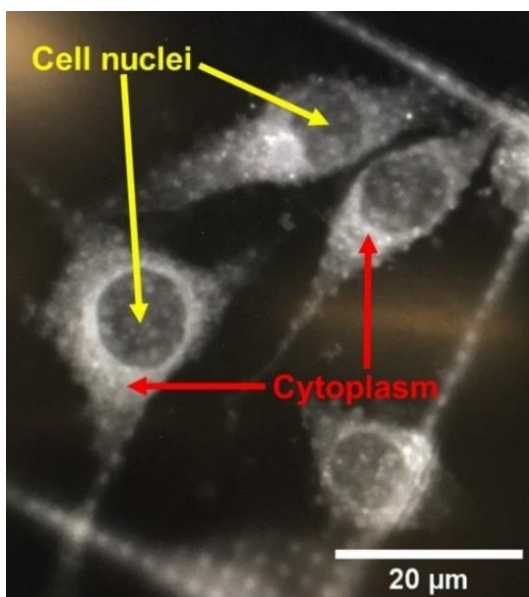


**Figure 5.5.** Representative example of a fluorescence microscopy image of cryopreserved, untreated PC3 prostate cancer cells (negative control) grown on a carbon-gold TEM grid under dark conditions, monitoring the fluorescence of LysoTracker Red ( $\lambda_{\text{ex/em}}=577/590$  nm). The image were recorded on a Zeiss Axioimager coupled to a Linkam cryostage. Showing elongated, cobble-stoned typical morphologies of PC3 cells (*ca.* 30-40  $\mu\text{m}$  in length),<sup>38, 39</sup> with clear cell nuclei.

### CryoSIM

Structure-Illumination Microscopy (SIM) can be used to gain super-resolution fluorescence information of biological samples beyond the Abbe diffract limit.<sup>40</sup> SIM is compatible with conventional fluorophores, including MitoTracker Deep Red ( $\lambda=644/665$  nm) and LysoTracker Red ( $\lambda=577/590$  nm).<sup>27</sup> Herein, cryopreserved PC3 cells treated with  $1\times\text{IC}_{50}$  of **12** (which forms blue fluorescent photoproducts upon irradiation with light)<sup>26</sup> and incubated with MitoTracker Deep Red and LysoTracker Red were monitored using cryo-SIM at the super-resolution light microscopy facility at the B24 beamline (DLS, Oxford).<sup>41</sup>

Cryopreserved PC3 cells incubated with MitoTracker Deep Red and LysoTracker Red revealed strong fluorescence emissions (**Fig. 5.6-9; Appendix, Fig. A19-23**), allowing the identification of mitochondrial and lysosomal organelles, and subsequently the nucleus (characterised by a lack of fluorescence). Blue fluorescence was not observed in the untreated control cells (dark and light). Additionally, blue fluorescence was not detectable in cells treated with  $1\times\text{IC}_{50}$  **12** under dark or photo-conditions.

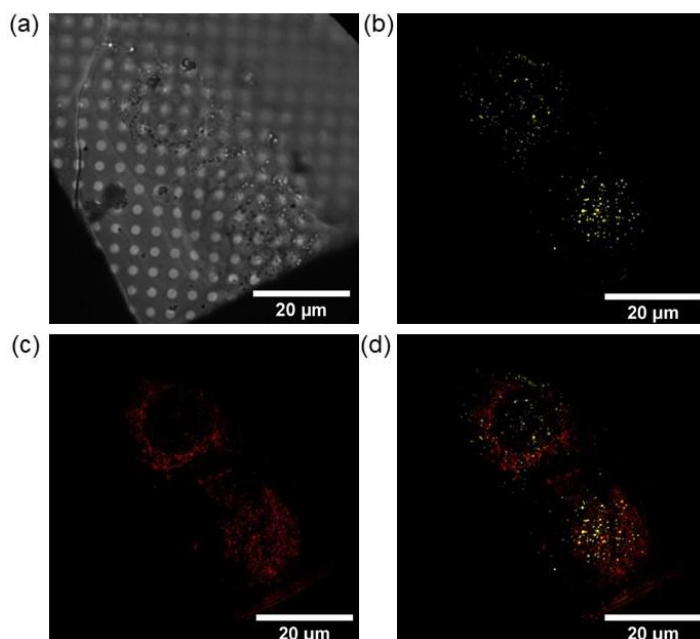


**Figure 5.6.** Two cryopreserved PC3 cells grown on carbon-gold TEM grids and to dark conditions (2 h, protected from light) and incubated with MitoTracker DeepRed ( $\lambda=644/665$  nm) and LysoTracker Red ( $\lambda=577/590$ nm). (a) Brightfield image. (b-d) Super-resolution fluorescence images showing (b) LysoTracker Red (lysosomes), (c) MitoTracker Red (mitochondria) and (d) overlay of LysoTracker Red and MitoTracker Deep Red. Images were generated in Fiji software.<sup>29</sup> Blue fluorescence was not observed.

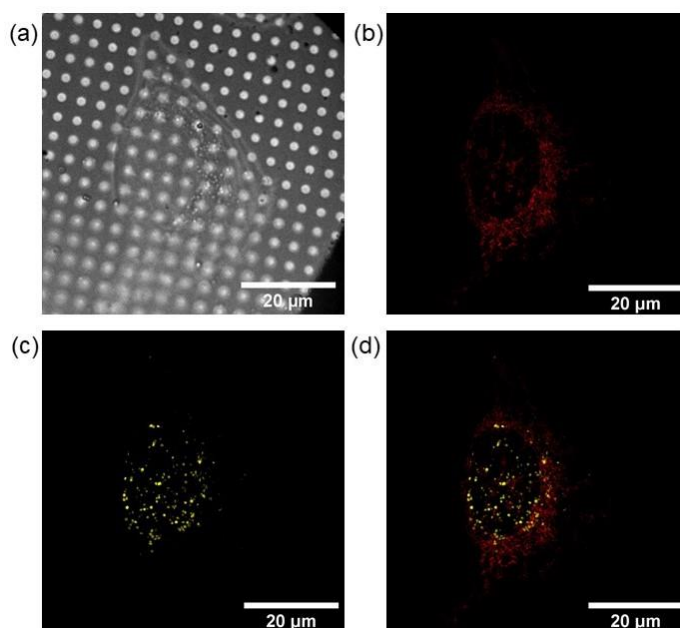


**Figure 5.7.** A cryopreserved PC3 cell grown on a carbon-gold TEM grids and exposed to dark conditions (1 h) followed by 1 h irradiation with blue light conditions (1 h, 465 nm) and incubated with MitoTracker DeepRed ( $\lambda=644/665$  nm) and LysoTracker Red ( $\lambda=577/590$ nm). (a) Brightfield image. (b-d) Super-resolution fluorescence images showing (b) LysoTracker Red (lysosomes), (c) MitoTracker DeepRed (mitochondria) and (d) overlay of LysoTracker Red and MitoTracker Deep Red. Images were generated in Fiji software.<sup>29</sup> Blue fluorescence was not observed.

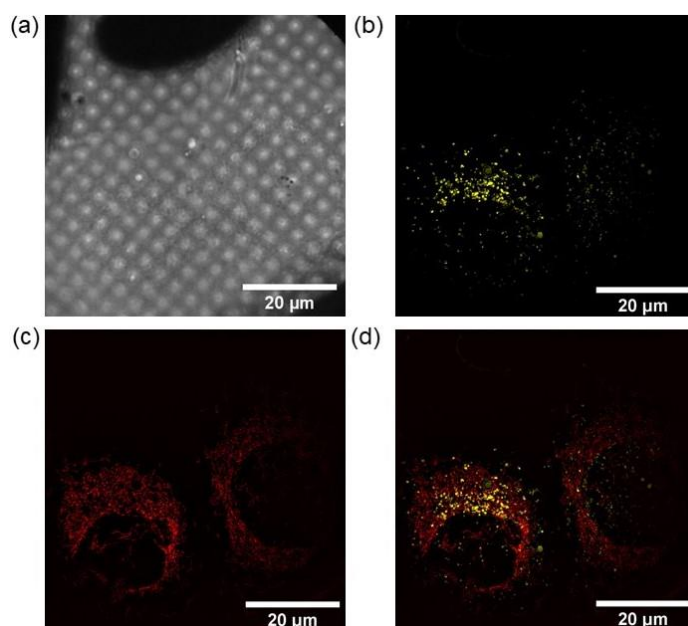


**Figure 5.8.** Two cryopreserved PC3 cells grown on a carbon-gold TEM grids and exposed  $1 \times IC_{50}$  of **12** for 2 h under dark conditions (2 h, protected from light) and incubated with MitoTracker DeepRed ( $\lambda=644/665$  nm) and LysoTracker Red ( $\lambda=577/590$ nm). (a) Brightfield image. (b-d) Super-resolution fluorescence images showing (b) LysoTracker Red (lysosomes), (c) MitoTracker Deep Red (mitochondria) and (d) overlay of LysoTracker Red and MitoTracker Deep Red. Images were generated in Fiji software.<sup>29</sup> Blue fluorescence was not observed.

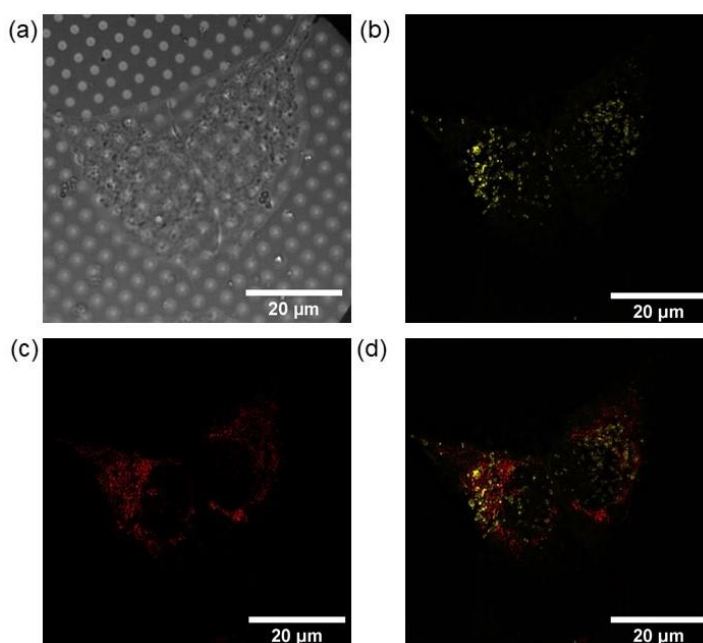


**Figure 5.9.** Two cryopreserved PC3 cells grown on a carbon-gold TEM grids and exposed  $1 \times IC_{50}$  of **12** dark conditions (1 h) followed by 1 h irradiation with blue light conditions (1 h, 465 nm) and incubated with MitoTracker DeepRed ( $\lambda=644/665$  nm) and LysoTracker Red ( $\lambda = 577/590$ nm). (a) Brightfield image. (b-d) Super-resolution fluorescence images showing (b) LysoTracker Red (lysosomes), (c) MitoTracker Deep Red (mitochondria) and (d) overlay of LysoTracker Red and MitoTracker Deep Red. Images were generated in Fiji software.<sup>29</sup> Blue fluorescence was not observed.

### Reconstructed x-ray tomograms

Cryo-XRT can be used to gain 3D structural information on cancer cells as close to their native physiological state as possible (besides live analysis),<sup>42-44</sup> avoiding the use of chemical fixatives. X-ray tomograms have been obtained using soft x-rays (500 eV), producing contrast between carbon-containing structures (*i.e.* organelles) and water (both from cells and the ice layer) on the sample.<sup>45</sup> Cryopreserved PC3 cells treated with 0.25–1.0× the irradiated IC<sub>50</sub> of **12** were analysed under both dark and irradiated ( $\lambda=465$  nm) conditions by cryo-XRT (Table 5.4).

**Table 5.4.** Summary of the tomograms obtained in this Chapter.

Conditions	Tomogram	Rotation (°)	Tilt range (°)	Figure	Video number
Untreated control (2 h, dark)	T1	0.5	-70 to +70	5.10	C5_Video_T1
	T2	0.2	-65 to +65	5.10	C5_Video_T2
	T3	0.2	-70 to +70	5.10	C5_Video_T3
Untreated control (1 h+1 h 465 nm)	T4	0.5	-70 to +60	5.11	C5_Video_T4
	T5	0.2	-65 to +65	5.11	C5_Video_T5
	T6	0.5	-65 to +65	5.11	C5_Video_T6
1×IC <sub>50</sub> (2 h, dark)	T7	0.2	-60 to +60	5.12	C5_Video_T7
	T8	0.5	-65 to +65	5.13	C5_Video_T8
	T9	0.5	-65 to +65	5.13	C5_Video_T9
0.25×IC <sub>50</sub> (1 h+1 h 465 nm)	T10	0.5	-65 to +65	5.14	C5_Video_T10
	T11	0.5	-65 to +65	5.14	C5_Video_T11
	T12	0.2	-65 to +70	5.15	C5_Video_T12
0.5×IC <sub>50</sub> (1 h+1 h 465 nm)	T13	0.5	-65 to +70	5.16	C5_Video_T13
	T14	0.2	-65 to +50	5.17	C5_Video_T14
1×IC <sub>50</sub> (1 h+1 h 465 nm)	T15	0.5	-55 to +60	5.18	C5_Video_T15
	T16	0.2	-60 to +60	5.19	C5_Video_T16
	T17	0.2	-65 to +65	5.19	C5_Video_T17
1×IC <sub>50</sub> (1 h+1 h 465 nm) <sup>[a]</sup>	T18	0.5	-55 to +55	5.20	C5_Video_T18
	T19	0.2	-65 to +65	5.21	C5_Video_T19

<sup>[a]</sup> Cells treated with 1×IC<sub>50</sub> (6.5  $\mu$ M) of **12** for 1 h, followed by 1 h irradiation with blue light (465 nm) and 2 h recovery in complex-free medium



A total of six tomograms ( $15.8 \times 15.8 \mu\text{m}^2$  regions) of cryopreserved untreated PC3 cells were obtained: (i) 2 h protected from the light (**T1-3**, **Fig. 5.10**); (ii) 1 h (protected from light) + 1 h exposure 465 nm (**T4-6**, **Fig. 5.11**). In all of these tomograms (**T1-6**), healthy, unmodified PC3 cells have been identified (showing well-rounded nuclei, clear nuclear membranes, nucleoli, plasma membrane, mitochondria, lipid droplets). The remarkable spatial resolution of B24 beamline (down to 40 nm) enabled the identification of cristae in elongated mitochondria (*e.g.* **T3**, **Fig. 5.10**).<sup>41</sup> Importantly, blue light (1 h, 465 nm) did not alter the morphology of PC3 cells – correlating with that reported in the literature.<sup>2</sup>

A total of four tomograms ( $15.8 \times 15.8 \mu\text{m}^2$ ) of cryopreserved PC3 cells treated with  $1 \times \text{IC}_{50}$  (6.5  $\mu\text{M}$ ) of **12** for 2 h in the dark were obtained (**T7-9**, **Fig. 5.12-13**). Typical features of an unmodified, healthy PC3 cell were observed, including a well-defined nuclear membrane and fused mitochondrial networks. Additionally, many lipid droplets were also observed, a common feature of prostate cancer cells.<sup>46, 47</sup> Two significant observations were made from cells treated with **12** in the dark, compared to that of the untreated control tomograms (**T1-6**; **Fig. 5.10-11**): (i) the presence of endosomes (**T7** and **T9**; **Appendix, Table A35**); (ii) dark, localised spots observed in cell nuclei (**T8-9**, **Fig. 5.13**).

The overall morphologies of PC3 cells treated with  $0.25 \times \text{IC}_{50}$  (1.5  $\mu\text{M}$ ) of **12** exposed to blue light (**T10-12**, **Fig. 5.14-15**) were similar to that of cells treated with **12** under dark conditions. Nuclei were still clearly identifiable, in addition to mitochondria and lipid droplets. However, two significant differences were observed in these treated cells, compared to both the untreated controls (**T1-6**; **Fig. 5.10-11**) and the cells treated under dark conditions (**T7-9**; **Fig. 5.12-13**): (i) presence of cytoplasmic vacuoles (**T10**, **Fig. 5.14**); (ii) membrane-blebbing and vesicle-shedding of the plasma membrane (**T10-11**, **Fig. 5.14**).

Two tomograms of PC3 cells treated with  $0.5 \times \text{IC}_{50}$  (3  $\mu\text{M}$ ) of **12** and exposed to blue light (465 nm) were obtained (**T13-14**, **Fig. 5.16-17**). Fused and separated mitochondria were clearly identifiable, with the nuclear membrane still defined. Interestingly, **T14** (**Fig. 5.17**) was significantly more rounded and darker in appearance, compared to **T13** (**Fig. 5.16**), despite exposure to the same conditions, highlighting the distribution and variability in drug uptake and dose response

exhibited by a population of cells. This is an important consideration in the analysis of individual cells, which inevitably leads to a biased selection of cell candidates. A large vacuole was also observed in the cell nucleus, which was surrounded by lipid droplets (**T14, Fig. 5.17**) – potentially as a cell repair mechanism to close the vacuole and prevent cell death.

Significant cellular damage was evident from the three tomograms obtained from cells treated with  $1\times\text{IC}_{50}$  (6.5  $\mu\text{M}$ ) of **12** for 1 h, followed by 1 h irradiation with blue light (**T15-17, Fig. 5.18-19**). Multiple cytoplasmic vacuoles were observed in all of the analysed cells. The outline of the nucleus can be identified, however, appears damaged, with increased granularity compared to that of the untreated controls (**T1-6; Fig. 5.10-11**). Mitochondria and lipids were difficult to identify in the cytoplasm, and severe membrane-blebbing was evident at the plasma membrane for **T16 (Fig. 5.19)**.

Finally, the extent of efflux of **12** from PC3 cells treated with  $1\times\text{IC}_{50}$  was investigated by treating cells with complex for 1 h exposure and 1 h irradiation (465 nm), followed by 2 h recovery in complex-free media (**T18-19, Fig. 5.20-21**). This is important for clinical translation, where patients are only exposed to drugs (or light) for short time periods. Interestingly, the cellular morphologies of recovered cells were significantly less damaged than the latter (with no recovery). Fused mitochondria, the nuclear membrane and lipids are visible in **T18**, with very few observable vacuoles (**Fig. 5.20**). The cell represented by **T19 (Fig. 5.21)** has a relatively healthy morphology, with significantly high numbers of lipid droplets observed (Total=88).

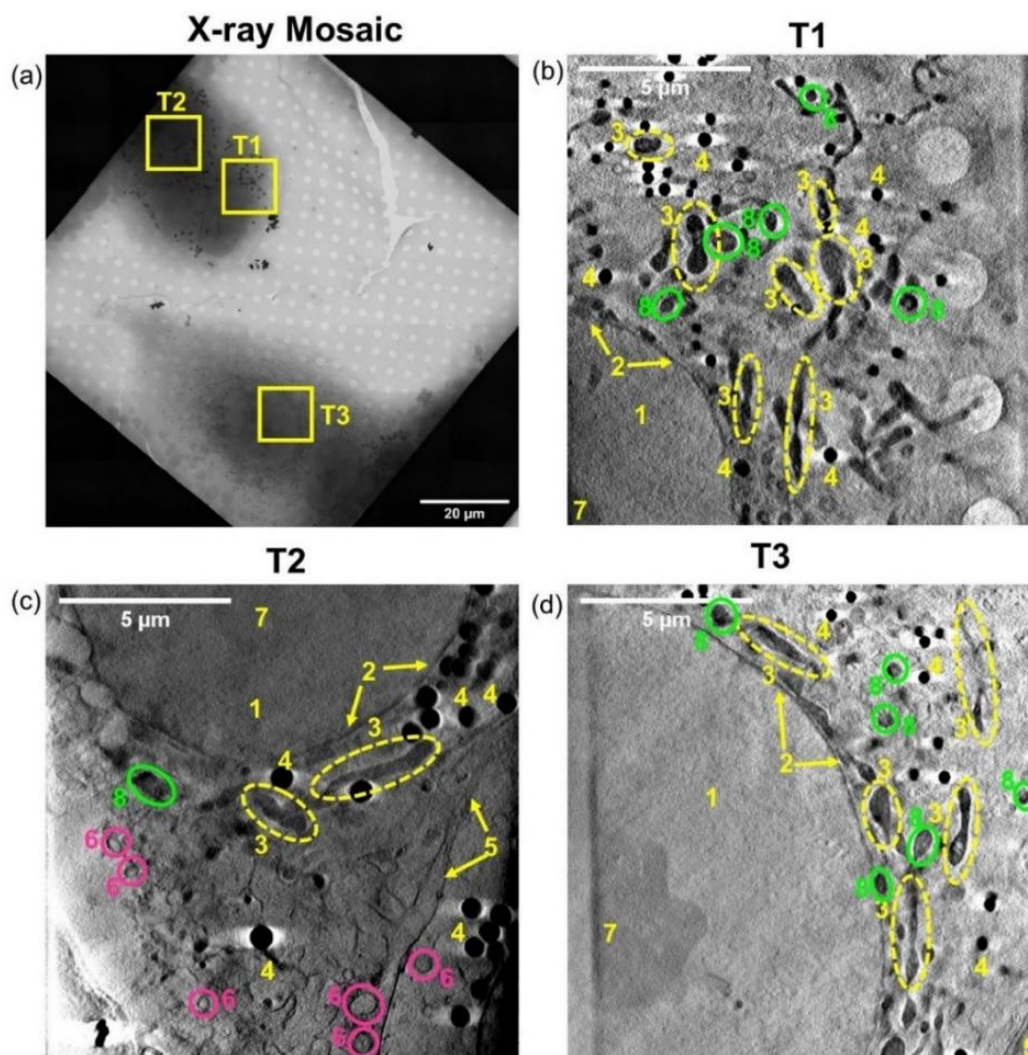


**Figure 5.10.** (a) X-ray mosaic of cryopreserved PC3 cells grown on Quantifoil TEM grids and exposed to dark conditions for 2 h and the areas of interest ( $15.8 \times 15.8 \mu\text{m}^2$ ) mapped using cryo-XRT; (b-d) reconstructed tomograms (T1-3, C5\_Video\_T1, T2, T3) showing cellular features: (1) nucleus; (2) nuclear membrane; (3) mitochondria; (4) lipid droplets; (5) plasma membrane; (6) vesicles; (7) nucleolus; (8) dense organelles; (9) endosomes.

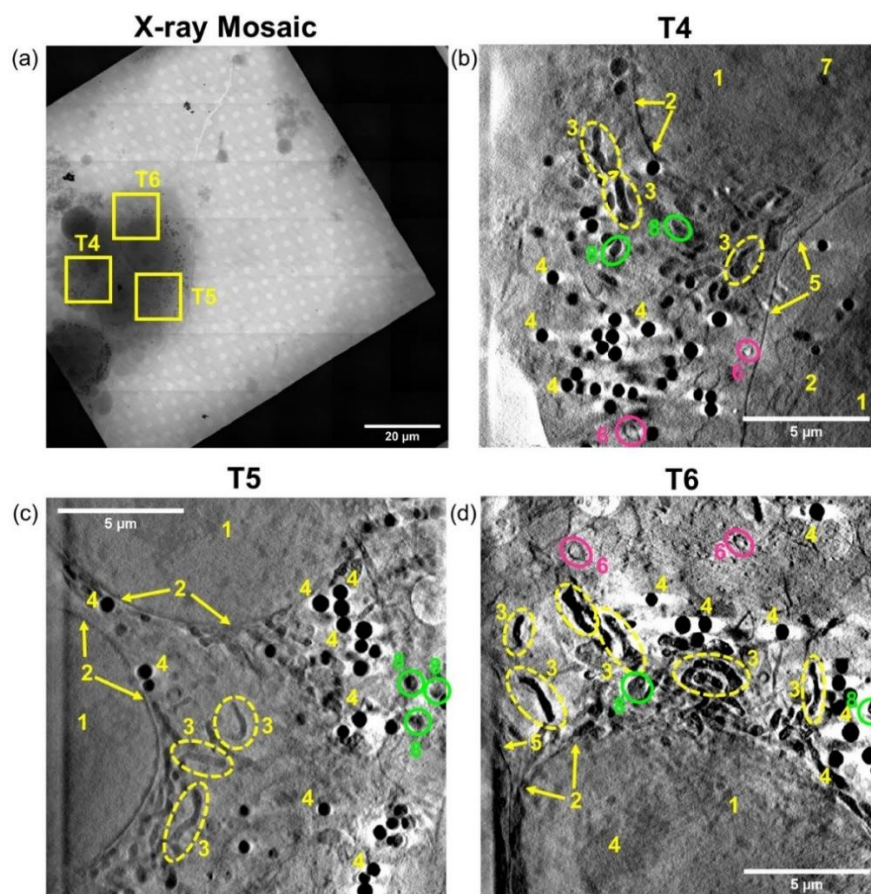


**Figure 5.11.** (a) X-ray mosaic of cryopreserved PC3 cells grown on Quantifoil TEM grids and exposed to 1 h irradiated (blue light,  $\lambda=465$  nm) conditions for 2 h and the areas of interest ( $15.8 \times 15.8 \mu\text{m}^2$ ) mapped using cryo-XRT. (b-d) reconstructed tomograms (**T4-6**, **C5\_Video\_T4**, **T5**, **T6**) showing cellular features: (1) nucleus; (2) nuclear membrane; (3) mitochondria; (4) lipid droplets; (5) plasma membrane; (6) vesicles; (7) nucleolus; (8) dense organelles; (9) endosomes.

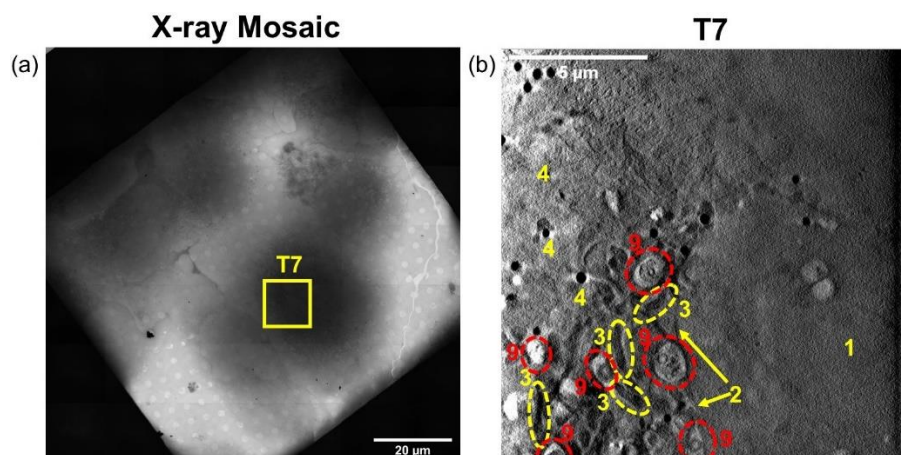


**Figure 5.12.** (a) X-ray mosaic of cryopreserved PC3 cells grown on Quantifoil TEM grids treated with  $1 \times$  irradiated  $\text{IC}_{50}$  ( $6.5 \mu\text{M}$ ) of **12** (2 h, dark conditions) and the areas of interest ( $15.8 \times 15.8 \mu\text{m}^2$ ) mapped using cryo-XRT; (b) reconstructed tomogram (**T7**, **C5\_Video\_T7**) showing cellular features: (1) nucleus; (2) nuclear membrane; (3) mitochondria; (4) lipid droplets; (5) plasma membrane; (6) vesicles; (7) nucleolus; (8) dense organelles; (9) endosomes.



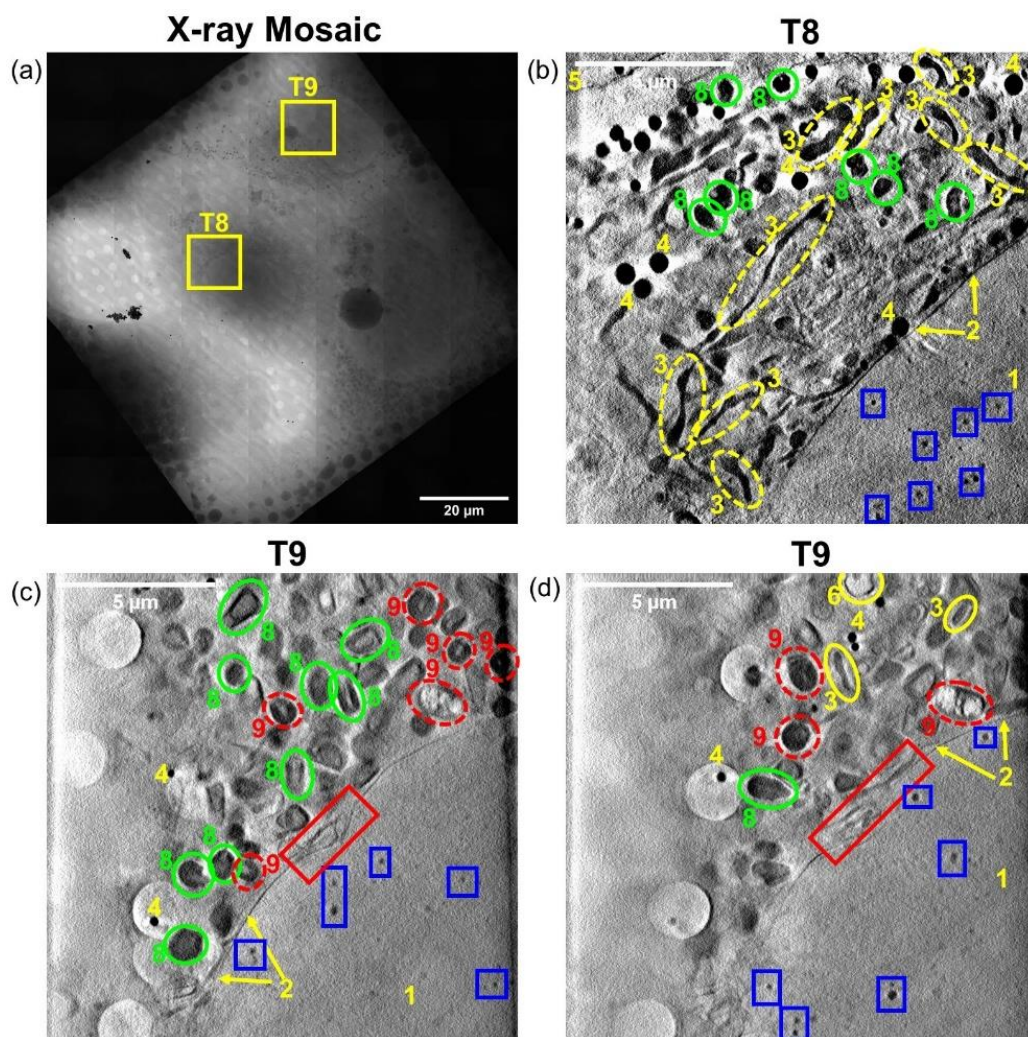


**Figure 5.13.** (a) X-ray mosaic of cryopreserved PC3 cells grown on Quantifoil TEM grids treated with  $1\times$  irradiated  $IC_{50}$  ( $6.5\ \mu\text{M}$ ) of **12** (2 h, dark conditions) and the areas of interest ( $15.8\times 15.8\ \mu\text{m}^2$ ) mapped using cryo-XRT. (b-d) reconstructed tomograms (**T8-9**, **C5\_Video\_T8**, **T9**) showing cellular features: (1) nucleus; (2) nuclear membrane; (3) mitochondria; (4) lipid droplets; (5) plasma membrane; (6) vesicles; (7) nucleolus; (8) dense organelles; (9) endosomes. Tiny black spots (high x-ray absorption) were observed in the nucleus of two independent PC3 cells treated with  $6.5\ \mu\text{M}$  of **12** under dark conditions as represented in the blue boxed regions. Nuclear membrane invaginations were also observed (identified by the red box), a typical feature of cancer cells.<sup>48</sup>

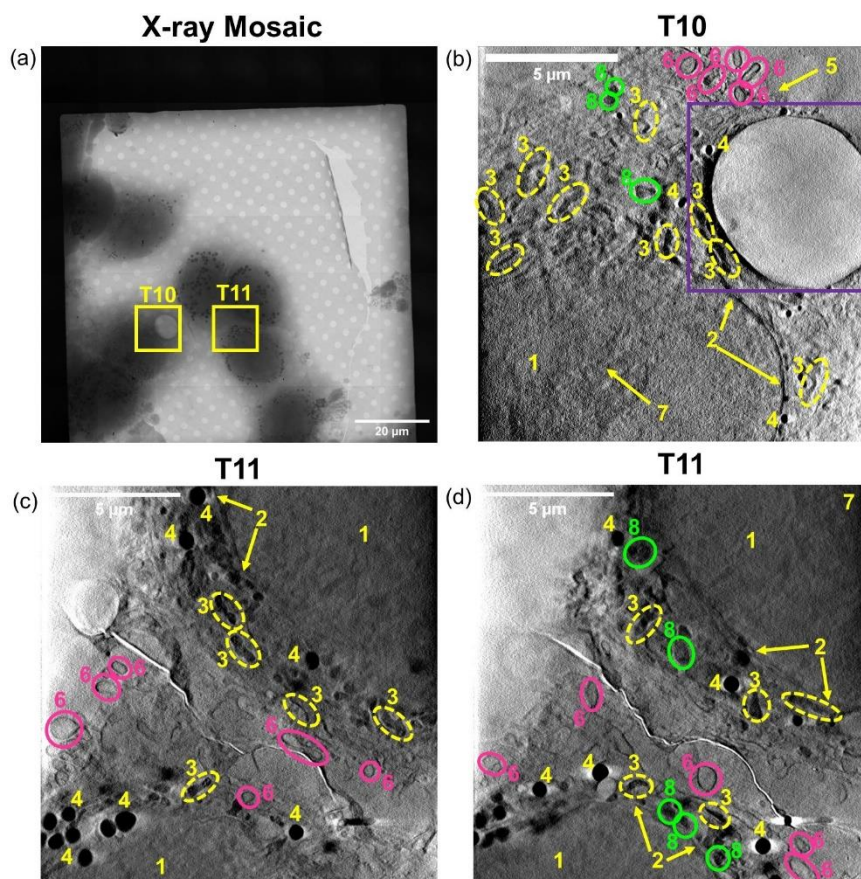


**Figure 5.14.** (a) X-ray mosaic of cryopreserved PC3 cells grown on Quantifoil TEM grids treated with  $0.25 \times IC_{50}$  ( $1.5 \mu M$ ) **12** for 1 h followed by 1 h irradiation (465 nm) the areas of interest ( $15.8 \times 15.8 \mu m^2$ ) mapped using cryo-XRT. (b-d) reconstructed tomograms (**T10-T11**, **C5\_Video\_T10**, **T11**) showing cellular features: (1) nucleus; (2) nuclear membrane; (3) mitochondria; (4) lipid droplets; (5) plasma membrane; (6) vesicles; (7) nucleolus; (8) dense organelles; (9) endosomes. A large cytoplasmic vacuole can be observed in **T10** independent PC3 cells (purple outline), a common feature of programmed cell death.<sup>49</sup>

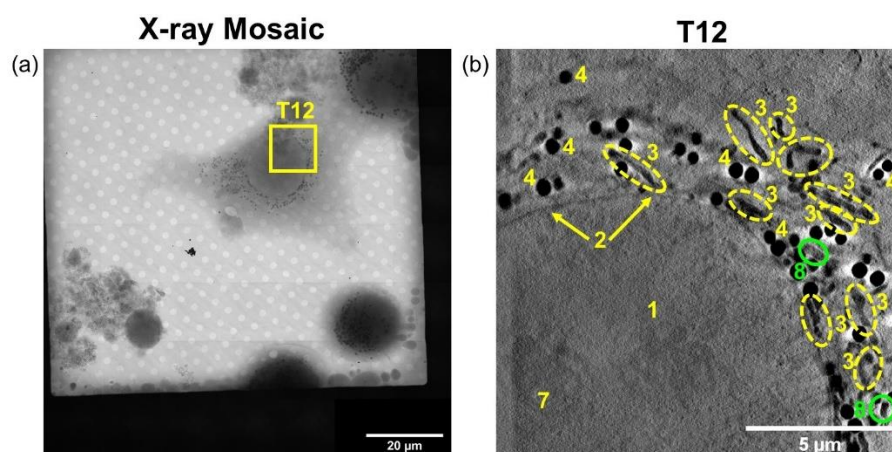


**Figure 5.15.** (a) X-ray mosaic of a cryopreserved PC3 cell grown on Quantifoil TEM grids treated with  $0.25 \times IC_{50}$  ( $1.5 \mu M$ ) of **12** for 1 h followed by 1 h irradiation (465 nm) the areas of interest ( $15.8 \times 15.8 \mu m^2$ ) mapped using cryo-XRT; (b) reconstructed tomogram (**T12**, **C5\_Video\_T12**) showing cellular features: (1) nucleus; (2) nuclear membrane; (3) mitochondria; (4) lipid droplets; (5) plasma membrane; (6) vesicles; (7) nucleolus; (8) dense organelles; (9) endosomes.



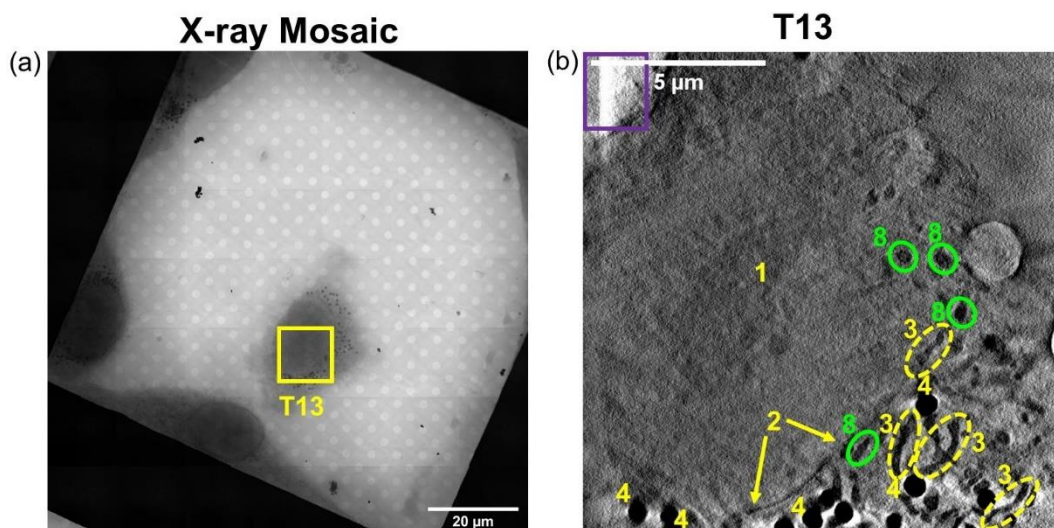


**Figure 5.16.** (a) X-ray mosaic of a cryopreserved PC3 cell grown on Quantifoil TEM grids treated with  $0.5 \times IC_{50}$  ( $3 \mu M$ ) of **12** for 1 h followed by 1 h irradiation (465 nm) the areas of interest ( $15.8 \times 15.8 \mu m^2$ ) mapped using cryo-XRT. (b) Reconstructed tomogram (**T13**, **C5\_Video\_T13**) showing cellular features: (1) nucleus; (2) nuclear membrane; (3) mitochondria; (4) lipid droplets; (5) plasma membrane; (6) vesicles; (7) nucleolus; (8) dense organelles; (9) endosomes. A nuclear vacuole was observed.

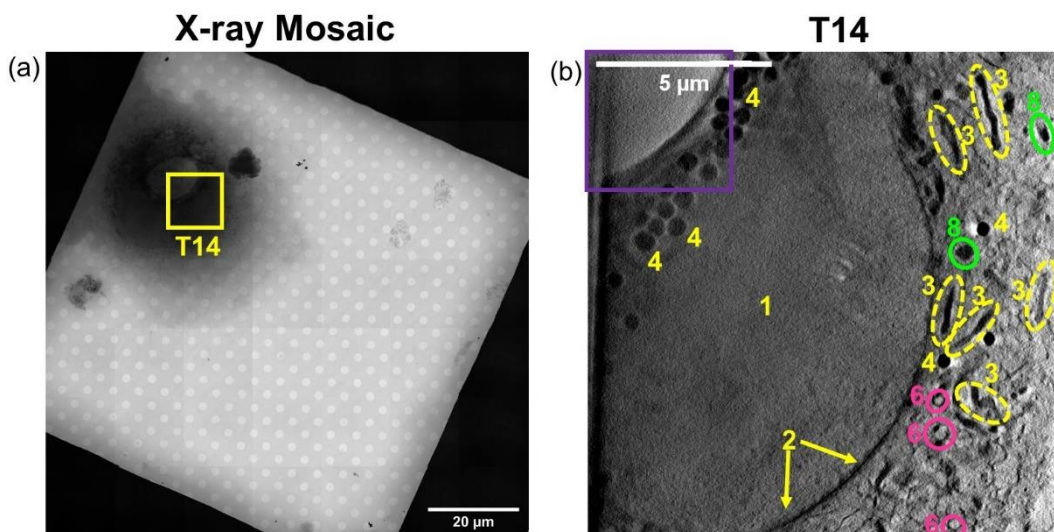


**Figure 5.17.** (a) X-ray mosaic of a cryopreserved PC3 cell grown on Quantifoil TEM grids treated with  $0.5 \times IC_{50}$  ( $3 \mu M$ ) of **12** for 1 h followed by 1 h irradiation (465 nm) the areas of interest ( $15.8 \times 15.8 \mu m^2$ ) mapped using cryo-XRT. (b) Reconstructed tomogram (**T14**, **C5\_Video\_T14**) showing cellular features: (1) nucleus; (2) nuclear membrane; (3) mitochondria; (4) lipid droplets; (5) plasma membrane; (6) vesicles; (7) nucleolus; (8) dense organelles; (9) endosomes. A large nuclear vacuole was observed.

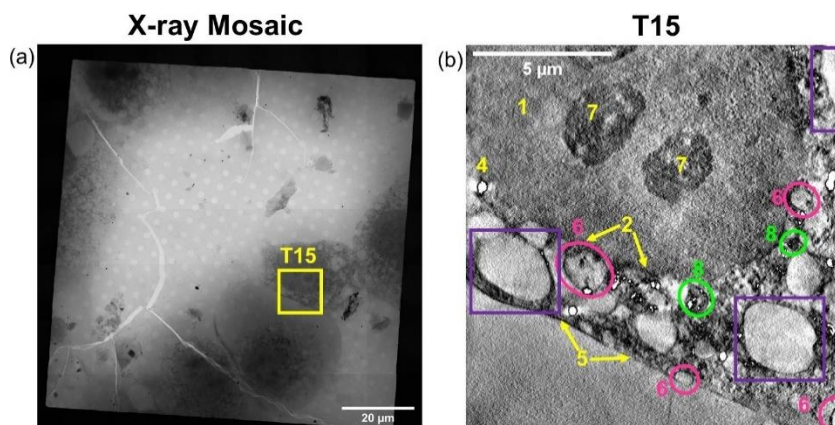


**Figure 5.18.** (a) X-ray mosaic of three prostate cancer cells grown on Quantifoil TEM grids treated with  $1 \times \text{IC}_{50}$  ( $6.5 \mu\text{M}$ ) of **12** for 1 h followed by 1 h irradiation (465 nm) the areas of interest ( $15.8 \times 15.8 \mu\text{m}^2$ ) mapped using cryo-XRT. (b) Reconstructed tomogram (**T15**, **C5\_Video\_T15**) showing cellular features: (1) nucleus; (2) nuclear membrane; (3) mitochondria; (4) lipid droplets; (5) plasma membrane; (6) vesicles; (7) nucleolus; (8) dense organelles; (9) endosomes. Cytoplasmic vacuoles were observed, which is a common feature of programmed cell death and is represented in purple.<sup>49</sup>

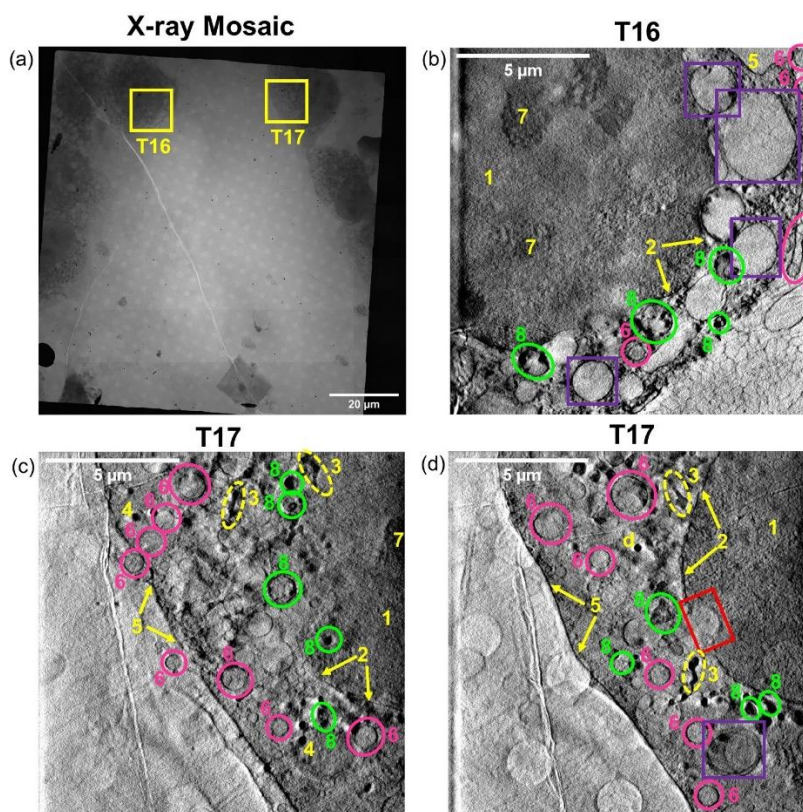


**Figure 5.19.** (a) X-ray mosaic of two PC3 cells grown on Quantifoil TEM grids treated with  $1 \times \text{IC}_{50}$  ( $6.5 \mu\text{M}$ ) of **12** for 1 h followed by 1 h irradiation (465 nm) the areas of interest ( $15.8 \times 15.8 \mu\text{m}^2$ ) mapped using cryo-XRT. (b-d) Reconstructed tomograms (**T16-17**, **C5\_Video\_T16**, **T17**) showing cellular features: (1) nucleus; (2) nuclear membrane; (3) mitochondria; (4) lipid droplets; (5) plasma membrane; (6) vesicles; (7) nucleolus; (8) dense organelles; (9) endosomes. Cytoplasmic vacuoles were observed (shown in purple), which is a common feature of programmed cell death.<sup>49</sup> Invaginations of the nuclear membrane were present in **T16-17** (shown in red), a common feature of cancer cells.<sup>48</sup>



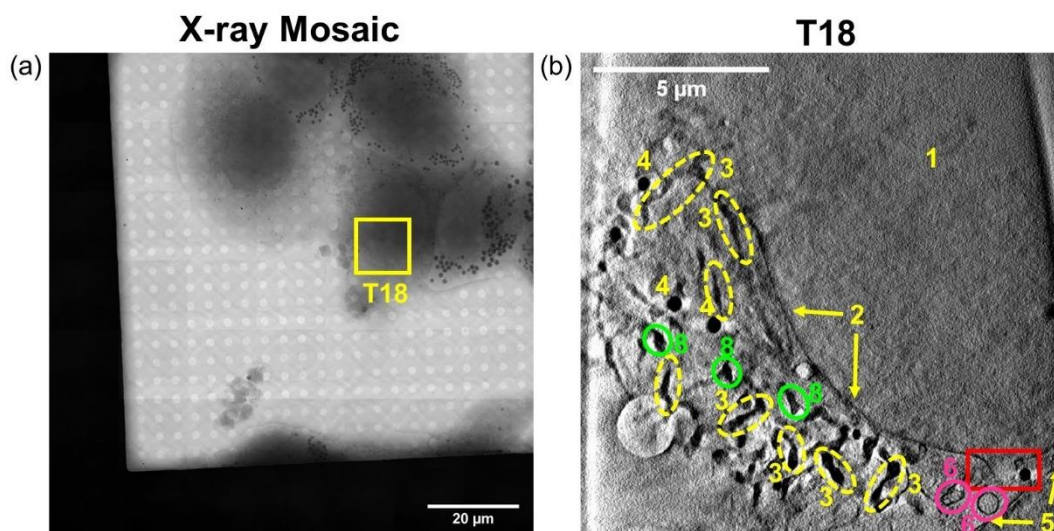


**Figure 5.20.** (a) X-ray mosaic of prostate cancer cells grown on Quantifoil TEM grids treated with  $1 \times \text{IC}_{50}$  ( $6.5 \mu\text{M}$ ) of **12** for 1 h followed by 1 h irradiation (465 nm) and 2 h recovery in drug-free media, the areas of interest ( $15.8 \times 15.8 \mu\text{m}^2$ ) mapped using cryo x-ray tomography. (b) Reconstructed tomogram (T18, C5\_Video\_T18) showing cellular features: (1) nucleus; (2) nuclear membrane; (3) mitochondria; (4) lipid droplets; (5) plasma membrane; (6) vesicles; (7) nucleolus; (8) dense organelles; (9) endosomes. Invaginations of the nuclear membrane were present (red), a common feature of cancer cells.<sup>48</sup>

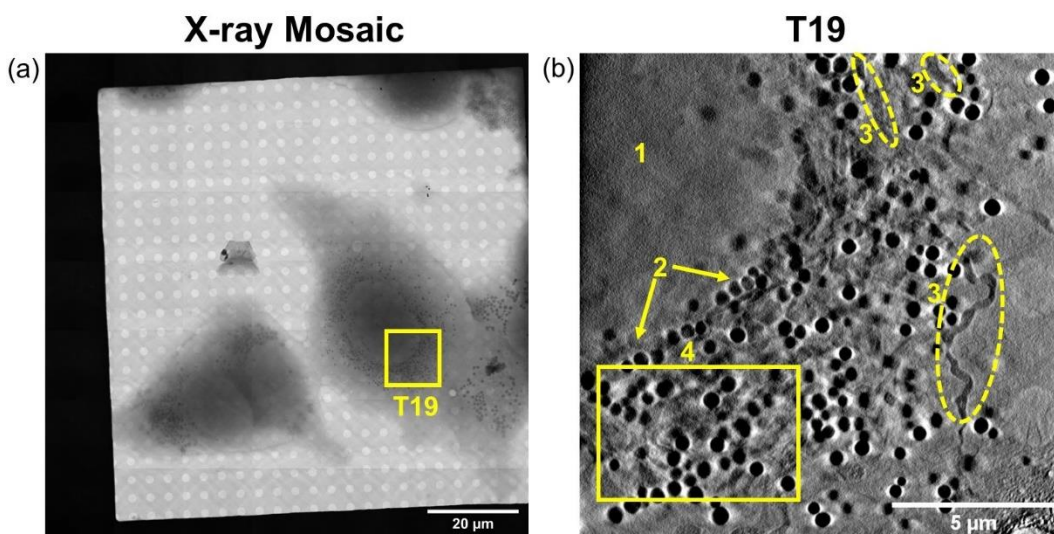


**Figure 5.21.** (a) X-ray mosaic of prostate cancer cells grown on Quantifoil TEM grids treated with  $1 \times \text{IC}_{50}$  ( $6.5 \mu\text{M}$ ) of **12** for 1 h followed by 1 h irradiation (465 nm) and 2 h recovery in drug-free media, showing the area of interest ( $15.8 \times 15.8 \mu\text{m}^2$ ) mapped using cryo x-ray tomography. (b) Reconstructed tomogram (T19, C5\_Video\_T19) showing cellular features: (1) nucleus; (2) nuclear membrane; (3) mitochondria; (4) lipid droplets; (5) plasma membrane; (6) vesicles; (7) nucleolus; (8) dense organelles; (9) endosomes. Note that this PC3 prostate cancer cell has a significantly enhanced number of lipid droplets (total = 88) compared to the control cells.

### 3D segmentation and visualisation

Organelles from the reconstructed tomograms can be segmented to gain information on drug-induced morphological changes in 3D. The volumes of mitochondria and lipid droplets ( $\mu\text{m}^3$ ) in each tomogram (**T1-19**; **Fig. 5.10-21**) were determined (**Table 5.5**; **Appendix, Tables A33-34**), revealing no statistically significant differences in mean mitochondrial or lipid droplet size between cells treated with  $0.1 \times \text{IC}_{50}$  of **12** under all conditions analysed. Endosomes (which can exhibit both dense and lucent interiors by cryo-XRT)<sup>41, 50</sup> were identified in two independent PC3 cells treated with **12** under dark conditions (**T7** and **T9**, **Section 5.3.2**, **Fig. 5.12-13**), and their volumes were segmented (**Appendix, Table A35**). The mean endosomal size were determined to be  $0.26 \pm 0.13$  and  $0.33 \pm 0.23$  for  $\mu\text{m}^3$  **T7** and **T9**, respectively. Additionally, small, dark spots observed in the cell nucleus of PC3 cells treated with **12** under dark conditions were found to range in volume between 0.002-0.042 and 0.003-0.031  $\mu\text{m}^3$  for **T8** and **T9**, respectively.

**Table 5.5.** The mean mitochondrial volume and lipid droplets ( $\mu\text{m}^3$ ) in cryopreserved PC3 cells treated with  $0.25-1 \times \text{IC}_{50}$  of **12** under dark (2 h) or blue light (1 h + 1 h 465 nm, 4.8 mW/cm<sup>2</sup>) conditions (**T1-19**) as determined in SuRVoS.<sup>31</sup> A minimum of 10 mitochondria and 6 lipid droplets per tomogram were segmented.

Conditions	Tomogram number	Mean mitochondrial volume ( $\mu\text{m}^3$ )	Total lipids	Mean lipid droplet volume ( $\mu\text{m}^3$ )
<b>Controls (Dark)</b>	<b>T1</b>	$0.25 \pm 0.12$	68	$0.07 \pm 0.02$
	<b>T2</b>	$0.19 \pm 0.08$	44	$0.09 \pm 0.02$
	<b>T3</b>	$0.35 \pm 0.14$	53	$0.23 \pm 0.01$
<b>Controls (465 nm)</b>	<b>T4</b>	$0.13 \pm 0.06$	51	$0.15 \pm 0.05$
	<b>T5</b>	$0.11 \pm 0.04$	45	$0.09 \pm 0.02$
	<b>T6</b>	$0.15 \pm 0.08$	35	$0.14 \pm 0.05$
<b><math>1 \times \text{IC}_{50}</math> (Dark)</b>	<b>T7</b>	$0.09 \pm 0.06$	24	$0.05 \pm 0.01$
	<b>T8</b>	$0.13 \pm 0.09$	26	$0.25 \pm 0.06$
	<b>T9</b>	$0.13 \pm 0.09$	28	$0.03 \pm 0.01$
<b><math>0.25 \times \text{IC}_{50}</math> (465 nm)</b>	<b>T10</b>	$0.12 \pm 0.07$	13	$0.05 \pm 0.01$
	<b>T11</b>	$0.24 \pm 0.06$	23	$0.15 \pm 0.04$
	<b>T12</b>	$0.13 \pm 0.07$	46	$0.20 \pm 0.06$
<b><math>0.5 \times \text{IC}_{50}</math> (465 nm)</b>	<b>T13</b>	$0.07 \pm 0.04$	42	$0.15 \pm 0.06$
	<b>T14</b>	$0.17 \pm 0.06$	36	$0.13 \pm 0.03$
<b><math>1 \times \text{IC}_{50}</math> (465 nm)</b>	<b>T15</b>	n.d	33	$0.03 \pm 0.02$
	<b>T16</b>	n.d	26	$0.03 \pm 0.01$
	<b>T17</b>	$0.08 \pm 0.03$	28	$0.03 \pm 0.01$
<b><math>1 \times \text{IC}_{50}</math> (465 nm)<sup>[a]</sup></b>	<b>T18</b>	$0.09 \pm 0.03$	6	$0.11 \pm 0.04$
	<b>T19</b>	$0.14 \pm 0.10$	88	$0.07 \pm 0.04$

<sup>[a]</sup> Cells treated with  $1 \times \text{IC}_{50}$  (6.5  $\mu\text{M}$ ) for 1 h, followed by 1 h irradiation with blue light (465 nm, 4.8 mW/cm<sup>2</sup>) and 2 h recovery in complex-free media.

Full segmentation of two tomograms was performed: (i) Untreated control (2 h dark conditions; **T3**, **Fig. 5.10**) (ii)  $1 \times \text{IC}_{50}$  of **11** (1 h + 1 h blue light irradiation; **T16**, **Fig. 5.18**) to show the extreme morphological differences in 3D (**Fig. 5.22-23**).

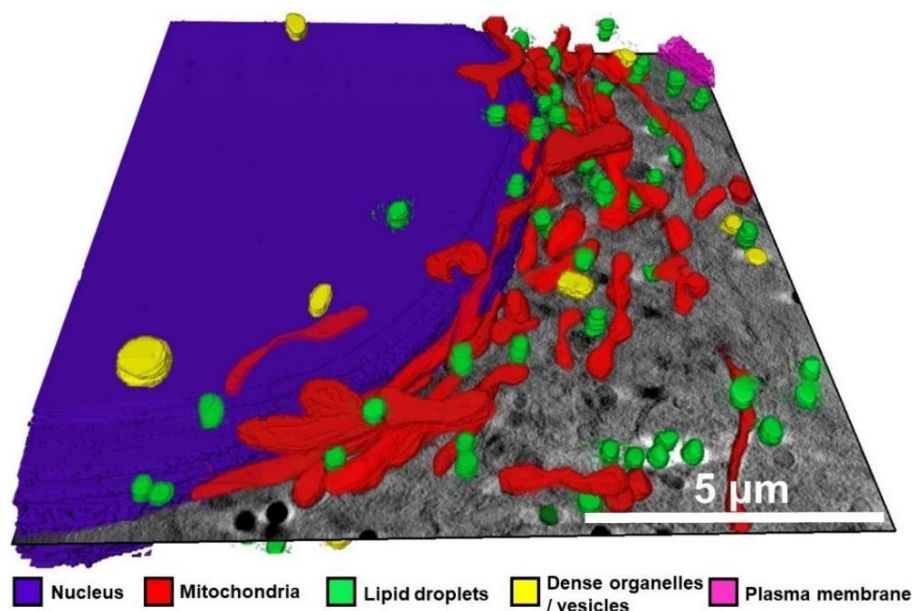


**Figure 5.22.** 3D representation of a  $15.8 \times 15.8 \mu\text{m}^2$  section of a cryo-preserved PC3 cell exposed to dark conditions (**T3**, **Section 5.3.2**, **Figure 5.10**), showing the volumes ( $\mu\text{m}^3$ ) of the nucleus (■), mitochondria (■), lipid droplets (■), dense organelles/vesicles (■) and the plasma membrane (■). Volume segmentation was performed in SuRVoS imaging software,<sup>31</sup> and visualized in 3D in Amira 2016 (**C5\_Video\_T3\_Segmented**).

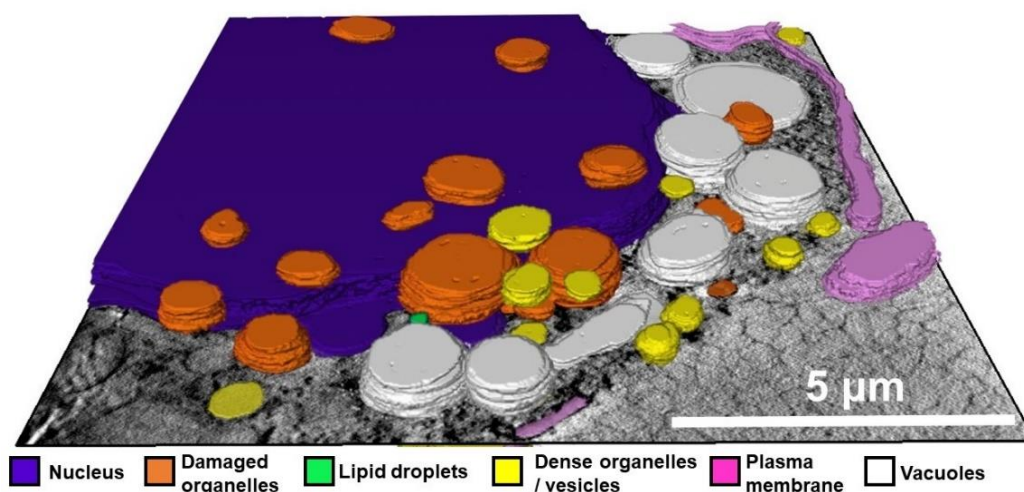


**Figure 5.23.** 3D representation of a  $15.8 \times 15.8 \mu\text{m}^2$  section of a cryopreserved PC3 cell treated with  $1 \times \text{IC}_{50}$  ( $6.5 \mu\text{M}$ ) **12** for 1 h followed by 1 h irradiation with 465 nm (**T16**, **Section 5.3.2**, **Figure 5.18**), showing the volumes ( $\mu\text{m}^3$ ) of the nucleus (■), damaged organelles (■), lipid droplets (■), dense organelles / vesicles (■), the plasma membrane (■) and cytoplasmic vacuoles (□). Volume segmentation was performed in SuRVoS imaging software,<sup>31</sup> and visualized in 3D in Amira 2016 (**C5\_Video\_T16\_Segmented**).



### 5.3.3 Synchrotron-XRF

Synchrotron-XRF has been used to probe the intracellular distribution of Pt in cryo-fixed and freeze-dried PC3 cells treated with 5 $\times$  irradiated IC<sub>50</sub> of **11** (275  $\mu$ M), **12** (32.5  $\mu$ M) and **cisplatin** (500  $\mu$ M) for 2 h (protected from light) or 1 h exposure with 1 h irradiation with blue light (465 nm, 4.8 mW/cm<sup>2</sup>). The Pt L<sub>3</sub>M<sub>5</sub>-emission (9.44 keV) was monitored in cryo-fixed and freeze-dried PC3 cells (**Table 5.6**).

**Table 5.6.** Summary of the XRF maps obtained in this Chapter.

Conditions	Cell number	Figure	Conditions	Cell number	Figure
Untreated (465 nm)	C1	5.24	12 (dark)	C10	5.27
	C2			C11	
	C3			C12	
11 (dark)	C4	5.25	12 (465 nm)	C13	5.28
	C5			C14	
	C6			C15	
11 (465 nm)	C7	5.26	Cisplatin (465 nm)	C16	5.29
	C8			C17	
	C9			C18	

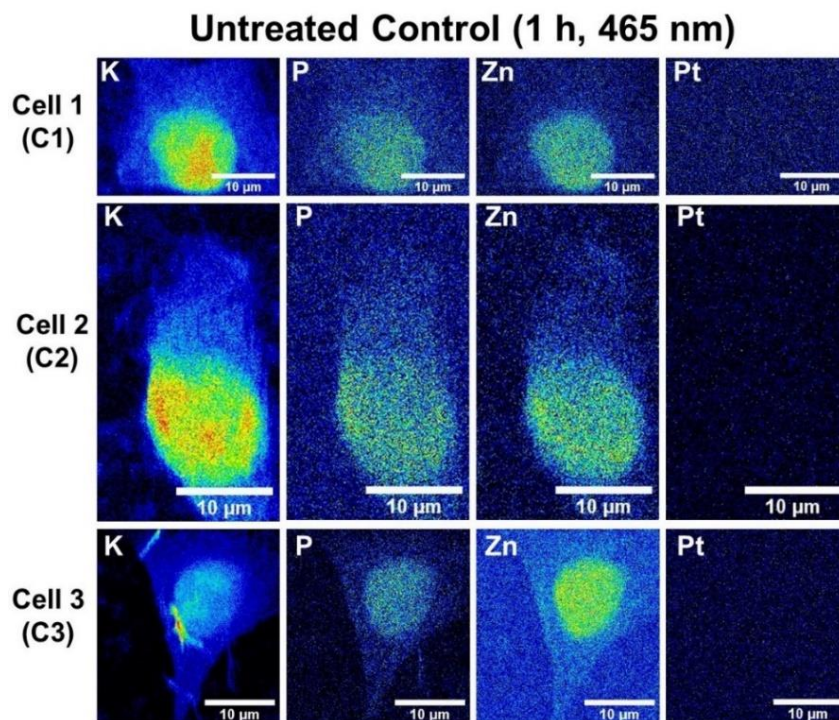


**Figure 5.24.** Synchrotron-XRF elemental maps of cryo-fixed and freeze-dried PC3 cells grown on a Si<sub>3</sub>N<sub>4</sub> membrane and exposed to 1 h irradiation at 465 nm (**C1-3**), obtained using incident energy 14 keV, showing potassium (K), phosphorus (P), zinc (Zn) and platinum (Pt). Images were generated in ImageJ software.<sup>33</sup>

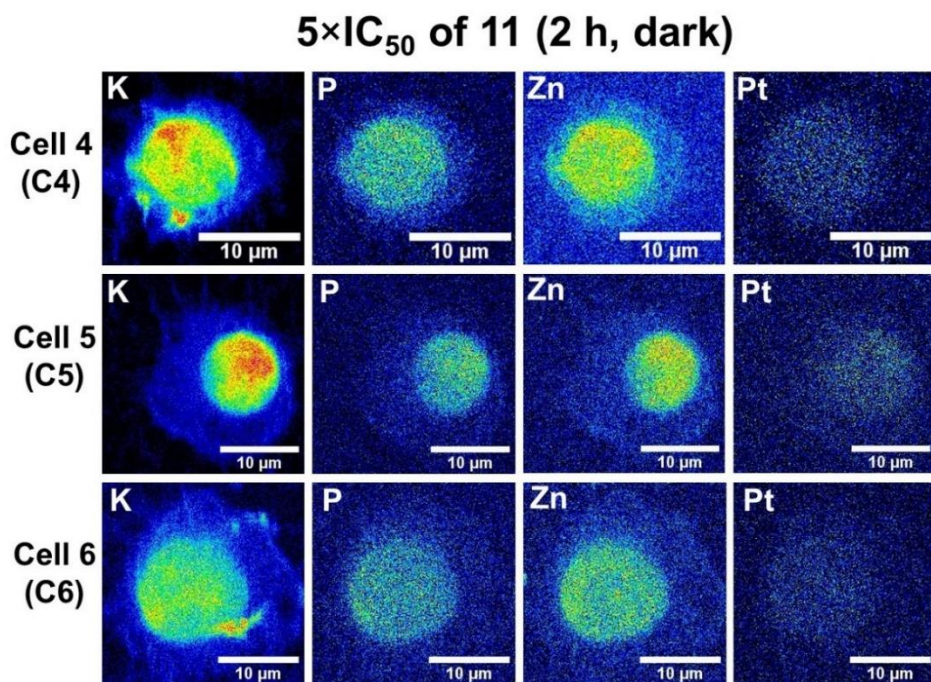


**Figure 5.25.** Synchrotron-XRF elemental maps of cryo-fixed and freeze-dried PC3 cells grown on a Si<sub>3</sub>N<sub>4</sub> membrane and treated with 5×IC<sub>50</sub> (275 μM) of **11** for 2 h in the dark (C4-6) obtained using incident energy 14 keV, showing potassium (K), phosphorus (P), zinc (Zn) and platinum (Pt). Images were generated in ImageJ software.<sup>33</sup>

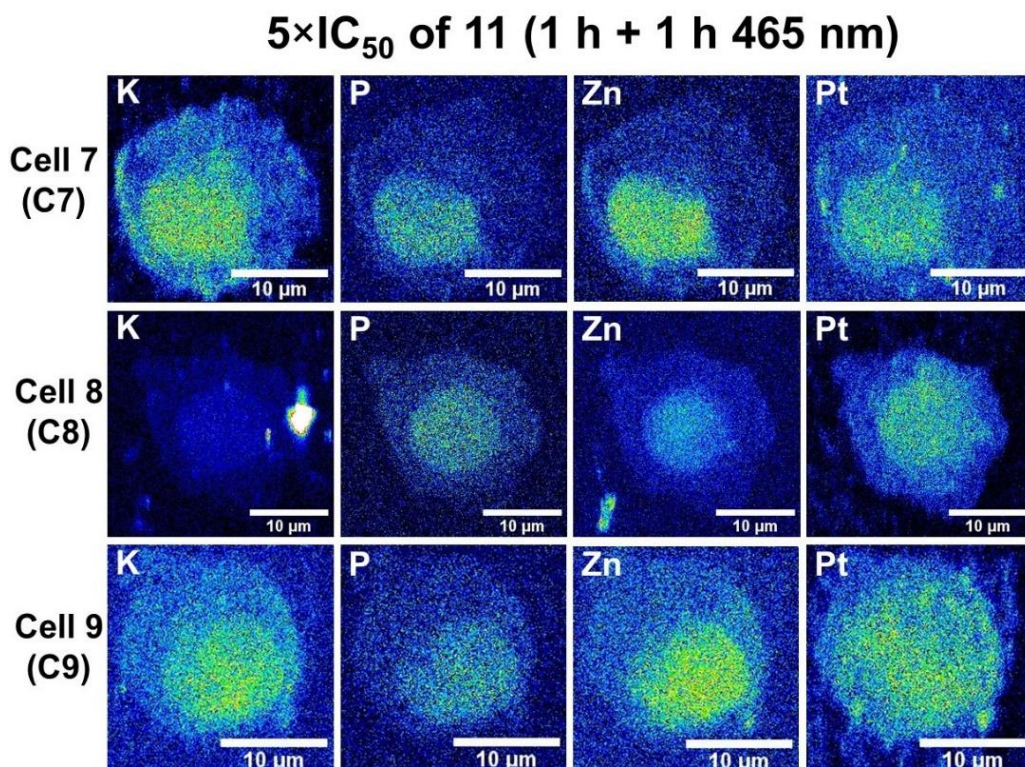


**Figure 5.26.** Synchrotron-XRF elemental maps of cryo-fixed and freeze-dried PC3 cells grown on a Si<sub>3</sub>N<sub>4</sub> membrane and treated with 5×IC<sub>50</sub> (275 μM) of **11** for 2 h (1 h exposure, 1 h irradiation at 465 nm) (C7-9) obtained using incident energy 14 keV, showing potassium (K), phosphorus (P), zinc (Zn) and platinum (Pt). Images were generated in ImageJ software.<sup>33</sup>



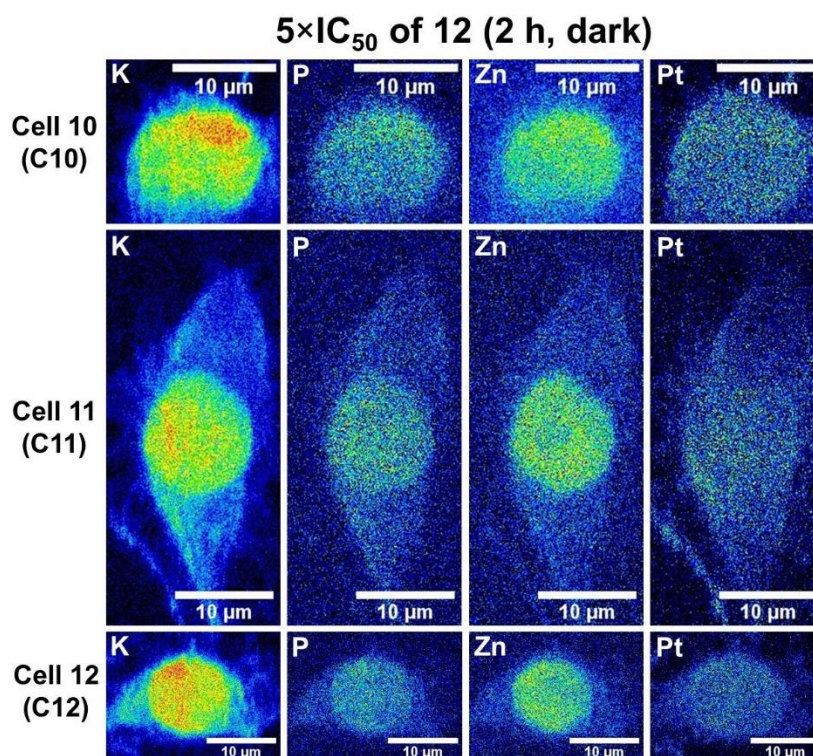


**Figure 5.27.** Synchrotron-XRF elemental maps of cryo-fixed and freeze-dried PC3 cells grown on a Si<sub>3</sub>N<sub>4</sub> membrane and treated with 5×IC<sub>50</sub> (32.5 μM) of **12** for 2 h in the dark (C10-11) obtained using incident energy 14 keV, showing potassium (K), phosphorus (P), zinc (Zn) and platinum (Pt). Images were generated in ImageJ software.<sup>33</sup>

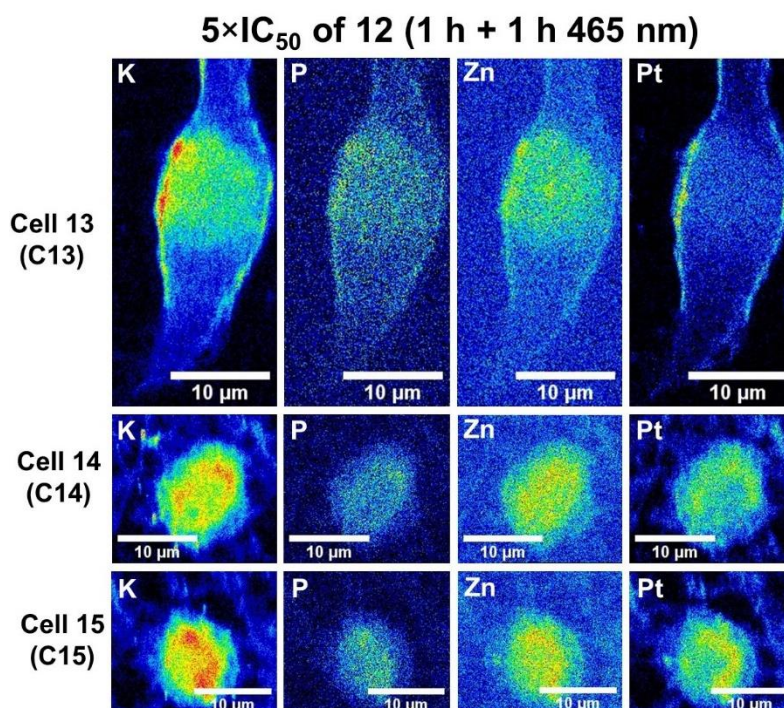


**Figure 5.28.** Synchrotron-XRF elemental maps of cryo-fixed and freeze-dried PC3 cells grown on a Si<sub>3</sub>N<sub>4</sub> membrane and treated with 5×IC<sub>50</sub> (32.5 μM) of **12** for 2 h (1 h exposure, 1 h irradiation at 465 nm – no recovery) (C13-15) obtained using incident energy 14 keV, showing potassium (K), phosphorus (P), zinc (Zn) and platinum (Pt). Images were generated in ImageJ software.<sup>33</sup>

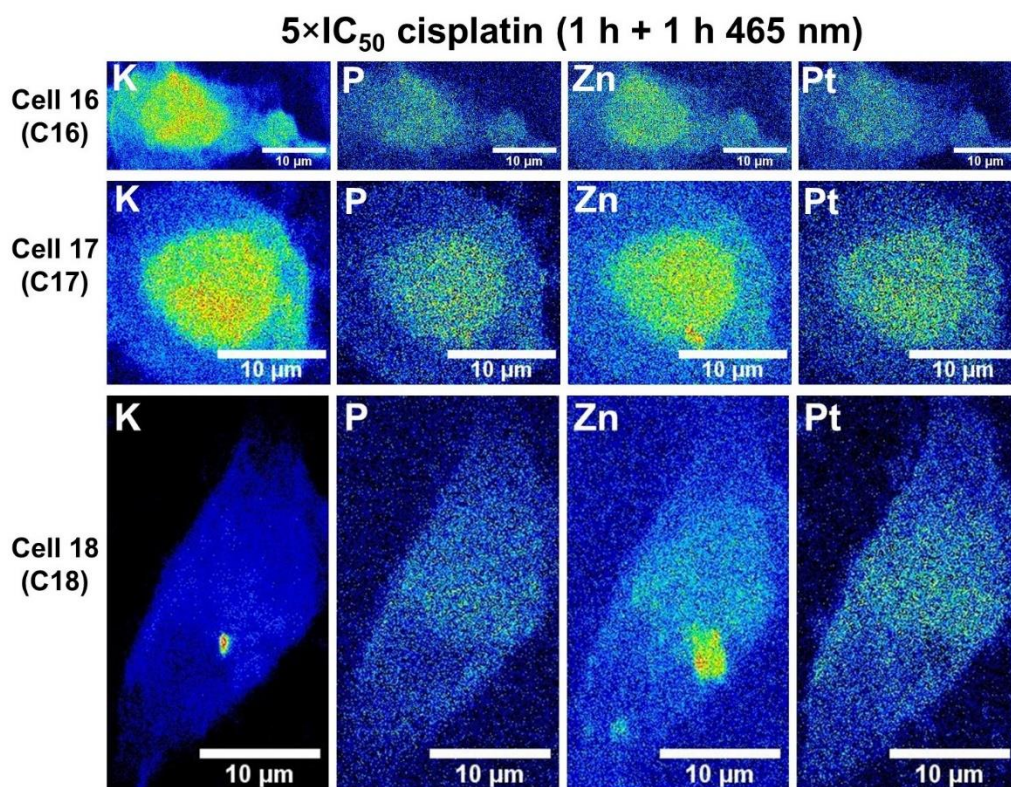


**Figure 5.29.** Synchrotron-XRF elemental maps of cryo-fixed and freeze-dried PC3 cells grown on a Si<sub>3</sub>N<sub>4</sub> membrane and treated with 5×IC<sub>50</sub> (500 μM) of **cisplatin** for 2 h (1 h exposure, 1 h irradiation at 465 nm – no recovery) (**C16-18**) obtained using incident energy 14 keV, showing potassium (K), phosphorus (P), zinc (Zn) and platinum (Pt). Images were generated in ImageJ software.<sup>33</sup>

#### Area and roundness factor

The area (μm<sup>2</sup>) and roundness factors of each individual cell (**C1-18**, **Fig. 5.24-29**) was determined in triplicate in ImageJ software (**Table 5.7**).<sup>33</sup> No statistically significant differences in cell areas (μm<sup>2</sup>) were observed between treated cells (**C4-18**, **Fig. 5.25-29**) and the controls (**C1-3**, **Fig. 5.24**). Similarly, no statistical differences in roundness factors were observed between treated cells (**C4-18**, **Fig. 5.22-26**) and untreated cells (**C1-3**, **Fig. 5.24**). No significant differences in cell area (μm<sup>2</sup>) or roundness factor were observed between cells treated with **11** under dark and irradiated conditions (**C4-6** with **C7-9**,  $p > 0.05$ ; **Fig. 5.25–26**) or with cells treated with **12** (**C10-12** with **C13-15**,  $p > 0.05$ ; **Fig. 5.27-28**).

Due to the diverse range of cell morphologies exhibited by cells, the area of cell nuclei and the percentage area of nuclei were obtained, revealing no statistically significant differences in the mean area of nuclei with respect to the whole cell area in cells treated with **11**, **12** and **cisplatin** (**Table 5.8**).



**Table 5.7.** Cell areas ( $\mu\text{m}^2$ ) and roundness factors of cryo-fixed and dried PC3 cells treated with  $5\times$  irradiated  $\text{IC}_{50}$  of **11** ( $\text{IC}_{50}=55.6\pm0.9\ \mu\text{M}$ ), **12** ( $\text{IC}_{50}=6.48\pm0.84\ \mu\text{M}$ ) or **cisplatin** ( $\text{IC}_{50}>100\ \mu\text{M}$ ) under both dark (2 h) or light (1 h + 1 h 465 nm,  $4.8\ \text{mW}/\text{cm}^2$ ) as determined from the S, K, P and Zn XRF elemental maps. Data were analysed in triplicate in ImageJ.<sup>33</sup>

Conditions	Cell number	Area ( $\mu\text{m}^2$ ) <sup>[a]</sup>	Mean	Roundness factor <sup>[b]</sup>	Mean
Controls	C1	482 $\pm$ 5	383 $\pm$ 75	0.87 $\pm$ 0.01	0.69 $\pm$ 0.20
	C2	334 $\pm$ 7		0.43 $\pm$ 0.01	
	C3	332 $\pm$ 5		0.78 $\pm$ 0.04	
11 (Dark)	C4	151 $\pm$ 3	283 $\pm$ 118	0.92 $\pm$ 0.01	0.94 $\pm$ 0.03
	C5	276 $\pm$ 5		0.94 $\pm$ 0.02	
	C6	423 $\pm$ 6		0.97 $\pm$ 0.01	
11 (465 nm)	C7	319 $\pm$ 2	302 $\pm$ 55	0.91 $\pm$ 0.01	0.90 $\pm$ 0.01
	C8	355 $\pm$ 6		0.82 $\pm$ 0.01	
	C9	231 $\pm$ 5		0.96 $\pm$ 0.01	
12 (Dark)	C10	133 $\pm$ 2	211 $\pm$ 67	0.97 $\pm$ 0.02	0.64 $\pm$ 0.26
	C11	287 $\pm$ 2		0.37 $\pm$ 0.02	
	C12	212 $\pm$ 2		0.59 $\pm$ 0.02	
12 (465 nm)	C13	265 $\pm$ 6	175 $\pm$ 68	0.33 $\pm$ 0.01	0.69 $\pm$ 0.27
	C14	141 $\pm$ 2		0.86 $\pm$ 0.02	
	C15	119 $\pm$ 4		0.89 $\pm$ 0.02	
Cisplatin (465 nm)	C16	398 $\pm$ 8	345 $\pm$ 40	0.48 $\pm$ 0.01	0.59 $\pm$ 0.24
	C17	313 $\pm$ 7		0.88 $\pm$ 0.02	
	C18	324 $\pm$ 6		0.37 $\pm$ 0.01	

**Table 5.8.** Individual areas of cell nuclei ( $\mu\text{m}^2$ ) and the percentage of intracellular area which is taken up by nuclei (%) in cryo-fixed and freeze-dried PC3 cells treated with  $5\times$  irradiated  $\text{IC}_{50}$  of **11** ( $\text{IC}_{50}=55.6\pm0.9\ \mu\text{M}$ ), **12** ( $\text{IC}_{50}=6.48\pm0.84\ \mu\text{M}$ ) or **cisplatin** ( $\text{IC}_{50}>100\ \mu\text{M}$ ) under both dark (2 h) or light (1 h + 1 h 465 nm,  $4.8\ \text{mW}/\text{cm}^2$ ) as determined from the Zn XRF elemental maps.

Conditions	Cell number	Area of nucleus ( $\mu\text{m}^2$ ) <sup>[a]</sup>	Area nucleus (%)	Mean area nucleus (%)
Controls	C1	139 $\pm$ 4	30	32 $\pm$ 7
	C2	136 $\pm$ 3	41	
	C3	92 $\pm$ 3	28	
11 (Dark)	C4	66 $\pm$ 1	43	35 $\pm$ 7
	C5	82 $\pm$ 3	30	
	C6	139 $\pm$ 1	33	
11 (465 nm)	C7	81 $\pm$ 4	25	30 $\pm$ 5
	C8	105 $\pm$ 4	30	
	C9	79 $\pm$ 2	34	
12 (Dark)	C10	91 $\pm$ 2	68	52 $\pm$ 16
	C11	106 $\pm$ 5	37	
	C12	107 $\pm$ 3	50	
12 (465 nm)	C13	94 $\pm$ 1	36	46 $\pm$ 11
	C14	82 $\pm$ 2	58	
	C15	53 $\pm$ 2	45	
Cisplatin (465 nm)	C16	123 $\pm$ 1	31	30 $\pm$ 1
	C17	92 $\pm$ 3	30	
	C18	97 $\pm$ 5	30	



### Elemental distribution and co-localisation

The correlation between Pt and Zn were determined for cells treated with **11** (C4-9, Fig. 5.25-26), **12** (C10-15, Fig. 5.27-28) and **cisplatin** (C16-18, Fig. 5.29) and are reported as Pearson R-values ( $r$ ) and Spearman Rank Correlations (**Appendix, Table A36**). The intracellular Pt in cells treated with **11** under dark conditions (C4-6, Fig. 5.25) showed a moderate co-localisation with Zn ( $r=0.14-0.23$ ; mean= $0.19\pm0.05$ ). Interestingly, the co-localisation between Pt and Zn was significantly enhanced in cells treated with **11** and exposed to blue light (C7-9, Fig. 5.26, ranging from  $r=0.40-0.49$ ; mean= $0.44\pm0.05$ ) when compared to dark conditions ( $p=0.0036$ ). The same trend was observed for cells treated with **12** in the dark (C10-12, Fig. 5.27, mean  $r=0.34\pm0.04$ ) and irradiated (C13-15, Fig. 5.28, mean  $r=0.58\pm0.08$ ;  $p=0.0423$ ). Finally, cells treated with **cisplatin** (C16-18, Fig. 5.29) showed moderate correlation between Pt and Zn (mean  $r=0.34\pm0.03$ ).

Cryo-fixed and dehydrated PC3 cells exposed to blue light (1 h, 465 nm) revealed clear, stretched-out morphologies (identified by endogenous elements: K, P and Zn) and well-rounded cell nuclei (C1-3, Fig. 5.24). Cells treated with **11** ( $5\times\text{IC}_{50}$ ) under dark conditions (C4-6, Fig. 5.25) appeared more rounded (compared to the untreated controls), with spherical nuclei. The Pt XRF in C4-6 was faint, but appears to somewhat co-localise with the spherical area of concentrated Zn in the cell nucleus. Cells treated with the same concentration of **11** but exposed to 1 h blue light (C7-9, Fig. 5.26) revealed significantly more intracellular Pt, sparsely distributed in the cell (including the cell nucleus).

Cells treated with **12** under both dark or irradiated conditions (1 h, 465 nm) revealed a variety of morphologies. Cells treated with **12** under dark conditions (C10-12, Fig. 5.27) showed significantly less Pt compared to irradiated cells (C13-15, Fig. 5.28). Overall, cells treated with **12** showed sparse distributions of Pt (cytoplasm and the nucleus). It is notable that one of the less damaged (elongated) cells treated with **12** exposed to blue light (C13, Fig. 5.28) showed highly localised Pt around the perimeter of the cell. Finally, PC3 cells treated with **cisplatin** ( $500\text{ }\mu\text{M}$ ) for 1 h and exposed to 1 h irradiation exhibited a variety of cell morphologies (C16-18, Fig. 5.29), with Pt distributed in the cell nucleus and the cytoplasm.

### Platinum quantification in PC3 cells

Mass fraction quantities of Pt were determined in PC3 cells treated with **11**, **12** and **cisplatin** (Fig. 5.30) by calibrating the flux to an AXO standard as previously described (Chapter 2, Section 2.6.1). Cells treated with **11** under irradiated conditions (465 nm) showed Pt levels *ca.* 3× higher than that of cells under dark conditions ( $p=0.0002$ ), with  $8.2\pm0.8$  and  $2.8\pm0.3$  ppm of Pt, respectively. The same trend was observed for **12**, with 3.5× more intracellular Pt detected under irradiation with blue light compared to dark conditions ( $p=0.0001$ ), with  $17\pm7$  and  $4.9\pm0.6$  ppm, respectively. In general, significantly more Pt was observed in cells treated with **12** when compared with those treated with **11** (both under dark conditions, and blue light irradiation;  $p=0.0061$  and  $p=0.0012$ , respectively). The mass fraction of Pt in cells treated with **cisplatin** ( $5.5\pm0.2$  ppm) closely resembled that of **12** ( $4.9\pm0.6$  ppm) under dark conditions (Table 5.9).

The percentage of intracellular Pt in nuclei in cells treated with **11** and **12** under dark conditions were determined to be  $74\pm15$  and  $52\pm17\%$ , respectively (Table 5.9). Similarly, the percentage of intranuclear Pt in cells treated with **11** or **12** under photo-conditions were  $57\pm9$  and  $55\pm15\%$ , respectively. Finally, cells treated with **cisplatin** under blue light conditions revealed  $42\pm8\%$  of intracellular Pt in the nucleus (Table 5.9).

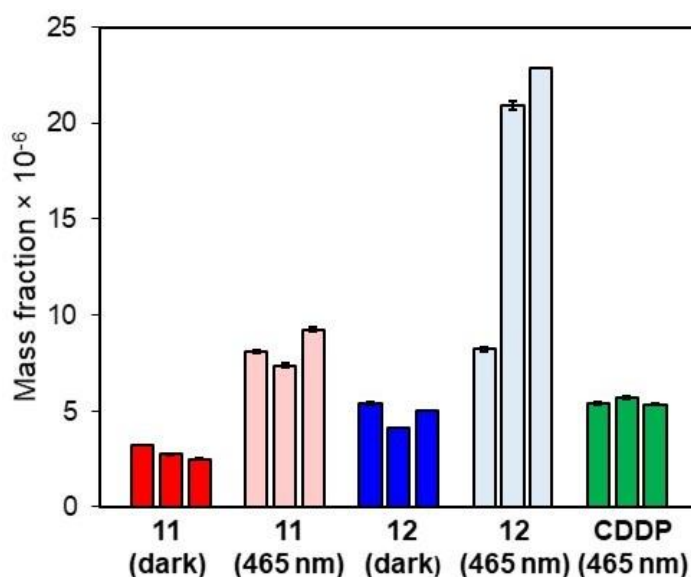


**Figure 5.30.** Mass fraction quantities of Pt in cryo-fixed and freeze-dried PC3 cells treated with  $5\times\text{IC}_{50}$  of **11** ( $\text{IC}_{50}=55.6\pm0.9\ \mu\text{M}$ ), **12** ( $\text{IC}_{50}=6.48\pm0.84\ \mu\text{M}$ ) and **cisplatin** ( $\text{IC}_{50}>100\ \mu\text{M}$ ) under dark (2 h) or 1 h exposure followed by 1 h blue light conditions (465 nm,  $4.8\ \text{mW cm}^{-2}$ , 1 h) as analysed by synchrotron-XRF.

**Table 5.9.** Intracellular quantities of Pt (ppm) in cryo-fixed and freeze-dried PC3 cells treated with 5× irradiated IC<sub>50</sub> of **11** (IC<sub>50</sub>=55.6±0.9 μM), **12** (IC<sub>50</sub>=6.48±0.84 μM) or **cisplatin** (IC<sub>50</sub>> 100 μM) under both dark (2 h) or irradiated (1 h exposure + 1 h 465 nm, 4.8 mW/cm<sup>2</sup>) conditions, as determined from the synchrotron-XRF maps.

Conditions	Cell	[Pt] per cell (ppm)	Mean [Pt] / cell (ppm)	% Pt / nucleus	Mean % Pt in nucleus
<b>11</b> (Dark)	<b>C4</b>	3.21±0.01	2.8±0.3	88±4	74±15
	<b>C5</b>	2.75±0.02		55±2	
	<b>C6</b>	2.51±0.01		78±3	
<b>11</b> (465 nm)	<b>C7</b>	8.10±0.05	8.2±0.8	52±4	57±9
	<b>C8</b>	7.4±0.1		50±2	
	<b>C9</b>	9.2±0.1		69±3	
<b>12</b> (Dark)	<b>C10</b>	5.41±0.07	4.9±0.6	70±7	52±17
	<b>C11</b>	4.12±0.02		31±3	
	<b>C12</b>	5.02±0.01		54±2	
<b>12</b> (465 nm)	<b>C13</b>	8.21±0.08	17±7	36±5	55±15
	<b>C14</b>	20.9±0.2		64±8	
	<b>C15</b>	22.88±0.03		64±4	
<b>Cisplatin</b>	<b>C16</b>	5.40±0.04	5.5±0.2	40±1	42±8
	<b>C17</b>	5.68±0.05		53±1	
	<b>C18</b>	5.34±0.02		34±1	

### 5.3.4 Pt XANES mapping

Solid pellets of **cisplatin**, K<sub>2</sub>PtCl<sub>4</sub> and **11**, as well as a platinum sheet were analysed by XANES over the energy range 11.46–11.73 keV, to monitor the Pt L<sub>3</sub>-edge absorption (11.56 keV),<sup>34</sup> as shown in **Fig. 5.31-32**. The XANES spectra of **cisplatin** and K<sub>2</sub>PtCl<sub>4</sub> were closely comparable owing to their Pt<sup>2+</sup> oxidation state and square-planar coordination environments. The spectrum of **11** revealed a slight shift in energy (*ca.* 2 eV), and a sharp increase in the edge absorption compared to the Pt(II) compounds (**cisplatin**; K<sub>2</sub>PtCl<sub>4</sub>). The ROI in cryo-fixed and freeze-dried PC3 cells treated with **11** and exposed to blue light were identified from the XRF of Pt. Two independent 5×5 μm<sup>2</sup> Pt-containing regions were monitored by XANES mapping using the nanofocussed beam in the range 11.46-11.73 keV (0.2s dwell time, 200 nm step size) using the “Compressed Sensing” and “Energy-Scanning” methods (**Section 5.2.4**).

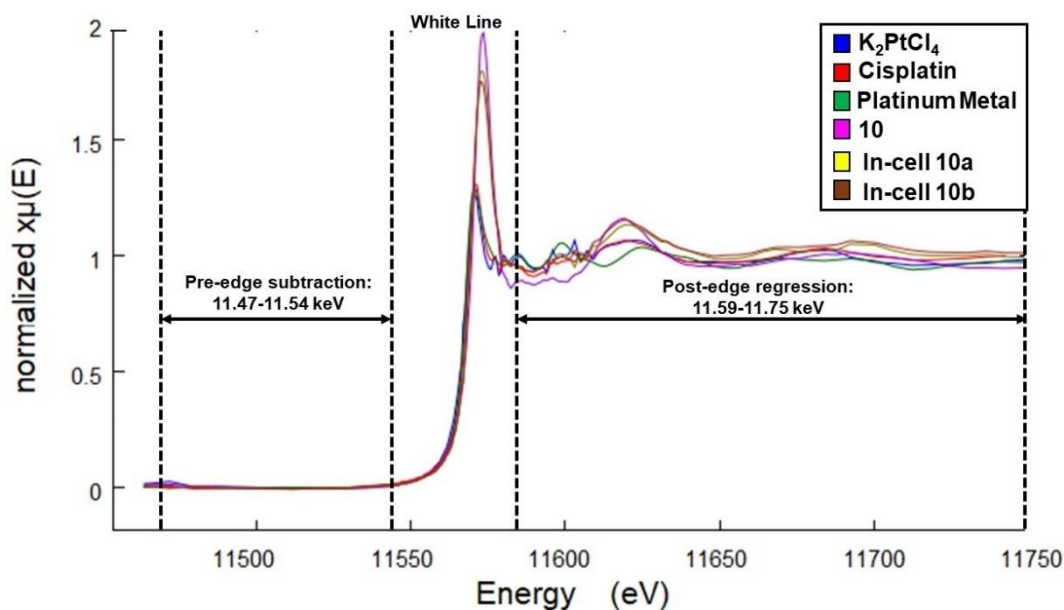


**Figure 5.31.** XANES spectra of solid pellets of  $\text{K}_2\text{PtCl}_4$  (■), cisplatin (■), **10** (■), and of platinum metal (■). XANES spectra of intracellular Pt in two independent  $5 \times 5 \mu\text{m}^2$  regions of cryo-fixed and dried PC3 cells treated with  $5 \times \text{IC}_{50}$  of **11** (1 h exposure + 1 h 465 nm), where 'In-cell 11a' (■) and 'In-cell 11b' (■) correspond to the Compressed Sensing and Energy-Scanning methods, respectively. Data were normalised using edge-step normalisation extrapolates the difference between pre-edge subtraction and post-edge regression to the edge itself. Pre-edge normalisation was performed in the energy range 11.47-11.54 keV and the post-edge normalisation was performed in the range 11.59-11.75 keV, and a normalisation order=2.

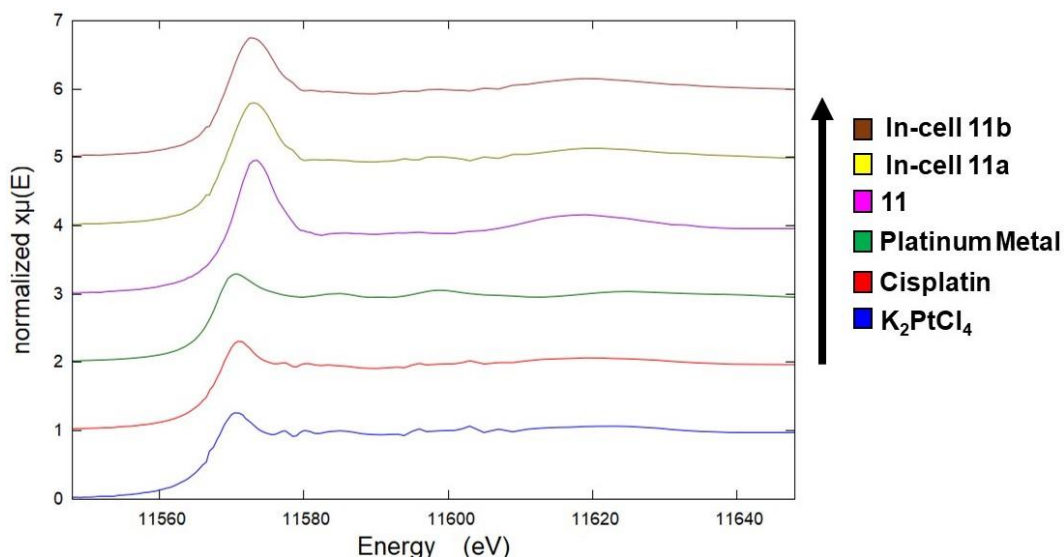


**Figure 5.32.** Stacked plot of XANES spectra of solid pellets of  $\text{K}_2\text{PtCl}_4$  (■), cisplatin (■), **10** (■), and of platinum metal (■). XANES spectra of intracellular Pt in two independent  $5 \times 5 \mu\text{m}^2$  regions of cryo-fixed and dried PC3 cells treated with  $5 \times \text{IC}_{50}$  of **11** (1 h exposure + 1 h 465 nm), where 'In-cell 11a' (■) and 'In-cell 11b' (■) correspond to the Compressed Sensing and Energy-Scanning methods, respectively. Pre-edge normalisation was performed in the energy range 11.47-11.54 keV and the post-edge normalisation was performed in the range 11.59-11.75 keV, and a normalisation order=2.

Data were processed using a method reported in the literature,<sup>36, 37</sup> to obtain normalized peak ratios (**Table 5.10**), as described previously in **Section 5.2.4**. Comparison of the normalized peak ratios of solid pellet of **11** and Pt in cells treated with **11** revealed *ca.* 18% reduction of Pt<sup>IV</sup> to Pt<sup>II</sup>. Whereas, comparison of cisplatin with intracellular **11** revealed *ca.* 25% reduction of Pt<sup>IV</sup> to Pt<sup>II</sup>. A linear combination fit (LCF) of the normalised data was also performed (between 11.55–11.60 keV), revealing *ca.* 80% intracellular Pt<sup>IV</sup> by the “Compressed Sensing” method and *ca.* 75% Pt<sup>IV</sup> by the “Energy-Scanning” XANES method (**Table 5.11**).

**Table 5.10.** Oxidation states, white line energies, normalised maximal absorption values and normalised peak ratios between the normalised maximum of the white line (a) and the post-edge minima (b) of **cisplatin**, **K<sub>2</sub>PtCl<sub>4</sub>**, **11** solid pellets, platinum metal and cryopreserved, freeze-dried PC3 cells treated with **11** under photo-conditions, as determined from XANES.

Compound	Oxidation state	White line (eV)	Normalised maximal absorption (a)	Normalized peak ratio (a/b)
<b>Cisplatin</b>	2+	11571.2	1.30	1.37
<b>K<sub>2</sub>PtCl<sub>4</sub></b>	2+	11570.7	1.26	1.32
<b>Pt metal</b>	0	11570.6	1.28	1.35
<b>11</b>	4+	11573.4	1.95	2.05
<b>In-cell 11a</b> <sup>[a]</sup>	n.d.	11572.9	1.64	1.73
<b>In-cell 11b</b> <sup>[a]</sup>	n.d.	11572.7	1.60	1.68

<sup>[a]</sup> Determined from 5×5 μm<sup>2</sup> regions of Pt in cryo-fixed and freeze-dried cells treated with 5×IC<sub>50</sub> **11** and exposed to 1 h blue light (465 nm) using the “Compressed Sensing” XANES method. <sup>[b]</sup> Determined from 5×5 μm<sup>2</sup> regions of Pt in cryopreserved and freeze-dried cells treated with 5×IC<sub>50</sub> **11** and exposed to 1 h blue light using the “Energy-Scanning” acquisition XANES method.

**Table 5.11.** Percentages of intracellular Pt<sup>IV</sup> and Pt<sup>II</sup> in cryofixed and dried PC3 cells treated with **11** under blue light conditions, determined by performing a linear combination fit (LCF) on the normalised data.

Pt compound	LCF standards	Percentage Pt <sup>IV</sup> (%)	Percentage Pt <sup>II</sup>
<b>In-cell 11a</b> <sup>[a]</sup>	<b>11 vs. cisplatin</b>	80.3±2.2	19.7±2.2
	<b>11 vs. K<sub>2</sub>PtCl<sub>4</sub></b>	81.8±1.9	18.2±1.9
<b>In-cell 11b</b> <sup>[b]</sup>	<b>11 vs. cisplatin</b>	76.5±1.7	23.5±1.7
	<b>11 vs. K<sub>2</sub>PtCl<sub>4</sub></b>	74.2±2.0	25.8±2.0

<sup>[a]</sup> Determined from 5×5 μm<sup>2</sup> regions of Pt in cryo-fixed and freeze-dried cells treated with 5×IC<sub>50</sub> **11** and exposed to 1 h blue light (465 nm) using the “Compressed Sensing” XANES method. <sup>[b]</sup> Determined from 5×5 μm<sup>2</sup> regions of Pt in cryopreserved and freeze-dried cells treated with 5×IC<sub>50</sub> **11** and exposed to 1 h blue light using the “Energy-Scanning” acquisition XANES method.

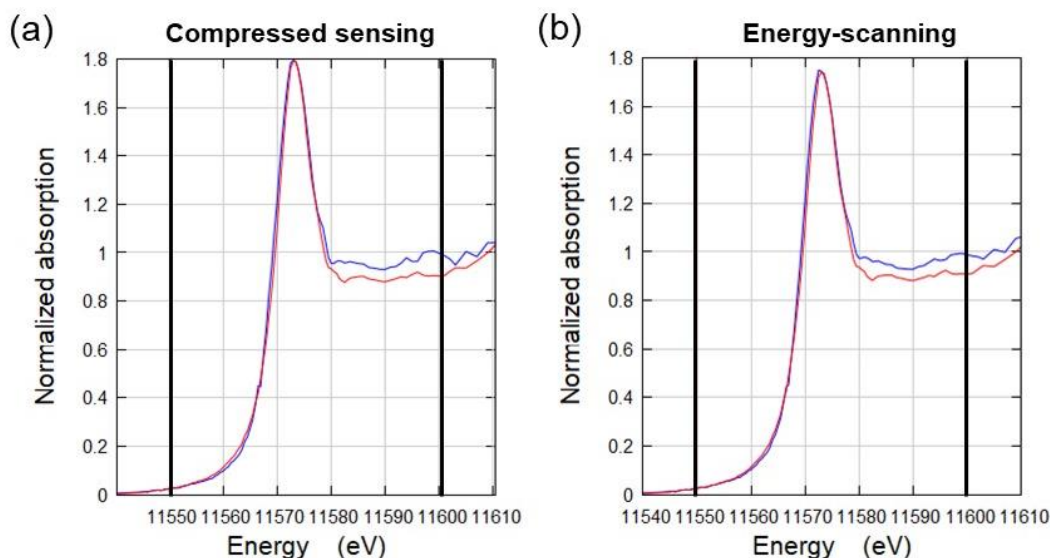


**Figure 5.33.** Representative example of Linear Combination Fit (LCF) analysis of  $5 \times 5 \mu\text{m}^2$  regions of cryo-fixed and dried PC3 cells treated with  $5 \times \text{IC}_{50}$  of **11** (1 h exposure + 1 h 465 nm), using (a) “Compressed-sensing” and (b) “Energy-Scanning” methods, respectively. The  $5 \times 5 \mu\text{m}^2$  analysed region is shown in blue and the LCF fit in red. LCF analysis was performed in the region 11.55–11.60 keV (20 eV below the edge and 30 eV above the edge).

## 5.4 Discussion

The aim of this Chapter was to gain insights into the antiproliferative mechanism(s) of action of diazido- $\text{Pt}^{\text{IV}}$  PACT prodrugs (**11**; **12**) in cancer cells as close to their native state as possible (without using chemical stains or labels). Correlative fluorescence microscopy, cryo-SIM and cryo-XRT can be used to investigate morphological or structural changes to cancer cells induced by **12** (a fluorescent, coumarin-labelled diazido- $\text{Pt}^{\text{IV}}$  complex) down to a 40 nm resolution at the B24 beamline. This may provide information into the mechanisms of cell death and subcellular targets of this family of photoactivatable diazido- $\text{Pt}^{\text{IV}}$  prodrugs. Complementary to this (although not analysed cryogenically) cryo-fixed and dried cells were analysed by nano-focussed XRF and XANES to probe the cellular distribution and speciation of Pt in cancer cells treated with the drug.

#### 5.4.1 Cryo-SIM of Pt-treated cancer cells

Structured Illumination Microscopy (SIM) is a powerful super-resolution technique which pushes the resolution of optical microscopes past the Abbe diffraction limit ( $d=\lambda/2NA$ , where  $\lambda$ =wavelength and  $NA$ =numerical aperture),<sup>40</sup> achieving 8-fold improved volumetric resolution compared to the diffraction limit.<sup>27</sup> SIM works on the basis of using “striped” or “patterned” illumination to excite a sample of interest by altering both the position and orientation of the pattern (Moiré effect). Advantages of 3D SIM include compatibility with conventional fluorophores, high sensitivity (compared to widefield techniques), it can be used for thick samples (>10  $\mu\text{m}$ ),<sup>51</sup> uses low doses and allows rapid data acquisition.<sup>27</sup> Importantly, cryo-SIM can be used in combination with cryo-XRT to gain insights into the intracellular localization and compartmentalization of fluorescent compounds in biological systems as close to their native state as possible.<sup>52</sup>

In this experiment, the fluorescence emissions of MitoTracker Deep Red ( $\lambda_{\text{ex/em}}$ =644/665 nm) and LysoTracker Red ( $\lambda_{\text{ex/em}}$ =577/590 nm) were intense, showing clearly where the mitochondrial and lysosomal organelles were inside the PC3 cells, allowing the identification of cell nuclei – characterised by the lack of fluorescence (**Section 5.3.2, Fig. 5.6–9**). The morphology of cells treated with  $1\times\text{IC}_{50}$  (6.5  $\mu\text{M}$ ) **12** and exposed to blue light (**Section 5.3.2, Fig. 5.6**) did not appear significantly different to that of the untreated controls, despite the known phototoxicity of **12**,<sup>26</sup> highlighting the limitations of 2D analysis. It is known that **12** forms blue fluorescent coumarin radicals upon photoactivation with light ( $\lambda_{\text{ex/em}}$ =405/450 nm),<sup>26</sup> however, the blue fluorescence could not be observed by cryo-SIM. This implies that, although **12** can release blue-fluorescent compounds in aqueous solution (7-hydroxycoumarin-3 carboxylate and radical photo-products containing hydroxido and coumarin-3 carboxylato ligands),<sup>26</sup> the fluorescence *inside* cells is likely not strong enough (perhaps due to short fluorescence lifetimes of the organic radicals). Nonetheless, the fluorophore emissions from the MitoTracker and LysoTracker were observed, providing 2D information of the cell outline, nucleus and cytoplasm as close to their native state as possible (**Section 5.3.2, Fig. 5.6–9**). As this was unsuccessful, future studies would aim to investigate a highly fluorescent diazido- $\text{Pt}^{\text{IV}}$  compound, such as the Ir-Pt conjugate (**7, Chapter 4**), to overlay the fluorescence with the 3D tomograms in a correlative approach.

## 5.4.2 Cryo-XRT and Pt-treated cancer cells

### Untreated PC3 cells

Cryo-XRT can provide morphological and subcellular information of cancer cells treated with diazido-Pt<sup>IV</sup> complexes under both dark and blue light (465 nm) conditions as close to their native state as possible. Three tomogram sections ( $15.8 \times 15.8 \mu\text{m}^2$ ) of representative untreated PC3 cells from a population of cells under dark conditions were obtained (**T1-3**, **Section 5.3.2**, **Fig. 5.10**). The tomograms were aligned (to account for drift and tilt) and reconstructed automatically in IMOD imaging software.<sup>30</sup> Tomograms **T1-3** exhibited features of typical PC3 cells, revealing well-defined nuclei (showing nucleolus and a thin nuclear membrane) and detailed cytoplasmic organelles, including mitochondria, lipid droplets and other (unassignable) dense organelles. Additionally, the plasma membrane can be identified in **T3** (**Section 5.3.2**, **Fig. 5.10**).

A particularly noticeable feature of these untreated PC3 cells was the presence of lipid droplets: carbon-dense spherical organelles,<sup>53</sup> with high x-ray absorptions (with x-ray absorption coefficients *ca.*  $1 \mu\text{m}^{-1}$  – almost 10× greater than that of vitreous ice).<sup>54</sup> These are structurally distinct from the AuNP fiducials ( $d=250 \text{ nm}$ ), which are isotropic, homogenous and spherical, have increased electron density (Au vs. C) and have “dark disk” appearances even at high sample tilt angles. Lipids are essential cellular components and have been reported to be significantly altered in certain disease states.<sup>55</sup> Lipid droplets are over-expressed in many prostate cancer cell lines, which can have detrimental consequences for cancer progression and pathogenesis,<sup>56</sup> making them a viable target for chemotherapeutics. The volumes of lipid droplets in these untreated “native” PC3 cells (**T1-3**, **Appendix, Table A34**) were determined using volume segmentation to compare to that of cells treated with **12**. In **T1-3** a wide distribution of lipid droplets was observed: ranging from  $0.05$ - $0.38 \mu\text{m}^3$  in size (SuRVoS software),<sup>31</sup> with between 44-68 lipids in each region ( $15.8 \times 15.8 \mu\text{m}^2$ ). The distribution and size of lipid droplets can be dependent on: (i) cell growth / adhesion; (ii) cell crowding (neighbouring cells); (iii) stage of cell growth (*i.e.* cell cycle). The 3D volume of lipid droplets is not well-reported in the literature, however, they are typically less than  $1 \mu\text{m}$  in diameter.<sup>57</sup> Overall, the mean volumes of lipid droplets in **T1-3** resides within the literature range.



Mitochondria were clearly identifiable in the cell cytoplasm: elongated and thin in nature (**Section 5.3.2, Fig. 5.10**), with cristae identifiable in many cases (*e.g.* **T3**). This differs to the general mitochondrial shape observed from the dark control cells in the iridium experiment (**Chapter 4**), which is likely due to the improved quality of samples in this experiment. This will also dependent on the cell passage used. The average volumes of mitochondria from PC3 cells exposed to dark conditions (**T1-3; Appendix, Table A33**) ranged between 0.09-0.58  $\mu\text{m}^3$ , emphasizing the large variance in mitochondrial volume observed in PC3 prostate cancer cells, as reported in **Chapter 4**. The area of mitochondria of healthy cells have been reported to range between 0.75–3  $\mu\text{m}^2$  in size,<sup>58</sup> and exhibit diverse mitochondrial arrangements (depending on the static, fusing and dynamic dividing status),<sup>59</sup> thus, the wide size variations are not surprising. Full 3D volume segmentation of **T3** (**Section 5.3.2, Fig. 5.23**) shows the nucleus, indisputable mitochondria, spherical lipid droplets, dense organelles/vesicles and the plasma membrane.

Vesicular structures were observed at the plasma membrane of one of the cells (**T2, Section 5.3.2, Fig. 5.10**), most likely corresponding to extracellular exosomes or shedding vesicles. Extracellular vesicles can be defined as membrane-enclosed particles released by a cell into extracellular space,<sup>60</sup> and are biomarkers for a variety of cancers.<sup>61</sup> In prostate cancer, the trafficking of extracellular vesicles (exosomes and prostasomes) can promote interactions with adjacent cells,<sup>61</sup> allowing cancer cells to invade new spaces. The presence of extracellular vesicles (exosomes) is a common feature in PC3 cells,<sup>61</sup> and was also observed in PC3 cells in the iridium experiment **Chapter 4 (Section 4.5.2)**.

PC3 cells exposed to 1 h irradiation with blue light ( $\lambda=465$  nm, **T4-6, Section 5.3.2, Fig. 5.11**) closely resembled that of cells exposed to dark conditions (**T1-3, Section 5.3.2, Fig. 5.10**). Nuclei, nucleoli and nuclear membranes were apparent, with elongated mitochondria (0.04–0.30  $\mu\text{m}^3$ ; **Appendix, Table A33**), extracellular vesicles, lipid droplets (0.07–0.24  $\mu\text{m}^3$ ; **Appendix, Table A34**) and well-defined cell membranes. No discernible morphological differences were identified between cells exposed to dark (**T1-3, Fig. 5.10**) or blue light (**T4-6, Fig. 5.11**) conditions, re-affirming that blue light (of this intensity and exposure) is non-toxic towards cancer cells, thus, can be utilized in PACT.<sup>2</sup> Moreover, both sets of untreated PC3 cells can be used as reliable negative controls in this experiment.

### Cells treated with **12** under dark conditions

In order to probe the in-cell effects of **12** under dark conditions (reported to be non-toxic,  $IC_{50} > 100 \mu M$ ),<sup>26</sup> cryopreserved PC3 cells treated with  $1 \times$  the irradiated  $IC_{50}$  ( $6.5 \mu M$ ) of **12** were analysed by cryo-XRT (**T7-9**, **Section 5.3.2**, **Fig. 5.12-13**). The cellular features showed attributes similar to that of the untreated controls (**T1-6**, **Section 5.3.2**, **Fig. 5.10-12**), with comparable lipid droplets ( $0.05\text{--}0.33 \mu m^3$ ), elongated mitochondria ( $0.02\text{--}0.34 \mu m^3$ ) and well-defined cell nuclei (**Appendix, Tables A33-34**). However, two noticeable features *not* evident in the untreated cells were observed: (i) endosomes (**T7** and **T9**, **Section 5.3.2**, **Fig. 5.12-13**); (ii) dark spots in cell nuclei (**T8-9**, **Section 5.3.2**, **Fig. 5.13**).

### Endosomes

Endosomes are membrane-bound compartments responsible for sorting and delivering internalized material to lysosomes or vacuoles for removal from the cell.<sup>62</sup> It has previously been reported that cisplatin-resistant cancer cells have altered endocytotic recycling pathways, which contributes to the development of acquired resistance.<sup>63</sup> Herein, endosomes were observed in two independent PC3 cells treated with **12** under dark conditions (**T7**, **T9**, **Section 5.3.2**, **Fig. 5.12-13**).

The endosomal size in cells treated with  $1 \times IC_{50}$  of **12** under dark conditions ranged between  $0.09\text{--}0.99 \mu m^3$  (**Appendix, Table A35**), with a variety of different transparencies (dense or lucent interiors) correlating with that of endosomes analysed by cryo-XRT in the literature.<sup>41, 50</sup> Endosomal size is dependent on the stage of post-internalisation (*i.e.* early, sorting or late endosomes) and can have 2D diameters of up to  $1 \mu m$ ,<sup>64</sup> explaining the variation in endosomal size observed. The endosomes in **T7** and **T9** (**Section 5.3.2**, **Fig. 5.12-13**) are different in appearance, which is likely attributed to different stages of cell growth and recovery in response to treatment with **12**. For example, it is evident from the x-ray mosaics that the cell mapped by **T9** (**Section 5.3.2**, **Fig. 5.13**) is less crowded, making it more exposed or vulnerable, compared with **T7** (**Section 5.3.2**, **Fig. 5.12**) which has more neighbouring cells (allowing extracellular interactions between adjacent cells, thus promoting cancer cell survival).<sup>65</sup>

The presence of endosomes may imply that PC3 cells can recognize **12** as an invader and attempts to secrete it from the cell *via* endocytotic pathways, thus, reduce the quantity of intracellular complex available for photo-activation. Therefore, the lack of dark toxicity of **12** may not *only* be attributed to the apparent complex ‘inertness’, but also a result of the active excretion/efflux from cancer cells. It is not all that surprising that Pt<sup>IV</sup>-prodrugs are being recognized by cancer cells in a similar manner to cisplatin, which emphasizes the crucial advantage of light-mediated selectivity in overcoming resistance. This may also warrant a further optimization of the antiproliferative screening protocol whereby cells are photoactivated earlier: for example, irradiation after 30 min dark drug exposure as opposed to 1 h drug exposure, which may increase the extent of cytotoxicity.

The postulated efflux of diazido-Pt<sup>IV</sup> complexes *via* active processes under dark conditions may be disadvantageous in the development of PACT prodrugs, however, this can also be exploited in general drug design. The conjugation of endosomal-targeting moieties to diazido Pt<sup>IV</sup> complexes may exploit the endosomal localisation of **12** under dark conditions (*e.g.* complexes which can be activated in these recycling compartments). For example, using endocytic-targeting ligands (such as riboflavin or mannose-6-phosphate – which rely on clathrin-dependent receptor-mediated endocytosis)<sup>66</sup> at the axial position of Pt<sup>IV</sup> prodrugs. This may exploit the “dark” endosomal-localisation of diazido-Pt<sup>IV</sup> prodrugs and enhance the overall antiproliferative effect.

### ***Nuclear spots and membrane invaginations***

The second major observation in cells treated with **12** (2 h, dark) was the presence of small black spots in the cell nucleus (**T8-9, Section 5.3.2, Fig. 5.13**), ranging from 0.002-0.042 and 0.003-0.031  $\mu\text{m}^3$  in size, for **T8** and **T9**. These dark spots were not attributed to fiducials as they are significantly smaller, non-spherical and inhomogeneous. Heavy metals have high atomic numbers, thus, causes strong electron scattering upon exposure to soft x-rays, appearing darker in tomography. This observation may provide evidence into the potential nuclear-targeting of **12** in PC3 cells. As soft x-rays (500 eV) cannot directly detect the XRF of heavy metals (*e.g.* Pt L<sub>3</sub>M<sub>5</sub>=9.44 keV), synchrotron-XRF was required to confirm this.

Nuclear membrane invaginations were also observed: 3D crevices formed when the nuclear membrane folds back on itself to encapsulate vesicles during endo- or exocytosis.<sup>67</sup> Tumour cells acquire nuclear membrane invaginations to enhance cell signalling (*i.e*  $\text{Ca}^{2+}$  signal transduction – as key component in the cell cycle and cell survival).<sup>48</sup> Moreover, as nuclear invaginations are common for many cancers,<sup>48</sup> this observation is likely not attributed to treatment with **12**, correlating with the lack of cytotoxicity of **12** ( $\text{IC}_{50} > 100 \mu\text{M}$ ) prior to photo-activation with blue light.

### Cells treated with **12** under photo-conditions

In order to probe the photo effects of **12**, PC3 cells were treated with  $0.25\text{--}1 \times \text{IC}_{50}$  ( $1.5\text{--}6.5 \mu\text{M}$ ) for 1 h, followed by 1 h exposure to blue light ( $\lambda = 465 \text{ nm}$ ) so as to compare directly to cell viability experiments (**Section 5.3.1, Table 5.3**). Significant differences in morphology were observed when treated with **12** under photo-conditions (**T10-17, Section 5.3.2, Fig. 5.14-19**), compared to those exposed to dark conditions (**T7-9, Section 5.3.2, Fig. 5.12-13**) including membrane-blebbing, vesicle-shedding, vacuolisation (cytoplasmic and nuclear), varying lipid droplet distributions, increased granularity of the nucleus and cell shrinkage. No statistically significant differences in the mean size of mitochondria or lipid droplets were observed between the untreated controls and cells treated with  $0.25\text{--}0.5 \times \text{IC}_{50}$  of **12** upon irradiation, with a wide range of 3D volumes ( $0.03\text{--}0.35 \mu\text{m}^3$  and  $0.04\text{--}0.29 \mu\text{m}^3$  for mitochondria and lipid droplets, respectively). The extent of cell damage was highly dose-dependent, with significantly damaged morphologies at higher concentrations of **12**. The mitochondria in severely damaged cells (treated with  $1 \times \text{IC}_{50}$  of **12**, **T15-16, Fig. 5.18-19**) could not confidently be identified in the cytoplasm, suggestive of drug-induced organelle damage.

Cells treated with **12** with the inclusion of a recovery period (**T18-19, Section 5.3.2, Fig. 5.20-21**) were significantly less damaged compared to that of cells treated with **12** without recovery (**T15-T17, Section 5.3.2, Fig. 5.18-19**): with healthy nuclei, well-defined lipid droplets, fused mitochondria and non-compromised plasma membranes. This may suggest a potential cytostatic contribution towards the antiproliferative activity of **12**. This may be a consequence of enhanced drug efflux or reduced cellular influx of **12** upon removal of extracellular drug solution. A

comparison of **T18** and **T19** ( $1 \times \text{IC}_{50}$  with recovery) revealed differences in 2D morphology, with **T19** being more elongated and resembling that of untreated PC3 cells grown on a 2D surface.<sup>38, 39</sup> This correlates with reduced cell damage in **T19** induced by **12**, emphasizing the differential uptake and efflux kinetics exhibited within cells in the population.

### ***Vesicle-shedding and membrane blebbing***

In general, there was a wide distribution in the 2D shape and morphology of cells treated with **12**, highlighting the varying dose response kinetics (*i.e.* uneven drug uptake) exhibited by individual cells in a population. Cryo-XRT has the advantage that it allows the rapid analysis of individual cells, as opposed to making an assumption about a large population of cells (*e.g.* metal ICP-MS cellular accumulation studies). Cells exposed to the lowest concentration ( $0.25 \times \text{IC}_{50}$ ) of **12** under photo-conditions revealed vesicle-shedding at the plasma membrane (**T10**, **Section 5.4.2**, **Fig. 5.14**). As vesicle-shedding is a common feature of many prostate cancer cell lines,<sup>61, 68</sup> it cannot confidently be attributed to damage induced by **12** – hence, complementary techniques are required to verify this.

Severe membrane-blebbing was also observed for cells treated with the highest concentration of **12** ( $1 \times \text{IC}_{50}$ ), but to a much greater extent, reaffirming concentration-dependent cell death. Membrane-blebbing is commonly associated with programmed cell-death mechanisms including apoptosis and necrosis.<sup>69</sup> Fluorescence imaging of structurally-similar light-activated diazido-Pt<sup>IV</sup> complexes did not exhibit the classical features of apoptosis (*e.g.* cell fragmentation), suggestive of predominantly non-apoptotic cell death.<sup>13</sup> It must be considered that **12** may exhibit multiple mechanisms of cell death, for example cisplatin induces apoptosis in addition to triggering autophagy.<sup>70</sup>

### ***Vacuolisation***

Cytoplasmic vacuoles were observed in cells treated with  $0.25-1 \times \text{IC}_{50}$  of **12** under photo-conditions (**T10-17**, **Section 5.3.2**, **Fig. 5.14-19**), with multiple cytoplasmic vacuoles at higher concentrations of **12**: dose-dependent cell damage. Cytoplasmic vacuoles are formed in response to harmful materials which have entered the cell, which may implicate a cellular attempt to remove or detoxify **12**, to evade cell death. Vacuolisation is commonly associated with autophagy or paraptosis.<sup>49</sup> Cytoplasmic vacuoles in autophagy are commonly double-membraned, whereas, in paraptosis they are single-membraned.<sup>71</sup> As the vacuoles in cells observed in these tomograms were predominantly enclosed by single-membranes, this may suggest paraptosis is involved in the cell death pathway induced by **12**.

The formation of vacuoles in cells treated with **12** (465 nm) may play an essential role in the initiation of non-apoptotic cell death. This is not the first report of drug-induced formation of vacuoles by Pt compounds in cancer cells.<sup>72-74</sup> Vacuolisation has also been linked to the generation of ROS, for example, curcumin (a compound with antitumour properties) can trigger extensive cytoplasmic vacuolation in PC-3M cells (metastatic cells derived from hepatic metastasis of PC3 cells),<sup>75</sup> which was attributed to the generation of ROS followed by non-apoptotic, non-autophagic cell death. As diazido-Pt<sup>IV</sup> complexes can generate toxic hydroxyl radicals, the formation of vacuoles under irradiated conditions may be associated with the production of ROS, however, further studies are required to confirm this. Overall, the observed dose-dependent vacuolisation may suggest that **12** does not predominantly induce apoptosis (unlike cisplatin).<sup>76</sup>

Interestingly, in **T14** ( $0.5 \times \text{IC}_{50}$ , 465 nm) a large *nuclear* vacuole surrounded by lipid droplets was observed (**Section 5.3.2**, **Fig. 5.17**). The cause of nuclear vacuoles is not well-understood, and have been postulated to be due to nuclear invaginations or direct formation of holes in the cell nucleus.<sup>77</sup> The observed nuclear vacuole may be associated with morphological damage induced by **12** under photo-conditions, with the lipid droplets attempting to repair the damage.

### ***Distribution of lipid droplets***

No statistically significant differences in the mean 3D size ( $\mu\text{m}^3$ ) and number of lipids (per tomogram) were observed in cells treated with different concentrations of **12** under photo-conditions when compared to the untreated controls (**Section 5.3.2, Table 5.5**). The distribution of lipids in 3 different cells treated with  $0.25 \times \text{IC}_{50}$  of **12** (**T10-12, Section 5.3.2, Fig. 5.14-15**) appeared to surround cell nuclei. Lipid droplets tend to congregate and cluster around cell nuclei (where they are synthesized at the endoplasmic reticulum),<sup>78</sup> and are re-distributed in the cytoplasm in response to intruding bodies (*i.e.* drugs), to generate energy from mitochondria. As this was also observed in the untreated controls (**T1-6, Section 5.3.2, Fig. 5.10-11**), hence, cannot be attributed to a cellular response to Pt treatment and requires further study.

Interestingly, there was a wide variety of lipid droplet size ( $\mu\text{m}^3$ ) in cells treated with  $0.25 \times \text{IC}_{50}$  of **12** when comparing individual cells (**T11-12** vs. **T10**,  $p < 0.001$ ; **Section 5.3.2, Fig. 5.14-15**). This was likely due to the variation in the metabolic state of the cell (which can cause rapid alterations in the number and size of lipid droplets).<sup>79</sup> Notably, the cell in **T10** has a large cytoplasmic vacuole and is more damaged than that of the latter, which may influence the nature of lipid droplets. The size of lipid droplets can also reflect the cellular energy storage capacity, which can be altered by environmental factors.<sup>80</sup> For example, HeLa cervical cancer cells treated with anticancer drug paclitaxel increased the size of lipid droplets in response to drug treatment.<sup>81</sup> Changes in the size of lipid droplets may be associated with cellular response to drug treatment, and requires further investigation into the lipid profiles in PC3 cells. This may be of particular interest in lipid-enriched prostate cancer cells (where lipids are highly implicated in cancer progression).<sup>82</sup>

The mean volume of lipid droplets in cells treated with  $0.5-1 \times \text{IC}_{50}$  of **12** (**T13-17**) were closely comparable to the untreated controls (**T1-6, Section 5.3.2, Table 5.5**), and to that of cells treated with lower concentrations (**T7-9**). Remarkably, lipid droplets surrounding a large nuclear vacuole were observed in **T14** ( $0.5 \times \text{IC}_{50}$ ). The physiological significance of lipid droplets in cell nuclei is not well-understood. Nuclear lipids have reported to be an alternative source of fatty acids and

cholesterol for membrane biosynthesis, signalling and transcription in the nucleus.<sup>83, 84</sup> It must be considered that the origin of these lipid droplets may be cytoplasmic, but become entrapped within the invaginations of the nuclear membrane (vacuoles).<sup>85</sup> Moreover, the lipids surrounding this vacuole are likely associated with cell repair mechanisms in response to cell damage. This highlights the remarkable ability to capture cellular events by cryo-XRT compared to conventional microscopy techniques.

Cells treated with **12** (465 nm) with the inclusion of a recovery period (**T18-19**, **Section 5.3.2**, **Fig. 5.20-21**) revealed significant differences in the number of lipid droplets. In contrast to **T18** (total lipid droplets=6), a significant number of lipid droplets were observed in **T19** (total=88), which may have been synthesized in response to cellular damage (*e.g.* releasing lipids for membrane biosynthesis, cell signalling or energy-generation). Both of the mapped cells (**T18-19**) resembled features comparable to that in the untreated PC3 control cells (**T1-6**, **Section 5.3.2**, **Fig. 5.10-11**). The difference in the number of dense lipids may be a consequence of different stages of cell growth or recovery in response to **12**. This is evident from the wide variety in the number and size of lipid droplets in other cells in the mosaic image (not imaged by cryo-XRT; **Fig. 5.20-21**). The importance of extracellular interactions between adjacent cells on a 2D surface can mediate cancer cell survival towards chemotherapeutics, hence, cell crowding may influence cell vulnerability (*e.g.* enhanced metal complex accumulation) resulting in differences in cellular response.<sup>61</sup> For example, the cell mapped in **T19** is more elongated, exhibiting a healthier cell morphology and is more exposed compared to **T18**, thus, may have a greater need for increased lipid droplets for cellular energy and repair once the extracellular drug medium is removed. However, no experimental evidence has been provided for this hypothesis, and goes beyond the scope of this thesis.



### ***Increase cell granularity***

In cells treated with  $1 \times \text{IC}_{50}$  of **12** under blue light conditions (**T15-17**, **Section 5.3.2**, **Fig. 5.18-19**) cell nuclei and nucleolus can be identified, but were less well-defined compared to the untreated controls (**T1-6**, **Fig. 5.10-11**) and were more granular in appearance. An increase in cellular granularity can be associated with growth arrest and cell death (particularly autophagy) in response to chemotherapeutics or irradiation,<sup>86</sup> which was demonstrated with organic test compounds in PC3 cells. Notably, the nuclei in cells treated with **12** ( $1 \times \text{IC}_{50}$ , 465 nm) were more granular, which may implicate the formation of nuclear stress granules: subnuclear compartments which form in response to stress stimuli as a means of protecting the cell,<sup>87</sup> and have been reported for chemotherapeutics including 5-Fluorouracil.<sup>88</sup> Cancer cells utilize the formation of stress granules in an attempt to evade drug treatment.<sup>89</sup> The extent of cell damage observed indicates that any cellular stress response was unsuccessful in restoring cell function and homeostasis, subsequently resulting in cell death. Overall, the increased granularity may be associated with autophagic cell death and potentially the formation of nuclear stress granules induced upon photo-treatment with **12**, however, techniques such as flow cytometry are required to probe this.

### ***Cytostatic vs. Cytotoxic***

Inclusion of a drug-free recovery period in antiproliferative screening is an important consideration for clinical translation, and can provide insights into the cytostatic or cytotoxic nature of drugs. Cells treated with **12** and recovered in complex-free media (**T18-19**, **Section 5.3.2**, **Fig. 5.20-21**) were significantly less damaged compared to the analogous cells without a recovery period (**T15-17**, **Section 5.3.2**, **Fig. 5.18-19**), which may implicate a cytostatic contribution to the antiproliferative activity of **12**.

Cytostatic drugs differ to cytotoxic drugs in that they can inhibit tumour growth upon drug exposure, whereas, cytotoxic drugs continuously kill the cancer cells even after drug removal. This may implicate a cytostatic contribution to the anticancer activity of **12**, in addition to the cytotoxicity of the  $\text{Pt}^{\text{II}}$  species. Cytostatic drugs prevent the proliferation of cancer cells by stabilization of a disease state,

which can be both beneficial and disadvantageous in cancer therapy. As cancer cells rapidly proliferative, they are extremely sensitive to cytostatic (growth-inhibiting) drugs,<sup>90</sup> compared to cytotoxic drugs – which affect all dividing cells (healthy and cancerous). In general, cytostatic complexes are less toxic towards healthy cells due to their improved target-specificity,<sup>90</sup> which can reduce off-target effects commonly experienced with cytotoxic drugs. Examples of drugs with cytostatic properties include 5-fluorouracil and rapamycin.<sup>91, 92</sup> However, common disadvantages of cytostatic drugs is that they require prolonged dosages for effective therapy,<sup>90</sup> thus, are frequently administered in combination with cytotoxic drugs. For example, rapamycin can enhance the cytotoxicity of cisplatin by inhibiting prostate cancer cell growth in a cytostatic manner.<sup>93</sup>

Overall, this data may suggest that complex **12** overcomes the predominantly cytotoxic nature of cisplatin by providing an additional cytostatic contribution to cell death, combined with the light-controlled *in situ* formation of cytotoxic Pt<sup>II</sup> species. This also correlates with the antiproliferative activity of coumarin, which exhibits both cytostatic and cytotoxic activity.<sup>94</sup> As cryo-XRT was only performed on coumarin-labelled **12**, the same conclusions cannot be drawn for all diazido-Pt<sup>IV</sup> PACT complexes from this family and requires further investigations (*e.g.* antiproliferative screening with different recovery periods).

### 5.4.3 Synchrotron-XRF

Synchrotron-XRF can be used to gain insights into the intracellular localisation and distribution of heavy metal elements with respect to endogenous biological elements. Herein, synchrotron-XRF has been used to investigate the potential cellular targets and distribution of Pt in cancer cells treated with diazido-Pt<sup>IV</sup> PACT complexes under both dark and blue light (465 nm) conditions. Synchrotron-XRF analysis was performed on cryo-fixed and dehydrated PC3 cells treated with 5× the irradiated IC<sub>50</sub> of **11**, **12** and **cisplatin** using an incident energy of 14 keV (100 nm step-size; 0.2 s exposure). Ideally, frozen-hydrated cells would be analysed by nano-focussed XRF to allow a direct comparison to cryo-XRT data. However, as these facilities were not available at the I14 beamline, cells were frozen and dried.

Elemental maps of three individual PC3 cells (from cell populations grown on Si<sub>3</sub>N<sub>4</sub> membranes) exposed to 1 h irradiation (465 nm) were obtained (**C1-3**, **Section 5.3.3**, **Fig. 5.24**). Overall, the cells revealed elongated, cobble-stoned morphologies *ca.* 30-40  $\mu\text{m}$  length, with small, rounded nuclei – correlating with the typical morphologies of untreated PC3 cells grown as a monolayer.<sup>38, 39</sup> Importantly, Pt L<sub>3</sub>M<sub>5</sub>-emission (9.44 keV) was not observed in these control cells.

### Cells treated with **11**, **12** or cisplatin

In order to analyse the in-cell effects of diazido-Pt<sup>IV</sup> complexes, cells were treated with 5 $\times$  the irradiated IC<sub>50</sub> of platinum complex under both dark (2 h protected from the light) and irradiated (1 h drug exposure followed by 1 h 465 nm exposure) conditions. A wide variety of cell shapes and sizes were observed, so that no statistically significant differences were evident when comparing the area or roundness factors (RF) of cells treated with **11**, **12** or **cisplatin** to the untreated controls. In general, Pt was distributed throughout cells treated with **11**, **12** or **cisplatin** (in the cytoplasm and nuclei). Interestingly, significantly higher levels of intracellular Pt were observed in cells treated with **11** or **12** upon blue light irradiation, compared to that in the dark.

### Cell morphology

Wide variations in 2D cell size ( $\mu\text{m}^2$ ) were observed in cells treated with **11** or **12**, under both dark and blue light conditions. The stage of cell growth / death and the heterogeneity of drug uptake can greatly influence the observed cellular morphology of individual cells treated with test compounds,<sup>95</sup> emphasizing the advantages of single-cell assays *vs.* population average data (*e.g.* ICP-MS). For example, a more elongated PC3 cell treated with **12** under dark conditions (**C11**, **Section 5.3.3**, **Fig. 5.27**) had an elongated cell morphology *ca.* 30  $\mu\text{m}$  in length with a centralised nucleus, with a roundness factor of  $0.37 \pm 0.02$  and area of  $287 \pm 2 \mu\text{m}^2$ . In contrast, analogous cell **C10** was significantly more rounded in shape (RF= $0.97 \pm 0.02$ ,  $p=0.0001$ ) and smaller in size ( $133 \pm 2 \mu\text{m}^2$ ,  $p=0.0001$ ). Finally, **C12** (**Section 5.3.3**, **Fig. 5.27**) revealed a morphology somewhat intermediate between **C10** and **C11**, with a stretched-out morphology with a centred nucleus

(Section 5.3.3, Fig. 5.27), moderate roundness properties ( $0.59 \pm 0.02$ ) and cell area of  $212 \pm 2 \mu\text{m}^2$ . Furthermore, emphasizing the variation in drug influx and efflux profiles of cells in a monolayer population. Wide variations in cell size and roundness factors were also observed for cells treated with **cisplatin** under irradiated conditions (mean area =  $345 \pm 40 \mu\text{m}^2$ ; mean roundness factor =  $0.59 \pm 0.24$ ).

No statistically significant trends in the mean nucleus-to-cytoplasmic ratios were observed between cells treated with **11**, **12** or **cisplatin** (Section 5.3.3, Table 5.8), with nuclei taking up *ca.* 30-40% of the overall cell area. Cell nuclei in PC3 cells have been reported to take up 66% of the cell volume,<sup>96</sup> thus, highlighting the limitations of imaging 3D objects using 2D XRF. In cells treated with **12**, the more elongated cells (roundness factor < 0.4) had smaller nuclear-to-cytoplasm ratios compared to the more rounded cells under the same conditions. Changes in the nucleus-to-cytoplasm area ratios can significantly alter cellular drug response and the metastatic proliferation (as demonstrated with cisplatin in breast cancer cells),<sup>97</sup> giving an indication of nuclear stress. Further work (ideally in 3D) with a greater statistical representation is required to investigate whether the rounding of a cell or changes in nucleus-to-cytoplasm ratios are associated with increased drug accumulation or cell damage.

#### *Distribution of Pt under dark conditions*

The Pt XRF ( $L_3M_5 = 9.44 \text{ keV}$ ) was very faint in cells treated with  $5 \times$  irradiated  $IC_{50}$  of **11** ( $IC_{50} = 6.5 \mu\text{M}$ ; C4-6, Section 5.3.3, Fig. 5.25) and **12** ( $IC_{50} = 55 \mu\text{M}$ ; C10-12, Fig. 5.27) under dark conditions (assumed to be non-toxic), but appears to mildly localise with Zn in the cell nucleus. This complements the dark spots observed in the cell nucleus in cryopreserved PC3 cells treated with **12** under dark conditions from cryo-XRT (T8-9, Section 5.3.2, Fig. 5.13). Moreover, the low levels of in-cell Pt may also be due to enhanced efflux under dark conditions, complementing the hypothesis of endosomal breakdown observed by cryo-XRT (T7-9, Section 5.3.2, Fig. 5.12-13). It may be hypothesized that some of **11** and **12** localizes in the nucleus of PC3 cells prior to photo-activation, however, XRF or  $^{195}\text{Pt}$  ICP-MS cell fraction studies at higher drug concentrations are required to confirm this.

The reduction of Pt<sup>IV</sup>-prodrugs to kinetically-labile Pt<sup>II</sup> square planar species is well-reported in the literature,<sup>4, 8, 10, 98</sup> with very few hypotheses involving Pt<sup>IV</sup>-DNA interactions.<sup>99, 100</sup> As cancer cells exist under redox stress, their intracellular environments are highly reducing and likely causes the unwanted chemical reduction of Pt<sup>IV</sup> PACT complexes prior to photoactivation. The chemical in-cell vulnerability of diazido-Pt<sup>IV</sup> complexes to form Pt<sup>II</sup> species may explain the observed nuclear-localisation of Pt under dark conditions. Alternatively, it must be considered that the intra-nuclear localisation of **11** and **12** under dark conditions may be associated with Pt<sup>IV</sup> interactions with nuclear DNA, however, this contradicts previous GMP-binding studies.<sup>4</sup> Further analytical techniques are required to probe the speciation of nuclear Pt (*e.g.* XANES or EPR).

#### ***Irradiation enhances Pt accumulation***

The Pt in cells treated with 5×IC<sub>50</sub> of **11** and **12** irradiated under blue light conditions revealed distributions in the cytoplasm and nucleus (**Section 5.3.3, Fig. 26, 5.28**), with more intense Pt XRF compared to that of analogous cells treated under dark conditions. This can be attributed to significantly higher concentrations of intracellular Pt upon irradiation (*ca.* 3× and 3.5× more for **11** and **12**, respectively), implying that irradiation with 465 nm not only activates the Pt<sup>IV</sup> complex, but may also enhance the cellular accumulation (influx/efflux). This has been reported for structurally-similar diazido Pt<sup>IV</sup> complexes upon irradiation with UVA light, achieving intracellular Pt levels of up to 20 ng/10<sup>6</sup> cells after 2 h in bladder cancer cells, almost 20× greater than that under dark conditions.<sup>101</sup> The enhanced accumulation of diazido-Pt<sup>IV</sup> complexes exposed to 465 nm may indicate the selective accumulation of photolysis products compared to the starting “inert” complexes.<sup>101</sup> Moreover, this may imply that reactive photoproducts can enter cells and irreversibly bind to cellular components,<sup>102</sup> To further probe this, ICP-MS cellular accumulation studies of cancer cells treated with equimolar concentrations of **11** or **12** under dark and irradiated conditions can be performed.

Alternatively, the increased levels of intracellular Pt may be attributed to photo-induced membrane damage. As the antiproliferative screening protocol involves irradiation with 1 h blue light whilst cells are still incubated with platinum test

compound, the extracellular formation of photo-products (*i.e.* photolysis) to enhance complex accumulation must be considered. Free radicals can alter the physiology of cell membranes (*i.e.* membrane fluidity or rigidity),<sup>103</sup> making biomembranes a viable target for attack by ROS.<sup>104</sup> In particular, hydroxyl radicals ( $\cdot\text{OH}$ ) have roles in modulating membrane permeability of cells.<sup>105</sup> As diazido- $\text{Pt}^{\text{IV}}$  complexes can generate toxic hydroxyl ( $\cdot\text{OH}$ ) and azidyl ( $\text{N}_3\cdot$ ) radicals upon 465 nm exposure, the extracellular formation of these radicals may influence the permeation of the now  $\text{Pt}^{\text{II}}$  square planer species (*e.g.* by lipid oxidation),<sup>106</sup> promoting the cellular accumulation. The extracellular activation of such  $\text{Pt}^{\text{IV}}$ -diazido prodrugs by light provides a means of killing cancer cells *via* radical-induced membrane damage, in addition to forming toxic  $\text{Pt}^{\text{II}}$  species which can bind to DNA. Moreover (providing the drug can reach the tumour microenvironment), this affords a combined *extra-* and *intracellular* mechanism to overcome resistance.

Although not observed from the synchrotron-XRF images of cells treated with **11** or **12** under 465 nm conditions, the extensive damage/blebbing of the plasma membrane was observed in analogous PC3 cells analysed by cryo-XRT (**Section 5.3.2, Fig. 5.23**), which supports the hypothesis of compromised membrane integrity upon blue light irradiation. Overall, the formation of extracellular photolysis products (*e.g.* radicals) may promote accumulation of Pt by altering membrane physiology, and potentially binding to cellular components to contribute to the antiproliferative effect.

#### ***Localisation of Pt in membrane***

Interestingly, in one of the cells treated with coumarin-labelled **12** under photo-conditions the Pt XRF was strongly localised at the perimeter of the cell (**C13, Section 5.3.3, Fig. 5.28**), suggestive of distribution in the plasma membrane. The elongated cell morphology (resembling the untreated controls) suggests that this particular cell is not significantly damaged - most likely as a result of reduced cellular accumulation of **12** (**Section 5.3.3, Fig. 5.30**). The localisation of Pt in the plasma membrane may suggest that Pt is being encapsulated in the membrane, which may be indicative of a cellular response to prevent intracellular entry of **12**. This may explain the minimal morphological damage observed in **C13** compared

to cells exposed to the same conditions (**C14-15**, **Section 5.3.3**, **Fig. 5.28**) – which were smaller, more rounded and exhibited higher intracellular Pt levels. The passive diffusion of lipophilic Pt<sup>IV</sup> complexes into cancer cells *via* the plasma membrane is well reported in the literature,<sup>16</sup> hence, the presence of Pt in the cell membrane is not surprising. For example, Pt<sup>IV</sup>-valproic acid derivatives of cisplatin primarily accumulated in the cell membrane of A2780 cells.<sup>107</sup> The hydrophobic nature of coumarin may also promote the membrane accumulation of **12** by forming favourable interactions with the hydrophobic core. Coumarins have high affinities for membrane phospholipids, which acts as a driving force for coumarin entry into cells.<sup>108</sup> The potential cellular efflux of **12** by membrane transporters must also be considered. The uptake pathways of diazido-Pt<sup>IV</sup> complexes can be probed using ICP-MS cellular accumulation studies in the presence of influx/efflux inhibitors, such as, verapamil (PGP) or ouabain (Na<sup>+</sup>-K<sup>+</sup> pump).<sup>109</sup>

Additionally, the potential *targeting* of the plasma membrane by **12** cannot be discounted. The lipophilic nature of coumarin may favour interactions with the phospholipid bilayer of plasma membranes. Pt-membrane interactions have been reported for cisplatin – which has shown to mediate cell uptake, cytotoxicity and resistance.<sup>110</sup> Overall, the observed accumulation of Pt in the plasma membrane of PC3 cells may be associated with interactions between coumarin (and/or Pt) and hydrophobic core of the lipid bilayer, which may mediate cellular influx/efflux mechanisms. This complements the significant membrane damage observed in PC3 cells treated with **12** by cryo-XRT (**Section 5.3.2**).

### ***Pt in the cell nucleus***

As Pt was found to mildly localize in the cell nuclei of PC3 cells treated with **11**, **12** or **cisplatin** (**C4-18**, **Section 5.3.3**, **Fig. 5.25-29**), the percentage of intracellular Pt in cell nuclei were determined (**Section 5.3.3**, **Table 5.9**). Note that when quantifying elements by 2D XRF mapping an assumption is made about the thickness and density of cells,<sup>111</sup> presuming homogeneity, thus, the cell nucleus is most likely not flat. As a result, the increased Pt XRF observed in nuclei of cells treated with **11**, **12** or **cisplatin** may be attributed to the increased cell thickness as opposed to increased concentrations of nuclear Pt. To overcome this, x-ray

tomography is required to determine the ratio between the nucleus and the cytoplasm in the z-plane. Overall, mean levels of nuclear Pt were found to be greater than 40% in cells treated with **11** or **12**, regardless of the photo-conditions, suggesting that the nucleus is likely a cellular target of these complexes. This correlates with the DNA-binding studies reported for this family of diazido-Pt<sup>IV</sup> PACT complexes.<sup>11</sup>

The nuclear-targeting of **11** and **12** (mean nuclear Pt percentages of 74±15 and 52±6%, respectively) may be independent on the photo-conditions, which may be indicative of the intracellular chemical reduction of Pt<sup>IV</sup> to Pt<sup>II</sup>. In cells, Pt<sup>IV</sup> complexes can be reduced by biological reducing agents to form active Pt<sup>II</sup> species which then bind to DNA, hence, the nuclear localisation of **11** and **12** under dark conditions is not surprising. Adversely, it must be considered that the Pt may be entering the nucleus as Pt<sup>IV</sup> under dark conditions, subsequently interacting or forming adducts with nuclear DNA.<sup>99, 100</sup> The intracellular reduction of Pt<sup>IV</sup>→Pt<sup>II</sup> (photo- or chemical) is generally assumed to be favourable for Pt<sup>IV</sup> prodrugs which rely on *in situ* reduction in their anticancer mechanisms of action. Further work is required to understand the intracellular stability, localisation and cellular accumulation profiles of different platinum species in order to elucidate the mechanism of action.

### ***Comparison of 11 and 12***

Higher quantities of intracellular Pt were determined in cells treated with **12** in the dark, compared to parent compound **11** – correlating with the lower potency of **11** (8× less potent). Additionally, the increased lipophilicity (due to the coumarin ligand) of **12** may promote cellular uptake through the hydrophobic core of the cell membrane (improving the bioavailability),<sup>108</sup> however, LogP studies are required to support this hypothesis.

A comparison of the normalised mass fraction quantities of Pt in cells treated with **12** and exposed to blue light showed *ca.* 2× more than that of **11**, potentially due to the enhanced hydrophobic properties of the latter. The improved antiproliferative potency of **12** (compared to **11**) may be facilitated by both the organic (coumarin) and inorganic (Pt modality) counterparts. This may have major implications in



future studies involving the conjugation of metallodrugs with modalities exhibiting antitumour properties or targeting groups. Tethering of conjugates may significantly improve the antiproliferative activity of a metal complex, however, the mechanism of action and uptake of these complexes may be altered with respect to the non-conjugate parental complex, thus, the mode of action cannot be assumed the same. This phenomenon has been reported for a variety of metallodrugs, including Pt<sup>IV</sup>-prodrugs,<sup>112</sup> Ru<sup>II</sup> complexes and Os<sup>VI</sup> nitride complexes.<sup>113, 114</sup> Additionally, fluorescent probes (which are typically large, conjugated structures) may also influence the cellular accumulation profiles, targeting and intracellular mechanism of actions of action compared to the parent compound.

The co-localisation between Pt and Zn in cells treated with equipotent concentrations of **11** or **12** was more pronounced for coumarin-labelled **12**, most likely due to the increased uptake of the coumarin derivative (2.8±0.3 and 4.9±0.6 ppm for **11** and **12**, respectively). Similarly, under blue light conditions the same trend was observed, with higher correlations between Pt and Zn for **12** vs. **11**, in agreement with the increased potency of **12** (IC<sub>50</sub>=6.5 µM) compared to **11** (IC<sub>50</sub>=55 µM). Intracellular Pt and Zn co-localised more strongly in PC3 cells treated with **11** upon blue light irradiation, compared to the those treated in the dark (r=0.44±0.05 and 0.19±0.05 for dark and irradiated, respectively). The same trend was observed for cells treated with **12** (r=0.58±0.08 and 0.34±0.04, respectively). Upon blue light irradiation, the accumulation of Pt from **11** and **12** is significantly enhanced which means that more of the now-cytotoxic Pt<sup>II</sup> species may be available to target the cell nucleus and form strong interactions with biomolecules. This may provide an explanation into the enhanced co-localisation of Pt and Zn in treated cells exposed to blue light compared to those treated in dark conditions. Moreover, as Zn is highly abundant in the nucleus, this supports the hypothesised DNA-interactions of photo-activated **11** and **12**.

### **Comparison to cisplatin**

**Cisplatin** has been used as a control in this study to allow a comparison to both the literature and to cancer cells treated with diazido-Pt<sup>IV</sup> complexes (**11** and **12**) under the same conditions (vitrified and freeze-dried). Cells were treated with 5×IC<sub>50</sub> of **cisplatin** (IC<sub>50</sub>>100 μM) for 1 h, followed by 1 h irradiation with 465 nm (**C16-18**, **Section 5.3.3**, **Fig. 5.29**). The cell nuclei in **C16-18** were clearly identified from the Zn XRF map, enabling the identification of Pt in the nucleus as well as the cytoplasm. Complementary to this, cells treated with **cisplatin** revealed moderate Pt-Zn co-localisation statistics ( $r=0.34\pm0.04$ ). This is not surprising considering that DNA-binding of cisplatin is well-known.<sup>115</sup> In the literature, the localisation of cisplatin is accepted to be primarily cytoplasmic (>50%),<sup>76</sup> with only 1% of cisplatin binding to nuclear DNA.<sup>116</sup> Other targets of **cisplatin** include mitochondria, lysosomes and endoplasmic reticuli.<sup>117</sup>

The disparity in the cellular distributions of **cisplatin** observed with that of the literature is likely dependent on factors including the type of cell, the stage of cell growth, sample preservation and the technique used to quantify them. For example, the predominant nuclear localisation of Pt of **cisplatin** (mean=42±8%) in vitrified and freeze-dried PC3 cells (**Section 5.3.3**, **Fig. 5.29**) correlates strongly with that of microprobe-XRF studies of cryo-fixed and freeze-dried A2780 cells treated with cisplatin (revealing the majority of Pt in the nucleus).<sup>118</sup> This predominant nuclear localisation of Pt is likely due to the presumption made about uniformity in cell thickness in 2D XRF mapping (as previously described). This highlights the importance of using complementary analytical techniques when probing the mechanisms of action of metallodrugs in biological systems.

The Pt XRF in cells treated with **cisplatin** (500 μM) was significantly lower than that of cells treated with much lower concentrations of **11** and **12** (5×IC<sub>50</sub>=275 and 32.5 μM, respectively) under blue light conditions, with 1.5 and 3× more Pt for **11** and **12**, respectively. This highlights the significant advantages of light-enhanced cellular accumulation (or membrane damage) induced upon photo-activation of **11** or **12**. Overall, the cellular distributions of **11** and **12** were comparable to that observed for **cisplatin** under the same conditions. As **cisplatin** is inactive in cancer cells up to 100 μM after 2 h exposure (IC<sub>50</sub>>100 μM, **Section 5.3.1**, **Table 5.3**), the

enhanced Pt accumulation in cells treated with equipotent concentrations of **11** or **12** ( $5 \times \text{IC}_{50}$ ) is a significant observation. This emphasizes the remarkable potency exhibited by  $\text{Pt}^{\text{IV}}$ -diazidyl PACT complexes, permitting lower doses of Pt compound to achieve the same antiproliferative effect – with the future potential to reduce adverse side effects and prevent drug diversion (decreased efficacy).

Comparison of Pt levels in cells treated with equipotent concentrations of **cisplatin** of **11** and **12** (dark conditions) revealed higher quantities for that of **cisplatin**. This is in strong agreement with low levels of intracellular Pt observed in cells treated with structurally-similar diazido- $\text{Pt}^{\text{IV}}$  compounds compared to **cisplatin** when treated with equimolar concentrations under dark conditions.<sup>101</sup> This may also imply that the accumulation of  $\text{Pt}^{\text{II}}$  species may be more favourable compared to  $\text{Pt}^{\text{IV}}$  species. The hypothesized extracellular photo-activation of  $\text{Pt}^{\text{IV}} \rightarrow \text{Pt}^{\text{II}}$  (e.g. membrane damage) may be a major contributor to the enhanced intracellular levels of Pt. Furthermore, the light-enhanced accumulation of **11** and **12** is likely crucial for antiproliferative activity.

#### 5.4.4 Pt XANES analysis

##### *Pt XANES mapping*

Complementary to XRF, x-ray absorption spectroscopy (XAS) can be used to gain insights into the oxidation state, speciation and coordination environments to elucidate the in-cell chemical form of heavy metal complexes and their potential targets or binding moieties. The main difference between XRF and XAS is the energy: for XRF mapping of cells we use a fixed energy which exceeds the electron-binding energy of elements of interest), whereas for XAS we acquire data using an energy range (in order to monitor the pre-edge, edge and post-edge regions). In particular, XANES (X-ray Absorption Near-Edge Spectroscopy) monitors the region within *ca.* 50-100 eV of the absorption edge.<sup>119</sup>

XANES analysis was performed on solid pellets of three platinum compounds with different oxidation states and coordination environments: (i)  $\text{K}_2\text{PtCl}_4$ ; (ii) **cisplatin**; (iii) **11**, in addition to a platinum metal sheet in the energy range 11.46-11.73 keV

(Section 5.3.4, Fig. 5.31-32). The XANES spectra of  $\text{K}_2\text{PtCl}_4$  and **cisplatin** were indistinguishable owing to the shared  $\text{Pt}^{2+}$  oxidation state, square planar coordination geometry, and the similarities of the ligands forming their coordination sphere. The  $\text{Pt}^0$  metal sheet has a white line at 11.570 keV and a normalised absorption maximum at 1.28. The XANES spectrum of solid **11** ( $\text{Pt}^{\text{IV}}$ ) was shifted to a higher energy (increased by *ca.* 2 eV), with a more intense absorption edge compared to  $\text{Pt}^{\text{II}}$  (white line=11.573 keV, maximum=1.95), correlating with that reported in the literature.<sup>36, 120</sup> This is due to the higher oxidation state of **11**, which requires a greater energy to excite core electrons.

XANES was performed on cryo-fixed and freeze-dried PC3 cells treated with **11** and irradiated with blue light using two methods: (i) “Compressed Sensing” (where 7 energies were selected and the XANES spectra monitored at those points over 1 h); (ii) “Energy Scanning” XANES (where a start and end energy were selected and the XRF spectra were collected every 0.5-1 eV around the edge and then 8 eV after the edge was monitored over a 12 h period). XANES spectra were obtained from XRF spectra by performing PCA and cluster analysis, as described in Section 5.2.4. The XANES spectra were normalised using edge-step normalisation in Athena.<sup>35</sup>

Although there are clear differences in the XANES spectra of  $\text{Pt}^{\text{II}}$  and  $\text{Pt}^{\text{IV}}$  species, the relative proportions of species in a mixture cannot be determined accurately by conventional curve-fitting techniques due to similarities in peak energy and shape. To overcome this, Hambley *et. al.* proposed a method which normalized the maximal absorption of the edge (height of peak) with the post-edge minima immediately after the white line.<sup>36</sup> This method has previously been validated with six known  $\text{Pt}^{\text{II}}$  and twelve  $\text{Pt}^{\text{IV}}$  compounds, to obtain average ratios for each oxidation state, respectively.<sup>36, 37</sup> Herein, this method was used to evaluate the oxidation state of platinum in PC3 cells treated with **11** under blue light conditions (Section 5.2.3, Fig. 5.4).

Initial observations revealed spectra comparable to that of an intracellular  $\text{Pt}^{4+}$  oxidation state (Section 5.3.4, Fig. 5.31-32) – which was reaffirmed for both XANES acquisition methods. Data were processed using the method proposed by Hambley *et. al.* (Section 5.4.4, Fig. 5.30, Table 5.3).<sup>36, 37</sup> The calculated maximum peak absorption ratio of platinum was determined to be  $1.71 \pm 0.04$  (considering both

the “Energy-scanning” and “Compressed Sensing” acquisition methods), which was found to be intermediate between the Pt<sup>IV</sup> and Pt<sup>II</sup> standards (2.05 and 1.35, respectively). The reduction in peak height from the solid pellet of **11** when compared to intracellular Pt revealed only an 18% decrease, whereas comparison to cisplatin revealed a 25% decrease – implying that the majority of intracellular Pt analysed exists at Pt<sup>IV</sup>.

This was reaffirmed by performing a LCF, revealing *ca.* 20% and 25% of intracellular platinum as Pt<sup>II</sup> for the “Compressed-Sensing” and “Energy-Scanning” methods, respectively. This may suggest the majority of Pt in cells treated with **11** under photo-conditions exists as Pt<sup>IV</sup>. This was unexpected, as diazido-Pt<sup>IV</sup> complexes are hypothesised to form Pt<sup>II</sup> species upon blue light irradiation). This may explain the low phototoxicity of **11** (IC<sub>50</sub>=55 µM), which is likely non-toxic in as Pt<sup>IV</sup> oxidation state. Alternatively, Pt<sup>IV</sup> photo-products may also be formed. For example, the intensity and light dosage of Pt-diazido complexes may favour ligand dissociation *vs.* photo-reductive elimination, thus resulting in Pt(IV) photo-products, as reported by Bednarski *et. al.*<sup>13, 121</sup>

As this experiment was not statistically representative (only two 5×5 µm<sup>2</sup> cell regions mapped), further XANES is required to corroborate this. Nonetheless, this preliminary data shows promise for the use of the “Compressed Sensing” XANES acquisition at the I14 beamline, which is significantly less time-consuming than conventional “Energy-Scanning”.

In this experiment, the XRF maps at each energy in the range 11.46–11.73 keV were averaged as opposed to obtaining spatially-resolved (pixel-by-pixel). This is because the per-pixel spectrum is extremely noisy because of the small region that is being scanned (200 nm step-size; 50×70 nm<sup>2</sup> beam size). The averaging of smaller pixels partially removes noise from the spectrum, giving a much higher confidence in the results. As a result, the averaging of spectra provides a ratio of oxidation states (Pt<sup>IV</sup>:Pt<sup>II</sup>) for the whole analysed region. Optimisation for spatially-resolved per-pixel XANES mapping is part of future plans for the I14 beamline.

### ***Beam damage during XANES mapping***

In order to obtain high spatial resolution (<100 nm) during XANES mapping of cells, the sample is exposed to high energy x-rays for a long period energy-scanning mode. This is not only time-consuming but can cause damage to cellular features and also the elemental distribution and speciation.<sup>122</sup> Likewise, even though the sample is exposed to the beam for a much shorter period of time (*ca.* 1.5 h vs. 12 h) using the “Compressed Sensing” method, sample beam damage may still occur. This may be detrimental for scientific reliability, particularly when studying photoactivatable drugs (some of which can be activated with x-rays). For example, a transferrin derivative of Ru<sup>II</sup> PDT photosensitiser TLD-1433 (which is in clinical trials for the treatment of bladder cancer) can be activated with x-rays to treat brain cancer.<sup>123</sup> Similarly, the continuous irradiation of A2780 ovarian cancer cells treated with an organo-osmium(II) complex by XANES mapping (100 nm resolution) caused oxidative damage.<sup>124</sup> X-ray induced photo-reduction of metals is a major drawback in monitoring the oxidation state of metals by XANES spectroscopy.<sup>122, 125</sup> Other concerns may also include the ablation of organic matter – endogenous elements in cells and tissues.<sup>126</sup> For example, the main radiation damage for chemically-fixed cells exposed to soft x-rays is the loss of mass thickness and cell shrinkage<sup>127</sup> – which can be reduced using cryo-preservation.

Multiple factors must be considered when assessing beam damage to the integrity of biological cells, which includes (i) x-ray energy (*e.g.* hard vs. soft), (ii) exposure time, (iii) spatial resolution, (iv) synchrotron beamline (*e.g.* photon flux), (v) reproducibility and (vi) cell preservation. The easiest way to investigate beam damage is to deliberately damage the sample using different x-ray exposure times at the desired energy and spatial resolution. This will inform on the limitations of x-ray exposure threshold of the sample, and provide insights into any changes in elemental distribution within the cells. From there, you can then analyse samples with suitable replicates to ensure that the results are reliable and reproducible concerning the elemental distribution, quantification, chemical speciation and cell morphology. Beam damage also depends on the synchrotron beamline, which can vary with factors including photon flux, energy and beam size. Finally, the method of preservation (*e.g.* hydrated or temperature) of biological samples may also be associated with beam damage.<sup>126</sup> For example, cryopreservation of samples can

reduce x-ray beam damage due to reduced thermal energy at lower temperatures.<sup>128</sup> X-ray beam damage during XRF and XANES has been discussed in detail in the literature.<sup>129, 130</sup> A proposed XANES mapping protocol to investigate sample beam damage is presented in **Appendix (Table A37)**. In this work, no obvious changes in cell morphology of elemental distribution in the two  $5 \times 5 \mu\text{m}^2$  regions of interest were observed, however, future assessment of the sample beam damage threshold is crucial for scientific reliability in XANES mapping of biological cells.

## 5.5 Conclusions and future work

The intracellular morphological damage induced by a coumarin-labelled diazido- $\text{Pt}^{\text{IV}}$  PACT complex (**12**) was investigated in cryopreserved PC3 cancer cells using cryo-SIM and cryo-XRT. Unfortunately the blue fluorescence of **12** formed upon photoactivation with 465 nm was not observed in cryopreserved PC3 cells treated with  $1 \times \text{IC}_{50}$  of **12** (1 h exposure followed by 1 h irradiation with light) by cryo-SIM, likely owing to the short life time of organic radicals. Cryo-XRT of PC3 cells treated with **12** under dark conditions revealed the presence of endosomes, implicating active (energy-dependent) influx/efflux accumulation pathways. This is likely a cellular response to unwanted materials and an attempt to excrete the platinum complex prior to *in situ* activation and antiproliferative activity upon blue light exposure. This could be further probed by  $^{195}\text{Pt}$  ICP-MS using endosomal inhibitors such as chloroquine or methyl- $\beta$ -cyclodextrin (as shown in **Chapter 3**).

The extent of cell damage may also be associated with the synthesis of lipid droplets (which play important roles in cell repair, growth and survival), however, this goes beyond the scope of work in this thesis. The physiological significance (if any) of the lipid droplets distributions in cancer cells treated with **12** is not understood, but may be involved in a cellular response to drug treatment (*i.e.* repair of membranes or vacuoles). As part of future studies, lipid-specific biological assays could be performed to identify any trends or alterations in lipids upon treatment with diazido- $\text{Pt}^{\text{IV}}$ , for example, investigating lipid metabolism enzymes by Western blotting, or fatty acids by GC-MS.<sup>131</sup>

Under photo-conditions, cells treated with **12** were significantly damaged – with multiple vacuoles (cytoplasmic and nuclear), membrane-blebbing, vesicle shedding and increased cell granularity– all of which are indicative of severe intracellular damage. Vacuolisation is not a classical feature of apoptosis, thus, it may be hypothesised that **12** does not predominantly induce apoptotic cell death, however, further studies are required to confirm this. In addition, cells treated with photo-activated **12** with the inclusion of a recovery period (in complex-free medium) were less damaged than that of cells treated without recovery, which may implicate a cytostatic contribution to the antiproliferative activity.

The distinct alterations in nuclear morphology (observed by cryo-XRT) may be attributed to Pt-induced damage, correlating with the nuclear localisation of platinum observed using nano-focussed synchrotron-XRF. Remarkably, XRF revealed that blue light significantly enhanced the cellular accumulation of Pt in PC3 cells treated with diazido-Pt<sup>IV</sup> PACT complexes (**11**, **12**). It can be hypothesized that this is most likely a consequence of increased Pt uptake as opposed to reduced efflux,<sup>132</sup> which may be associated with photo-induced membrane-damage and extracellular photolysis products. This could be probed using flow cytometry (membrane integrity analysis) or <sup>195</sup>Pt ICP-MS cell accumulation studies by irradiating cells in drug-containing medium (1 h) and comparing it to that of irradiation in drug-free medium. Determination of the chemical speciation of diazido-Pt<sup>IV</sup> complexes in biological medium upon irradiation may be crucial in understanding the photo-enhanced Pt uptake, and can be probed using analytical techniques such as EXAFS or capillary-electrophoresis ICP-MS).<sup>120, 133</sup>

Preliminary XANES analysis of PC3 cells treated with diazido-Pt<sup>IV</sup> complex **11** under photo-activated conditions revealed *ca.* 83% of intracellular Pt existed as Pt<sup>4+</sup>. This was unexpected as it is hypothesised that diazido-Pt<sup>IV</sup> prodrugs are photo-reduced to form toxic Pt<sup>II</sup> species inside cancer cells. Further XANES work is required with a greater population of cells for statistical relevance is required to confirm this hypothesis.



A further development on this research would be to perform correlative cryo-XRT and XRF on the same cells close to their native state (cryopreserved cells) to further understand the in-cell activity of PtIV-diazidyl PACT prodrugs (demonstrated by Pizarro *et. al.* with a potent half-sandwich Ir complex)<sup>134</sup> or alternatively combined XRF and X-ray holographic nanotomography (as demonstrated for human macrophage cells).<sup>135</sup> Finally, the use of a molecular probe (*e.g.* Br or I) at inert sites of the complex would allow dual-mapping by XRF and ICP-MS, to determine the fate of ligands in cancer cells, as demonstrated with Br-labelled Os complexes in **Chapter 3** and I-labelled rhenium complexes in the literature.<sup>136</sup>

## 5.6 References

1. H. Shi, C. Imberti, G. J. Clarkson and P. J. Sadler, *Inorg Chem Front*, 2020, **1**, 1-10.
2. S. Bonnet, *Dalton Trans*, 2018, **47**, 10330-10343.
3. N. J. Farrer, L. Salassa and P. J. Sadler, *Dalton Trans*, 2009, **48**, 10690-10701.
4. H. Shi, C. Imberti and P. J. Sadler, *Inorg Chem Front*, 2019, **7**, 1623-1638.
5. A. Vogler, A. Kern and J. Hüttermann, *Angew Chem Int Ed*, 1978, **17**, 524-525.
6. M. Imran, W. Ayub, I. S Butler, Z.-u. Rehman and I. Muhammad, *Coordin Chem Rev*, 2018, **376**, 405-429.
7. P. J. Bednarski, F. S. Mackay and P. J. Sadler, *Anticancer Agents Med Chem*, 2007, **7**, 75-93.
8. T. C. Johnstone, K. Suntharalingam and S. J. Lippard, *Chem Rev*, 2016, **116**, 3436-3486.
9. K. Mitra, *Dalton Trans*, 2016, **45**, 19157-19171.
10. C. Imberti, P. Zhang, H. Huang and P. J. Sadler, *Angew Chem Int Ed*, 2020, **59**, 61-73.
11. N. J. Farrer, J. A. Woods, L. Salassa, Y. Zhao, K. S. Robinson, G. Clarkson, F. S. Mackay and P. J. Sadler, *Angew Chem Int Ed*, 2010, **49**, 8905-8908.
12. F. S. Mackay, J. A. Woods, H. Moseley, J. Ferguson, A. Dawson, S. Parsons and P. J. Sadler, *Chemistry*, 2006, **12**, 3155-3161.

13. P. J. Bednarski, R. Grunert, M. Zielzki, A. Wellner, F. S. Mackay and P. J. Sadler, *Chem Biol*, 2006, **13**, 61-67.
14. F. S. Mackay, J. A. Woods, P. Heringová, J. Kaspárková, A. M. Pizarro, S. A. Moggach, S. Parsons, V. Brabec and P. J. Sadler, *PNAS*, 2007, **104**, 20743-20748.
15. H. Shi, G. J. Clarkson and P. J. Sadler, *Inorganica Chim Acta*, 2019, **489**.
16. A. M. Pizarro, R. J. McQuitty, F. S. Mackay, Y. Zhao, J. A. Woods and P. J. Sadler, *ChemMedChem*, 2014, **9**, 1169-1175.
17. P. R. Ortiz de Montellano, *Future Med Chem*, 2013, **5**, 213-228.
18. J. Rautio, H. Kumpulainen, T. Heimbach, R. Oliyai, D. Oh, T. Jarvinen and J. Savolainen, *Nat Rev Drug Discov*, 2008, **7**, 255-270.
19. D. Gibson, *Dalton Transactions*, 2016, **45**, 12983-12991.
20. H. I. Phillips, L. Ronconi and P. J. Sadler, *Chemistry*, 2009, **15**, 1588-1596.
21. R. R. Vernooij, T. Joshi, M. D. Horbury, B. Graham, E. I. Izgorodina, V. G. Stavros, P. J. Sadler, L. Spiccia and B. R. Wood, *Chem Eur*, 2018, **24**, 5790-5803.
22. H. Shi, I. Romero-Canelón, M. Hreusova, O. Novakova, V. Venkatesh, A. Habtemariam, G. J. Clarkson, J.-i. Song, V. Brabec and P. J. Sadler, *Inorg Chem*, 2018, **57**, 14409-14420.
23. H. Shi, C. Imberti, H. Huang, I. Hands-Portman and P. J. Sadler, *Chem Comm*, 2020, **56**, 2320-2323.
24. V. Venkatesh, C. J. Wedge, I. Romero-Canelón, A. Habtemariam and P. J. Sadler, *Dalton Trans*, 2016, **45**, 13034-13037.
25. T. M. Pereira, D. P. Franco, F. Vitorio and A. E. Kummerle, *Curr Top Med Chem*, 2018, **18**, 124-148.
26. H. Shi, *PhD Thesis*, 2019.
27. I. Kounatidis, M. L. Stanifer, M. A. Phillips, P. Paul-Gilloteaux, X. Helligenstein, H. Wang, C. A. Okolo, T. M. Fish, M. C. Spink, D. I. Stuart, I. Davis, S. Boulant, J. M. Grimes, I. M. Dobbie and M. Harkiolaki, *Cell*, 2020, **182**, 515-530.
28. M. A. Phillips, M. Harkiolaki, D. M. Susano Pinto, R. M. Parton, A. Palanca, M. Garcia-Moreno, I. Kounatidis, J. W. Sedat, D. I. Stuart, A. Castello, M. J. Booth, I. Davis and I. M. Dobbie, *Optica*, 2020, **7**, 802-812.

29. J. Schindelin, I. Arganda-Carreras, E. Frise, V. Kaynig, M. Longair, T. Pietzsch, S. Preibisch, C. Rueden, S. Saalfeld, B. Schmid, J. Y. Tinevez, D. J. White, V. Hartenstein, K. Eliceiri, P. Tomancak and A. Cardona, *Nat Methods*, 2012, **9**, 676-682.
30. J. R. Kremer, D. N. Mastronarde and J. R. McIntosh, *J Struct Biol*, 1996, **116**, 71-76.
31. I. Luengo, M. C. Darrow, M. C. Spink, Y. Sun, W. Dai, C. Y. He, W. Chiu, T. Pridmore, A. W. Ashton, E. M. H. Duke, M. Basham and A. P. French, *J Struct Biol*, 2017, **198**, 43-53.
32. V. A. Solé, E. Papillon, M. Cotte, P. Walter and J. Susini, *Spectrochim Acta B*, 2007, **62**, 63-68.
33. C. T. Rueden, J. Schindelin, M. C. Hiner, B. E. DeZonia, A. E. Walter, E. T. Arena and K. W. Eliceiri, *BMC Bioinformatics*, 2017, **18**, 529-529.
34. A. Thompson, A. D., E. Gullikson, H. M., K.-J. Kim, J. Kirtz, J. Kortright, I. Lindau, Y. Liu, P. Pianetta, A. Robinson, J. Scofield, J. Underwood, G. Williams and H. Winick, *X-ray Data Booklet*, 2009.
35. B. Ravel and M. Newville, *J Synchrotron Radiat*, 2005, **12**, 537-541.
36. M. D. Hall, H. L. Daly, J. Z. Zhang, M. Zhang, R. A. Alderden, D. Pursche, G. J. Foran and T. W. Hambley, *Metallomics*, 2012, **4**, 568-575.
37. M. D. Hall, G. J. Foran, M. Zhang, P. J. Beale and T. W. Hambley, *J Am Chem Soc*, 2003, **125**, 7524-7525.
38. B. Kamalidehghan, S. Ghafouri-Fard, E. Motevaseli and F. Ahmadipour, *Drug Des Dev Ther*, 2018, **12**, 1119-1133.
39. M. Marra, G. Salzano, C. Leonetti, P. Tassone, M. Scarsella, S. Zappavigna, T. Calimeri, R. Franco, G. Liguori, G. Cigliana, R. Ascani, M. Rotonda, A. Abbruzzese, P. Tagliaferri, M. Caraglia and G. De Rosa, *Nanomedicine*, 2011, **7**, 955-964.
40. R. Heintzmann and T. Huser, *Chem Rev* 2017, **117**, 13890-13908.
41. R. Carzaniga, M. C. Domart, E. Duke and L. M. Collinson, *Methods Cell Biol*, 2014, **124**, 151-178.
42. A. E. Weston, H. E. J. Armer and L. M. Collinson, *J Chem Biol*, 2009, **3**, 101-112.
43. M. Harkiolaki, M. C. Darrow, M. C. Spink, E. Kosior, K. Dent and E. Duke, *Emerg Top Life Sci*, 2018, **2**, 81-92.

44. J. Groen, J. J. Conesa, R. Valcárcel and E. Pereiro, *Biophys Rev*, 2019, **11**, 611-619.
45. Berglund, Rymell, Peuker, Wilhein and Hertz, *J Microsc*, 2000, **197**, 268-273.
46. A. Sorvina, C. A. Bader, C. Caporale, E. A. Carter, I. R. D. Johnson, E. J. Parkinson-Lawrence, P. V. Simpson, P. J. Wright, S. Stagni, P. A. Lay, M. Massi, D. A. Brooks and S. E. Plush, *Oncotarget*, 2018, **9**, 35541-35552.
47. M. Roman, T. P. Wrobel, A. Panek, C. Paluszkievicz and W. M. Kwiatek, *BBA-MOL CELL BIOL L*, 2020, **1865**, 158753.
48. K.-H. Chow, R. E. Factor and K. S. Ullman, *Nat Rev Cancer*, 2012, **12**, 196-209.
49. A. V. Shubin, I. V. Demidyuk, A. A. Komissarov, L. M. Rafieva and S. V. Kostrov, *Oncotarget*, 2016, **7**, 55863-55889.
50. S. Gil, E. Solano, F. Martínez-Trucharte, J. Martínez-Esaín, A. J. Pérez-Berná, J. J. Conesa, C. Kamma-Lorger, M. Alsina and M. Sabés, *PLoS One*, 2020, **15**, 230022.
51. J. Demmerle, C. Innocent, A. J. North, G. Ball, M. Müller, E. Miron, A. Matsuda, I. M. Dobbie, Y. Markaki and L. Schermelleh, *Nat Protoc*, 2017, **12**, 988-1010.
52. E. M. H. Duke, M. Razi, A. Weston, P. Guttmann, S. Werner, K. Henzler, G. Schneider, S. A. Tooze and L. M. Collinson, *Ultramicroscopy*, 2014, **143**, 77-87.
53. F. Jamme, B. Cinquin, Y. Gohon, E. Pereiro, M. Réfrégiers and M. Froissard, *J Synchrotron Radiat*, 2020, **27**, 772-778.
54. N. Varsano, T. Dadosh, S. Kapishnikov, E. Pereiro, E. Shimoni, X. Jin, H. S. Kruth, L. Leiserowitz and L. Addadi, *J Am Chem Soc*, 2016, **138**, 14931-14940.
55. A. L. S. Cruz, E. d. A. Barreto, N. P. B. Fazolini, J. P. B. Viola and P. T. Bozza, *Cell Death Dis*, 2020, **11**, 105.
56. R. Mitra, T. T. Le, P. Gorjala and O. B. J. B. C. Goodman Jr., *BMC Cancer*, 2017, **17**, 631.
57. F. Geng and D. Guo, *Intern Med Rev*, 2017, **3**, 1-9.
58. L. Wiemerslage and D. Lee, *J Neurosci Methods*, 2016, **262**, 56-65.

59. J. G. McCarron, C. Wilson, M. E. Sandison, M. L. Olson, J. M. Girkin, C. Saunter and S. Chalmers, *J Vasc Res*, 2013, **50**, 357-371.
60. M. C. Cufaro, D. Pieragostino, P. Lanuti, C. Rossi, I. Cicalini, L. Federici, V. De Laurenzi and P. Del Boccio, *J Oncol*, 2019, **1**, 1639854-1639854.
61. V. Vlaeminck-Guillem, *Front Oncol*, 2018, **8**, 222-222.
62. A. L. Contento and D. C. Bassham, *J Cell Sci*, 2012, **125**, 3511-3518.
63. X. J. Liang, S. Mukherjee, D. W. Shen, F. R. Maxfield and M. M. Gottesman, *Cancer Res*, 2006, **66**, 2346-2353.
64. J. Huotari and A. Helenius, *EMBO Rep*, 2011, **30**, 3481-3500.
65. K. Kamińska, C. Szczylik, Z. F. Bielecka, E. Bartnik, C. Porta, F. Lian and A. M. Czarnecka, *J Cell Mol Med*, 2015, **19**, 283-296.
66. L. M. Bareford and P. W. Swaan, *Adv Drug Deliv Rev*, 2007, **59**, 748-758.
67. S. Brady, D. R. Colman and P. Brophy, in *From Molecules to Networks* eds. J. H. Byrne, R. Heidelberger and M. N. Waxham, Academic Press, Boston, 2014, pp. 23-52.
68. D. Millimaggi, C. Festuccia, A. Angelucci, S. D'Ascenzo, N. Rucci, S. Flati, M. Bologna, A. Teti, A. Pavan and V. Dolo, *Int J Oncol*, 2006, **28**, 909-914.
69. Y. Zhang, X. Chen, C. Gueydan and J. Han, *Cell Res*, 2018, **28**, 9-21.
70. J. Chen, L. Zhang, H. Zhou, W. Wang, Y. Luo, H. Yang and H. Yi, *Mol Med Rep*, 2018, **17**, 6859-6865.
71. D. Kessel, *Photochem Photobiol*, 2019, **95**, 119-125.
72. W.-J. Guo, Y.-M. Zhang, L. Zhang, B. Huang, F.-F. Tao, W. Chen, Z.-J. Guo, Q. Xu and Y. Sun, *Autophagy*, 2013, **9**, 996-1008.
73. F. Hu, F. Wei, Y. Wang, B. Wu, Y. Fang and B. Xiong, *J Pharmacol Sci*, 2015, **128**, 27-34.
74. A. F. Westendorf, J. A. Woods, K. Korpis, N. J. Farrer, L. Salassa, K. Robinson, V. Appleyard, K. Murray, R. Grünert, A. M. Thompson, P. J. Sadler and P. J. Bednarski, *Mol Cancer Ther*, 2012, **11**, 1894-1904.
75. W.-J. Lee, M.-H. Chien, J.-M. Chow, J.-L. Chang, Y.-C. Wen, Y.-W. Lin, C.-W. Cheng, G.-M. Lai, M. Hsiao and L.-M. Lee, *Sci Rep*, 2015, **5**, 10420-10420.
76. V. M. Gonzalez, M. A. Fuertes, C. Alonso and J. M. Perez, *Mol Pharmacol*, 2001, **59**, 657-663.
77. R. M. Bavle, *J Oral Maxillofac Pathol*, 2016, **20**, 339-341.

78. A. D. Barbosa, H. Sembongi, W.-M. Su, S. Abreu, F. Reggiori, G. M. Carman and S. Siniosoglou, *Mol Biol Cell*, 2015, **26**, 3641-3657.
79. T. C. Walther and R. V. Farese, Jr., *Annu Rev Biochem*, 2012, **81**, 687-714.
80. J. Yu and P. Li, *Sci China Life Sci*, 2017, **60**, 46-56.
81. D. Zietkowski, G. S. Payne, E. Nagy, M. A. Mobberley, T. A. Ryder and N. M. deSouza, *Magn Reson Med*, 2012, **68**, 369-377.
82. Q. Dang, Y.-A. Chen and J.-T. Hsieh, *Am J Clin Exp Urol*, 2019, **7**, 273-280.
83. J. P. Layerenza, P. Gonzalez, M. M. Garcia de Bravo, M. P. Polo, M. S. Sisti and A. Ves-Losada, *Biochim Biophys Acta*, 2013, **1831**, 327-340.
84. K. Softysik, Y. Ohsaki, T. Tatematsu, J. Cheng and T. Fujimoto, *Nat Comm*, 2019, **10**, 473.
85. R. Uzbekov and P. Roingeard, *BMC Res Notes*, 2013, **6**, 386.
86. M. K. Haynes, J. J. Strouse, A. Waller, A. Leitao, R. F. Curpan, C. Bologa, T. I. Oprea, E. R. Prossnitz, B. S. Edwards, L. A. Sklar and T. A. Thompson, *J Biomol Screen*, 2009, **14**, 596-609.
87. A. Sandqvist and L. Sistonen, *J Cell Biol*, 2004, **164**, 15-17.
88. P. Anderson, N. Kedersha and P. Ivanov, *Biochim Biophys Acta*, 2015, **1849**, 861-870.
89. S. Timalina, K. Arimoto-Matsuzaki, M. Kitamura, X. Xu, Q. Wenzhe, M. Ishigami-Yuasa, H. Kagechika and Y. Hata, *J Biochem*, 2018, **164**, 381-391.
90. S. Kummar, M. Gutierrez, J. H. Doroshov and A. J. Murgu, *Br J Clin Pharmacol*, 2006, **62**, 15-26.
91. J. V. Anttila, M. Shubin, J. Cairns, F. Borse, Q. Guo, T. Mononen, I. Vázquez-García, O. Pulkkinen and V. Mustonen, *PLoS Comput Biol*, 2019, **15**, 1007493.
92. C. Focaccetti, A. Bruno, E. Magnani, D. Bartolini, E. Principi, K. Dallaglio, E. O. Bucci, G. Finzi, F. Sessa, D. M. Noonan and A. Albini, *PLoS One*, 2015, **10**, e0115686-e0115686.
93. A. Imrali, X. Mao, M. Yeste-Velasco, J. Shamash and Y. Lu, *Am J Cancer Res*, 2016, **6**, 1772-1784.
94. M. A. Musa, M. O. F. Khan and J. S. Cooperwood, *Lett Drug Des Discov*, 2009, **6**, 133-138.

95. M. Niepel, M. Hafner, M. Chung and P. K. Sorger, *Curr Protoc Chem Biol*, 2017, **9**, 55-74.
96. M. Moore, J. Sebastian and M. Kolios, *J Biomed Opt*, 2019, **24**, 106502.
97. R. Domura, R. Sasaki, Y. Ishikawa and M. Okamoto, *J Funct Biomater*, 2017, **8**, 18.
98. D. Gibson, *Dalton Trans*, 2009, **48**, 10681-10689.
99. O. Nováková, O. Vrána, V. I. Kiseleva and V. Brabec, *Eur J Biochem*, 1995, **228**, 616-624.
100. E. G. Talman, Y. Kidani, L. Mohrmann and J. Reedijk, *Inorganica Chim Acta*, 1998, **283**, 251-255.
101. A. F. Westendorf, L. Zerzankova, L. Salassa, P. J. Sadler, V. Brabec and P. J. Bednarski, *J Inorg Biochem*, 2011, **105**, 652-662.
102. P. J. Bednarski, K. Korpis, A. F. Westendorf, S. Perfahl and R. Grünert, *Philos T R Soc B*, 2013, **371**, 20120118.
103. R. C. Petersen, *AIMS Biophys* 2017, **4**, 240-283.
104. R. M. Cordeiro, *Biochim Biophys Acta*, 2014, **1838**, 438-444.
105. T.-Y. Wang, M. D. J. Libardo, A. M. Angeles-Boza and J.-P. Pellois, *ACS Chem Biol*, 2017, **12**, 1170-1182.
106. J. Wong-Ekkabut, Z. Xu, W. Triampo, I. M. Tang, D. P. Tieleman and L. Monticelli, *Biophys J*, 2007, **93**, 4225-4236.
107. V. Novohradsky, L. Zerzankova, J. Stepankova, O. Vrana, R. Raveendran, D. Gibson, J. Kasparkova and V. Brabec, *Biochem Pharmacol*, 2015, **95**, 133-144.
108. T. Taechowisan, C. Lu, Y. Shen and S. Lumyong, *J Cancer Res Ther*, 2007, **3**, 86-91.
109. I. Romero-Canelón, A. M. Pizarro, A. Habtemariam and P. J. Sadler, *Metallomics*, 2012, **4**, 1271-1279.
110. N. Martinho, T. C. B. Santos, H. F. Florindo and L. C. Silva, *Front Physiol*, 2019, **9**, 1898-1898.
111. J. L. Gregg, K. M. McGuire, D. C. Focht and M. A. Model, *Pflugers Arch*, 2010, **460**, 1097-1104.
112. X. Li, Y. Liu and H. Tian, *Bioinorg Chem Appl*, 2018, **2018**, 8276139.
113. K. Suntharalingam, T. C. Johnstone, P. M. Bruno, W. Lin, M. T. Hemann and S. J. Lippard, *J Am Chem Soc*, 2013, **135**, 14060-14063.

114. L. Zeng, P. Gupta, Y. Chen, E. Wang, L. Ji, H. Chao and Z.-S. Chen, *Chem Soc Rev*, 2017, **46**, 5771-5804.
115. A. Basu and S. Krishnamurthy, *Nucleic Acids Res*, 2010, **10**, 1-16.
116. A. Mandic, J. Hansson, S. Linder and M. C. Shoshan, *J Biol Chem*, 2003, **278**, 9100-9106.
117. T. Makovec, *Radiol Oncol*, 2019, **53**, 148-158.
118. M. D. Hall, C. T. Dillon, M. Zhang, P. Beale, Z. Cai, B. Lai, A. P. Stampfl and T. W. Hambley, *J Biol Inorg Chem*, 2003, **8**, 726-732.
119. F. Sepulcre, M. G. Proietti, M. Benfatto, S. Della Longa, J. García and E. Padrós, *Biophys J*, 2004, **87**, 513-520.
120. A. A. Hummer and A. Rompel, *Metallomics*, 2013, **5**, 597-614.
121. A. F. Westendorf, A. Bodtke and P. J. Bednarski, *Dalton Transactions*, 2011, **40**, 5342-5351.
122. E. J. New, V. C. Wimmer and D. J. Hare, *Cell Chemical Biology*, 2018, **25**, 7-18.
123. S. Monro, K. L. Colón, H. Yin, J. Roque, 3rd, P. Konda, S. Gujar, R. P. Thummel, L. Lilge, C. G. Cameron and S. A. McFarland, *Chem Rev*, 2019, **119**, 797-828.
124. C. Sanchez-Cano, D. Gianolio, I. Romero-Canelon, R. Tucoulou and P. J. Sadler, *Chem Commun (Camb)*, 2019, **55**, 7065-7068.
125. J. Yang, T. Regier, J. J. Dynes, J. Wang, J. Shi, D. Peak, Y. Zhao, T. Hu, Y. Chen and J. S. Tse, *Analytical Chemistry*, 2011, **83**, 7856-7862.
126. J. F. Collingwood and F. Adams, *Spectrochim Acta B*, 2017, **130**, 101-118.
127. A. Gianoncelli, L. Vaccari, G. Kourousias, D. Cassese, D. E. Bedolla, S. Kenig, P. Storici, M. Lazzarino and M. Kiskinova, *Scientific reports*, 2015, **5**, 10250-10250.
128. G. Schneider, P. Guttmann, S. Rehbein, S. Werner and R. Follath, *J Struct Biol*, 2012, **177**, 212-223.
129. F. Porcaro, S. Roudeau, A. Carmona and R. Ortega, *Trends Analyt Chem*, 2018, **104**, 22-41.
130. A. Gianoncelli, L. Vaccari, G. Kourousias, D. Cassese, D. E. Bedolla, S. Kenig, P. Storici, M. Lazzarino and M. Kiskinova, *Sci Rep*, 2015, **5**, 10250.
131. L. Gomes, L. Viana, J. L. Silva, C. Mermelstein, G. Atella and E. Fialho, *Biomed Res Int*, 2020, **20**, 1-10.



132. L. X. Yang, E. B. Douple and H. J. Wang, *Int J Radiat Oncol Biol Phys*, 1995, **33**, 641-646.
133. H. U. Holtkamp, S. Movassaghi, S. J. Morrow, M. Kubanik and C. G. Hartinger, *Metallomics*, 2018, **10**, 455-462.
134. J. J. Conesa, A. C. Carrasco, V. Rodriguez-Fanjul, Y. Yang, J. L. Carrascosa, P. Cloetens, E. Pereiro and A. M. Pizarro, *Angew Chem Int Ed*, 2020, **59**, 1270-1278.
135. C. Gramaccioni, Y. Yang, A. Pacureanu, N. Vigano, A. Procopio, P. Valenti, L. Rosa, F. Berlutti, S. Bohic and P. Cloetens, *Anal Chem*, 2020, **92**, 4814-4819.
136. C. C. Konkankit, J. Lovett, H. H. Harris and J. J. Wilson, *Chem Comm*, 2020, **56**, 6515-6518.

# **Chapter 6**

## **Conclusions and future work**

## 6.1 Conclusions

The *in vitro* biological activity of a diverse range of precious metal complexes in cancer cells have been investigated using advanced synchrotron imaging techniques at DLS (Oxford), alongside complementary antiproliferative screening assays. Namely, synchrotron-XRF, DPC imaging and XANES (at the I14 beamline) have been used to probe the intracellular distribution, stability and speciation of metal complexes in cancer cells down to a 100 nm resolution. Complementary studies using correlative cryo-SIM and cryo-XRT (at the B24 beamline) were used to investigate the localisation of fluorescent compounds at a subcellular level (40 nm resolution), in addition to drug-induced morphological changes and cellular events as close to their physiological state as possible.

- **Synthesis, characterisation and screening of Os<sup>II</sup> 16-electron catalysts**

One of the aims of **Chapter 3** was to synthesize and characterize a series of 16-electron Os<sup>II</sup> catalysts of the formulae [Os<sup>II</sup>(*p*-cymene)(RBsDPEN)] (where BsDPEN=benzylidiphenylethylene diamine), and assess their catalytic and biological activity *in vitro*. One of the main aims was to probe the *in-cell* stability of such complexes, which has been achieved using a Br-labelled complex [Os<sup>II</sup>(*p*-cymene)(BrBsDPEN)] (**RR/SS-2**, **Section 3.1**, **Fig. 3.3**) using ICP-MS and synchrotron-XRF. **RR/SS-2** exhibited similar chemical (x-ray crystal structure, DFT, LogP, solution stability and transfer hydrogenation catalytic activity) and biological activity (cytotoxicity, selectivity, cell accumulation, membrane integrity, cell cycle analysis, in-cell catalysis) compared to that of parent compound [Os<sup>II</sup>(*p*-cymene)(TsDPEN)] (**RR-1**, where TsDPEN= tosyldiphenylethylene diamine).<sup>1-3</sup>

Cellular accumulation studies of the Br-labelled Os<sup>II</sup> catalysts (**RR/SS-2**) were performed in cancer cells under varying conditions (temperature, inhibition of caveolae endocytosis, inhibition of efflux, time and cellular distribution), which consistently revealed significantly higher levels of Br *vs.* Os (>10-fold, **Section 3.3.10**). This is highly indicative of intracellular complex degradation *via* dissociation of the Br-labelled sulfonamide ligand, which may account for the low

intracellular catalytic turnover of pyruvate to lactate reported for parent compound **RR-1** over 24 h.<sup>2, 3</sup> The Os accumulation was highly-dependent on caveolae endocytosis and PGP-mediated efflux, whereas, the Br-labelled sulfonamide modality was much less dependent on these pathways. It is hypothesized that caveolae endocytosis can mediate the uptake of the ‘intact’ osmium catalyst (**2**), but once inside the cells, **2** is rapidly degraded, with the Br-labelled ligand being retained inside the cells for longer. Additionally, inhibition of the PGP efflux pump increased the levels of intracellular Os but not Br, which may implicate different efflux pathways for the ‘intact’ catalyst (**RR/SS-2**) and ‘free’ Br-labelled ligand. Cellular distribution ICP-MS studies revealed the predominant deposition of both Os and Br in the membrane and cytoskeletal fractions in cells treated with **SS-2**, implying that some of the complex is intact in the cytoplasm, where catalysis likely occurs. Negligible quantities of Os were present in the nuclear fraction (<6%) which may rule out an Os-DNA mechanism of action (**Section 3.3.11**), whereas, 10-20% of intracellular Br was present in the nucleus. It is now hypothesized that the 16-electron Os complex may facilitate cell permeation of the sulfonamide ligand where it can dissociate and enter the cell nucleus, however, its contribution to the antiproliferative activity (if any) is not yet understood and requires further work.

The concentration-dependent cellular distribution of Br-labelled **SS-2** was also investigated using synchrotron-XRF by monitoring the Br (KL<sub>3</sub>=11.92 keV) and Os (L<sub>3</sub>M<sub>5</sub>=8.91 keV) emissions. Os and Br co-localized in the cell cytoplasm (**Section 3.3.12**), with significantly higher levels of intracellular Br vs. Os, in strong agreement with cellular accumulation <sup>189</sup>Os-<sup>79</sup>Br ICP-MS studies (**Section 3.3.10**). The Br was also distributed in the nucleus, corroborating cell fractionation ICP-MS studies. Os and Br co-localized in small cytoplasmic compartments of size *ca.* 0.7 μm<sup>2</sup>, which are likely attributed to endosomes or lysosomes. Moreover, this may implicate the lysosomal breakdown and efflux of **SS-2**. This hypothesis was further probed using chloroquine (which can deactivate lysosomes):<sup>5, 6</sup> cells pre-incubated in chloroquine followed by treatment with **RR-1** or Br-labelled **SS-2** revealed a 25-50% increase in potency (IC<sub>50</sub>), which was accompanied by an increase in Os cellular accumulation (**Section 3.3.13**). Chloroquine-dependent membrane integrity analysis (by flow cytometry) was also used to reaffirm the increase in potency and intracellular Os was not due to membrane damage.

Overall, the work in **Chapter 3** successfully probed the *in-cell* mechanism of action, targeting and stability of a Br-labelled 16-electron Os(II) catalyst by utilising a dual-quantitative approach using correlative ICP-MS and synchrotron-XRF. This provided direct evidence for the cellular distribution and instability of this family of Os<sup>II</sup> complexes in cancer cells, revealing a dependence on active (energy-dependent) influx/efflux mechanisms and the delivery of the dissociated sulfonamide ligand into the cell nucleus. The reduced intracellular amount of intact “active” catalyst observed may explain the low catalytic turnover number of pyruvate to lactate reported for **RR-1**.<sup>3</sup>

- **Distribution and cell damage by cyclometallated Ir<sup>III</sup> photosensitisers**

The main aim of **Chapter 4** was to utilize both cryo-XRT and XRF to probe the cellular distribution and cell damage induced by potent cyclometallated Ir(III) PDT photosensitisers in cancer cells using correlative cryo-SIM, cryo-XRT and XRF, as close to their native state as possible.<sup>8-10</sup> Cryo-XRT analysis of PC3 prostate cancer cells treated of a promising Ir<sup>III</sup>-diketonate photosensitiser (**7**, **Section 4.1**, **Fig. 4.1**) was successfully achieved, providing quantitative 3D insights into the changes in mitochondrial morphology and volume upon photo-activation. Although no direct evidence for the localization of this complex in the mitochondria was obtained, it can be hypothesized that the observed mitochondrial damage is likely caused by the generation of singlet oxygen (<sup>1</sup>O<sub>2</sub>) in close proximity to these organelles. Unfortunately, the phosphorescence of **7** ( $\lambda_{\text{ex/em}}=458/620$  nm) was not observed using fluorescence microscopy, thus, was not analysed by super-resolution cryo-SIM. Nonetheless, cryo-XRT provided crucial 3D insights into the cell damage induced by **7** down to a subcellular resolution (40 nm), in their near-native state.

The second aim of **Chapter 4** was to probe the *in-cell* distribution of a potent Ir-Pt PDT-PACT conjugate (**8**, **Section 4.1**, **Fig. 4.1**) in cancer cells, using synchrotron-XRF under both dark (non-toxic) and irradiated conditions. Unfortunately, due to poor sample quality (poorly preserved and damaged cells), only cells treated with **8** under dark conditions could be mapped, and requires further study. Nonetheless, XRF revealed the localisation of Pt in the nucleus and cytoplasm, and Ir in small, concentrated regions (most likely in the cytoplasm). This is in agreement with the

absence of adducts formed between Ir and model DNA bases, suggesting that the nucleus is not a major target for the Ir-PDT moiety,<sup>13</sup> and may imply organelle-targeting. The nuclear-targeting of Pt (which is well-reported for Pt<sup>II</sup> drugs) may be associated with the chemical reduction of Pt<sup>IV</sup> → Pt<sup>II</sup> (*e.g.* by low molecular weight antioxidants), correlating with the ability of Pt of **8** to form adducts with DNA after photo-activation. Interestingly, 5× more intracellular Pt *vs.* Ir was observed, which is indicative of Ir<sup>III</sup>-Pt<sup>IV</sup> cleavage and different cellular targets of the cleaved Pt and Ir parts. Alternatively, the hypothesis of extracellular complex cleavage cannot be discounted, thus the speciation of **8** in biological media requires further study. Overall, the work in **Chapter 4** successfully utilised cryo-XRT and XRF to investigate the cellular damage, distribution and stability and of Ir<sup>III</sup> PDT photosensitisers in cancer cells.

- **In-cell x-ray studies of diazido-Pt<sup>IV</sup> photoactivatable prodrugs**

The main aims of **Chapter 5** were to build on the x-ray techniques used in both **Chapters 3** and **4** to investigate the concentration-dependent intracellular targeting and morphological damage induced by a fluorescent coumarin-labelled diazido-Pt<sup>IV</sup> PACT complex (**12**, **Section 5.1**) in cancer cells using cryo-SIM, cryo-XRT, synchrotron-XRF and XANES. Unfortunately, the blue fluorescence photo-products of **12** (upon blue light irradiation) were not observed by cryo-SIM, however, cryo-XRT produced significant results which may impact the future design of diazido-Pt<sup>IV</sup> complexes for photoactivatable chemotherapy (PACT). Diazido-Pt<sup>IV</sup> complexes are non-toxic to cancer cells up to 100 μM,<sup>13</sup> which is assumed to be a consequence of the remarkable chemical stability exhibited by these complexes. However, cryo-XRT of cells treated with 1×IC<sub>50</sub> (6.5 μM) of **12** under dark conditions revealed endosomes which may implicate active mechanisms of efflux (*i.e.* removal of Pt complex) prior to photo-activation. In addition, small black spots were observed in nuclei of cells treated with **12** under dark conditions, which may implicate the nuclear-targeting of these complexes (dark absorption of heavy metals by soft x-rays). This was reaffirmed using synchrotron-XRF by directly mapping the Pt with respect to the highly localised Zn of cell nuclei.

Cryo-XRT revealed that, under blue light conditions, diazido-Pt<sup>IV</sup> complexes caused significant morphological damage including cytoplasmic/nuclear vacuoles, membrane-blebbing, vesicle-shedding, increased cell granularity and damaged cytoplasmic organelles. Interestingly, the cellular accumulation of Pt in cancer cells treated with diazido-Pt<sup>IV</sup> complexes (**11** and **12**) was significantly enhanced upon blue light exposure (shown by XRF), which may implicate the formation of extracellular photolysis products to promote Pt influx.<sup>14</sup> It may be hypothesized that **12** can be activated with 465 nm both intracellularly and extracellularly (in drug-medium) to exert its antiproliferative effect. Finally, cells treated with diazido-Pt<sup>IV</sup> prodrugs under photo-conditions and recovered in complex-free media confirmed that cells did not continue to die, hence, revealing a cytostatic (growth inhibition) contribution to cell death, in addition to the cytotoxicity (tumour shrinkage) of the Pt<sup>II</sup> species formed upon irradiation. Overall, the work in **Chapter 5** has provided direct evidence into the cellular distribution and targeting of Pt<sup>IV</sup>-diazido PACT prodrugs, in addition to providing insights into the morphological damage and mechanisms of cell death, which may be crucial for clinical translation.

## 6.2 Future work

### 6.2.1 Improving the efficacy of osmium sulfonamide catalysts

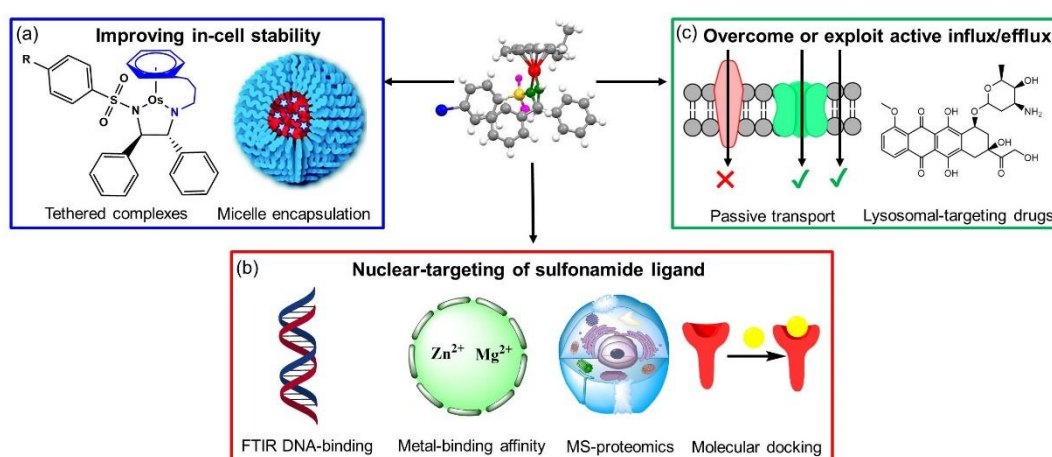


**Figure 6.1.** Possible ways of improving the drug efficacy of half-sandwich [Os<sup>II</sup>(arene)(BsDPEN)] complexes: (a) Improving the in-cell stability; (b) nuclear-targeting studies of the sulfonamide ligand; (c) Overcome or exploit active cellular influx/efflux mechanisms. The micelle-encapsulation image was taken from the literature.<sup>15</sup>

The *in-cell* catalytic activity of Os<sup>II</sup> *para*-cymene 16-electron sulfonamide complexes is dependent on the complex remaining intact, to facilitate favourable substrate binding in the transition state (*via* the Re or Si face). This research has demonstrated that these complexes have limited stability in cancer cells, which likely explains the low turnover of pyruvate to unnatural lactate over 24 h.<sup>2, 3</sup> The stability of transition metal complexes is highly dependent on the coordinated ligands, hence, improving the stability of this family of complexes may be to synthesize tethered analogues,<sup>16</sup> in which the diamine ligand is tethered to the arene group (as shown for many iridium and ruthenium half-sandwich complexes).<sup>10, 17</sup> Alternatively, polymer-coating or micelle-encapsulation of Os<sup>II</sup> 16-electron catalysts may significantly improve the stability in a cellular environment. This has previously been shown for 16-electron Ru<sup>II</sup> and Os<sup>II</sup> carborane complexes encapsulated in P123 core-shell micelles,<sup>15</sup> which enhanced the intracellular stability and aqueous solubility, whilst maintaining the antiproliferative activity.

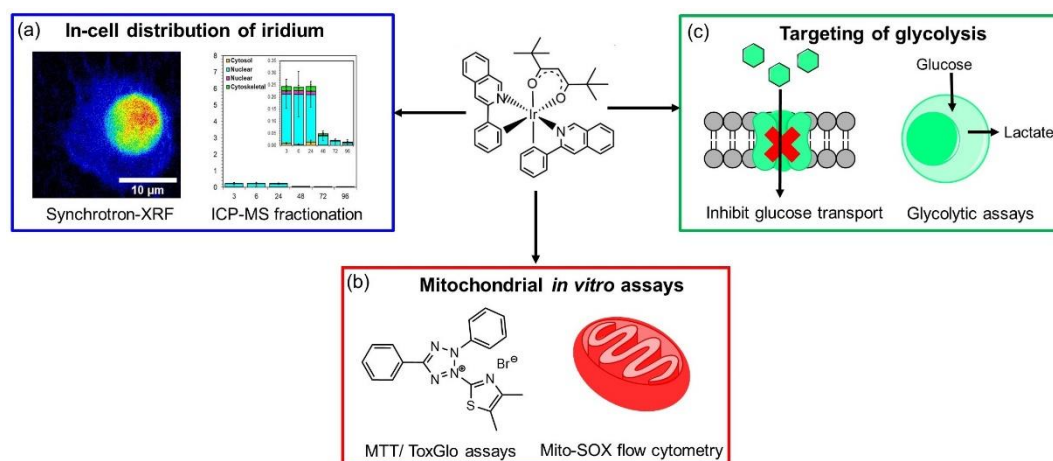
The dissociation of the bidentate sulfonamide ligand from Os was demonstrated by ICP-MS and synchrotron-XRF using a Br-probe at an apparent inert site (**Chapter 3**). Remarkably, significantly higher levels of the unbound sulfonamide ligand were retained intracellularly, which was found to localise with the Os in the cytoplasm, but also independently in the cell nucleus. It is known that uncoordinated sulfonamide ligands are non-toxic to cancer cells (IC<sub>50</sub>>100 µM), thus, metal complexation may provide a means of delivering the sulfonamide ligand inside cells. The potential binding modalities of Br-labelled sulfonamide ligands to intracellular biomolecules could be elucidated using mass spectrometry proteomics, which has previously been used to identify the binding of organo-osmium(II) complexes to nucleobases.<sup>18</sup> As Zn<sup>2+</sup> and Mg<sup>2+</sup> are abundant cell nuclei and stabilize DNA, hence, cell nuclei metal-binding studies or molecular docking may provide insights into the binding preferences of the sulfonamide ligand. In addition, FTIR can be used to gain insights into DNA or RNA inhibition of the intact Os<sup>II</sup> complex and “free” ligand by exploiting the hydrated and dehydrated forms of DNA.<sup>19</sup>

Additional approaches to improving the efficacy of Os<sup>II</sup> sulfonamide complexes might be to overcome the dependence on active (energy-dependent) influx and efflux pathways. It is well-known that the cellular accumulation of lipophilic drugs is predominantly facilitated *via* passive diffusion,<sup>20</sup> since they readily diffuse



across cell membranes. Hence, extending the hydrophobicity of these complexes may shift the dependence away from active pathways (*i.e.* endocytosis), however, this is a compromise with aqueous solubility. Alternatively, as lysosomes have been implicated in the breakdown of Os<sup>II</sup> sulfonamide complexes, this can be exploited through a targeting approach. For example, tethering pH-activated<sup>21</sup> or lysosomal-targeting drugs (*i.e.* doxorubicin)<sup>22</sup> at inert sites of the Os<sup>II</sup> complexes may lead to enhanced antiproliferative activity.

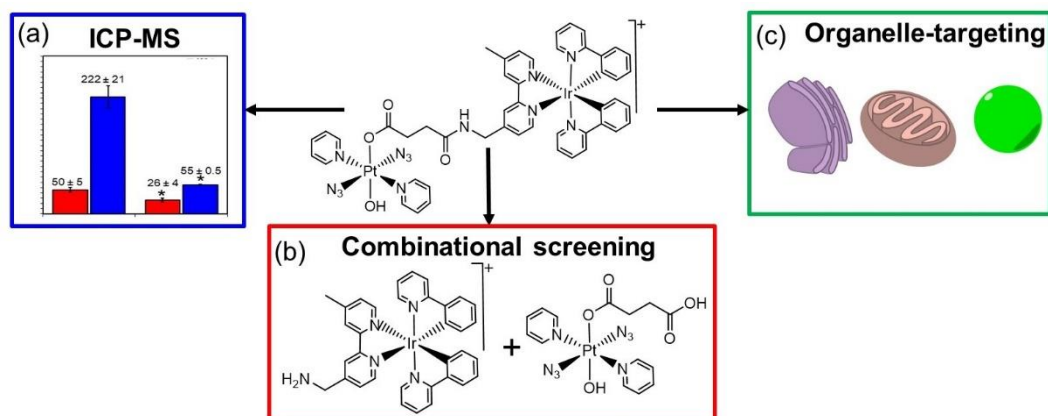
## 6.2.2 Targeting of iridium PDT photosensitizers



**Figure 6.2.** Possible ways of further probing the targeting of iridium photosensitisers: (a) in-cell distribution of iridium; (b) mitochondrial *in vitro* assays; (c) targeting of glycolysis.

Cryo-XRT revealed damage to mitochondrial organelles in cancer cells treated with **7** (Chapter 4). The cellular distribution of **7** can be probed using synchrotron-XRF (Ir L<sub>3</sub>M<sub>5</sub>=9.18 keV) or cell fractionation <sup>192</sup>Ir ICP-MS studies. Mitochondrial-dependent cell viability assays can be used to elucidate cellular targets of cyclometallated Ir<sup>III</sup> photosensitizers, including mitochondrial dysfunction ToxGlo assay and flow cytometry mitochondrial assays.<sup>23, 24</sup> As **7** can enhance levels of glycolytic enzymes, further studies may involve investigating the effect of inhibiting glucose transporters or glycolytic enzymes. For example, screening against GLUT1 and using glucose analogues (*e.g.* 2-NBDG) to quantify and visualize inhibition of glucose uptake by fluorescence microscopy,<sup>25</sup> or pyruvate/lactate colorimetric assays.<sup>3</sup>

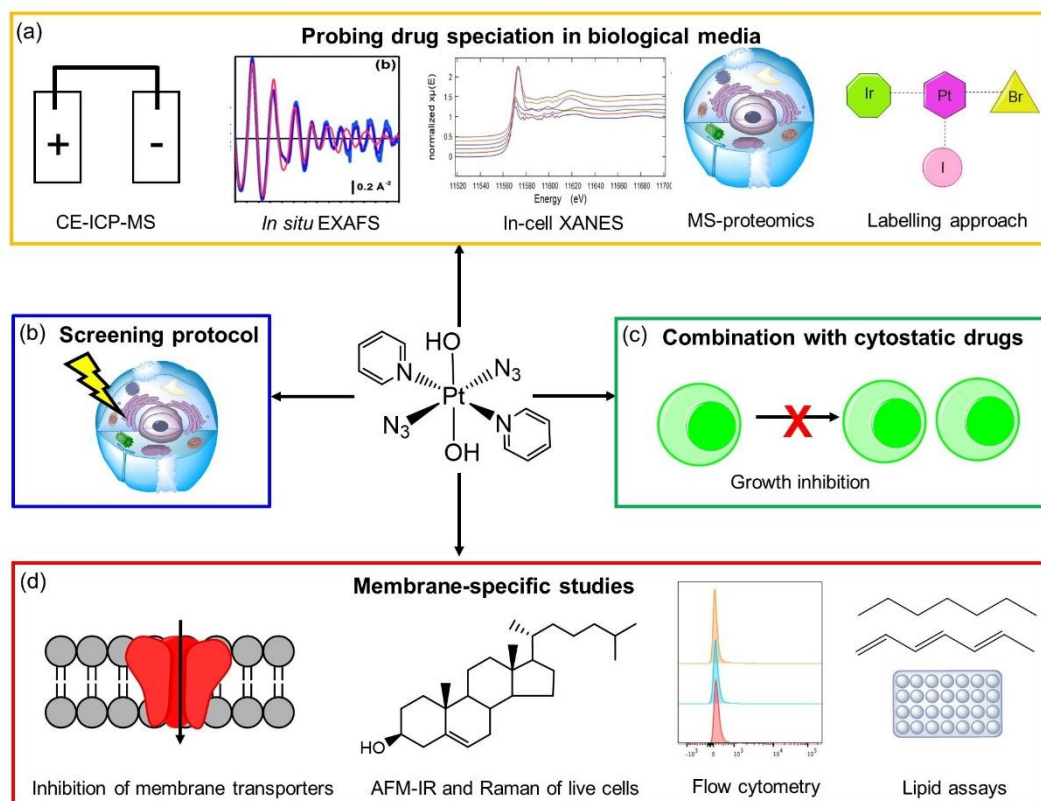
## 6.2.3 Cellular accumulation, targeting and stability of Ir-Pt



**Figure 6.3.** Further work for investigating the in-cell targets of a potent PDT-PACT complex (**8**): (a) ICP-MS accumulation studies; (b) combinational *in vitro* screening; (c) organelle-targeting assays.

The cellular influx and efflux mechanisms of **8** have not yet been probed, thus, ICP-MS  $^{192}\text{Ir}$  and  $^{195}\text{Pt}$  studies under varying conditions (as described in **Chapter 3**) could be used to gain an insight into cleavage of the linker between the two metal centres under both dark and irradiation conditions (465 nm). As Ir was concentrated in small, cytoplasmic regions and the Pt was sparsely distributed throughout the cell, cellular fractionation ICP-MS studies could provide insights into the potential cellular targets and cleavage of **8**. Complementary to this, organelle-specific cell viability assays can be employed to probe the therapeutic targets of intact and cleaved **8**, for example lysosomal (chloroquine; NeutralRed assay)<sup>6, 26</sup> or mitochondrial (ToxGlo assay or cytochrome c assays).<sup>25, 27</sup> As the cellular accumulation of diazido- $\text{Pt}^{\text{IV}}$  complexes was significantly enhanced upon blue light exposure (**Chapter 5**), the same concept can be probed for **8** using ICP-MS.

Synchrotron-XRF alone cannot confirm the nature of specific organelles or cellular features, analytical techniques such as FT-ICR mass spectrometry can be used to elucidate specific binding of the metal fragments to biomolecules.<sup>28</sup> The concept of combinational therapeutic screening can be employed to determine whether the antiproliferative activity of **8** is dependent on the Pt-Ir modalities being intact prior to photoactivation: for example, performing cell viability assays with combinations of the individual  $\text{Ir}^{\text{III}}$ -PDT and  $\text{Pt}^{\text{IV}}$ -PACT modalities (complexes **9** and **10**, **Chapter 4**, **Section 4.1**, **Fig. 4.3**).

6.2.4 Future design of diazido-Pt<sup>IV</sup> PACT complexes

**Figure 6.4.** Further work in optimising the antiproliferative activity of diazido-Pt<sup>IV</sup> PACT prodrugs: (a) probing drug speciation in biological media; (b) optimisation of antiproliferative screening protocols; (c) combinational screening with other cytostatic drugs; (d) membrane-specific studies to assess membrane damage upon blue light exposure. The *in situ* EXAFS image was taken from the literature.<sup>29</sup>

This thesis has demonstrated that the cellular accumulation of diazido-Pt<sup>IV</sup> PACT complexes in cancer cells is highly dependent on the photo-conditions (*ca.* 3× more upon blue light irradiation), which may prove significant in the future development of these complexes for phototherapy (**Chapter 5**). Further research into the potential extracellular activation of diazido-Pt<sup>IV</sup> complexes by blue light may involve membrane integrity flow cytometry (demonstrated in **Chapter 3**) to determine whether photoactivation damages the cell membrane, resulting in enhanced Pt influx. In addition, specific dose-dependent (blue light) cellular accumulation ICP-MS studies associated with cell membranes and / or influx mechanisms can be investigated: ouabain (inhibitor of Na<sup>+</sup> / K<sup>+</sup> pump), CTR1 (copper transporters utilized by various Pt compounds), amphotericin B (protein-

mediated uptake) or methyl- $\beta$ -cyclodextrin (inhibitor of caveolae endocytosis).<sup>30</sup> Alternative methods for investigating membrane damage induced by diazido-Pt<sup>IV</sup> complexes at different light dosages might involve AFM-Raman and AFM-IR spectroscopy, biologically (live cells) or chemically (solution experiments with membrane saturated and unsaturated lipids).<sup>31</sup> Further to this, <sup>195</sup>Pt ICP-MS accumulation studies of cells treated with diazido-Pt<sup>IV</sup> complexes but irradiated in complex-free medium (*not* in extracellular drug solution) may provide essential insights into the photo-mediated uptake of these complexes.

The chemical speciation of test compounds in biologically-relevant media may be essential in elucidating extra- and intracellular mechanisms of drug activation for *in vivo* and clinical translation. With this in mind, this research would benefit from investigating the speciation of diazido-Pt<sup>IV</sup> compounds in cell culture media using techniques such as capillary-electrophoresis ICP-MS, EXAFS or XANES *in situ* studies.<sup>32-34</sup> Further in-cell Pt XANES studies are required to build on the preliminary work in **Chapter 5**. Additionally, a labelling approach can be employed using readily detectable exogenous elements (*e.g.* Br or I by ICP-MS/XRF),<sup>35, 36</sup> which can be used to monitor the fate of the axial OR groups of diazido-Pt<sup>IV</sup> complexes and in a cellular environment.

An optimization of methodology (exposure times, light intensity or dosage) may be essential in overcoming the endosomal-breakdown of diazido-Pt<sup>IV</sup> complexes under dark conditions – which may be associated with the lack of toxicity observed. Complementary to this, investigations into the detoxification and efflux mechanisms of this family of Pt<sup>IV</sup> complexes under dark and blue light conditions can be investigated using various endocytotic or lysosomal inhibitors by ICP-MS (as shown in **Chapter 3**).<sup>30</sup>

Finally, the cytostatic nature of diazido-Pt<sup>IV</sup> compounds can further be exploited by investigating the combination with other known cytostatic compounds (*i.e.* rapamycin or paclitaxel),<sup>37, 38</sup> either by complex conjugation or combination therapy. This is important for the clinical translation of these complexes, as cytostatic drugs are commonly administered in combination with other drugs (*i.e.* cytotoxic drugs) to increase the drug efficacy.<sup>39</sup>

## 6.2.5 Further utilization of synchrotron techniques

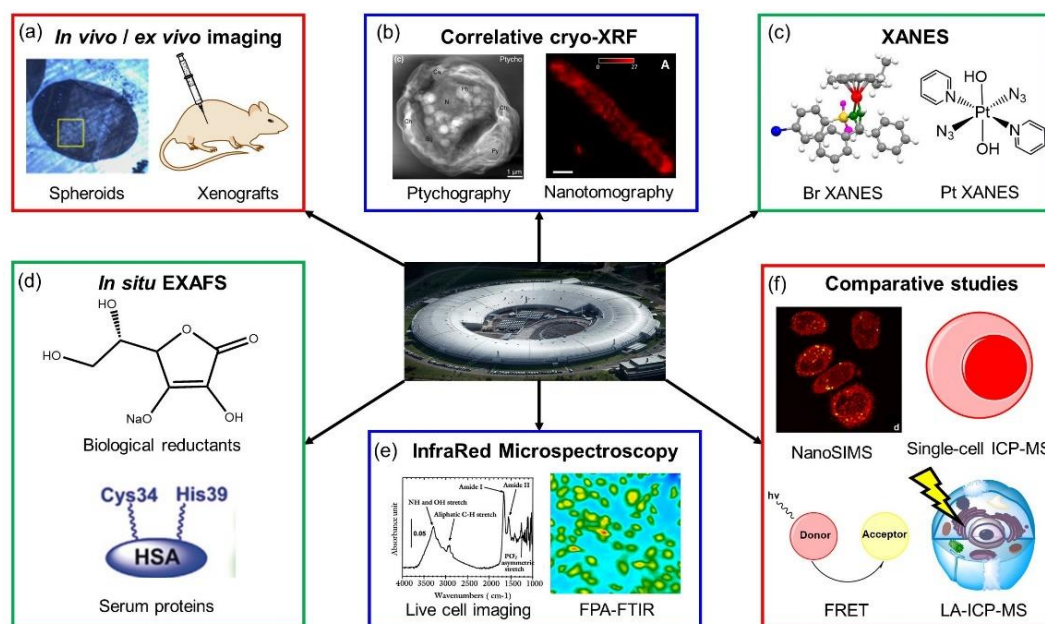


**Figure 6.5.** Further utilisation of synchrotron techniques: (a) *in vivo* and *ex vivo* synchrotron imaging; (b) correlative cryo-XRF techniques; (c) XANES; (d) *In situ* EXAFS studies; (e) InfraRed microspectroscopy; (f) comparative techniques for metal speciation. The following images were taken from the literature: spheroids,<sup>40</sup> ptychography,<sup>41</sup> nanotomography,<sup>42</sup> serum proteins,<sup>43</sup> live cell imaging<sup>44</sup> and nanoSIMS.<sup>45</sup>

This thesis has used a variety of synchrotron-based techniques, including soft cryo-XRT, synchrotron-XRF, DPC imaging and XANES analysis to investigate the mechanisms of action of organometallic compounds in cancer cells. Further hard x-ray synchrotron techniques can be utilized on the same complex systems to gain complementary information of the different families of complexes studied in this thesis. Synchrotron-XRF forms a large proportion of this thesis and has provided new information on the *in-cell* activities of Os, Ir and Pt anticancer complexes. XRF can also be applied to *ex vivo* (tumour spheroids or tissue) or *in vivo* models (tumour xenografts in mice). This is important as the translation from *in vitro* studies to a clinical scenario can be drastically different. Correlative cryo-XRF and cryo-XRT can provide native-state information on the morphological and targeting effects of metallodrugs *in vitro* and *in vivo* (e.g. using two different beamlines, or performing hard x-ray ptychography).<sup>9, 46</sup> In addition, cryo-XRF can be coupled with hard x-ray ptychography or nanotomography to provide further insights into the in-cell metal localisation in 3D,<sup>41, 42</sup> to elucidate cellular targets to a higher resolution (e.g.

sub-15 nm beam available at NSLS-II).<sup>42</sup> As synchrotron-XRF is time-consuming, the need for high-throughput analysis of samples proves necessary for increasing the statistical relevance of mapped cells, which may be obtained using lower emittance sources – which is planned for the Diamond II synchrotron upgrade.

The platinum XANES analysis of diazido-Pt<sup>IV</sup> complexes in cancer cells in this thesis (**Chapter 5**) was a preliminary attempt to validate and optimize different data acquisition methods, thus, the “compressed-sensing” method can be employed for future *in vitro* and *in vivo* analysis of Pt<sup>II</sup> and Pt<sup>IV</sup> compounds at beamline I14. XANES analysis of both Os and Br would be particularly interesting for the Br-labelled Os<sup>II</sup> catalysts reported in this thesis (**Chapters 3**),<sup>47-49</sup> to gain insights into the intracellular speciation and binding modalities of the intact complex and the dissociated ligand. The potential adducts or binding modalities of the Os, Ir or Pt complexes reported herein can be investigated chemically by performing *in situ* EXAFS solution analysis (>100 eV from the absorption edge), which has previously been used to analyse the GSH-activation of half-sandwich Os<sup>II</sup>-azopyridine complexes.<sup>29</sup> For example, the interactions between Os<sup>II</sup> 16-electron catalysts with L-cysteine (which are highly abundant in lysosomes) can be investigated using EXAFS, which may elucidate potential chemical species which lead to complex detoxification and degradation.

Other synchrotron techniques can be used to investigate the cellular changes and potential binding partners of organometallic complexes. Synchrotron InfraRed microspectroscopy can be used to monitor the changes in DNA, lipids and proteins in live, single cells (avoiding fixation),<sup>31, 50</sup> which can provide direct insights into drug-induced biochemical and morphological changes. This may be particularly interesting for monitoring the C-Br band in Br-labelled Os complexes (**Chapters 3-4**). Complementary to this, focal-plane array synchrotron InfraRed microscopy can provide high-throughput, depth-resolved chemical information of treated cells with high spatial resolution.<sup>51, 52</sup> Finally, it would be interesting to utilize complementary techniques to investigate the distribution, speciation and quantification of elements in biological systems, and compare it to results obtained by synchrotron-XRF and XANES. Notably, techniques for the speciation of metals includes mass cytometry,<sup>53</sup> LA-ICP-MS,<sup>54</sup> NanoSIMS,<sup>55</sup> single-cell ICP-MS<sup>56</sup> and FRET ratiometric sensors.<sup>57-59</sup>

### 6.3 References

1. J. P. C. Coverdale, C. Sanchez-Cano, G. J. Clarkson, R. Soni, M. Wills and P. J. Sadler, *Chem Eur J*, 2015, **21**, 8043-8046.
2. J. P. C. Coverdale, *PhD Thesis (University of Warwick)*, 2017.
3. J. P. C. Coverdale, I. Romero-Canelon, C. Sanchez-Cano, G. J. Clarkson, A. Habtemariam, M. Wills and P. J. Sadler, *Nat Chem*, 2018, **10**, 347-354.
4. L. Svorc, P. Tomčík, J. Durdiak, M. Rievaj and D. Bustin, *Pol J Environ Stud*, 2012, **21**, 7-13.
5. A. Kondratskyi, K. Kondratska, F. Vanden Abeele, D. Gordienko, C. Dubois, R.-A. Toillon, C. Slomianny, S. Lemière, P. Delcourt, E. Dewailly, R. Skryma, C. Biot and N. Prevarskaya, *Sci Rep*, 2017, **7**, 15896-15896.
6. M. Mauthe, I. Orhon, C. Rocchi, X. Zhou, M. Luhr, K. J. Hijlkema, R. P. Coppes, N. Engedal, M. Mari and F. Reggiori, *Autophagy*, 2018, **14**, 1435-1455.
7. C. K. C. Chiu, H. Huang, Y. P. Y. Lam, A. Habtemariam, T. Malcomson, M. Paterson, G. Clarkson, P. O'Connor, H. Chao and P. Sadler, *Angew Chem Int Ed*, 2017, **129**, 14898-14902.
8. M. Chiappi, J. J. Conesa, E. Pereiro, C. O. S. Sorzano, M. J. Rodríguez, K. Henzler, G. Schneider, F. J. Chichón and J. L. Carrascosa, *J Nanobiotechnology*, 2016, **14**, 15-15.
9. J. J. Conesa, A. C. Carrasco, V. Rodríguez-Fanjul, Y. Yang, J. L. Carrascosa, P. Cloetens, E. Pereiro and A. M. Pizarro, *Angew Chem Int Ed*, 2020, **59**, 1270-1278.
10. S. Gil, E. Solano, F. Martínez-Trucharte, J. Martínez-Esaín, A. J. Pérez-Berná, J. J. Conesa, C. Kamma-Lorger, M. Alsina and M. Sabés, *PLoS One*, 2020, **15**, e0230022-e0230022.
11. H. Huang, S. Banerjee and P. J. Sadler, *ChemBioChem*, 2018, **19**, 1574-1589.
12. H. Shi, C. Imberti and P. J. Sadler, *Inorg Chem Front*, 2019, **6**, 1623-1638.
13. H. Shi, *PhD Thesis (University of Warwick)*, 2019.
14. A. F. Westendorf, L. Zerzankova, L. Salassa, P. J. Sadler, V. Brabec and P. J. Bednarski, *J Inorg Biochem*, 2011, **105**, 652-662.

15. N. P. E. Barry, A. Pitto-Barry, I. Romero-Canelón, J. Tran, J. J. Soldevila-Barreda, I. Hands-Portman, C. J. Smith, N. Kirby, A. P. Dove, R. K. O'Reilly and P. J. Sadler, *Faraday Discuss*, 2014, **175**, 229-240.
16. J. Hannedouche, G. J. Clarkson and M. Wills, *J Am Chem Soc*, 2004, **126**, 986-987.
17. F. Chen, I. Romero-Canelón, J. J. Soldevila-Barreda, J.-I. Song, J. P. C. Coverdale, G. J. Clarkson, J. Kasparkova, A. Habtemariam, M. Wills, V. Brabec and P. J. Sadler, *Organometallics*, 2018, **37**, 1555-1566.
18. C. A. Wootton, C. Sanchez-Cano, H.-K. Liu, M. P. Barrow, P. J. Sadler and P. B. O'Connor, *Dalton Trans*, 2015, **44**, 3624-3632.
19. B. R. Wood, *Chem Soc Rev*, 2016, **45**, 1980-1998.
20. N. J. Yang and M. J. Hinner, *Methods Mol Biol*, 2015, **1266**, 29-53.
21. S. Moromizato, Y. Hisamatsu, T. Suzuki, Y. Matsuo, R. Abe and S. Aoki, *Inorg Chem*, 2012, **51**, 12697-12706.
22. M. Alvi, R. Nicoletto, B. A. Eshmawi and C. M. Ofner, *Cancer Res*, 2019, **79**, 2091-2091.
23. L. Kamalian, A. E. Chadwick, M. Bayliss, N. S. French, M. Monshouwer, J. Snoeys and B. K. Park, *Toxicol In Vitro*, 2015, **29**, 732-740.
24. L. d. B. Monteiro, G. G. Davanzo, C. F. de Aguiar and P. M. M. Moraes-Vieira, *MethodsX*, 2020, **7**, 100938.
25. C. Granchi, S. Fortunato and F. Minutolo, *MedChemComm*, 2016, **7**, 1716-1729.
26. G. Repetto, A. del Peso and J. L. Zurita, *Nat Protoc*, 2008, **3**, 1125-1131.
27. M. E. Christensen, E. S. Jansen, W. Sanchez and N. J. Waterhouse, *Methods*, 2013, **61**, 138-145.
28. H. Li, Y. Zhao, H. I. Phillips, Y. Qi, T. Y. Lin, P. J. Sadler and P. B. O'Connor, *Anal Chem*, 2011, **83**, 5369-5376.
29. X. Zhang, F. Ponte, E. Borfecchia, A. Martini, C. Sanchez-Cano, E. Sicilia and P. J. Sadler, *Chem Comm*, 2019, **55**, 14602-14605.
30. I. Romero-Canelón, A. M. Pizarro, A. Habtemariam and P. J. Sadler, *Metallomics*, 2012, **4**, 1271-1279.
31. J. L. Denbigh, D. Perez-Guaita, R. R. Vernooij, M. J. Tobin, K. R. Bambery, Y. Xu, A. D. Southam, F. L. Khanim, M. T. Drayson, N. P. Lockyer, R. Goodacre and B. R. Wood, *Sci Rep*, 2017, **7**, 2649.



32. H. U. Holtkamp, S. Movassaghi, S. J. Morrow, M. Kubanik and C. G. Hartinger, *Metallomics*, 2018, **10**, 455-462.
33. G. N. George and I. J. Pickering, in *Encyclopedia of Biophysics*, ed. G. C. K. Roberts, Springer Berlin Heidelberg, Berlin, Heidelberg, 2013, pp. 2762-2767.
34. C. K. J. Chen, P. Kappen, D. Gibson and T. W. Hambley, *Dalton Trans*, 2020, **49**, 7722-7736.
35. M. D. Hall, R. A. Alderden, M. Zhang, P. J. Beale, Z. Cai, B. Lai, A. P. J. Stampfl and T. W. Hambley, *J Struct Biol*, 2006, **155**, 38-44.
36. C. C. Konkankit, J. Lovett, H. H. Harris and J. J. Wilson, *Chem Comm*, 2020, **56**, 6515-6518.
37. J. Li, S. G. Kim and J. Blenis, *Cell Metab*, 2014, **19**, 373-379.
38. E. Pasquier, M. Carre, B. Pourroy, L. Camoin, O. Rebai, C. Briand and D. Braguer, *Mol Cancer Ther*, 2004, **3**, 1301-1310.
39. D. Lu, T.-R. Lu and S. Cao, *Adv Pharmacoevidemiol Drug Saf*, 2013, **2**, 124.
40. C. Sanchez-Cano, I. Romero-Canelón, K. Geraki and P. J. Sadler, *J Inorg Biochem*, 2018, **185**, 26-29.
41. J. Deng, D. J. Vine, S. Chen, Q. Jin, Y. S. G. Nashed, T. Peterka, S. Vogt and C. Jacobsen, *Sci Rep*, 2017, **7**, 445.
42. T. W. Victor, L. M. Easthon, M. Ge, K. H. O'Toole, R. J. Smith, X. Huang, H. Yan, K. N. Allen, Y. S. Chu and L. M. Miller, *Sci Rep*, 2018, **8**, 13415.
43. P. Zhang, H. Huang, S. Banerjee, G. J. Clarkson, C. Ge, C. Imberti and P. J. Sadler, *Angew Chem Int Ed*, 2019, **58**, 2350-2354.
44. N. Jamin, P. Dumas, J. Moncuit, W.-H. Fridman, J.-L. Teillaud, G. L. Carr and G. P. Williams, *PNAS*, 1998, **95**, 4837-4840.
45. S. Lacombe and C. Le Sech, *Surface Sci*, 2009, **603**, 1953-1960.
46. S. H. Shahmoradian, E. H. R. Tsai, A. Diaz, M. Guizar-Sicairos, J. Raabe, L. Spycher, M. Britschgi, A. Ruf, H. Stahlberg and M. Holler, *Sci Rep*, 2017, **7**, 6291.
47. C. Sanchez-Cano, D. Gianolio, I. Romero-Canelon, R. Tucoulou and P. J. Sadler, *Chem Comm*, 2019, **55**, 7065-7068.
48. K. Uno, Y. Notoya, T. Fujikawa, H. Yoshikawa and K. Nishikawa, *Jpn J Appl Phys*, 2005, **44**, 4073-4079.

49. A. Leri and B. Ravel, *J Synchrotron Radiat*, 2014, **21**, 623-626.
50. J. Doherty, A. Raoof, A. Hussain, M. Wolna, G. Cinque, M. Brown, P. Gardner and J. Denbigh, *Analyst*, 2019, **144**, 997-1007.
51. B. R. Wood, K. R. Bambery, M. W. A. Dixon, L. Tilley, M. J. Nasse, E. Mattson and C. J. Hirschmugl, *Analyst*, 2014, **139**, 4769-4774.
52. M. J. Tobin, J. Vongsvivut, D. E. Martin, K. H. Sizeland, M. J. Hackett, R. Takechi, N. Fimorgnari, V. Lam, J. C. Mamo, E. A. Carter, B. Swarbrick, P. A. Lay, D. A. Christensen, D. Perez-Guaita, E. Lowery, P. Heraud, B. R. Wood, L. Puskar and K. R. Bambery, *Infrared Phys Techn*, 2018, **94**, 85-90.
53. Q. Chang, O. I. Ornatsky, I. Siddiqui, R. Straus, V. I. Baranov and D. W. Hedley, *Sci Rep*, 2016, **6**, 36641-36641.
54. K. Löhr, H. Traub, A. J. Wanka, U. Panne and N. Jakubowski, *J Anal At Spectrom*, 2018, **33**, 1579-1587.
55. R. Lee, S. Escrig, M. Croisier, S. Clerc-Rosset, G. Knott, A. Meibom, C. Davey, K. Johnsson and P. Dyson, *Chem Comm*, 2015, **51**, 16486-16489.
56. M. Corte Rodríguez, R. Álvarez-Fernández García, E. Blanco, J. Bettmer and M. Montes-Bayón, *Anal Chem*, 2017, **89**, 11491-11497.
57. K. Hwang, Q. Mou, R. J. Lake, M. Xiong, B. Holland and Y. Lu, *Inorg Chem*, 2019, **58**, 13696-13708.
58. W. Maret, *Metallomics*, 2015, **7**, 202-211.
59. R. Berrocal-Martin, C. Sanchez-Cano, C. K. C. Chiu, R. J. Needham, P. J. Sadler and S. W. Magennis, *Chem Eur J*, 2020, **26**, 4980-4987.

# **Chapter 7**

## **Appendix**

**Tables A1-A37****Table A1.** Biological elements that exist in fetal calf serum (FCS) used in tissue culture.<sup>1</sup>

Element	Total Concentration (mM)
Calcium (Ca)	3.6
Chloride (Cl)	96
Copper	<0.001
Manganese (Mn)	<0.001
Phosphorus (P)	3.35
Potassium (K)	13.5
Sodium (Na)	140
Iron (Fe)	<0.001
Zinc (Zn)	<0.001

**Table A2.** Biological elements that exist in DMEM tissue culture media as salts, amino acids or vitamins, and the concentrations they exist at.<sup>[a]</sup>

Element	Chemical Form	Concentration (mg/L)
Calcium (Ca)	Calcium chloride	200.00
	D-Calcium pantothenate	4.00
Chloride (Cl)	Calcium chloride	200.00
	Choline chloride	4.00
	L-Arginine hydrochloride	84.00
	L-Cystine 2HCl	63.00
	L-Histidine hydrochloride-H <sub>2</sub> O	42.00
	L-Lysine hydrochloride	146.00
	Potassium Chloride	400.00
	Pyridoxine hydrochloride	4.00
	Sodium Chloride	6400.00
	Thiamine hydrochloride	4.00
Iron (Fe)	Ferric Nitrate	0.10
Magnesium (Mg)	Magnesium Sulfate	97.67
Phosphorus (P)	Sodium Phosphate monobasic	125.00
Potassium (K)	Potassium Chloride	400.00
Sodium (Na)	L-Tyrosine disodium salt dihydrate	104.00
	Phenol red	0.01
	Sodium Bicarbonate	3700.00
	Sodium Chloride	6400.00
	Sodium Phosphate monobasic	125.00
	L-Cystine 2HCl	63.00
	L-Methionine	0.20
	Magnesium Sulfate	97.67
	Thiamine hydrochloride	4.00

<sup>[a]</sup> Information was obtained from <https://www.thermofisher.com/uk/en/home/technical-resources/media-formulation.183.html> (Accessed on 7th October 2020).

**Table A3.** Biological elements that exist in RPMI-1640 tissue culture media as salts, amino acids or vitamins, and the concentrations they exist at.<sup>[a]</sup>

Element	Chemical Form	Concentration (mg/L)
Calcium (Ca)	Calcium Nitrate	100.00
	D-calcium pantothenate	0.25
Chloride (Cl)	Choline chloride	3.00
	L-Cystine 2HCl	65.00
	L-Lysine hydrochloride	40.00
	Potassium chloride	400.00
	Pyridoxine hydrochloride	1.00
	Sodium chloride	6000.00
	Thiamine hydrochloride	1.00
Magnesium (Mg)	Magnesium sulphate	48.84
Phosphorus (P)	Sodium phosphate dibasic	800.00
Potassium (K)	Potassium chloride	400.00
Sodium (Na)	L-Tyrosine disodium salt dihydrate	29.00
	Sodium bicarbonate	2000.00
	Sodium chloride	6000.00
	Sodium phosphate dibasic	800.00
Sulfur (S)	Glutathione (reduced)	1.00
	L-Cystine 2HCl	65.00
	L-Methionine	15.00
	Magnesium sulphate	48.84
	Thiamine hydrochloride	1.00

<sup>[a]</sup> Information was obtained from <https://www.thermofisher.com/uk/en/home/technical-resources/media-formulation.114.html> (Accessed on 7th October 2020).

**Table A4.** Biological elements that exist in PBS used in tissue culture.<sup>[a]</sup>

Element	Chemical Form	Concentration (mg/L)
Chloride (Cl)	Sodium chloride	8006.28
	Potassium chloride	201.29
Phosphorus (P)	Sodium phosphate dibasic	1419.60
	Monopotassium phosphate	250.00
Potassium (K)	Potassium chloride	201.29
	Monopotassium phosphate	250.00
Sodium (Na)	Sodium chloride	8006.28
	Sodium phosphate dibasic	1419.60

<sup>[a]</sup> Information was obtained from <https://www.thermofisher.com/uk/en/home/technical-resources/media-formulation.160.html> (Accessed on 7th October 2020).

**Table A5.** Biological elements that exist in HBSS used in tissue culture.<sup>[a]</sup>

Element	Chemical Form	Concentration (mg/L)
Calcium (Ca)	Calcium chloride	110.98
Chloride (Cl)	Calcium chloride	110.98
	Magnesium chloride hexahydrate	203.30
	Potassium chloride	373.75
	Sodium chloride	8181.60
Magnesium (Mg)	Magnesium chloride hexahydrate	203.30
	Magnesium sulfate hydrate	98.59
Phosphorus (P)	Disodium phosphate	53.40
	Potassium dihydrogen phosphate	54.43
Potassium (K)	Potassium chloride	373.75
	Potassium dihydrogen phosphate	54.43
Sodium (Na)	Disodium phosphate	53.40
	Sodium bicarbonate	336.04
	Sodium chloride	8181.60
Sulfur (S)	Magnesium sulfate hydrate	98.59

<sup>[a]</sup> Information was obtained from <https://www.thermofisher.com/uk/en/home/technical-resources/media-formulation.153.html> (Accessed on 7th October 2020).

**Table A6.** X-ray crystallographic data for *SS-1*, *SS-2* and *SS-3* (Chapter 3).

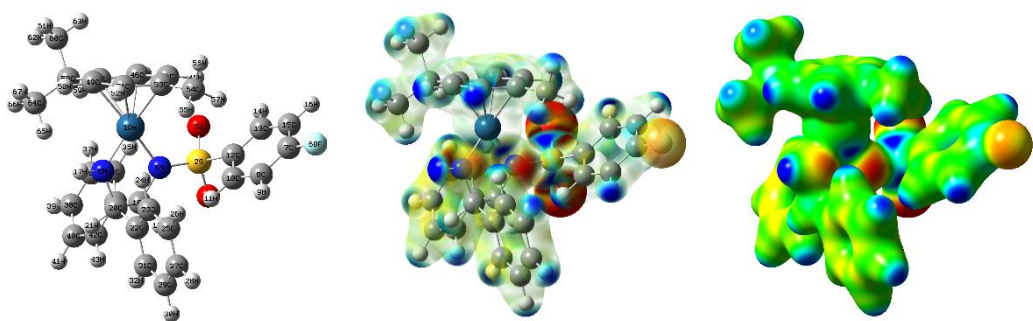
Complex	<i>SS-1</i> <sup>[a]</sup>	<i>SS-2</i>	<i>SS-3</i>
<b>a</b> (Å)	10.6100(3)	9.9784(1)	9.33638(14)
<b>b</b> (Å)	13.8464(3)	14.2370(1)	14.31887(15)
<b>c</b> (Å)	18.9530(5)	19.7954(2)	21.7165(3)
<b>α</b> (°)	90	90	90
<b>β</b> (°)	90	90	90
<b>γ</b> (°)	90	90	90
<b>Crystal system</b>	Orthorhombic	Orthorhombic	Orthorhombic
<b>Temperature (K)</b>	150	150	150
<b>Reported volume</b> (Å <sup>3</sup> )	2788.79(11)	2812.18(4)	2903.21(6)
<b>Space group</b>	P2 <sub>1</sub> 2 <sub>1</sub> 2 <sub>1</sub>	P2 <sub>1</sub> 2 <sub>1</sub> 2 <sub>1</sub>	P2 <sub>1</sub> 2 <sub>1</sub> 2 <sub>1</sub>
<b>D<sub>x</sub></b> (g cm <sup>-3</sup> )	1.641	1.780	1.832
<b>Z</b>	4	4	4
<b>Empirical formula</b>	C <sub>31</sub> H <sub>34</sub> N <sub>2</sub> O <sub>2</sub> OsS	C <sub>30</sub> H <sub>31</sub> BrN <sub>2</sub> O <sub>2</sub> OsS	C <sub>30</sub> H <sub>31</sub> IN <sub>2</sub> O <sub>2</sub> OsS
<b>MW</b> (g/mol)	688.86	754.74	800.73
<b>μ</b> (mm <sup>-1</sup> )	4.678	11.157	17.545
<b>F(000)</b>	1368.0	1472	1544
<b>Reflections measured</b>	33345	5531	5624
<b>WR<sub>2</sub> reflections</b>	0.0927	0.0771	0.0665

<sup>[a]</sup> Literature crystallographic data.<sup>2</sup>

**Table A7.** Mulliken partial charges calculated for complexes **RR-6** (X=F), **theoretical compound (EB1, X=Cl)**, **RR-2** (X=Br) and **RR-3** (X=I), at the PBE0/Lanl2DZ/6-31+G\*\* level of theory (**Chapter 3**).

	Mulliken partial charge			
	<b>RR-6</b>	<b>EB1</b>	<b>RR-2</b>	<b>RR-3</b>
Os 1	0.566	0.566	0.566	0.566
S 2	1.369	1.369	1.371	1.371
O 3	-0.599	-0.597	-0.597	-0.597
O 4	-0.551	-0.551	-0.550	-0.550
N 5	-0.891	-0.890	-0.889	-0.889
N 6	-0.821	-0.819	-0.820	-0.821
X 68	-0.323	0.017	0.065	0.172

**Table A8.** Cartesian coordinates and electrostatic potential surface (EPS) calculated for [Os(*p*-cymene)(*N*-(4-fluorobenzenesulfonyl)-1,2-diphenylethylenediamine)] (**RR-6**, X= F) calculated at the PBE0/Lanl2DZ/6-31+G\*\* level. EPS is shown mapped onto the total electron density. Isovalue=0.04. (*R,R*)-catalyst only. Surface mapping colours range from red (-0.025 au) to blue (+0.30 au), **Chapter 3**.

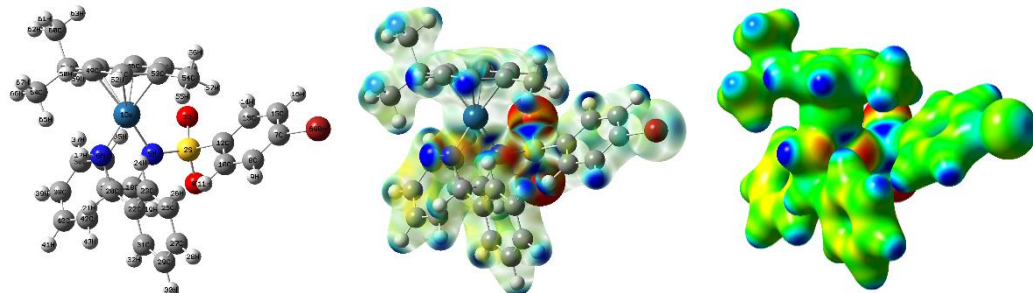


Atom	x	y	z
Os 1	-0.6540	-0.7843	-0.6626
S 2	0.7115	0.2380	2.1218
O 3	0.0200	-0.8779	2.7792
O 4	0.8909	1.4910	2.8562
N 5	0.0344	0.5768	0.6629
N 6	-0.8765	0.8563	-1.6271
C 7	4.8976	-1.2587	1.2232
C 8	4.4061	-0.1790	0.4999
H 9	5.0303	0.2991	-0.2473
C 10	3.1141	0.2636	0.7541
H 11	2.7022	1.0948	0.1913
C 12	2.3380	-0.3848	1.7132
C 13	2.8472	-1.4611	2.4362
H 14	2.2233	-1.9400	3.1843
C 15	4.1416	-1.9094	2.1885
H 16	4.5695	-2.7456	2.7310
H 17	-1.1952	0.9232	-2.5864
C 18	-0.3919	1.9608	0.4335
H 19	0.3366	2.6472	0.8788
C 20	-0.3833	2.1137	-1.0993
H 21	-1.0820	2.9207	-1.3600
C 22	0.9861	2.5123	-1.6403
C 23	1.7889	1.6338	-2.3681
H 24	1.4249	0.6281	-2.5578
C 25	3.0415	2.0334	-2.8340
H 26	3.6528	1.3355	-3.4005
C 27	3.5084	3.3188	-2.5793
H 28	4.4833	3.6308	-2.9431
C 29	2.7117	4.2068	-1.8579
H 30	3.0639	5.2145	-1.6556
C 31	1.4624	3.8058	-1.3989
H 32	0.8466	4.5074	-0.8390
C 33	-1.7578	2.2925	1.0247
C 34	-2.5191	1.3547	1.7215

Atom	x	y	z
H 35	-2.1229	0.3546	1.8677
C 36	-3.7600	1.7012	2.2537
H 37	-4.3343	0.9584	2.8013
C 38	-4.2570	2.9913	2.1021
H 39	-5.2224	3.2611	2.5208
C 40	-3.4964	3.9406	1.4228
H 41	-3.8640	4.9572	1.3122
C 42	-2.2585	3.5918	0.8940
H 43	-1.6680	4.3487	0.3805
C 44	-0.1004	-2.7557	0.3184
H 45	0.5294	-2.8456	1.1955
C 46	-1.4752	-2.4890	0.4993
H 47	-1.8639	-2.4001	1.5071
C 48	-2.3165	-2.1701	-0.6209
C 49	-1.7516	-2.2266	-1.9334
H 50	-2.3546	-1.9494	-2.7905
C 51	-0.3561	-2.3953	-2.0967
H 52	0.0872	-2.2852	-3.0813
C 53	0.5010	-2.6387	-0.9616
C 54	1.9775	-2.8007	-1.1502
H 55	2.3403	-2.1619	-1.9598
H 56	2.2123	-3.8407	-1.4071
H 57	2.5203	-2.5390	-0.2399
C 58	-3.7743	-1.8475	-0.3796
H 59	-3.8208	-1.3884	0.6164
C 60	-4.5851	-3.1478	-0.3515
H 61	-4.5564	-3.6450	-1.3274
H 62	-5.6324	-2.9395	-0.1113
H 63	-4.1980	-3.8484	0.3946
C 64	-4.3567	-0.8449	-1.3709
H 65	-3.7412	0.0586	-1.4177
H 66	-5.3648	-0.5568	-1.0586
H 67	-4.4417	-1.2685	-2.3783
F 68	6.1412	-1.6882	0.9780

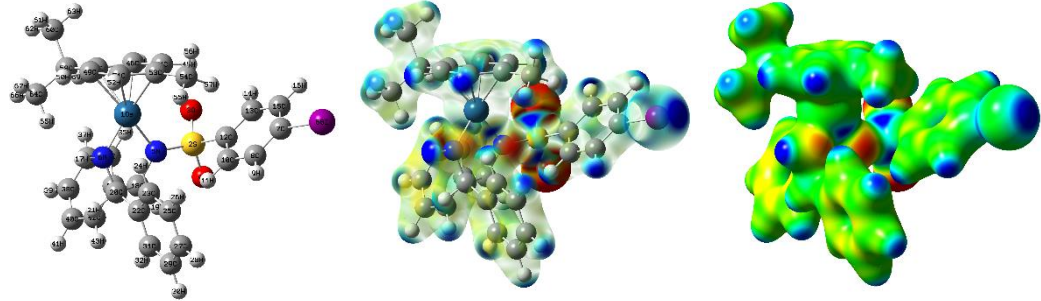


**Table A9.** Cartesian coordinates and electrostatic potential surface (EPS) calculated for [Os(*p*-cymene)(*N*-(4-bromobenzenesulfonyl)-1,2-diphenylethylenediamine)] (**RR-2**, X=Br) calculated at the PBE0/Lanl2DZ/6-31+G\*\* level. EPS is shown mapped onto the total electron density. Isovalue=0.04. (*R,R*)-catalyst only. Surface mapping colours range from red (-0.025 au) to blue (+0.30 au), **Chapter 3**.



Atom	x	y	z
Os 1	-1.0486	-0.8113	-0.6906
S 2	0.2446	0.3755	2.0625
O 3	-0.2102	-0.8538	2.7228
O 4	0.2540	1.6268	2.8207
N 5	-0.5498	0.6199	0.6479
N 6	-1.5834	0.7881	-1.6005
C 7	4.5748	-0.3864	0.9239
C 8	3.8801	0.6265	0.2721
H 9	4.3653	1.2356	-0.4823
C 10	2.5468	0.8444	0.6017
H 11	1.9821	1.6193	0.0934
C 12	1.9336	0.0449	1.5629
C 13	2.6434	-0.9586	2.2160
H 14	2.1441	-1.5588	2.9704
C 15	3.9804	-1.1830	1.8940
H 16	4.5473	-1.9624	2.3908
H 17	-1.9529	0.8207	-2.5432
C 18	-1.2107	1.9167	0.4694
H 19	-0.5917	2.7061	0.9094
C 20	-1.2818	2.0991	-1.0579
H 21	-2.1103	2.7864	-1.2777
C 22	-0.0113	2.7213	-1.6286
C 23	0.8691	2.0065	-2.4404
H 24	0.6375	0.9716	-2.6745
C 25	2.0311	2.6028	-2.9300
H 26	2.7056	2.0300	-3.5613
C 27	2.3277	3.9249	-2.6149
H 28	3.2326	4.3903	-2.9952
C 29	1.4500	4.6515	-1.8113
H 30	1.6690	5.6859	-1.5616
C 31	0.2909	4.0546	-1.3290
H 32	-0.3880	4.6313	-0.7034
C 33	-2.5914	2.0024	1.1110
C 34	-3.1575	0.9444	1.8213
H 35	-2.5927	0.0256	1.9443
C 36	-4.4217	1.0703	2.3955
H 37	-4.8428	0.2366	2.9514
C 38	-5.1369	2.2567	2.2735
H 39	-6.1207	2.3540	2.7239
C 40	-4.5719	3.3267	1.5829
H 41	-5.1112	4.2659	1.4954
C 42	-3.3106	3.1980	1.0122
H 43	-2.8751	4.0480	0.4896
C 44	-0.0790	-2.6675	0.1747
H 45	0.6322	-2.6606	0.9920
C 46	-1.4587	-2.6585	0.4771
H 47	-1.7666	-2.6541	1.5161
C 48	-2.4353	-2.4698	-0.5569
C 49	-1.9852	-2.3968	-1.9134
H 50	-2.6994	-2.2138	-2.7081
C 51	-0.6015	-2.3204	-2.1992
H 52	-0.2711	-2.1184	-3.2131
C 53	0.3790	-2.4270	-1.1472
C 54	1.8401	-2.3348	-1.4631
H 55	2.0235	-1.6270	-2.2759
H 56	2.2158	-3.3156	-1.7788
H 57	2.4153	-2.0130	-0.5925
C 58	-3.9026	-2.4175	-0.1933
H 59	-3.9466	-2.0536	0.8414
C 60	-4.4854	-3.8344	-0.2315
H 61	-4.4559	-4.2406	-1.2487
H 62	-5.5297	-3.8263	0.0961
H 63	-3.9297	-4.5164	0.4194
C 64	-4.7154	-1.4520	-1.0509
H 65	-4.2623	-0.4561	-1.0505
H 66	-5.7314	-1.3677	-0.6538
H 67	-4.8039	-1.8005	-2.0863
Br 68	6.4409	-0.7006	0.4586

**Table A10.** Cartesian coordinates and electrostatic potential surface (EPS) calculated for [Os(*p*-cymene)(*N*-(4-iodobenzenesulfonyl)-1,2-diphenylethylenediamine)] (**RR-3**, X=I) calculated at the PBE0/Lanl2DZ/6-31+G\*\* level. EPS is shown mapped onto the total electron density. Isovalue=0.04. (*R,R*)-catalyst only. Surface mapping colours range from red (-0.025 au) to blue (+0.30 au), **Chapter 3**.



Atom	x	y	z
Os 1	-1.3565	-0.8153	-0.6914
S 2	-0.0670	0.3984	2.0515
O 3	-0.4760	-0.8468	2.7125
O 4	-0.0865	1.6462	2.8155
N 5	-0.8846	0.6254	0.6472
N 6	-1.9504	0.7711	-1.5873
C 7	4.2775	-0.2185	0.8501
C 8	3.5297	0.7639	0.2060
H 9	3.9737	1.3894	-0.5605
C 10	2.1939	0.9362	0.5530
H 11	1.5929	1.6854	0.0477
C 12	1.6240	0.1221	1.5278
C 13	2.3790	-0.8514	2.1747
H 14	1.9132	-1.4659	2.9391
C 15	3.7184	-1.0284	1.8332
H 16	4.3130	-1.7869	2.3305
H 17	-2.3367	0.7962	-2.5235
C 18	-1.5929	1.8991	0.4854
H 19	-0.9968	2.7065	0.9245
C 20	-1.6864	2.0882	-1.0397
H 21	-2.5398	2.7485	-1.2466
C 22	-0.4438	2.7566	-1.6204
C 23	0.4432	2.0821	-2.4592
H 24	0.2400	1.0444	-2.7065
C 25	1.5777	2.7213	-2.9592
H 26	2.2580	2.1792	-3.6109
C 27	1.8396	4.0469	-2.6281
H 28	2.7229	4.5456	-3.0165
C 29	0.9546	4.7334	-1.7978
H 30	1.1466	5.7700	-1.5350
C 31	-0.1768	4.0937	-1.3049
H 32	-0.8616	4.6396	-0.6584
C 33	-2.9687	1.9325	1.1421
C 34	-3.4870	0.8531	1.8569
H 35	-2.8878	-0.0447	1.9708
C 36	-4.7478	0.9318	2.4467
H 37	-5.1309	0.0823	3.0062
C 38	-5.5075	2.0913	2.3362
H 39	-6.4884	2.1518	2.7991
C 40	-4.9908	3.1823	1.6407
H 41	-5.5653	4.1012	1.5613
C 42	-3.7327	3.1009	1.0544
H 43	-3.3353	3.9673	0.5284
C 44	-0.3244	-2.6433	0.1626
H 45	0.3890	-2.6160	0.9773
C 46	-1.7026	-2.6778	0.4707
H 47	-2.0064	-2.6862	1.5109
C 48	-2.6892	-2.5171	-0.5589
C 49	-2.2470	-2.4261	-1.9169
H 50	-2.9698	-2.2646	-2.7086
C 51	-0.8677	-2.3028	-2.2074
H 52	-0.5482	-2.0860	-3.2217
C 53	0.1205	-2.3829	-1.1600
C 54	1.5757	-2.2384	-1.4829
H 55	1.7297	-1.5048	-2.2788
H 56	1.9796	-3.1988	-1.8253
H 57	2.1470	-1.9191	-0.6088
C 58	-4.1562	-2.5132	-0.1907
H 59	-4.2084	-2.1573	0.8464
C 60	-4.6943	-3.9474	-0.2352
H 61	-4.6580	-4.3459	-1.2553
H 62	-5.7365	-3.9743	0.0981
H 63	-4.1140	-4.6160	0.4080
C 64	-5.0017	-1.5686	-1.0400
H 65	-4.5818	-0.5582	-1.0319
H 66	-6.0196	-1.5214	-0.6416
H 67	-5.0794	-1.9113	-2.0782
I 68	6.3183	-0.4877	0.3171

**Table A11.** Viable (FL2-) and non-viable (FL2+) membrane integrity analysis of a normalized population of A549 (human lung) cancer cells treated with  $1 \times \text{IC}_{50}$  of **SS-2** ( $31 \pm 1 \mu\text{M}$ ) or **RR-2** ( $29.5 \pm 0.5 \mu\text{M}$ ) for 24 h (310 K, 5%  $\text{CO}_2$ ) and co-administered with sodium formate (0-2 mM) as determined by flow cytometry (**Chapter 3**).

Complex	Viable membrane (FL2-)	Non-viable membrane (FL2+)	P-value <sup>[a]</sup>
Untreated control	99.73 $\pm$ 0.07	0.27 $\pm$ 0.07	1.0000
Untreated + formate	99.76 $\pm$ 0.05	0.24 $\pm$ 0.05	0.6184
<b>SS-2</b>	99.82 $\pm$ 0.11	0.18 $\pm$ 0.11	0.3079
<b>SS-2</b> + formate	99.76 $\pm$ 0.05	0.24 $\pm$ 0.05	0.6668
<b>RR-2</b>	99.53 $\pm$ 0.09	0.47 $\pm$ 0.09	0.0382
<b>RR-2</b> + formate	99.44 $\pm$ 0.03	0.56 $\pm$ 0.03	0.0099

<sup>[a]</sup> P-values were calculated using a two-tailed t-test assuming unequal variables. All t-tests were comparison to the untreated control.

**Table A12.** Time-dependent ICP-MS  $^{189}\text{Os}$  cellular accumulation in A2780 (human ovarian) cancer cells treated with  $1 \times \text{IC}_{50}$  concentration of **RR-1** ( $15.5 \pm 0.5 \mu\text{M}$ ), **SS-2** ( $30.8 \pm 1.6 \mu\text{M}$ ) or **RR-2** ( $27.4 \pm 0.6 \mu\text{M}$ ) for 3-24 h (**Chapter 3**). The extent of efflux was determined by  $1 \times \text{IC}_{50}$  for 24 h, followed by recovery period in complex-free media (24, 48 and 72 h).

Time / h	<b>RR-1</b> <sup>[a]</sup>	<b>SS-2</b>	<b>RR-2</b>
<b>3</b>	32 $\pm$ 4	37 $\pm$ 2	35 $\pm$ 3
<b>6</b>	42 $\pm$ 1	32 $\pm$ 7	39 $\pm$ 8
<b>18</b>	33 $\pm$ 1	29 $\pm$ 2	28 $\pm$ 2
<b>24</b>	30 $\pm$ 2	29.5 $\pm$ 0.5	22 $\pm$ 3
<b>48</b> <sup>[b]</sup>	19 $\pm$ 2	18.3 $\pm$ 0.6	22 $\pm$ 4
<b>72</b> <sup>[b]</sup>	13 $\pm$ 2	16 $\pm$ 5	18 $\pm$ 2
<b>96</b> <sup>[b]</sup>	5.1 $\pm$ 0.5	7.2 $\pm$ 1.5	7.7 $\pm$ 2.5

<sup>[a]</sup> Time-dependent cellular accumulation of **RR-1** in A2780 cells as reported in the literature.<sup>2, 3</sup>

<sup>[b]</sup> 24 h exposure, followed by 24, 48 or 72 h recovery in complex-free media.

**Table A13.** Formate-dependent ICP-MS  $^{189}\text{Os}$  cellular accumulation in A2780 cells treated with  $1 \times \text{IC}_{50}$  of **RR-1** ( $15.5 \pm 0.5 \mu\text{M}$ ) or **SS-2** ( $30.8 \pm 1.6 \mu\text{M}$ ) for 24 h upon co-administration with sodium formate (0 or 2 mM).

[Formate] / mM	ng of Os/ $10^6$ cells	
	<b>RR-1</b> <sup>[a]</sup>	<b>SS-2</b>
<b>0</b>	29 $\pm$ 3	30 $\pm$ 1
<b>2</b>	28 $\pm$ 3	31 $\pm$ 2

<sup>[a]</sup> Formate-dependent cellular accumulation of **RR-1** in A2780 cells as reported in the literature.<sup>2, 3</sup>

**Table A14.** Verapamil-dependent efflux of  $^{189}\text{Os}$  and  $^{79}\text{Br}$  in A549 cells treated with  $1\times \text{IC}_{50}$  of **SS-2** ( $30.8\pm 1.6\ \mu\text{M}$ ) for 24 h, and recovery in 0-20  $\mu\text{M}$  of verapamil hydrochloride (prepared in 5% v/v DMSO, 95% v/v DMEM) for 24-72 h (**Chapter 3**). Statistical analysis was performed using Welch's unpaired t-test, assuming unequal variances.

Recovery time / h	Complex-free media		Verapamil	
	Os ng/ $10^6$ cells	Br ng/ $10^6$ cells	Os ng/ $10^6$ cells	Br ng/ $10^6$ cells
24	$9.1\pm 2.4$	$275\pm 54$	$11.5\pm 2.4$	$243\pm 35$
48	$3.9\pm 0.8$	$176\pm 31$	$6.6\pm 0.06$	$178\pm 20$
72	$3.0\pm 0.9$	$151\pm 44$	$5.7\pm 2.3$	$187\pm 64$

**Table A15.** Intracellular ratio of bromine-to-osmium (Br/Os) in A549 (human lung) cancer cells treated with  $1\times \text{IC}_{50}$  of **SS-2** ( $30.8\pm 1.6\ \mu\text{M}$ ) for 24 h, and recovered in 0-20  $\mu\text{M}$  of erapamil hydrochloride (prepared in 5% v/v DMSO, 95% v/v DMEM) for 24-72 h (**Chapter 3**). Statistical analysis was performed using the Welch's unpaired t-test, assuming unequal variances.

Recovery time / h	Br / Os molar ratio	
	Complex-free media	Verapamil
24 <sup>[a]</sup>	$72\pm 23$	$51\pm 13$
48 <sup>[a]</sup>	$107\pm 29$	$64\pm 7$
72 <sup>[a]</sup>	$48\pm 21$	$76\pm 40$

**Table A16.** Time-dependent ICP-MS  $^{189}\text{Os}$  and  $^{79}\text{Br}$  accumulation in A549 (human lung) cancer cells treated with  $1\times \text{IC}_{50}$  of **SS-2** ( $30.8\pm 1.6\ \mu\text{M}$ ) for different exposure times (3, 6, 24 h) and 24 h with different recovery times (24, 48 and 72 h), **Chapter 3**.

Time / h	ng/ $10^6$ cells	
	Osmium	Bromine
0	$0.03\pm 0.01$	$4.6\pm 1.8$
3	$46\pm 3$	$186\pm 20$
6	$46\pm 9$	$249\pm 39$
24	$46\pm 3$	$571\pm 11$
48	$9.1\pm 2.4$	$275\pm 54$
72	$3.9\pm 0.8$	$176\pm 31$
96	$3.0\pm 0.9$	$151\pm 44$

<sup>[a]</sup> 24 h exposure, followed by 24, 48 or 72 h recovery in complex-free media.

**Table A17.** Time-dependent ICP-MS  $^{189}\text{Os}$  cellular distribution in A549 (human lung) cancer cells treated with  $1\times\text{IC}_{50}$  of **SS-2** ( $30.8\pm 1.6\ \mu\text{M}$ ) for 3-24 h and determined using a cell fractionation kit (**Chapter 3**). The extent of efflux was determined by  $1\times\text{IC}_{50}$  for 24 h followed by recovery in complex-free media (24-72 h).

Time / h	Average % Osmium			
	Cytosolic	Membrane	Nuclear	Cytoskeletal
3	$3.4\pm 0.6$	$84\pm 12$	$5.7\pm 0.5$	$7.1\pm 1.4$
6	$1.67\pm 0.8$	$86\pm 9$	$6.0\pm 0.3$	$6.2\pm 0.5$
24	$5.6\pm 2.8$	$81\pm 9$	$5.5\pm 0.4$	$8.2\pm 1.4$
24+24	$1.4\pm 0.1$	$80\pm 5.2$	$5.5\pm 0.3$	$12.9\pm 0.9$
24+48	$1.6\pm 0.2$	$84\pm 18$	$4.6\pm 1.6$	$9.4\pm 2.1$
24+72	$4.7\pm 2.9$	$66\pm 9$	$9.2\pm 2.7$	$19.6\pm 6.7$

**Table A18.** Time-dependent ICP-MS  $^{79}\text{Br}$  cellular distribution in A549 (human lung) cancer cells treated with  $1\ \text{IC}_{50}$  of **SS-2** ( $30.8\pm 1.6\ \mu\text{M}$ ) for 3-24 h and determined using a cell fractionation kit (**Chapter 3**). The extent of efflux was determined by  $1\times\text{IC}_{50}$  for 24 h followed by recovery in complex-free media (24-72 h).

Time / h	Average % Bromine			
	Cytosolic	Membrane	Nuclear	Cytoskeletal
3	$17.2\pm 1.4$	$58.1\pm 7.4$	$19.7\pm 1.2$	$4.9\pm 2.1$
6	$8.9\pm 6.1$	$72.9\pm 6.9$	$15.3\pm 0.4$	$2.9\pm 0.2$
24	$10.6\pm 2.6$	$74.9\pm 9.8$	$11.8\pm 0.8$	$2.7\pm 0.004$
24+24	$6.5\pm 0.2$	$79.5\pm 3.5$	$11.2\pm 0.3$	$2.8\pm 0.2$
24+48	$7.1\pm 0.8$	$77.6\pm 16.2$	$11.1\pm 1.4$	$4.2\pm 0.9$
24+72	$10.3\pm 2.3$	$64.5\pm 0.649$	$17.6\pm 1.4$	$7.5\pm 1.8$

**Table A19.** Normalized fractional moles of  $^{189}\text{Os}$  and  $^{79}\text{Br}$  in the nuclear fractions in A549 cells treated with  $1\times\text{IC}_{50}$  of **SS-2** ( $30.8\pm 1.6\ \mu\text{M}$ ) for different exposure times, as reported in fractional  $\text{nmol} \times 10^{-8}$  per cell and determined by ICP-MS (**Chapter 3**).

Time / h	Fraction $\text{nmol} \times 10^{-8}$ per cell	
	Osmium	Bromine
3	$1.4\pm 0.4$	$46.4\pm 15.5$
6	$1.5\pm 0.6$	$48\pm 19$
24	$1.3\pm 0.3$	$85\pm 13$
24+24	$0.3\pm 0.1$	$39\pm 17$
24+48	$0.10\pm 0.05$	$25\pm 11$
24+72	$0.13\pm 0.07$	$28\pm 8$

**Table A20.** Cell areas ( $\mu\text{m}^2$ ) and roundness factors (RF) of cryo-fixed and freeze-dried A549 cells treated with  $0.5 \times \text{IC}_{50}$  of *SS-2* (0-150  $\mu\text{M}$ ) for 24 h (no recovery), as identified by S, K, P and Zn distributions in the synchrotron-XRF elemental maps (**Chapter 3**): **C1-4** (untreated controls), **C5-7** (30  $\mu\text{M}$ ), **C9-15** (90  $\mu\text{M}$ ) and **C16-18** (150  $\mu\text{M}$ ). Data were analysed in triplicate using ImageJ.<sup>4</sup>

Cell	Area ( $\mu\text{m}^2$ )	Mean area ( $\mu\text{m}^2$ )	Roundness factor	Mean RF
C1	925 $\pm$ 42	766 $\pm$ 126	0.33 $\pm$ 0.02	0.33 $\pm$ 0.04
C2	685 $\pm$ 19		0.34 $\pm$ 0.01	
C3	829 $\pm$ 23		0.36 $\pm$ 0.02	
C4	624 $\pm$ 28		0.28 $\pm$ 0.01	
C5	747 $\pm$ 21	599 $\pm$ 103	0.32 $\pm$ 0.01	0.49 $\pm$ 0.17
C6	602 $\pm$ 5		0.61 $\pm$ 0.01	
C7	476 $\pm$ 36		0.34 $\pm$ 0.02	
C8	572 $\pm$ 23		0.68 $\pm$ 0.01	
C9	453 $\pm$ 7	411 $\pm$ 88	0.72 $\pm$ 0.03	0.75 $\pm$ 0.16
C10	331 $\pm$ 5		0.89 $\pm$ 0.03	
C11	556 $\pm$ 5		0.43 $\pm$ 0.02	
C12	411 $\pm$ 6		0.77 $\pm$ 0.01	
C13	279 $\pm$ 3		0.94 $\pm$ 0.02	
C14	373 $\pm$ 6		0.80 $\pm$ 0.05	
C15	476 $\pm$ 22		0.719 $\pm$ 0.004	
C16	478 $\pm$ 3	569 $\pm$ 62	0.83 $\pm$ 0.02	0.88 $\pm$ 0.04
C17	611 $\pm$ 9		0.886 $\pm$ 0.003	
C18	590 $\pm$ 9		0.91 $\pm$ 0.03	

**Table A21.** Area of cell nuclei ( $\mu\text{m}^2$ ) in cryo-fixed and freeze-dried A549 cells treated with  $0.5 \times \text{IC}_{50}$  of *SS-2* (0-150  $\mu\text{M}$ ) for 24 h (no recovery), as identified by the Zn distributions in the synchrotron-XRF elemental maps: **C1-4** (untreated controls), **C5-7** (30  $\mu\text{M}$ ), **C9-15** (90  $\mu\text{M}$ ) and **C16-18** (150  $\mu\text{M}$ ). Data were analysed in triplicate using ImageJ.<sup>4</sup>

Cell	Area ( $\mu\text{m}^2$ )	Mean area ( $\mu\text{m}^2$ )
C1	147 $\pm$ 6	127 $\pm$ 18
C2	119 $\pm$ 3	
C3	138 $\pm$ 5	
C4	104 $\pm$ 7	
C5	108 $\pm$ 3	138 $\pm$ 28
C6	123 $\pm$ 3	
C7	139 $\pm$ 9	
C8	180 $\pm$ 4	
C9	150 $\pm$ 5	130 $\pm$ 21
C10	87 $\pm$ 3	
C11	140 $\pm$ 4	
C12	128 $\pm$ 6	
C13	136 $\pm$ 4	
C14	122 $\pm$ 5	
C15	150 $\pm$ 8	
C16	223 $\pm$ 10	266 $\pm$ 34
C17	296 $\pm$ 13	
C18	280 $\pm$ 6	

**Table A22.** Pearson R-value and Spearman Rank Correlation between **Os** and **Br** in the cytoplasm, nucleus or whole cryo-fixed and freeze-dried A549 cells treated with 1-5×IC<sub>50</sub> of SS-2 (0-150 µM) as determined from the synchrotron-XRF maps (**Chapter 3**): **C5-7** (30 µM), **C9-15** (90 µM) and **C16-18** (150 µM). Data were analysed in triplicate using ImageJ.<sup>4</sup>

Cell	Pearson R-value			Spearman Rank Correlation		
	All	Cytoplasm	Nucleus	All	Cytoplasm	Nucleus
<b>C5</b>	0.45	0.13	-0.02	0.346	0.120	-0.022
<b>C6</b>	0.29	0.19	0.10	0.284	0.178	0.093
<b>C7</b>	0.15	0.21	0.00	0.125	0.206	-0.003
<b>C8</b>	0.42	0.42	0.04	0.364	0.364	-0.030
<b>C9</b>	0.48	0.42	-0.08	0.417	0.345	-0.073
<b>C10</b>	0.56	0.48	0.03	0.510	0.469	-0.031
<b>C11</b>	0.43	0.33	0.00	0.397	0.316	0.002
<b>C12</b>	0.43	0.38	-0.08	0.406	0.349	-0.079
<b>C13</b>	0.09	0.32	-0.05	0.139	0.301	-0.062
<b>C14</b>	0.24	0.39	-0.05	0.160	0.356	-0.043
<b>C15</b>	0.07	0.41	-0.11	0.074	0.423	-0.13
<b>C16</b>	0.22	0.18	0.08	0.214	0.172	0.043
<b>C17</b>	0.11	0.16	0.02	0.100	0.147	0.022
<b>C18</b>	0.22	0.17	0.04	0.139	0.159	0.031

**Table A23.** Pearson R-value and Spearman Rank Correlation between **Os** and **Zn** in the cytoplasm, nucleus or whole cryo-fixed and freeze-dried A549 cells treated with 1-5×IC<sub>50</sub> of SS-2 (0-150 µM) as determined from the synchrotron-XRF maps (**Chapter 3**): **C5-7** (30 µM), **C9-15** (90 µM) and **C16-18** (150 µM). Data were analysed in triplicate using ImageJ.<sup>4</sup>

Cell	Pearson R-value			Spearman Rank Correlation		
	All	Cytoplasm	Nucleus	All	Cytoplasm	Nucleus
<b>C5</b>	0.07	0.05	-0.03	0.077	0.049	-0.022
<b>C6</b>	0.02	0.00	0.00	0.014	-0.012	0.000
<b>C7</b>	0.00	-0.02	-0.01	-0.009	-0.018	-0.011
<b>C8</b>	-0.01	0.00	-0.02	0.002	-0.003	-0.025
<b>C9</b>	-0.03	-0.03	-0.03	-0.021	-0.040	-0.023
<b>C10</b>	0.06	0.03	-0.09	0.078	0.028	-0.084
<b>C11</b>	-0.03	-0.02	-0.01	-0.018	-0.027	-0.014
<b>C12</b>	-0.02	0.03	-0.02	-0.007	0.031	-0.017
<b>C13</b>	-0.15	0.03	-0.08	-0.145	0.025	-0.068
<b>C14</b>	-0.08	0.03	-0.03	-0.083	0.020	-0.032
<b>C15</b>	-0.02	0.03	-0.01	-0.015	0.014	-0.018
<b>C16</b>	-0.02	0.00	0.00	-0.022	-0.005	-0.003
<b>C17</b>	0.00	0.03	0.02	-0.002	0.020	0.024
<b>C18</b>	0.01	0.01	0.01	0.005	0.006	0.004

**Table A24.** Pearson R-value and Spearman Rank Correlation between **Br** and **Zn** in the cytoplasm, nucleus or whole cryo-fixed and freeze-dried A549 cells treated with 1-5×IC<sub>50</sub> of **SS-2** (0-150 µM) as determined from the synchrotron-XRF maps (**Chapter 3**): **C5-7** (30 µM), **C9-15** (90 µM) and **C16-18** (150 µM). Data were analysed in triplicate using ImageJ.<sup>4</sup>

Cell	Pearson R-value			Spearman Rank Correlation		
	All	Cytoplasm	Nucleus	All	Cytoplasm	Nucleus
<b>C5</b>	0.36	0.13	0.06	0.342	0.128	0.049
<b>C6</b>	0.18	0.05	0.07	0.176	0.054	0.068
<b>C7</b>	0.16	0.06	0.07	0.168	0.063	0.024
<b>C8</b>	0.18	0.03	0.11	0.192	0.038	0.094
<b>C9</b>	0.11	0.05	0.08	0.126	0.046	0.097
<b>C10</b>	0.28	0.12	0.17	0.286	0.118	0.172
<b>C11</b>	0.09	0.00	0.08	0.104	-0.001	0.077
<b>C12</b>	0.21	0.11	0.13	0.207	0.105	0.116
<b>C13</b>	0.33	0.08	0.22	0.278	0.077	0.204
<b>C14</b>	0.17	0.08	0.08	0.185	0.079	0.087
<b>C15</b>	0.26	0.09	0.08	0.246	0.088	0.081
<b>C16</b>	0.29	0.21	0.05	0.214	0.173	0.043
<b>C17</b>	0.10	0.16	0.02	0.099	0.147	0.022
<b>C18</b>	0.22	0.17	0.04	0.139	0.158	0.031

**Table A25.** Membrane integrity analysis determined by flow cytometry for a normalized population of A549 cells pre-incubated with either medium alone or with added chloroquine diphosphate (**CQ**, 150 µM) for 2 h, followed by treatment with 1×IC<sub>50</sub> **RR-1** or **SS-2** for 24 h, with no recovery (**Chapter 3**). P-values were determined using Welch's unpaired t-test, assuming unequal variables.

Conditions	Viable membrane (FL2-)	Non-viable membrane (FL2+)
Untreated (control)	99.51±0.05	0.49±0.05
<b>CQ</b> (control)	99.43±0.11	0.57±0.11
<b>1</b>	98.92±0.13	1.08±0.13
<b>1 + CQ</b>	98.78±0.16	1.22±0.16
<b>2</b>	98.31±0.02	1.69±0.02
<b>2 + CQ</b>	99.05±0.05	0.95±0.05



**Table A26.** The average calculated volumes ( $\mu\text{m}^3$ ) of individually segmented mitochondria in cryopreserved PC3 cells grown on carbon-gold TEM grids and treated with 0-1  $\mu\text{M}$  of **7** for 2 h (protected from light), followed by 10 min in the dark or irradiated with blue light ( $\lambda=465$  nm, 4.8 mW/cm<sup>2</sup>), followed by 24 h recovery in complex-free media. One tomogram from each condition was volume segmented (**T1-4, Chapter 4**). Data were acquired in SuRVoS imaging software.<sup>5</sup> A total number of mitochondria per tomogram were determined to be: (i) **T1**=14; (ii) **T2**=20; (iii) **T3**=26; (iv) **T4**=19.

3D volume ( $\mu\text{m}^3$ )				
Mitochondria number	Untreated control (Dark) <sup>[a]</sup>	Untreated control ( $\lambda = 465$ nm) <sup>[b]</sup>	Treated (Dark) <sup>[c]</sup>	Treated ( $\lambda = 465$ nm) <sup>[d]</sup>
1	1.193	0.785	1.444	0.0693
2	0.725	0.638	1.454	0.0498
3	0.401	0.952	1.001	0.0588
4	2.221	1.393	0.864	0.1010
5	4.405	1.132	0.733	0.1249
6	0.252	0.481	1.283	0.1211
7	0.553	0.568	0.384	0.0922
8	0.258	0.368	1.217	0.0739
9	0.167	0.619	0.564	0.0455
10	0.945	0.494	0.236	0.1030
11	0.228	1.293	0.223	0.0558
12	0.361	0.638	0.914	0.1197
13	1.650	0.304	1.348	0.0463
14	0.312	0.204	0.609	0.0898
15		0.292	0.410	0.0615
16		1.019	0.722	0.0991
17		0.562	1.197	0.0942
18		0.702	0.602	0.0693
19		0.313	1.026	0.0693
20		0.315	0.511	
21			0.479	
22			0.569	
23			0.207	
24			0.487	
25			0.748	
26			0.656	
Mean	0.98±1.2	0.65±0.35	0.77±0.38	0.08±0.03

<sup>[a]</sup> Exposed to 2 h protected from the light, followed by 24 h recovery in complex-free media. <sup>[b]</sup> Exposed to 10 min irradiation (465 nm, 4.8 mW/cm<sup>2</sup>) followed by 24 h recovery in complex-free media. <sup>[c]</sup> Exposed to 1  $\mu\text{M}$  of **7** for 2 h, followed by 10 min (protected from light) and 24 h recovery in complex-free medium. <sup>[d]</sup> Exposed to 1  $\mu\text{M}$  of **7** for 2 h, followed by 10 min irradiation (465 nm, 4.8 mW/cm<sup>2</sup>) and 24 h recovery in complex-free medium

**Table A27.** The cell areas ( $\mu\text{m}^2$ ) and roundness factors coefficients of cryo-fixed and freeze-dried A549 lung cancer cells treated with 0 (**C1-3**) or  $5\times\text{IC}_{50}$  (**C4-6**) of **8** (500  $\mu\text{M}$ , 2 h) under dark conditions as determined from the K, S, P and Zn synchrotron-XRF elemental maps (**Chapter 4**). Data were analysed in triplicate in ImageJ.<sup>4</sup>

Cell	Area ( $\mu\text{m}^2$ )	Mean area ( $\mu\text{m}^2$ )	Roundness factor	Mean roundness
<b>C1</b>	540 $\pm$ 18	438 $\pm$ 82	0.43 $\pm$ 0.05	0.37 $\pm$ 0.07
<b>C2</b>	415 $\pm$ 11		0.40 $\pm$ 0.02	
<b>C3</b>	361 $\pm$ 32		0.29 $\pm$ 0.02	
<b>C4</b>	378 $\pm$ 13	407 $\pm$ 31	0.87 $\pm$ 0.02	0.81 $\pm$ 0.08
<b>C5</b>	427 $\pm$ 34		0.85 $\pm$ 0.03	
<b>C6</b>	418 $\pm$ 21		0.71 $\pm$ 0.05	

**Table A28.** The Pearson R-value statistical co-localization between Ir, Pt and Zn in cryo-fixed and freeze-dried A549 lung cancer cells treated with **8** (500  $\mu\text{M}$ , 2 h) under dark conditions as determined from the elemental synchrotron-XRF maps (**Chapter 4**). Data were analysed in triplicate in ImageJ software.<sup>4</sup>

Cell	Ir-Zn	Mean Ir-Zn	Pt-Zn	Mean Pt-Zn	Ir-Pt	Mean Ir-Pt
<b>C4</b>	0.20	0.33 $\pm$ 0.12	0.59	0.65 $\pm$ 0.05	0.44	0.51 $\pm$ 0.10
<b>C5</b>	0.38		0.66		0.47	
<b>C6</b>	0.42		0.69		0.63	

**Table A29.** The Spearman Rank Correlation statistical co-localization between Ir or Pt with Zn in cryopreserved and freeze-dried A549 lung cancer cells treated with **8** (500  $\mu\text{M}$ , 2 h) under dark conditions as determined from the synchrotron-XRF elemental maps (**Chapter 4**). Data were analysed in triplicate in ImageJ software.<sup>4</sup>

Cell	Ir-Zn	Mean Ir-Zn	Pt-Zn	Mean Pt-Zn	Ir-Pt	Mean Ir-Pt
<b>C4</b>	0.17	0.26 $\pm$ 0.08	0.49	0.55 $\pm$ 0.08	0.36	0.44 $\pm$ 0.07
<b>C5</b>	0.30		0.64		0.48	
<b>C6</b>	0.32		0.53		0.49	

**Table A30.** The mole fraction quantities and molar platinum-to-iridium ratios (Pt/Ir) in cryo-fixed and freeze-dried A549 lung cancer cells treated with **8** (500  $\mu\text{M}$ , 2 h) under dark conditions as determined from the K, S, P and Zn synchrotron-XRF elemental maps (**Chapter 4**). Data were analysed in triplicate in ImageJ software.<sup>4</sup>

Cell	Pt mole fraction / $10^{-8}$	Mean area ( $\mu\text{m}^2$ )	Ir mole fraction / $10^{-8}$	Mean roundness factor	Pt / Ir ratio
<b>C4</b>	0.75 $\pm$ 0.01		0.182 $\pm$ 0.001		4.13
<b>C5</b>	1.03 $\pm$ 0.02	0.97 $\pm$ 17	0.223 $\pm$ 0.004	0.23 $\pm$ 0.04	4.62
<b>C6</b>	1.12 $\pm$ 0.03		0.271 $\pm$ 0.003		4.15

**Table A31.** Individual lengths and mean lengths ( $\mu\text{m}$ ) of the dark, elongated cytoplasmic organelles identified from the Differential Phase Contrast Images of cryo-fixed and freeze-dried A549 cells treated with **8** (500  $\mu\text{M}$ , 2 h) under dark conditions (**Chapter 4**). Data were analysed in ImageJ software.<sup>4</sup>

Number	Organelle length ( $\mu\text{m}$ )		
	C4	C5	C6
<b>1</b>	2.04 $\pm$ 0.08	3.08 $\pm$ 0.12	2.73 $\pm$ 0.13
<b>2</b>	1.22 $\pm$ 0.04	4.14 $\pm$ 0.10	2.79 $\pm$ 0.07
<b>3</b>	1.60 $\pm$ 0.05	2.20 $\pm$ 0.03	3.66 $\pm$ 0.09
<b>4</b>	0.98 $\pm$ 0.11	1.55 $\pm$ 0.04	2.87 $\pm$ 0.11
<b>5</b>	1.24 $\pm$ 0.07	2.67 $\pm$ 0.04	2.43 $\pm$ 0.16
<b>6</b>	0.76 $\pm$ 0.07	1.86 $\pm$ 0.09	1.66 $\pm$ 0.09
<b>7</b>	0.94 $\pm$ 0.12	2.07 $\pm$ 0.02	1.86 $\pm$ 0.07
<b>8</b>	0.98 $\pm$ 0.13	2.15 $\pm$ 0.03	3.12 $\pm$ 0.14
<b>9</b>	1.04 $\pm$ 0.08	5.14 $\pm$ 0.12	
<b>Mean</b>	1.2 $\pm$ 0.4	2.8 $\pm$ 1.1	2.6 $\pm$ 0.6

**Table A32.** Individual and mean areas ( $\mu\text{m}^2$ ) of the dark, elongated cytoplasmic organelles identified from the DPC images of cryopreserved and freeze-dried A549 cells treated with **8** (500  $\mu\text{M}$ , 2 h) under dark conditions (**Chapter 4**). Data were analysed in ImageJ software.<sup>4</sup>

Number	Organelle area ( $\mu\text{m}^2$ )		
	C4	C5	C6
<b>1</b>	2.83 $\pm$ 0.23	2.26 $\pm$ 0.15	2.41 $\pm$ 0.25
<b>2</b>	1.66 $\pm$ 0.19	2.59 $\pm$ 0.26	3.98 $\pm$ 0.38
<b>3</b>	1.99 $\pm$ 0.22	2.04 $\pm$ 0.27	1.86 $\pm$ 0.17
<b>4</b>	1.432 $\pm$ 0.30	0.59 $\pm$ 0.11	1.66 $\pm$ 0.19
<b>5</b>	0.86 $\pm$ 0.14	2.31 $\pm$ 0.34	1.41 $\pm$ 0.16
<b>6</b>	1.04 $\pm$ 0.11	1.15 $\pm$ 0.19	1.04 $\pm$ 0.14
<b>7</b>	1.00 $\pm$ 0.23	0.81 $\pm$ 0.22	1.07 $\pm$ 0.12
<b>8</b>	0.98 $\pm$ 0.31	0.93 $\pm$ 0.10	
<b>9</b>	1.25 $\pm$ 0.28		
<b>Mean</b>	1.5 $\pm$ 0.6	1.6 $\pm$ 0.8	1.9 $\pm$ 1.0

**Table A33.** Individual and mean mitochondrial volumes in cryopreserved PC3 cells treated with  $0.25-1 \times \text{IC}_{50}$  of **12** under dark (2 h) or blue light (1 h exposure + 1 h 465 nm conditions, **T1-15; T18-20**) as determined in SuRVoS (**Chapter 5**).<sup>5</sup> A minimum of 10 mitochondria per tomogram were segmented.

<b>T1</b>	<b>T2</b>	<b>T3</b>	<b>T4</b>	<b>T5</b>	<b>T6</b>
0.20	0.18	0.53	0.24	0.17	0.11
0.49	0.21	0.42	0.14	0.12	0.05
0.28	0.19	0.22	0.10	0.08	0.17
0.09	0.26	0.25	0.17	0.13	0.21
0.14	0.38	0.17	0.17	0.08	0.14
0.17	0.20	0.58	0.09	0.16	0.10
0.27	0.11	0.45	0.15	0.04	0.11
0.34	0.12	0.31	0.11	0.10	0.30
0.33	0.12	0.32	0.04	0.08	0.09
0.17	0.13	0.29	0.10	0.10	0.23
0.25±0.12	0.19±0.08	0.35±0.14	0.13±0.06	0.11±0.04	0.15±0.08
<b>T7</b>	<b>T8</b>	<b>T9</b>	<b>T10</b>	<b>T11</b>	<b>T12</b>
0.06	0.05	0.05	0.03	0.35	0.09
0.08	0.34	0.19	0.04	0.24	0.14
0.26	0.08	0.30	0.06	0.28	0.13
0.09	0.07	0.15	0.07	0.20	0.15
0.09	0.21	0.21	0.11	0.21	0.07
0.12	0.08	0.07	0.15	0.15	0.09
0.06	0.08	0.15	0.19	0.17	0.19
0.09	0.19	0.04	0.23	0.21	0.28
0.05	0.07	0.07	0.12	0.29	0.05
0.05	0.13	0.03	0.16	0.27	0.13
0.09±0.06	0.13±0.09	0.13±0.09	0.12±0.07	0.24±0.06	0.13±0.07
<b>T13</b>	<b>T14</b>	<b>T15</b>	<b>T18</b>	<b>T19</b>	<b>T20</b>
0.05	0.11	0.12	0.12	0.35	
0.11	0.14	0.13	0.03	0.15	
0.14	0.20	0.14	0.08	0.07	
0.07	0.13	0.08	0.09	0.30	
0.06	0.30	0.07	0.14	0.12	
0.11	0.17	0.09	0.08	0.12	
0.02	0.21	0.06	0.10	0.04	
0.06	0.23	0.05	0.11	0.07	
0.04	0.13	0.04	0.05	0.06	
0.04	0.11	0.07	0.05	0.11	
0.07±0.04	0.17±0.06	0.08±0.03	0.09±0.03	0.14±0.10	

**Table A34.** Individual and mean lipid droplet volumes in cryopreserved PC3 cells treated with  $0.25-1 \times IC_{50}$  of **12** under dark (2 h) or blue light (1 h exposure and 1 h 465 nm) conditions (**T1-20**) as determined in SuRVoS (**Chapter 5**).<sup>5</sup> A minimum of 6 lipid droplets per tomogram were segmented.

<b>T1</b>	<b>T2</b>	<b>T3</b>	<b>T4</b>	<b>T5</b>	<b>T6</b>	<b>T7</b>
0.11	0.12	0.18	0.14	0.12	0.23	0.04
0.09	0.10	0.13	0.12	0.09	0.10	0.05
0.05	0.08	0.14	0.16	0.07	0.17	0.04
0.05	0.09	0.26	0.24	0.09	0.09	0.04
0.07	0.08	0.38	0.15	0.07	0.12	0.07
0.06	0.09	0.31	0.10	0.12	0.12	0.04
0.07±0.02	0.09±0.02	0.23±0.01	0.15±0.05	0.09±0.02	0.14±0.05	0.05±0.01
<b>T8</b>	<b>T9</b>	<b>T10</b>	<b>T11</b>	<b>T12</b>	<b>T13</b>	<b>T14</b>
0.32	0.02	0.04	0.11	0.12	0.17	0.14
0.26	0.03	0.05	0.29	0.15	0.17	0.11
0.24	0.02	0.05	0.20	0.23	0.13	0.15
0.18	0.03	0.04	0.20	0.12	0.16	0.09
0.20	0.03	0.06	0.20	0.12	0.11	0.16
0.33	0.04	0.04	0.21	0.18	0.13	0.11
0.25±0.06	0.03±0.01	0.05±0.01	0.15±0.04	0.20±0.06	0.15±0.06	0.13±0.03
<b>T15</b>	<b>T16</b>	<b>T17</b>	<b>T18</b>	<b>T19</b>		
0.04	0.05	0.05	0.11	0.09		
0.04	0.03	0.01	0.03	0.09		
0.02	0.03	0.02	0.09	0.11		
0.02	0.01	0.04	0.15	0.05		
0.05	0.02	0.03	0.14	0.10		
0.02	0.02	0.01	0.13	0.01		
0.03±0.02	0.03±0.01	0.03±0.01	0.11±0.04	0.07±0.04		

**Table A35.** Volumes ( $\mu\text{m}^3$ ) of endosome-like structures observed in two independent cryopreserved PC3 cells treated with  $1\times$  irradiated  $\text{IC}_{50}$  ( $6.48\pm 0.84\ \mu\text{M}$ ) of **12** for 2 h under dark conditions (**T7** and **T9**, respectively). Data were analysed in SuRVoS (**Chapter 5**).<sup>5</sup>

Number	Endosomal volume ( $\mu\text{m}^3$ )	
	T7	T9
1	0.58	0.99
2	0.53	0.42
3	0.19	0.20
4	0.17	0.37
5	0.39	0.21
6	0.33	0.19
7	0.21	0.33
8	0.24	0.38
9	0.16	0.27
10	0.23	0.19
11	0.14	0.26
12	0.09	0.13
13	0.31	
14	0.23	
15	0.30	
16	0.21	
17	0.16	
Mean	$0.26\pm 0.13$	$0.33\pm 0.23$

**Table A36.** Pearson's R-values and Spearman Rank coefficients between Pt and Zn in cryo-fixed and freeze-dried PC3 cells treated with  $5\times$  irradiated  $\text{IC}_{50}$  of **11** ( $\text{IC}_{50}=55.6\pm 0.9\ \mu\text{M}$ ), **12** ( $\text{IC}_{50}=6.48\pm 0.84\ \mu\text{M}$ ) or **cisplatin** ( $\text{IC}_{50}> 100\ \mu\text{M}$ ) under both dark (2 h) or irradiated conditions (1 h exposure 1 h 465 nm,  $4.8\ \text{mW}/\text{cm}^2$ ), as determined from the synchrotron-XRF maps (**Chapter 5**). Data were analysed in ImageJ.<sup>4</sup>

Conditions	Cell number	Pearson's R-value	Spearman rank coefficient
<b>10</b> (Dark)	<b>C4</b>	0.23	0.17
	<b>C5</b>	0.20	0.12
	<b>C6</b>	0.14	0.11
<b>10</b> (465 nm)	<b>C7</b>	0.49	0.44
	<b>C8</b>	0.42	0.38
	<b>C9</b>	0.40	0.41
<b>11</b> (Dark)	<b>C10</b>	0.35	0.38
	<b>C11</b>	0.29	0.24
	<b>C12</b>	0.37	0.34
<b>11</b> (465 nm)	<b>C13</b>	0.48	0.46
	<b>C14</b>	0.63	0.57
	<b>C15</b>	0.62	0.59
<b>Cisplatin</b>	<b>C16</b>	0.30	0.31
	<b>C17</b>	0.38	0.36
	<b>C18</b>	0.33	0.35

**Table A37.** Proposed method for assessing sample beam damage during XANES mapping using a nano-focussed beamline, specifically in cryo-fixed and dried cells treated with photoactivatable drugs.

Step	Overview	Experiment
1	Test the limits of x-ray beam exposure on the sample (e.g. what exposure time damages the sample)	Expose cell sample to long exposure times (at the desired resolution and energy) until visible damage to the cell morphology is observed. This can be performed by obtaining brightfield microscopy images of specific cells before and after beam exposure.
2	Identify the beam exposure time at which the cell morphology is <i>not</i> damaged	Once the ultimate limit of beam damage is known, lower exposure times can be used to determine the maximum x-ray exposure time which does not damage the cell morphology.
3	Assess whether the elemental distribution and quantification at this maximal x-ray exposure is the same as those in cells exposed for shorter periods.	Analyse the differences in the distribution of endogenous elements (Fe, Zn, S, P, K etc.) in addition to the exogenous complex being investigated (e.g. Pt, Ir, Os). Additionally, estimate the quantity of these elements using an AXO standard to assess any differences. From this, the x-ray exposure time which does not damage the cell morphology OR affect the elemental distribution or elemental quantities can be determined.
4	Assess whether the chemical speciation of the element of interest changes (e.g. Pt, Ir, Os) at the edge of interest at this x-ray exposure.	Perform XANES mapping at this x-ray exposure over the edge of interest, and at lower x-ray exposures to determine whether the chemical speciation changes at higher exposures. From this, a suitable x-ray exposure can be determined for the experiment.
5	For photoactivatable drugs in which light may alter the oxidation state, solid pellets of the “inactive” and “active” drug can be prepared.	“Dark” solid pellets protected from the light should be analysed at the optimised x-ray exposure using both the full beam or the nano-focussed beam (XANES mapping) to determine whether the oxidation state changes throughout analysis. This will allow identification of the x-ray exposure at which the chemical speciation changes as a result of repeated beam exposure, thus, the point at which the results become invalid. The “irradiated” slid pellet (irradiated with UV/Vis light prior to XANES mapping) should also be analysed to determine when the x-ray beam changes the elemental speciation.
6	Start the experiment	Perform XANES mapping on regions of interest in cells against solid pellets of known oxidation state using the optimized x-ray exposure time.

## Figures A1-A23

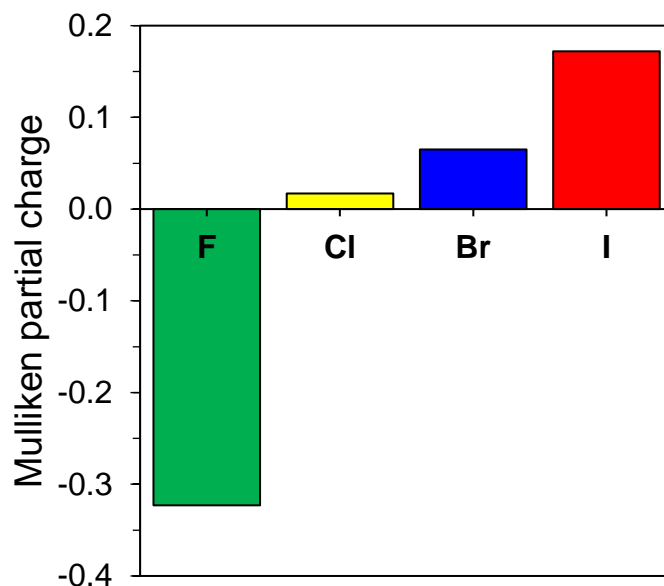


**Figure A1.** Mulliken partial charges calculated for halide atom (X) in complexes **RR-6** (X=F), **theoretical compound (EB1, X=Cl)**, **RR-2** (X=Br) and **RR-3** (X=I), at the PBE0/Lanl2DZ/6-31+G\*\* level of theory (**Chapter 3**).

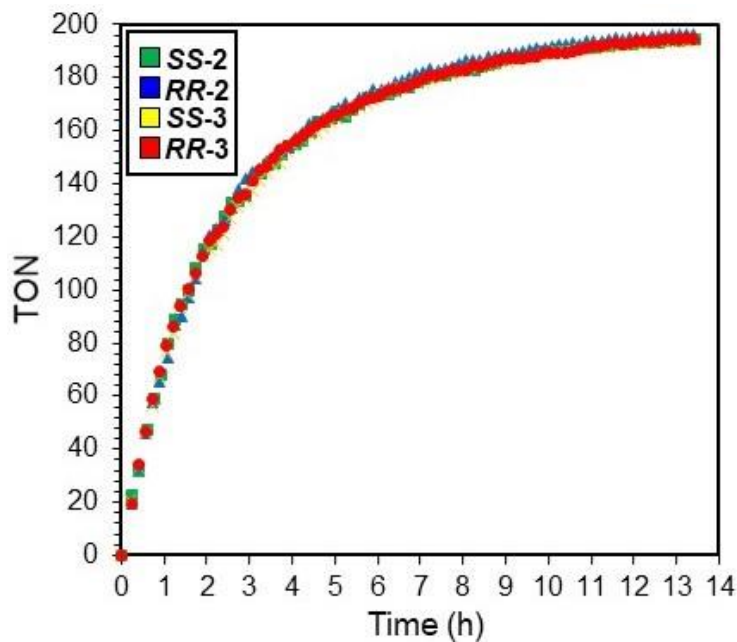


**Figure A2.** The  $^1\text{H}$  NMR catalytic turnover number (TON) of acetophenone to (*S*) or (*R*)-1-phenylethanol for complexes **SS/RR-2** (*p*-Br) and **SS/RR-3** (*p*-I) over 14 h (310 K) in the presence of 5:2 formic acid/TEA azeotrope and  $\text{d}_6$ -benzene (**Chapter 3**).



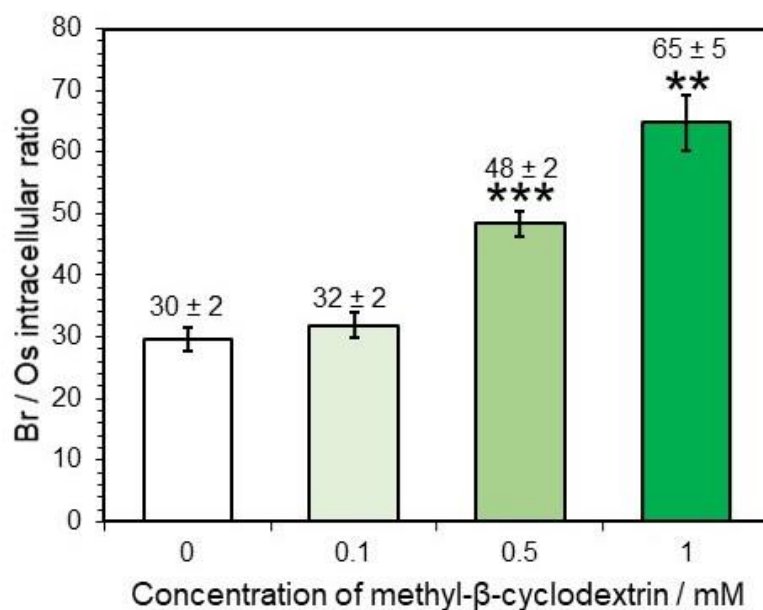


**Figure A3.** The intracellular bromine-to-osmium (Br/Os) molar ratios calculated for A549 (human lung) cancer cells treated with  $1 \times \text{IC}_{50}$  **SS-2** ( $30.8 \pm 1.6 \mu\text{M}$ ) upon co-administration with 0-1 mM methyl-β-cyclodextrin for 24 h (**Chapter 3**). Statistical analysis was performed using the Welch's unpaired t-test, assuming unequal variances, and compared to untreated control (0  $\mu\text{M}$  methyl-β-cyclodextrin).

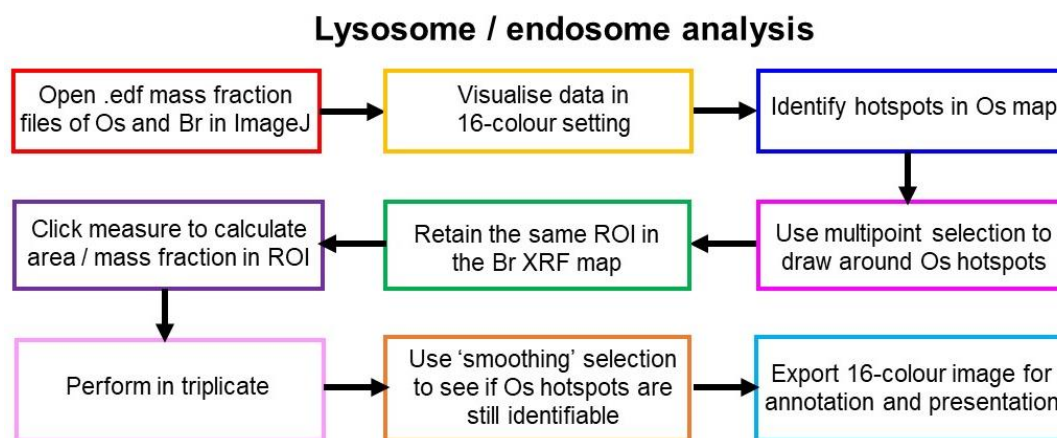


**Figure A4.** Workflow for the analysis of lysosomes / endosomal structures from the XRF elemental maps of A549 cells treated with **2** (**Chapter 3**). Firstly, the fitted and calibrated .edf mass fraction files of both Os and Br were opened in ImageJ software and visualised using 16-colour imaging setting. Hotspots of Os were identified as ROI using the multipoint selection tool. The same ROI was identified in the Br map (Edit>Selection>Retain Selection). The area ( $\mu\text{m}^2$ ) and mass fraction of each ROI were measured (Analyze>Measure) for both Os and Br, and performed in triplicate. After this, the 'smoothing' selection tool was used (Process>Smooth), which replaces each pixel with the average of its  $3 \times 3$  neighbours (blurs the image). This is to see if the Os hotspots are still clearly visible and reaffirm the ROI selection. For presentation and printing purposes, the 'smoothed' 16-colour image was exported.

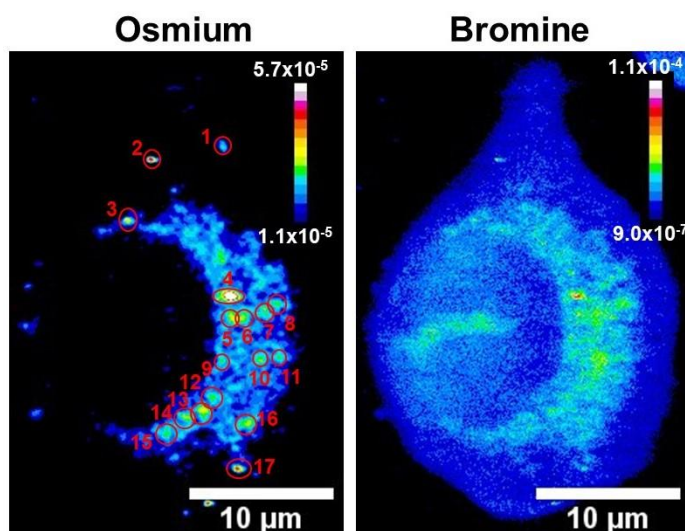


**Figure A5.** Synchrotron-XRF elemental maps of a cryo-fixed and freeze-dried A549 (human lung) cancer cell (C9) treated with  $3 \times \text{IC}_{50}$  of **SS-2** (90  $\mu\text{M}$ ) for 24 h (no recovery) as represented in 16-colour setting in ImageJ,<sup>4</sup> showing small vesicle-sized co-localisation of Os and Br (**Chapter 3**) as represented identified with red circles. Images were prepared in ImageJ using the 16-colour settings, using the multipoint selections tools to identify small compartments. Data were acquired using 15 keV energy, 0.1 s exposure, 100 nm stepsize with *ca.*  $50 \times 70 \text{ nm}^2$  beam size. Data were analysed in PyMCA software,<sup>6</sup> and images generated in ImageJ.<sup>7</sup> Note that, the presented images are shown as using the smoothing tool for clarity and presentation purposes, but all analysis was performed on the original pixelated mass fraction image. See Appendix **Fig. A12** for more information. A total of 17 lysosomes were identified with an average area of  $0.63 \pm 0.29 \mu\text{m}^2$  and a calculated average bromine-to-osmium (Br/Os) ratio of  $3.4 \pm 0.4$ .

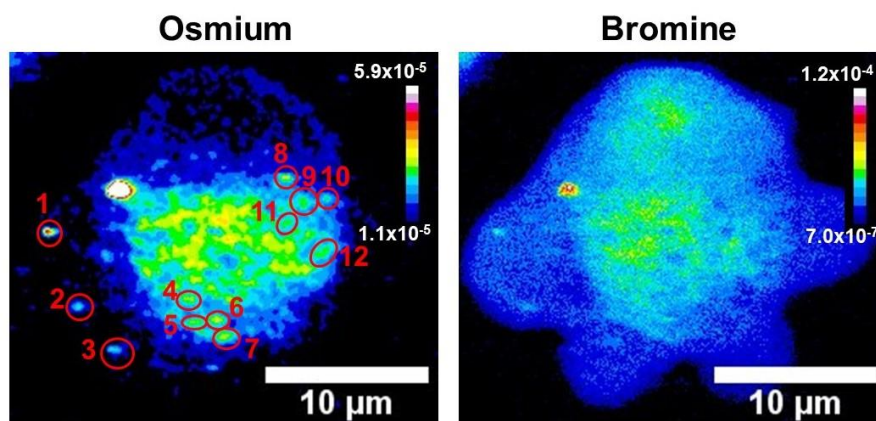


**Figure A6.** Synchrotron-XRF elemental maps of a cryo-fixed and freeze-dried A549 cell (C10) treated with  $3 \times \text{IC}_{50}$  of **SS-2** (90  $\mu\text{M}$ ) for 24 h (no recovery) as represented in 16-colour setting in ImageJ,<sup>4</sup> showing small vesicle-sized co-localisation of Os and Br (**Chapter 3**) as represented identified with red circles. Images were prepared in ImageJ using the 16-colour settings, using the multipoint selections tools to identify small compartments. Data were acquired using 15 keV energy, 0.1 s exposure, 100 nm stepsize with *ca.*  $50 \times 70 \text{ nm}^2$  beam size. Data were analysed in PyMCA software,<sup>6</sup> and images generated in ImageJ.<sup>7</sup> Note that, the presented images are shown as using the smoothing tool for clarity and presentation purposes, but all analysis was performed on the original pixelated mass fraction image. See Appendix **Fig. A12** for more information. A total of 12 lysosomes were identified with an average area of  $0.57 \pm 0.23 \mu\text{m}^2$  and a calculated average bromine-to-osmium (Br/Os) ratio of  $3.1 \pm 0.6$ .

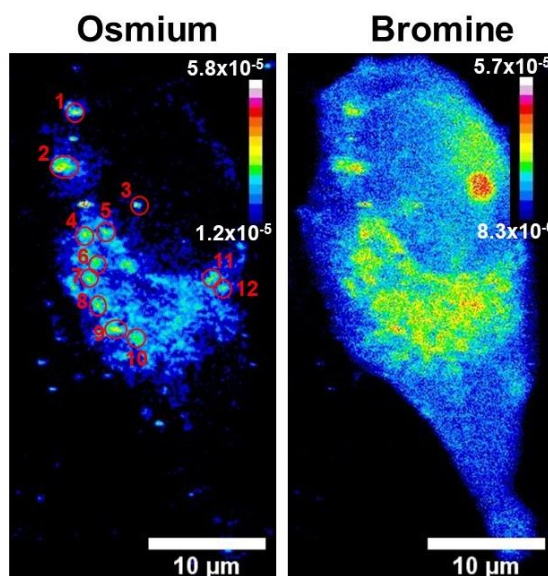


**Figure A7.** Synchrotron-XRF elemental maps of a cryo-fixed and freeze-dried A549 cell (C11) treated with  $3 \times \text{IC}_{50}$  of **SS-2** (90  $\mu\text{M}$ ) for 24 h (no recovery) as represented in 16-colour setting in ImageJ,<sup>4</sup> showing small vesicle-sized co-localisation of Os and Br (**Chapter 3**) as represented identified with red circles. Images were prepared in ImageJ using the 16-colour settings, using the multipoint selections tools to identify small compartments. Data were acquired using 15 keV energy, 0.1 s exposure, 100 nm stepsize with *ca.*  $50 \times 70 \text{ nm}^2$  beam size. Data were analysed in PyMCA software,<sup>6</sup> and images generated in ImageJ.<sup>7</sup> Note that, the presented images are shown as using the smoothing tool for clarity and presentation purposes, but all analysis was performed on the original pixelated mass fraction image. See Appendix **Fig. A12** for more information. A total of 12 lysosomes were identified with an average area of  $0.70 \pm 0.17 \mu\text{m}^2$  and a calculated average bromine-to-osmium (Br/Os) ratio of  $2.6 \pm 0.3$ .

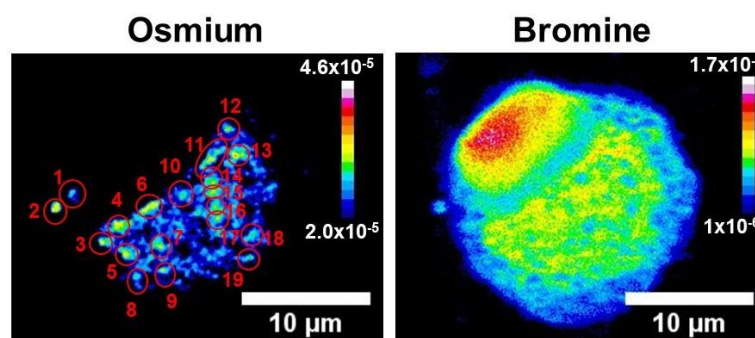


**Figure A8.** Synchrotron-XRF elemental maps of a cryo-fixed and freeze-dried A549 cell (C12) treated with  $3 \times \text{IC}_{50}$  of **SS-2** (90  $\mu\text{M}$ ) for 24 h (no recovery) as represented in 16-colour setting in ImageJ,<sup>4</sup> showing small vesicle-sized co-localisation of Os and Br (**Chapter 3**) as represented identified with red circles. Images were prepared in ImageJ using the 16-colour settings, using the multipoint selections tools to identify small compartments. Data were acquired using 15 keV energy, 0.1 s exposure, 100 nm stepsize with *ca.*  $50 \times 70 \text{ nm}^2$  beam size. Data were analysed in PyMCA software,<sup>6</sup> and images generated in ImageJ.<sup>7</sup> Note that, the presented images are shown as using the smoothing tool for clarity and presentation purposes, but all analysis was performed on the original pixelated mass fraction image. See Appendix **Fig. A12** for more information. A total of 19 lysosomes were identified with an average area of  $0.67 \pm 0.19 \mu\text{m}^2$  and a calculated average bromine-to-osmium (Br/Os) ratio of  $5.7 \pm 0.8$ .



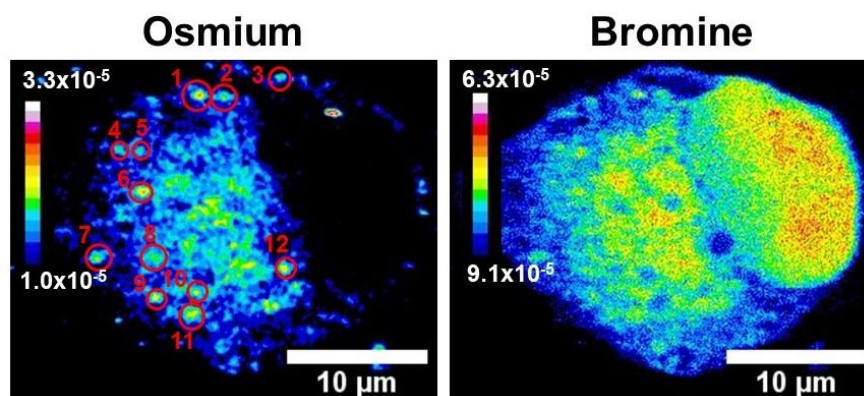


**Figure A9.** Synchrotron-XRF elemental maps of a cryo-fixed and freeze-dried A549 cell (C15) treated with  $3\times\text{IC}_{50}$  (90  $\mu\text{M}$ ) of *SS-2* for 24 h (no recovery) as represented in 16-colour setting in ImageJ,<sup>4</sup> showing small vesicle-sized co-localisation of Os and Br (Chapter 3) as represented identified with red circles. Images were prepared in ImageJ using the 16-colour settings, using the multipoint selections tools to identify small compartments. Data were acquired using 15 keV energy, 0.1 s exposure, 100 nm stepsize with *ca.*  $50\times 70\text{ nm}^2$  beam size. Data were analysed in PyMCA software,<sup>6</sup> and images generated in ImageJ.<sup>7</sup> Note that, the presented images are shown as using the smoothing tool for clarity and presentation purposes, but all analysis was performed on the original pixelated mass fraction image. See Appendix Fig. A12 for more information. A total of 12 lysosomes were identified with an average area of  $0.58\pm 0.18\text{ }\mu\text{m}^2$  and a calculated average bromine-to-osmium (Br/Os) ratio of  $3.6\pm 0.4$ .

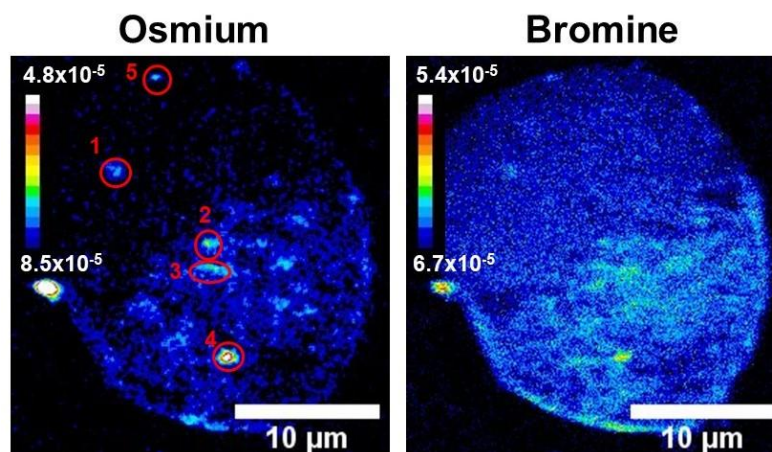


**Figure A10.** Synchrotron-XRF elemental maps of a cryo-fixed and freeze-dried A549 cell (C16) treated with  $5\times\text{IC}_{50}$  (90  $\mu\text{M}$ ) of *SS-2* for 24 h (no recovery) as represented in 16-colour setting in ImageJ,<sup>4</sup> showing small vesicle-sized co-localisation of Os and Br (Chapter 3) as represented identified with red circles. Images were prepared in ImageJ using the 16-colour settings, using the multipoint selections tools to identify small compartments. Data were acquired using 15 keV energy, 0.1 s exposure, 100 nm stepsize with *ca.*  $50\times 70\text{ nm}^2$  beam size. Data were analysed in PyMCA software,<sup>6</sup> and images generated in ImageJ.<sup>7</sup> Note that, the presented images are shown as using the smoothing tool for clarity and presentation purposes, but all analysis was performed on the original pixelated mass fraction image. See Appendix Fig. A12 for more information. A total of 12 lysosomes were identified with an average area of  $0.84\pm 0.42\text{ }\mu\text{m}^2$  and a calculated average bromine-to-osmium (Br/Os) ratio of  $1.57\pm 0.14$ .

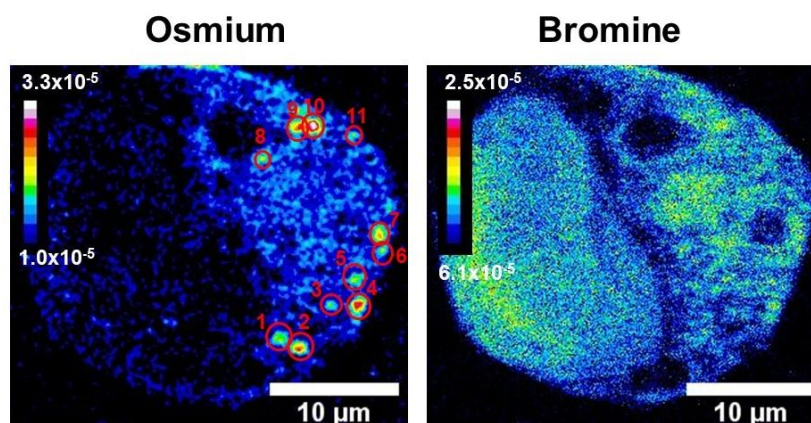


**Figure A11.** Synchrotron-XRF elemental maps of a cryo-fixed and freeze-dried A549 cell (C17) treated with  $5 \times \text{IC}_{50}$  (150  $\mu\text{M}$ ) of SS-2 for 24 h (no recovery) as represented in 16-colour setting in ImageJ,<sup>4</sup> showing small vesicle-sized co-localisation of Os and Br (Chapter 3) as represented identified with red circles. Images were prepared in ImageJ using the 16-colour settings, using the multipoint selections tools to identify small compartments. Data were acquired using 15 keV energy, 0.1 s exposure, 100 nm stepsize with *ca.*  $50 \times 70 \text{ nm}^2$  beam size. Data were analysed in PyMCA software,<sup>6</sup> and images generated in ImageJ.<sup>7</sup> Note that, the presented images are shown as using the smoothing tool for clarity and presentation purposes, but all analysis was performed on the original pixelated mass fraction image. See Appendix Fig. A12 for more information. A total of 11 lysosomes were identified with an average area of  $0.80 \pm 0.28 \mu\text{m}^2$  and a calculated average bromine-to-osmium (Br/Os) ratio of  $1.53 \pm 0.12$ .

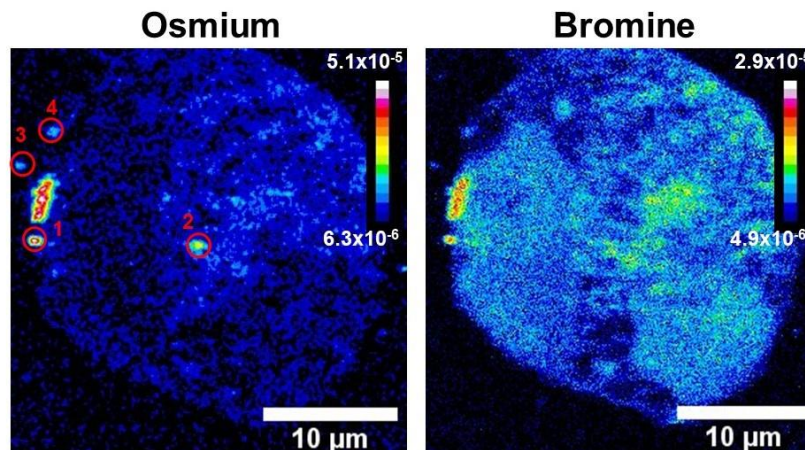


**Figure A12.** Synchrotron-XRF elemental maps of a cryo-fixed and freeze-dried A549 cell (C18) treated with  $5 \times \text{IC}_{50}$  (150  $\mu\text{M}$ ) of SS-2 for 24 h (no recovery) as represented in 16-colour setting in ImageJ,<sup>4</sup> showing small vesicle-sized co-localisation of Os and Br (Chapter 3) as represented identified with red circles. Images were prepared in ImageJ using the 16-colour settings, using the multipoint selections tools to identify small compartments. Data were acquired using 15 keV energy, 0.1 s exposure, 100 nm stepsize with *ca.*  $50 \times 70 \text{ nm}^2$  beam size. Data were analysed in PyMCA software,<sup>6</sup> and images generated in ImageJ.<sup>7</sup> Note that, the presented images are shown as using the smoothing tool for clarity and presentation purposes, but all analysis was performed on the original pixelated mass fraction image. See Appendix Fig. A12 for more information. A total of 2 lysosomes were identified with an average area of  $0.63 \pm 0.05 \mu\text{m}^2$  and a calculated average bromine-to-osmium (Br/Os) ratio of  $1.24 \pm 0.13$ .



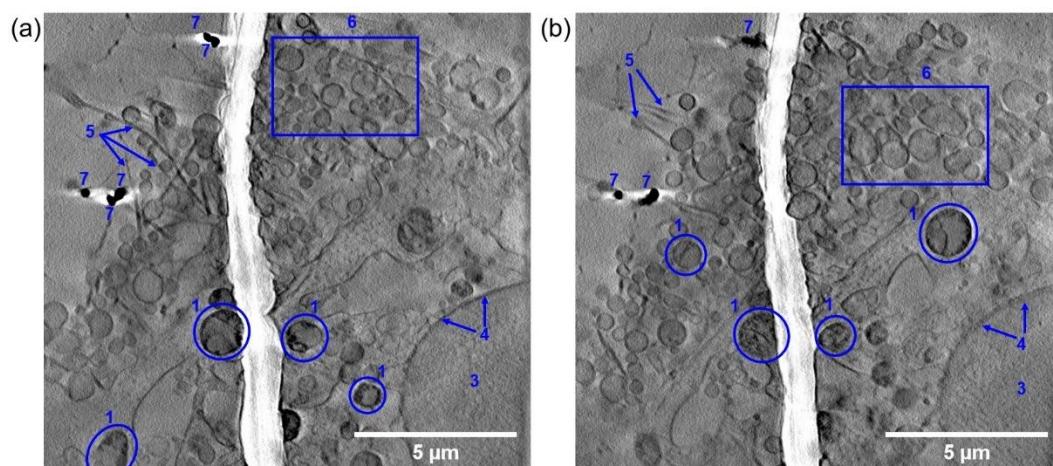


**Figure A13.** 2D projections of a reconstructed x-ray tomogram ( $15.8 \times 15.8 \mu\text{m}^2$ ) showing cellular and organelle morphology of a cryopreserved PC3 cell grown on carbon-gold TEM grid under dark conditions (protected from light) followed by 24 h in fresh medium (310 K, 5%  $\text{CO}_2$ ; **T5, C4\_Video\_T5, Chapter 4**). Images were generated in IMOD imaging software,<sup>8</sup> showing two different sample views (tilt angles): 0°; (b) +14°. Showing (1) mitochondria, (2) nucleolus, (3) nucleus, (4) nuclear membrane, (5) features of lamellipodium, (6) spherical vesicles, (7) gold nanoparticle fiducials ( $d=250 \text{ nm}$ ).

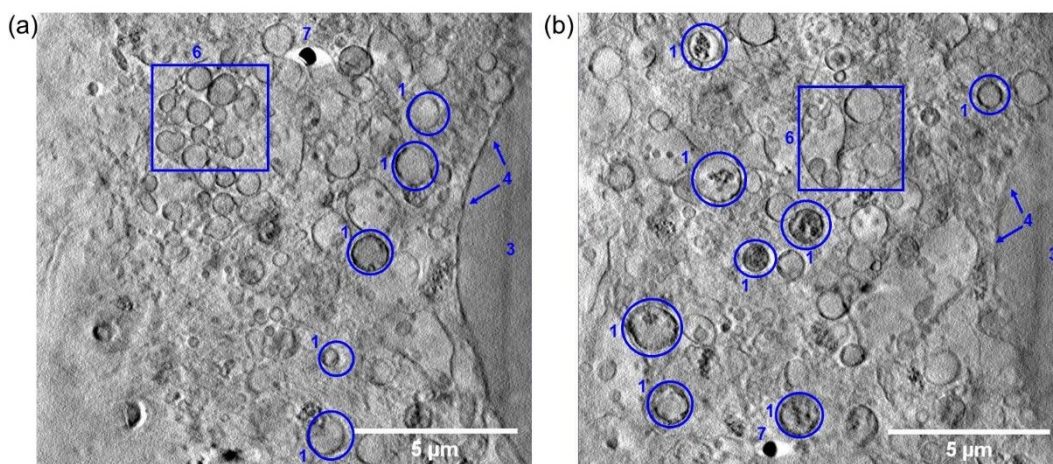


**Figure A14.** 2D projections of a reconstructed x-ray tomogram ( $15.8 \times 15.8 \mu\text{m}^2$ ) showing cellular and organelle morphology of a cryopreserved PC3 cell grown on carbon-gold TEM grid treated with **7** ( $1 \mu\text{M}$ ) for 2 h under dark conditions (protected from light), followed by 24 h recovery in complex-free media (310 K, 5%  $\text{CO}_2$ ; **T6, C4\_Video\_T6, Chapter 4**). Images were generated in IMOD imaging software,<sup>8</sup> showing two different sample views (tilt angles): 0°; (b) +15°. Showing (1) mitochondria, (2) nucleolus, (3) nucleus, (4) nuclear membrane, (5) features of lamellipodium, (6) spherical vesicles, (7) gold nanoparticle fiducials ( $d=250 \text{ nm}$ ).

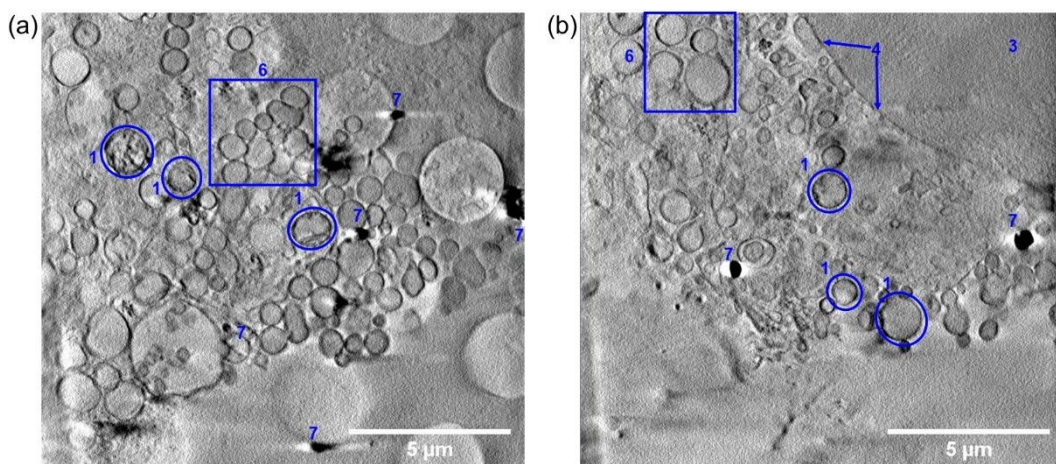


**Figure A15.** 2D projections of a reconstructed x-ray tomogram ( $15.8 \times 15.8 \mu\text{m}^2$ ) showing cellular and organelle morphology of a cryopreserved PC3 cell grown on carbon-gold TEM grid treated with **7** ( $1 \mu\text{M}$ ) for 2 h under dark conditions (protected from light), followed by recovery in complex-free media (310 K, 5%  $\text{CO}_2$ ; **T7**, **C4\_Video\_T7**, **Chapter 4**). Images were generated in IMOD imaging software,<sup>8</sup> showing two different sample views (tilt angles):  $0^\circ$ ; (b)  $+24^\circ$ . Showing (1) mitochondria, (2) nucleolus, (3) nucleus, (4) nuclear membrane, (5) features of lamellipodium, (6) spherical vesicles, (7) gold nanoparticle fiducials ( $d=250 \text{ nm}$ ).

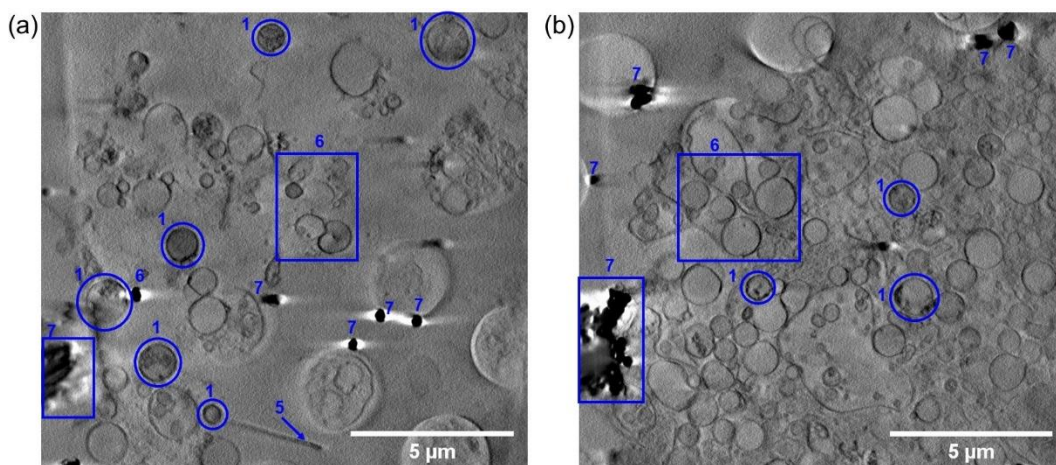


**Figure A16.** 2D projections of a reconstructed x-ray tomogram ( $15.8 \times 15.8 \mu\text{m}^2$ ) showing cellular and organelle morphology of a cryopreserved PC3 cell grown on carbon-gold TEM grid treated with **7** ( $1 \mu\text{M}$ ) for 2 h under dark conditions (protected from light), followed by recovery in complex-free media (310 K, 5%  $\text{CO}_2$ ; **T8**, **C4\_Video\_T8**, **Chapter 4**). Images were generated in IMOD imaging software,<sup>8</sup> showing two different sample views (tilt angles):  $0^\circ$ ; (b)  $+39^\circ$ . Showing (1) mitochondria, (2) nucleolus, (3) nucleus, (4) nuclear membrane, (5) features of lamellipodium, (6) spherical vesicles, (7) gold nanoparticle fiducials ( $d=250 \text{ nm}$ ).



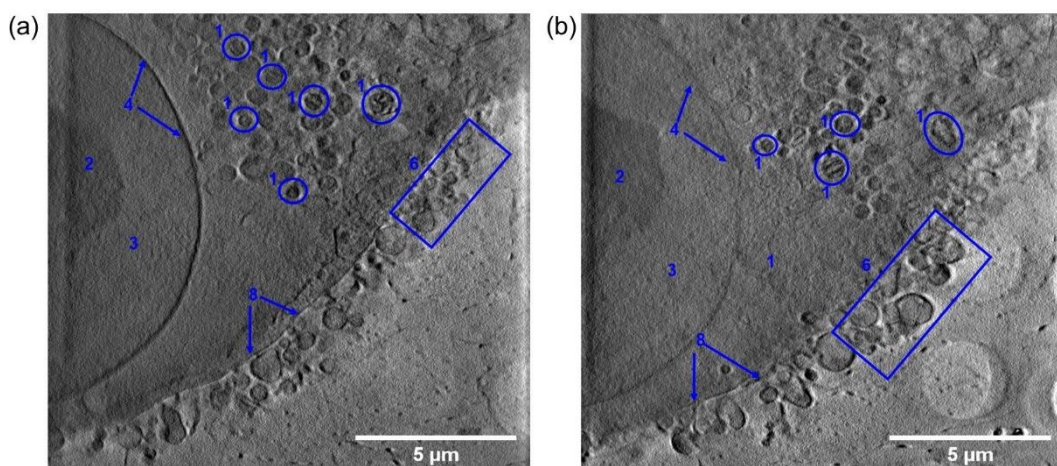


**Figure A17.** 2D projections of a reconstructed x-ray tomogram ( $15.8 \times 15.8 \mu\text{m}^2$ ) showing cellular and organelle morphology of a cryopreserved PC3 cell grown on carbon-gold TEM grid and treated with **7** ( $1 \mu\text{M}$ ) for 2 h (protected from the light), 10 min irradiation ( $465 \text{ nm}$ ,  $4.8 \text{ mW/cm}^2$ ) followed by 24 h recovery in complex-free media ( $310 \text{ K}$ ,  $5\% \text{ CO}_2$ ; **T9**, **C4\_Video\_T9**, **Chapter 4**). Images were generated in IMOD imaging software,<sup>8</sup> showing two different sample views (tilt angles):  $0^\circ$ ; (b)  $+10^\circ$ . Showing (1) mitochondria, (2) nucleolus, (3) nucleus, (4) nuclear membrane, (5) features of lamellipodium, (6) spherical vesicles, (7) gold nanoparticle fiducials ( $d=250 \text{ nm}$ ), (8) plasma membrane.

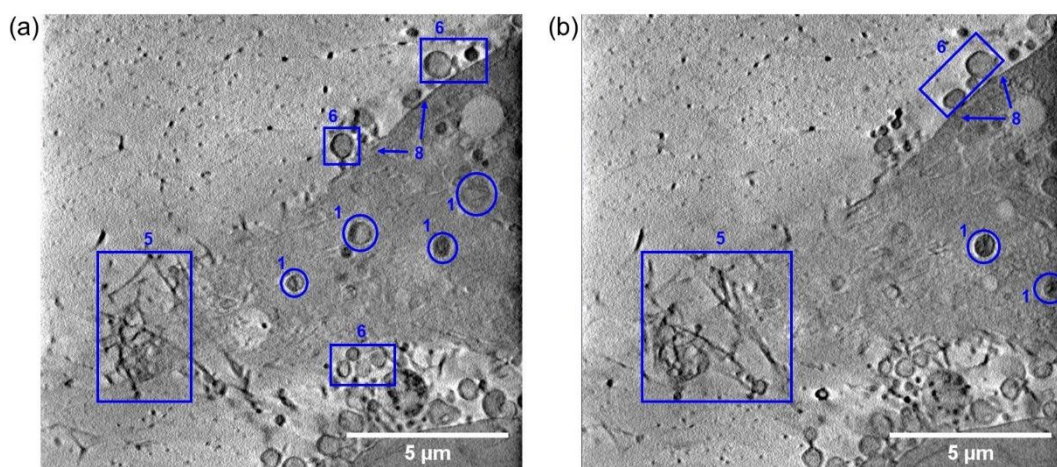


**Figure A18.** 2D projections of a reconstructed x-ray tomogram ( $15.8 \times 15.8 \mu\text{m}^2$ ) showing cellular and organelle morphology of a cryopreserved PC3 cell grown on carbon-gold TEM grid and treated with **7** ( $1 \mu\text{M}$ ) for 2 h (protected from the light), 10 min irradiation ( $465 \text{ nm}$ ) followed by 24 h recovery in complex-free media ( $310 \text{ K}$ ,  $5\% \text{ CO}_2$ ; **T10**, **C4\_Video\_T10**, **Chapter 4**). Images were generated in IMOD imaging software,<sup>8</sup> showing two different sample views (tilt angles):  $0^\circ$ ; (b)  $+6.5^\circ$ . Showing (1) mitochondria, (2) nucleolus, (3) nucleus, (4) nuclear membrane, (5) features of lamellipodium, (6) spherical vesicles, (7) gold nanoparticle fiducials ( $d=250 \text{ nm}$ ), (8) plasma membrane.



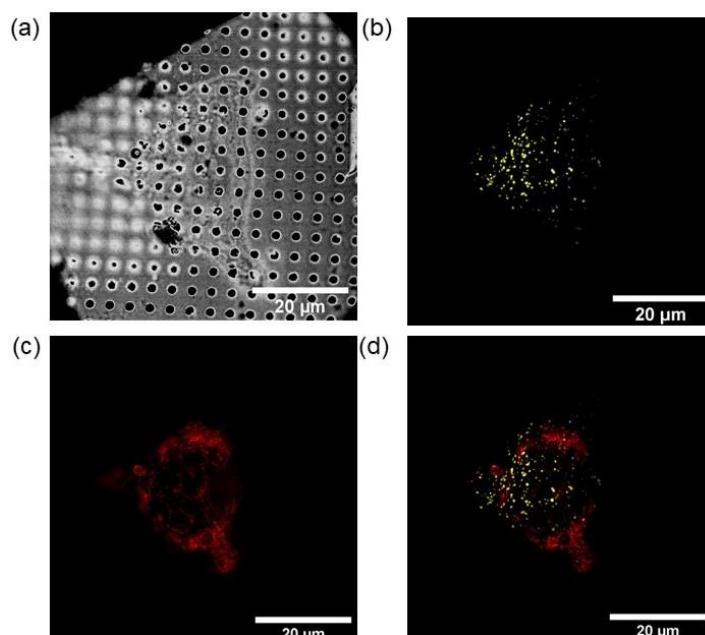


**Figure A19.** A cryopreserved PC3 cell grown on carbon-gold TEM grids and exposure to dark conditions (2 h, protected from light) and incubated with MitoTracker DeepRed ( $\lambda=644/665$  nm) and LysoTracker Red ( $\lambda=577/590$ nm) from **Chapter 5**. (a) Brightfield image. (b-d) Super-resolution fluorescence images obtained at the cryoSIM facility (B24, DLS): (b) LysoTracker Red (lysosomes), (c) MitoTracker Red (mitochondria) and (d) overlay of LysoTracker Red and MitoTracker Deep Red. Images were generated in Fiji.<sup>9</sup> Blue fluorescence was not observed.

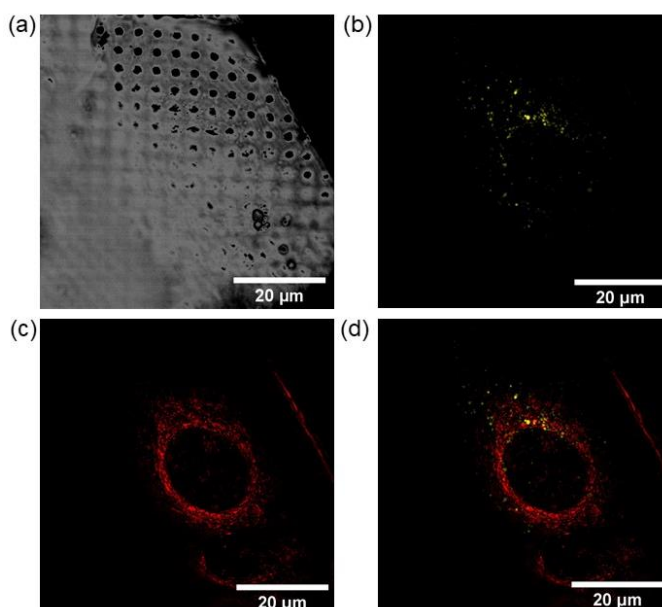


**Figure A20.** A cryopreserved PC3 cell grown on carbon-gold TEM grids and to dark conditions (2 h, protected from light) and incubated with MitoTracker DeepRed ( $\lambda=644/665$  nm) and LysoTracker Red ( $\lambda=577/590$ nm) from **Chapter 5**. (a) Brightfield image. (b-d) Super-resolution fluorescence images obtained at the cryoSIM facility (B24, DLS): (b) LysoTracker Red (lysosomes), (c) MitoTracker Red (mitochondria) and (d) overlay of LysoTracker Red and MitoTracker Deep Red. Images were generated in Fiji.<sup>9</sup> Blue fluorescence was not observed.

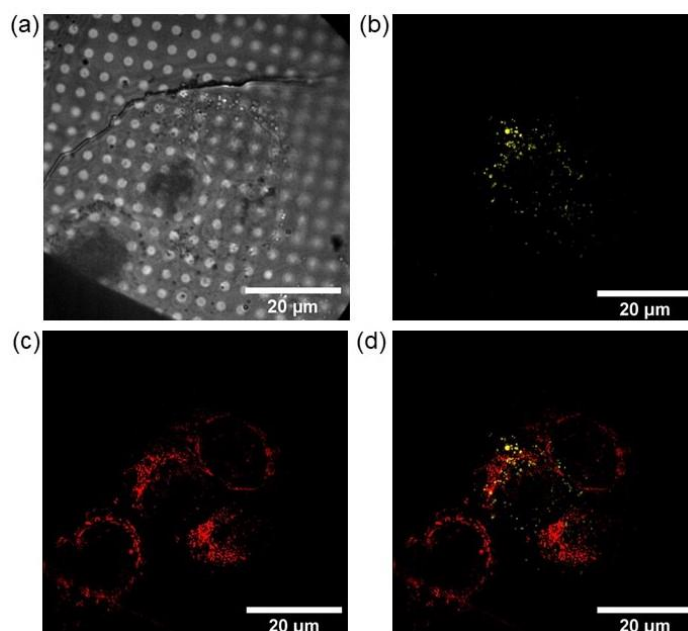


**Figure A21.** A cryopreserved PC3 cell grown on carbon-gold TEM grids and to dark conditions (1 h irradiation, 465 nm) and incubated with MitoTracker DeepRed ( $\lambda=644/665$  nm) and LysoTracker Red ( $\lambda=577/590$ nm) from **Chapter 5**. (a) Brightfield image. (b-d) Super-resolution fluorescence images obtained at the cryoSIM facility (B24, DLS): (b) LysoTracker Red (lysosomes), (c) MitoTracker Red (mitochondria) and (d) overlay of LysoTracker Red and MitoTracker Deep Red. Images were generated in Fiji.<sup>9</sup> Blue fluorescence was not observed.

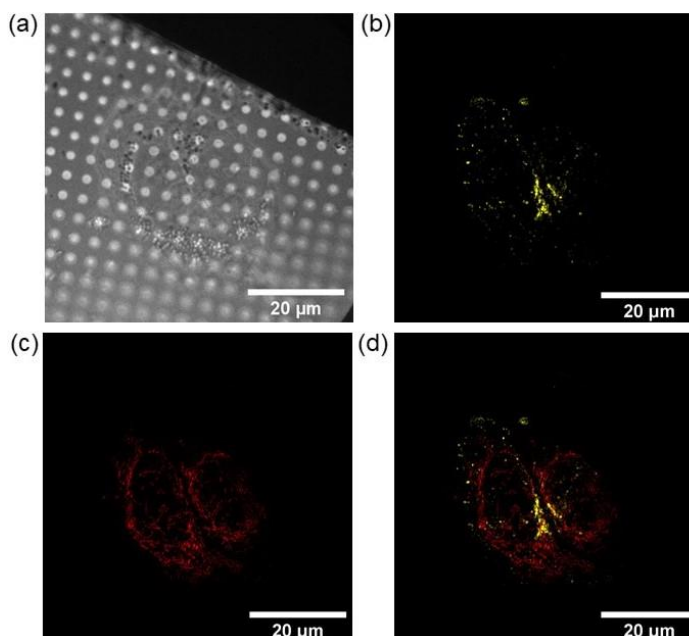


**Figure A22.** A cryopreserved PC3 cell grown on carbon-gold TEM grids and to dark conditions (1 h irradiation, 465 nm) and incubated with MitoTracker DeepRed ( $\lambda=644/665$  nm) and LysoTracker Red ( $\lambda=577/590$ nm) from **Chapter 5**. (a) Brightfield image. (b-d) Super-resolution fluorescence images obtained at the cryoSIM facility (B24, DLS): (b) LysoTracker Red (lysosomes), (c) MitoTracker Red (mitochondria) and (d) overlay of LysoTracker Red and MitoTracker Deep Red. Images were generated in Fiji.<sup>9</sup> Blue fluorescence was not observed.

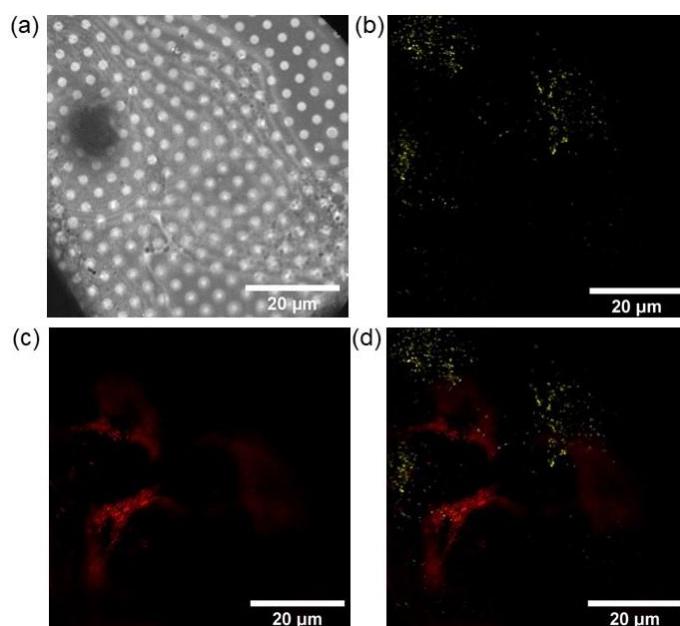


**Figure A23.** Two cryopreserved PC3 cells grown on a carbon-gold TEM grids and exposed  $1 \times \text{IC}_{50}$  of **12** for 2 h under dark conditions (2 h, protected from light) and incubated with MitoTracker DeepRed ( $\lambda=644/665$  nm) and LysoTracker Red ( $\lambda=577/590\text{nm}$ ) from **Chapter 5**. (a) Brightfield image. (b-d) Super-resolution fluorescence images obtained at the cryoSIM facility (B24, DLS): (b) LysoTracker Red (lysosomes), (c) MitoTracker Red (mitochondria) and (d) overlay of LysoTracker Red and MitoTracker Deep Red. Images were generated in Fiji.<sup>9</sup> Blue fluorescence was not observed.

## References

1. Z. Yang and H.-R. Xiong, in *Biomedical Tissue Culture*, ed. L. Ceccherini-Nelli, Matteoli, B., 2012, vol. 1, ch. 2, p. 1.
2. J. P. C. Coverdale, *PhD Thesis*, 2017.
3. J. P. C. Coverdale, I. Romero-Canelón, C. Sanchez-Cano, G. J. Clarkson, A. Habtemariam, M. Wills and P. J. Sadler, *Nat Chem*, 2018, **10**, 347-354.
4. C. T. Rueden, J. Schindelin, M. C. Hiner, B. E. DeZonia, A. E. Walter, E. T. Arena and K. W. Eliceiri, *BMC Bioinformatics*, 2017, **18**, 529-529.
5. I. Luengo, M. C. Darrow, M. C. Spink, Y. Sun, W. Dai, C. Y. He, W. Chiu, T. Pridmore, A. W. Ashton, E. M. H. Duke, M. Basham and A. P. French, *J Struct Biol*, 2017, **198**, 43-53.
6. V. A. Solé, E. Papillon, M. Cotte, P. Walter and J. Susini, *Spectrochim Acta B*, 2007, **62**, 63-68.
7. C. T. Rueden, J. Schindelin, M. C. Hiner, B. E. DeZonia, A. E. Walter, E. T. Arena and K. W. Eliceiri, *BMC Bioinform*, 2017, **18**, 529-529.
8. D. N. Mastronarde and S. R. Held, *J Struct Biol*, 2017, **197**, 102-113.
9. J. Schindelin, I. Arganda-Carreras, E. Frise, V. Kaynig, M. Longair, T. Pietzsch, S. Preibisch, C. Rueden, S. Saalfeld, B. Schmid, J. Y. Tinevez, D. J. White, V. Hartenstein, K. Eliceiri, P. Tomancak and A. Cardona, *Nat Met*, 2012, **9**, 676-682.